

INFORMATION TO USERS

This manuscript has been reproduced from the microfilm master. UMI films the text directly from the original or copy submitted. Thus, some thesis and dissertation copies are in typewriter face, while others may be from any type of computer printer.

The quality of this reproduction is dependent upon the quality of the copy submitted. Broken or indistinct print, colored or poor quality illustrations and photographs, print bleedthrough, substandard margins, and improper alignment can adversely affect reproduction.

In the unlikely event that the author did not send UMI a complete manuscript and there are missing pages, these will be noted. Also, if unauthorized copyright material had to be removed, a note will indicate the deletion.

Oversize materials (e.g., maps, drawings, charts) are reproduced by sectioning the original, beginning at the upper left-hand corner and continuing from left to right in equal sections with small overlaps. Each original is also photographed in one exposure and is included in reduced form at the back of the book.

Photographs included in the original manuscript have been reproduced xerographically in this copy. Higher quality 6" x 9" black and white photographic prints are available for any photographs or illustrations appearing in this copy for an additional charge. Contact UMI directly to order.

UMI

A Bell & Howell Information Company
300 North Zeeb Road, Ann Arbor MI 48106-1346 USA
313/761-4700 800/521-0600

NOTE TO USERS

The original manuscript received by UMI contains pages with indistinct and/or slanted print. Pages were microfilmed as received.

This reproduction is the best copy available

UMI

Architecture of Submarine Channel Levees

by

Kenneth Ian Skene

Submitted in partial fulfillment of the requirements
for the degree of Doctor of Philosophy

at

Department of Oceanography
Dalhousie University
Halifax, Nova Scotia
August, 1998

© Copyright by Kenneth I. Skene, 1998



National Library
of Canada

Acquisitions and
Bibliographic Services

395 Wellington Street
Ottawa ON K1A 0N4
Canada

Bibliothèque nationale
du Canada

Acquisitions et
services bibliographiques

395, rue Wellington
Ottawa ON K1A 0N4
Canada

Your file Votre référence

Our file Notre référence

The author has granted a non-exclusive licence allowing the National Library of Canada to reproduce, loan, distribute or sell copies of this thesis in microform, paper or electronic formats.

The author retains ownership of the copyright in this thesis. Neither the thesis nor substantial extracts from it may be printed or otherwise reproduced without the author's permission.

L'auteur a accordé une licence non exclusive permettant à la Bibliothèque nationale du Canada de reproduire, prêter, distribuer ou vendre des copies de cette thèse sous la forme de microfiche/film, de reproduction sur papier ou sur format électronique.

L'auteur conserve la propriété du droit d'auteur qui protège cette thèse. Ni la thèse ni des extraits substantiels de celle-ci ne doivent être imprimés ou autrement reproduits sans son autorisation.

0-612-36591-3

Canada

DALHOUSIE UNIVERSITY

FACULTY OF GRADUATE STUDIES

The undersigned hereby certify that they have read and recommend to the Faculty of Graduate Studies for acceptance a thesis entitled "Architecture of Submarine Channel Levees"

by Kenneth Skene

in partial fulfillment of the requirements for the degree of Doctor of Philosophy.

Dated: August 21, 1998

External Examiner _____
Research Supervisor _____
Research Supervisor _____
Examining Committee _____



DALHOUSIE UNIVERSITY

DATE: 21 August 1998

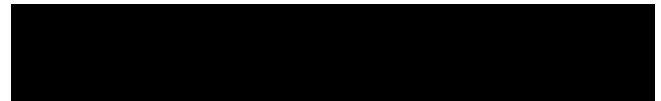
AUTHOR: Kenneth I. Skene

TITLE: Architecture of Submarine Channel Levees

DEPARTMENT OR SCHOOL: Oceanography

DEGREE: Ph.D. CONVOCATION: Fall YEAR: 1998

Permission is herewith granted to Dalhousie University to circulate and to have copied for non-commercial purposes, at its discretion, the above title upon the request of the individuals or institutions.



Signature of Author

THE AUTHOR RESERVES OTHER PUBLICATION RIGHTS, AND NEITHER THE THESIS NOR EXTENSIVE EXTRACTS FROM IT MAY BE PRINTED OR OTHERWISE REPRODUCED WITHOUT THE AUTHORS WRITTEN PERMISSION.

THE AUTHOR ATTESTS THAT PERMISSION HAS BEEN OBTAINED FOR THE USE OF ANY COPYRIGHTED MATERIAL APPEARING IN THIS THESIS (OTHER THAN BRIEF EXCERPTS REQUIRING ONLY PROPER ACKNOWLEDGEMENT IN SCHOLARLY WRITING), AND THAT SUCH USE IS CLEARLY ACKNOWLEDGED.

*“There comes a moment in the day when you have written your pages in the morning,
attended to your correspondence in the afternoon, and have nothing further to do.
Then comes that hour when you are bored;
that’s the time for”*

H.G. Wells, quoted by Charlie Chaplin in *My Autobiography*

TABLE OF CONTENTS

Table of Contents.....	v
List of Tables	viii
List of Figures.....	x
Abstract.....	xvii
List of Abbreviations and Symbols Used	xviii
Acknowledgments.....	xxi
Chapter 1 — Introduction.....	1
1.1 General Statement.....	1
1.2 Goal and Objectives.....	2
1.3 Organization of Thesis.....	3
1.4 Introduction to Levee Architecture and Turbidity Current Theory	4
1.4.1 Architectural Elements.....	4
1.4.2 Channel-Levee Classification	6
1.4.3 General Flow Processes	8
1.4.4 Architecture-Flow Parameter Relationships	11
Chapter 2 — Methods	24
2.1 General Statement.....	24
2.2 Seismic Stratigraphy.....	24
2.2.1 Basic Theory	24
2.2.2 Correlation	27
2.2.3 Depositional Sequences	28
2.3 Architectural measurements.....	30
2.3.1 Positioning	30
2.3.2 Channel Morphology	32
2.3.3 Depositional Sequence Thickness.....	32
2.3.4 Sediment Wave Morphology	33
2.4 Statistical Analysis.....	35
2.5 Characterizing the Large-scale Structure of Channel-Levee Systems.....	42
Chapter 3 — Levee Architecture of NAMOC.....	46
3.1 General Statement.....	46
3.2 Data Set.....	46
3.3 Setting of NAMOC.....	49
3.3.1 Channel Morphology	49
3.3.2 Previous Work on Geology of NAMOC	51
3.3.3 Nature of Turbidity Currents	54
3.4 Levee Architecture of NAMOC.....	57
3.4.1 Levee Stratigraphy	57
3.4.2 Stratigraphic Evolution	75
3.4.3 Architectural Data from NAMOC	83
3.5 Synthesis of Levee Architecture	97
3.5.1 Downchannel Variability.....	97

3.5.2 Stratigraphic Variability.....	98
3.6 Key Features	105
Chapter 4 — Levee Architecture of Hueneme Fan	107
4.1 General Statement.....	107
4.2 Data Set.....	107
4.3 Setting of Hueneme Fan.....	110
4.3.1 Channel Morphology	110
4.3.2 Previous Work on Geology of Hueneme Fan	110
4.3.3 Nature of Turbidity Currents	113
4.4 Levee Architecture of Hueneme Fan	118
4.4.1 Levee Stratigraphy	118
4.4.2 Stratigraphic Evolution	130
4.4.3 Architectural Data from Hueneme Fan.....	134
4.5 Synthesis of Levee Architecture	151
4.5.1 Downchannel Variability.....	151
4.5.2 Stratigraphic Variability.....	155
4.6 Key Features	158
Chapter 5 — Levee Architecture of Other Systems	161
5.1 General Statement.....	161
5.2 Reserve Fan.....	161
5.2.1 Levee Architecture.....	164
5.2.2 Synthesis of Levee Architecture on Reserve Fan	165
5.2.3 Key Features	168
5.3 Amazon Fan.....	169
5.3.1 General Setting.....	169
5.3.2 Levee Architecture.....	177
5.3.3 Synthesis of Levee Architecture on Amazon Fan.....	202
5.3.4 Key Features	208
5.4 Var Fan.....	209
5.4.1 General Setting.....	209
5.4.2 Levee Architecture.....	215
5.4.3 Synthesis of Levee Architecture on Var Fan	226
5.4.4 Key Features	232
5.5 General Summary	233
Chapter 6 — Levee Architecture of Laurentian Fan	234
6.1 General Statement.....	234
6.2 Data Set.....	234
6.3 Setting of Laurentian Fan.....	238
6.3.1 Channel Morphology	238
6.3.2 Previous Work on Geology of Laurentian Fan	240
6.3.3 Nature of Turbidity Currents	243
6.4 Levee Architecture of Laurentian Fan	245
6.4.1 Levee Stratigraphy	245

6.4.2 Stratigraphic Evolution	269
6.4.3 Levee Architecture	273
6.5 Synthesis of Levee Architecture	283
6.5.1 Downstream Variability	283
6.5.2 Stratigraphic Variability	283
6.6 Key Features	285
Chapter 7 — Synthesis of Levee Architecture	286
7.1 General Statement	286
7.2 Observations of Levee Architecture	286
7.2.1 Thickness Patterns	286
7.2.2 Levee Asymmetry	296
7.2.3 Levee Crest Evolution	300
7.2.4 Sediment Waves	306
7.3 Physical Interpretation of Depositional Lengthscales in Levee Architecture	309
7.3.1 General Interpretation of Across-Levee Lengthscale	310
7.3.2 Constant Thickness Model	313
7.4 Discussion	321
7.4.1 Application of the Empirical Relationships	323
7.4.2 Differences Between Channel-Levee Systems	327
7.4.3 Physical Process of Overbanking	328
7.4.4 Implications for Downchannel Structure of Channel-Levee Systems	330
7.5 Closing Statement	336
Chapter 8 — Conclusions, Contributions, and Directions for Future Research	338
8.1 General Statement	338
8.2 Characterization of Channel-Levee Architecture	338
8.3 Empirical Relationships	340
8.3.1 Inter-system Variability	340
8.3.2 Downchannel Variability	331
8.3.3 Stratigraphic Variability	342
8.4 Physical Interpretation of Thickness Patterns	343
8.5 Generic Model for Channel-Levee Architecture	345
8.6 Suggestions for Future Research	346
Appendix A: Derivation of Constant Thickness Model	347
References	353

LIST OF TABLES

Table 3.1. Summary of characteristic sequence thicknesses on NAMOC.....	53
Table 3.2. Regression data for cross-section 1 of NAMOC.	84
Table 3.3. Regression data for cross-section 2 of NAMOC.	87
Table 3.4. Regression data for western levee of NAMOC at cross-section 3.....	89
Table 3.5. Regression data for interchannel high on NAMOC.....	89
Table 3.6. Regression data for western levee of NAMOC at cross-section 4.....	91
Table 3.7. Regression data for eastern levee of NAMOC at cross-section 4.....	92
Table 3.8. Regression data for western levee of NAMOC at cross-section 5.....	92
Table 3.9. Regression data for eastern levee of NAMOC at cross-section 5.....	94
Table 3.10. Summary of levee crest elevation differences and distances between conjugate levee crests.....	95
Table 4.1. Data on volume and initiation mechanism for six turbidites in Santa Monica Basin deposited over the last five centuries (data and interpreted mechanism from Malouta et al. (1981), Reynolds (1987), Gorsline (1996).....	115
Table 4.2. Estimates of hemipelagic sediments for each depositional sequence.	140
Table 4.3. Regression data for cross-section 1: western levee.....	142
Table 4.4. Regression data for cross-section 1: eastern levee.....	142
Table 4.5. Regression data for cross-section 2: western levee.....	144
Table 4.6. Regression data for cross-section 2: eastern levee.....	144
Table 4.7. Regression data for cross-section 3: western levee.....	146
Table 4.8. Regression data for cross-section 3: eastern levee.....	146
Table 4.9. Reconstruction of Hueneme Fan levee crest asymmetry taking account of the paleobathymetry on J (Figure 4.15).	147
Table 4.10. Across-levee elevation difference calculated from data in Table 4.9 and across-levee slope calculated using channel width equal to 4 km	148
Table 5.1. Mean grain size characterizing general location on Reserve Fan (data from Normark & Dickson, 1976b).	164
Table 5.2. Values of channel dimensions and flow parameters taken from Normark (1989) at 2 km downchannel at the site of the 1975 current meter location (Figure 5.1).	164
Table 5.3. Summary of regression parameters for western levee of Reserve Fan.	165
Table 5.4. Summary of regression parameters at Site 939 for depositional sequences identified in 3.5 kHz data.	187

Table 5.5. Summary of regression parameters at Site 940 for depositional sequences identified in 3.5 kHz data	195
Table 5.6. Summary of regression parameters at Site 940 for depositional sequences identified in watergun data.....	197
Table 5.7. Summary of regression parameters at Site 944 for depositional sequences identified in 3.5 kHz data	202
Table 5.8. Summary of regression parameters for line D8 on Var Fan.	223
Table 5.9. Summary of regression parameters for DS1 on Var Fan.....	224
Table 5.10. Regression parameters for DS1 on Var Fan calculating different regression equations for the proximal levee and levee flank.....	224
Table 6.1. Summary of regression parameters calculated for thickness patterns in 3.5 kHz data	274
Table 6.2. Summary of regression data for thickness variations between horizon G and the surface.	276
Table 6.3. Summary of regression data for thickness variations between horizon O and the surface.	276
Table 7.1. Summary of regression results from exponential fit to downchannel variations in sediment thickness at levee crest.	287
Table 7.2. Dominant control, origin, and patterns in cross-channel slope.....	296
Table 7.3. Summary of sediment wave characteristics and associated channel and levee morphology.....	308
Table 7.4. Values of Γ_1 and Γ_2 and the corresponding value of E/C_D used to produce model results in Figure 7.14.....	318
Table 8.1. Summary of figures showing across-levee variations in depositional sequence thickness.....	339

LIST OF FIGURES

Figure 1.1. Schematic diagram of simplified canyon-channel-levee-lobe system.....	5
Figure 1.2. Cross sectional channel-levee classification of Nelson & Kulm (1973) showing: A. erosional; B. erosional/depositional; and C. depositional systems.	7
Figure 1.3. Planform channel-levee classification (modified after Clarke, 1992) based on relationship between channel slope and sinuosity.	9
Figure 1.4. Simplification of Normark & Piper's (1991) facies model showing the depositional features on levees of various turbidity current flow types.	12
Figure 1.5. Definition sketch for cross-flow slope equation.....	20
Figure 2.1. Examples of seismic data.	26
Figure 2.2. Generic cross-section of channel-levee system showing locations of levee flank, levee crest, levee edge, and channel edge.....	31
Figure 2.3. Profile of sediment waves defining architectural measurements including, wavelength, amplitude, SRR, and migration.	34
Figure 2.4. Comparison of F-score between linear model and exponential model for systems used in this study.	37
Figure 2.5. Sample plots of thickness data.	40
Figure 2.6. Sample plots of trend data, showing the downchannel variation in k for depositional sequences.....	43
Figure 2.7. Schematic representation of a submarine fan system showing the approximate downchannel extent of data investigated in this study.....	45
Figure 3.1. Bathymetric map of the Labrador Sea showing trend of NAMOC and the location of the study area.	47
Figure 3.2. Generalized channel patterns draining the slope off Hudson Strait and Labrador Slope (after Klaucke, 1995) and distribution of acoustic data and cores available for this study.	48
Figure 3.3. Profiles of channel morphology for NAMOC (from Klaucke, 1995).	50
Figure 3.4. Airgun type section from western levee of NAMOC showing definition of reflectors and depositional sequences.	52
Figure 3.5. 3.5 kHz type section from western levee of NAMOC showing definition of reflectors and depositional sequences.	58
Figure 3.6. Interpreted line drawings of 3.5 kHz data from NAMOC.....	60
Figure 3.7. Sediment waves on NAMOC.	64
Figure 3.9. Character of interchannel high at cross-section 2.....	66
Figure 3.10. 3.5 kHz profile at cross-section 4.	67
Figure 3.11. 3.5 kHz profile at cross-section 5.	69

Figure 3.12. 3.5 kHz profile showing surface debris flow west of NAMOC near cross-sections 4 and 5.....	70
Figure 3.13. Summary core descriptions of 87025-012 (core 012) and 92045-005 (core 005).	71
Figure 3.14. 3.5 kHz profile over core site for 92045-005.	73
Figure 3.15. Frequency of laminae per metre of section in core 012 plotted beside summary core description.	74
Figure 3.16. Airgun seismic profile across NAMOC at cross-section 4.....	76
Figure 3.17. Sleevegun seismic profile across NAMOC at cross-section 5.	77
Figure 3.18. Buried channel-levee system, possibly ancestral NAMOC or tributary channel draining Labrador Slope.	78
Figure 3.19. Cross-plot of levee crest water depth.	80
Figure 3.20. Thickness data from cross-section 1.....	85
Figure 3.21. Thickness data from cross-section 2.....	86
Figure 3.22. Thickness data from cross-section 3.....	88
Figure 3.23. Thickness data from cross-section 4.....	90
Figure 3.24. Thickness data from cross-section 5.....	93
Figure 3.25. Asymmetry in regression parameters.	96
Figure 3.26. Downchannel variation in k.....	99
Figure 3.27. Downchannel variation in thickness of depositional sequences.....	100
Figure 3.28. Downchannel variation in across-channel asymmetry.	101
Figure 3.29. Stratigraphic variation in the spatial decay constant, k, at each of the five sections across NAMOC.....	102
Figure 3.30. Inter-relationship between decay constant ratio and cross-channel slope. ...	104
Figure 4.1. Location of Hueneme Fan within Santa Monica Basin.....	108
Figure 4.2. General bathymetry of Santa Monica Basin showing location of Hueneme Fan and distribution of acoustic data from CSS Parizeau cruise 91062.	109
Figure 4.3. Detailed bathymetric map of Hueneme Fan (after Normark et al., 1998).	111
Figure 4.4. Morphology of Hueneme Channel showing profiles of axial water depth, slope, and sinuosity as a function of distance down-channel.	112
Figure 4.5. Acoustic character of sediments as imaged by Hunttec DTS records.	119
Figure 4.6. Hunttec DTS type section from western levee of Hueneme Channel.	120
Figure 4.7. NSRF type section from western levee of Hueneme Channel.	123

Figure 4.8. NSRF profile of upper Hueneme Channel showing stratigraphic and geographic relationship between modern channel and buried channel-levee system to the east of the modern channel.....	124
Figure 4.9. Interpreted line drawings of seismic sections perpendicular and parallel to Hueneme Channel.	125
Figure 4.10. Hunttec DTS profile from inner, western levee of Hueneme Channel.....	126
Figure 4.11. Hunttec DTS profile showing sediment waves on levee flank.	128
Figure 4.12. NSRF profile across distal end of Hueneme Channel.	129
Figure 4.13. Continuation of NSRF profile shown in Figure 4.8 showing the feature interpreted as a buried levee and the high reflectivity package immediately adjacent to the levee interpreted to be channel fill.	131
Figure 4.14. Hunttec DTS profile on western, outer levee of Hueneme Channel.	132
Figure 4.15. Paleobathymetry map of horizon J.	133
Figure 4.16. Hunttec DTS profile over crest of western levee.....	135
Figure 4.17. Hunttec DTS profile from eastern side of Hueneme Channel showing evenly bedded depositional sequences all characterized by weak to moderate acoustic stratification.	136
Figure 4.18. Hunttec DTS profile from eastern side of Hueneme Channel.	137
Figure 4.19. Thickness data from cross-section 1.....	141
Figure 4.20. Thickness data from cross-section 2.....	143
Figure 4.21. Thickness data from cross-section 3.....	145
Figure 4.22. Asymmetry of regression parameters.	149
Figure 4.23. Hunttec DTS profile showing relationship between depositional sequences and northernmost topographic high observed in modern bathymetry (Figure 4.3) and paleobathymetry of horizon J (Figure 4.15).....	152
Figure 4.24. A. Downchannel plot of the elevation difference between conjugate levee crests. B. Downchannel plot of cross-channel slope.....	153
Figure 4.25. Down-channel variation in regression parameters.	154
Figure 4.26. Thickness of sediment at the western levee crest above horizon J plotted against distance downchannel.	156
Figure 4.27. Stratigraphic evolution of decay constants for DS1 and DS2 calculated for the western levee at cross-sections 1 and 2.....	157
Figure 5.1. Bathymetry of Reserve Fan showing location of current meter stations and acoustic profiles.	162
Figure 5.2. Data from profiles 1-3 on Reserve Fan	166
Figure 5.3. Downchannel variation in spatial decay constant and thickness of sediment at the levee crest on western levee of Reserve Fan.....	167

Figure 5.4. Location map for Amazon Fan.....	170
Figure 5.5. Schematic cross-section showing middle fan architecture (modified after Flood, Piper, Klaus et al., 1995).	171
Figure 5.6. Morphology of Amazon Channel.....	173
Figure 5.7. Total aggradation of Amazon system measured from base of ULC to modern levee crest of Amazon Channel (data from Pirmez, 1994).	175
Figure 5.8. Trend of Amazon Channel in the vicinity of Site 939 showing location of boreholes and 3.5 kHz profiles.	178
Figure 5.9. 3.5 kHz profile over Site 939.	179
Figure 5.10. 3.5 kHz profile across Site 939 collected in 1984 by RV Conrad.....	181
Figure 5.11. Borehole stratigraphy at Site 939.	182
Figure 5.12. Turbidite character at Site 939.....	185
Figure 5.13. Bed to bed correlation of silt packet identified at Site 939.	186
Figure 5.14. Thickness variations across the eastern levee of Amazon Channel at Site 939.....	188
Figure 5.15. Channel trend in the vicinity of Site 940 showing location of borehole and seismic profile.....	189
Figure 5.16. Line drawings of 3.5 kHz profiles across sites 940 and 944 showing location of boreholes relative to Amazon Channel.....	190
Figure 5.17. Watergun profile over Site 940 showing relationship of borehole stratigraphy to seismic units.....	191
Figure 5.18. Borehole stratigraphy of the upper 95 m at Site 940.....	193
Figure 5.19. Complete borehole stratigraphy of Site 940 showing major seismic units defined in watergun and 3.5 kHz data.....	194
Figure 5.20. Thickness data from sites 940 and 944 for depositional sequences defined in 3.5 kHz profiles.....	196
Figure 5.21. Thickness variations across eastern levee of Amazon Channel in vicinity of Site 940 for depositional sequences defined in watergun seismic profile.	198
Figure 5.22. Channel trend in the vicinity of Site 944 showing location of boreholes and 3.5 kHz profile.	199
Figure 5.23. Borehole stratigraphy of upper 80 m of section at Site 944.	200
Figure 5.24. Grain size data for sites 939, 940 and 944 taken from Piper & Deptuck (1997).	203
Figure 5.25. Grain size data for sites 939, 940 and 944 (from Hiscott et al., 1997).	204
Figure 5.26. Downchannel variation in cross-channel slope of Amazon Channel and Froude number calculated from Komar's (1969) model assuming that flow thickness equals channel depth.	206

Figure 5.27. Location of Var Fan showing major geomorphological zones referred to in text.....	210
Figure 5.28. Seismic lines available for study of Var Fan.....	211
Figure 5.29. Morphology of Var fan valley (from Piper & Savoye, 1993).	213
Figure 5.30. Airgun seismic profile, D8 showing acoustic stratigraphy developed for Var Fan.....	216
Figure 5.31. Line drawings of successive downchannel profiles, D7, D8, D9, D10, D12, D13.....	218
Figure 5.32. Seismic profile D10.....	220
Figure 5.33. Thickness variations across Var Sedimentary Ridge for depositional sequences identified in profile D8.	222
Figure 5.34. Thickness variations across Var Sedimentary Ridge for DS1 identified in profiles D7, D8, D9, D10, D12, and D13.	225
Figure 5.35. Sediment waves on Var Fan (modified after Savoye et al., 1993).	227
Figure 5.36. Downchannel variability in regression parameters.	228
Figure 5.37. Downchannel variability in regression parameters.	229
Figure 5.38. Schematic depiction of sediment wave evolution for seismic profile shown in Figure 5.35.....	231
Figure 6.1. General map of the continental margin off Nova Scotia showing the location of Laurentian Fan and the study area.	235
Figure 6.2. Data distribution for study of Laurentian Fan.	236
Figure 6.3. Detailed bathymetry of Laurentian Fan (after Hughes-Clarke, 1988).....	237
Figure 6.4. Longitudinal profiles of Eastern Valley with distances measured along the channel from the 400 m isobath.....	239
Figure 6.5. Longitudinal profiles of Western Valley with distance measured along the channel from the 400 m isobath.....	241
Figure 6.6. Sparker seismic profile across WLEV showing the four regional reflectors identified in this study.....	246
Figure 6.7. Multichannel seismic line, GAD008.	248
Figure 6.8. Comparison of sediment thickness at crest of fan valleys on Laurentian Fan showing the predominance of sediment accumulation west of Eastern Valley since horizon L and the shift of maximum sediment accumulation to west of Western Valley since horizon Q.....	251
Figure 6.9. Sleevegun seismic profile across WLEV south of type section shown in Figure 6.6.	252
Figure 6.10. Airgun seismic profile across ELEV.	254

Figure 6.11. Sleevegun seismic profile across ELEV showing erosional surface associated with debris flow.	255
Figure 6.12. Sleevegun seismic profile across ELEV showing debris flows above horizons B and Q.	256
Figure 6.13. Airgun seismic profile along ELEV showing toplap at horizon B.....	257
Figure 6.14. Sleevegun seismic profile along WLEV.	259
Figure 6.15. Sleevegun seismic profile along WLWV.	260
Figure 6.16. Sleevegun seismic profile of WLWV at cross-section 3.....	261
Figure 6.17. Sleevegun seismic profile of WLWV at cross-section 2.....	262
Figure 6.18. Sleevegun seismic profile of WLWV near cross-section 2 showing debris flows.....	264
Figure 6.19. 3.5 kHz profile of WLWV at cross-section 3.....	265
Figure 6.20. 3.5 kHz profile of WLWV at cross-section 2.....	266
Figure 6.21. Summary descriptions of selected piston cores.....	267
Figure 6.22. Frequency of laminae or beds per metre of sections for cores 069, 070, and 072.....	270
Figure 6.23. Summary of grain size analyses on Laurentian Fan (from Schell, 1996)....	271
Figure 6.24. Thickness variations for interval above R1 in 3.5 kHz data.....	275
Figure 6.25. Thickness variations for interval above horizon O at cross-sections 2-5.	277
Figure 6.26. Longitudinal profiles of Eastern Valley showing: A. cross-channel slope; and B. estimated velocity from cross-channel slope.....	279
Figure 6.27. Schematic depiction of sediment wave evolution on WLWV.	280
Figure 6.28. Stratigraphic variation in amount of thinning across hinge line.....	282
Figure 6.29. Downchannel variation in regression parameters.....	284
Figure 7.1. Downchannel variations in sediment thickness at levee crest for all systems in thesis.	288
Figure 7.2. Relationship between inverse decay constant and channel half-width.....	290
Figure 7.3. Relationship between inverse decay constant and channel relief.....	291
Figure 7.4. Relationship between decay constant and downchannel slope.	292
Figure 7.5. A. Generalized pattern of downchannel thickness variations. B. Downchannel e-folding length of thickness variations, λ^{-1} (m), plotted against channel half-width. C. E-folding length plotted against channel relief.	293
Figure 7.6. Relationship between channel width and channel depth for channel-levee systems in this study (filled squares), including data from the literature (open circles) taken from maps published in Bouma et al. (1985).	295

Figure 7.7. (Top) Downchannel trend in cross-channel thickness gradient ($m\ km^{-1}$) on Hueneme Fan. (Bottom) Definition sketch showing parameters used to calculate the cross-channel gradient in sediment thickness at the levee crest.	297
Figure 7.8. Schematic showing interpretation of downchannel patterns in levee asymmetry.....	299
Figure 7.9. Evolution of levee crests on Hueneme Fan and Var Fan.	302
Figure 7.10. Evolution of levee crests on Laurentian Fan.	303
Figure 7.11. Geometric model for evolution of levee crests.....	304
Figure 7.12. Schematic representation of the stratigraphic development of sediment waves, synthesizing observations from NAMOC, Hueneme Fan, Var Fan, and Laurentian Fan.	307
Figure 7.13. Definition sketch for constant thickness model.....	314
Figure 7.14. Flow behaviour in constant thickness model.....	319
Figure 7.15. Observed relationship between channel relief, D , and the product of k^{-1} and λ^{-1}	322
Figure 7.16. A. Schematic depiction of western levee and reconstruction of channel fill history at cross-section 1 of Hueneme Fan.	325
Figure 7.17. Application of empirical relationships to levee architecture from Zaire Fan; A. Interpreted line drawing of seismic profile; B. Thickness data plotted against distance from channel axis; C. Predictions of scaling relationships.	326
Figure 7.18. General downchannel patterns in A. levee width and B. sediment thickness at levee crest. C. Extent of data used to ground-truth patterns and schematic representation of average channel dimensions. D. Potential difference in flow processes responsible for bipartite division of channel. E. Expression of overspilling and spreading flow on Hueneme Fan.....	331
Figure 7.19. Experimental results from investigation of spreading turbidity currents by Luthi (1981).	333
Figure 7.20. Experimental results from the investigation of axisymmetric turbidity currents by Bonneau et al. (1995).....	334

ABSTRACT

Levee architecture of six submarine channel-levee systems was investigated using seismic reflection profiles, piston cores, and boreholes. The systems span a wide range of geological environments and comprise the Northwestern Atlantic Mid-Ocean Channel (NAMOC), and Hueneme, Reserve, Amazon, Var, and Laurentian fans. Quantitative measures of architecture were defined and used to investigate the spatial and stratigraphic evolution of levees. Depositional sequences on levees display regular variations in thickness both across-levee and downchannel. Perpendicular to channel trend, depositional sequences thin following an exponential trend that can be quantified by a spatial decay parameter, k . Along the upper reaches of a system, downchannel exponential thinning of levee sediment is quantified by a second spatial decay parameter, λ . Stratigraphically, the growth of sediment waves and the evolution of levee crests followed consistent patterns not previously recognized. No significant stratigraphic pattern was observed for k .

Characterization of thickness variations using k and λ allows the direct comparison of levee architecture and channel morphology. Using data from all the systems investigated, correlations were found between the inverse of k and both channel half-width, W , and channel relief, D , and between the inverse of λ and W and D . Based on the downchannel behaviour of k and sediment thickness at the levee crest, submarine channels divide into two discrete reaches: an upper reach where k is uniform and sediment thickness decays exponentially downchannel, and a lower reach where k tends to decrease and sediment thickness is uniform or decays abruptly in the downchannel direction.

The channel-levee systems studied here have a wide range of sediment sources and different mechanisms for flow initiation. Nevertheless, levee architecture correlates with channel morphology, suggesting that flow processes rather than external conditions control this architecture. A simple model of flow behaviour suggests reasons for the observed geometric relationships provided that channel geometry relates to through-channel volume discharge in a manner analogous to the relationships between channel geometry and volume discharge established for rivers.

LIST OF ABBREVIATIONS AND SYMBOLS USED

b		exponent in hydraulic geometry equation relating channel width to volume discharge
b_o	m	obstacle height related to formation of lee waves
B	m	sediment wave amplitude
c		volume concentration
C		layer-averaged volume concentration
C_D		drag coefficient for flow
C_P		drag coefficient for sinking particles
d	m	grain size
D	m	channel relief
E		entrainment coefficient
f		exponent in hydraulic geometry equation relating channel relief to volume discharge
f	s⁻¹	Coriolis parameter
F		Fisher's F-ratio
F_{exp}		Fisher's F-ratio for exponential model
F_{lin}		Fisher's F-ratio for linear model
Fi		Froude number
g	m s⁻²	acceleration due to gravity
g_o	m s⁻²	modified gravity, $g(\rho_s - \rho)/\rho$
h	m	overbank flow thickness
H	m	through-channel flow thickness
ΔH	m	elevation difference between conjugate levee crests
∇H	m km⁻¹	cross-channel slope
I	kg m⁻² s⁻¹	acoustic impedance
K	kg⁻¹ m⁻¹ s⁻²	bulk modulus

k	m^{-1}	spatial decay constant for thickness variations across levee
k⁻¹	m	inverse spatial decay constant or quantitative definition of levee width
k_{sw}	m^{-1}	wave number of sediment waves, $2\pi/L_{sw}$
L_e	m	e-folding length for downchannel variations in sediment thickness at levee crest
L_{sw}	m	wavelength of sediment waves
L_v	m	levee width
m		exponent in hydraulic geometry equation relating velocity to volume discharge
n		number of turbidites within a depositional sequence
N	s^{-1}	buoyancy frequency
p		probability
Q	$m^3 s^{-1}$	through-channel volume discharge
R		reflection coefficient
Re_p		particle Reynolds number
Ri_o		bulk Richardson number
SSR		sedimentation rate ratio in lee wave model for sediment waves
u	$m s^{-1}$	through-channel velocity
u_*	$m s^{-1}$	frictional velocity
v	$m s^{-1}$	across-levee velocity
v_o	$m s^{-1}$	velocity of sound
w	$m s^{-1}$	vertical velocity
w_s	$m s^{-1}$	settling velocity of particles
x	m	downchannel distance
Δx_c	m	change in lateral position of sediment wave crest
Δx_t	m	change in lateral position of sediment wave trough
y	m	across-levee distance

z	m	elevation
β		downchannel slope
η	m	depositional sequence thickness
η_{lc}	m	depositional sequence thickness at levee crest
η_0	m	y-intercept of regression equation for across levee variations in depositional sequence thickness
$\nabla\eta$	m km ⁻¹	cross-channel gradient in depositional sequence thickness at levee crest
Γ_1, Γ_2		parameters in constant thickness model
λ	m ⁻¹	downchannel decay constant for exponential decay of sediment thickness at levee crest
λ^{-1}	m	inverse of downchannel channel decay constant or levee length
μ	kg m ⁻¹ s ⁻¹	dynamic viscosity
ν	m ² s ⁻¹	kinematic viscosity
ρ	kg m ⁻³	ambient fluid density
ρ_B	kg m ⁻³	bulk density of sediment
ρ_s	kg m ⁻³	grain density
τ	s	flow duration

ACKNOWLEDGMENTS

Because this project looked at a wide variety of fans I am greatly indebted to those persons and organizations who graciously supplied me with data, including Reinhard Hesse at McGill University, Bruno Savoye at IFREMER, and Carlos Pirmez at Lamont-Doherty Earth Observatory.

I would like to acknowledge the support and hospitality of Geological Survey of Canada Atlantic and the guidance of my co-supervisors, Dr. David Piper at GSC Atlantic and Dr. Paul Hill at Dalhousie. I am also indebted to Drs. Chris Beaumont, Tony Bowen, and Martin Gibling at Dalhousie for their input during the course of the research and thoughtful reviews of this thesis.

Others that have helped me during my time at Dalhousie — over beers, at barbeques, Grey Cup and Thanksgiving dinner — are many and I would like to thank Trent and Nicole, Jason and Carol-Ann, Scott and Tracy, Darryl and Renee, Ken, and Jeff. Many of the great times I had in Halifax were because of you.

Most of all, I would like to acknowledge the love and support of my wife, Karen, and my parents, Ian and Mary-Pat, and my inlaws, Bill and Mary.

Funding for this work was provided by an NSERC Post-graduate Scholarship and an NSERC Operating Grant to David Piper.

Chapter 1

Introduction

1.1 General Statement

Submarine channel-levee systems are major pathways for the transfer of terrigenous sediment to the deep-sea. The levees are repositories of important geological information. They consist of both terrigenous and pelagic sediments, with their respective fauna and flora, accumulating at rates far exceeding those of contemporaneous deep-sea environments; thus, they can provide decadal resolution of continental and oceanic history approaching the resolution of ice cores. The juxtaposition in time and space of potential reservoir and source rocks makes these geological environments attractive for hydrocarbon exploration.

The levees of submarine channels have received little attention and consequently lack a comprehensive depositional model relating levee architecture to the depositional mechanisms responsible for levee growth. The literature typically describes submarine levees as wedges of fine-grained sediment adjacent to channels created by overbank deposition from turbidity currents flowing down the main channel of a submarine fan (e.g., Normark & Piper, 1991). Middleton & Southard (1984) defined turbidity currents as sediment gravity flows in which the gravitational driving force is supplied by a suspension of particles supported by fluid turbulence, making them a class of density currents (Simpson, 1987). However, unlike density currents, where the gravitational driving force arises from differences in state variables, like temperature or salinity, turbidity currents are driven primarily by the presence of suspended sediment. The turbidity currents responsible for levee deposition have been pictured as having episodic or continuous overspill that transfers sediment from the channel to the levees (Chough & Hesse, 1976; Piper & Normark, 1983; Normark & Piper, 1991; Clark et al., 1992; Clark & Pickering, 1996; Hiscott et al., 1997). Beyond these general descriptions, only a few other features of levees have received attention. The most notable of these features include: 1) the presence of sediment waves on the backsides of some levees (Normark et al., 1980); and 2) the asymmetry of levee height across a channel (Komar, 1969).

Levees require much additional research because they record most, if not all, through-channel turbidity current flows, the duration of channel activity, and paleo-climatological data for both the source area (i.e., the adjacent continent) and the overlying water column (Clark & Pickering, 1996). Because the propensity of an individual turbidity current to spill from the channel to the levees depends on channel depth and because levee aggradation partly controls channel depth, an intimate relationship between the character of the through-channel turbidity currents and the architecture of the levees has been suggested (e.g., Menard, 1964; Komar, 1973; Hiscott et al., 1997), but has never been thoroughly quantified. Levees contribute, in part, to the lateral boundaries of a channel, thus the architecture and stability of levees determine the possibility of avulsion (e.g., Flood et al., 1991) and the changing of sediment pathways in a submarine fan. Because channels transport and often fill with coarse-grained sediment the geometry of channel bodies controlled, in part, by levee stability will play a role in determining the reservoir characteristics — for example, thickness and continuity — of a channel sand (e.g., Clark & Pickering, 1996). The fine-grained sands that characterize some levees have also been the target of hydrocarbon exploration because, in spite of their fine-grained nature and therefore low primary porosity and permeability, the exceptional continuity of these sands has been proven to make these reservoirs a productive source of hydrocarbons (e.g., Gulf of Mexico, M. DeVries, pers. comm., 1997). The ultimate fate of sediment introduced as or subsequently evolving into turbidity currents also plays a role in the disposal of mining tailings into subaqueous settings (Ellis & Poling, 1995). In this case, levees act as repositories for some of the tailings and levee stability will partially control the dispersal of tailings into the environment.

1.2 Goal and Objectives

The investigation of levee architecture in this thesis has three main objectives:

1. to systematically and quantitatively characterize features in levee architecture from several geologically distinct systems;
2. to define controls on levee architecture with simple models of turbidity currents;
3. to investigate the potential for using levee architecture to infer environmentally relevant turbidity current flow parameters.

Meeting these objectives will lead to a depositional model for levees, the insights from which will be used to understand overall fan evolution. The main goal of the thesis is to discern what aspects of through-channel flow character are preserved in levee architecture.

1.3 Organization of Thesis

Chapter 2 presents some of the general methodology used in the thesis, including the basic principles of seismic stratigraphy, the measurements of levee architecture, and the statistical analysis. Chapters 3 and 4 investigate the levee growth patterns from the Northwestern Atlantic Mid-Ocean Channel (NAMOC) and Hueneme Fan off southern California, respectively. Both chapters first present a general statement about the topics covered and then summarize available data. The next section details the setting of each channel-levee system starting with channel morphology, followed by summaries of previous geological investigations and the controls on the character of turbidity currents active in each system. These controls on character include sediment delivery, initiation mechanisms, and previous work on flow parameter reconstruction. Following this presentation of background material, each chapter then documents the levee architecture of the system including the depositional history revealed by acoustic and core stratigraphy, ending with a synthesis of the levee growth patterns.

Chapter 5 presents data on the architecture of other systems including Reserve, Amazon, and Var fans. Discussion of each system takes on a condensed form of the previous two chapters. These systems augment the pool of observations of levee architecture although data for characterizing the levee architecture of these systems is less comprehensive than for NAMOC and Hueneme Fan. Chapter 6 is devoted exclusively to the more complex Laurentian Fan and follows a structure similar to Chapters 3 and 4.

Chapters 3-6 present data from submarine channel-levee systems sampling a wide range of geological environments. The application of consistent analytical and quantitative techniques, discussed in Chapter 2, provides a basis for making meaningful comparisons between systems. Chapter 7 synthesizes these data and interprets variability in channel-levee architecture comparing the predictions of simple physical models with empirically-derived relationships. At the end of Chapter 7, implications for the

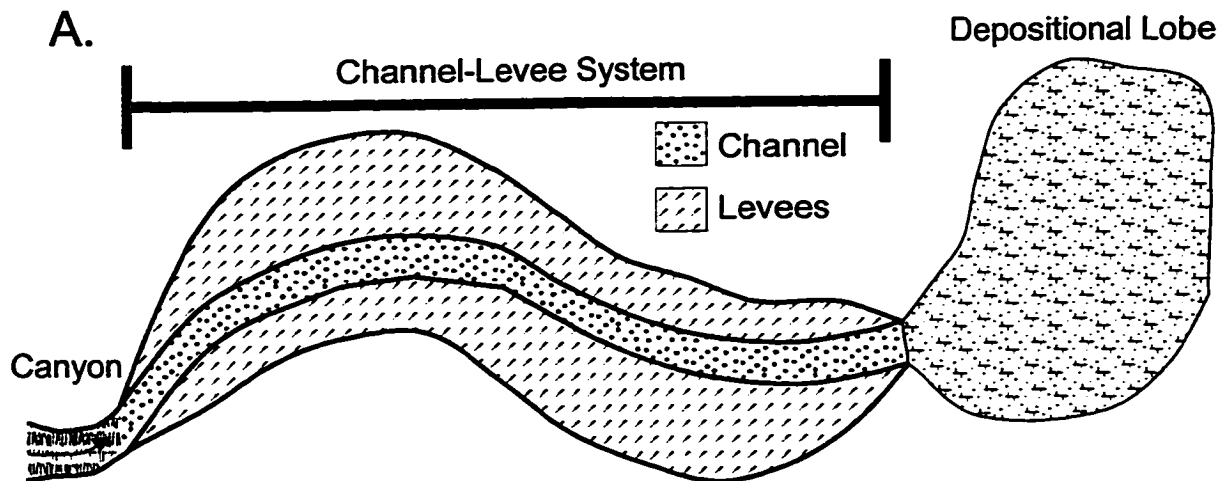
investigation of modern and ancient submarine channel-levee systems are explored in the light of the new understanding of levee architecture gained from this study. Chapter 8 summarizes the major conclusions of the thesis and suggests avenues for future research.

1.4 Introduction to Levee Architecture and Turbidity Current Theory

1.4.1 Architectural Elements

Miall (1985) was the first to systematically describe sedimentary sequences in terms of architectural elements. For submarine fans, the major elements or building blocks of the stratigraphic sequence include canyon, channel-levee, and lobe elements (Figure 1.1) (e.g., Piper & Normark, 1983; Mutti & Normark, 1987, 1991; Clark & Pickering, 1996). The channel-levee element may be subdivided into three sub-elements, the channel and its associated left-hand and right-hand levees (looking downstream). While these elements — canyon, channel-levee, and lobe — represent major features, they do not encompass the entire range of elements within a turbidite system (see Mutti & Normark, 1987, 1991).

Canyons focus the transfer of terrigenous sediment from the continental shelf to the deep sea. Consequently, the canyon is often considered the sediment source, although transport of sediment to the canyon head is implicit in any discussion of sediment supply. Stow et al. (1985) suggested that the presence of a canyon represents a necessary condition for the development of a submarine fan. Without a canyon, the continental shelf acts more like a line source that feeds a slope-apron depositional environment (Stow et al., 1985). The focusing of sediment by the canyon may also be necessary for the development of turbidity currents (e.g., Hill & Bowen, 1983; Baltzer et al., 1994). Canyons certainly play a role in focusing the cross-shelf transport of suspended sediment (e.g., Shepard et al., 1979; Gorsline et al., 1984). Just as the canyon represents a sediment source, the depositional lobe is a depocentre or sink for sediment carried by a turbidity current. Lobes tend to be broad sedimentary deposits found on the basin plain, characterized by coarser-grained detrital sediment than the surrounding pelagic and hemipelagic sediments. Morphologically, the lobes begin at the termination of significant channel relief, operationally defined as the limit of resolution of deep-tow instruments



General Downslope Trends

- Decreasing channel slope (Clarke et al., 1992)
- Initially increasing, then decreasing sinuosity (Clarke et al., 1992)
- Initially increasing, then decreasing channel depth (Menard, 1964; Komar, 1973)
- Increasing overall grain size of levee sediments (e.g., Amazon Fan, Hiscott et al., 1997)

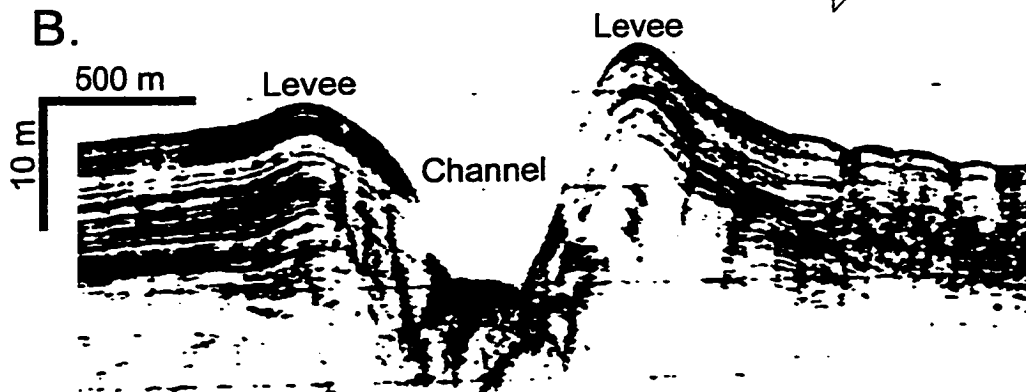


Figure 1.1. A. Schematic diagram of simplified canyon-channel-levee-lobe system showing channel-levee system within overall submarine fan setting. B. High resolution sub-bottom profile across a channel-levee system (modified after Ricci Lucchi et al., 1985). Note the difference in acoustic penetration between the channel and the levees and the substantial stratigraphic information contained within the levees.

(~1-2 m, Normark et al., 1979) and end as they merge into basin plain sediments or abut against basin margins.

A channel-levee system (or systems) occupies the region between the canyon and depositional lobe. The channel acts as a conduit for sediment transport seaward of the canyon mouth and can act either as a sink (deposition) or source (erosion) of sediment for the flow, depending upon the types of turbidity currents traversing the channel. Levees act mostly as depocentres for sediment supplied to them by overspill from the channel. However, the slumping of levee material into the channel supplies sediment to the channel and erosion of the levees may feed sediment to more distal overbank locations or to the depositional lobe. Nevertheless, the predominantly depositional character of levees makes these sites attractive for the study of fan evolution (Clark & Pickering, 1996).

1.4.2 Channel-Levee Classification

Cross-sectional Morphology

Submarine channel-levee systems have been classified based on their cross-sectional morphology (Nelson & Kulm, 1973; Mutti & Normark, 1987, 1991) and channel sinuosity (Clark et al., 1992). Nelson & Kulm (1973) classified channel-levee systems as erosional, depositional-erosional, and depositional based on cross-sectional morphology (Figure 1.2). Erosional channels downcut into older sediments and no levees form. Depositional channels show aggradation of both the channel and levees. Depositional-erosional channels represent a hybrid between purely erosional and purely depositional channels. The levees are predominantly sites of deposition while periods of erosion, bypass, and deposition characterize the channel, producing a complex channel-fill stratigraphy. Any one channel-levee system can show all three morphologies, typically having a proximal erosional channel, followed by a depositional-erosional channel that, farther downstream, grades into a depositional channel.

Planform Morphology

Imaging of the surficial morphology of submarine channels, especially using sidescan sonar and multibeam bathymetry, has demonstrated that channels have a range of sinuosities (e.g., Damuth et al., 1983; Flood & Damuth, 1987; Clark et al., 1992). The ratio of along-channel distance between two points in the channel to the straight line

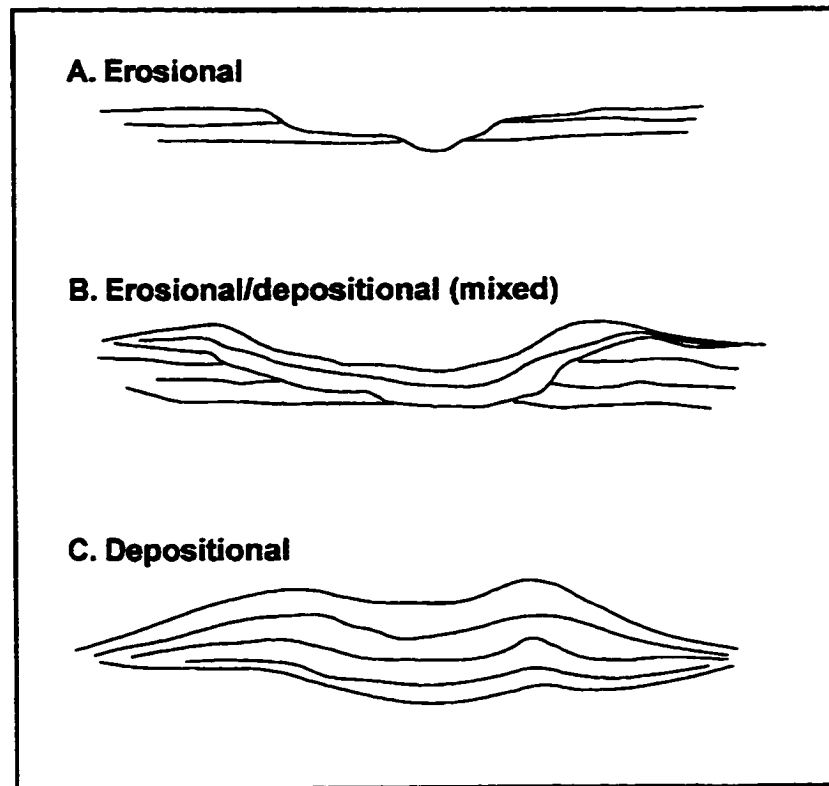


Figure 1.2. Cross sectional channel-levee classification of Nelson & Kulm (1973) showing: A. erosional; B. erosional/depositional; and C. depositional systems.

distance between these same points defines sinuosity. Thus, values for sinuosity vary from a minimum of unity for straight channels to greater than two for meandering channels. In a review of 16 modern submarine channels, Clark et al. (1992) found sinuosity to be a useful parameter for classifying submarine channels. In addition, Clark et al. (1992) showed from plots of sinuosity versus channel slope (Figure 1.3) that submarine channels resemble large river systems in that they have a peak sinuosity related to a specific value of downchannel slope that uniquely characterizes a system. Laboratory studies, notably by Schumm & Khan (1972), suggested that this slope-sinuosity relationship depends on the hydraulic conditions of the through-channel flows. In addition, many workers (e.g., Hesse et al., 1987; Flood & Damuth, 1987) have shown that channels tend to an equilibrium or graded profile (concave upward channel profile). The tendency toward a graded profile and the sinuosity-slope relationship suggest that channel-levee systems evolve to a morphology that in some way relates to the types of turbidity currents flowing through them. Pirmez (1994) demonstrated that sinuosity correlates directly with regional slope, i.e., the difference in elevation between two points divided by the straight-line distance between them. Where the regional slope is high, sinuosity increases such that the local channel gradient, i.e., the difference in elevation divided by the along-channel distance between them, is much less than the regional slope. Such behaviour suggests that channel morphology evolves in order to accommodate a particular downchannel profile, likely in equilibrium with the hydraulics of the average through-channel flows (Clark et al., 1992).

1.4.3 General Flow Processes

Levee deposition occurs as turbidity currents within the channel exceed the local channel depth and spread out away from the channel. This can occur for the head and body of the flow, but because the head of a turbidity is about as long as it is thick, overspill from the head does not contribute volumetrically significant amounts of sediment to the levees. A general term for the escape of fluid and sediment from the through-channel flow to the levees is overbanking. During overbanking the channel acts as the source of sediment for deposition on the levees. Two types of overbanking can

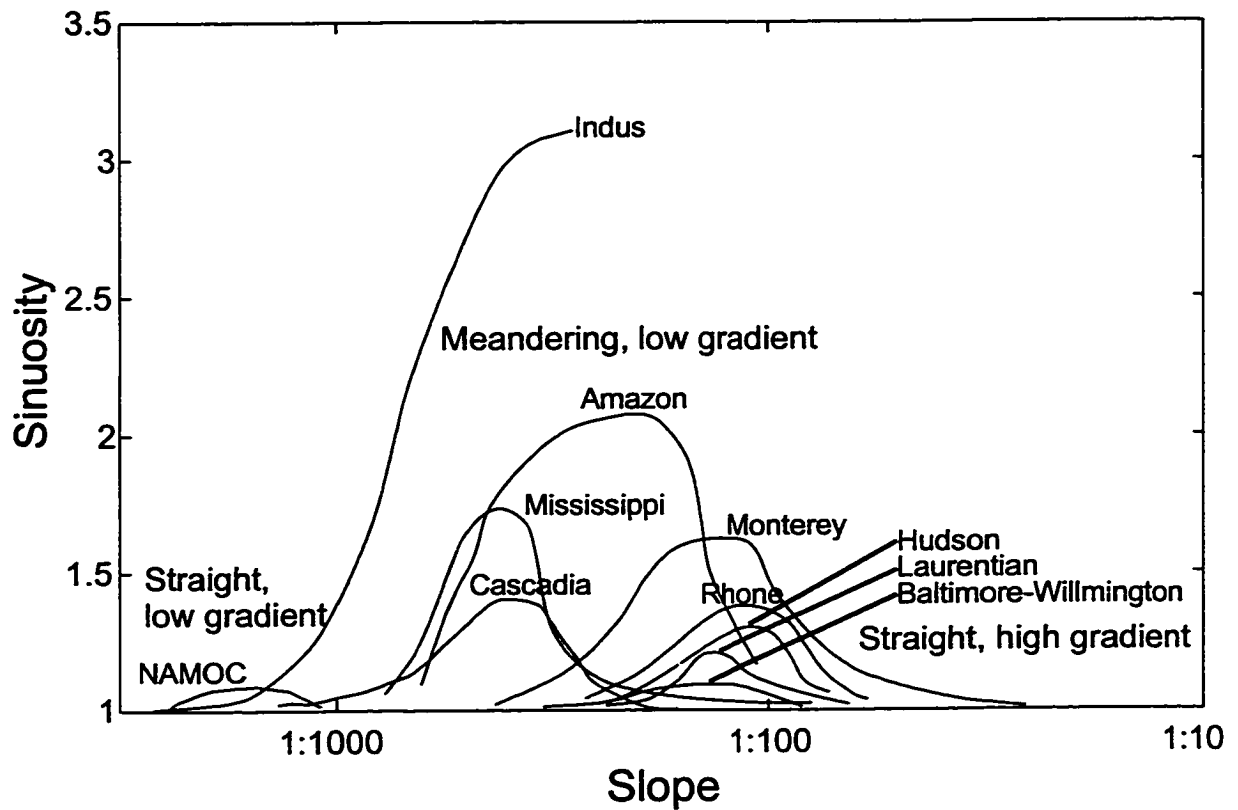


Figure 1.3. Planform channel-levee classification (modified after Clarke et al., 1992) based on relationship between downchannel slope and sinuosity. Two end-members in this classification scheme are straight, steep channels and meandering, low gradient channels. From his investigation of the Northwestern Atlantic Mid-Ocean Channel (NAMOC), Klaucke (1995) proposed a third end-member, a low sinuosity, low gradient channel.

potentially occur, differentiating this behaviour into overbanking that is focused at a particular location along the channel (flow-stripping) and overbanking that occurs along significant reaches of the channel (flow-spilling or continuous overspill).

Piper & Normark (1983) proposed the term flow-stripping to explain the behaviour of a Holocene turbidity current on Navy Fan. The distribution of this turbidite suggests that most of the turbidity current left the channel at an abrupt bend becoming a new, discrete turbidity current while the flow remaining in the channel quickly decelerated. Although deceleration of the residual channel flow was integral to the original definition of flow-stripping, the term has since been used to describe any overbanking that primarily occurs at a particular location along the channel. These locations can be channel bends where flow-stripping in some cases produces spillover lobes (Bute Inlet, Zeng et al., 1991) or low points in the levee crest, perhaps caused by sediment failure (Var Fan, Savoye et al., 1993). In these examples, residual channel flow does not necessarily die out. Continuation of the residual channel flow does place limits on how much sediment is lost to flow-stripping; if a large portion of the flow is “stripped off”, downchannel negative buoyancy and inertia of the current may not be enough to overcome friction, promoting rapid deceleration. Another version of flow-stripping was proposed by Hay (1987) and termed inertial overspill. In this process, flow-stripping occurs when the radius of curvature of the flow path in the channel is greater than the radius of curvature of the levee crests. Deflection of the flow by centrifugal forces diverts fluid to one side of the channel, potentially increasing flow thickness above channel relief. Presumably, thalwegs represent the morphological expression of the dominant flow path and so comparison of thalweg sinuosity with overall channel sinuosity should determine whether inertial overspill is important in a channel-levee system.

Flow-spilling or continuous overspill refers to the process by which overbanking occurs over long reaches of a channel, reaching an equilibrium between loss of material to the levees, changes in channel depth or channel cross-sectional area, and entrainment of water through the upper interface of the flow (e.g., Hiscott et al., 1997). Such a process was invoked to explain the long-distance (> 300 km) correlation of individual turbidites on the western levee of the Northwestern Atlantic Mid-Ocean Channel

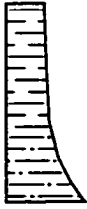
(NAMOC) (Hesse, 1995). Continuous overspill may also explain the apparent equilibrium between channel depth and the thickness of through-channel flows (Menard, 1964; Komar, 1973). On Amazon Fan, Pirmez (1994) used a simple continuous overspill model to explain the variation in flow parameters that he calculated using more conventional methods of flow parameter reconstruction (see Bowen et al., 1984 and following section). For continuous overspill, the channel acts as a line source of sediment to the levees.

1.4.4 Architecture-Flow Parameter Relationships

Facies models for submarine fans commonly imply a relationship between fan architecture and character of the turbidity currents that both create and interact with this morphology. Piper & Normark (1983; their Figure 8) proposed a range of flows moving through Navy Fan. Sandy flows were generally considered to be thin, high density, fast-moving, and confined to the channel. Muddy flows that aggrade or, with increasing intensity, possibly erode the levees were envisioned to be thick, low density, and slower moving than sandy flows. The model of Piper & Normark (1983) explicitly showed the interaction of differing flow types with the morphological elements of a submarine fan, but it did not make predictions about the nature of the turbidites deposited from the various flow types. Walker (1965) proposed a facies model showing the predominance of massive to graded thick-bedded sands and gravels within the channel, thin-bedded, finer-grained material on the levees, and proximal to distal fining and thinning of beds on the depositional lobe. However, this model requires a full range of grain sizes and applies to only a single type of flow capable of delivering this range of grain sizes. Normark & Piper (1991) combined variations in flow type with predictions about the nature of the resulting turbidites (Figure 1.4). The Normark & Piper (1991) model predicts the deposits and some of the expected bedforms from large sandy flows, large muddy flows, large mixed grain-size flows, and repeated thin muddy flows. Large sandy flows contribute mostly to deposition in the channel and on the depositional lobe. Their contribution to shaping channel morphology affects only indirectly levee architecture by changing channel relief and the potential for subsequent flows to overbank. Large muddy flows deposit relatively thick-bedded turbidites on the levees, possibly moulding these deposits into sediment waves. Large mixed flows also deposit relatively thick-bedded

Levee deposits from different flow types

Large muddy flow



Large mixed flow



Repeated thin muddy flows



Of the four flow types in Normark & Piper's (1991) facies model, only three contribute to levee deposition. In their model, sediment waves only form from large muddy flows.

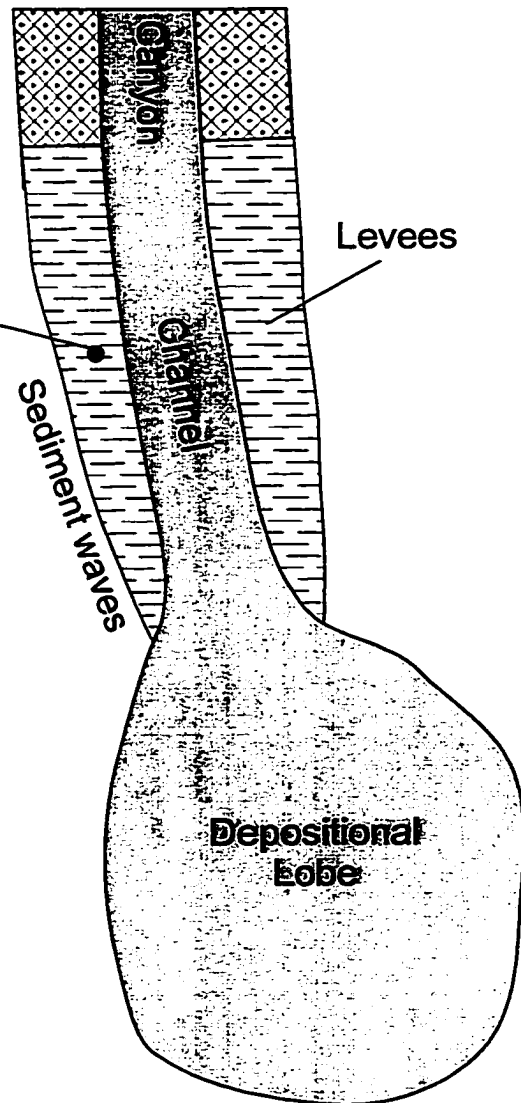


Figure 1.4. Simplification of Normark & Piper's (1991) facies model showing the depositional features on levees of various turbidity current flow types: large muddy flows with the deposition of thin silt laminae and the generation of mud waves on the levees; large mixed flows with the deposition of coarse material (perhaps up to fine sand) on the levees; repeated thin muddy flows which develop thin-bedded muddy turbidites with basal silt laminae on the levees. The large sandy flows discussed by Normark & Piper (1991) do not contribute directly to levee deposition.

turbidites on the levees which may be coarser-grained than the deposits of large muddy flows. Thin muddy flows deposit relatively thin-bedded turbidites on the levees and may not contribute to the development of sediment waves.

Although general statements can be made about the type of flow responsible for various facies associations, specific determinations of flow type arise from flow parameter reconstruction (e.g., Bowen et al., 1984). For example, using the facies model of Normark & Piper (1991), the presence of sediment waves suggests large muddy flows and the equation of Normark et al. (1980) provides a relationship between wavelength of sediment waves and flow thickness. Methods for the reconstruction of flow parameters and their successful application depend upon the types of data available and can be divided into three general categories: flow parameters derived from 1) sediments; 2) channel morphology; and 3) levee morphology.

Flow Parameters from Sediments

Turbidites record the character of the turbidity current from which deposition occurred. Walker (1965) described the idealized vertical sequence in a turbidite bed, or Bouma sequence, in terms of the flow regime under which each Bouma division deposits. The A-division of the sequence consists of massive sandstones deposited under upper flow regime conditions (possibly antidune conditions). A great deal of work concerning deposition of these massive sands by high concentration turbidity currents (or sandy debris flows; Shamugam, 1996) is available in the literature. At the very least, the absence of such beds in levee sediments suggests that high concentration flows do not play a direct role in levee sedimentation. B-division sediments show planar lamination and normal grading ascribed to deposition under upper-flow-regime plane-bed conditions. The boundary between B and C division marks the transition from upper- to lower-flow-regime. C-division sediments are ripple cross-laminated. The D division of the Bouma sequence comprises finer-grained laminated sediments deposited under lower-flow-regime, plane-bed conditions. Finally, the uppermost E division of the Bouma sequence consists of pelitic sediments, representing hemipelagic and pelagic sedimentation. Using the bedform stability fields summarized by Allen (1985), Komar (1985) estimated flow velocities of $0.5-1 \text{ m s}^{-1}$ for the C-D boundary in sand composed of $140 \mu\text{m}$ particles.

Examination of silt laminae in muddy turbidites led Stow & Bowen (1980) to propose a depositional model for these structures from which estimates of flow parameters could also be made. They proposed a four stage depositional model where silt grains initially settle through the viscous sublayer at the base of a turbidity current. Continued supply of sediment to the boundary layer immediately above the viscous sublayer increases the concentration of particles in this layer, promoting flocculation. At some critical concentration, the flocs are sufficiently large to overcome the boundary layer shear and deposit as a “mud blanket”. Predictions of this model — an upward fining and thinning of the silt laminae and relatively constant thickness of the mud layer — compare favourably with sediment samples from the Scotian Slope and Laurentian Fan (Stow & Bowen, 1980). Stow & Bowen (1980), using the deposition rate equation of McCave & Swift (1976), derived expressions for turbidity current flow parameters as a function of the sedimentological characteristics of silt laminae, primarily the grain size distribution, bulk density, and thickness of individual laminae. From such data, Stow & Bowen (1980) were able to estimate the velocity, thickness, and duration of turbidity currents. Other models for the formation of silt laminae have been proposed including: 1) velocity fluctuations (Lombard, 1963); 2) reflection of turbidity currents by basin walls (Van Andel & Komar, 1969); 3) passage of a series of small distinct flows (Dzulynski & Radomski, 1955); and 4) burst-and-sweep cycles (Hesse & Chough, 1980). The literature still does not contain a consensus view for the formation of silt laminae, and although other models for laminae formation may be more appropriate than the Stow & Bowen (1980) model, they have no direct applicability to the estimation of flow parameters and will not be discussed further.

Various suspension criteria have been used to estimate flow velocity as a function of particle settling velocity. The conditions implied by each method can be divided into three categories: 1) autosuspension conditions; 2) threshold for sediment movement conditions; and 3) washload conditions. Observations of turbidites generally describe grain size distributions; consequently the general application of suspension criteria requires a relationship between observed grain size and settling velocity.

For single particles, balancing the gravitational force due to settling against frictional forces acting to retard sinking predicts that the settling velocity, w_s (m s^{-1}), of grain of diameter, d (m), varies according to

$$w_s^2 = \frac{4 g_o d}{3 C_p} \quad (1.1)$$

where

$$g_o = g \frac{\rho_s - \rho}{\rho} \quad (1.2)$$

and where g (m s^{-2}) is acceleration due to gravity, ρ_s (kg m^{-3}) is grain density, ρ (kg m^{-3}) is fluid density, and C_p is a particle drag coefficient (e.g., Allen, 1970). For particles less than about 200 μm , C_p is a function of the particle Reynolds number defined by

$$\text{Re}_p = \frac{\rho}{\mu} w_s d \quad (1.3)$$

where μ ($\text{kg m}^{-1} \text{s}^{-1}$) is the dynamic viscosity. Substituting the dependence of C_p on Re_p given by

$$C_p = \frac{24}{\text{Re}_p}$$

into (1.1) yields Stokes' Law, which predicts that settling velocity scales with the square of grain diameter according to

$$w_s = \frac{1}{18} \frac{g(\rho_s - \rho)}{\mu} d^2 \quad (1.4)$$

For particles much greater than 200 μm (i.e., $\text{Re}_p > 1$), C_p is relatively constant and settling velocity scales with the square root of grain diameter.

The relationship between grain size and settling velocity is useful only when single-grain settling characterizes a deposit, but single-grain settling is only one mode by which particles may gain the bed. Individual grains may combine to form particle aggregates, also known as flocs. The disaggregated grain size distribution of a floc is identical to the disaggregated grain size distribution of the flow, but floc size is not a readily predictable function of disaggregated grain size (Kranck, 1975). However, disaggregated grain size distributions can provide clues to the nature of the parent particle size distribution (Kranck, 1975; 1984). For turbidites from offshore eastern Canada,

Kranck (1984) showed that two distinct populations of grains can exist: a single-grain population and a flocculated population. While settling velocity of the single-grain population can be derived using (1.1) or (1.4), the settling velocity of the floc population requires additional information. In situ measurements of floc settling velocity under a wide range of environmental conditions suggest that this settling velocity is approximately 0.001 m s^{-1} (e.g., Alldredge & Gotschalk, 1989; Kinecke & Sternberg, 1989; Syvitski et al., 1995; Dyer et al., 1996).

The concept of an autosuspension limit was first proposed by Bagnold (1962) who suggested that turbidity currents must expend energy not only in overcoming the frictional resistance to flow but also in keeping sediment in suspension. Closely related to autosuspension is the concept of ignition (Parker, 1982). A current is said to "ignite" when net erosion by the current increases the driving force for the flow which in turn increases the erosion rate again increasing the driving force. Such a current accelerates downslope. Autosuspension, on the other hand, only specifies conditions for which the current has power in excess of that required to suspend its sediment. Bagnold (1962) proposed that when

$$\frac{w_s \cos\beta}{u \sin\beta} < \varepsilon \quad (1.5)$$

with $\varepsilon = 1$, the current would possess energy in excess of that needed to overcome friction and keep particles in suspension. Pantin (1979) suggested the use of an efficiency factor which reduced the value of ε to 0.01, thereby making the condition for autosuspension more limiting. Stacey & Bowen (1988b) derived an autosuspension criterion from simplifications to the equations of motion governing the vertical structure of a turbidity current that took the form

$$\frac{w_s \cos\beta}{uC_D} < S_0 \quad (1.6)$$

where S_0 lies between 0.02 and 0.06. Note that the drag coefficient, C_D , in this case, reflects a constant of proportionality relating the square of flow velocity to the stress at the base of the flow and should not be confused with the drag coefficient associated with sediment grains introduced in the above discussion of settling velocity. Because the drag coefficient, C_D , is a function of slope and bottom roughness, these forms of the

autosuspension criterion are qualitatively similar. In each, flow velocity must be greater than some multiple of the settling velocity for autosuspension to occur. Given the settling velocity derived from grain size analysis of the deposited sediment, the autosuspension criterion gives what most would consider an erroneous velocity estimate because if flow conditions exceeded the autosuspension limit, the current would not be depositing sediment. Application of the autosuspension criterion does provide, however, a maximum velocity for the current upstream of the sample location.

A very popular method for relating flow velocity to the grain size of turbidites uses

$$\frac{u_*}{w_s} = b \quad (1.7)$$

where the friction velocity, u_* , relates to the mean flow velocity, u , by

$$u_*^2 = C_D u^2 \quad (1.8)$$

The coefficient, b , may take a range of values centred around unity with many workers using $b = 1$ (e.g., Reynolds, 1987; Syvitski & Schafer, 1996). With $b = 1$, the critical velocity for erosion equals the settling velocity of the sediment. Such conditions hold for single particles, but not for grains bound in flocs. Settling velocity relates to particle size using (1.1) or (1.4), but the selection of the particle size remains controversial. The controversy hinges on deciding which grain size within the deposit characterizes the flow conditions for which (1.7) is valid. Bowen et al. (1984) used the median grain size, arguing that applying this grain size should average out over the turbulent velocity fluctuations within the flow. In addition, using median grain size, one might expect coarser grains in the deposit to have moved as bedload and perhaps the finest grains to have been trapped between larger grains. Strictly speaking, the median size required by the arguments for Bowen et al. (1984) is the median particle size of the flow rather than the median grain size determined from a disaggregated sample. In such a case, determination of the settling velocity for the single grain population as defined by Kranck (1984) might be the scale for which (1.7) is most valid. Komar (1985) favoured the grain size representing the 95th percentile of the grain size distribution, although he stated that the choice was pragmatic rather than physically justified. Skene et al. (1997, in press)

argued that the frictional velocity represented by the coarsest grains in the flow sets an upper limit on the turbulent velocity fluctuations of the flow; all turbulent velocities should be smaller than this amount and may well average to the frictional velocity represented by the median grain size. The presence of sediment grains smaller than the coarsest grain size was attributed to asymmetry between erosion and deposition rates, especially for fine-grained sediment.

From a review of data relating grain size to flow condition, Bowen et al. (1984; and references therein) constructed a plot of settling velocity versus frictional velocity that was divided into fields pertaining to bedload conditions, suspended sediment conditions, and washload conditions. They suggested that washload conditions, whereby sediment is evenly distributed throughout the flow thickness, occurs for $b > 7-30$ in (1.7). As with application of an autosuspension criterion, washload conditions apparently preclude the deposition of sediment in the channel, the flow being too vigorous to allow sedimentation. However, sediment carried as washload within the channel may be deposited on the levees. Consequently, the application of the washload criterion to levee sediments offers an independent constraint on velocity in the channel measured, for example, using the threshold criterion (Bowen et al., 1984).

Flow Parameters from Channel Morphology

Two avenues exist for extracting flow parameters from channel morphology. Both methods use simplified models of turbidity current dynamics. The first method solves a depth-integrated, downstream momentum balance for steady, uniform flow (Komar, 1977; Bowen et al., 1984; Stacey & Bowen, 1988a), resulting in a Chezy-type equation,

$$u^2 = g_0 C H \frac{\sin \beta}{E + C_D} \quad (1.9)$$

where u (m s^{-1}) is the average velocity, C is the dimensionless volume concentration of particles, H (m) is the flow thickness, β is the channel slope, E is the entrainment coefficient, and C_D is the drag coefficient. Equation (1.9) represents the balance between the gravitational driving force provided by the suspended sediment and the frictional resistance to motion at the base and upper interface of the flow. As such, (1.9) applies to the steady, uniform flow of the turbidity current body. Typically, estimates of flow

thickness assume bankfull conditions (e.g., Komar, 1977), so equation (1.9) yields velocity as a function of volume concentration for chosen values of E and C_D . Alternatively, knowing velocity independently, (1.9) can be rearranged to solve for volume concentration; estimates of volume concentration derived in this manner must be less than 0.09 (Bagnold's Limit; Bagnold, 1962) because at volume concentrations above 0.09, grain-to-grain interactions become significant.

A second method for relating flow parameters to channel morphology solves the depth-average, cross-channel, momentum balance for steady, uniform flow in a channel (Komar, 1969). This method assumes that the important balance of forces across the channel is between the pressure gradient force, the Coriolis force, and the centrifugal force caused by channel curvature. Balancing these terms produces

$$-g_o C \frac{\partial H}{\partial y} = f u + \frac{u^2}{R} \quad (1.10)$$

where f (s^{-1}) is the Coriolis parameter, and R is the radius of curvature of the channel. The height difference across the channel divided by channel width or twice channel half-width, W (Figure 1.5), serves as an estimate of the cross-flow slope (Komar, 1969) such that

$$\frac{\partial H}{\partial y} \approx \frac{\Delta H}{2W} = \nabla H \quad (1.11)$$

where ΔH (m) is the difference in elevation between the left- and right-hand levee crests, and W (m) is the horizontal distance between the channel axis and the levee crest. Bowen et al. (1984) rearranged (1.10) using the Froude number, Fi , yielding

$$-\frac{\partial H}{\partial y} = H \left(\frac{f}{u} + \frac{1}{R} \right) Fi^2 \quad (1.12)$$

where

$$Fi^2 = \frac{u^2}{g_o C H} \quad (1.13)$$

In either form, the cross-flow slope equation provides a relationship between levee asymmetry and flow velocity for a given value of Fi or C . In (1.10) the predicted cross-levee slope is directly related to velocity while inversely related to volume concentration. In (1.12) this same slope is directly proportional to Fi^2 , suggesting that supercritical flows

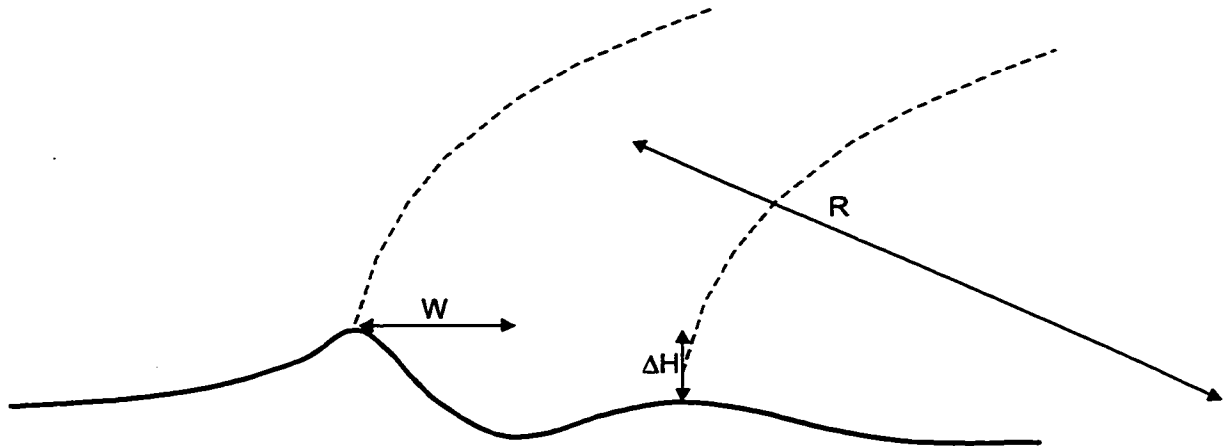


Figure 1.5. Definition sketch for cross-flow slope equation. The slope of the upper interface of the flow responds both to the action of the Coriolis and centrifugal forces. These forces are balanced a the cross-flow pressure gradient. In order to use levee asymmetry for insights into flow parameters, the cross-flow slope is assumed to be equal to the difference in levee crest elevation divided by the distance from levee crest to levee crest.

($Fi > 1$) have larger cross-flow slopes than subcritical flows ($Fi < 1$). In addition, (1.12) implies that the cross-flow slope goes to zero when

$$\frac{f}{u} = -\frac{1}{R}. \quad (1.14)$$

In the northern hemisphere, the cross-flow slope produced by right-turning meander bends counteracts the slope produced from the Coriolis force which diverts water to the right of the flow direction.

Estimates of flow duration from channel morphology require estimates of the total volume of sediments within an individual turbidite. Assuming that all the sediment in a turbidite flowed through a channel cross-section for which a mean flow velocity and volume concentration are known, then the mean sediment discharge equals the product of cross-sectional area, velocity, and volume concentration. Dividing the total volume of sediment by this sediment discharge then gives an estimate of flow duration.

Flow Parameters from Levee Morphology

A feature of many submarine channel levees is the presence of sediment waves aligned obliquely to the channel trend with an acoustic morphology suggesting upstream migration. From Var Fan, Savoye et al. (1993) showed an excellent example of sediment waves and their apparent upstream migration imaged using high resolution airgun seismic reflection profiles. Similar observations led Normark et al. (1980) to propose that these features represent giant antidunes with their wavelength, L_{sw} (m), theoretically related to volume concentration, C , and velocity, u , by

$$L_{sw} = 2\pi \frac{u^2}{g_0 C} \quad (1.15)$$

Alternatively, using (1.13), (1.15) becomes

$$L_{sw} = 2\pi Fi^2 h \quad (1.16)$$

For $Fi = 1$, depth of flow is approximately one-sixth the wavelength. Applying (1.16) to sediment waves on Monterey Fan, Normark et al. (1980) suggested flow thicknesses ranging from 50-800 m. Sediment waves on Var Fan described by Savoye et al. (1993) have $L_{sw} \geq 1000$ m suggesting flows hundreds of metres thick.

An alternative model for sediment wave formation employs the analytical streamfunction solution to flow over a sinusoidal bed proposed by Queney (1948). By

differentiating the stream function in the direction of flow, Flood (1988) calculated the velocity field finding a nearbed velocity maximum at $1/4L_{sw}$ and a velocity minimum at $3/4L_{sw}$. Using these expressions for velocity and McCave & Swift's (1976) equation for sediment deposition, Flood (1988) formed a ratio of the minimum to maximum sedimentation rates, termed the sedimentation rate ratio (SRR), given by

$$SRR = \frac{\tau_c - \rho_f C_D u^2 (1 + Bk'_w)^2}{\tau_c - \rho_f C_D u^2 (1 - Bk'_w)^2} \quad (1.17)$$

where

$$k'_w = k_w \left(\frac{k_s^2 - k_w^2}{k_f^2 - k_w^2} \right) \quad (1.18)$$

$$k_w = \frac{2\pi}{L} \quad (1.19)$$

$$k_s = \frac{N}{u} \approx Fi^{-1} \frac{1}{h} \quad (1.20)$$

$$N = \left(\frac{g}{\rho_f} \frac{\partial \rho_f}{\partial z} \right)^{1/2} \approx \left(\frac{g_o C h u^2}{h h u^2} \right)^{1/2} = Fi^{-1} \frac{u}{h} \quad (1.21)$$

$$k_f = \frac{f}{u} \quad (1.22)$$

where B (m) is the sediment wave amplitude, τ_c ($\text{kg m}^{-1} \text{s}^{-2}$) is the critical shear stress for deposition, ρ_f (kg m^{-3}) is the flow density, k_w (m^{-1}) is the wave number of the sediment waves, and N is the buoyancy frequency. The streamfunction solution used by Flood (1988) applies to the case when $k_f \leq k_w \leq k_s$, i.e., when the vertical variation in streamline displacement is sinusoidal and out of phase with the sediment wave. Assuming constant conditions across a sediment wave, the SRR is a function of the flow velocity.

Flood (1988) initially derived his SRR relationship and the lee wave model to describe sediment waves formed under thermohaline bottom currents. Applications of the lee wave model to sediment waves associated with turbidity current flow remain sparse in the literature. Howe (1996) invoked the lee wave model as a possible mechanism for, if not the formation, at least the maintenance, of a sediment wave field found distal to Barra Fan, Rockall Trough, off the northwestern UK. Howe (1996)

presented core evidence that convincingly argues for turbidite deposition as the process responsible for sediment wave growth. However, the criteria used to discount the antidune model of Normark et al. (1980) are not made entirely clear, except to point out that the antidune model requires $Fi \geq 1$. The common predictions of sediment wave architecture made by the competing models leaves little evidence with which one can easily choose between them.

In reviewing what is known about levee architecture and the various approaches generally used to extract process information from the deposits of turbidity currents, some features of levees have been used, like elevation differences between conjugate levee crests and sediment waves, while more basic features of levee morphology have been neglected. An enlightening comparison can be made between the quantitative analysis of channel morphology versus levee architecture. Channel morphology — relief, width, and slope — can be relatively easily quantified and these basic features of channel geometry have been rigorously investigated in many studies (e.g., Hesse et al., 1987; Clark et al., 1992; Pirmez & Flood, 1995). Part of what this study accomplishes is to extend the quantifiable parameters of a channel-levee system to include information recorded by levee architecture, systematically characterizing the analogous basic features (i.e., dimensions) of levees. In addition, previous studies of submarine channels have generally focused on the modern expression of the channel and, while important, they cannot be used to infer anything more about turbidity current processes than those active during the most recent phase of channel-levee development. Levees, on the other hand, can record a high resolution stratigraphy imaged using conventional seismic profiling techniques. Consequently, quantitative analysis of levee architecture and the relationships between this architecture and channel morphology have the potential to enhance our understanding not only of the geometry of channel-levee systems but also their stratigraphic evolution.

Chapter 2

Methods

2.1 General Statement

The thesis analyzes a wide range of data collected over the last 30 years from a variety of fans. Consequently, no single methodology strictly applies to all the systems under investigation. However, some techniques are used throughout the thesis. Acoustic profiles constitute the key data set that is common to each system. As such, the basic premises and techniques of seismic stratigraphy are reviewed below. From these data and their seismic interpretation, architectural measurements have been made. The first of these measurements is the location of a data point within the system. The rest of the measurements characterize some feature of this data point, for example, depositional sequence thickness.

2.2 Seismic Stratigraphy

2.2.1 Basic Theory

The basic theory behind seismic stratigraphy deals with the propagation of sound waves through layered media. Elastic sound waves generated by a surface source reflect off discontinuities in the subsurface and return to the surface where their time of arrival and their intensity are recorded. Arrival time depends upon the distance traveled by the wave divided by the velocity at which the wave traveled. The intensity of the reflected wave depends upon the amount of acoustic energy returned to the surface from the discontinuity. The velocity of elastic waves, or P-waves, v_p (m s^{-1}), in the earth depends upon the density, ρ_B (kg m^{-3}), bulk modulus, K ($\text{kg m}^{-1} \text{s}^{-2}$), and shear modulus, μ ($\text{kg m}^{-1} \text{s}^{-2}$), of the material according to

$$v_p = \left(\frac{K + \frac{4}{3}\mu}{\rho_B} \right)^{1/2} \quad (2.1)$$

The discontinuities that generate reflections occur at contrasts in acoustic impedance, I ($\text{kg m}^{-2} \text{s}^{-1}$), the product of seismic wave velocity and bulk density. The contrast in acoustic impedance between two layers defines the reflectivity coefficient, R (dimensionless), according to

$$R = \frac{I_{\text{layer2}} - I_{\text{layer1}}}{I_{\text{layer2}} + I_{\text{layer1}}} \quad (2.2)$$

where layer 2 underlies layer 1. In general, large reflectivity coefficients generate a strong seismic reflection and hence a high intensity signal arrives at the receiver. For example, $R = 0.9995$ between air and water (Kearey & Brooks, 1984, p. 39). However, for most geological material, R rarely exceeds ± 0.5 ; typical reflection coefficients are less than ± 0.2 (Kearey & Brooks, 1984, p. 39). Consequently, most seismic energy is transmitted and only a small amount reflected.

The relationship between seismic reflections and bedding is not simple, but major contrasts in acoustic impedance and therefore high reflectivity coefficients tend to coincide with unconformities and stratal surfaces (e.g., Mitchum et al., 1977; Brown & Fisher, 1982). Unconformities generate large contrasts because they represent hiatuses in the depositional record and therefore bring sediments of different ages and different properties into vertical contact with each other. Stratal surfaces generate reflections owing to the vertical stacking of sediments with different characteristics, for example, interbedded sands and shales. It is these relationships between the acoustic properties of sedimentary successions and geologically-important interfaces that spawned the development of seismic stratigraphy.

A single-channel seismic record displays a series of seismic reflection traces collected at a known horizontal offset; each trace (or line of data) represents the returns in response to a single pulse (or shot) from the sound source (Figure 2.1). In marine surveys, the sound source and receiver move continuously with the ship, with the time between shots being held constant. Therefore, the distance between individual traces is the elapsed time between shots multiplied by the speed of the vessel. The individual traces are recorded and displayed such that two-way travel time (TWTT) increases vertically downward. TWTT is the time elapsed between the shot and the return of the seismic energy detected by the receiver. True depth is then the velocity of the sound in the sediment multiplied by half the two-way travel time.

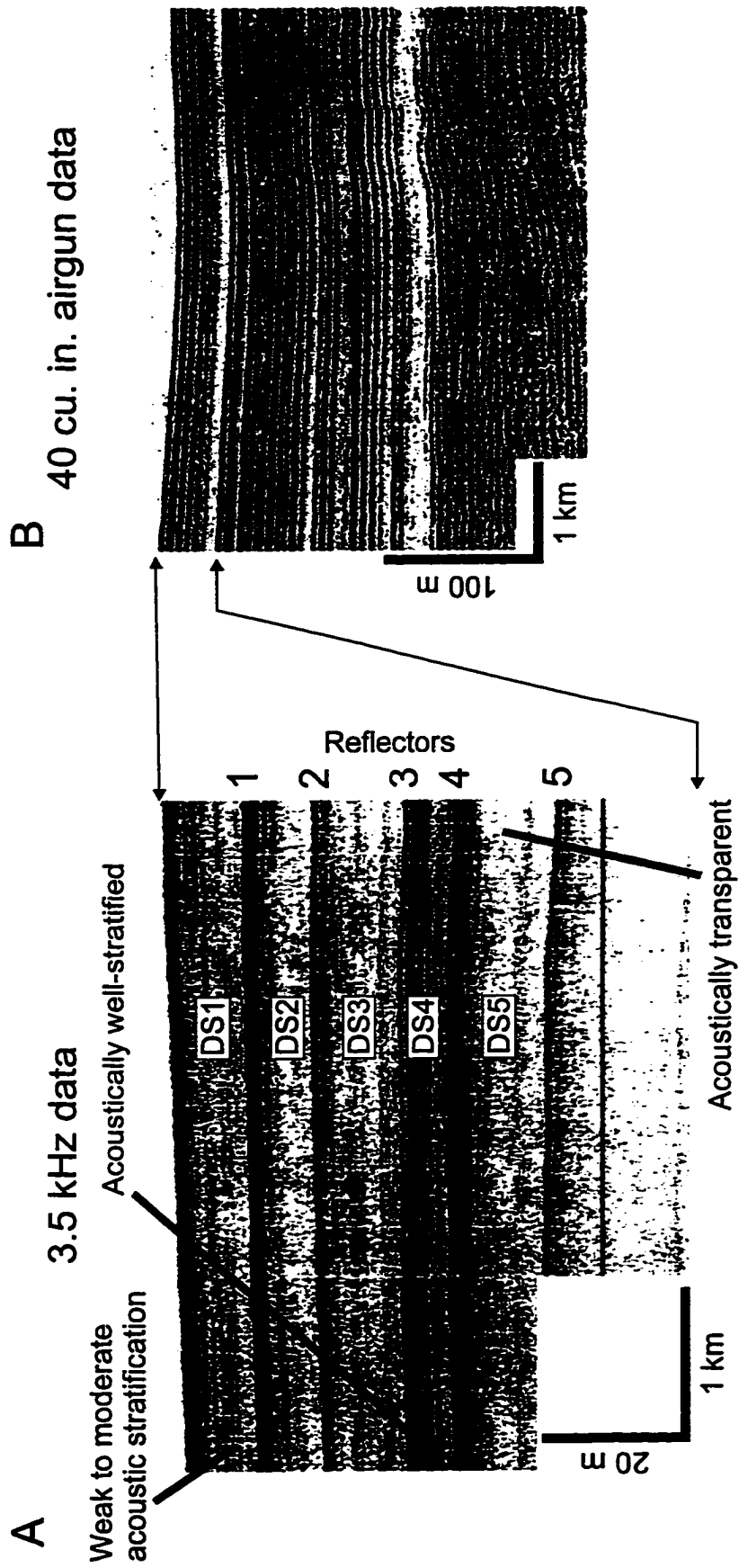


Figure 2.1. Examples of seismic data: A. High resolution 3.5 kHz sub-bottom profile and B. Lower resolution 40 cubic inch airgun profile. The 3.5 kHz data provide a detailed record of the stratigraphy but only image the upper 80 m of the sedimentary succession. On the other hand, the airgun data provide information extending several hundred metres below the sediment surface but, owing to the lower frequency of the sound source, airgun data lack detailed resolution.

A final note important to the thesis concerns the fidelity of seismic data. The resolution of seismic data corresponds to the smallest vertical spacing between interfaces that have the potential to generate a seismic reflection, i.e., $R \neq 0$. The frequency of the sound source and the velocity of the sound in the sediments determines resolution. In other words, the smallest vertical spacing between reflection horizons that can be resolved is greater than the wavelength of the source signal. Frequency of the source also determines attenuation of seismic energy, with high frequencies attenuated more quickly than low frequencies. More precisely, attenuation due to absorption of seismic energy by the medium through which it propagates is directly proportional to wavelength. For most materials, the attenuation of seismic energy takes a value between 0.25-0.75 decibels per wavelength (Kearey & Brooks, 1984, p. 37). For a given velocity, a low-frequency source like an airgun will produce a low resolution record of the subsurface, but because of the low attenuation it will image material deeper in the sedimentary succession (Figure 2.1b). Higher frequency sources like boomers or 3.5 kHz profilers, produce high resolution records but only of the upper few tens of metres of the sediment column due to attenuation (Figure 2.1a). In the following chapters, the type of seismic system employed determines the level of detail with which the architecture of levees can be studied.

2.2.2 Correlation

It is instructive to think of each seismic trace as a sample of the acoustic properties of the sub-bottom sediments just as a piston core or borehole samples the actual sediment. The positions at which these acoustic properties generate seismic reflections can be noted on any one trace just as sedimentary units can be distinguished in a core. Seismic reflections can be correlated between traces thereby defining a surface or reflector (also called horizon). It should be noted that at its most fundamental level, the development of a seismic stratigraphy represents the correlations made between individual traces. Thus interpretation begins very early on in the analysis of seismic data.

The correlation of reflections defines a reflector that may represent an unconformity or stratal surface because these interfaces tend to produce reflections. Stratal surfaces generally represent near-isochronous horizons, dividing sedimentary successions into packages that span a definite interval of stratigraphic time. They

represent previous depositional surfaces, and through the mapping of such surfaces, the development of a sedimentary succession can be divided into time slices.

Unconformities, on the other hand, represent diachronous surfaces, their age potentially changing along the reflector identified as an unconformity. Unconformities do possess some degree of chronostratigraphic information as all the sediment overlying an unconformity is younger than the event which produced the unconformity.

In the thesis, reflectors in particular geographic area were defined in a type section and subsequently correlated throughout the available seismic profiles. Direct tracing of reflectors corresponds to the correlations of reflections between individual traces. The accuracy with which this is accomplished can be checked at cross-overs in the seismic profiles, i.e., where two profiles cross the same point in space. The basic methodology is to trace a reflector through the data and then to check the sub-bottom depths at cross-overs for internal consistency. The thesis also required correlation of reflectors based on acoustic character, defined below, and stratigraphic position, in particular when correlating horizons across a channel. This type of correlation compares the expression of the sediment column in seismic records, matching similar vertical successions between separate locations.

2.2.3 Depositional Sequences

The identification and mapping of sub-bottom horizons divides the sedimentary succession into discrete packages, termed depositional sequences. The character of each sequence is described according to the expression of its upper and lower bounding surfaces, its acoustic stratification, and the internal geometry of the reflections.

Important aspects of a bounding surface of a depositional sequence include its amplitude, relief, and concordance. The intensity of a reflection, or its amplitude, depends upon the impedance contrast between layers. Qualitatively, amplitude is described as weak, moderate, or high. The relief of the surface denotes the deviation of the horizon from a planar surface. For levees this relief can be divided into large- and small-scale relief. For example, large-scale relief is associated with the reflectors as they rise toward a levee crest; small-scale relief corresponds to the shorter wavelength fluctuations in sub-bottom depth associated with, for example, sediment waves. Finally,

concordance denotes the relationship between a reflector and the underlying or overlying reflectors (Mitchum et al., 1977). Basal discordance includes downlap, onlap, and erosional truncations. Discordance along an upper interface includes toplap and erosional truncation. Discordant relationships imply gaps in the stratigraphic column. In the thesis, care was taken to identify discordance in the seismic profiles so that the depositional sequences comprised a conformable succession of strata. As such, their geometry reflects depositional processes.

One can also describe depositional sequences by their internal character or seismic facies. Seismic facies analysis describes the reflections within a depositional sequence (e.g., Mitchum et al., 1977), and in this thesis the important aspects were the degree of acoustic stratification and the internal geometry of the reflections. Generally, levees consist of acoustically transparent to weakly to strongly acoustically stratified sediment, the distinctions depending in part on the resolution of the seismic system. An acoustically transparent depositional sequence lacks internal reflections suggesting that it consists of homogenous material lacking internal contrasts in acoustic impedance. However, it can also mean that the vertical scale of contrasts in acoustic impedance is less than the resolution of the seismic system. When the sediments are acoustically stratified, this stratification can vary from weakly to well developed. The degree of stratification reflects the presence and magnitude of contrasts in acoustic impedance at vertical scales greater than the resolution of the seismic system. It can also correspond to internal multiples where acoustic energy reflects between sub-bottom interfaces before returning to the surface. Generally, using high resolution seismic data (<0.5 m), submarine levees show varying degrees of acoustic stratification. Typically, weakly developed stratification is interpreted to reflect interbedded sands and silts within predominantly muddy sediment (e.g., Piper & Fader, 1990).

A final important consideration when describing the character of depositional sequences is the internal geometry of the reflections. Within the seismic data used in this thesis, the internal geometry of reflections varies from sub-parallel (either wavy or flat-lying) to divergent. Subparallel reflections possess approximately constant vertical spacing between reflections while their overall form can have low-relief (flat-lying) or small-scale relief (wavy, e.g., sediment waves). Divergent reflections show progressive

changes in inter-reflection spacing, suggesting that the depositional sequence as a whole is changing in thickness while still consisting of a conformable succession of strata.

2.3 Architectural measurements

2.3.1 Positioning

Absolute position in any marine survey is probably the single most important measurement. Without it, any data collected are of only limited value as they cannot be placed geographically. The navigation for data in this thesis is generally of two types and can be divided into surveys prior to 1993 and those after 1993. Prior to 1993, positioning was provided by an integrated LORAN C and transit satellite navigation system. With this system, navigational accuracy is generally ± 150 m for survey lines run at constant heading and speed. After 1993, the global position system (GPS) became the navigational tool of choice, providing resolution first at the scale of 5 m, and then with the advent of differential GPS (DGPS) resolution increased to the sub-metre scale.

Beyond knowledge of absolute geographic position, an important consideration in the thesis was the definition of relative positions within a channel-levee system (Figure 2.2), including such features as levee flank, levee crest, etc. Throughout the thesis, a right-handed coordinate system was used, having the positive x-axis pointing downslope. The axis of the modern channel, selected either as the midpoint of the channel or the deepest point within the channel, defined the origin of the y-axis. In this coordinate system, the z axis was positive upward. For a channel that slopes southward, the positive y-axis points east, the negative y-axis points west. Some phrases used throughout the thesis include: 1) across-levee, meaning increasing distance from the channel axis perpendicular to channel trend; and 2) across-channel, generally referring to differences in a parameter on one side of the channel as compared with the opposite or conjugate side of the channel.

The bathymetrically highest point adjacent to the channel typically defines the levee crest (Figure 2.2). The levee crest also divides strata dipping toward the channel from strata dipping away from the channel. It, therefore, tends to be characterized by a near zero across-levee slope. Some, but not all, levee crests coincide with the position of maximum thickness of depositional sequences. A well-defined levee crest separates

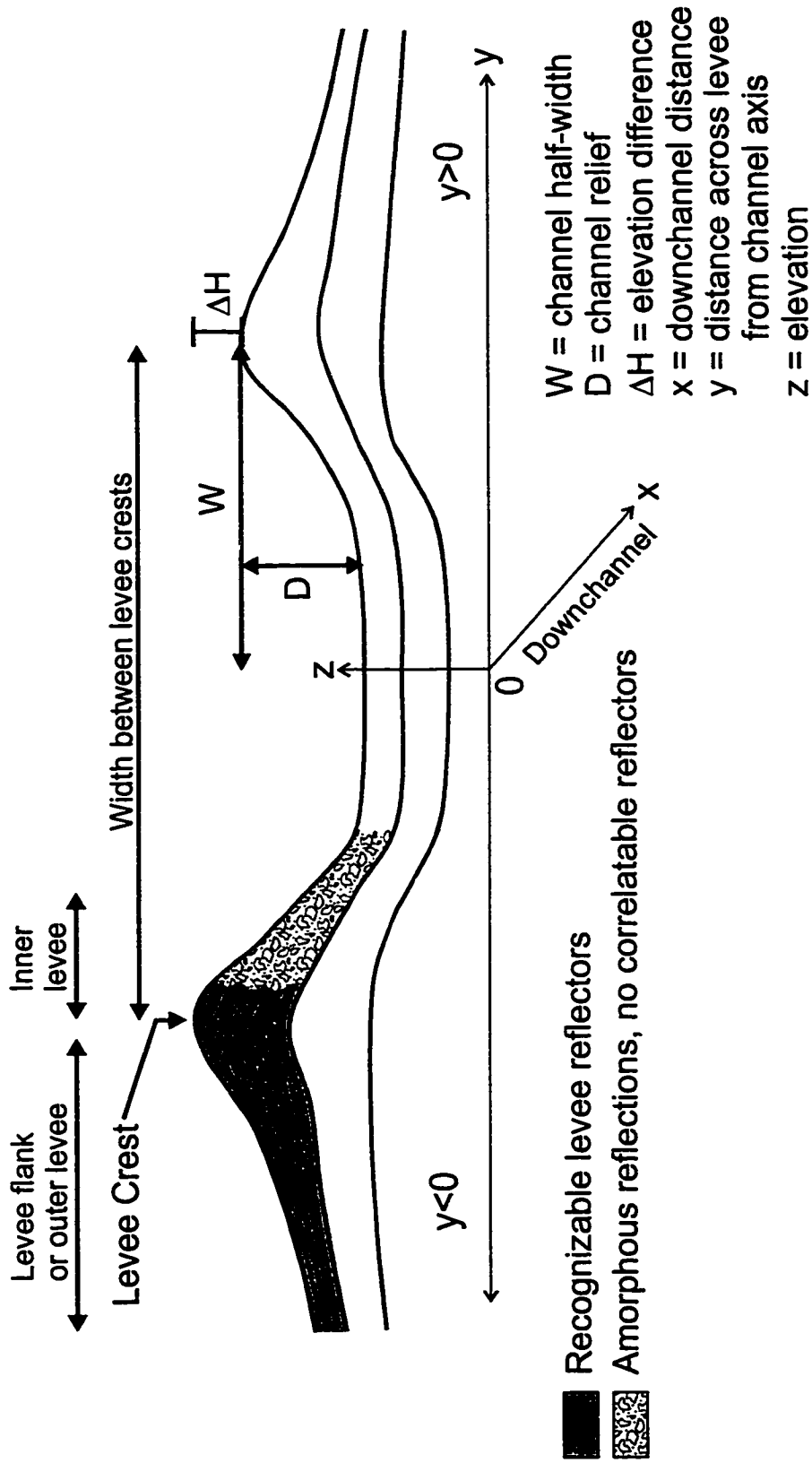


Figure 2.2. Generic cross-section of channel-levee system showing locations of levee flank or outer levee, levee crest, and inner levee. Also shown are the definitions of various parameters describing the morphology of the channel and the coordinate system used in the thesis. The elevation difference, ΔH , represents the difference in the elevation of conjugate levee crests.

strata that dip in opposite directions; thus in many cases levee sediments can be followed for many kilometres from the levee crest to the channel not changing their character until near the channel. This region between the levee crest and the channel has been termed the inner levee (Figure 2.2). The outer levee or levee flank denotes the region distal from the levee crest (Figure 2.2).

2.3.2 Channel Morphology

Channel morphology was generally parameterized by downchannel slope, relief, depth, half-width, and asymmetry. Slope is reported in units of metres per kilometre and calculated as the change in elevation between two points divided by the horizontal distance between them. Channel relief is the elevation difference between the channel floor and the levee crest. Channel depth corresponds to the average of the channel relief taken from opposite sides of the channel. Channel half-width, W (m), represents the distance the levee crest and the channel axis. Asymmetry in the elevation of conjugate levee crests was reported in two ways: 1) as the elevation difference between conjugate levee crests, ΔH (m); and 2) as the elevation difference divided by the distance between conjugate levee crests, yielding what is often termed the cross-channel slope, ∇H (m km^{-1}) (e.g., Bowen et al., 1984).

2.3.3 Depositional Sequence Thickness

The calculation of depositional sequence thickness, η (m), proceeded in three steps. The first step was simply to calculate the difference in two-way travel time between reflector horizons. Half of this time multiplied by an estimate of the velocity of sound in the sediments produced an estimate of depositional sequence thickness in metres. Typically, a value of 1500 m s^{-1} was used to convert two-way travel time to depth. In some cases, the velocity structure of the sediment column was supported by measurements on sediment samples which confirmed the use of an average velocity of 1500 m s^{-1} .

The final step in calculating the thickness of a depositional sequence was the removal of the thickness of hemipelagic and pelagic sediments. It was assumed that for any one cross-section the hemipelagic and pelagic contribution to the thickness of a depositional sequence was uniform across the levee. Pelagic and hemipelagic

sedimentation represent settling of particles from the overlying water column and no immediate reason exists for the thickness of such sediments to systematically vary with distance from a submarine channel. Different methods were employed to estimate the absolute magnitude of hemipelagic and pelagic sediments, including the use of recent sedimentation rates, the investigation of sediment cores, and the analysis of seismic facies. Because no single method was employed, the presentation of each system includes a discussion of how the hemipelagic sediments were accounted for in the calculation of depositional sequence thickness. Of note, however, is that they rarely accounted for more than 20% of the stratigraphic succession.

2.3.4 Sediment Wave Morphology

The morphology of sediment waves was parameterized by four measurements (Figure 2.3). As with any wave, a sediment wave can be characterized by a wavelength, L_{sw} (m), and amplitude, B (m). Wavelength was calculated as the distance between crests or troughs of the sediment waves. This measurement was denoted apparent wavelength when the orientation of the seismic profile could not be placed unequivocally at right angles to the orientation of the wave crests. When dealing strictly with the surface expression of these features, the collection of high-resolution bathymetric data rectifies this problem; however, when looking at the stratigraphic evolution of sediment waves, precise imaging of their geometry requires three-dimensional seismic data, a technique not yet applied to the study of sediment waves. The wavelengths reported for sediment waves are principally apparent wavelength measured from trough to trough or crest to crest on seismic profiles. Wave amplitude was calculated as half the vertical distance between crest and trough. A third measurement for characterizing sediment waves is the SRR (sedimentation rate ratio) which was defined by Flood (1988) as the ratio of sediment thickness at one-quarter and three-quarters of a wavelength, respectively (Figure 2.3). This measurement, along with wave amplitude, is required by Flood's (1988) lee wave model for sediment wave development. The final measurements on sediment waves quantify the character of sediment wave propagation. Most important of these is the distance that individual troughs, Δx_t (m), or crests, Δx_c (m), move between overlying and underlying sediment waves giving some indication of the amount of migration. Both

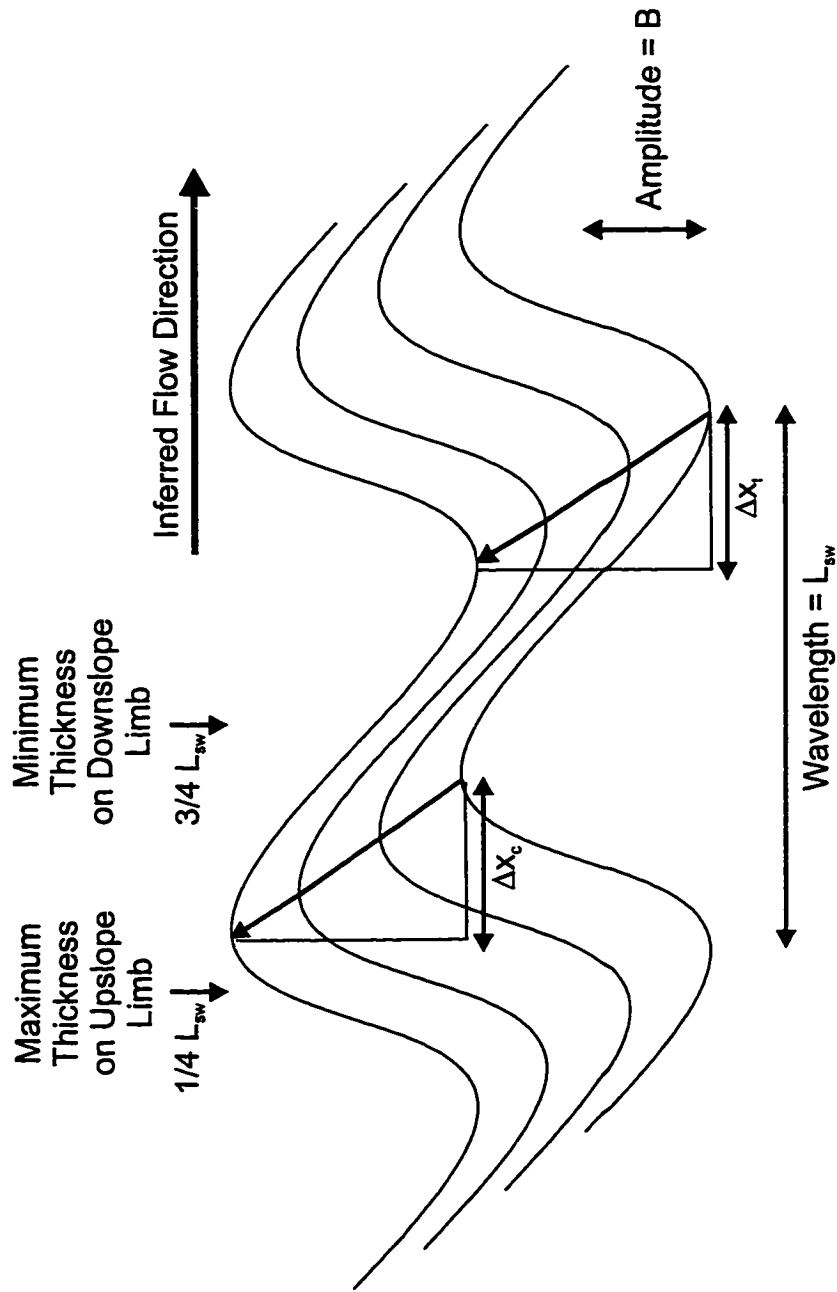


Figure 2.3. Profile of sediment waves defining architectural measurements including, wavelength, amplitude, and migration. The minimum thickness on the downslope limb divided by the maximum thickness on the upslope limb defines the sedimentation rate ratio (SRR) used in Flood's (1988) model for sediment waves.

the antidune model of Normark et al. (1980) and the lee wave model of Flood (1988) predict upstream migration of actively developing sediment waves. Quantifying this migration delineates the stratigraphic intervals when sediment waves were actively migrating and may help to differentiate between the two models explaining their formation.

2.4 Statistical Analysis

Depositional sequences tend to thin perpendicular to channel trend according to a concave-upward function of distance from the channel axis. The variations in depositional sequence thickness, after removal of hemipelagic and pelagic sediments, were fit to an exponential model that has the form

$$\eta(y) = \eta_0 e^{ky} \quad (2.3)$$

where η (m) is depositional sequence thickness, η_0 (m) is depositional sequence thickness $y = 0$, y (m) is distance from the channel axis, and k (m^{-1}) is the exponential decay constant. In such a coordinate system, η_0 is not an observable quantity as it represents the thickness of the depositional sequence at the channel axis, which by definition has no levee sediments. However, (2.3) can be used to predict the value of η for any value of y , namely the levee crest, y_{lc} . Note that the levees tend to show thinning away from the channel axis. Consequently, k is positive for negative y and k is negative for positive y .

Characterization of thickness patterns perpendicular to channel trend using the exponential model has been employed throughout the thesis. Theoretically, exponential-thinning occurs because deposition from a steady-uniform flow can be described as a first-order rate process, having an exponential solution (e.g., McCave & Swift, 1976). The exponential model was also chosen because of the ease with which it can be manipulated, i.e., continuously differentiable, and the potential process information contained within the decay constant. Beyond these theoretical and analytical considerations, the initial data analysis of NAMOC and Hueneme Fan appeared to favour the exponential model, suggesting its use in more complex systems investigated later like Laurentian Fan.

In some cases, the exponential trend in thickness variations is obvious not only from visual inspection of plots but also in the statistical analysis of these variations. In

other cases, thickness trends can be fit to an exponential model while visually these patterns may look linear or appear to be composed of a small number of linear segments. A third possibility is that the thickness patterns are highly variable and therefore cannot be fit to any model or that thickness patterns show almost no variability, i.e., depositional sequences have a uniform thickness, not producing a statistically significant regression. Sources of error in the fitting of an exponential model to the thickness variations include: 1) small thickness variations relative to the horizontal extent of the seismic data; 2) difficulties in correlating reflectors toward the channel; and 3) resolution limits of seismic data, especially airgun data, with respect to imaging depositional sequences and assessing erosion. The appropriate statistic for comparing different models is the F-score which measures the ratio of the mean square of the regression to the mean square of the residuals (Davis, 1986). Critical values of F depend upon significance level of the regression and the number of degrees of freedom (i.e., $n-2$, where n is number of observations). Both exponential and linear fits can be significant, i.e., $p < 0.05$, but the value of F provides a basis for choosing one model over another. For example, in deciding between an exponential fit and a linear fit, the one with the larger F-score would be chosen. If the F-scores do not differ, then there is no statistical reason for choosing one model over another. The comparison between the F-scores for the linear model, F_{lin} , and those for the exponential model, F_{exp} , show that the F_{exp} is equal or greater than F_{lin} , suggesting that there is either no difference between the two models or that the exponential model is favoured (Figure 2.4).

In order to calculate the parameters, η_0 and k , needed in (2.3), linear regression was performed on the natural logarithm of (2.3) or

$$\ln \eta = \ln \eta_0 + ky \quad (2.4)$$

using SPSS for Windows 3.1. For linear regression, the SPSS output includes several parameters besides the values of the regression parameters. It also reports the standard error of the regression parameters, the p value for the parameters, and the correlation coefficient. The equations for linear regression and estimation of errors based on confidence limits were taken from Hamilton (1992).

Linear regression estimates the value of k using

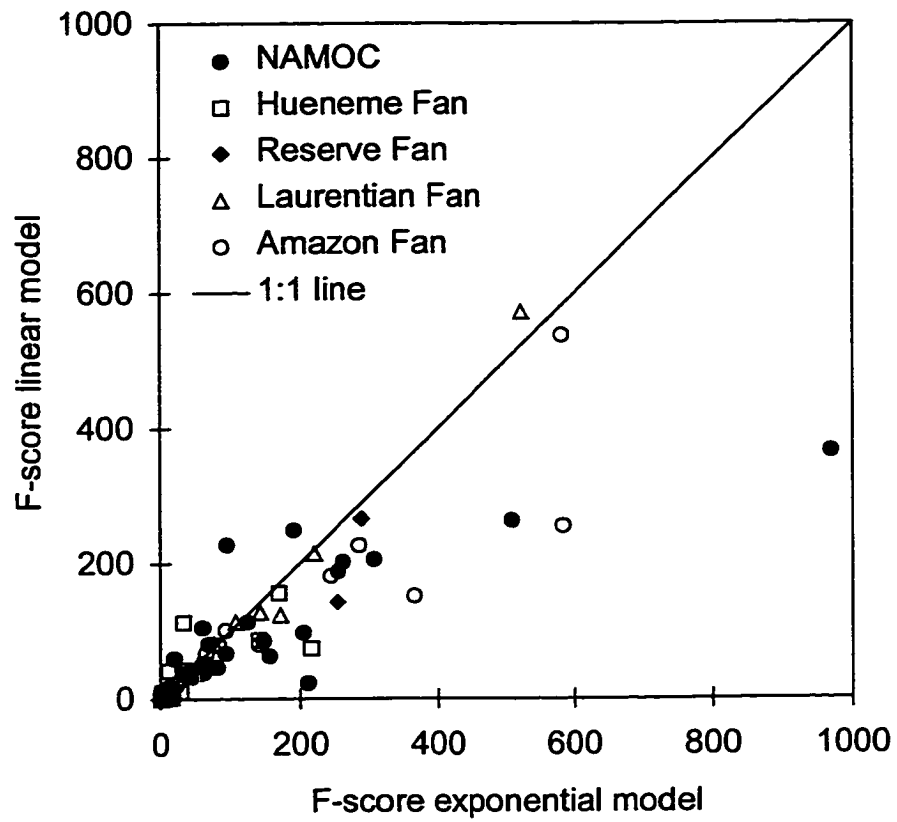


Figure 2.4. Comparison of F-score between linear model and exponential model. Comparison shows that, in general, there is either no significant difference between the models or that the exponential model is favoured.

$$k = \frac{\sum y(\ln \eta) - \left[\frac{\sum y \sum \ln \eta}{n} \right]}{\sum y^2 - \left[\frac{(\sum y)^2}{n} \right]} \quad (2.5)$$

and the value of $\ln \eta_0$ using

$$\ln \eta_0 = \bar{y} - k \cdot \overline{\ln \eta} \quad (2.6)$$

where the overbars denote mean values, and n is the number of data points. These equations provide estimates for the parameters, k and η_0 , which can be used to produce estimated values for y . An indication of the degree to which the regression parameters provide a reasonable description of the data is reported as the correlation coefficient, r , which is calculated according to

$$r^2 = 1 - \frac{\sum (y - \hat{y})^2}{\sum (y - \bar{y})^2} \quad (2.7)$$

where \hat{y} is the estimated value of y from the regression equation. The value of r^2 reports the amount of variance explained by the regression.

Another method for assessing the regression parameters is to calculate their standard errors and from these confidence intervals. The standard error of the regression parameters is found first by calculating the standard error of the residuals given by

$$s_e = \left(\frac{\sum (y - \hat{y})^2}{n - 2} \right)^{1/2} = \left(\frac{SSR}{n - 2} \right)^{1/2} \quad (2.8)$$

For the slope of the regression line, k , the standard error is

$$s_k = \frac{s_e}{\sqrt{SSY}} \quad (2.9)$$

where

$$SSY = \sum y^2 - \left[\frac{(\sum y)^2}{n} \right] \quad (2.10)$$

while for the intercept of the regression line, the standard error is

$$s_y = s_e \left(\frac{1}{n} + \frac{\bar{y}}{\sqrt{SSY}} \right)^{1/2} \quad (2.11)$$

The confidence interval around the regression parameter is, using k as an example,

$$k \pm t_{\text{crit}} s_k \quad (2.12)$$

where t_{crit} is the critical value of the t-statistic for the specified degrees of freedom and chosen confidence interval. At the 95% confidence level, $t_{\text{crit}} = 1.96$ for infinite degrees of freedom while $t_{\text{crit}} = 2$ for 60 degrees of freedom and it equals 2.086 for 20 degrees of freedom (e.g., Hamilton, 1992).

Throughout the statistical analysis of the thickness data, a 95% confidence level was used with the null hypothesis stating that the regression parameter was equal to zero and the alternative hypothesis stating that the regression parameter was not equal to zero. To reject the null hypothesis, i.e., calculate a regression parameter that is significantly different from zero, at the 95% confidence level the calculated value of p had to be less than 0.05. In cases where the null hypothesis could not be rejected, the value of k was found to be not significantly different than zero. These cases could mean that depositional sequence thickness is truly uniform with distance from the channel or entirely irregular. It could also mean that the rate of decay was so small that the seismic data did not extend to sufficient distances from the channel to capture this behaviour; consequently, the depositional sequences only appear to be uniform. Operationally, values of k on the order of 10^{-7} m^{-1} or less would not be differentiated from uniform sedimentation. At such small values of k , the lengthscale for changes in sediment thickness is several thousand kilometres. Even if seismic data existed over such lengthscales, theoretically allowing for the measurement of thickness variations, it is unlikely that deposition from an overbanking turbidity current would be the only operative depositional mechanism.

For significant statistical fits of the data, the 95% confidence interval around the regression parameter was used to depict uncertainty in the parameter. In the plots of depositional sequence thickness presented in the following chapters, the data are plotted as circles with five lines (Figure 2.5): the regression line, confidence intervals, upper and lower; and prediction intervals, upper and lower. The regression line uses the estimated regression parameters. The prediction interval around the regression represents the confidence that the regression parameters can predict individual values of thickness at a

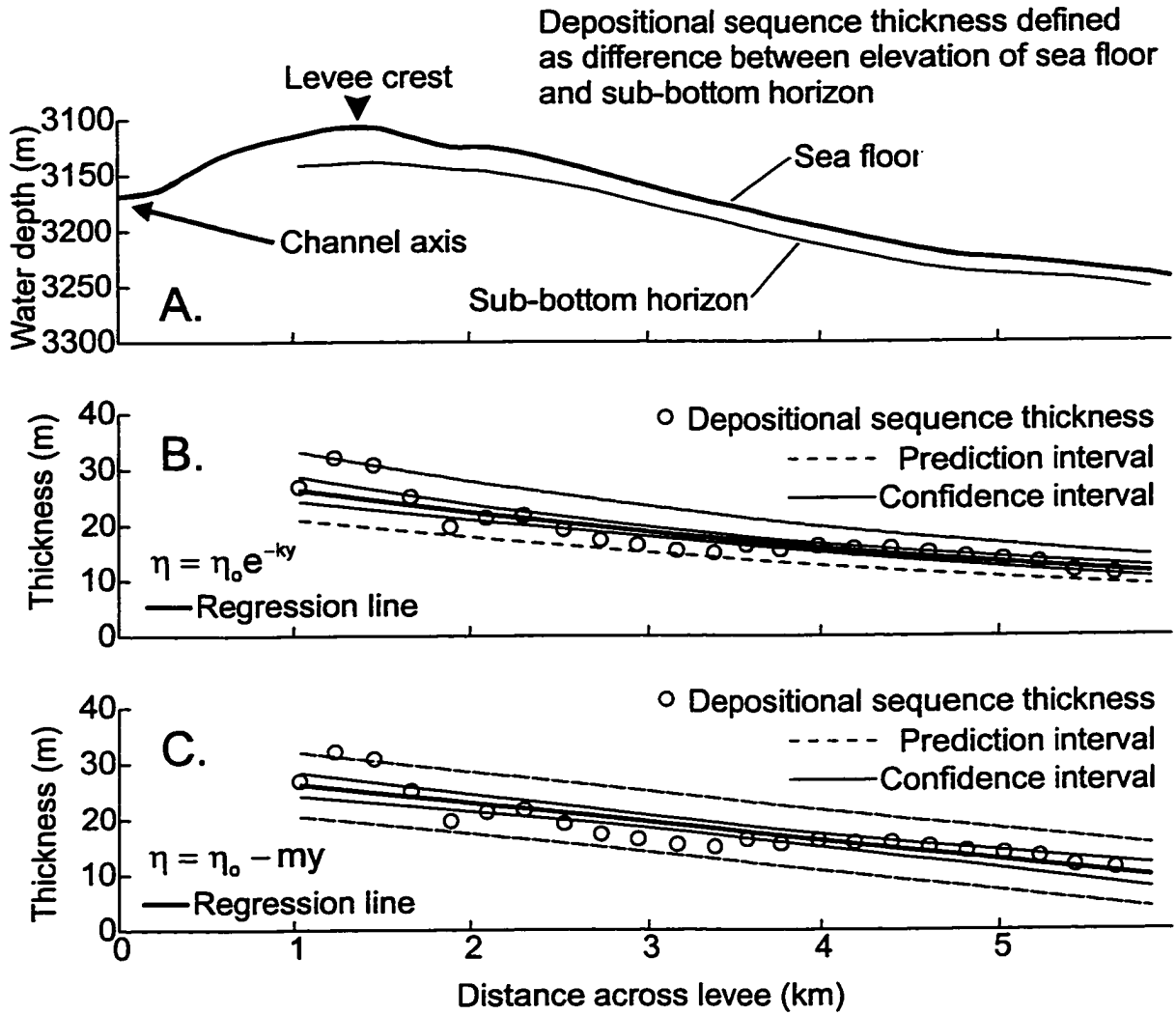


Figure 2.5. Sample plots of thickness data: A. Interpreted line drawing of 3.5 kHz profile across Amazon Channel near Ocean Drilling Program Site 940; B. Thickness data plotted with exponential fit; C. Thickness data plotted with linear fit.

given value of y . Like the confidence interval on the regression parameters, the confidence intervals around the regression line follow the equation,

$$\hat{y} \pm t_{\text{crit}} \cdot SE_y \quad (2.13)$$

where t_{crit} is again the critical value of t at the chosen confidence level for the specified degrees of freedom. To calculate the prediction intervals, SE_y has the form

$$SE_y = s_e \left(1 + \frac{1}{n} + \frac{(y - \bar{y})^2}{SSY} \right)^{1/2} \quad (2.14)$$

The confidence intervals reflect the ability of the regression parameter to predict the mean value of thickness. To calculate the confidence intervals, SE_y has a slightly different form given by

$$SE_y = s_e \left(\frac{1}{n} + \frac{(y - \bar{y})^2}{SSY} \right)^{1/2} \quad (2.15)$$

Figure 2.5 displays data from a high resolution 3.5 kHz profile across the eastern levee of Amazon Fan. Figure 2.5a shows an interpreted line drawing of the data while Figure 2.5b and Figure 2.5c show the plot of depositional sequence thickness versus distance from the channel axis as well as exponential and linear fits to these data. In Figure 2.5b and Figure 2.5c, the data points are plotted as open circles. The bold solid line represents the regression equation. The thin solid lines depict the upper and lower confidence limits on the regression and the dashed lines depict the upper and lower prediction intervals. Visual inspection of the thickness data might suggest that the data are as well represented by the linear model (Figure 2.5c) as they are by the exponential model (Figure 2.5b). For both the exponential model and the linear model, the regression parameters were significant, i.e., $p < 0.05$, with $r = 0.93$ for the exponential model and $r = 0.88$ for the linear model, suggesting that the exponential model better describes the data than the linear model. As mentioned, a more statistically meaningful comparison of the degree to which the models describe the data is the F-score. The larger this value, the more accurately the regression describes the variations in the data. For the example in Figure 2.5, the F-score for the exponential model is 136.6 while for the linear model it is 78.8, supporting the contention that the exponential is a statistically better fit to the data.

The regression parameters in the following chapters are reported with error estimates representing the 95% confidence limit. In this example (Figure 2.5), the regression was conducted on 24 data points leaving 22 degrees of freedom. The estimated value of k and η_0 for the exponential model are $-17.9 \times 10^{-5} \text{ m}^{-1}$ and 32.0 m, respectively. The critical value of t for this number of degrees of freedom is 2.074. The standard error for k was $0.15 \times 10^{-5} \text{ m}^{-1}$ so that the 95% confidence limits around k are $\pm 2.074(0.15 \times 10^{-5}) \text{ m}^{-1}$ or $\pm 0.31 \times 10^{-5} \text{ m}^{-1}$. The standard error for the y-intercept, η_0 , was 1.83 m so that its confidence limits are $\pm 2.074(1.83) \text{ m}$ or $\pm 3.80 \text{ m}$.

Another common set of plots used in the thesis shows an architectural parameter versus downstream distance or stratigraphic position (Figure 2.6). These plots are especially useful in summarizing the behaviour of a parameter within a system. Each data point is plotted with its error bars denoting the 95% confidence interval around the parameter estimate. Visual inspection of such plots allows for a qualitative assessment of trends. For no system does more than a handful of data points exist to characterize any trend; consequently, statistical analysis of trends was not warranted.

2.5 Characterizing the Large-scale Structure of Channel-Levee Systems

The major data for characterization of levee architecture comprise seismic profiles. In the ideal case, downchannel variation in channel morphology and levee architecture would be quantified over the entire length of a submarine channel. Parameterization of levee architecture at particular locations downchannel includes a spatial decay constant, k , and the thickness of sediment at the levee crest, η_{lc} , for individual depositional sequences. These parameters extend the quantifiable variables of channel-levee morphology to include characterization of levee architecture. Typical variables of channel morphology were also measured including relief, half-width, radius of channel curvature, and slope. Where correlation of horizons could be made across the channel, the elevation difference, ΔH , and the difference in depositional sequence thickness at the levee crest, $\Delta \eta_{lc}$ were also quantified.

For modern channels, echosoundings are sufficient to delineate the present bathymetry and are all that is necessary for the characterization of channel morphology and the difference in elevation between conjugate levee crests. On the other hand,

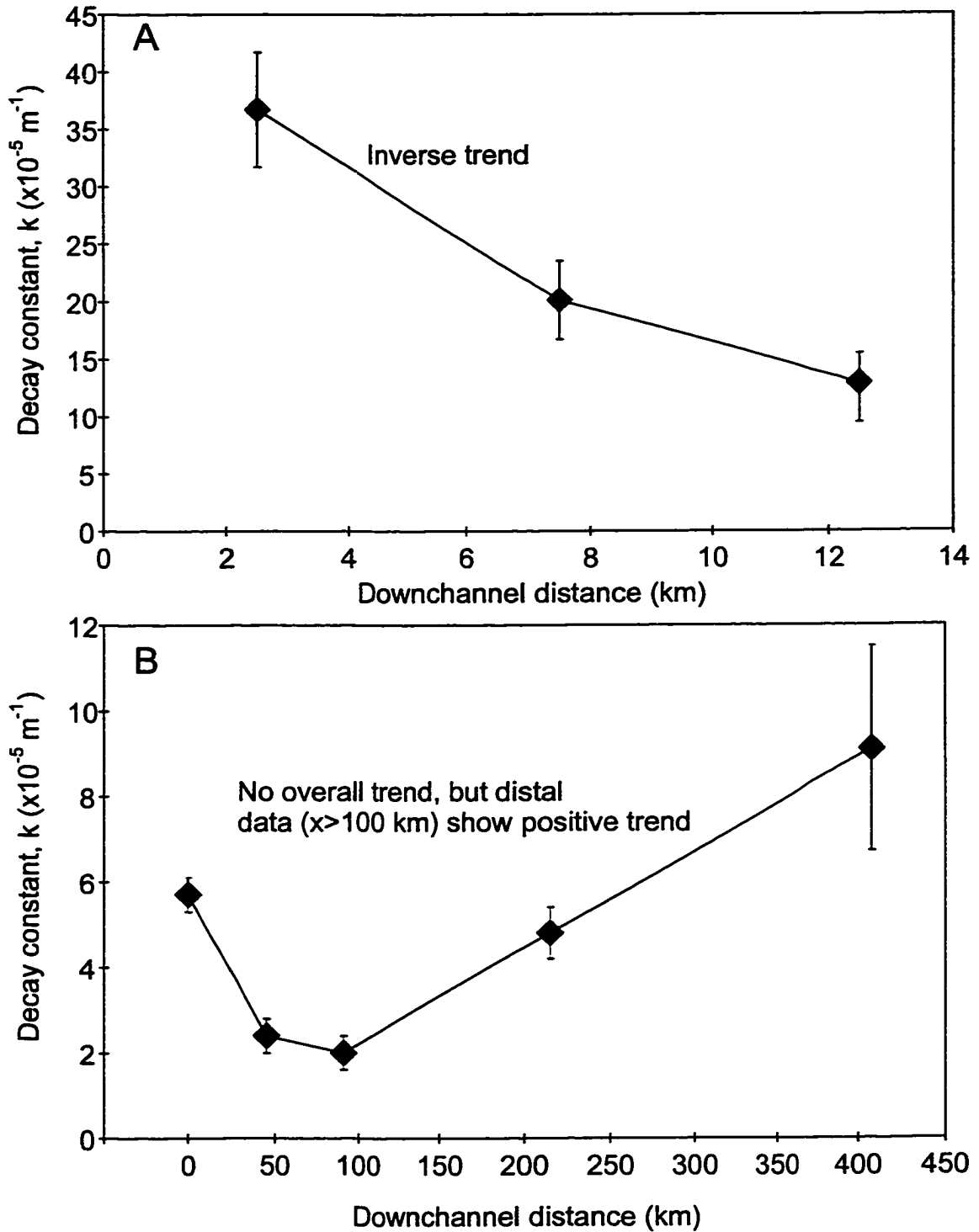


Figure 2.6. Sample plots of trend data showing the downchannel variation in the across-levee spatial decay constant, k , which parameterizes the variations in thickness of depositional sequences perpendicular to channel trend: A. Hueneme Fan and B. NAMOC. The error bars denote the 95% confidence limits on k .

quantitative data on levee architecture require acoustic profiles that image the sub-bottom. Furthermore, to enable meaningful downchannel comparisons, the development of acoustic stratigraphies that could be widely correlated was necessary. However, neither the distribution of available data nor their quality allowed for the complete characterization of the downchannel structure of a submarine channel-levee system. Figure 2.7 schematically depicts the location and horizontal extent of detailed data from each of the systems studied in this thesis. Note the relative position of the detailed data within the overall structure of a generic submarine fan system (canyon, channel-levee, and depositional lobe). For example, the data from NAMOC cover over 400 km of the channel length but only encompass a small portion of the overall system. Data from Hueneme Fan cover about 20 km, but these data encompass a significant portion of this small sandy fan. In addition, the data from NAMOC, for example, sample the upper reaches of the channel-levee system while the data from Hueneme Fan extend to the depositional lobe.

The strategy for investigating channel-levee architecture follows from the limitations imposed by the available data. Downchannel patterns in architectural parameters were sought when looking at individual systems, but not without regard for the relationship that these parameters have in the general setting of the data with respect to distance along the system in question. Consequently, given that detailed data exist along various reaches of a channel-levee system, it was possible to construct a generic pattern for channel-levee architecture, encompassing the entire extent of a channel-levee system. Not only patterns in individual architectural parameters were sought but also the relationship between parameters. The data cover systems sampling a wide range of geological environments. Consequently, relationships between parameters likely reflect underlying physical controls rather than local effects.

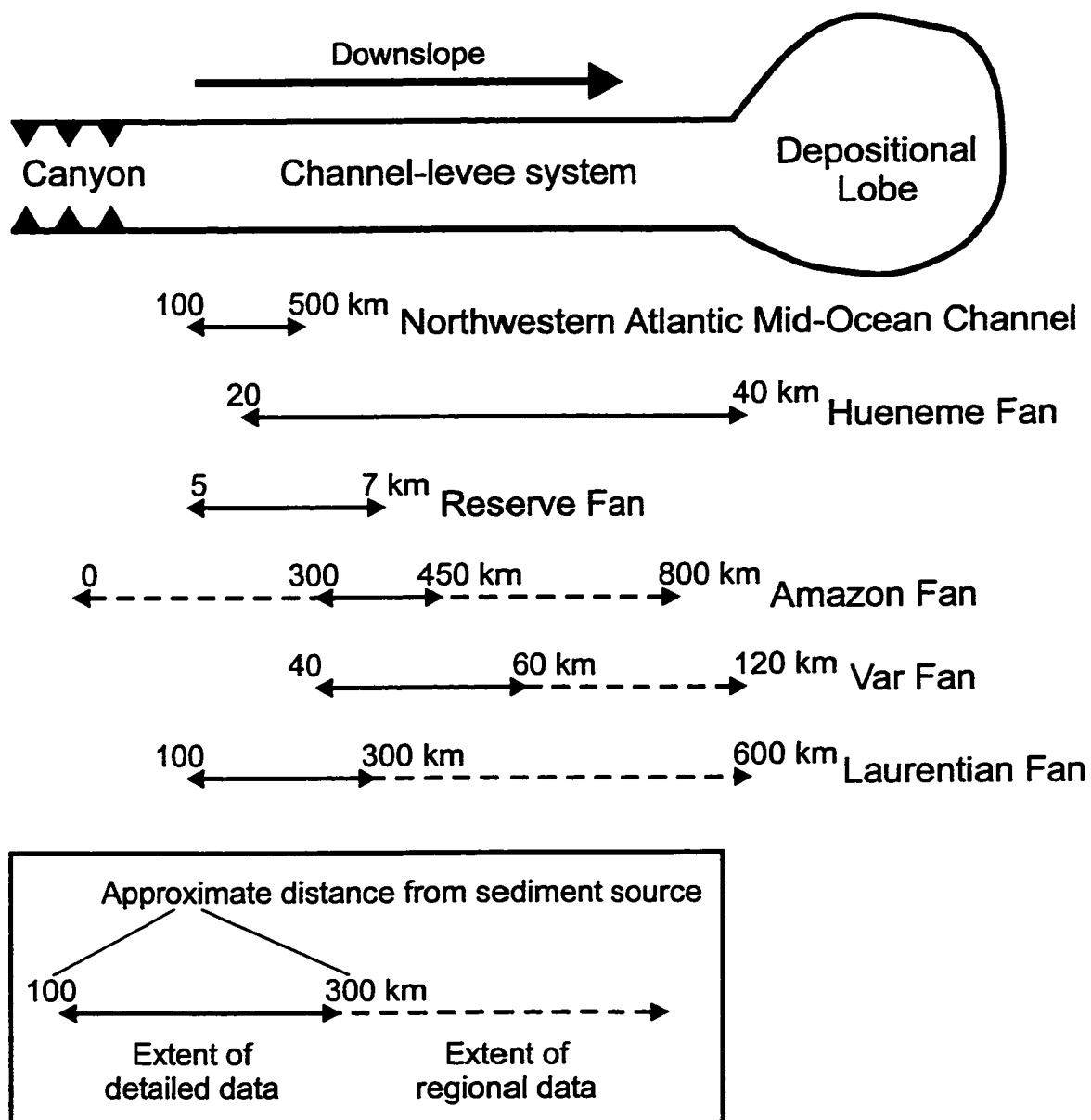


Figure 2.7. Schematic representation of a submarine fan system showing the approximate downchannel extent of data investigated in this study. Solid lines depict the length of individual systems that were studied in detail while the dashed lines depict the length of the system covered by regional data reported in the literature or investigated by the author. Reaches with detailed data refer to locations where a stratigraphy could be defined and correlated along the channel with reasonable confidence. In the regional data only general correlations could be made, it therefore lacks an exact stratigraphy. The distances associated with each system represent approximate distances from the inferred sediment source.

Chapter 3

Levee Architecture of NAMOC

3.1 General Statement

The Northwest Atlantic Mid-ocean Channel (NAMOC) traverses the Labrador Sea from the base of the continental slope off Hudson Strait southward to the Sohm Abyssal Plain (Figure 3.1). The system has low sinuosity and a low bathymetric gradient, leading Klaucke (1995) to identify it as a third end-member in the classification scheme of Clark et al. (1992). In cross-section, NAMOC displays asymmetric levees whose long-term growth is imaged by acoustic profiles. NAMOC provides the opportunity to study levee growth from a glacially-fed system which is of the same size as better known fluviially-fed systems like Amazon Fan (e.g., Manley & Flood, 1988). The ease with which cross-channel correlations of acoustic data can be made provides insight into the behaviour of conjugate levees and possible constraints on flow character that differences in the growth patterns on opposite sides of the channel may provide. Furthermore, the presence of a stable channel bifurcation along the upper reach of NAMOC provides the opportunity to investigate the behaviour of a relatively simple spillover channel.

3.2 Data Set

The primary data set for the investigation of levee growth on NAMOC consists of high resolution 3.5 kHz acoustic profiles, supplemented by sidescan sonar, shallow piston cores, and airgun seismic profiles (Figure 3.2) made available by GSC (Atlantic) and McGill University. Data coverage is somewhat sparse but excellent continuity of reflectors in 3.5 kHz data allowed for widespread correlation of up to five subbottom horizons. Re-interpretation of airgun seismic profiles has led to slightly different correlations of the acoustic stratigraphy originally developed by Klaucke (1995). Deep seismic reflection profiles have been interpreted by Myers & Piper (1988). Shallow subsurface stratigraphy sampled by piston cores was initially investigated by Chough & Hesse (1980) and subsequently by Hesse et al. (1987), Hesse (1995), and Wang & Hesse (1996). Klaucke (1995), Klaucke & Hesse (1996), and Hesse et al. (1996) reported on the results of sidescan sonar data collected in 1993, groundtruthed by available piston cores and 3.5 kHz acoustic profiles. Resolution of the 3.5 kHz data is better than 0.5 m while

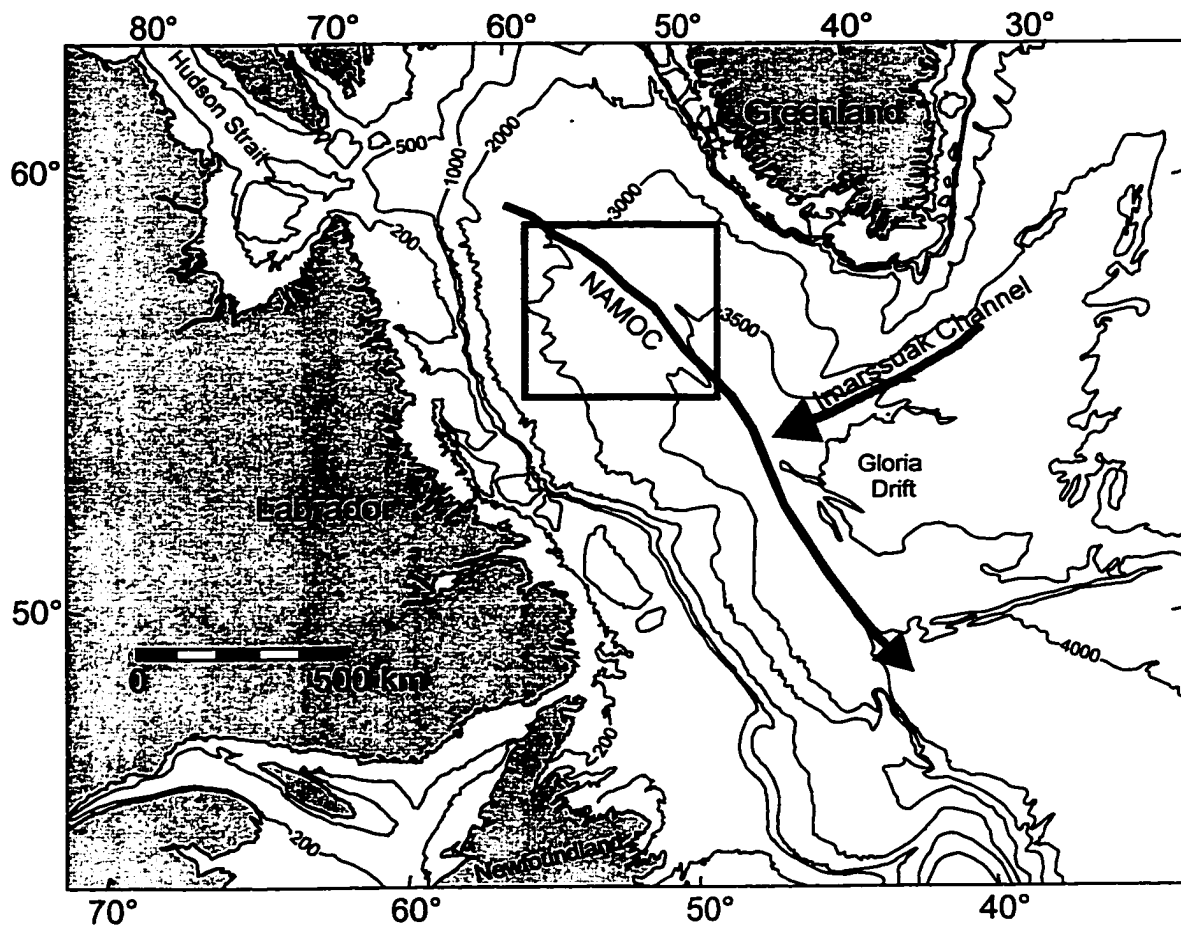


Figure 3.1. Bathymetric map of the Labrador Sea showing trend of NAMOC and location of study area. NAMOC continues southward of the region shown in this map, covering a total distance of about 4000 km.

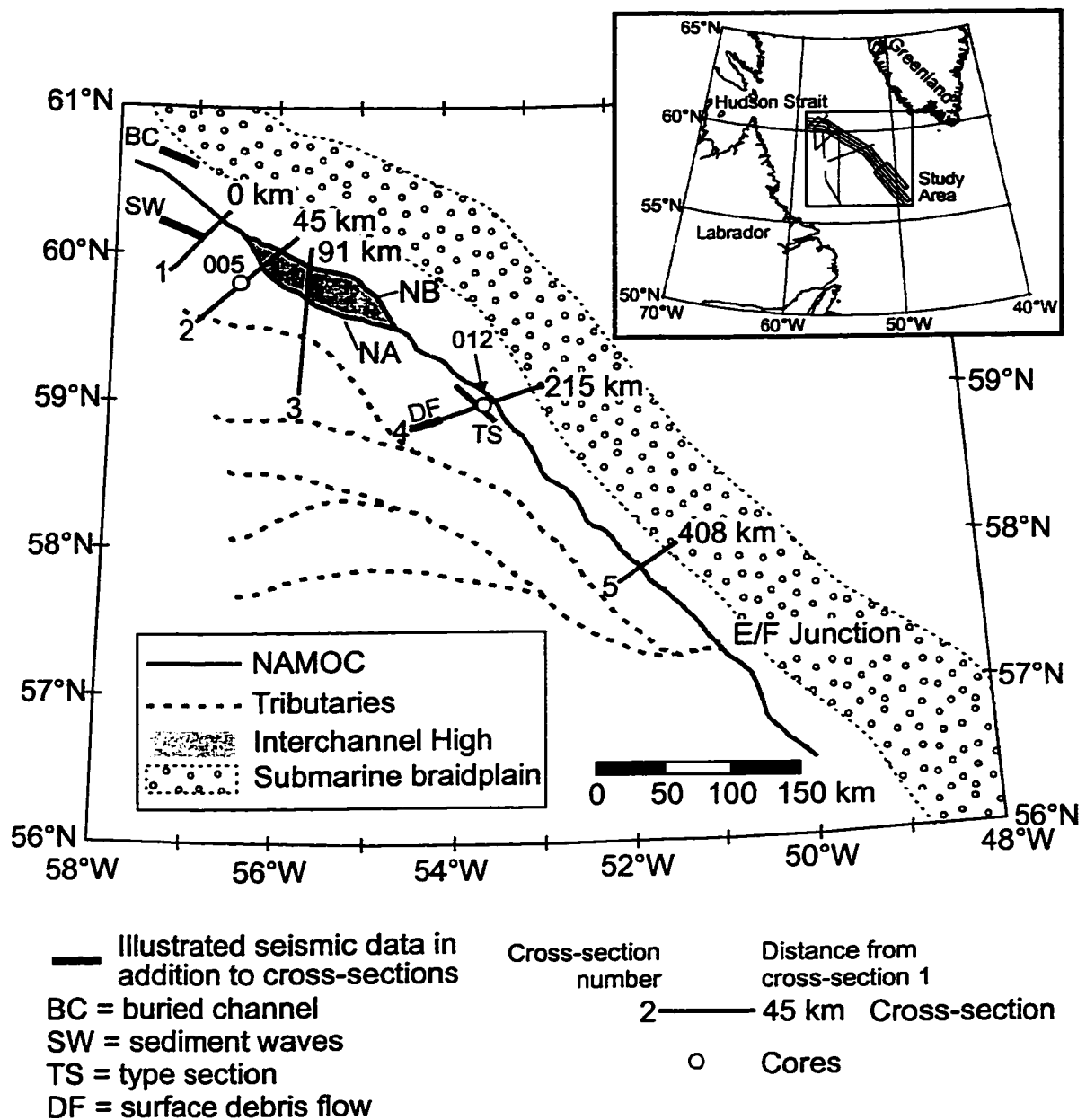


Figure 3.2. Generalized channel patterns draining the slope off Hudson Strait and Labrador Slope (after Klaucke, 1995) and distribution of acoustic data and cores available for this study. Also shown is the approximate extent of the submarine braidplain east of NAMOC, identified by Klaucke (1995). Inset shows general location of study area and regional seismic data used in this study.

resolution in the airgun data ranges from 10-20 m.

3.3 Setting of NAMOC

3.3.1 Channel Morphology

NAMOC is approximately 4000 km long (Figure 3.1), stretching from the base of the slope off Hudson Strait southward to the Sohm Abyssal Plain (Hesse et al., 1987). Based on recently collected sidescan sonar, Klaucke (1995) subdivided NAMOC into three sections based on channel sinuosity: a 350 km upper reach possessing low sinuosity (1.01-1.05) with little variation, a 700 km middle reach having low sinuosity (1.01-1.14), but moderate variations in sinuosity, and a 1050 km lower reach characterized by sinuosities ranging from straight (1.0) to meandering (almost 1.5). The relatively unchanging values of sinuosity in the upper reach led Klaucke (1995) to suggest that this section of NAMOC had reached an equilibrium with the hydrodynamics of the turbidity currents flowing through the channel. The merging of tributaries draining the Labrador Slope (Figure 3.2) played a role in the morphological development of the middle reach of NAMOC (Klaucke, 1995). The morphology of the lower reach of NAMOC is partially to completely controlled by pre-existing bathymetric relief (Klaucke, 1995). The present study focuses on the upper reach of NAMOC north of the E/F tributary junction (Figure 3.2).

The equilibrium channel (term from Klaucke, 1995) possesses radii of curvature ranging from 17-55 km and channel slopes on the order of 1 m km^{-1} , ranging from 1.5 to 0.5 m km^{-1} (Figure 3.3a, b). Channel depth varies from about 120-180 m generally decreasing over the upper 400 km of NAMOC (Figure 3.3b). The western levee (right-hand side looking downstream) is consistently higher than the eastern levee, with the elevation difference between conjugate levee crests averaging about 70 m over the upper 400 km of NAMOC (Figure 3.3c). Channel cross-sectional area decreases rapidly over the first 100 km from $1800 \times 10^3 \text{ m}^2$ to $600 \times 10^3 \text{ m}^2$ and then varies between $600 \times 10^3 \text{ m}^2$ and $800 \times 10^3 \text{ m}^2$ over the rest of the upper reach of NAMOC (Figure 3.3c).

Within the upper channel reach, NAMOC bifurcates into a western (NA) and eastern (NB) channel segment separated by a small interchannel high (Figure 3.2). The eastern channel segment is bathymetrically lower than the western segment, suggesting that it may be the preferred pathway for turbidity currents flowing through this section of

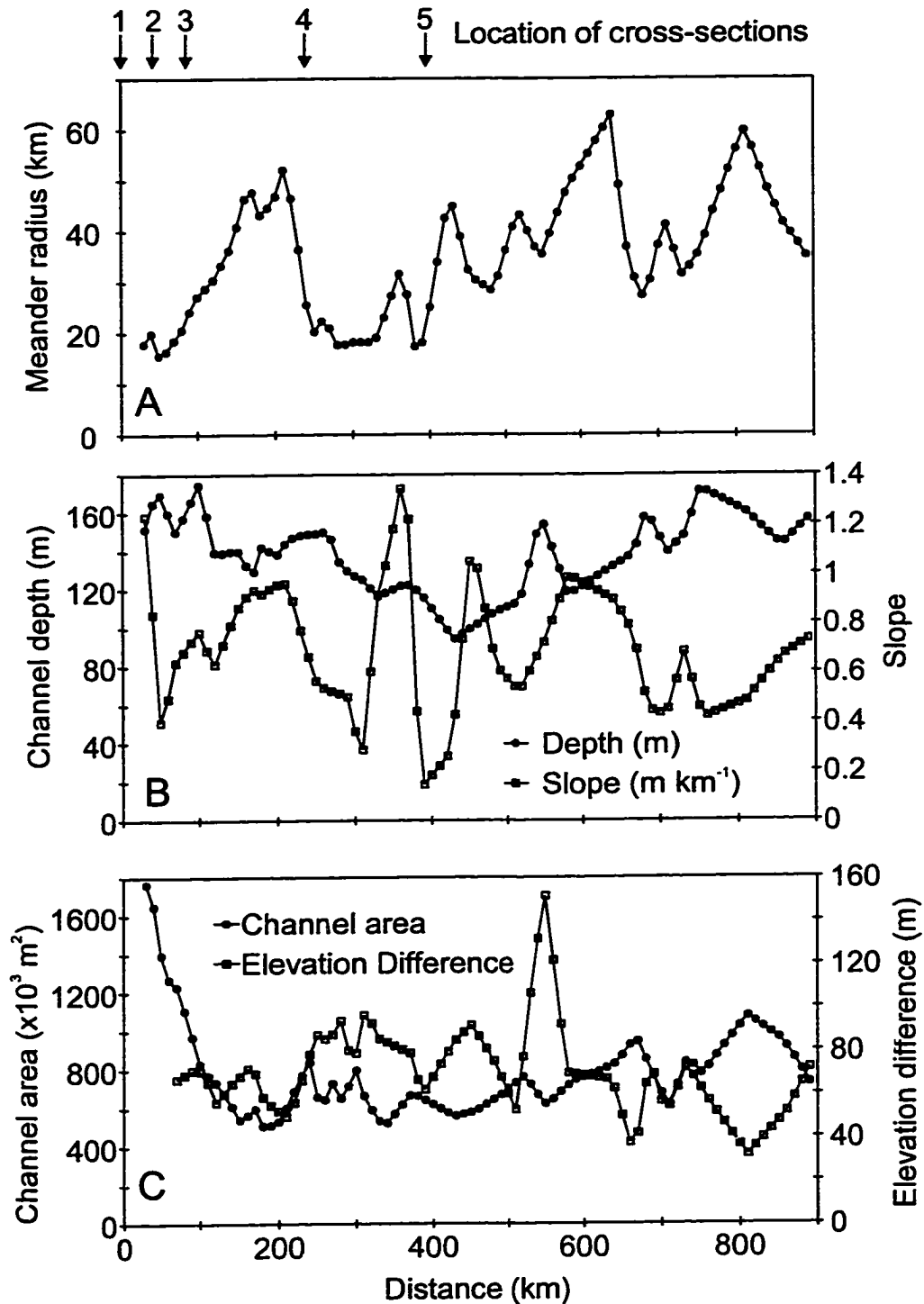


Figure 3.3. Profiles of channel morphology for NAMOC (data from Klaucke, 1995). A. Meander radius. B. Channel depth (filled circles) and channel slope (open squares). C. Channel cross-sectional area (filled circles) and the elevation difference between the western (right-hand) and eastern (left-hand) levees (open squares). The uppermost reach, less than 400 km, was termed the "equilibrium channel" by Klaucke (1995). Approximate downchannel location of cross-sections used to characterize levee architecture given by arrows at top of figure.

NAMOC. At the bifurcation point, the western channel may act like a spillover channel, tapping the upper portions of the main flow moving down the eastern channel segment. Klaucke (1995) hypothesized that the eastern branch may transport the coarsest grain sizes because of the elevation difference between the two branches and the concentration of the larger grain sizes near the base of the flow.

3.3.2 Previous Work on Geology of NAMOC

Recent work on the architecture of NAMOC has focused on the relative importance of sediment delivery through Hudson Strait and sediment derived from tributary channels draining the continental slope off Labrador and other deep-ocean channels (Imarssuak Mid-Ocean Channel or IMOC) (Hesse et al., 1987). In turn, some evidence exists for the separation of grain sizes at Hudson Strait with coarse sediment feeding a submarine braidplain east of NAMOC (Figure 3.2) and the finer-sediment maintaining NAMOC (Klaucke, 1995; Klaucke & Hesse, 1996; Hesse et al., 1996).

General Late Cenozoic Stratigraphy

Myers & Piper (1988) defined the deep seismic stratigraphy using low resolution airgun seismic profiles. These workers defined four regional reflectors of which the uppermost horizon, D, separates flat-lying, high amplitude discontinuous reflections from the channel-levee complex associated with NAMOC. Consequently, horizon D dates the beginning of channel-levee growth associated with NAMOC. Extrapolating dates from DSDP and ODP sites in the Labrador Sea, horizon D dates around mid-Pleistocene (Myers & Piper, 1988). Interpretation of higher resolution sleevegun seismic profiles led Klaucke (1995) to suggest that D does not represent an isochronous surface, becoming younger with distance down-channel. Such an interpretation suggests that NAMOC has prograded southward through the Pleistocene. Klaucke (1995) divided the sequence above D, as imaged in sleevegun records, into seven depositional sequences (Figure 3.4). The lowest five units have a consistent acoustic signature possessing a basal stratified unit and an overlying transparent unit. Unit F consists entirely of acoustically well-stratified sediment while the surficial unit, G, is acoustically transparent throughout. Table 3.1 summarizes the characteristic thickness of the acoustic units measured at both the western and eastern levee

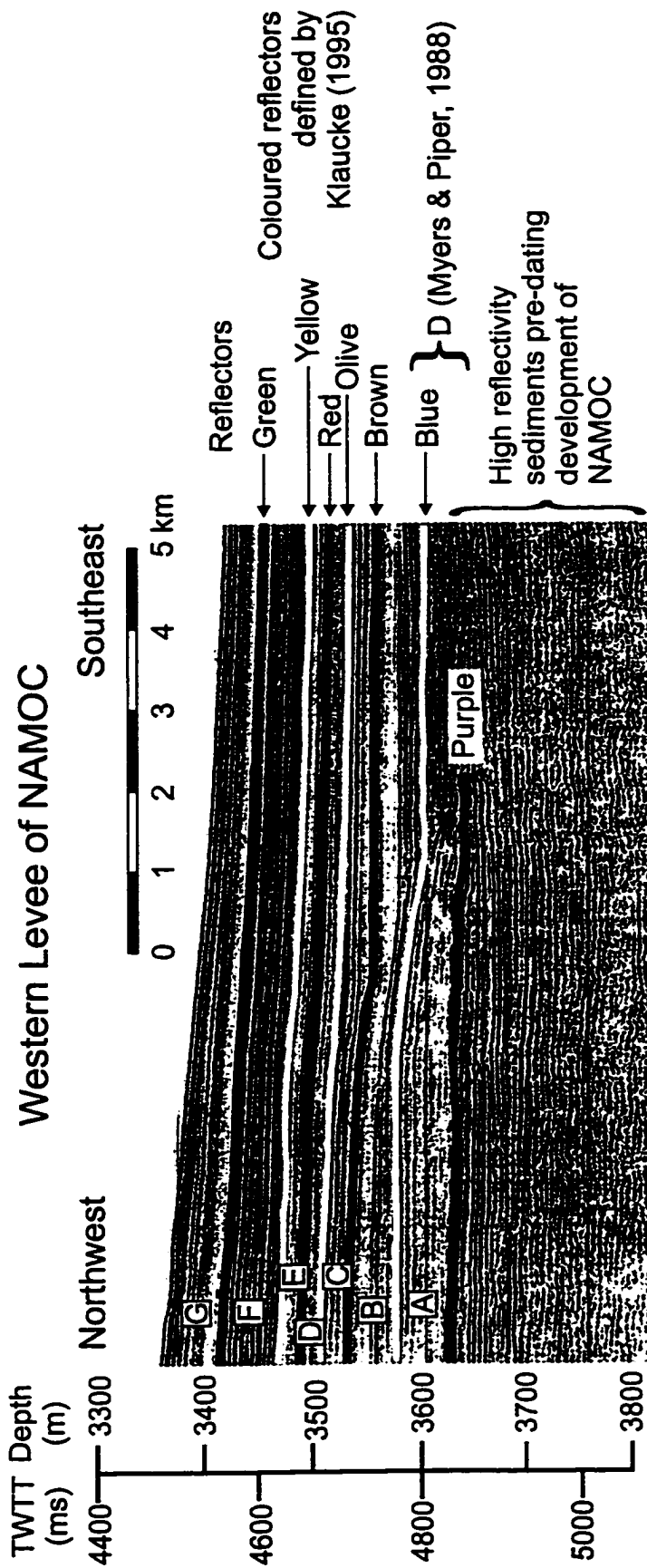


Figure 3.4. Airgun type section from western levee of NAMOC showing definition of reflectors (green, yellow, red, olive, brown, blue, and purple, in order of increasing subbottom depth) and depositional sequences (A to G). Location given in Figure 3.2. Transition between discontinuous, high amplitude reflections and more continuous reflections associated with the development of NAMOC occurs around horizon purple or blue. This same transition was identified as horizon D in lower resolution seismic data of Myers & Piper (1988).

crests as reported by Klaucke (1995). The approach toward equal thickness of sediment at the levee crest on opposite sides of the channel was taken by Klaucke (1995) to represent the approach to an equilibrium channel-levee system.

Table 3.1. Summary of characteristic depositional sequence thicknesses on NAMOC. Data and definition of depositional sequences taken from Klaucke (1995). Oldest depositional sequence is A, youngest depositional sequence is G.

Depositional Sequence	Characteristic Thickness	
	Right-hand levee	Left-hand levee
A	50-60	
B	40	
C	30	<18
D	20-30	15
E	30-40	13
F	50	20
G	50	50

General Late Quaternary Stratigraphy

Previous investigations of the shallow stratigraphy of NAMOC have generally focused on the sedimentary sequence recovered from shallow (<10 m) piston cores (Chough & Hesse, 1980; Hesse et al., 1987; Hesse, 1995; Wang & Hesse, 1996). Chough & Hesse (1980) differentiated between laminated, fine-grained levee sediments and coarser-grained, poorly-sorted levee sediments. The laminated levee sediments were interpreted as body-spill turbidites while the poorly-sorted levee sediments were regarded as head-spill turbidites (Chough & Hesse, 1980), but are now recognized as ice-rafted deposits (Wang & Hesse, 1996). Chough & Hesse (1980) defined body-spill turbidites as the deposits resulting from overbanking of the body of a turbidity current. Individual turbidite beds range up to 0.1 m thick and average around 0.03 m. Hesse et al. (1987) divided the late Quaternary section sampled by piston cores into four units: upper hemipelagic, upper turbidite, lower hemipelagic, and lower turbidite. Correlation of lithologic units and individual beds both across and down NAMOC shows that the levees are generally uniform in composition along channel, although tending towards a coarser overall grain size in the downchannel direction (Hesse et al., 1987). Wang & Hesse (1996) focused mainly on the continental slope stratigraphy, although some of their work extended to NAMOC. Radiocarbon dates reported by Wang & Hesse (1996) distinguish up to six phases of

turbidity current activity that they correlated with glacial conditions: deglacial period from 8 to 15 ka, ice growth phase from about 20 to 30 ka, a second deglacial phase from 35 to 40 ka, and three interstadial phases characterized by turbidites, the first of which is tentatively dated between 44 to 50 ka. These phases were recognized on the Labrador Slope. The first two phases of turbidite deposition likely correspond to the upper and lower turbidite units identified by Hesse et al. (1987). Wang & Hesse (1996) found no turbidite deposition, at least on the Labrador Slope, corresponding to the last glacial maximum.

3.3.3 Nature of Turbidity Currents

Sediment Delivery

Pleistocene sediment delivery to NAMOC was by glacio-marine processes including subglacial, englacial and supraglacial outwash, ice-rafting, and downslope remobilization ice-contact deposits. As in most glacially-fed systems the magnitudes of sediment supply are poorly known. However, examination of their deposits can constrain the volume of sediment supplied and deposited by glacio-marine processes. Wang & Hesse (1996) divided the sedimentary facies of the Labrador Slope into three groups: hemipelagic, sediment gravity flow, and contourite/nepheloid plume deposits. The hemipelagic sediments consist of bioturbated muds with diverse faunas and muds rich in IRD (ice-rafted detritus) with sparse faunas interpreted as Heinrich events (Broecker et al., 1992). According to Wang & Hesse (1996), hemipelagic sediment makes up approximately 53% of the sediments sampled by shallow piston cores with 50% consisting of bioturbated muds and 3% consisting of Heinrich layers. Sediment gravity flow deposits represent 41% of the sediments. Of this 41%, the majority of the deposits are turbidites (34%) with only minor debris flows (7%). The least abundant facies found by Wang & Hesse (1996) are contourites and nepheloid plume deposits making up less than 6% of the sediments.

The volume of sediment contained within the NAMOC system has been estimated at about 10^{15} m^3 (Piper et al., 1990). Using the middle Pleistocene age inferred for the inception of NAMOC (Myers & Piper, 1988) a rough estimate of sediment input comes to $10^9 \text{ m}^3 \text{ a}^{-1}$. This estimate includes turbidites, hemipelagites, and ice-rafted sediment,

so it cannot be regarded as anything other than a guide to rate at which sediment entered the NAMOC system.

Initiation

Several mechanisms for initiation of turbidity currents on NAMOC have been proposed, including failure of sediment supplied by ice-rafting or meltwater and hyperpycnal inflow of meltwater. Hesse et al. (1987) favoured failure by oversteepening of glacially-supplied sediment leading to large-scale turbidity current surges. Hesse et al. (1996) and Klauke & Hesse (1996) suggested that hyperpycnal inflow of, at least, the bedload portion of proglacial meltwater streams supplied the coarse-grained material making up the submarine braidplain east of NAMOC (Figure 3.2). The separation of outwash into a bedload hyperpycnal flow and a suspended load hypopycnal (or surface) plume has been demonstrated for modern tidewater glaciers (Syvitski et al., 1987). The association of debris flows and evidence of retrogressive failure of the slope off Hudson Strait with the turbidites of NAMOC supports the notion that sediment failure spawned turbidity currents (Hesse et al., 1987). For the 1929 event off the Grand Banks of Newfoundland, Piper et al. (1992) and Piper et al. (1998a, submitted) provided evidence for the long-term (greater than a few hours) feeding of turbidity currents by debris flows that experience a hydraulic jump. If such a process also occurred off Hudson Strait, it may account for the prolonged turbidity currents required not only to traverse the nearly 4000-km channel path of NAMOC but also to produce the tractional bedding structures (ripples) observed in levee cores (Hesse et al., 1987).

The frequency of turbidity currents on NAMOC has been estimated using sedimentation rates and benthic recolonization times for cores sampling the late Pleistocene section. Given that the average turbidite appears to be 0.03 m thick and a sedimentation rate for turbidites of 0.13 m ka^{-1} , Hesse et al. (1987) reported recurrence intervals of approximately 230 years. Benthic organisms generally require from 1 to greater than 10 years to recolonize an area after being wiped out by a turbidity current event (Hecker, 1980). The lack of bioturbation between successive turbidites led Hesse et al. (1987) to suggest possible recurrence intervals of as little as 10 years. These estimates suggest that the frequency of events on NAMOC could be one every 10 to 200 years.

Flow Parameter Estimates

Klaucke (1995) reconstructed the flow parameters for the most recent phase of turbidity current activity on NAMOC. His reported velocity estimates using the cross-flow slope equation (Komar, 1969; Bowen et al., 1984) range up to 1.5 m s^{-1} . Velocity estimates from the maximum grain size of levee-crest sediments (0.25 mm, settling velocity 0.025 m s^{-1}) ranged from $0.35\text{-}0.45 \text{ m s}^{-1}$, depending on the assumed value of the drag coefficient (0.003-0.005). In all cases, Klaucke (1995) quoted Rubey (1933) as the source for his estimates of settling velocity from grain size. The channel sediments are markedly coarser than levee sediments, having a maximum grain size of up to 20 mm (locally as high as 60 mm). Velocity estimates for the channel flows from this grain size (settling velocity 0.44 m s^{-1}) range from $6.5\text{-}8 \text{ m s}^{-1}$. The large difference in grain size characteristics between the channel flow and levee crest prompted Klaucke (1995) to suggest strong vertical velocity gradients within flows traversing NAMOC. He refuted the interpretation of the channel sediments as a lag deposit because they were poorly-sorted. However, the muds present in the piston core samples of such coarsely grained sediments may not be in situ, having being mixed with the gravel by coring disturbance. It could be that the coarsest grains in the channel fill were ice-rafted to their present location and have little bearing on turbidity current flow character, except to set an upper limit on flow velocity within the channel (less than that required to erode grains 20 mm in diameter).

Excess flow densities related to these velocity estimates range from 4 kg m^{-3} (~ 0.002 , volume concentration) for the levee sediments to $67\text{-}87 \text{ kg m}^{-3}$ (0.04-0.05) for the channel sediments to $1\text{-}12 \text{ kg m}^{-3}$ (0.0006-0.007) for flow velocities estimated using the cross-flow slope equation. Again, the large difference in flow densities between the channel and levees was ascribed by Klaucke (1995) to vertical gradients within the flow. Estimated flow thicknesses have generally been taken to be not much larger than channel depth, which ranges from about 180 m to 160 m over the first 350 km (Figure 3.3b). From the estimates of excess density and velocity provided by Klaucke (1995), his assumed flow thicknesses ranged between 15 m and 60 m; however, no evidence is given by Klaucke (1995) for how these thickness estimates were substantiated.

In summary, the available evidence from NAMOC suggests that this glacially-fed system was supplied with large volumes of sediment possessing a wide range of grain sizes. Turbidity current activity on NAMOC ranged from possibly as frequent as one event every ten years to one every 230 years. The velocities attained by these currents was likely on the order of 1 m s^{-1} , possibly as high as 10 m s^{-1} . Flow thicknesses and volume concentrations may have been on the order of 100 - 200 m and 10^{-3} - 10^{-4} , respectively.

3.4 Levee Architecture of NAMOC

The present study investigates the levee architecture of the most recent phase of channel-levee growth on NAMOC that has been imaged by 3.5 kHz sub-bottom profiler records. Lower resolution airgun seismic data were used to delineate the long term history of NAMOC and to establish the setting for this latest phase of levee growth. The following section presents the general stratigraphy of the most recent phase of levee growth, the stratigraphic evolution of NAMOC, and an analysis of levee architecture.

3.4.1 Levee Stratigraphy

A 3.5 kHz profile located on the western levee of NAMOC was chosen as the type section for the acoustic stratigraphy (Figure 3.5). This area also represents the type section chosen by Klaucke (1995) for his sleevegun seismic data (Figure 3.4). The 3.5 kHz type section (Figure 3.5) shows a conformable succession of weakly acoustically stratified to acoustically transparent sediment separated by moderate amplitude, continuous reflections that can be widely correlated. In order of increasing subbottom depth, the regional reflectors include O, G, R, L, and A. The lowermost horizon in 3.5 kHz records, horizon A, lies above the first correlatable sub-bottom horizon in sleevegun seismic records (green of Klaucke, 1995; Figure 3.4). Note that the acoustic stratigraphy for the 3.5 kHz data uses letters (O, G, R, L, and A) to designate sub-bottom horizons; the acoustic stratigraphy identified in airgun profiles uses the colour scheme of Klaucke (1995). The reflectors define the bounding surfaces of five depositional sequences. DS1 lies between the surface and horizon O; DS2 lies between O and G; DS3 lies between G and R; DS4 lies between R and L; and DS5 lies between L and A. Unlike the character of the other depositional sequences, the sediments of DS4, bounded by horizons R and L,

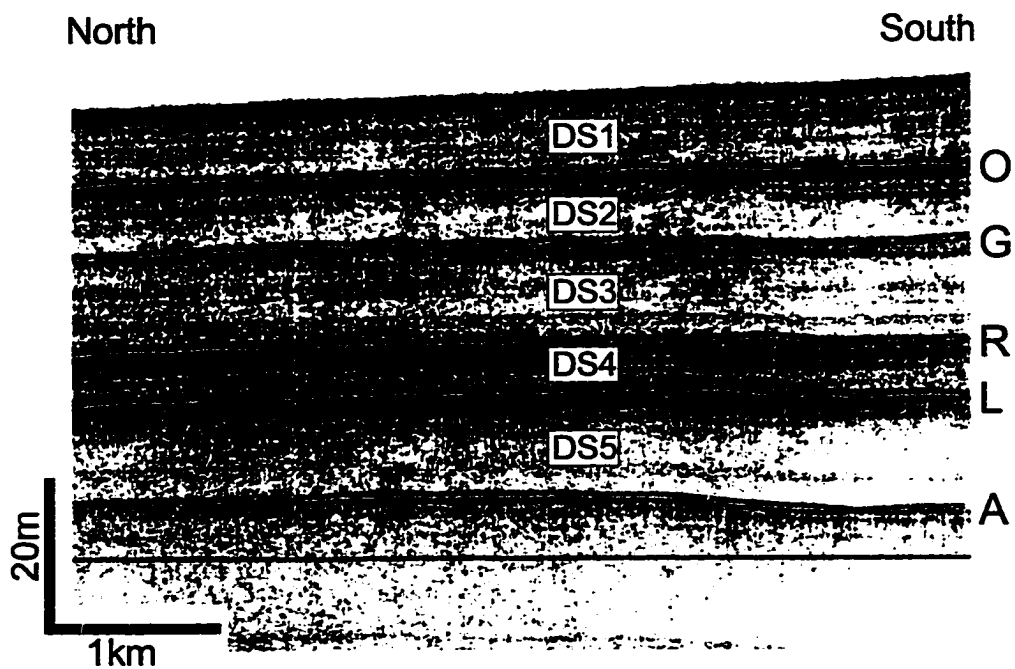


Figure 3.5. 3.5 kHz type section from western levee of NAMOC showing definition of reflectors and depositional sequences. Location given in Figure 3.2.

are acoustically well-stratified throughout. In the type section, the thickness of depositional sequences 1 through 5 are 10 m, 10 m, 13 m, 7 m, and 14 m, respectively. Radiocarbon ages reported by Wang & Hesse (1996) suggest that horizon O may date from around 30 ka, potentially placing the entire section above horizon A within the Wisconsin glacial (i.e., < 70 ka).

The reflectors identified in the type section could be correlated over almost the entire length of the upper reach of NAMOC (i.e., upstream of the E/F junction, Figure 3.2). Successive, channel-perpendicular cross-sections show the down-channel evolution of the NAMOC levees from broad, lenticular bodies, to narrower wedge-shaped features (Figure 3.6). Each cross-section was manually digitized and converted to subbottom depth based on a sound velocity of 1500 m s⁻¹.

Cross-section 1, the most proximal channel crossing, shows a broad levee (Figure 3.6) with some evidence for sediment waves west of the channel (Figure 3.7). The sediment waves have apparent amplitudes up to 5 m and an apparent wavelength of 2-4 km. Small sediment waves (apparent amplitude and wavelength 2-5 m and 200-500 m, respectively) are also seen on a dip line immediately upstream of cross-section 1 (Figure 3.7b, c), but cannot be detected on subsequent cross-sections downchannel. The sediment waves imaged across-strike (Figure 3.7a) began their development prior to horizon R. These waves appear to migrate westward. When imaged on oblique dip lines (Figure 3.7b, c) the sediment waves have apparent amplitudes of about 5 m, wavelengths around 500 m, and appear stationary (Figure 3.7b) or migrate north or northwestward (Figure 3.7c). In addition, the sediment waves in Figure 3.7b do not begin to develop until after deposition of R while those waves seen in Figure 3.7a and Figure 3.7c appear to have begun developing prior to R.

Cross-section 2 like cross-section 1, possesses broad levees. The depositional sequences at cross-section 2 dip gently toward the channel between the levee crest and the channel axis (Figure 3.8). At greater distances from the channel the depositional sequences all dip away from the channel. In spite of this long wavelength relief, the depositional sequences thin uninterruptedly perpendicular to channel trend.

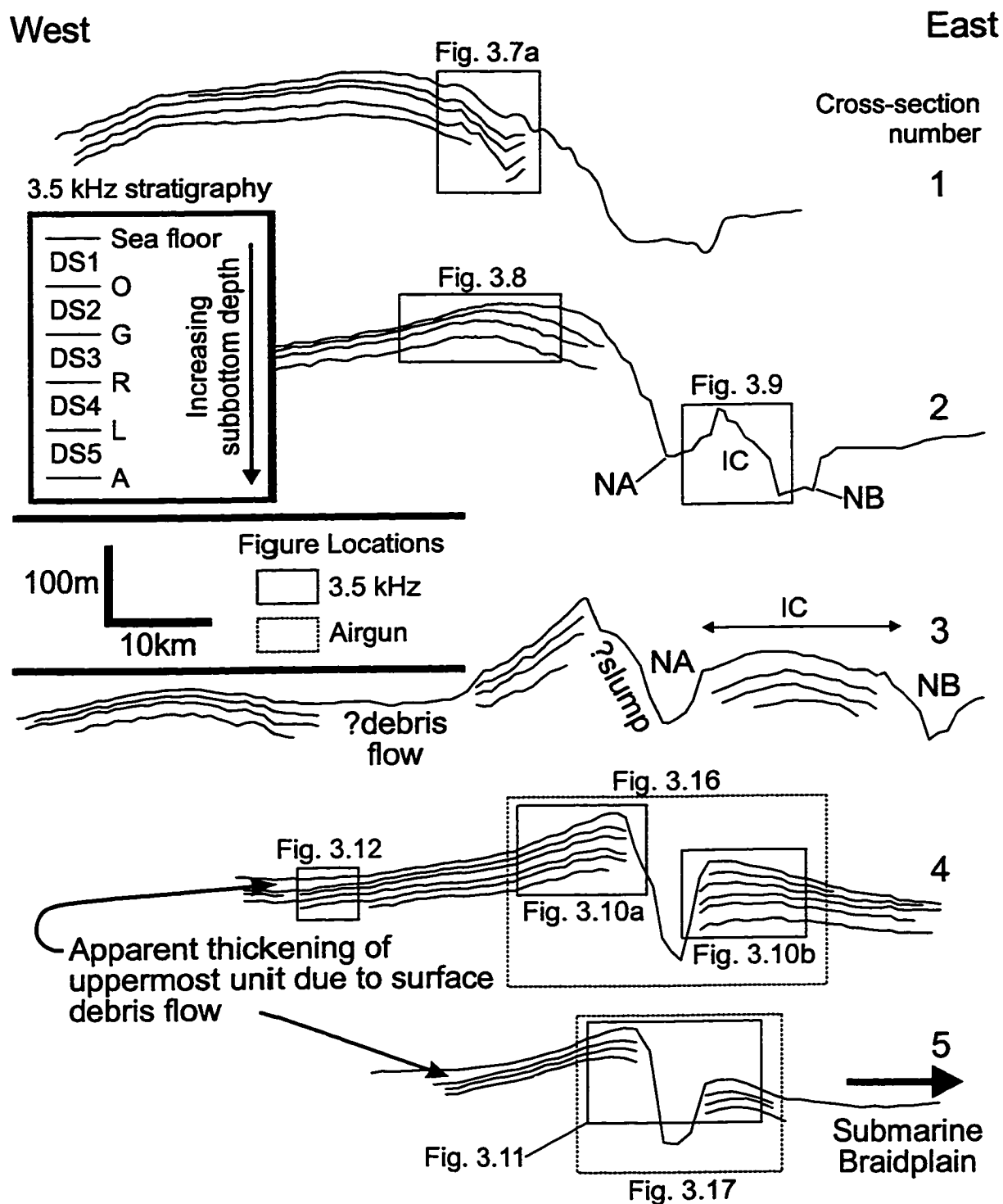


Figure 3.6. Interpreted line drawings of 3.5 kHz data from NAMOC. These lines represent successive cross-sections down NAMOC. Boxes denote location of seismic examples. IC = interchannel high separating western (NA) and eastern (NB) branches of NAMOC.

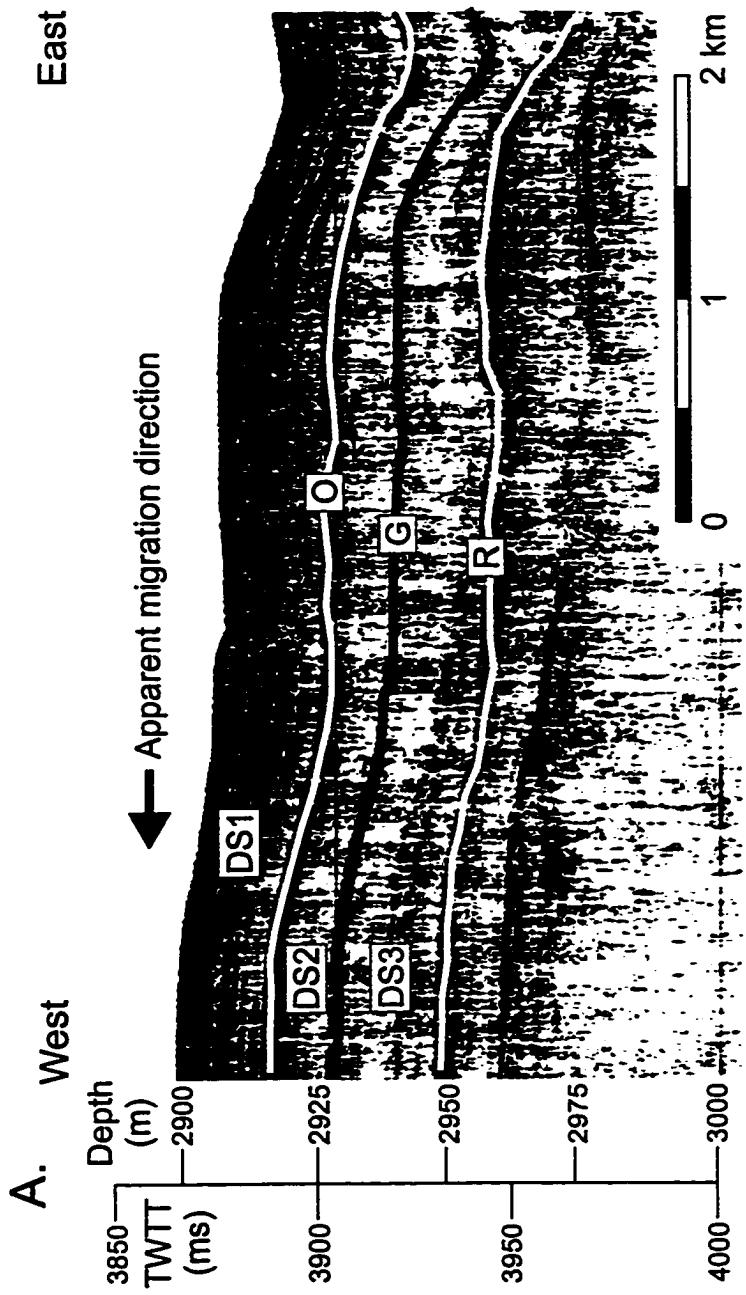


Figure 3.7. Sediment waves on NAMOC. A. On cross-section 1, showing apparent migration to the west. B. Immediately north of cross-section 1, showing migration to the northwest. C. Further north of cross-section 1, showing migration to the west. Locations given in Figure 3.2 and Figure 3.6.

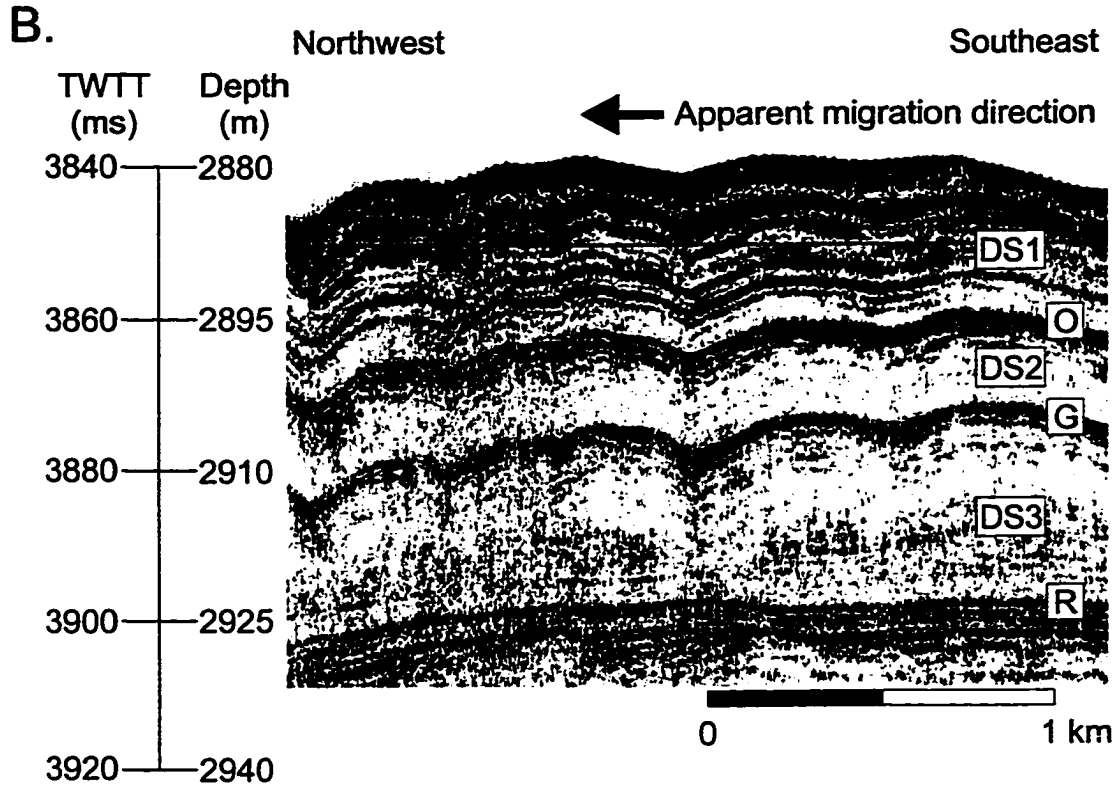


Figure 3.7. *Continued.*

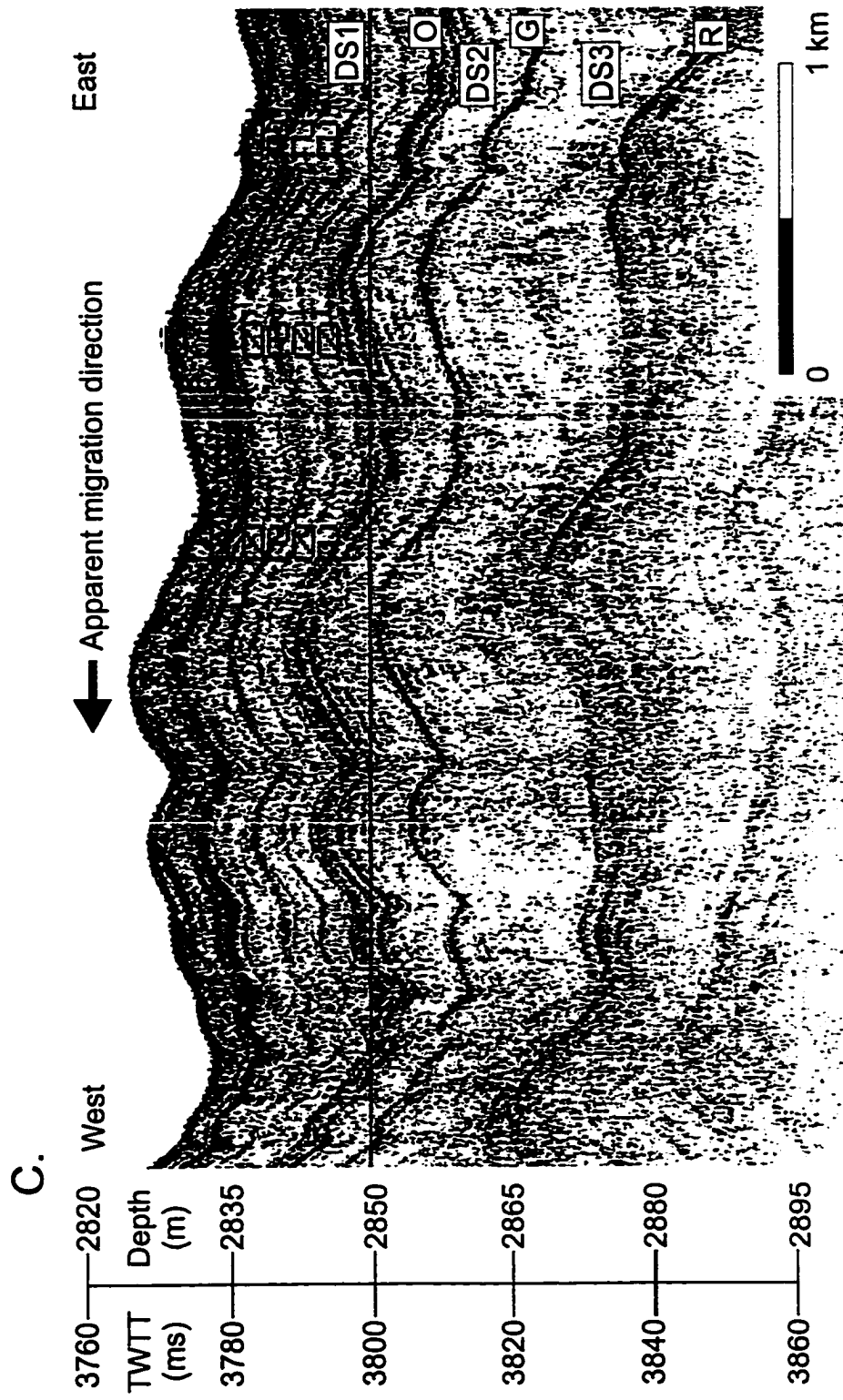


Figure 3.7. Continued.

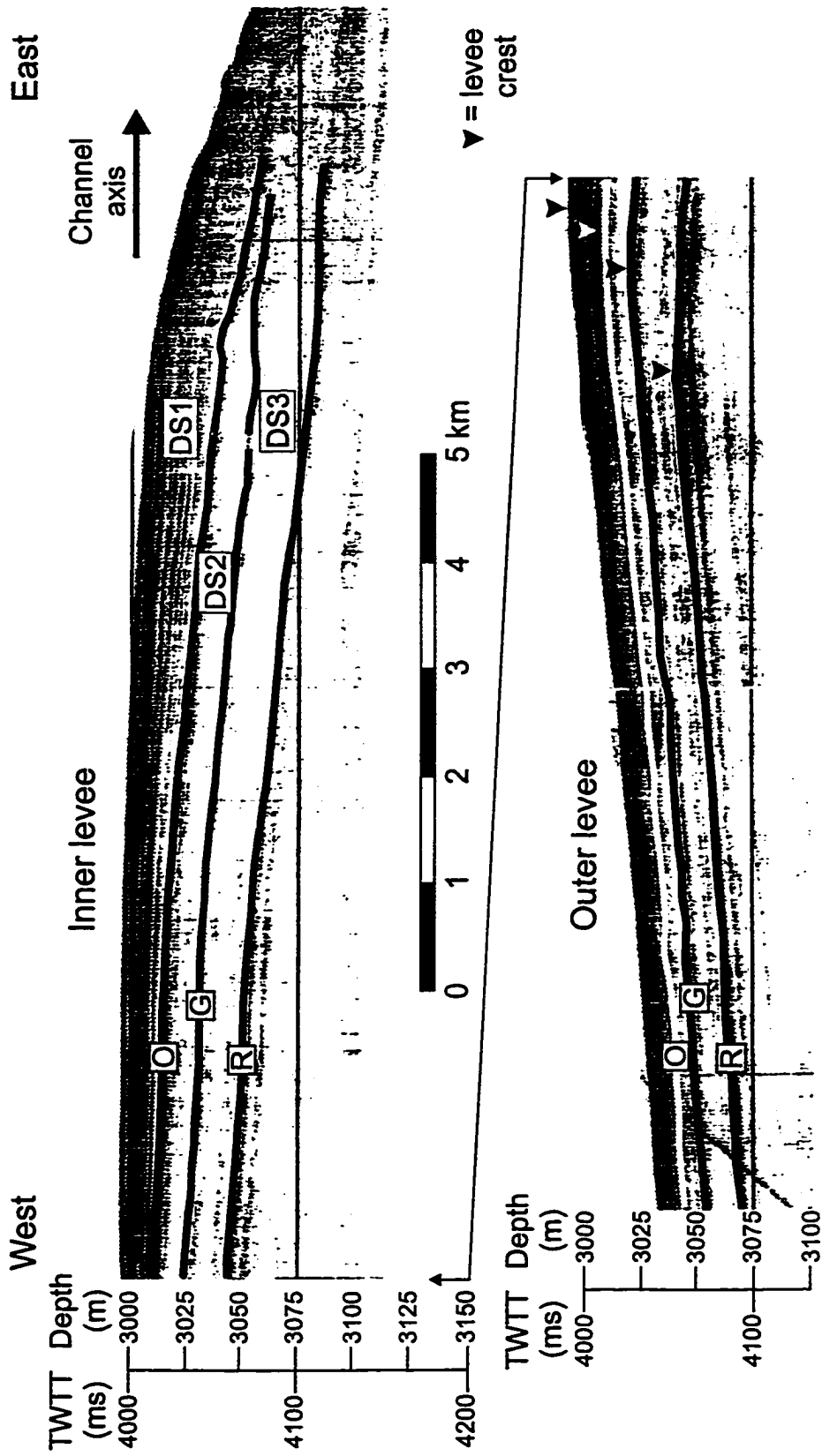


Figure 3.8. 3.5 kHz profile at cross-section 2. Location given in Figure 3.2 and Figure 3.6.

Cross-sections 3-5 all show a more classic levee form with a distally thinning wedge of sediment occurring adjacent to the channel. Each horizon displays an easily identifiable levee crest, except those on the western levee at cross-section 3. Here, probable slumping of the levee has truncated reflector continuity and partially obscured levee crest locations. Between cross-sections 2 and 3, the character of the interchannel high between channel segments NA and NB changes. At cross-section 2, this high is erosional in character (Figure 3.9) while at cross-section 3 it is depositional (Figure 3.6) and reflectors could be correlated into this area. The depositional sequences on the interchannel high at cross-section 3 show some evidence of levee morphology, thinning away from the NA channel axis. At cross-section 4 (Figure 3.6 and Figure 3.10) and cross-section 5 (Figure 3.6 and Figure 3.11) both sides of the channel possess a typical levee morphology. DS1 at cross-sections 4 and 5 apparently thickens away from the channel, but this behaviour results from the presence of a surface debris flow (Figure 3.12). The acoustic character — transparent and smoothing of underlying topography — supports the identification of this feature as a debris flow. Cores sampling this sediment recovered gravelly-sandy mud with clay clasts (Wang & Hesse, 1996). Pebbles and mud clasts are uniformly distributed throughout a finer mud matrix also supporting a debris flow origin for the deposit. Possibly this same debris flow exists at cross-section 3, obscuring reflector correlations.

The acoustic character and external geometry of DS4 are notably different than the other depositional sequences. Channel-perpendicular profiles of this unit at cross-sections 1 and 4, show it to be of relatively uniform thickness (Figure 3.6, Figure 3.10, Figure 3.11). The uniform thickness of DS4 along with its acoustically well-stratified character suggest that it may not be the result of turbidite deposition or, at least, that the turbidite deposition active during the accumulation of DS4 was markedly different than that characterizing the other depositional sequences.

Most of the groundtruth available for the seismic profiles comes from shallow piston cores that have been presented elsewhere (e.g., Hesse et al., 1987; Wang & Hesse, 1996) and have not been the focus of the present study. However, in order to provide some appreciation for the sediments making up the levees of NAMOC, several cores were examined. Figure 3.13 shows summary descriptions of two cores, encompassing

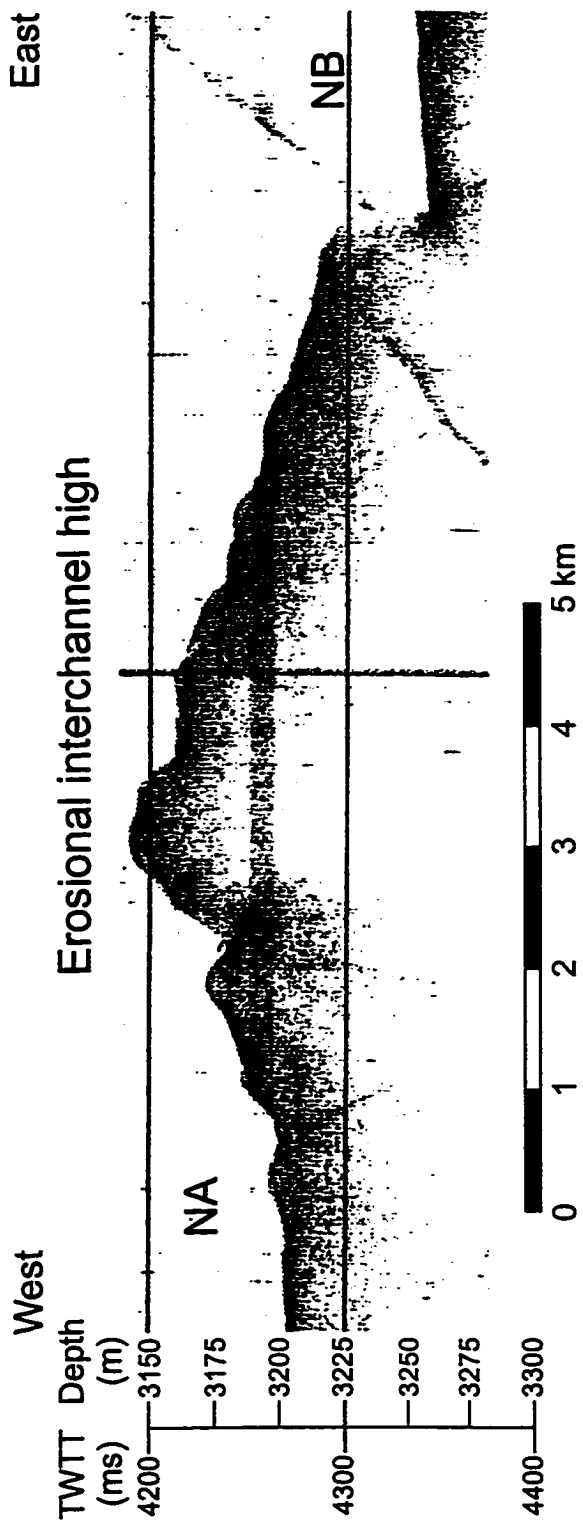


Figure 3.9. Character of interchannel high at cross-section 2. Note erosional character indicated by roughness of seafloor and poor penetration of acoustic energy. Location given in Figure 3.2 and Figure 3.6.

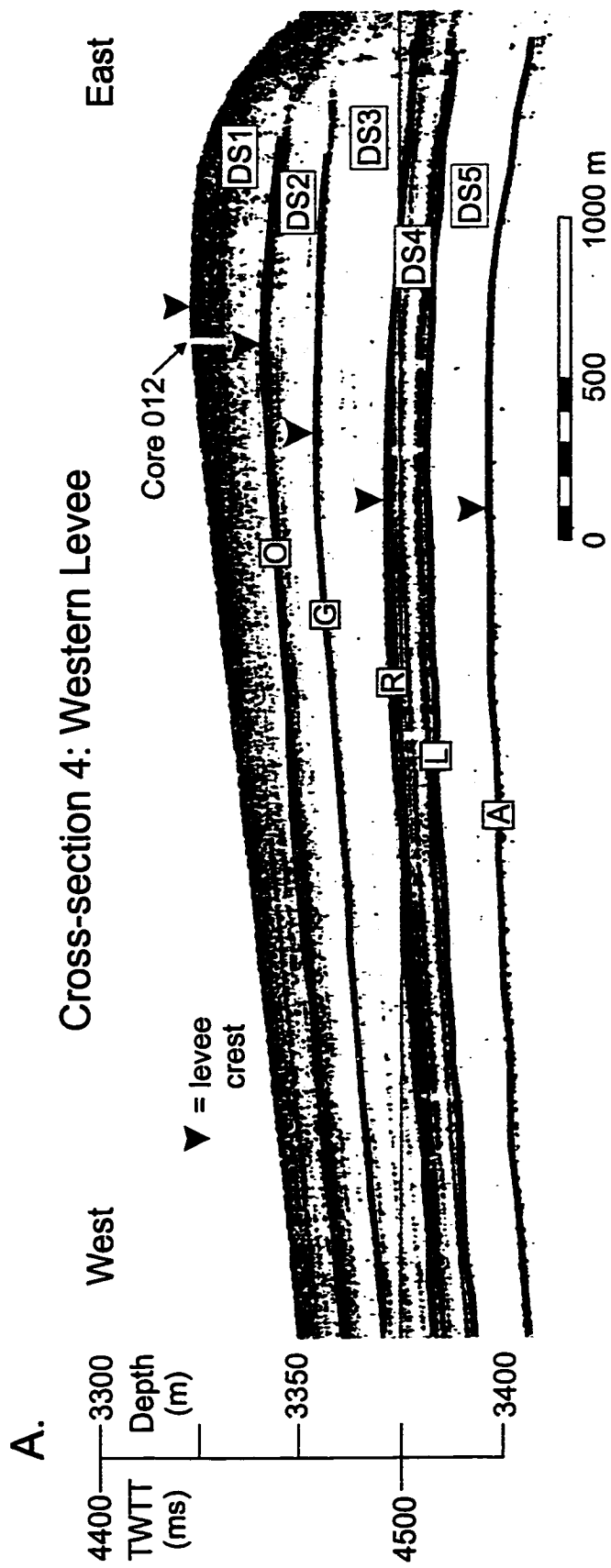


Figure 3.10. 3.5 kHz profile at cross-section 4: A. Western levee; B. Eastern levee. Location given in Figure 3.2 and Figure 3.6.

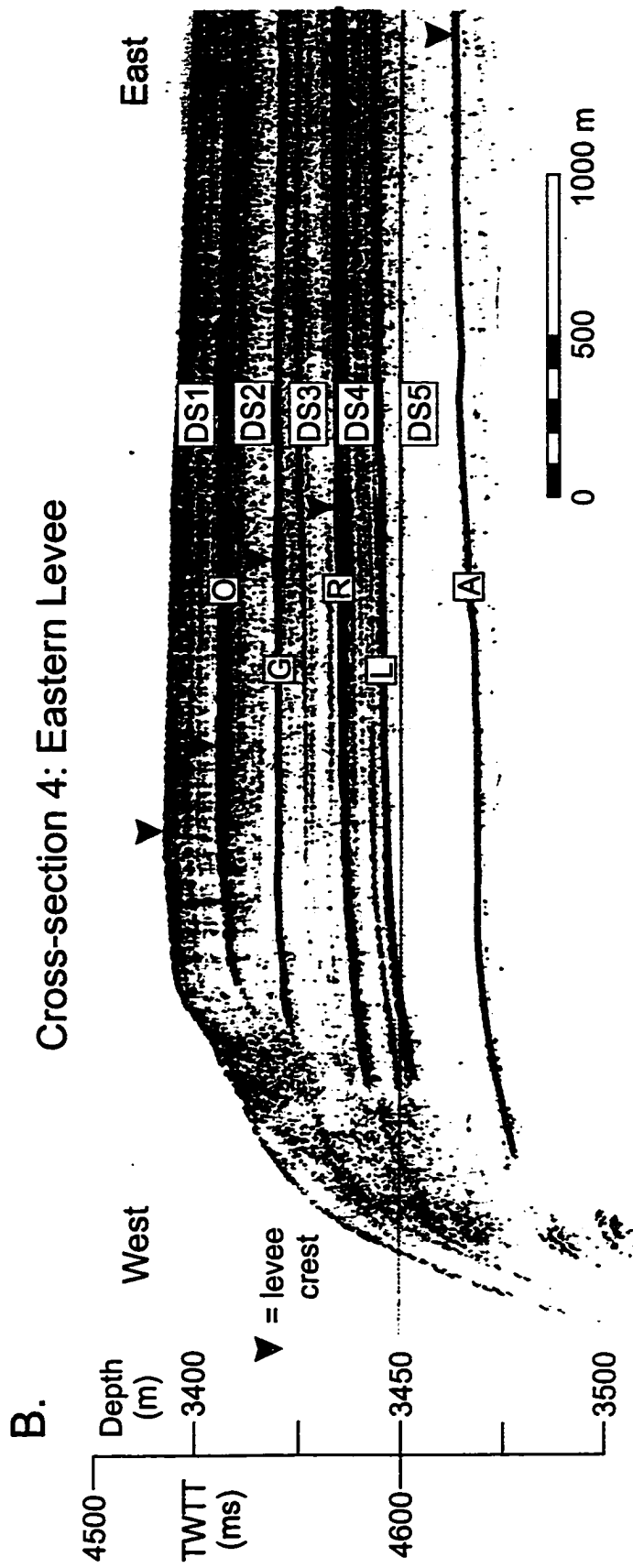


Figure 3.10. *Continued.*

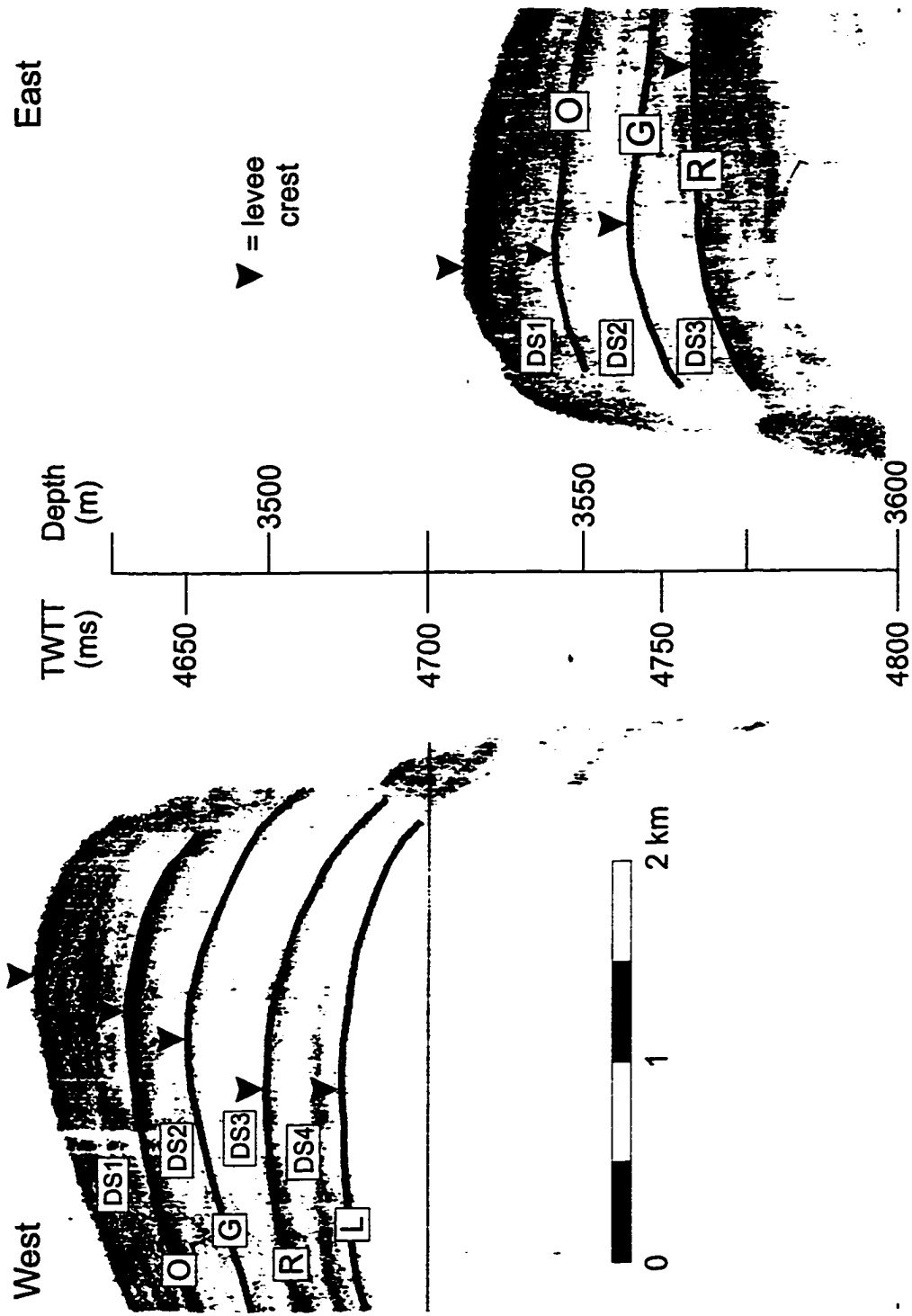


Figure 3.11. 3.5 kHz profile at cross-section 5. Location given in Figure 3.2 and Figure 3.6.

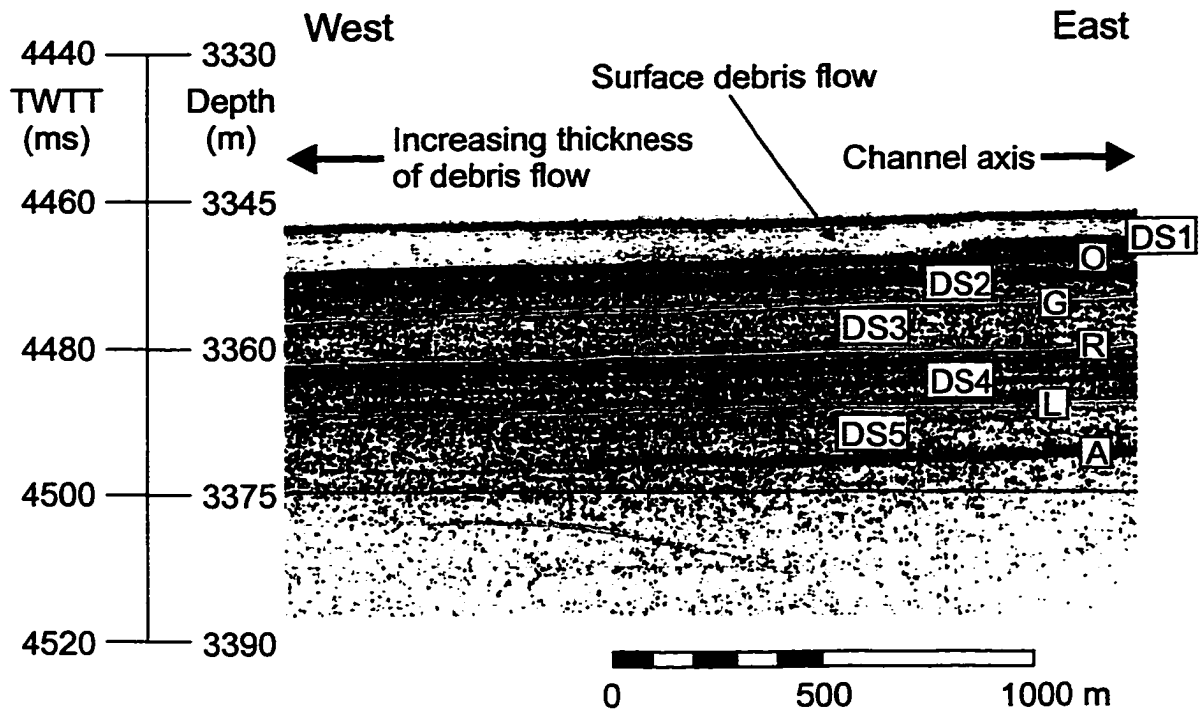


Figure 3.12. 3.5 kHz profile showing surface debris flow west of NAMOC near cross-sections 4 and 5. Location given in Figure 3.6.

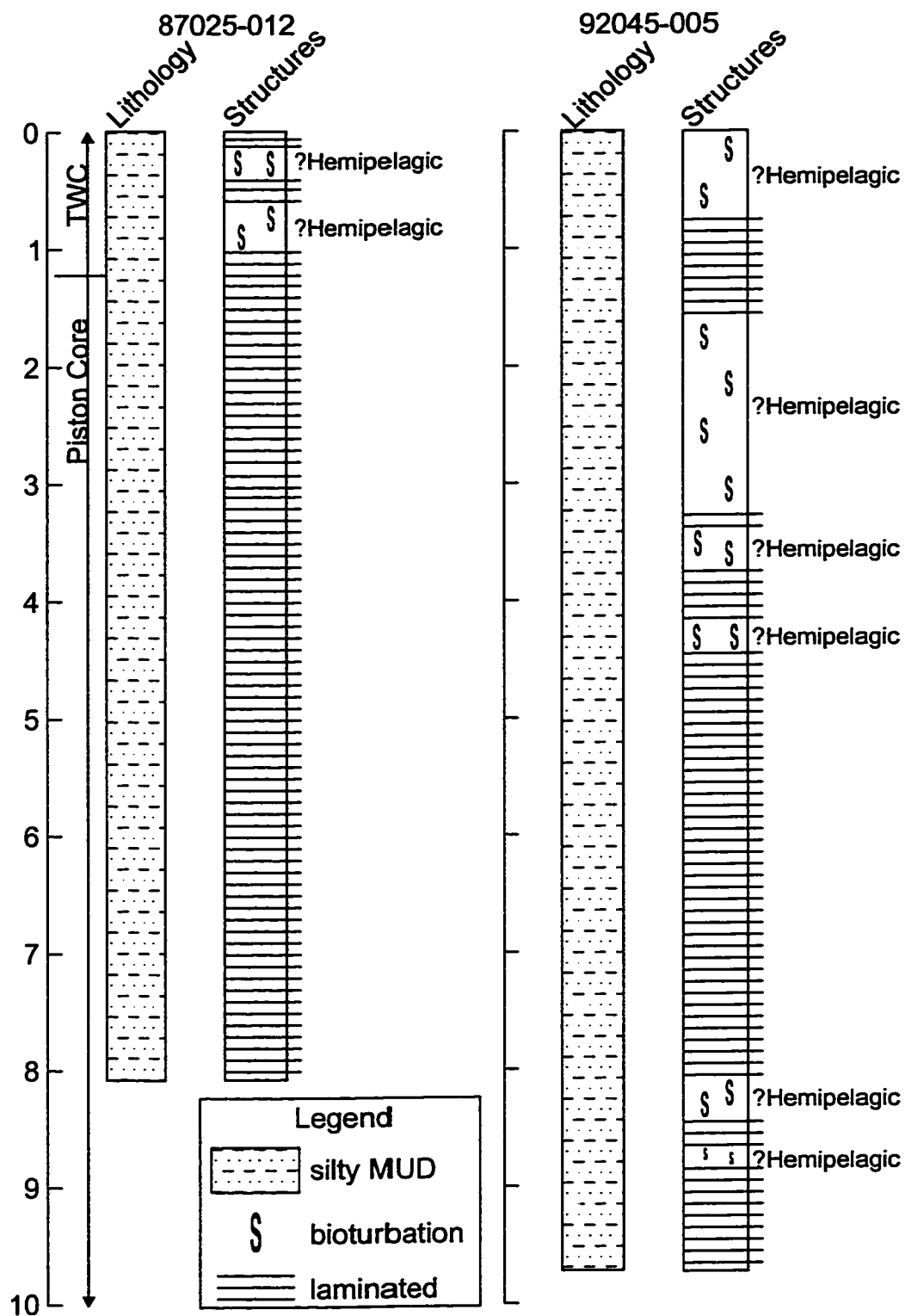


Figure 3.13. Summary core descriptions of 87025-012 (core 012) and 92045-005 (core 005). Locations given in Figure 3.2. Bioturbated sediments may have hemipelagic origin, but could be muddy turbidites.

the variability in those described. Core 87025-012 (core 012) was collected near the crest of the western levee of NAMOC at cross-section 4 and penetrated to a sub-bottom depth of 8.1 m, sampling about half the stratigraphic succession of DS1 (Figure 3.10). Core 92045-005 (core 005) was collected from the levee flank at cross-section 2, penetrating to a sub-bottom depth of 9.8 m sampling almost the entire stratigraphic thickness of DS1 at this location (Figure 3.14). Core 012 consists of ~1 m of interbedded dark olive-grey, bioturbated silty muds and laminated, light olive-grey, silty mud turbidites overlying > 7 m of laminated, light olive-grey silty mud turbidites. Tan-coloured silt laminae, rich in detrital carbonate, mark the base of many of the turbidites. The distinction between hemipelagic and turbiditic mud was confirmed by smear slide analysis showing the hemipelagic mud to consist of a significant fraction of coccoliths, foraminifera, and diatoms while the turbidite mud has significant amounts of detrital carbonate and rare biogenic particles. The turbidites grade upward into darker olive-grey sediment, presumably due to decreasing amounts of detrital carbonate, but exact bed thickness is difficult to assess. An objective method for characterizing the sediments reports the frequency of laminae and beds per meter of section. Such data circumvent the troublesome and controversial picking of turbidite bases and tops involved in assessing bed thickness. In core 012, no trend in the frequency of laminae or beds exists (Figure 3.15). In core 005, the interbedded dark olive-grey, bioturbated silty muds and laminated silt mud turbidites extend to about 4.5 m below sea floor (Figure 3.13). This unit, like in core 012, overlies laminated, light olive-grey, silty mud turbidites, but has some interbedded bioturbated silty mud between 8 and 9 m below sea floor. In this core, the bioturbated silty muds may be hemipelagic sediments or bioturbated muddy turbidites.

The turbidite facies of these cores and all those examined from NAMOC are dominated by a monotonous succession of laminated sediment without readily identifiable trends in sediment properties, suggesting that the character of the flows from which they were deposited remained relatively unchanged. Comparison of the cores with the 3.5 kHz character suggests that the weakly stratified acoustic signature of the levees corresponds to muddy turbidites (Figure 3.10 and Figure 3.14).

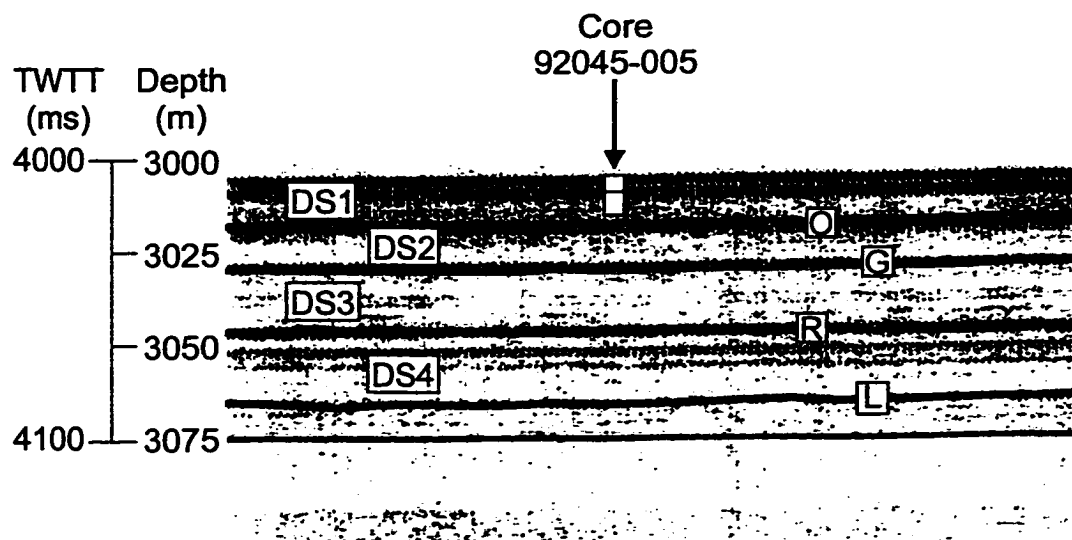


Figure 3.14. 3.5 kHz profile over core site for 92045-005. Note that the piston core penetrates almost the entire thickness of DS1. The solid line within the white bar that is used to denote the piston core depicts the approximate depth of the boundary between interbedded hemipelagic and laminated silty mud and predominantly laminated silty mud.

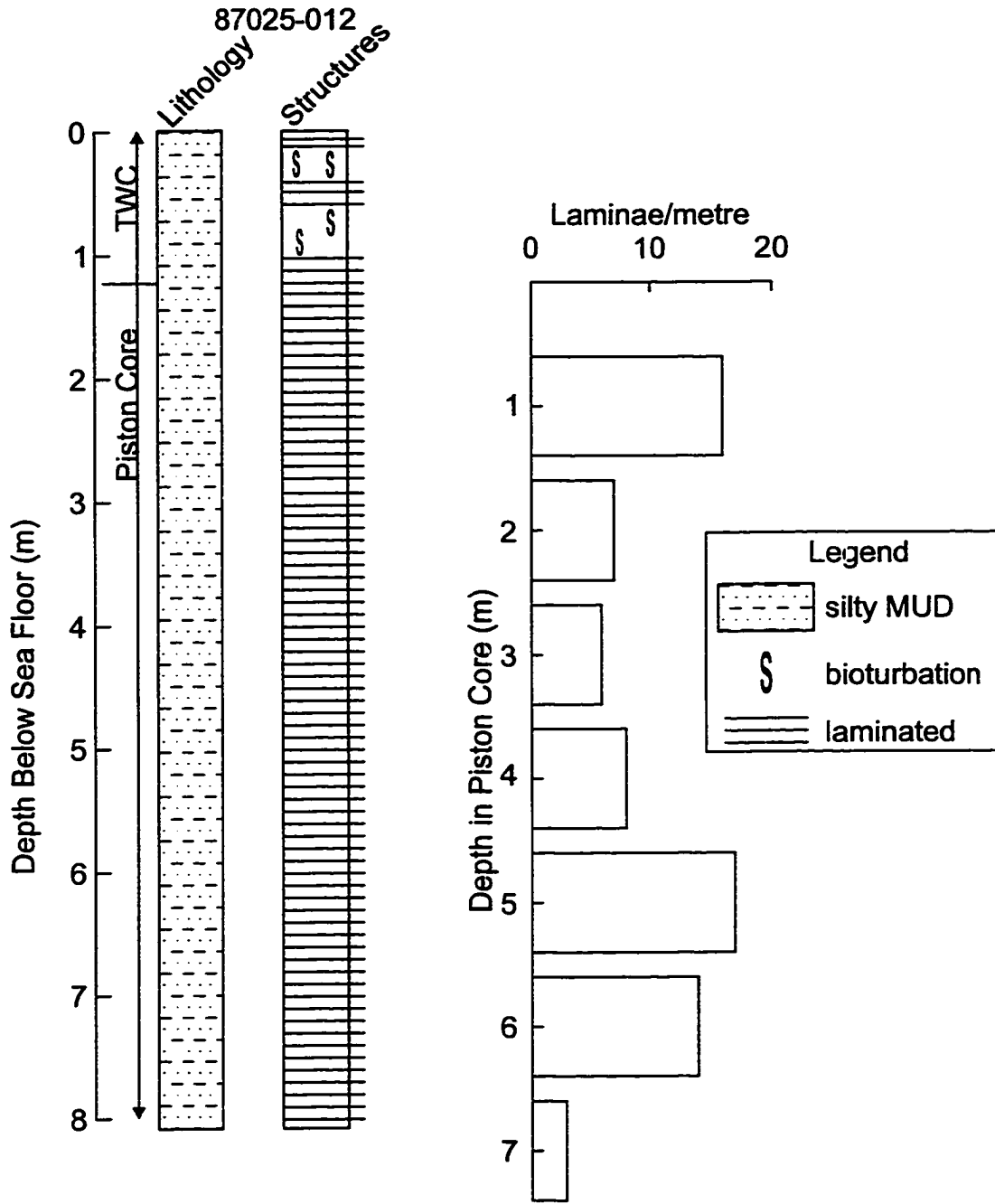


Figure 3.15. Number of laminae per metre of section in core 012 plotted beside summary core description. Depths on the histogram are depth in piston core.

3.4.2 Stratigraphic Evolution

Airgun Seismic Data

According to the chronology of Myers & Piper (1988), NAMOC became an active conduit for sediment sometime around mid-Pleistocene time. This activity began at cross-sections 4 (Figure 3.16) and 5 (Figure 3.17) after deposition of blue. The airgun seismic records reveal possible switching of the channel location through time (Figure 3.16 and Figure 3.18). The brown reflector underlying the western levee at cross-section 4 (Figure 3.16) shows little indication of rising to a levee crest as it approaches the channel, but does appear to form a levee crest beneath the eastern levee. The reflectors above brown on both sides of NAMOC, however, all appear to form levee crests that are associated with the present location of NAMOC. The abandoned and buried channel (Figure 3.18) occurs below olive. The channel could be the ancestral NAMOC or it may be a tributary. Nevertheless, no evidence for abandoned channels can be seen above olive, suggesting that the modern NAMOC has been in its present location since deposition of olive.

Besides the relative stability of the channel, the record of long-term channel-levee evolution preserved in the airgun seismic records depicts a history of channel bypassing. Comparing the thickness of channel fill with the thickness of the levees suggests that relatively little aggradation of the channel has occurred since blue. Presuming that blue represents the approximate base of the channel fill then at cross-section 4 less than 50 m of sediment have accumulated in the channel compared to over 200 m of sediment west of the channel and about 150 m of sediment east of the channel. At cross-section 5, the channel also has less than 50 m of fill while the modern western levee crest has about 150 m of sediment above blue and the modern eastern levee crest has about 100 m of sediment above blue.

Between olive and yellow the bulk of levee deposition consisted of acoustically transparent depositional sequences separated by thin intervals of high amplitude, laterally continuous reflectors (Figure 3.16 and Figure 3.17). At cross-section 4, each of these reflectors rises toward NAMOC forming an identifiable levee crest (Figure 3.16). At cross-section 5, the western levee possesses a similar morphology while the eastern levee

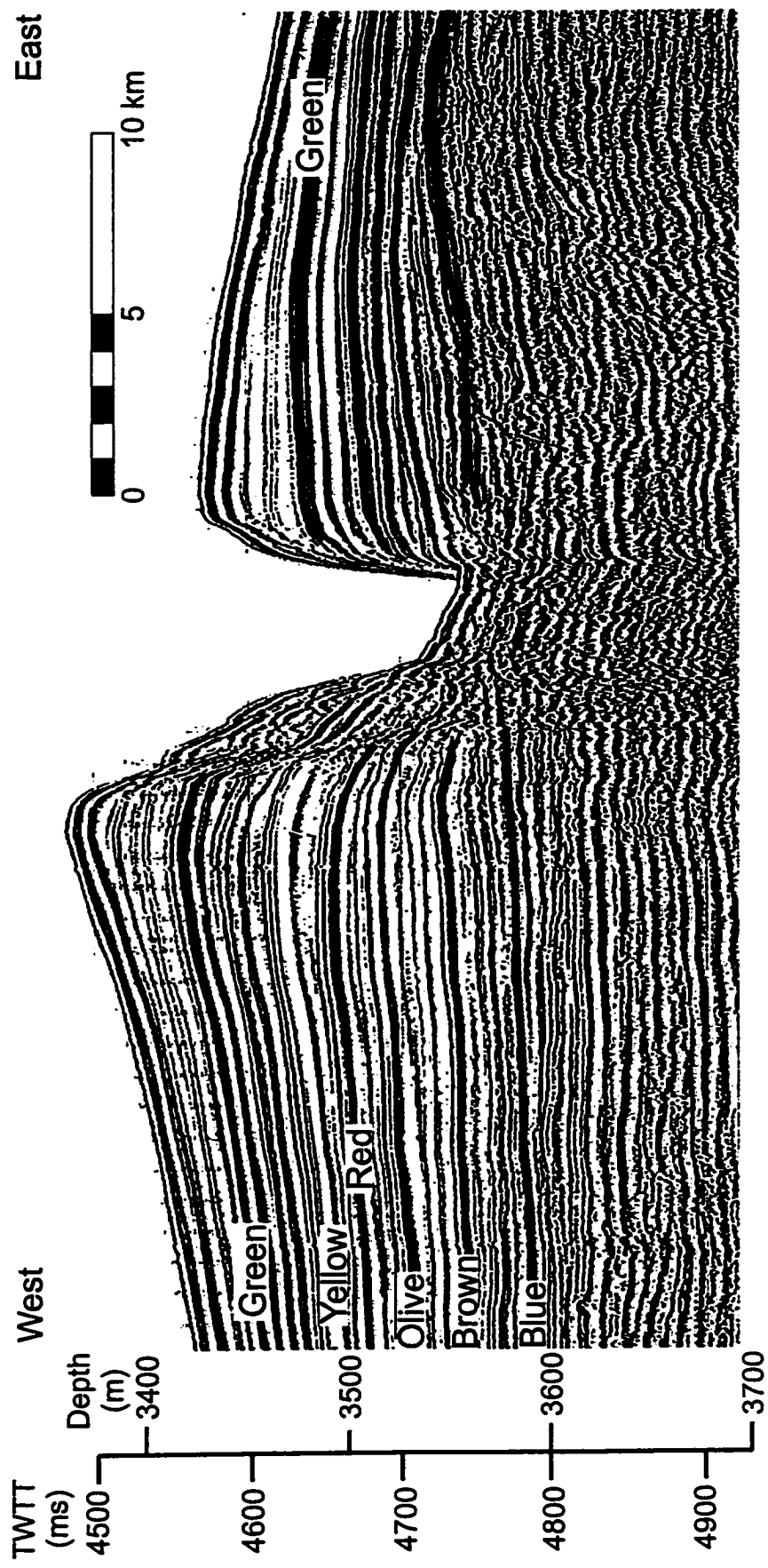


Figure 3.16. Airgun seismic profile across NAMOC at cross-section 4. Location given in Figure 3.2 and Figure 3.6.

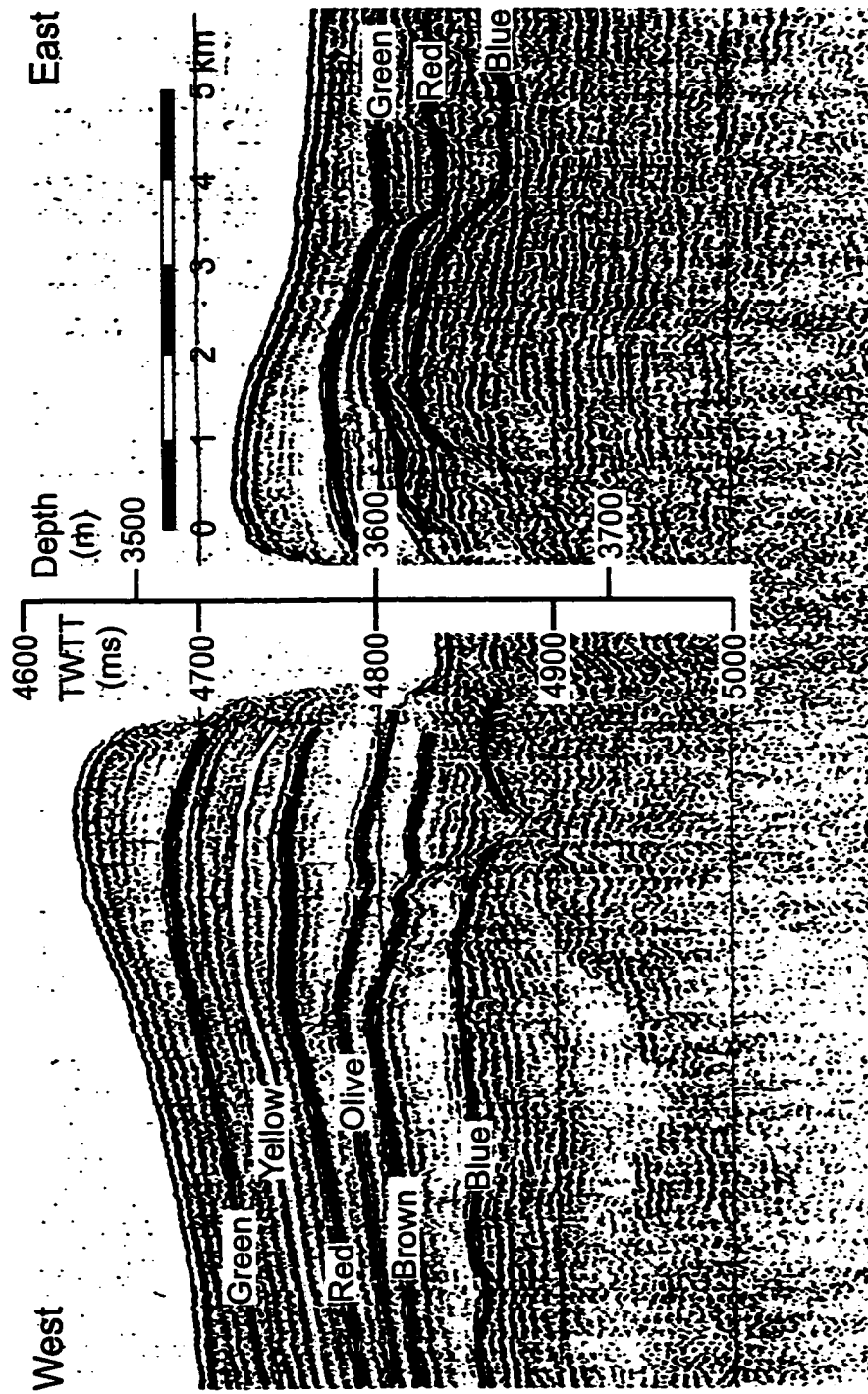


Figure 3.17. Sleevegun seismic profile across NAMOC at cross-section 5. Location given in Figure 3.2 and Figure 3.6.

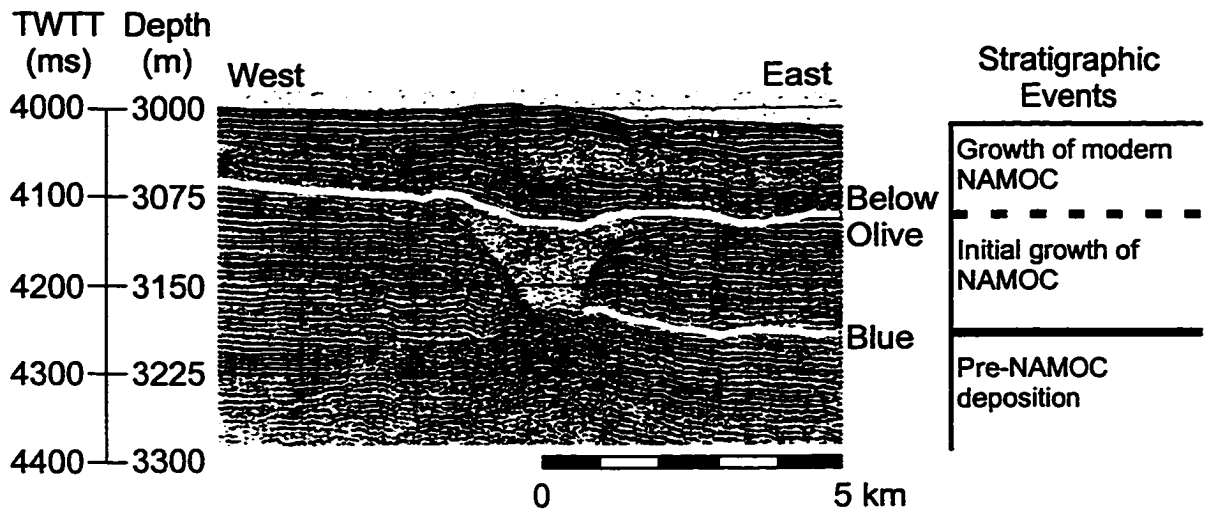


Figure 3.18. Buried channel-levee system, possibly ancestral NAMOC or tributary draining Labrador Slope. Location given in Figure 3.2.

has a more complicated morphology, likely because of relief that can be seen at reflector blue (Figure 3.17). However, the overall reflector geometry as well as the acoustically transparent nature of the sediment suggest that this phase of deposition along NAMOC was characterized by the aggradation of the levees through the accumulation of muddy turbidites.

A steady increase in the elevation difference between conjugate levee crests accompanied this aggradation of the levees. At cross-section 4, elevation differences began to develop after deposition of brown and increased with the emplacement of successive depositional sequences until deposition of green. At cross-section 5, although resolution of the depositional sequences prohibits a detailed analysis, the levee development appears to mimic that seen at cross-section 4. Cross-plotting the water depth of conjugate levee crests confirms these similarities: the history of differences in levee crest elevation at cross-section 4 is almost identical to that at cross-section 5 (Figure 3.19a). The plot shows two phases in this development. Before green, elevation differences increased between the deposition of successive reflectors as seen by the deviation of the trends away from the 1:1 line depicting equal elevation. After green, levee asymmetry increases only slightly, the trend in levee crest elevation parallels the 1:1 line and is best seen in the 3.5 kHz data (Figure 3.19b). This behaviour is reflected in the observation made by Klauke (1995) that the surface depositional sequence, G (Figure 3.16 and Figure 3.17), possesses approximately equal thickness on either side of NAMOC.

The history of elevation differences between conjugate levee crests appears insensitive to the character of the depositional sequences. Deposition between yellow and green consisted of acoustically well-stratified sediments very different from the acoustic character of the underlying sequences. This unit displays the largest increase in asymmetry between successive depositional sequences, but it continues the overall evolution of asymmetric levees established after deposition of olive (Figure 3.19a). The origin of the change in acoustic character may lie in one or several factors. The change may reflect increases in grain size of the levee sediment. Alternatively it may represent changes in the bedding character of the turbidites. And finally, the change in

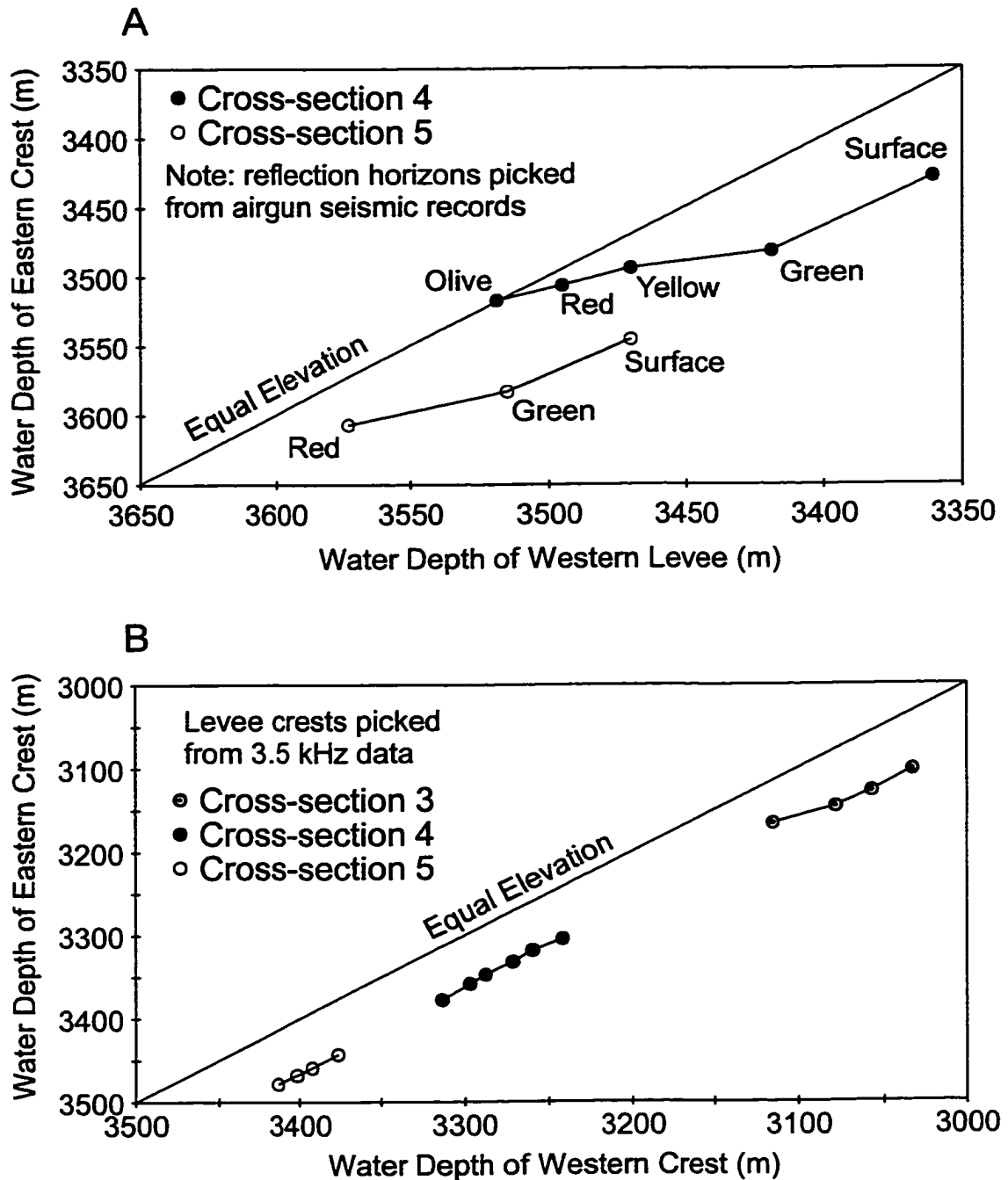


Figure 3.19. Cross-plot of levee crest water depth: A. Levee crests picked from airgun data; and B. Levee crests picked from 3.5 kHz data. The 1:1 line is labeled as equal elevation. Trends in the water depths of the levee crests that run parallel to the 1:1 line show cases where the elevation difference remains unchanged while trends that diverge away from the 1:1 line show cases where the elevation different increases through time.

acoustic character may reflect that depositional processes other than turbidity currents were active during this time.

The last depositional sequence that can be distinguished in the airgun seismic data lies above the green reflector. The transparent acoustic character of this unit suggests muddy turbidite deposition like the deposition prior to yellow. However, this phase of levee growth left approximately equal amounts of sediment on either side of NAMOC (Figure 3.16 and Figure 3.17). This behaviour also shows up in the relatively unchanging values of the elevation difference between conjugate levees (Figure 3.19b).

In summary, the long term growth of NAMOC can be divided into four stages. The first stage, between blue and olive, represents the initial development of NAMOC. The second stage between olive and yellow reflects the growth of an asymmetrical levee system through the deposition of muddy turbidites. The third stage of NAMOC evolution is represented by the sequence between yellow and green where deposition of acoustically well-stratified sediment occurred while elevation differences between conjugate levees continued to increase. The fourth and final stage of NAMOC evolution is represented by a return to levee aggradation through the deposition of muddy turbidites; however, in this phase of levee growth, elevation differences remained relatively unchanged through time. Thus the modern differences in the elevation of the levees crests of NAMOC appear to be inherited from the differences in sediment accumulation that characterized the depositional sequences older than green.

3.5 kHz Data

It is above green in airgun seismic data that the depositional sequences analyzed in the 3.5 kHz data occur. Having a much higher resolution than the airgun data, the 3.5 kHz data across the levees show that this succession has a slightly more complex expression than that suggested by the airgun profiles.

Between horizons green and A as seen on the airgun seismic profile (Figure 3.16) and continuing from horizon A to horizon L (DS5) as seen on the 3.5 kHz profile, the levee continued to grow through deposition of acoustically transparent (Figure 3.10) to weakly acoustically stratified sediment (Figure 3.5). Its acoustic character mimics that of DS1 where the available sediment samples suggest that this character is indicative of muddy turbidites.

DS4 conformably overlies L but possesses a different acoustic character than that of the overlying and underlying depositional sequences. This may reflect the same changes as were suggested for the change from transparent to acoustically well-stratified sediment seen in the airgun data, i.e., changes in bedding, grain size, and/or depositional mechanism. In cross-section, this sedimentary package possesses a more uniform thickness unlike the other depositional sequences (Figure 3.6 and Figure 3.10), suggesting that, if turbidity currents were the active depositional process, then the character of the overbanking turbidity currents differed from that of the currents responsible for deposition of the other sequences. Relief on R changes from displaying sediment waves at cross-section 1 (Figure 3.7a, c) to flat-lying immediately north of cross-section 1 (Figure 3.7b) and to flat-lying at cross-sections 2-5 (Figure 3.6, Figure 3.8, Figure 3.10, and Figure 3.11).

Above R, the character of DS3 marked the return to deposition of acoustically transparent sediment interpreted to be muddy turbidites. Similar character and inferred depositional processes continued for DS2 and DS1 (e.g., Figure 3.5). Sediment waves continued to develop in the north (Figure 3.7). A surface debris flow overlies and possibly eroded DS1 on the western levee flank at cross-sections 4 (Figure 3.12) and 5 and possibly 3. Otherwise, this phase of deposition witnessed the accumulation of muddy turbidites on both the eastern and western levees of NAMOC. At cross-sections 3-5, elevation differences between conjugate levees throughout the succession remained nearly identical (Figure 3.19b, trend of levee crest positions parallel to 1:1 line representing equal elevation). One exception is the increase in the elevation difference between horizon R and G at cross-section 3 (Figure 3.19b).

In summary, the most recent phase of levee evolution shows little deviation from the accumulation of muddy turbidites except for the interval represented by DS4. Elevation differences between conjugate levee crests were approximately constant at cross-section 4 and 5 and for most of the succession distinguished at cross-section 3. Sediment waves developed around deposition of horizon R although the exact timing of their development varies from just below R to above R over spatial scales of less than 10 km.

3.4.3 Architectural Data from NAMOC

Depositional Sequence Thickness

A primary component of levee architecture is the variations in depositional sequence thickness across a levee. To investigate possible patterns in this variable, plots of thickness versus across-levee distance were constructed for each depositional sequence at each cross-section. The distances reported are along the seismic profile from the modern channel axis. The variations in thickness were then parameterized by fitting them to an exponential model (see Chapter 2 for methodology). Tables of regression data show the calculated regression parameters, k and η_0 , as well as the horizontal distance from channel axis to levee crest and the calculated value of thickness at the levee crest, η_{lc} . After presenting the thickness data for depositional sequences identified in the high resolution 3.5 kHz profiles, attention is briefly turned to the longer term history of the NAMOC levees revealed by the airgun seismic data collected at cross-sections 4 and 5.

As mentioned in Chapter 2, the contribution of hemipelagic sediments to the depositional sequence thickness must be accounted for before investigating patterns in the thickness of depositional sequences, ideally isolating turbidite deposition from other processes. Analysis of piston cores, e.g. core 005 and 012 (Figure 3.13), suggests that the hemipelagic contribution to depositional sequence thickness is anywhere from 0-30%. In core 012, hemipelagic sediments compose about 0.8 m of the core which penetrated to a sub-bottom depth of about 8 m. In other words, hemipelagic sediments make up about 10% of the core. In core 005, recognizable hemipelagic sediments make up about 3 m of the core which has a total thickness of about 10 m. In this case, hemipelagic sediments make up about 30% of the core. The hemipelagic component is perhaps over-estimated in core 005 because of the difficulties in distinguishing bioturbated muddy turbidites from hemipelagic mud without detailed smear slide analyses. For simplicity, the regression results reported below assume that 10% of the depositional sequence thickness at the western levee crest is hemipelagic sediments as was found in core 012 and that this sediment is of uniform thickness across the levee. The plots of thickness versus across-levee distance have this amount of sediment removed. Note that because it is not a significant proportion of the depositional sequence, removal of the hemipelagic sediments does not significantly alter the calculated regression parameters.

At cross-section 1, DS1, DS2, and DS3 show a simple pattern of thinning across the levee (Figure 3.20). Data for DS1 and DS2 extend from the levee flank to almost 20 km from the channel while DS3 could only be identified with certainty for distances > 30 km from the channel axis. DS4 is dominated by long wavelength variations in thickness with peaks at about 15 km, 40 km and 55 km. No simple thinning pattern characterizes DS4; however, some of the complexity in DS4 could result from the difficulties in correlating horizons R and L toward the channel. For the upper three depositional sequences, the maximum thickness of sediment on the levee occurs channelward of the levee crest (arrows in Figure 3.20).

Table 3.2 summarizes the regression parameters for cross-section 1. Significant regressions exist for each depositional sequence; however, the regression performed on DS4 is notably weaker, $r = 0.45$, than for the overlying depositional sequences where r ranges from 0.85 to 0.98. The decay constant, k , shows an upsection increase. The depositional sequence thickness at the levee crest does not display any trend, varying between a minimum of 7.4 m for DS2 and a maximum of 17.7 m for DS3. The position of the levee crest remains fairly stable at -36 km for DS2, DS3 and DS4, moving to -34 km at the surface.

Table 3.2. Regression data for cross-section 1. All results are statistically significant, i.e., $p < 0.05$. DS = depositional sequence, k ($\times 10^{-5} \text{ m}^{-1}$) = decay constant, δk ($\times 10^{-5} \text{ m}^{-1}$) = 95% confidence limit on k , η_o (m) = y-intercept of regression, $\delta\eta_o$ (m) = 95% confidence limit on η_o , r = correlation coefficient, y_{lc} (km) = distance from channel axis to levee crest, and η_{lc} (m) = calculated thickness of depositional sequence at levee crest.

DS	k	δk	η_o	$\delta\eta_o$	r	y_{lc}	η_{lc}
1	5.7	0.4	76.1	5.0	0.98	-34.2	10.8
2	3.1	0.6	22.6	2.7	0.85	-36.1	7.4
3	1.8	0.2	33.9	2.1	0.92	-36.2	17.7
4	0.6	0.4	16.1	1.2	0.45	-36.1	13.0

All the depositional sequences at cross-section 2 display channel-perpendicular thinning (Figure 3.21); however the penetration of acoustic energy only allowed identification of the upper three depositional sequences. Like cross-section 2, the maximum thickness of each depositional sequence occurs channelward of the levee crest.

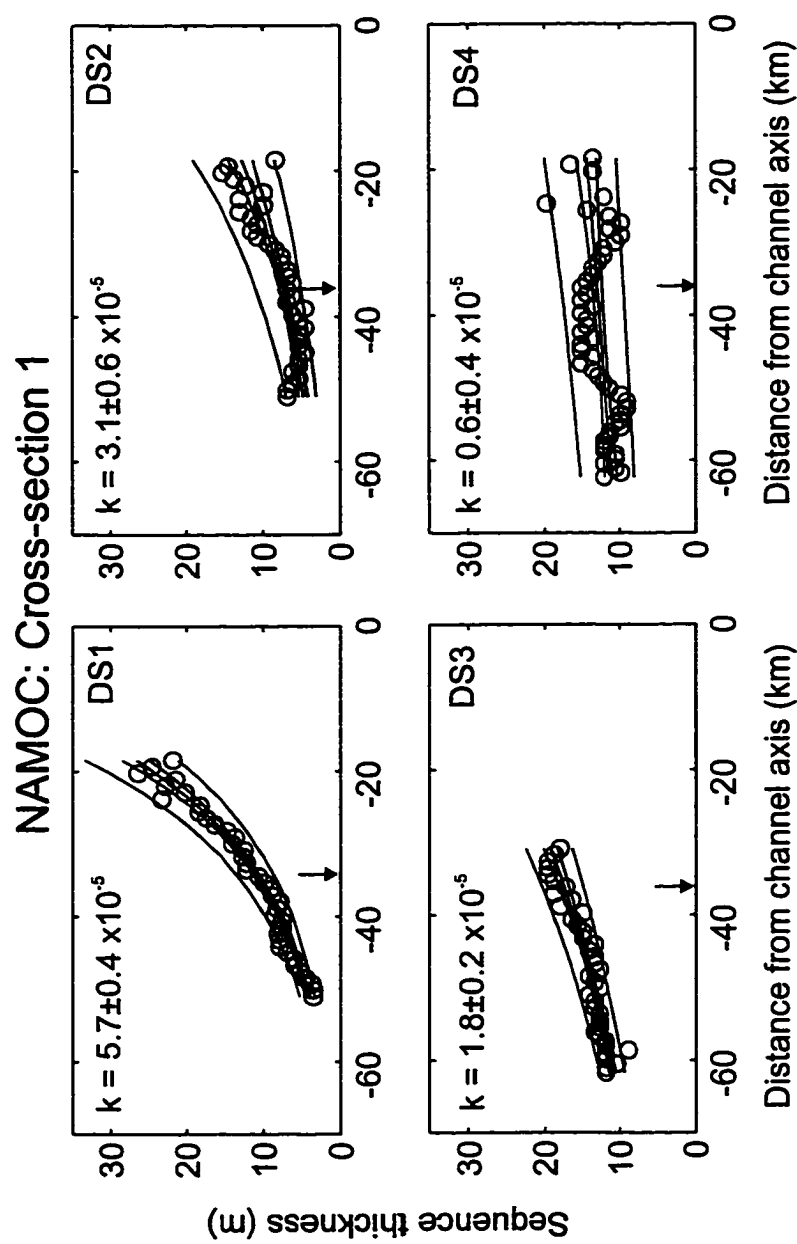


Figure 3.20. Thickness data from cross-section 1. Arrows denote location of levee crest. The decay constants for across-levee variations in thickness, k , are given with the 95% confidence limits reported as errors. Also plotted are the regression line, confidence intervals and prediction intervals. See Chapter 2.

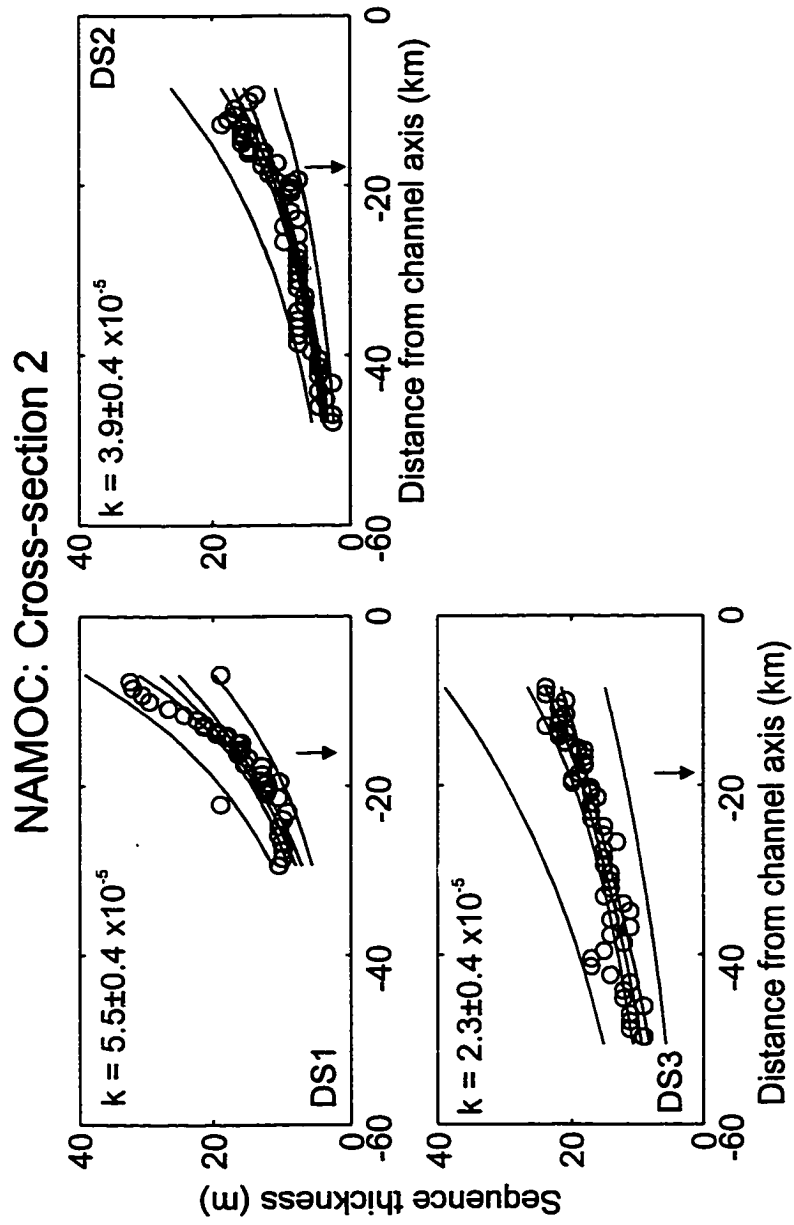


Figure 3.21. Thickness data from cross-section 2 of NAMOC. For explanation see Figure 3.20.

The regression data (Table 3.3) show that k progressively increases upsection from $2.3 \times 10^{-5} \text{ m}^{-1}$ to $5.5 \times 10^{-5} \text{ m}^{-1}$. The thickness of sediment at the levee crest, η_{lc} , decreases upsection. This decrease coincides with a channelward shift of the levee crest — y_{lc} decreases upsection. However, the thickness data do not appear to show that the underlying levee crest affects the variations in thickness of the overlying depositional sequence. In all the cases, the data show no interruption of the thinning pattern that might be attributed to the change in the dip of the underlying surface associated with the levee crest (Figure 3.8).

Table 3.3. Regression data for cross-section 2. See Table 3.2 for explanation of data and symbols.

DS	k	δk	η_o	$\delta\eta_o$	r	y_{lc}	η_{lc}
1	5.5	0.4	24.3	3.2	0.79	-16.2	10.0
2	3.9	0.4	23.5	3.2	0.91	-17.8	11.7
3	2.3	0.4	29.0	4.2	0.78	-18.7	18.9

For cross-section 3, depositional sequences could be identified on the interchannel high that separates the NA and NB branches of NAMOC (Figure 3.6) as well as the western levee. Depositional sequences on the interchannel high possess the weak acoustic stratification and divergent reflections that suggest levee deposition. DS1 and DS3 thin to the east, away from the channel (Figure 3.22), suggesting sediment delivery from the NA channel branch rather than the NB channel branch. Sediment thickness in DS2 appears uniform. The correlation of reflectors on the western levee of NAMOC at cross-section 3 was hampered by a surface debris flow. It is this feature that accounts for the gap in the data between about -20 km and -35 km (Figure 3.22). The crests of the western levee correspond to the maximum thickness of the depositional sequences and these crests do not appear to shift their position. However, slumping of the channel proximal sediments may have partially obscured the levee crests.

Table 3.4 summarizes the regression data from the western levee of NAMOC at cross-section 3; Table 3.5 contains the regression data for the interchannel high at cross-section 3. On the western levee, all the identifiable depositional sequences produced a

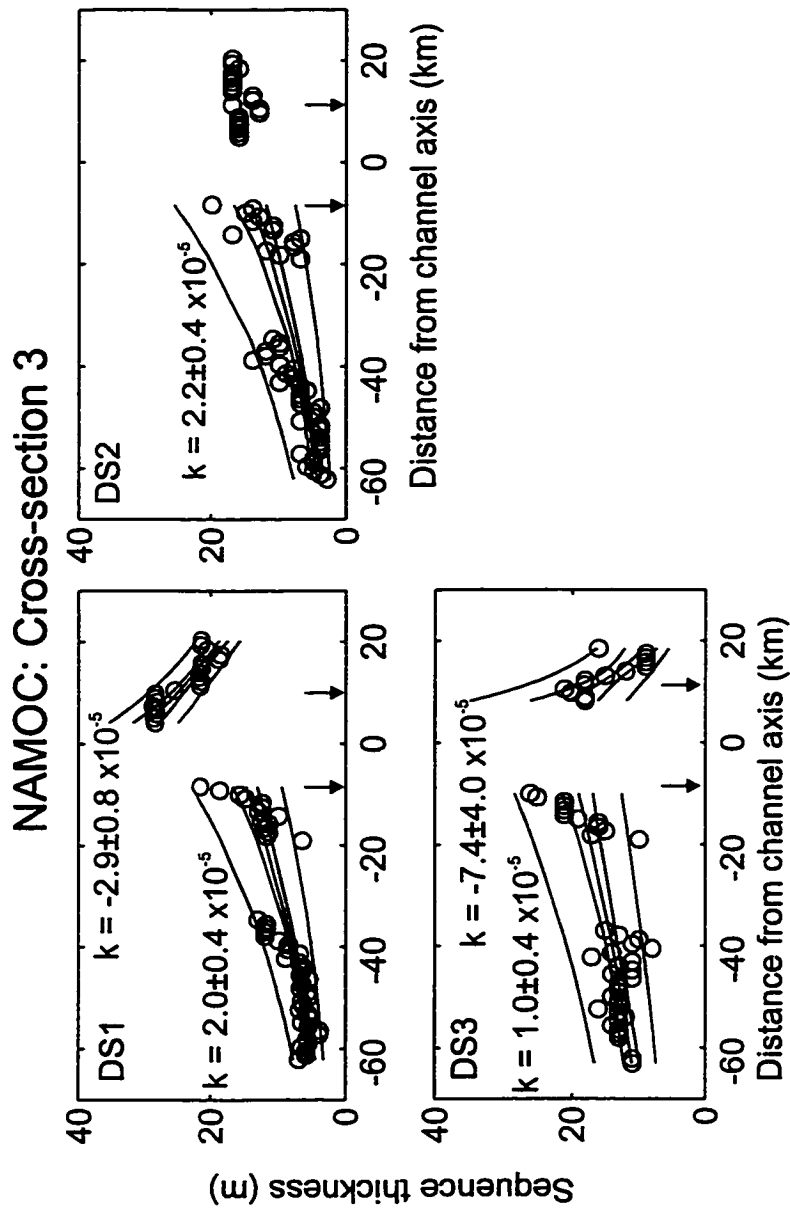


Figure 3.22. Thickness data from cross-section 3 of NAMOC. For explanation see Figure 3.20.

significant regression. Almost no difference exists in the parameterization of DS1 and DS2 at a 95% significance level. DS3 has a lower decay constant.

Table 3.4. Regression data for western levee at cross-section 3. See Table 3.2 for explanation of data and symbols.

DS	k	δk	η_o	$\delta\eta_o$	r	y_{lc}	η_{lc}
1	2.0	0.4	17.4	2.6	0.85	-8.4	14.7
2	2.2	0.4	16.8	3.4	0.80	-8.4	14.0
3	1.0	0.4	21.0	3.2	0.67	-8.4	19.3

On the interchannel high, the variation in thickness for each depositional sequence could be fitted by a statistically significant regression equation. For DS1 and DS3, the thinning pattern produced a negative decay constant corresponding to thinning away from the NA channel segment. For DS2, the calculated k is small but positive corresponding to a weak thickening of DS2 moving away from the NA channel segment. The correlation coefficient for this regression is small ($r = 0.35$) indicating a relatively poor description of DS2 by the regression equation. This can be easily confirmed by visual inspection of the thickness patterns (Figure 3.22). The decay constant decreases between DS3 and DS1, but the large errors around k for DS3 suggest that this difference is not significant at the 95% confidence level.

Table 3.5. Regression data for interchannel high at cross-section 3. See Table 3.2 for explanation of data and symbols.

DS	k	δk	η_o	$\delta\eta_o$	r	y_{lc}	η_{lc}
1	-2.9	0.8	33.6	3.2	0.88	8.9	26.0
2	0.7	0.8	14.4	1.6	0.35	11.3	15.6
3	-7.4	4.0	37.5	20.4	0.74	11.5	16.0

Cross-section 4 has the longest record of levee growth in the 3.5 kHz data. At this cross-section, the depositional sequences, except DS4, show a well-developed pattern of thinning perpendicular to the channel trend both east and west of NAMOC (Figure 3.23). DS4 stands out from the rest of the depositional sequences, having nearly uniform thickness. The maximum thickness of levee sediments is slightly channelward of the levee crests but never more than a few kilometres, unlike, for example, cross-section 2 where this distance can be more than 10 km.

NAMOC: Cross-section 4

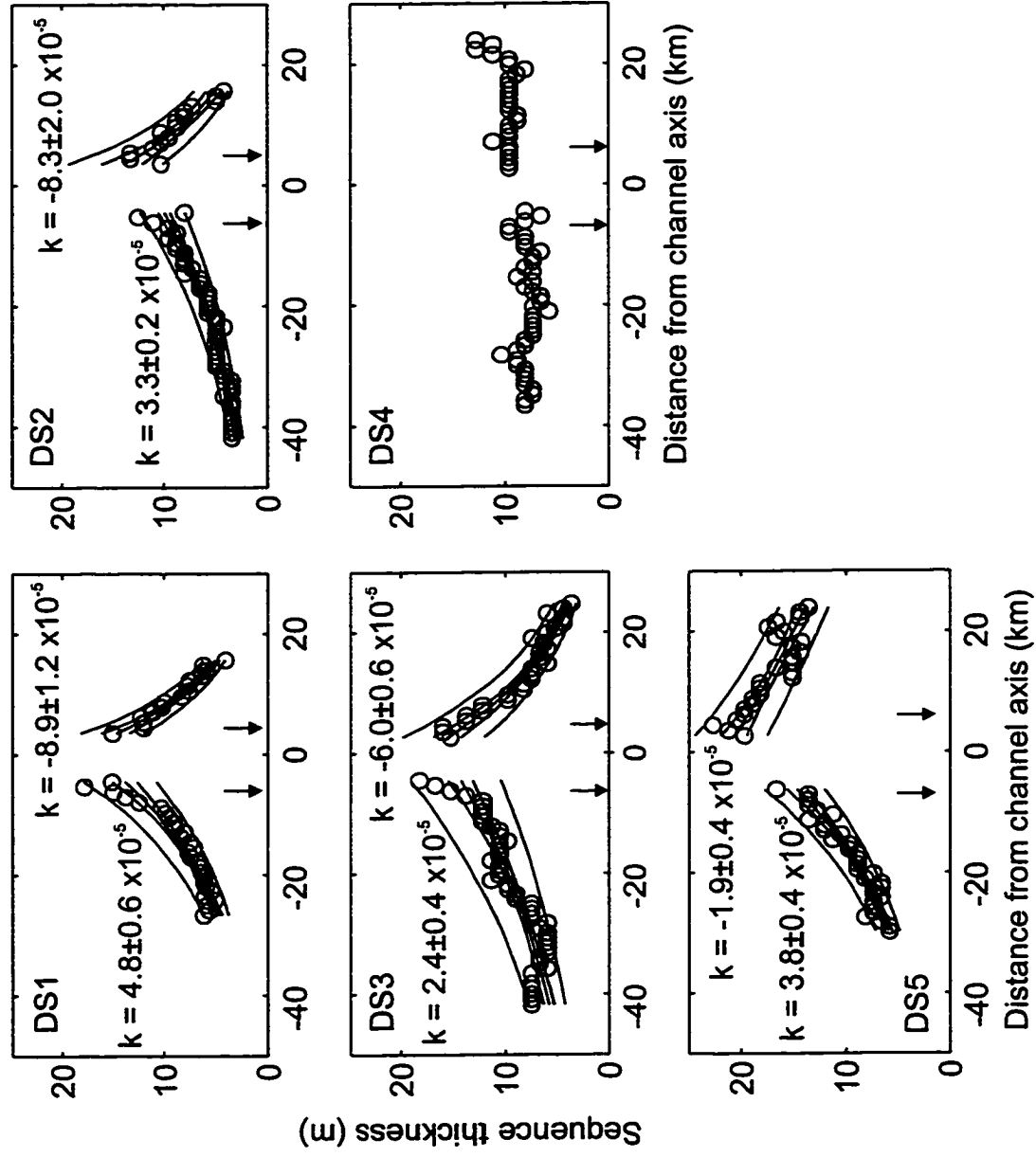


Figure 3.23. Thickness data from cross-section 4 of NAMOC. For explanation see Figure 3.20.

In keeping with the well-developed thinning patterns observed for cross-section 4, the regression parameters, again except for DS4, have high r values (Table 3.6 and Table 3.7). The western levee at cross-section 4 shows an upsection increase in k from $2.4 \times 10^{-5} \text{ m}^{-1}$ to $4.8 \times 10^{-5} \text{ m}^{-1}$ for the three uppermost depositional sequences. The thickness of sediments at the levee crest, η_{lc} , dips to 9.4 m for DS2 from an otherwise relatively constant value of 13-14 m. The change between DS2 and DS1 occurs in the distribution of levee sediment from a thin, broad depositional sequence to a more wedge-shaped unit. The upsection increase in k coincides with a channelward shifting of the levee crest that has also been observed at cross-section 2. However, a straightforward correlation between levee crest position and k may not exist because DS5 possesses the most distal levee crest at -6.8 km but has a decay constant that does not statistically differ from DS2 whose levee crest occurs at -6.1 km.

Table 3.6. Regression data for western levee at cross-section 4. See Table 3.2 for explanation of data and symbols. For DS4, the regression equation was not statistically significant.

DS	k	δk	η_o	$\delta \eta_o$	r	y_{lc}	η_{lc}
1	4.8	0.6	17.2	2.0	0.94	-5.8	13.0
2	3.3	0.2	11.5	0.8	0.96	-6.1	9.4
3	2.4	0.4	15.7	1.6	0.88	-6.5	13.4
4							
5	3.8	0.4	18.4	1.6	0.95	-6.8	14.2

The eastern levee at cross-section 4 also shows an upsection increase in k for the upper three depositional sequences; although, k for DS1 is not significantly different than k for DS2. The same is true of η_{lc} . Thus the only apparent difference between DS3 and the overlying depositional sequences is in k . DS4 has weakly significant regression parameters ($r = 0.37$) with a positive k . Examination of the data (Figure 3.23) shows that this relationship exists because of slight increase in thickness that occurs for $y > 20$ km. Otherwise, DS4 is uniform in thickness. The decay constant of DS5 is significantly less than the other depositional sequences while η_{lc} is significantly greater.

Three of the five depositional sequences could be identified at cross-section 5, allowing for the investigation of their thickness patterns (Figure 3.24). The presence of

Table 3.7. Regression data for eastern levee at cross-section 4. See Table 3.2 for explanation of data and symbols.

DS	k	δk	η_o	$\delta\eta_o$	r	y_{lc}	η_{lc}
1	-8.9	1.2	20.3	1.4	0.97	4.6	13.6
2	-8.3	2	18.8	2	0.92	5.1	12.1
3	-6	0.6	18.1	1	0.96	5.7	12.5
4	0.6	0.6	9.1	0.4	0.37	6.2	9.7
5	-1.9	0.4	21.7	0.8	0.85	8.2	18.0

the braidplain east of NAMOC hampered the unequivocal identification of depositional sequences for distances greater than 10 km east of the channel axis (Figure 3.6). On the western levee, the greater data coverage for DS2 and DS3 compared with DS1 results from the complicating presence of a near-surface debris flow, obscuring the true thickness of DS1. On the eastern levee, DS3 suffers from the poorest data, mostly because of poor penetration of acoustic energy at this location.

The regression data from the western levee of NAMOC at cross-section 5 (Table 3.8) show a distinct difference between DS1 and the underlying depositional sequences. The decay constant increases to $9.1 \times 10^{-5} \text{ m}^{-1}$ for DS1 from around $3 \times 10^{-5} \text{ m}^{-1}$ for DS2 and DS3. The increase in k coincides with an increase in η_{lc} . Thus thinner, broader depositional sequences (DS2 and DS3) underlie a much more wedge-shaped depositional sequence consisting of less sediment. Although the levee crests move toward the channel axis, the decrease in k does not correlate simply with levee crest position.

Table 3.8. Regression data for western levee at cross-section 5. See Table 3.2 for explanation of data and symbols.

DS	k	δk	η_o	$\delta\eta_o$	r	y_{lc}	η_{lc}
1	9.1	1.2	21.4	2.4	0.95	-5.3	13.2
2	3.1	0.7	9.5	1.0	0.76	-5.4	8.0
3	3.0	0.8	10.4	1.3	0.69	-5.9	8.7

While the upper two depositional sequences on the eastern levee at cross-section 5 can be fit to with an exponential model, DS3 lacks the data for the calculation of significant regression parameters (Table 3.9, Figure 3.24). Although accepting the null hypothesis in the regression may mean that sedimentation patterns were uniform, all that

NAMOC: Cross-section 5

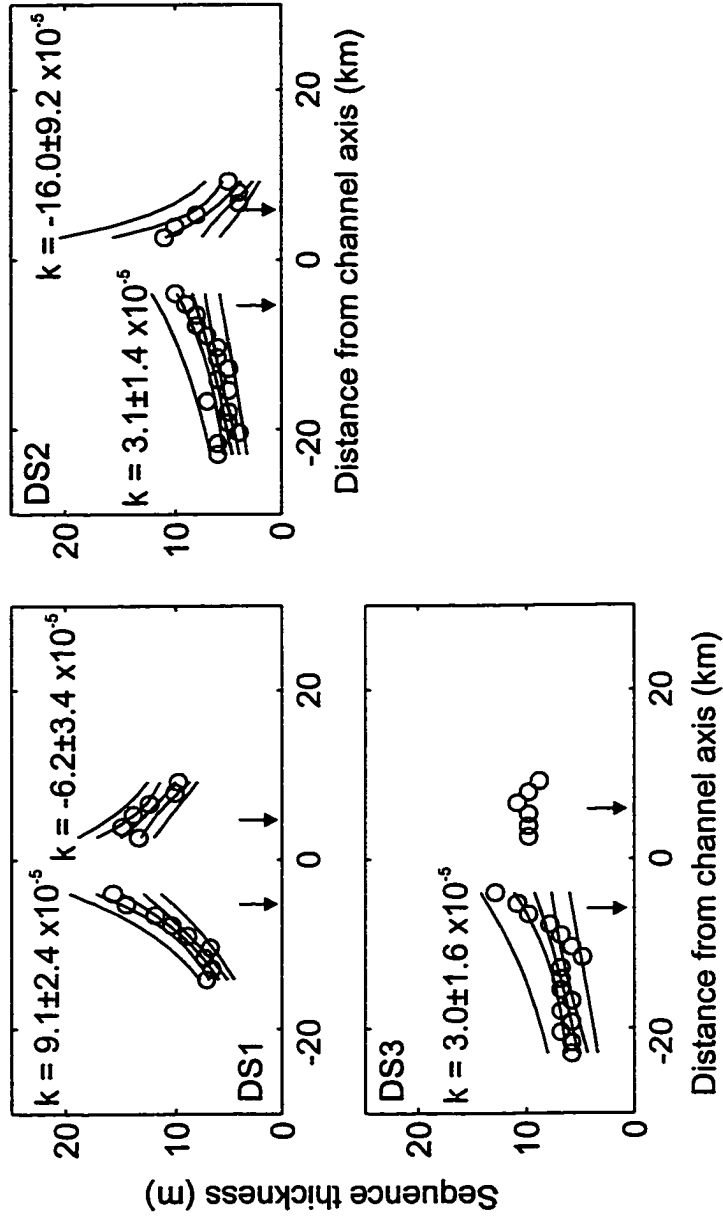


Figure 3.24. Thickness data from cross-section 5 of NAMOC. For explanation see Figure 3.20.

can be robustly said is that the data do not statistically support a k different from zero. This is not so for the overlying depositional sequences which also suffer from limited data coverage. For this levee, k decreases between DS2 and DS1 while η_{lc} remains unchanged at 95% confidence level. The eastern levee at cross-section 5 has a small wedge-shaped levee overlain by a more uniform levee — a relationship not often seen on NAMOC.

Table 3.9. Regression data for eastern levee at cross-section 5. See Table 3.2 for explanation of data and symbols. For DS3, the regression equations was not statistically significant.

DS	k	δk	η_o	$\delta\eta_o$	r	y_{lc}	η_{lc}
1	-6.2	-1.7	17.7	1.9	0.88	4.6	13.3
2	-16	-4.6	16.6	4.9	0.87	4.9	7.2
3							

Across-channel Asymmetry

The asymmetry of levee architecture on NAMOC could be assessed where depositional sequences could be identified on either side of the channel at cross-sections 3, 4 and 5. The following section presents the asymmetry data for these cross-sections. These data include elevation differences between conjugate levee crests, the width between conjugate levee crests, the cross-channel slope, and comparison of the regression parameters presented in the preceding section.

Tabulating the data on across-channel differences in the elevation of conjugate levee crests shows that the elevation difference is notably unchanged with stratigraphic position and downchannel location (Table 3.10). Generally, the elevation difference is 60-70 m with a minimum of 51 m for horizon R at cross-section 3. More variability is seen in the position of the levee crests measured from the modern channel axis. The crests generally move toward the channel axis through time producing an overall decrease in the distance between conjugate levee crests. The net result is that the cross-channel slope becomes more negative both upsection and downchannel.

The regression parameters calculated above can also be used to characterize the asymmetry in levee architecture. Cross-plots of k on the western levee against k on the

eastern levee show that k tends to be greater on the eastern levee than on the western levee (Figure 3.25a). In three of the nine cases, k is greater on the western levee than the eastern levee including DS2 at cross-section 3, DS5 at cross-section 4, and DS1 at cross-section 5. Except in these cases, the NAMOC has broader (i.e., lower k) western levees than eastern levees. The thickness of sediment on conjugate levee crests tends to be more nearly equal with the only significant outlier being for DS1 at cross-section 3 (Figure 3.25b). At this location DS1 is substantially thicker on the interchannel high than on the western levee. Otherwise, sediment thickness at the levee crests is about equal. Such behaviour is not unexpected for the latest phase of levee growth considering the approximately equal thickness of sediments on either side of the channel seen in airgun profiles (Figure 3.16 and Table 3.1).

Table 3.10. Summary of levee crest elevation differences and distances between conjugate levee crests.

Cross-section 3					
Reflector	ΔH (m)	y_{lc} for $y < 0$	y_{lc} for $y > 0$	width (km)	∇H (m km ⁻¹)
Surface	69	-8.4	8.9	17.3	-3.99
O	71	-8.4	11.3	19.7	-3.60
G	68	-8.4	11.5	19.9	-3.42
R	51	-10.0	11.9	21.9	-2.33
Cross-section 4					
Reflector	ΔH (m)	y_{lc} for $y < 0$	y_{lc} for $y > 0$	width (km)	∇H (m km ⁻¹)
Surface	63	-5.8	4.6	10.4	-6.06
O	59	-6.1	5.1	11.2	-5.27
G	61	-6.5	5.7	12.2	-5.00
R	61	-6.8	6.2	13.0	-4.69
L	61	-6.8	6.2	13.0	-4.69
A	65	-7.1	8.2	15.3	-4.25
Cross-section 5					
Reflector	ΔH (m)	y_{lc} for $y < 0$	y_{lc} for $y > 0$	width (km)	∇H (m km ⁻¹)
Surface	67	-5.3	4.6	9.9	-6.77
O	67	-5.4	4.9	10.3	-6.50
G	67	-5.9	5.8	11.7	-5.73
R	65	-6.3	5.8	12.1	-5.37

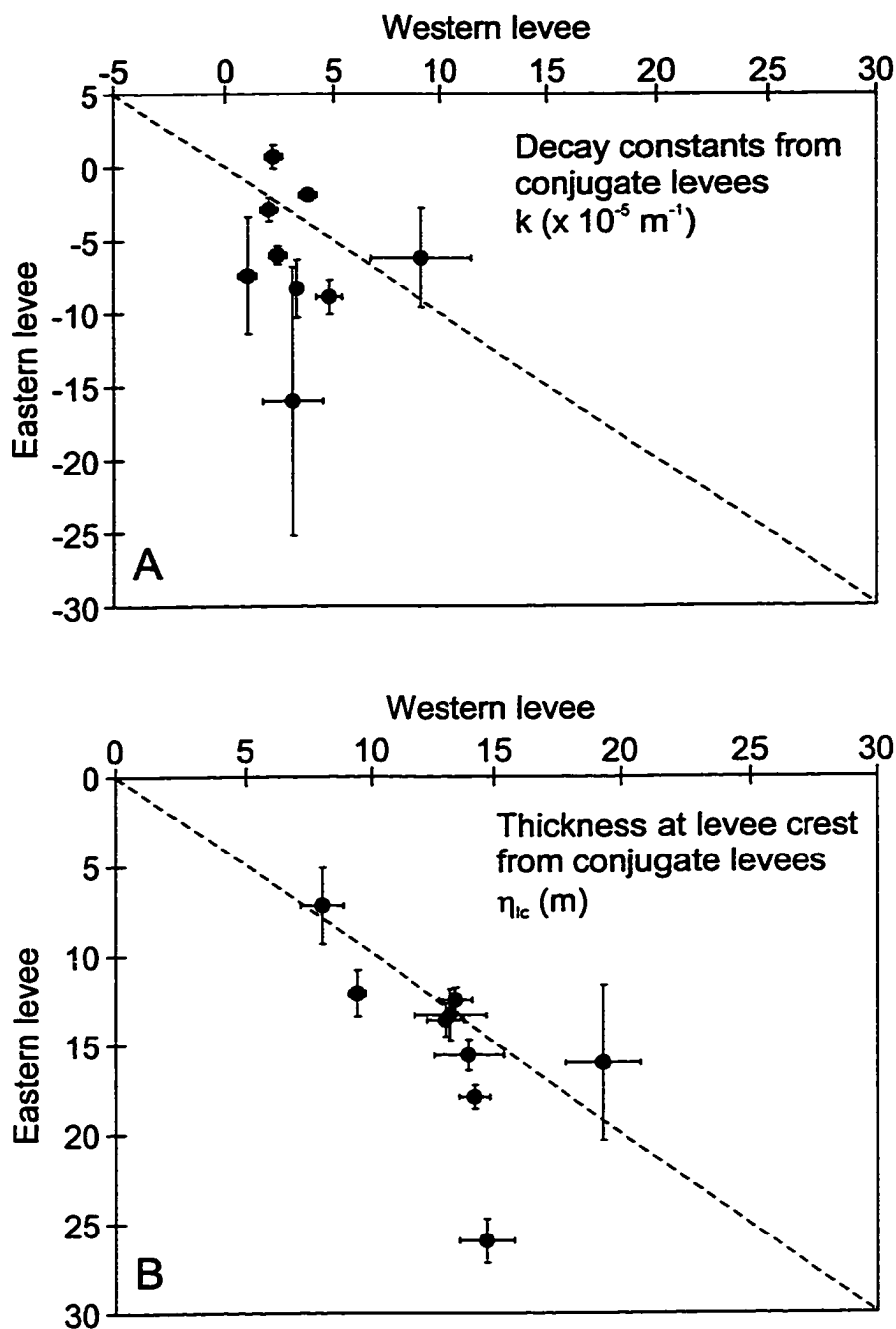


Figure 3.25. Asymmetry in regression parameters: A. decay constant for across-level variations in thickness, k ($\times 10^{-5} \text{ m}^{-1}$); B. thickness of sediment at levee crest in metres. The decay constants tend to be similar or larger on the eastern levee than the western levee. The thickness of sediment at the levee crest tends to equal for conjugate levees.

Sediment Waves

Sediment waves characterize a small portion of NAMOC around cross-section 1. However, they are potentially useful indicators of flow character and thus their morphology bears attention. Because of their limited areal extent and the paucity of data available to characterize them, only general statements can be made concerning their morphology. On seismic profiles running approximately subparallel to NAMOC, the sediment waves appear to migrate north to northwest (Figure 3.7b,c); whereas, on the one strike profile that shows sediment waves (cross-section 1), the waves appear to migrate west (Figure 3.7a). Considering that the exact orientation of the wave crests is unknown, only an approximate indication of the direction of wave migration is possible and it appears to be northwest. The waves appear to continue their migration up to the surface. Amplitude of the waves decreases slightly upsection while their wavelength appears unchanged. As previously noted, sediment waves begin at different times in the stratigraphic evolution of NAMOC. However, initial wave development does not show a coherent spatial pattern, likely because of the lack of data.

3.5 Synthesis of Levee Architecture

This section compiles the data on the levee morphometry of NAMOC in order to explore trends in the downchannel, stratigraphic, and across-channel variations in levee architecture.

3.5.1 Downchannel Variability

Downchannel plots of the decay constant show no consistent trend for any of the depositional sequences (Figure 3.26). The decay constant is more variable on the eastern levee than the western levee, but to within the 95% confidence limits of k , no overall increase or decrease in k occurs. DS1 and to lesser extents DS2 and DS3 display increases in k spanning cross-sections 3 to 5. Focusing especially on variability in the first four cross-sections, the downchannel uniformity of k exists in spite of two major changes in channel morphology. First of all, k varies only slightly even though the channel bifurcates between cross-section 1 and 2 and merges again between cross-section 3 and 4 (Figure 3.2). Secondly, the character of the interchannel high between cross-section 2 and 3 changes from erosional to depositional, without an identifiable response

in the value of k . The lack of a trend in the decay constant coincides with the lack of significant trends in channel slope. It does, however, coincide with a gradual decrease in channel depth over the upper reach of NAMOC (Figure 3.3b).

At the scale of individual depositional sequences, downchannel plots of the thickness of sediments at the levee crest lack a strong trend (Figure 3.27a). Some evidence exists for a downchannel decrease in sediment thickness, especially for DS2 and DS3 on the western levee and for DS1-DS3 on the eastern levee. When the thickness above horizon R (encompassing DS1, DS2, and DS3) on the western levee is calculated and plotted downchannel (Figure 3.27b), an identifiable decrease in sediment thickness emerges. It shows that the thickness of sediment at the levee crest decreases significantly between cross-section 1 and 3 in comparison to only a minor change between cross-sections 3 and 5. The distance over which this change from large downchannel gradients in η_{lc} to small gradients defines a lengthscale for downchannel evolution of levee architecture that is of order 300 km (Figure 3.27b).

Distance between conjugate levee crests shows a consistent trend downchannel (Figure 3.28a). Values for the elevation difference between conjugate levee crests remains relatively uniform (Figure 3.28b). The downchannel evolution of cross-channel slope calculated from the data presented in Figure 3.28a also shows a consistent trend becoming more negative downchannel (Figure 3.28b). This pattern is predominantly a function of decreasing distance between conjugate levee crests. The pattern weakly corresponds to greater values of k on the eastern levee than the western levee where six out nine cases have k on the eastern levee greater than k on the western levee (Figure 3.25a). The values of η_{lc} on either side of the channel are approximately the same (Figure 3.25b) suggesting again that trends in ∇H result primarily from movement of the levee crests toward the channel axis and not preferential depositional on the western levee.

3.5.2 Stratigraphic Variability

Stratigraphically, the decay constant shows an upsection increase in some cases while in others no trend appears to exist (Table 3.2-Table 3.9, Figure 3.29). At cross-sections 1 and 2, depositional sequences from the western levee display an upsection

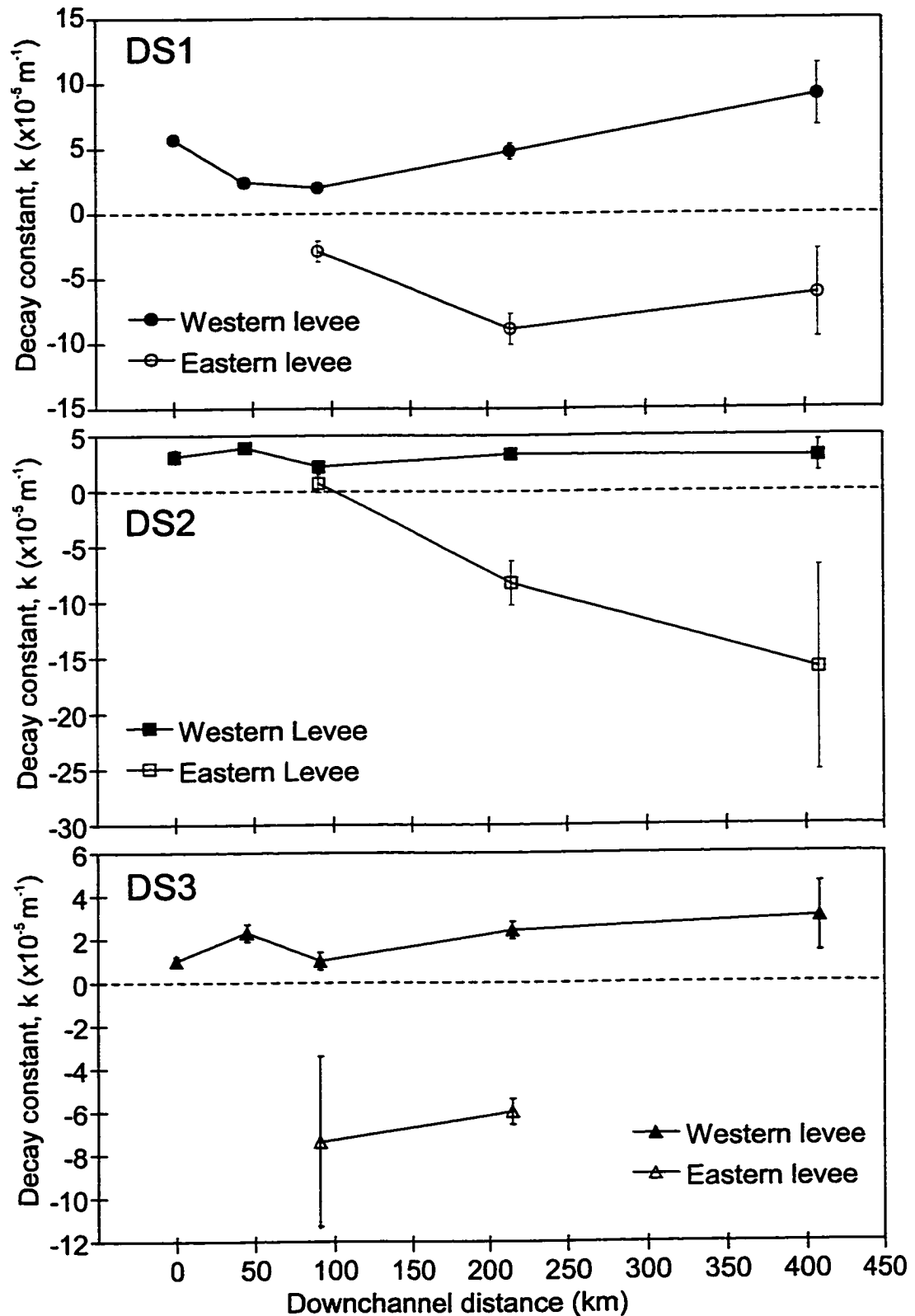


Figure 3.26. Downchannel variation in k . None of the depositional sequences show a strong overall trend. However, DS1 and DS3 on the western levee show an increase for distances greater than 100 km downchannel.

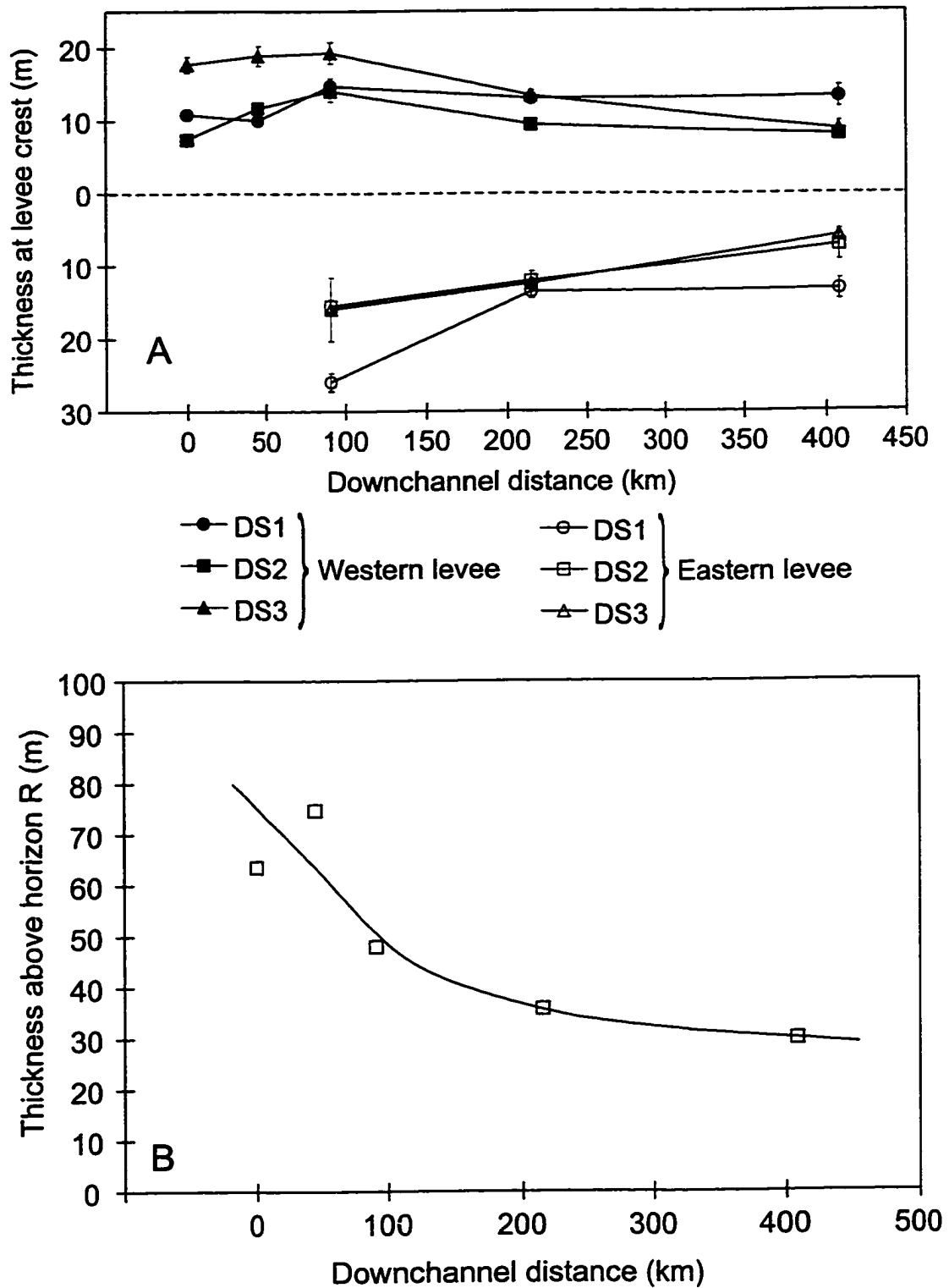


Figure 3.27. Downchannel variation in thickness of depositional sequences on NAMOC: A. thickness at levee crest for individual depositional sequences; and B. thickness at levee crest above horizon R down western levee.

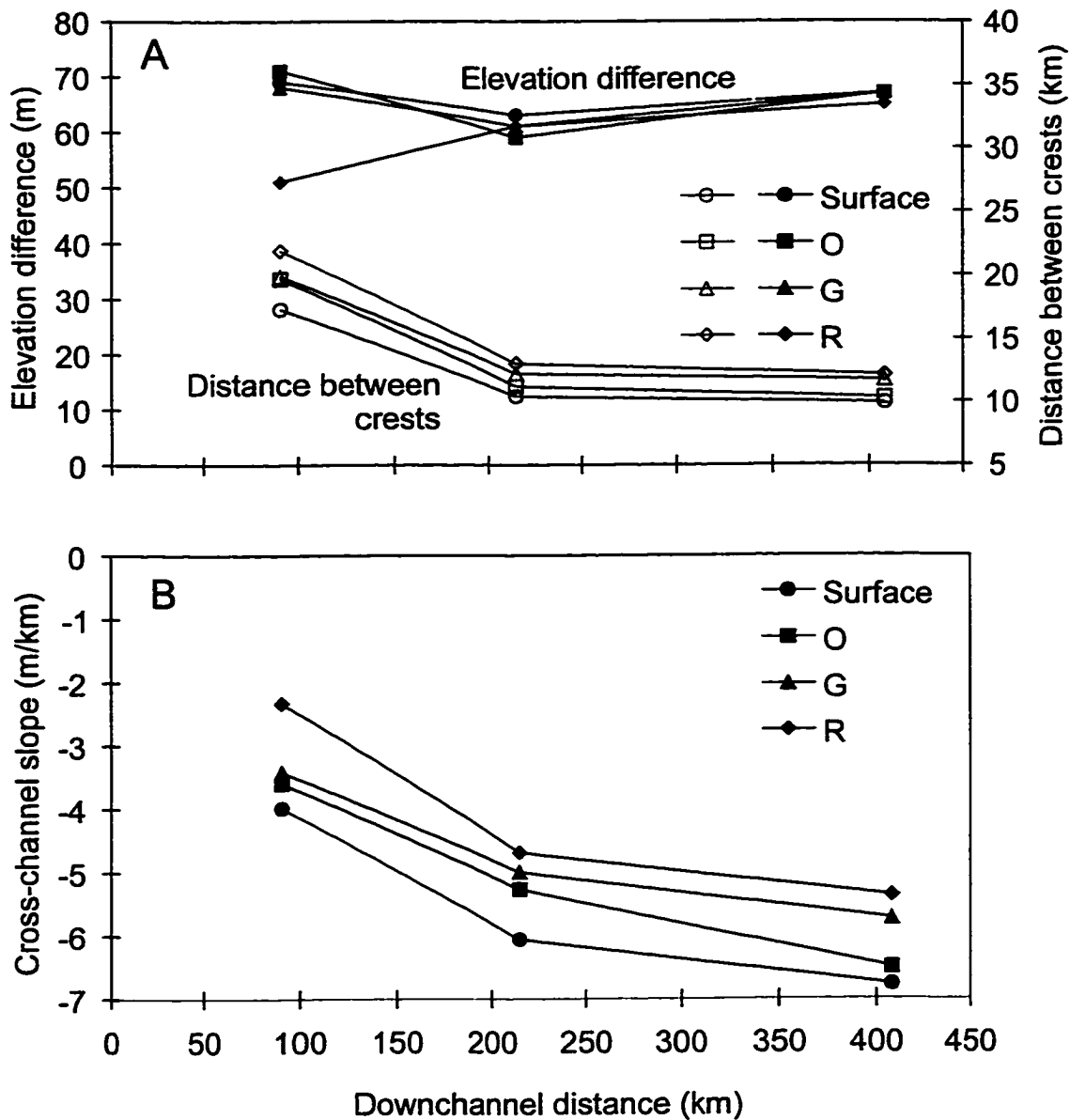


Figure 3.28. Downchannel variation in cross-channel asymmetry: A. plot of elevation difference between conjugate levees (filled symbols) and distance between levee crests (open symbols) versus downchannel distance; and B. downchannel variation in cross-channel slope. The cross-channel slope shows a trend toward increasingly negative values that is mostly due to the decrease in the distance between conjugate levee crests and not variations in the elevation difference.

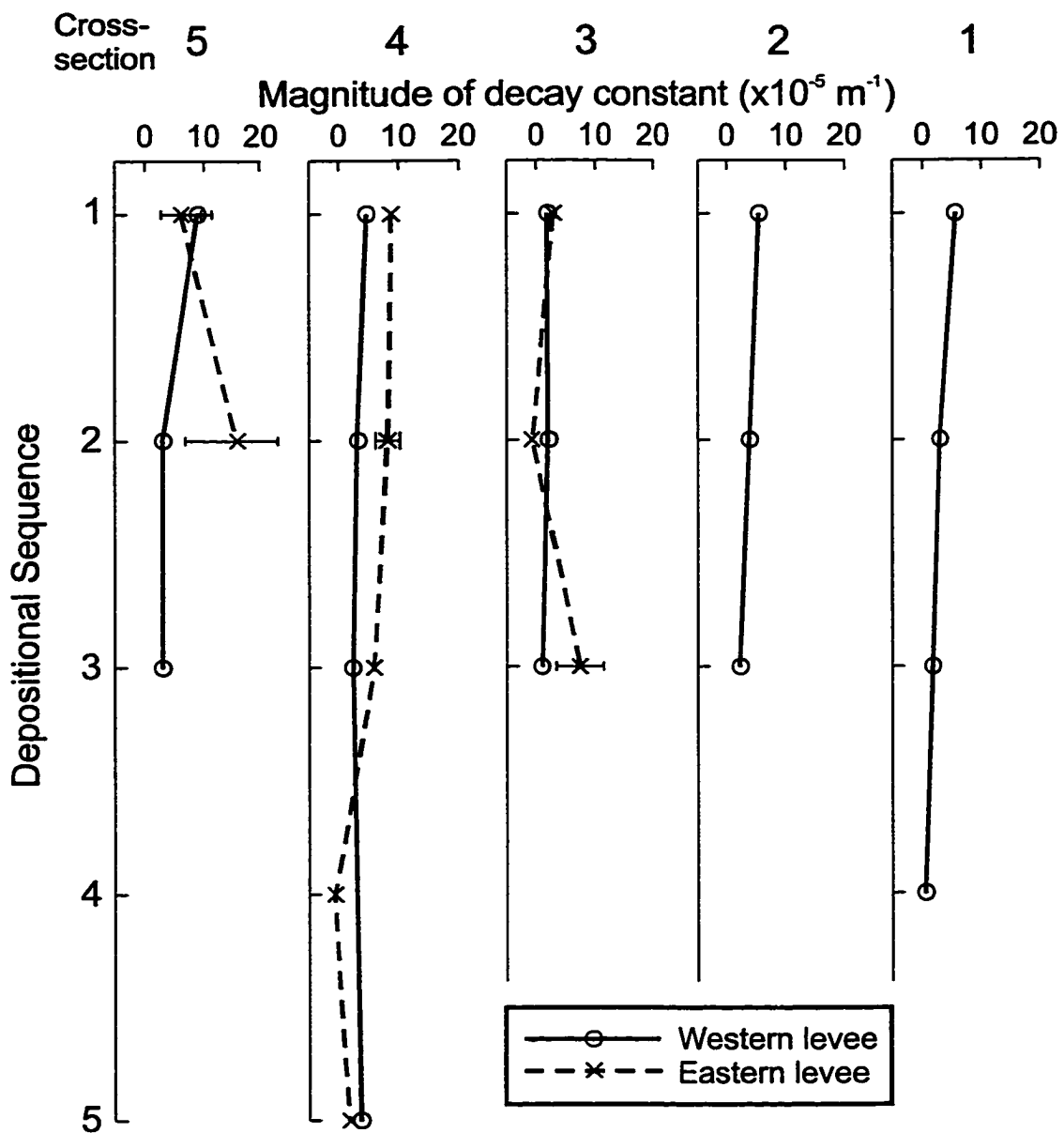


Figure 3.29. Stratigraphic variation in the spatial decay constant for across-levee variations in thickness, k , at each of the five cross-sections on NAMOC.

increase in k while at cross-section 3, k increases between DS3 and DS2, but no significant difference exists between DS2 and DS1. On the interchannel high at cross-section 3, k shows no stratigraphic trend. At cross-section 4, k increases slightly from DS3 to DS1. DS4 has uniform thickness; k does not statistically differ from zero. On the eastern levee, the magnitude of k shows a slight increase, but this increase is within the errors of k . The stratigraphic pattern in k is almost identical on the conjugate levees at cross-section 4. Data from cross-section 5 displays an increase in k on the western levee while k decreases on the eastern levee between DS2 and DS1.

The history of asymmetry on NAMOC shows that the increasingly negative values of ∇H arise from decreases in the distance between conjugate levee crests — the same mechanism responsible for the downchannel pattern in ∇H . The thickness on opposite sides of the channel remains approximately equal (Figure 3.25b). The strongest upsection trends in k characterize cross-section 1 and 2, but these cross-sections, especially cross-section 1, show no strong trend in levee crest movement. Asymmetry in k across the channel also lacks a stratigraphic trend. Although k tends to be greater on the eastern levee than the western levee (Figure 3.25a) the degree of asymmetry in k is not in a direct relationship with ∇H (Figure 3.30). Asymmetry in k was parameterized using the ratio of decay constants, western levee to eastern levee, termed k -ratio.

The history of asymmetry imaged by lower resolution airgun seismic profiles shows that the elevation difference between conjugate levee crest reflects preferential deposition on the western levee of NAMOC prior to deposition of green (Figure 3.16, Figure 3.17, and Figure 3.19a). Between olive and yellow at cross-section 4, deposition on the western levee was always greater, often twice as great, than on the eastern levee. Consequently, the elevation difference between conjugate levee crests progressively increased prior to green. During this time the levee crests moved toward the channel axis as they appear to do in the higher resolution 3.5 kHz data. With the elevation differences increasing and the distance between levee crests decreasing, the cross-channel slope between olive and green increased dramatically.

The stratigraphic evolution of the sediment waves north of cross-section 1 display a variable history. In some cases, the waves show no evidence for migration while in

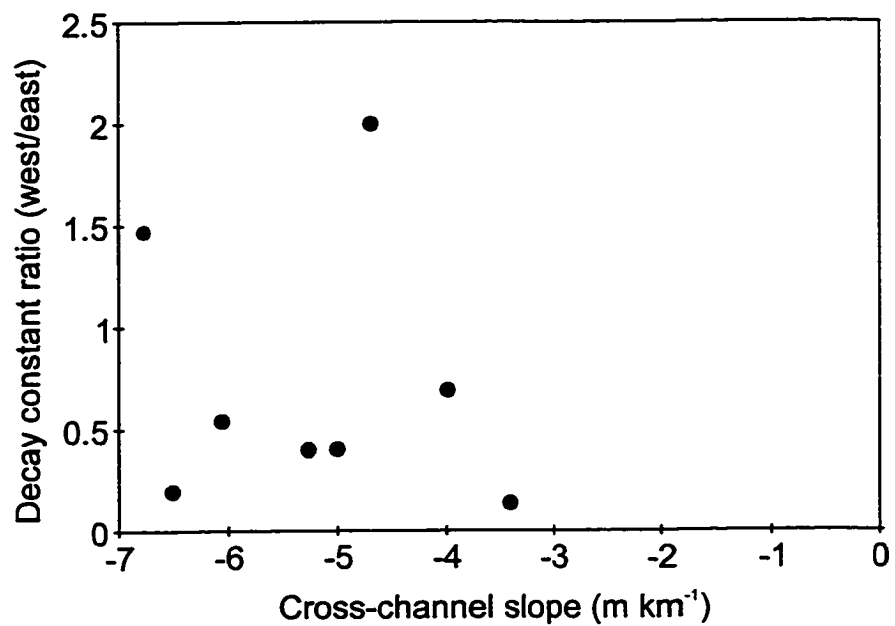


Figure 3.30. Inter-relationship between decay constant ratio and cross-channel slope. Ratio of decay constants given by magnitude of k on western levee divided by magnitude of k on eastern levee.

other cases a steady migration from their inception is seen. Alternations between periods of migration and periods of stagnation could not be unequivocally detected. Apparent wavelength does not appear to change for any one wave while wave amplitude remains constant or decreases slightly upsection. The sedimentation rate ratio (SRR) of the waves tends to unity suggesting uniform deposition across the waveform. This evolution suggests that the conditions responsible for the bedforms displayed only minor fluctuations through time or that these sediment waves do not respond linearly to changes in flow conditions.

3.6 Key Features

1. Data from NAMOC provide information on the variation in architecture and morphometry along the upper reach of a very long, glacially-fed, channel-levee system. Although, the spatial extent of data relative to the total length of NAMOC is small, the downchannel distance of over 400 km covered by the available data offers some constraint on the absolute spatial scales over which turbidity-current processes operate.
2. The most recent phase of levee growth, imaged by 3.5 kHz records, represents the continued building of levees along a relatively stable channel pathway. Evidence suggests that the channel path of NAMOC has remained stable since deposition of reflector olive (airgun data) well before the phase of levee growth imaged by the 3.5 kHz data. Long-term evolution of NAMOC is characterized by channel bypassing with the accumulation of a thick succession of levee sediments and only minor channel fill.
3. Thickness patterns on NAMOC imaged by high-resolution seismic data can be well-characterized by exponentially thinning depositional sequences aligned perpendicular to channel trend. The depositional sequences were fit to an exponential model using linear regression (Chapter 2).
4. During the most recent phase of levee growth, cross-channel slope on NAMOC is primarily a function of the distance between conjugate levee crests and not the elevation difference between levee crests. This slope increases both upsection and downchannel. Prior to deposition of reflector green (airgun data) the levees of NAMOC grew due to preferential deposition of sediment west of the channel. This,

more than variations in the distance between levee crests, dictated the increase in cross-channel slope of the system during deposition between olive and green.

5. The strongest downchannel pattern in levee architecture is characterized by increasingly negative ∇H which is due mostly to the progressive migration of the levee crests toward the channel axis rather than increases in the elevation difference between conjugate levee crests. This pattern coincides with values of k and η_{lc} that show relatively weak downchannel trends.
6. The downchannel uniformity of the decay constant, k , exists in spite of a gradual shallowing of the channel, the bifurcation and merging of NAMOC, and the spatial transition between erosion and deposition on the interchannel high.
7. The strongest stratigraphic pattern in levee architecture is also characterized by increasingly negative values of ∇H caused by migration of the levee crests toward the channel. At cross-sections 1 and 2 and to a lesser extent on the western levee at cross-section 4, a stratigraphic increase in k occurs.

Chapter 4

Levee Architecture of Hueneme Fan

4.1 General Statement

Hueneme Fan lies within the Santa Monica Basin, off Los Angeles, California (Figure 4.1). It is a low sinuosity, high gradient system in the classification scheme of Clark et al. (1992). Hueneme Fan is a small, sandy fan, lying within a tectonically active borderland basin; these characteristics make it an excellent analogue of many ancient sand-rich systems now exposed on land or actively pursued as oil and gas exploration targets. Hueneme Fan offers the opportunity to study the levee growth patterns of a relatively steep, sandy system, where the nature of turbidity current initiation is reasonably well-constrained. Hueneme Fan developed an asymmetric levee system from a well-defined initial basin configuration. Development of asymmetry, both inherited from pre-existing bathymetric relief and that presumably resulting from the action of the Coriolis force, are seen through the stratigraphic development of Hueneme Fan.

4.2 Data Set

The data for investigating the levee growth patterns of Hueneme Fan consist almost exclusively of acoustic imagery (Figure 4.2). In 1992, single channel sleevegun, Hunttec Deep Tow System (DTS) boomer, and 12 kHz records were collected from CSS Parizeau. These data were made available by GSC (Atlantic). For the present study, Hunttec DTS formed the primary data. Penetration on Hunttec DTS records was typically up to 50 ms on the levee flanks with a resolution of < 0.5 m. Some use was also made of the sleevegun data recorded by the Nova Scotia Research Foundation (NSRF) hydrophone array (hereafter referred to as "NSRF data"). These records have greater acoustic penetration, up to 1 s, but lower resolution (< 10 m). Core data that can be used for groundtruthing the acoustic records were taken from the literature, especially Malouta et al. (1981), Reynolds (1987), and Gorsline (1996).

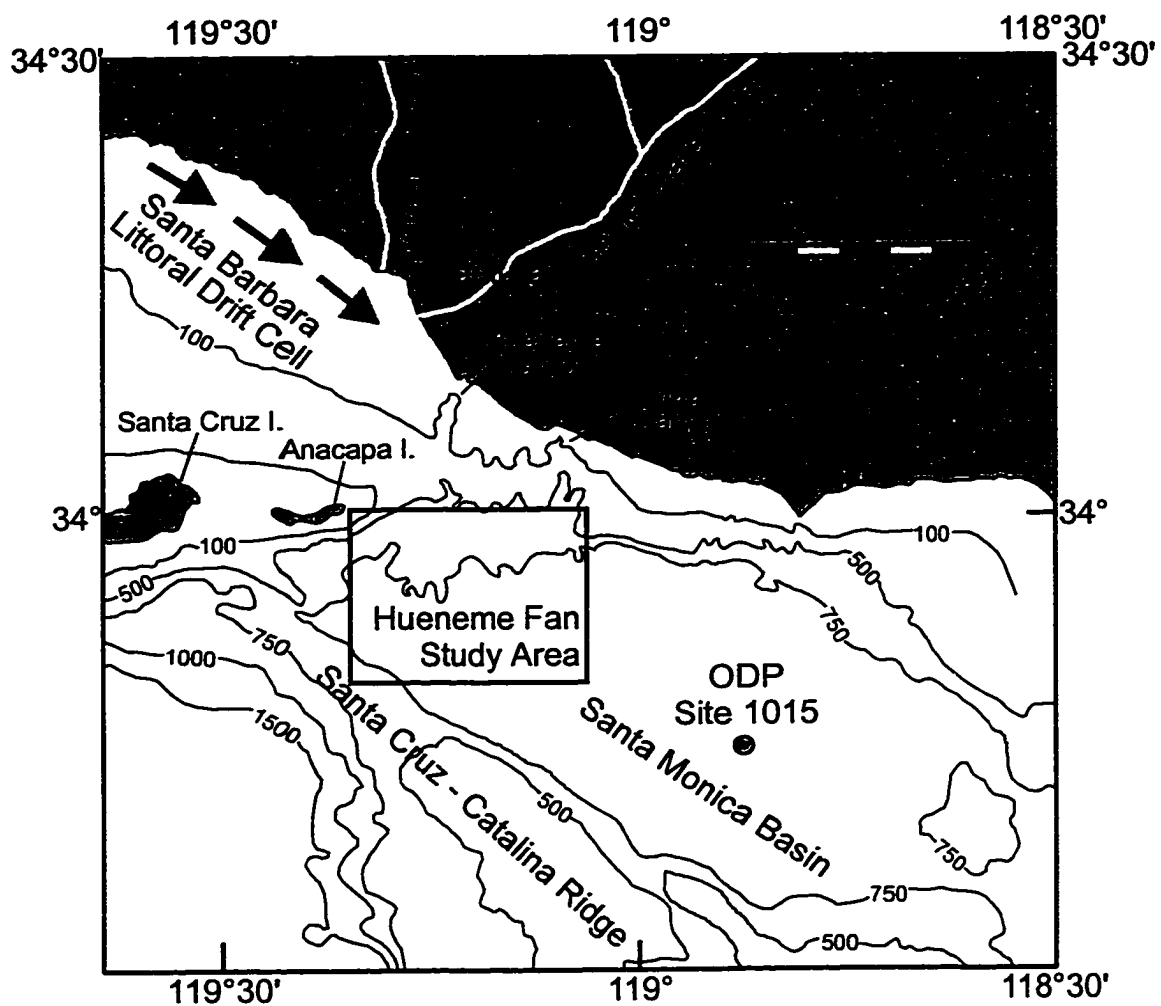


Figure 4.1. Location of Hueneme Fan within Santa Monica Basin. Also shown is the location of Ocean Drilling Program Site 1015.

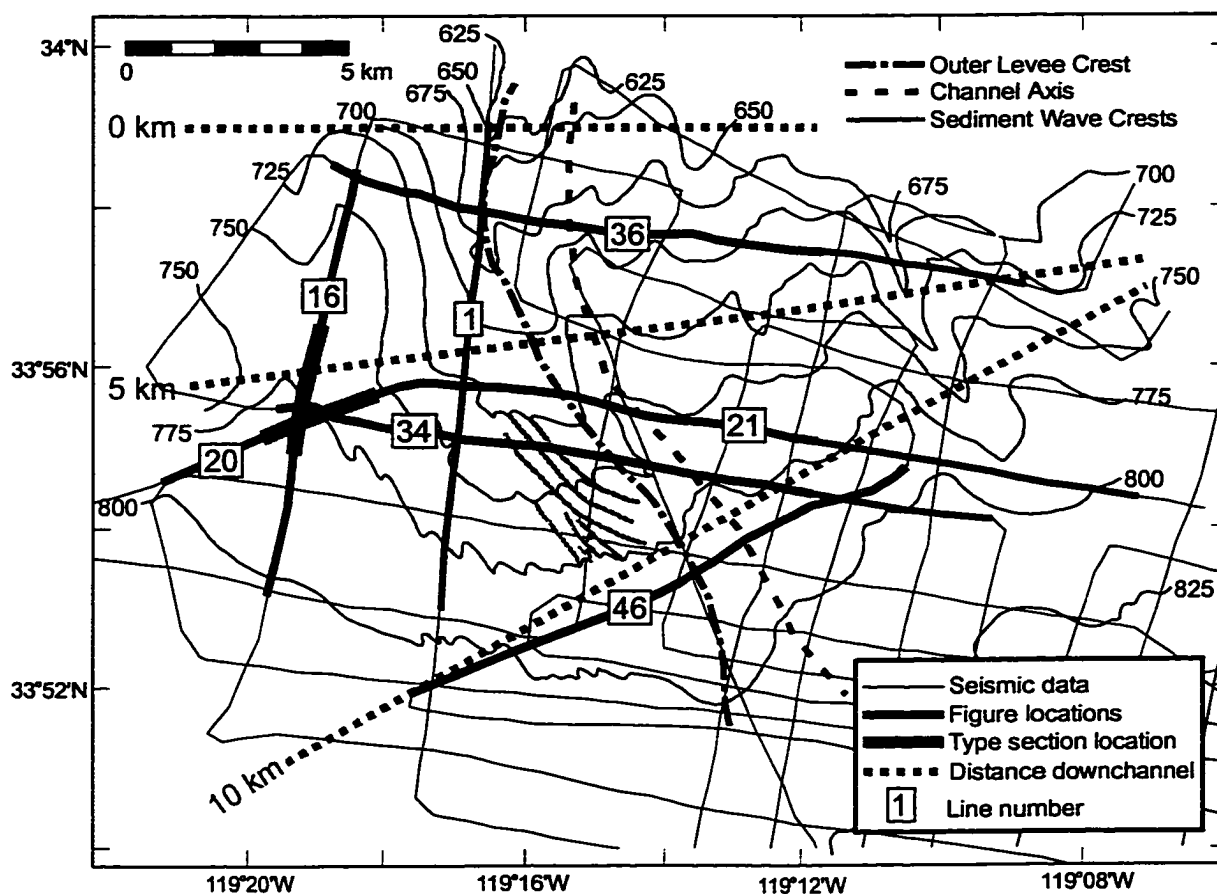


Figure 4.2. General bathymetry of Santa Monica Basin showing location of Hueneme Fan and distribution of acoustic data from CSS Parizeau cruise 91062. Also shown are trends of the modern levee crest and channel axis. Bold lines denote seismic lines displayed in figures. Distance downchannel from the 650 m isobath (0, 5, and 10 km) referred to in text.

4.3 Setting of Hueneme Fan

4.3.1 Channel Morphology

The Hueneme Canyon/Channel system extends approximately 30 km from the head of Hueneme Canyon, which deeply incises the continental shelf, heading in water depths of only 30 m (Figure 4.1). The detailed bathymetric map of Hueneme Fan covers a region between the 650 m isobath and the 800 m isobath with its most prominent feature being Hueneme Channel (Figure 4.3). The channel profile follows a weakly exponential trend (Figure 4.4). Many other submarine channels behave this way and have commonly been interpreted as graded (e.g., Clark et al., 1992), suggesting that the channel has reached an equilibrium with the hydrodynamics of the turbidity currents responsible for shaping its morphology. In Figure 4.4 and all subsequent discussion of Hueneme Fan, distance along-channel is measured from the 650 m isobath. The channel has a low sinuosity with one notable bend at approximately 6 km (Figure 4.4). The channel slope varies from 5-16 m km^{-1} , decreasing downfan (Figure 4.4). Relief between the western levee crest and the channel floor decreases from about 30 m on the upper fan to < 4 m on mid-fan, at which point the channel loses its morphological expression (Figure 4.3). The elevation difference between conjugate levee crests varies from 20 m to < 4 m, with the western (right-hand side looking downchannel) levee higher than the eastern (left-hand) levee. Channel width remains relatively constant downslope, averaging 4 km from levee crest to levee crest. In the detailed bathymetric map (Figure 4.3) sediment waves can be seen on the right-hand levee between 6 km and 10 km. The upper fan possesses both an inner low levee and outer, higher levee. Distance between the crests of the inner levees averages around 1 km.

4.3.2 Previous Work on Geology of Hueneme Fan

The architecture of Hueneme Fan has most recently been investigated by Normark et al. (1998), Piper et al. (1994) and Piper et al. (1998b, submitted). These studies have investigated the long term growth of Hueneme Fan and the most recent phase of channel-levee growth, building upon the initial work of Nardin (1983).

General Quaternary Stratigraphy

Normark et al. (1998) used NSRF data to develop an acoustic stratigraphy of

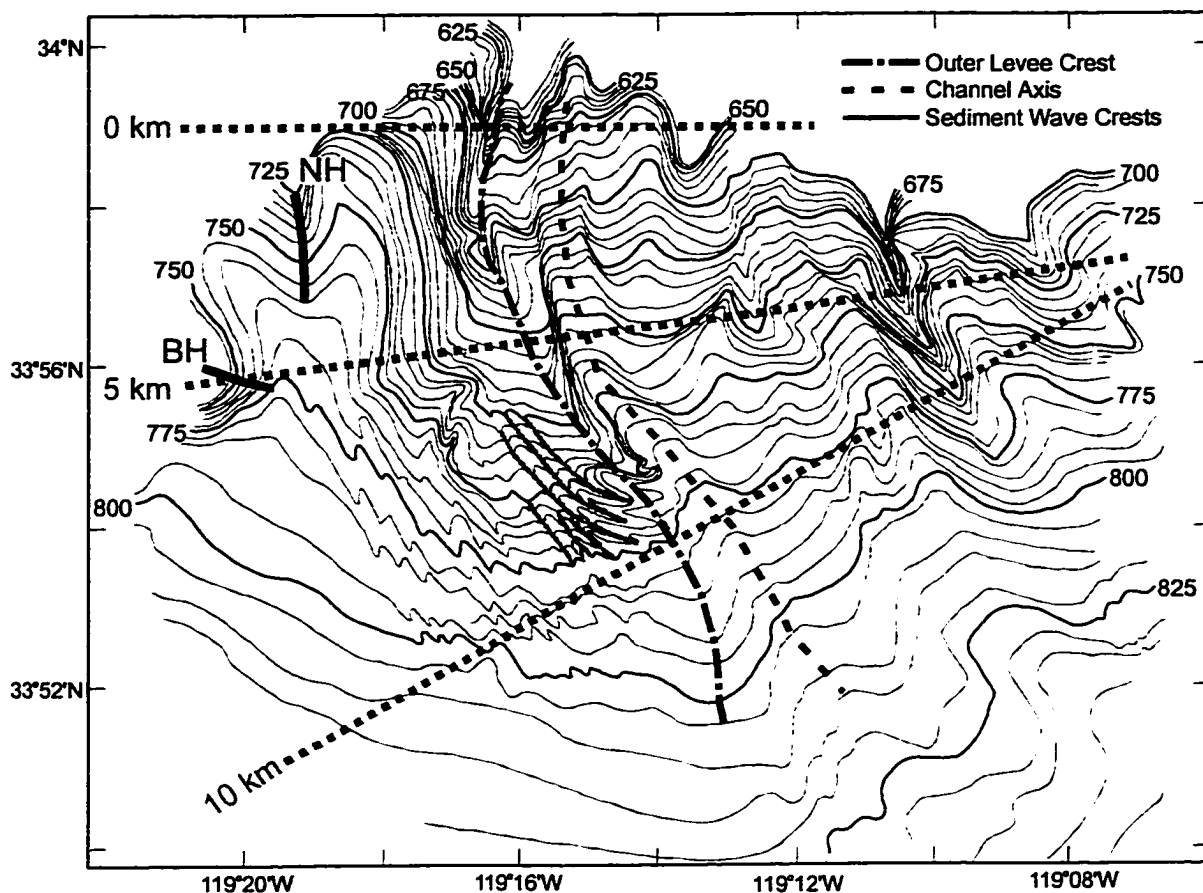


Figure 4.3. Detailed bathymetric map of Hueneme Fan (after Normark et al., 1998). Trend of the modern channel and levee crest depict the eastward turn of the channel. Sediment wave crests are highlighted although crest to crest correlations are speculative, based solely on the contours as drawn. BH denotes possible surface expression of subsurface high discussed in text. NH denotes trend of northernmost topographic high referred to in text.

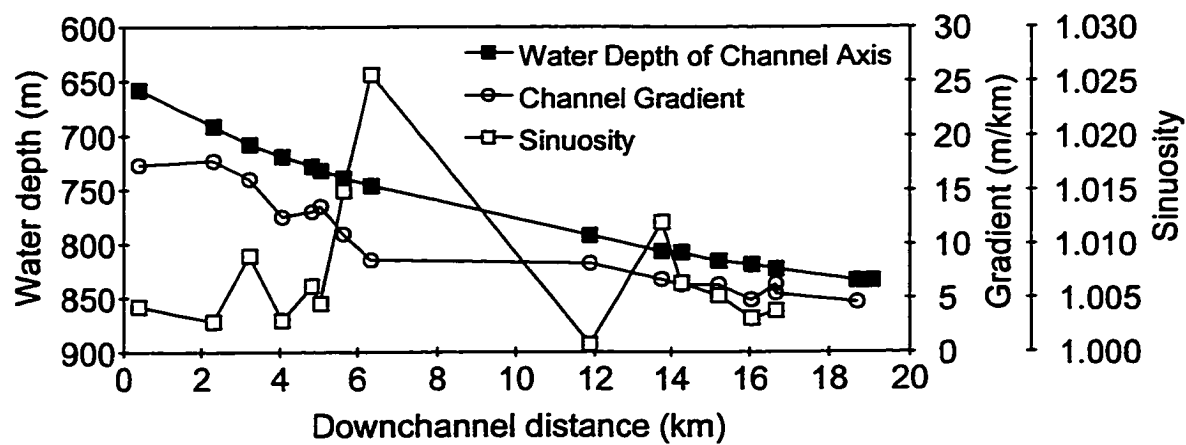


Figure 4.4. Morphology of Hueneme Channel showing profiles of axial water depth (filled squares), slope (open circles), and sinuosity (open squares) as a function of distance down-channel. Distance is measured along the channel trend from the 650 m isobath.

Hueneme Fan that showed the stacking of channel-levee sequences and the migration of the sediment source along the continental shelf. This migration was attributed to delta lobe switching as the Santa Clara river crossed the narrow continental shelf, depositing deltaic sediments that prograded onto the continental slope. These workers suggested that the nature of fan development depended on the mechanism responsible for generating turbidity currents which, in turn, depended on relative sea level. At lowstands of sea level, Normark et al. (1998) suggested that direct hyperpycnal inflow from the Santa Clara River may have been the dominant initiation mechanism. At highstands of sea level, they attributed turbidity current initiation to resuspension of sediment supplied by littoral drift and trapped in the canyon heads. Important to the later discussion of levee growth on Hueneme Channel is the definition by Normark et al. (1998) of a reflector, termed J, as the base of the most recent phase of channel-levee growth fed through Hueneme Canyon. This reflector was tentatively dated at around the last glacial maximum based on extrapolation of sedimentation rates at the basin margins.

General Late Quaternary Stratigraphy

Piper et al. (1998b, submitted) investigated high resolution Huntec DTS profiles, developing an acoustic stratigraphy for the latest phase of channel-levee growth. Important findings of this study, pertinent to levee growth on Hueneme Channel are: 1) the presence of an inner and outer levee on the upper fan; 2) the change from sandier to muddier sediments implied by the acoustic signature of channel-proximal sediments comprising the inner levee; and 3) the transition from weakly acoustically stratified sediments interspersed with continuous reflections to acoustically well-stratified sediments, likely at the 6 ka highstand of sea level.

4.3.3 Nature of Turbidity Currents

From a survey of the literature, several broad constraints may be placed on the character of turbidity currents delivering sediment to the fan. Each of these constraints — sediment delivery, initiation mechanisms, and flow parameter reconstructions — is reviewed in the following section.

Sediment Delivery

The character of present-day sediment input into Santa Monica Basin gives some indication of the rates and grain sizes supplied to the basin during the late Quaternary evolution of Hueneme Fan. It should be noted that exact estimates of these parameters are not well-known for earlier times; consequently, modern sediment input rates can only establish order-of-magnitude estimates for past sediment delivery.

Santa Monica Basin receives sediment via littoral drift and fluvial input. Hueneme Canyon lies at the downdrift end of the long Santa Barbara littoral cell (Figure 4.1) (Nardin, 1983). Malouta et al. (1981) estimated that the present rate of littoral drift in the Santa Barbara cell supplies approximately $10^6 \text{ m}^3 \text{ yr}^{-1}$ of sediment, mainly sand, that is intercepted by the head of Hueneme Canyon. The present fluvial sediment discharge into the basin ranges from 10^6 - $10^7 \text{ m}^3 \text{ yr}^{-1}$, depending on rainfall, and comes mainly from Santa Clara River. Given the relative proximity of the canyon head and the mouth of the Santa Clara, it seems likely that this river fed the canyon head directly during lowstands of sea level (Dahlen et al., 1990). In fact, the present water depth of the canyon head at only 30 m suggests that direct fluvial input to the canyon head persisted well into the Holocene (Normark et al., 1998).

Within Santa Monica Basin, i.e., seaward of the 750 m isobath, Gorsline (1996) mapped the distribution of six turbidites that were deposited within the last 500 years based on a ^{210}Pb chronology (Table 4.1). He compared estimates of turbidite volume with the volume of sediment that could have accumulated in the canyon heads due to fluvial input and littoral drift. According to Gorsline (1996), basin-floor turbidites exceeding $50 \times 10^6 \text{ m}^3$ required both canyon emptying and slope failures. The smaller events are coincident with major flood events (Gorsline, 1996); however, their volumes are small enough that floods or failure of sediment in the canyon head could have supplied the requisite sediment volumes.

Malouta et al. (1981) mapped the present day sediment cover, finding that the shelf had sediment with grain sizes between 16-250 μm , whereas the slope had finer material ranging from 8-16 μm and even finer material, with grain sizes ranging from 4-8

μm , characterized the basin floor. These data suggest that only a limited range ($< 250 \mu\text{m}$) of grain sizes was available for redeposition by turbidity currents.

Table 4.1. Data on volume and initiation mechanism for six turbidites in Santa Monica Basin deposited over the last five centuries (data and interpreted mechanism from Malouta et al. (1981), Reynolds (1987), Gorsline (1996)).

Turbidite	Volume $\times 10^6 \text{ m}^3$	Initiation Mechanism	Supporting Evidence
1969	10	hyperpycnal inflow or failure of canyon head sediments	1969-1970 floods
1880's	28	hyperpycnal inflow or failure of canyon head sediments	Mission records of floods, 1884-1891
1811-1812	55	seismic trigger	Mission records of seismic events, 1812 "Mission 'Quakes"
280 a	58	seismic trigger	sediment volume
400 a	75	seismic trigger	sediment volume
560 a	105	seismic trigger	sediment volume

Initiation

The position of relative sea level apparently influences the mechanisms initiating turbidity currents on Hueneme Fan (Normark et al., 1998). Normark et al. (1998) suggested that during highstands of sea level, turbidity currents are initiated by the remobilization of littoral drift intercepted by and accumulating in the canyon heads. Downslope remobilization of this canyon head sediment may have occurred due to storm surges or earthquake loading, likely following the mechanisms proposed by Inman et al. (1976) for Scripps Canyon and Anastasakis & Piper (1991) for Aegean turbidites, respectively.

The turbidites identified by Gorsline (1996) over the past 500 years (Table 4.1) were subdivided based on sediment volume in comparison to the total amount of sediment that could have accumulated in the canyon heads using modern values for littoral drift and fluvial input. On this basis, Gorsline (1996) attributed the four oldest events to seismic triggering of sediment failure. The coincidence in the age of the 200-year-old turbidite with historical records of an earthquake in this area offers some support

for this conclusion; however, the accuracy of ^{210}Pb -dating ($\pm 3\text{-}50$ years) precludes a definitive correlation. The two most recent events coincided with times of major floods of the Santa Clara River. Reynolds (1987) suggested that hyperpycnal inflow may have triggered the 100-year-old-turbidite, using historical records of floods as supporting evidence. Gorsline (1996) also suggested that hyperpycnal inflow may have triggered this event as well as the most recent turbidite, but his comparison of sediment volumes could not differentiate between hyperpycnal inflow and the emptying of the canyons due to sediment failure.

Normark et al. (1998) invoked hyperpycnal inflow as an initiation mechanism that was active during lowstands of sea level. The Santa Clara River is a steep, medium-sized river; thus, it is a likely candidate for creating hyperpycnal inflows (Mulder & Syvitski, 1995). During lowstands, the Santa Clara fed directly to the head of Hueneme Canyon (Dahlen et al., 1990), making hyperpycnal inflow even more likely.

Flow Parameter Estimates

Previous estimates of flow parameters for turbidity currents active in the Hueneme Fan system have focused on recent events described by Malouta et al. (1981) (200-year turbidite) and Reynolds (1987) (100-year turbidite). Malouta et al. (1981) and Reynolds (1987) made comparisons between their studied turbidites and the underlying turbidites sampled by some of their cores; however, similar analyses of late Pleistocene turbidites were hampered by the inability to correlate individual events. Normark et al. (1998) suggested some constraints on the flows responsible for fan growth during lowstands of sea level.

Malouta et al. (1981) mapped a near-surface turbidite having a volume of about 10^8 m^3 . Using ^{210}Pb methods, they dated this turbidite at 200 a and correlated the event with an 1812 earthquake documented in mission records. From its distribution, Malouta et al. (1981) suggested Mugu Canyon (Figure 4.1) as the likely sediment source. This turbidite has well developed Bouma C-D-E divisions.

Reynolds (1987) mapped the distribution of a turbidite overlying the 200-year turbidite of Malouta et al. (1981). She estimated an age of 100 a for this event and correlated it with the Santa Clara River flood of 1884. From its distribution, Hueneme Canyon appears as the most likely source. The 100-year turbidite has a bimodal grain

size with sand ranging from 90-150 μm and silt from 20-50 μm . Using suspension criteria, Reynolds (1987) estimated flow velocities from 0.9 m s^{-1} on the upper middle fan to 0.1 m s^{-1} on the lower middle fan. Flow thickness estimates were taken from the distribution of the turbidite relative to bathymetric obstacles on the floor of Santa Monica Basin and ranged from 5 m to 15 m. Using her velocity and flow thickness estimates, Reynolds (1987) used the Chezy equation to estimate the excess density of the flow as between 1 and 5 kg m^{-3} , decreasing downfan. The total volume of sediment deposited was 10^7 m^3 and, with the previous flow parameter estimates, a sediment discharge can be calculated that yields a flow duration of approximately 10 days. The long flow duration estimate and the distribution of the turbidite seaward of Hueneme Canyon led Reynolds (1987) to suggest that hyperpycnal inflow from the Santa Clara initiated the turbidity current.

Comparison between the two recent turbidites shows that the 100-year turbidite is approximately an order of magnitude less in volume and finer-grained than the 200-year turbidite (Reynolds, 1987). The well-developed C-D-E divisions in the 200-year turbidite compared to the D-E divisions of the 100-year turbidite suggest that the older event had a higher flow regime. Comparing the thicknesses of these turbidites with older events, Malouta et al. (1981) suggested that older events were of greater volume than the 200-year turbidite, thus placing a lower limit of 10^8 m^3 on the sediment volume of past events. Malouta et al. (1981) also estimated the frequency of events at less than one per 100 years by comparing the volume of the 200-year turbidite to the rate of sediment supply to Santa Monica Basin.

Evidence for the nature of turbidity currents on Hueneme Fan further back in time is sparse due to the lack of core data. The lowstand turbidity currents envisioned by Normark et al. (1998) built high levees and were responsible for sediment wave formation. Using the relationship between wavelength and flow thickness proposed by Normark et al. (1980) and assuming a Froude number of unity, the morphology of the sediment waves suggests that flows on the western levee were on the order of 100 m. Consequently, at least some lowstand turbidity currents were likely thick, long duration flows (Normark & Piper, 1991).

In summary, the available evidence suggests that the turbidity currents responsible for the construction of Hueneme Fan had velocities on the order of $< 1 \text{ m s}^{-1}$ and volume concentrations around $10^{-3} - 10^{-4}$. Flow thickness is less well constrained, but may have been several times greater than channel relief. The flows transported grain sizes that likely reflected those presently supplied by Santa Clara river or by the southerly littoral drift, i.e., no greater than coarse sand. The frequency of turbidity currents over the last 500 years has been about one per century; during the late Pleistocene the frequency may have been higher. The relatively small size of Hueneme Fan may reflect the relatively low rates of sediment delivery to the system, estimated to be around $10^6 - 10^7 \text{ m}^3 \text{ yr}^{-1}$, based on modern values.

4.4 Levee Architecture of Hueneme Fan

The present study investigates the levee architecture of the most recent phase of channel-levee growth on Hueneme Fan that is imaged by Hunttec DTS boomer records. This section presents the general stratigraphy of this phase of levee growth followed by an analysis and synthesis of the architectural measures introduced in Chapter 2.

In the seismic examples and the treatment of the levee architecture of Hueneme Fan, two-way travel time was converted to depth in metres using an average velocity of 1500 m s^{-1} . Ocean Drilling Program (ODP) site 1015 in the central Santa Monica Basin (Figure 4.1) recovered sandy turbidites that had velocities averaging 1600 m s^{-1} (Shipboard Scientific Party, 1997). Acoustic character of these sediments, particularly their high reflectivity, typifies sandy sediments (Figure 4.5). Comparison of this acoustic character with that of the levees (Figure 4.5) with their moderate reflectivity strongly suggests that the levees comprise muddier sediments. In addition, velocity data from ODP boreholes on Amazon Fan suggest that an average velocity of 1500 m s^{-1} is appropriate for the first 100 m of section in muddy turbidites (Flood, Piper, Klaus et al., 1995; Flood et al., 1997).

4.4.1 Levee Stratigraphy

In the Hunttec DTS data, three regional reflectors were traced from the type section on the western levee of Hueneme Channel (Figure 4.6) throughout the levee sediments both to the west and east of Hueneme Channel. In order of increasing

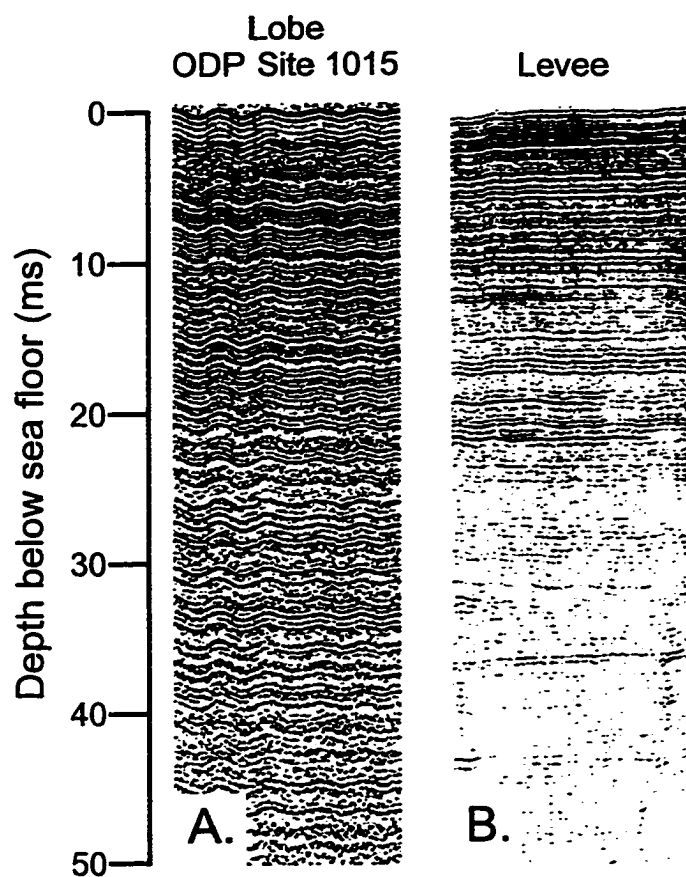


Figure 4.5. Acoustic character of sediments as imaged in Hunttec DTS boomer records: A. in central Santa Monica Basin sampled by ODP Site 1015 having velocities averaging 1600 m s^{-1} ; B. typical levee sediments having an assumed velocity of 1500 m s^{-1} .

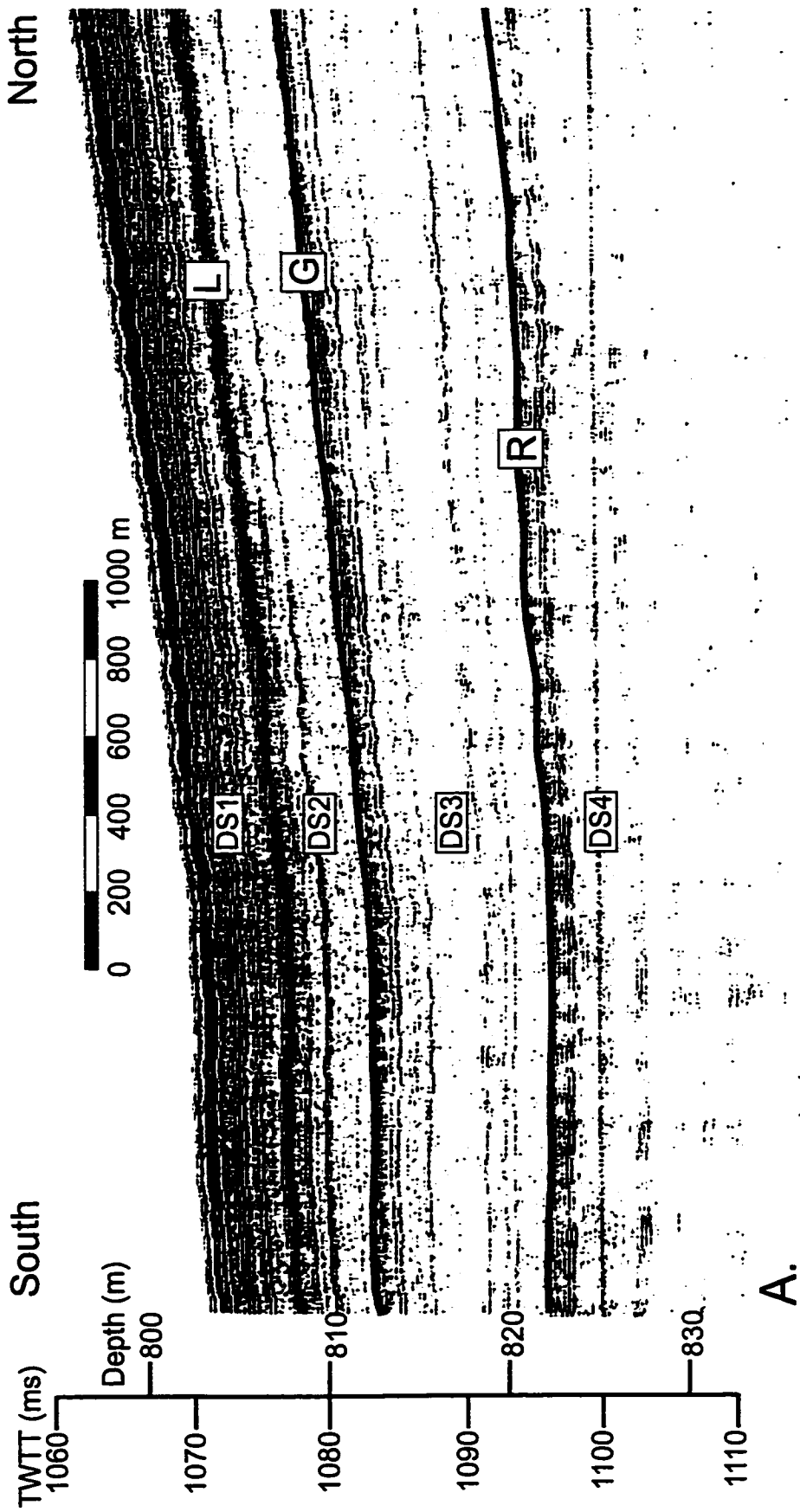


Figure 4.6. Huntect DTS type section from western levee of Hueneme Channel: A. dip section; B. strike section. Locations given in Figure 4.2 and Figure 4.9. Reflectors defined in text; DS = depositional sequence, TWTT = two-way travel time.

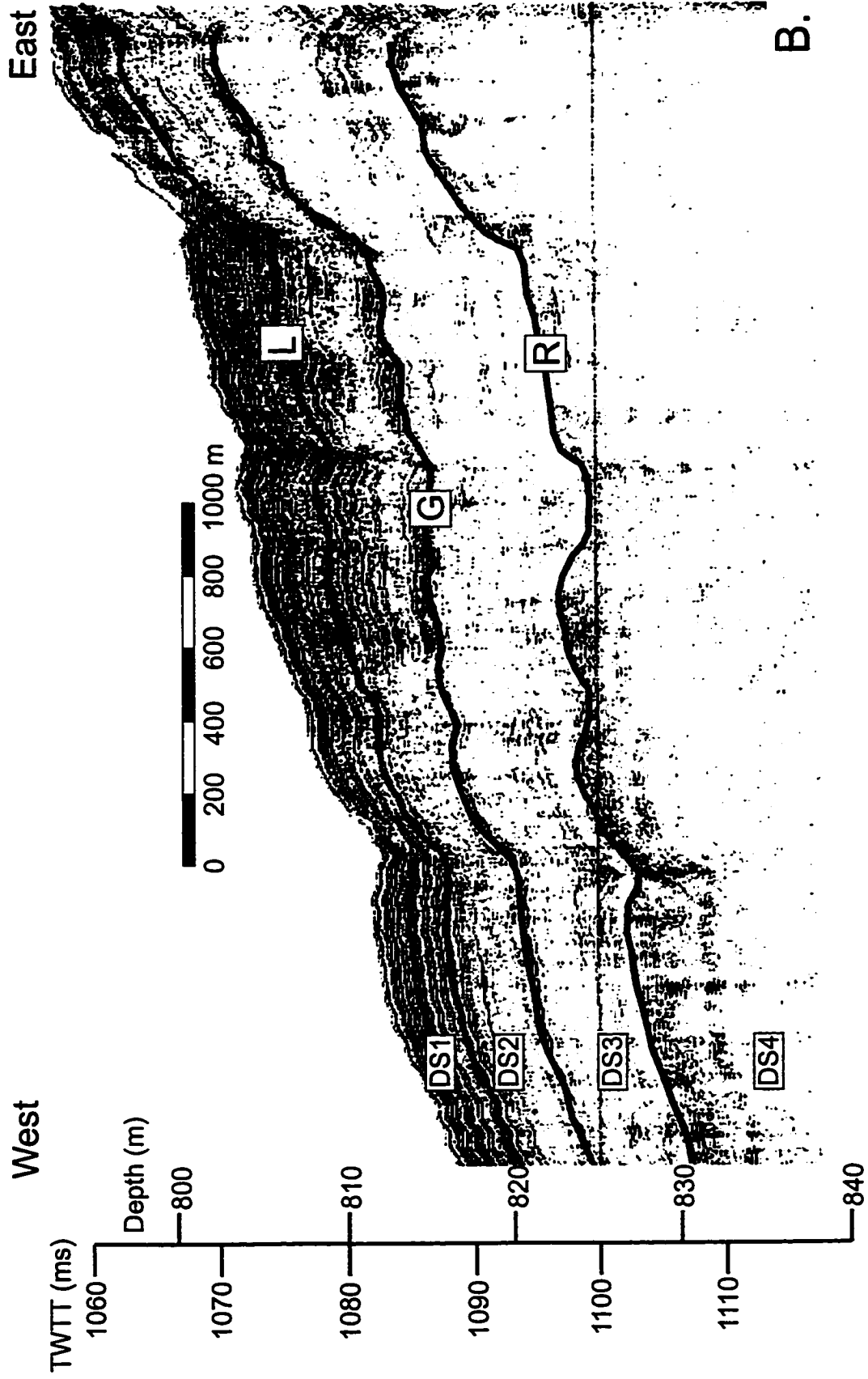


Figure 4.6. Continued.

subbottom depth, these reflectors are L, G, and R (Figure 4.6). A fourth widely correlatable reflector, J, was identified by Normark et al. (1998) in their data (Figure 4.7). Horizon J could be directly traced beneath the channel and into the levee sediments east of Hueneme Channel (Figure 4.8). The overlying reflectors were correlated across the channel on the basis of reflector character and stratigraphic position relative to J. The reflectors form the boundaries of four depositional sequences: DS4 bounded by J and R, DS3 bounded by R and G, DS2 bounded by G and L, and DS1 bounded by L and the sea floor. Horizon J marks the beginning the most recent phase of channel-levee growth seaward of Hueneme Canyon (Normark et al., 1998) and the base of DS4. DS4 occurs near the limit of acoustic penetration on the Hunttec DTS records; however, in its upper sections it appears weakly acoustically stratified (Figure 4.6). On the lower resolution NSRF records, DS4 appears weakly to strongly acoustically stratified. DS2 and DS3 are best imaged in the Hunttec DTS records. They appear weakly acoustically stratified, making up a conformable succession at the resolution of the Hunttec DTS data. DS3 can be locally distinguished on NSRF records where it appears weakly acoustically stratified to acoustically transparent (Figure 4.7 and Figure 4.8). DS1 can only be distinguished on Hunttec DTS records where it appears acoustically well-stratified throughout.

Line drawings from seismic profiles that obliquely cross Hueneme Channel show that the morphology of the channel-levee system progresses downfan from distinct to subtle (Figure 4.9). On line 36, the inner and outer levees are pronounced while by line 20-21 the distinction between the two is less evident and finally by Line 46 little evidence for a inner/outer levee morphology remains. DS1 and DS2 on the inner levee at line 36 (Figure 4.10a) are acoustically well-stratified, indicative of muddy sediments. Here, DS3 appears acoustically amorphous, suggesting sandier sediments. At line 20-21 (Figure 4.10b) the transition from acoustically amorphous to acoustically stratified sediment is less distinct. At line 46, reflectors are difficult to correlate close to the channel because of limited penetration of seismic energy. On the levee flank, the character of the depositional sequences is similar to upstream locations (Figure 4.11). Nearer Hueneme Channel, only R can be confidently traced toward the levee crest and then only when using the NSRF records (Figure 4.12). At line 46, DS4 appears to thicken westward while above horizon R, sediments have much more uniform thickness (Figure 4.12) than

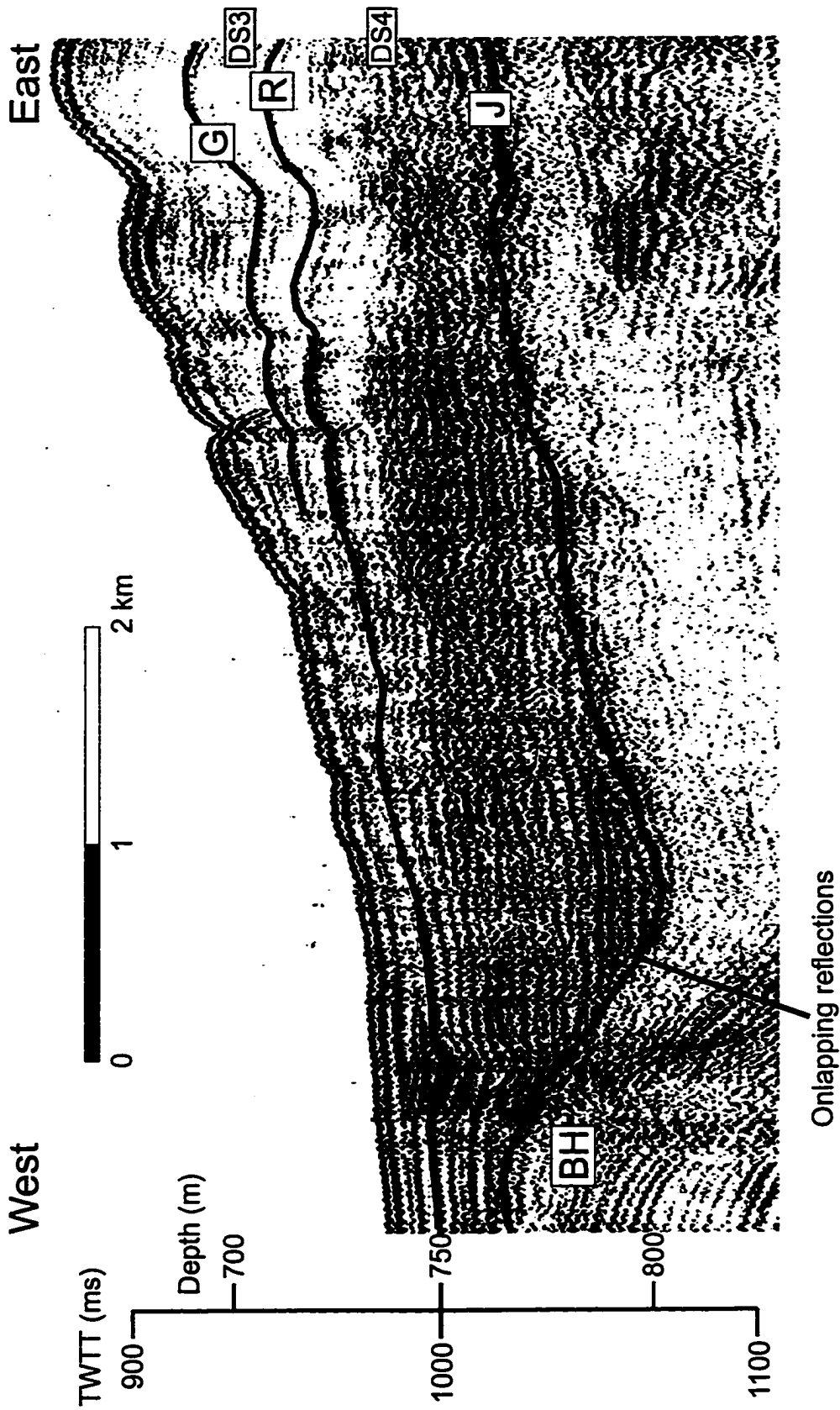


Figure 4.7. NSRF type section from western levee of Hueneme Channel. Locations given in Figure 4.2 and Figure 4.9. Reflectors defined in text. Note onlapping of reflections against buried subsurface high (BH).

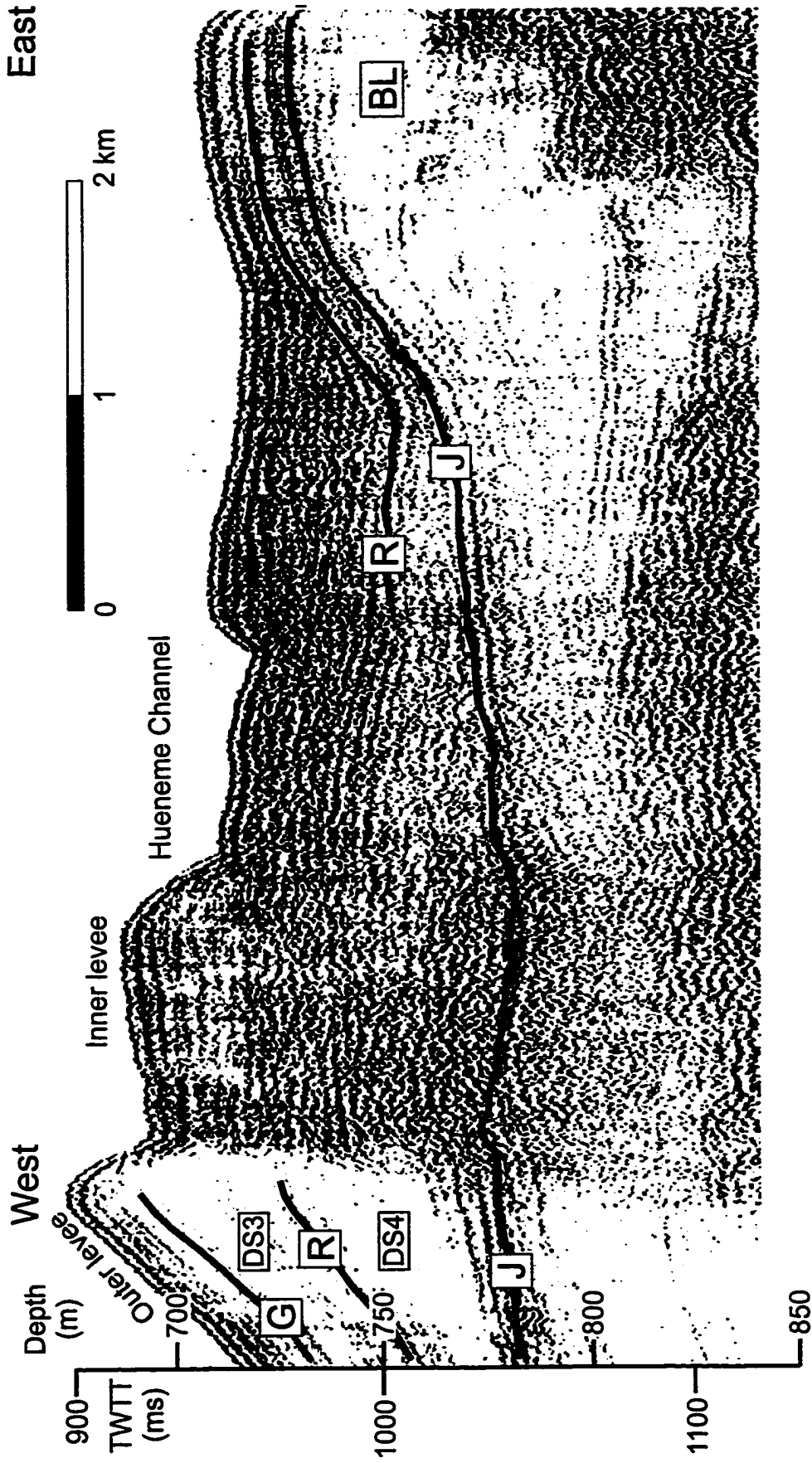


Figure 4.8. NSRF profile (Line 36) of upper Hueneme Channel showing stratigraphic and geographic relationship between modern channel and buried channel-levee system (BL) to the east of the modern channel. Location given in Figure 4.2 and Figure 4.9.

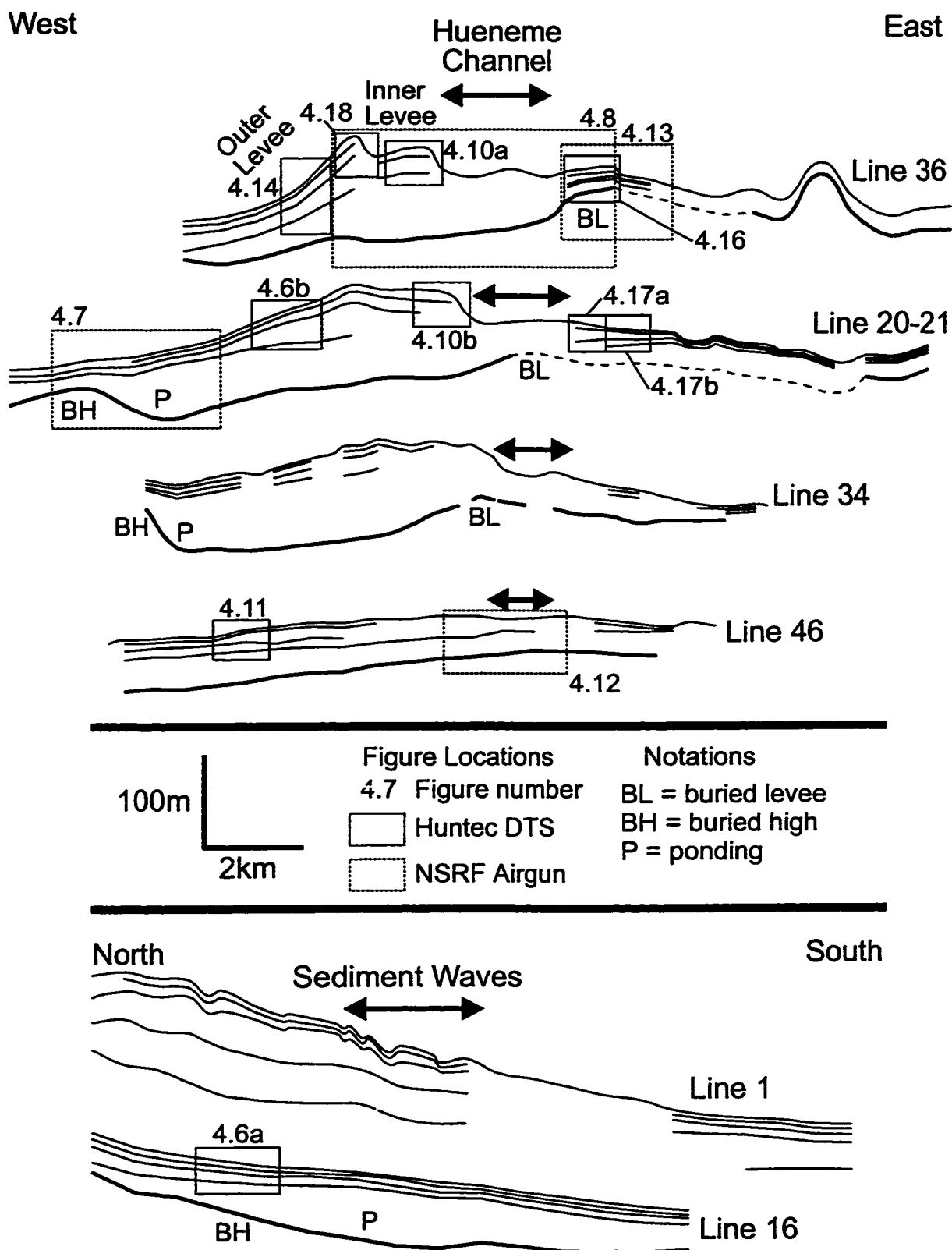


Figure 4.9. Interpreted line drawings of seismic sections perpendicular and parallel to Hueneme Channel. These sections have been grouped into predominantly across-channel, or west-east (top), and down-channel, or north-south (bottom), lines. Locations given in Figure 4.2.

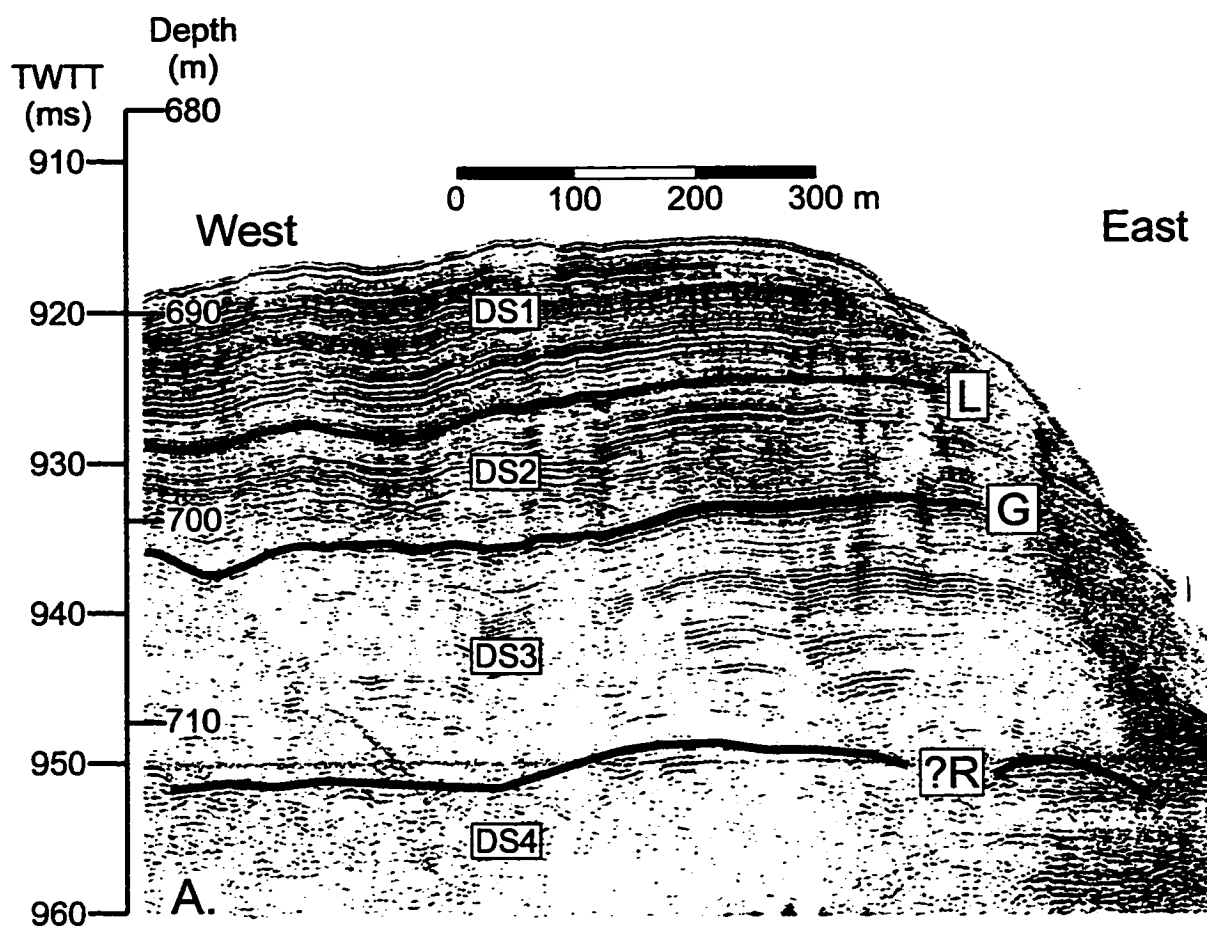


Figure 4.10. Hunttec DTS profile from inner, western levee of Hueneme Channel: A. at line 36; B. at line 20-21. Locations given in Figure 4.2 and Figure 4.9. Note the transition from discontinuous reflections below horizon G to continuous reflections with good acoustic stratification above G at line 36 while this transition appears to occur after horizon G at line 20-21.

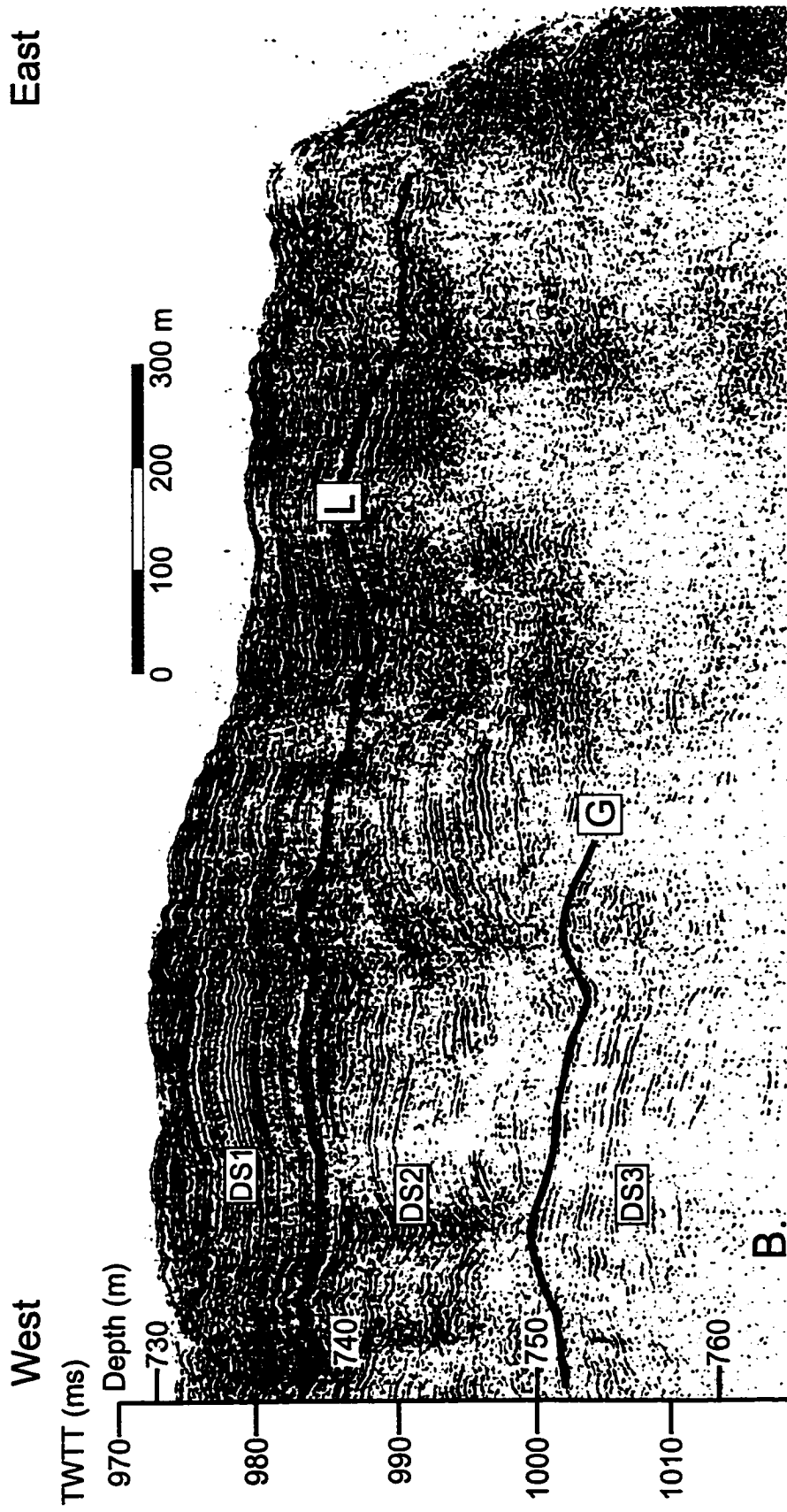


Figure 4.10. Continued.

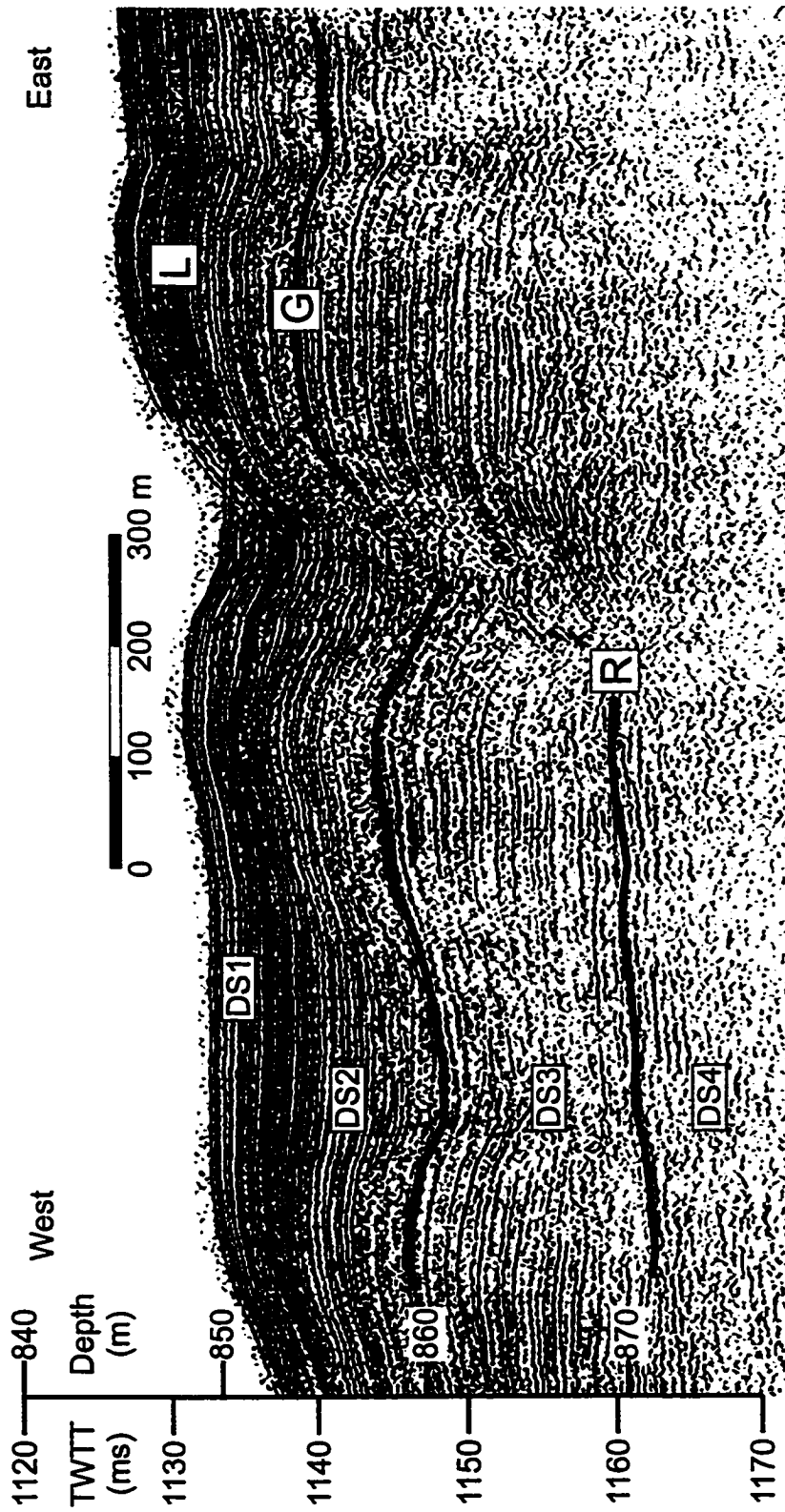


Figure 4.11. Huntect DTS profile (Line 46) showing sediment waves on levee flank. At this location, the bedforms appear to begin after deposition of horizon R. Their migration appears to be eastward, i.e., toward the channel. At some stratigraphic intervals the waves appear to be aggradational lacking eastward migration. However this behaviour characterizes individual waves and does not appear to be consistent for any particular stratigraphic interval except perhaps for deposition after horizon L. Location given in Figure 4.2 and Figure 4.9.

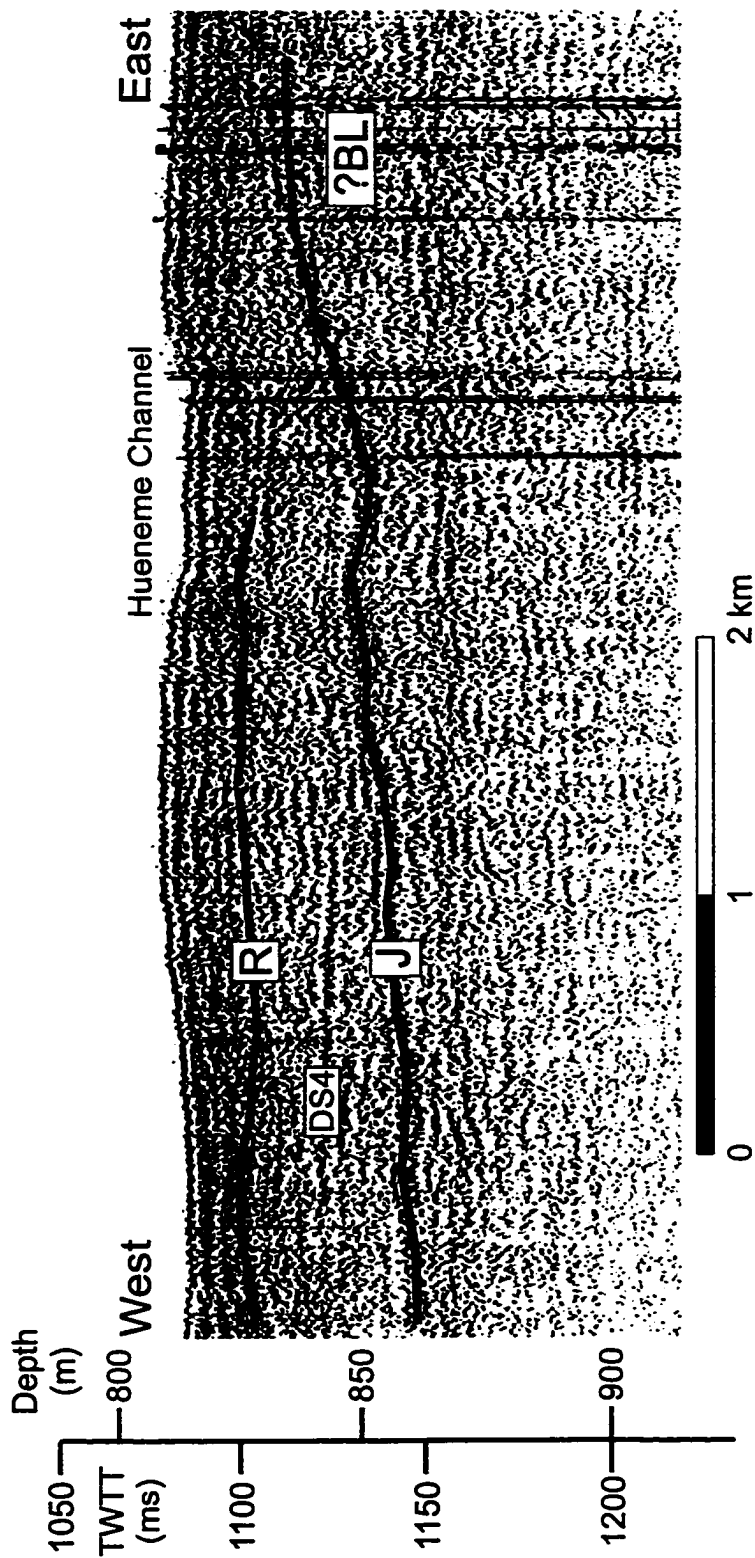


Figure 4.12. NSRF profile (Line 46) across distal end of Hueneme Channel. Location given in Figure 4.2 and Figure 4.9. At this location Hueneme Channel has very low relief. Note westward thickening of DS4 between horizons J and R.

at locations upfan (i.e., line 36, Figure 4.9).

The cross-sections also illustrate the effect of the buried channel-levee system (BL on Figure 4.8 and Figure 4.9) and a subsurface high (BH on Figure 4.7 and Figure 4.9) on overlying depositional sequences. On line 36, the buried channel-levee system occurs east of the modern Hueneme Channel and lies stratigraphically below J (Figure 4.8). This feature is interpreted to be a buried levee because it has a low overall reflectivity with divergent internal reflections and lies adjacent to high reflectivity, acoustically amorphous sediment indicative of sandy channel fill (Figure 4.13). By line 46 (Figure 4.12), the modern channel axis occurs adjacent to but stratigraphically well-above the flank of this buried levee. Ponding of sediment along the subsurface high is seen in both strike (line 20-21 on Figure 4.9 and Figure 4.7) and dip (line 16) lines (BH on Figure 4.9). Apparent relief of this subsurface high (Figure 4.7) is approximately 40 m.

On the outer levee west of Hueneme Channel, the two most proximal cross-sections display thinning of depositional sequences perpendicular to the channel trend (Figure 4.6b, Figure 4.9, Figure 4.14). Although not captured by the line drawings, sediment waves exist on the levee backside. These waves are absent from the levee backside at line 36 (Figure 4.14), but are well-developed only a few kilometres further downstream at line 20-21 (Figure 4.6b). They can also be seen at line 46 although their apparent (i.e., profiles not perpendicular to wave crest) amplitude and wavelength have decreased (Figure 4.11). At line 20-21 evidence for sediment wave development can be seen as deep as horizon R, and at line 46 sediment wave development apparently began around horizon G. This suggests that the conditions for sediment wave development shifted basinward between deposition of DS4 and DS3.

4.4.2 Stratigraphic Evolution

The surface defined by J delineates the initial conditions for the most recent phase of levee growth (Figure 4.15). The most prominent feature on J is the channel-levee system that exists east of the modern channel trend (Figure 4.8 and Figure 4.13). The modern channel trend over the first 5 km appears to be guided by the presence of this buried levee. However, at distances greater than 5 km, the modern channel partially overrides this feature.

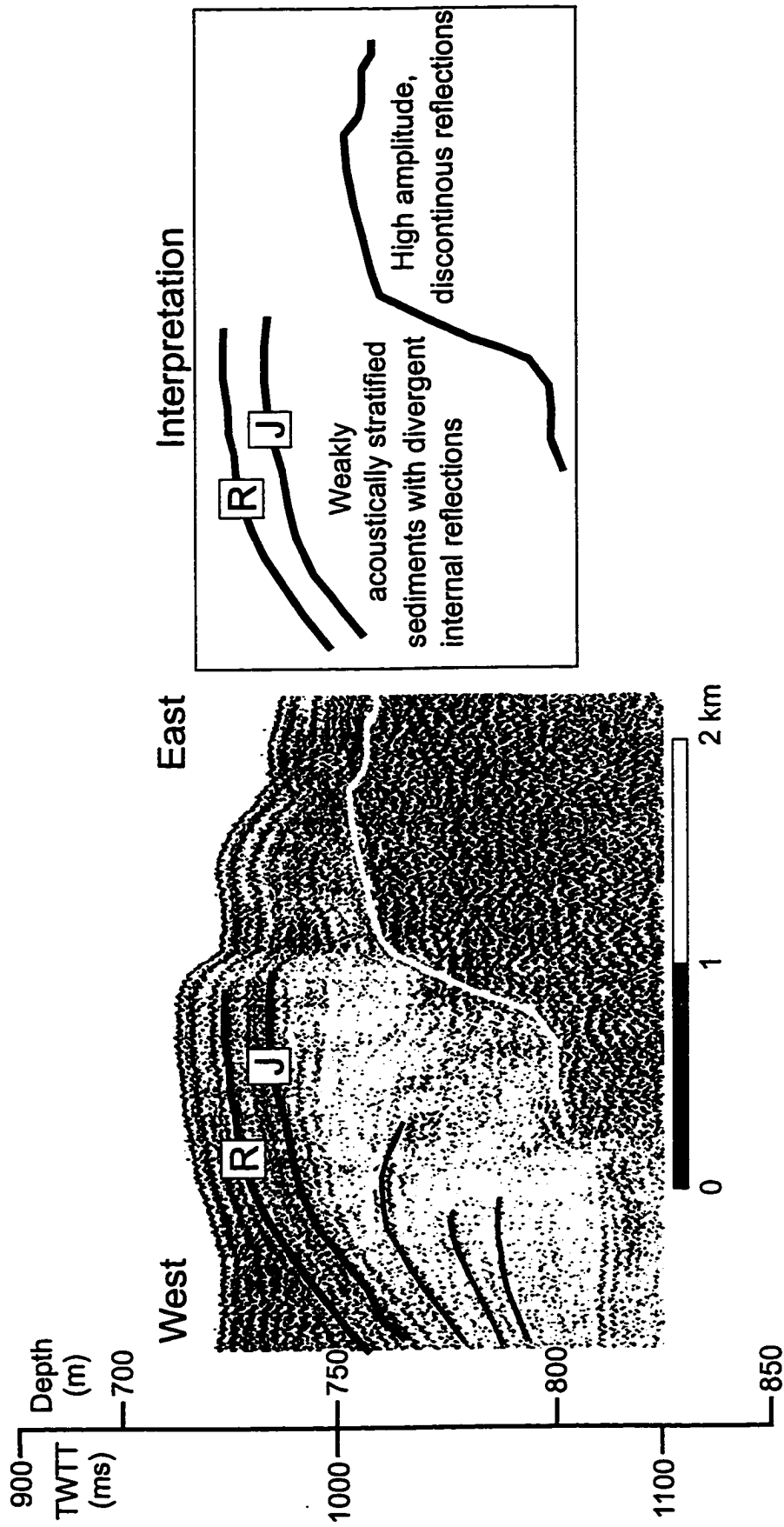


Figure 4.13. Continuation of NSRF profile (Line 36) illustrated in Figure 4.8 showing the feature interpreted to be a buried levee and the high reflectivity package immediately adjacent to the levee interpreted to be channel fill. Location given in Figure 4.2 and Figure 4.9.

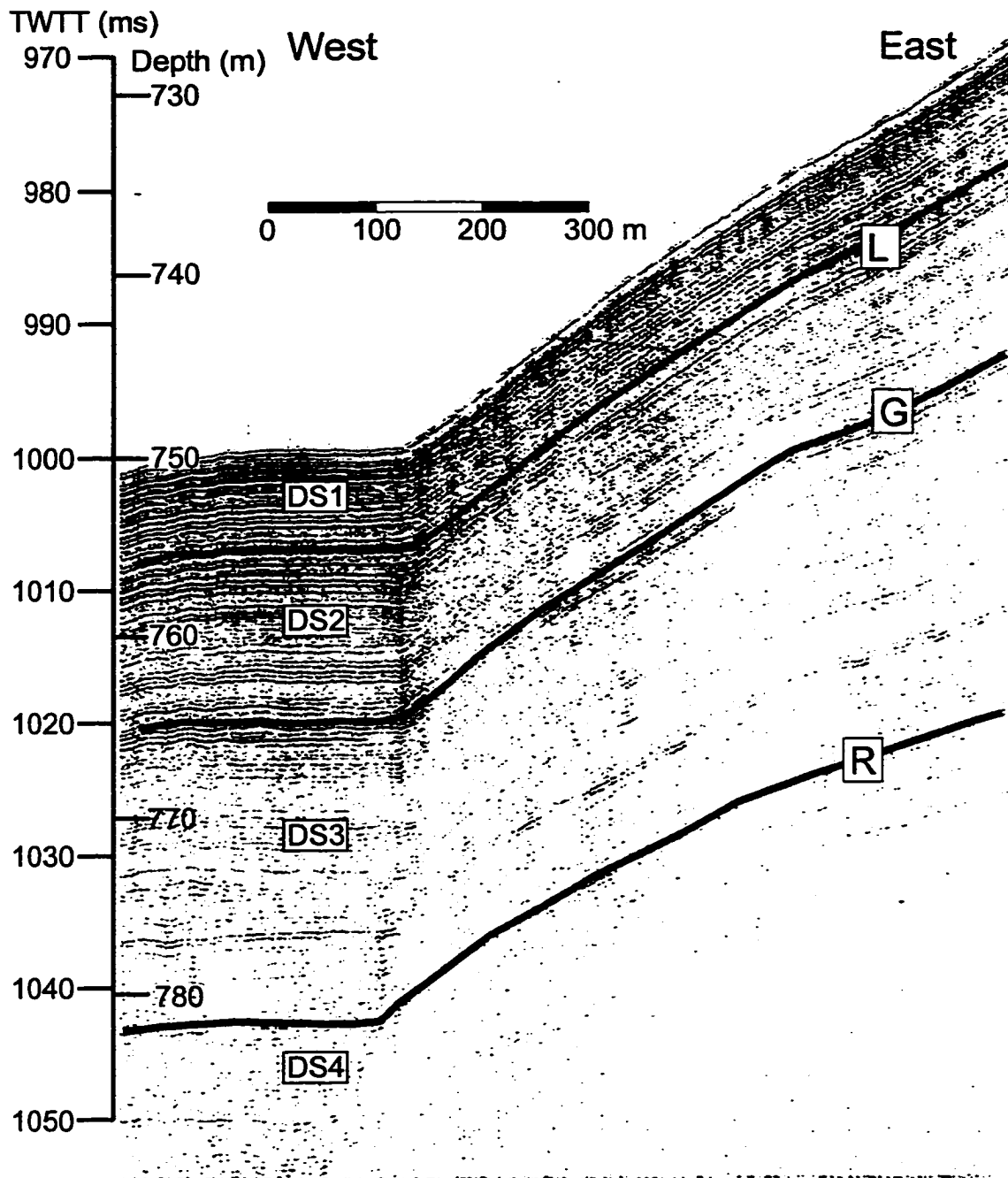


Figure 4.14. Hunttec DTS profile (Line 36) on western, outer levee of Hueneme Channel. Location given in Figure 4.2 and Figure 4.9.

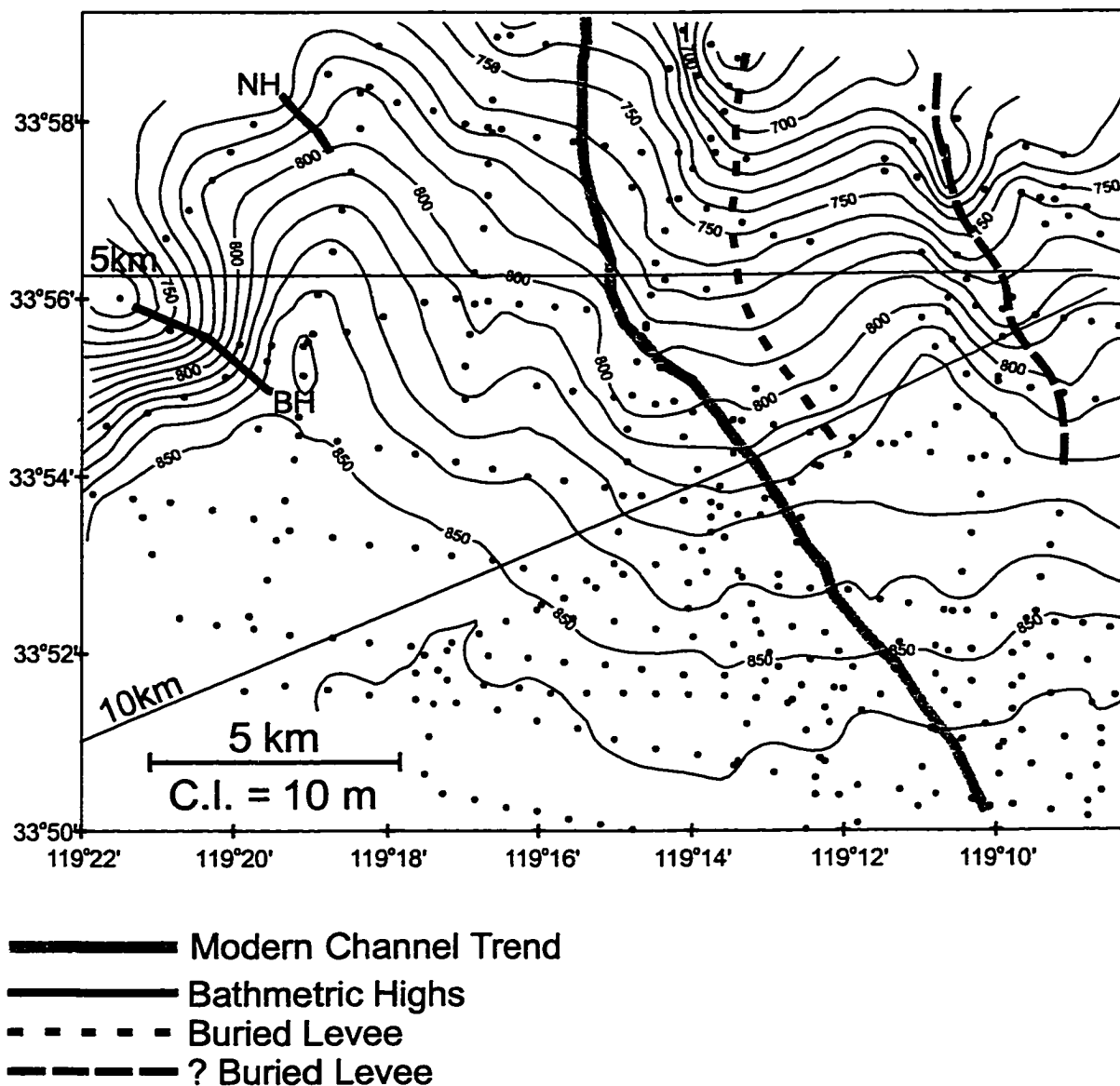


Figure 4.15. Paleobathymetry map of horizon J. Each dot represents a digitized data point. Contour interval is 10 m based on sound velocity of 1500 m s^{-1} . Also shown is the modern channel trend (thick, grey, solid line). This surface shows the initial configuration of the basin prior to the latest phase of channel-levee growth seaward of Hueneme Canyon.

The stratigraphic evolution of the levees since horizon J has differed between areas west and east of Hueneme Channel and between upfan and downfan locations. On the upper fan, the western levee of Hueneme Channel became well-established by horizon R and this outer levee continued to aggrade throughout the recent evolution of the fan (Figure 4.8, Figure 4.16). Around horizon G, an inner levee began to grow. The eastern levee on the upper fan also aggraded, but because deposition tended to drape the preexisting surface defined by horizon J (Figure 4.17), a typical levee morphology did not develop.

Further downfan, the western levee had a similar development but also includes the development of sediment waves just below horizon R (Figure 4.6b). The eastern levee is poorly defined until at least horizon G and has an acoustic character suggesting somewhat sandier sediment (Figure 4.18).

At the most distal locations covered by the data, the levees of Hueneme Channel are subtle features. At horizon R, the western levee thickens to the west (Line 46, Figure 4.9). Above horizon R, the western levee tends to have a uniform thickness but reflectors could not be confidently traced toward the channel, leaving the western levee poorly defined at this downfan location. In this area sediment waves on the distal western levee only began to develop after deposition of horizon R. Conversely, the eastern levee is better defined and the depositional sequences above R show evidence for thinning away from the channel.

4.4.3 Architectural Data from Hueneme Fan

From the acoustic stratigraphy of Hueneme Fan, the character of each depositional sequence can be quantified in terms of its thickness patterns. This section details the architectural data for each depositional sequence, first discussing the data distribution, then presenting the architectural data, and finally presenting a statistical analysis of the data.

Data Distribution

As can be seen in Figure 4.2, much of the acoustic data does not cross the channel at right angles to its trend. Consequently, only the apparent geometry of the system is imaged along any one seismic line. Because the purpose of this study is to characterize

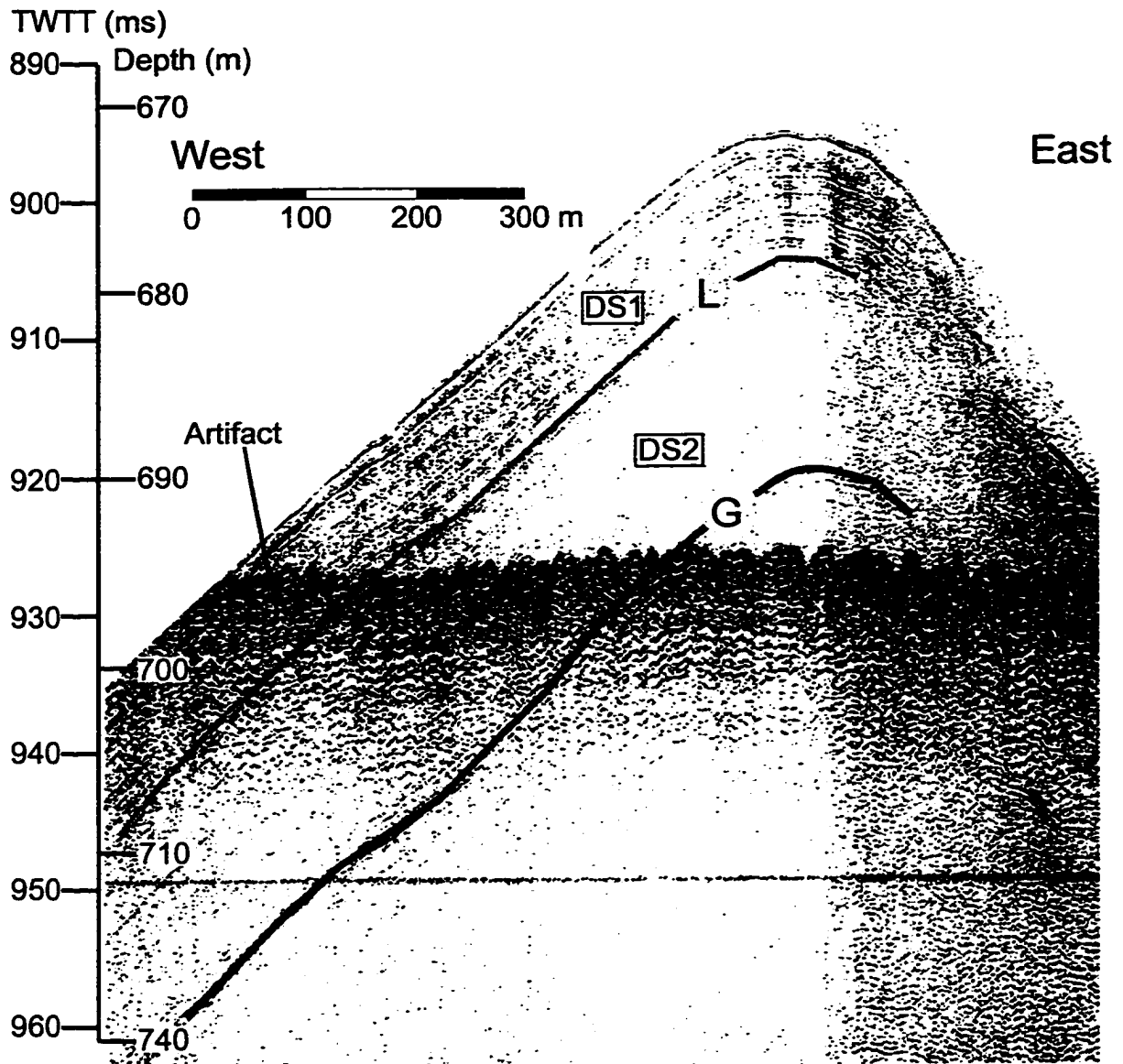


Figure 4.16. Hunttec DTS profile (Line 36) over crest of western levee. Location given in Figure 4.2 and Figure 4.9. Note that the modern levee crest, the crest at horizon L and the crest at horizon G stack vertically showing no evidence for significant movement of the levee crest through time.

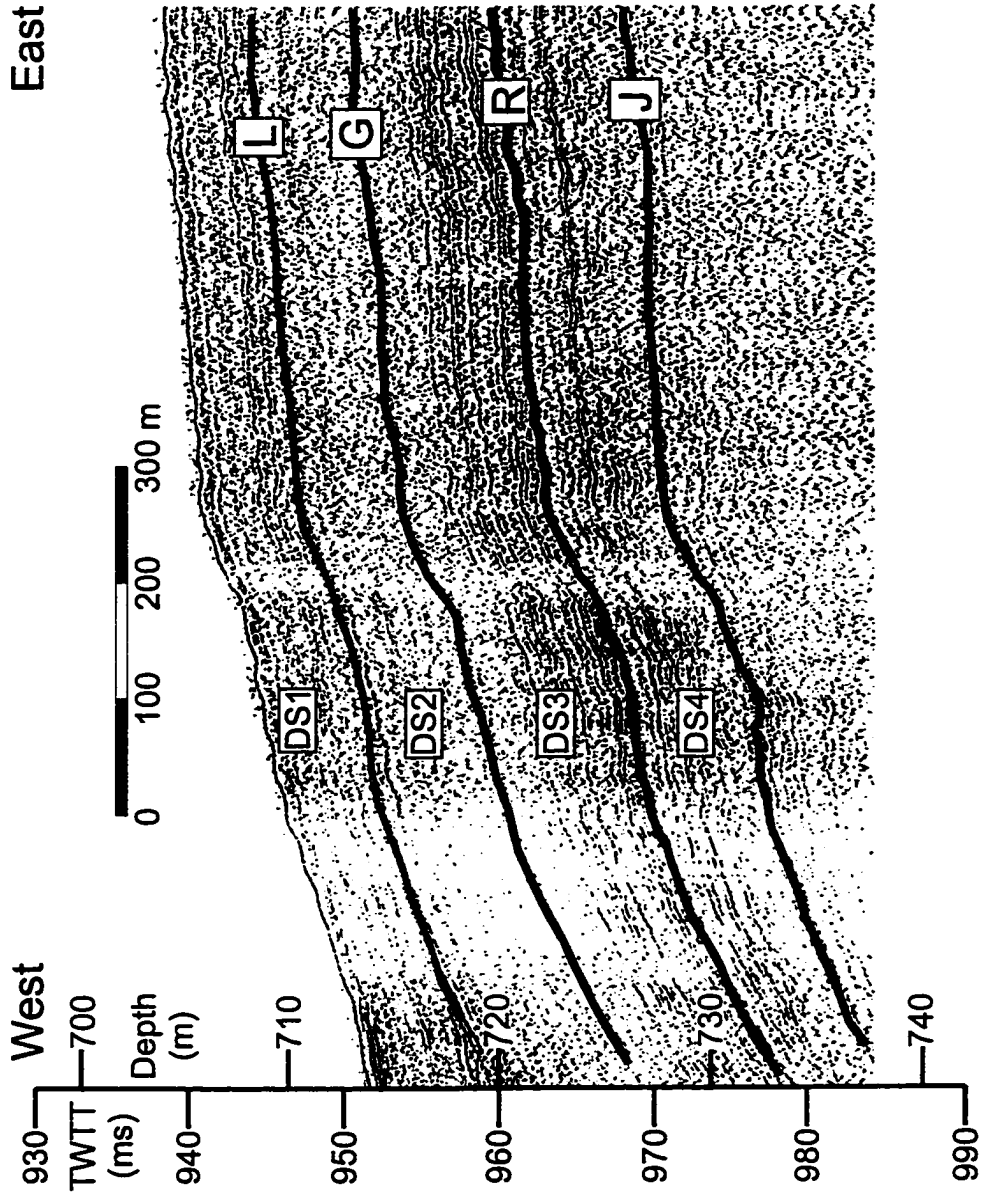


Figure 4.17. Hunttec DTS profile (Line 36) from eastern side of Hueneme Channel showing evenly bedded depositional sequences all characterized by weak to moderate acoustic stratification. Location given in Figure 4.2 and Figure 4.9.

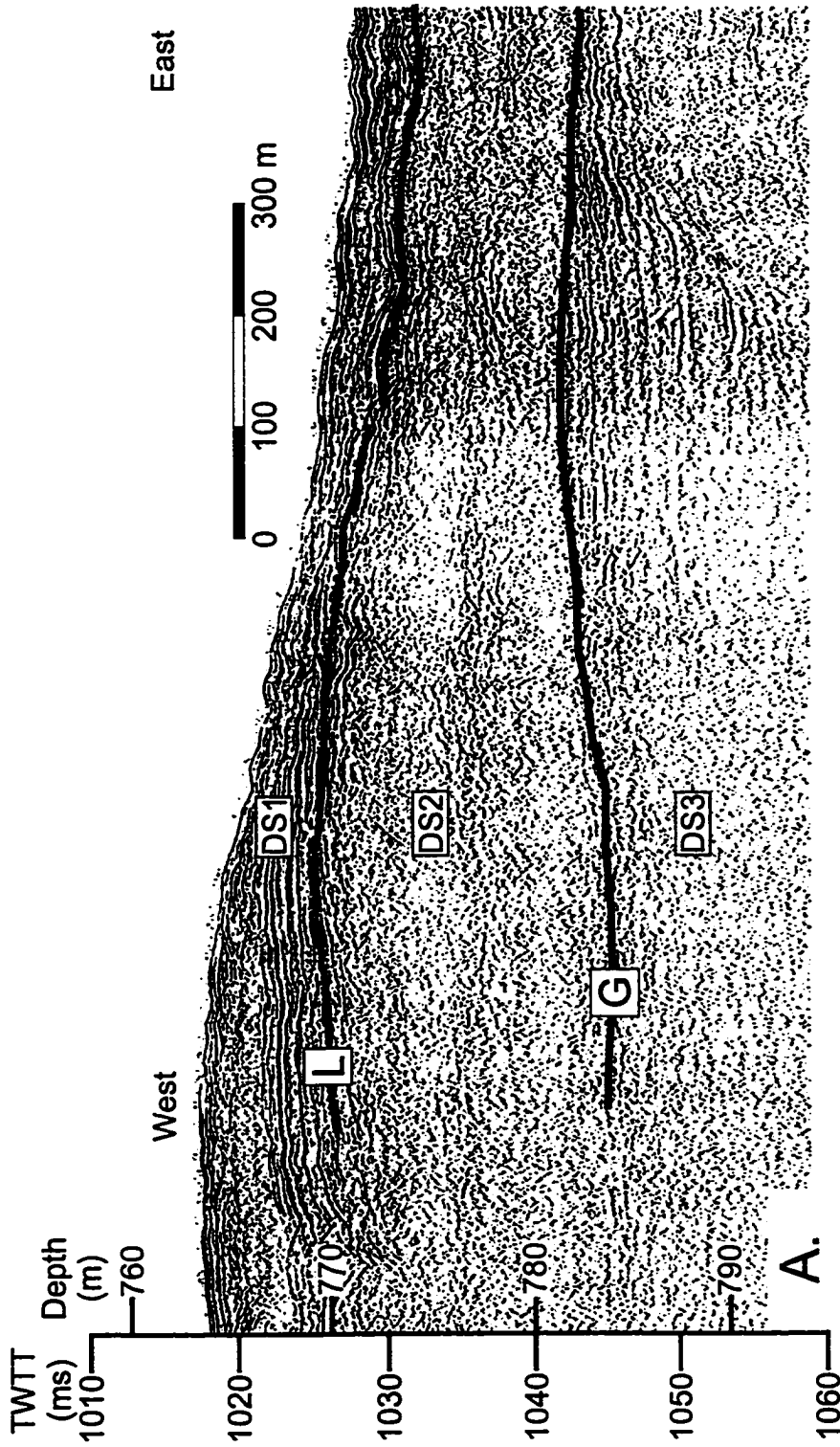


Figure 4.18. Huntect DTS profile (Line 20-21) from eastern side of Hueneme Channel: A. levee crest. B. levee flank. Locations given in Figure 4.2 and Figure 4.9. Levee appears characterized by acoustically amorphous material interspersed with high amplitude discontinuous reflections that grade laterally into acoustically stratified sediments.

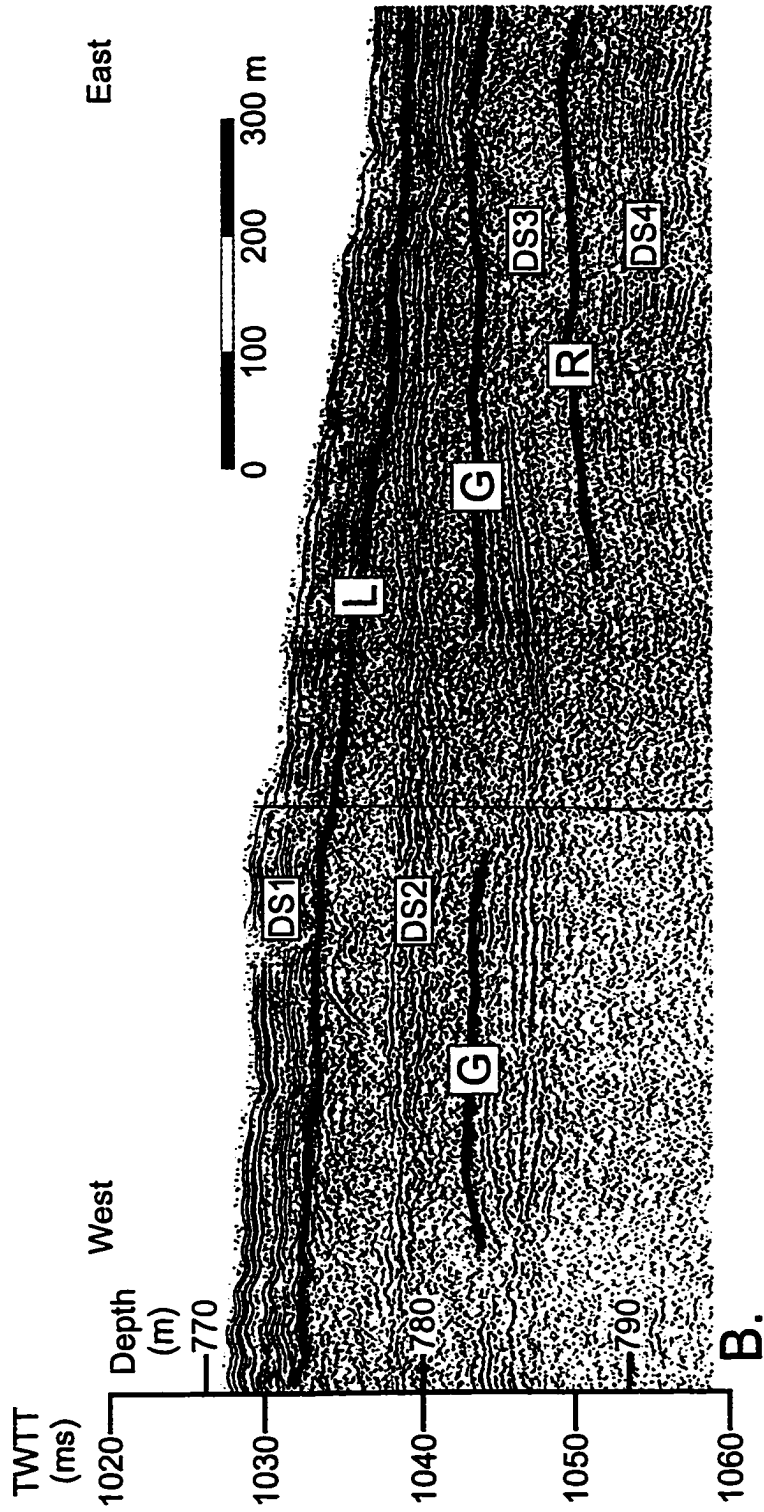


Figure 4.18. Continued.

levee morphology, the lack of channel-perpendicular crossings required that the bathymetric and paleobathymetric picks be transformed into a more suitable coordinate system. Each point was given in latitude and longitude and transformed first to an x-y coordinate system using a Lambert Conformable projection. In these coordinates, x represents distances east (positive) and west (negative) of origin and y represents distances north (positive) and south (negative) of the origin. These Cartesian coordinates were then transformed into a streamwise coordinate system using the modern channel trend. In this coordinate system, the x-axis represents down-channel distance and the y-axis represents distance perpendicular to the channel trend with negative values corresponding to the western levee (or right-hand levee looking downstream) and positive values corresponding to the eastern levee (or left-hand levee looking downstream). As noted above, the morphology of Hueneme Channel progresses from distinct to subtle (e.g., Figure 4.9). To investigate downstream changes in levee architecture the data set was divided into three sections depending upon distance down-channel from the 650 m isobath: less than 5 km (cross-section 1), 5-10 km (cross-section 2), and 10-15 km (cross-section 3). These divisions separate the data into a proximal section characterized by a well-developed western levee having both an inner and outer levee, a middle section having sediment waves, and a distal section possessing subtle channel-levee relief.

Depositional Sequence Thickness

As in Chapter 3, which presented data from the Northwestern Atlantic Mid-Ocean Channel, patterns in the thickness of depositional sequences were investigated on Hueneme Fan. The following sections discuss the strategy for accounting for hemipelagic sediments in the depositional sequences and the thickness data and regression parameters for depositional sequences from each cross-section.

The lack of published core data from Hueneme Fan required that the contribution of hemipelagic sediments to depositional sequence thickness be estimated indirectly. The hemipelagic contribution to Hueneme Fan sediment thickness is relatively uniform basinwide (Christensen, 1991), having a value of about $16 \pm 0.4 \text{ mg cm}^{-2} \text{ yr}^{-1}$ over the past several centuries (Christensen et al., 1994). Reported bulk densities range from 1100-1500 kg m^{-3} (Christensen et al., 1994), yielding a hemipelagic accumulation rate equal to 0.11-0.15 m ka^{-1} . Using this range for the accumulation rate and estimates of the age of

reflector J as anywhere from 18 to 28 ka (Normark et al., 1998) provides an estimate of 2-3 m of hemipelagic sediment deposited since J. The amount of hemipelagic sediments in each depositional sequence was estimated by first determining either the minimum or median thickness of each depositional sequence. Each of these values divided by their sum yields an estimate of the percentage of the total sediment column that each depositional sequence represents. Using these percentages the total thickness of hemipelagic sediments was partitioned between the depositional sequences. In no case did the method for removing hemipelagic sediments contribute to more than a 1% change in the parameter values calculated by the regression analysis. Table 4.2 summarizes the estimated contribution of hemipelagic sediments for each depositional sequence.

At cross-section 1, the depositional sequences west of Hueneme Channel all show pronounced thinning away from the channel (Figure 4.19) and, where evidence exists, stable, aggradational levee crests (Figure 4.16). The values of k do not differ significantly at the 95% confidence level except for DS3 for which k is about twice as large as for the other depositional sequences.

Table 4.2. Estimates of hemipelagic sediment thickness for each depositional sequence.

Depositional Sequence	Hemipelagic Sediment Thickness
DS1	0.3 m
DS2	0.3 m
DS3	0.3 m
DS4	1.6 m
Total	2.5 m

East of Hueneme Channel, only DS1 and DS2 show any evidence of thinning away from the channel (Figure 4.19). DS3 east of the channel thickens slightly to the east and as a result, k is greater than zero for this depositional sequence. DS4 east of the channel displays no discernible thickness patterns, varying from 5 m to 25 m with an average thickness of 10 m. For DS1 and DS2, across-channel comparison of k shows that it does not differ significantly while the value of η_{lc} is greater on the western levee than the eastern levee by as much as 7 m for DS2 and 3 m for DS1.

Hueneme Fan: Cross-section 1

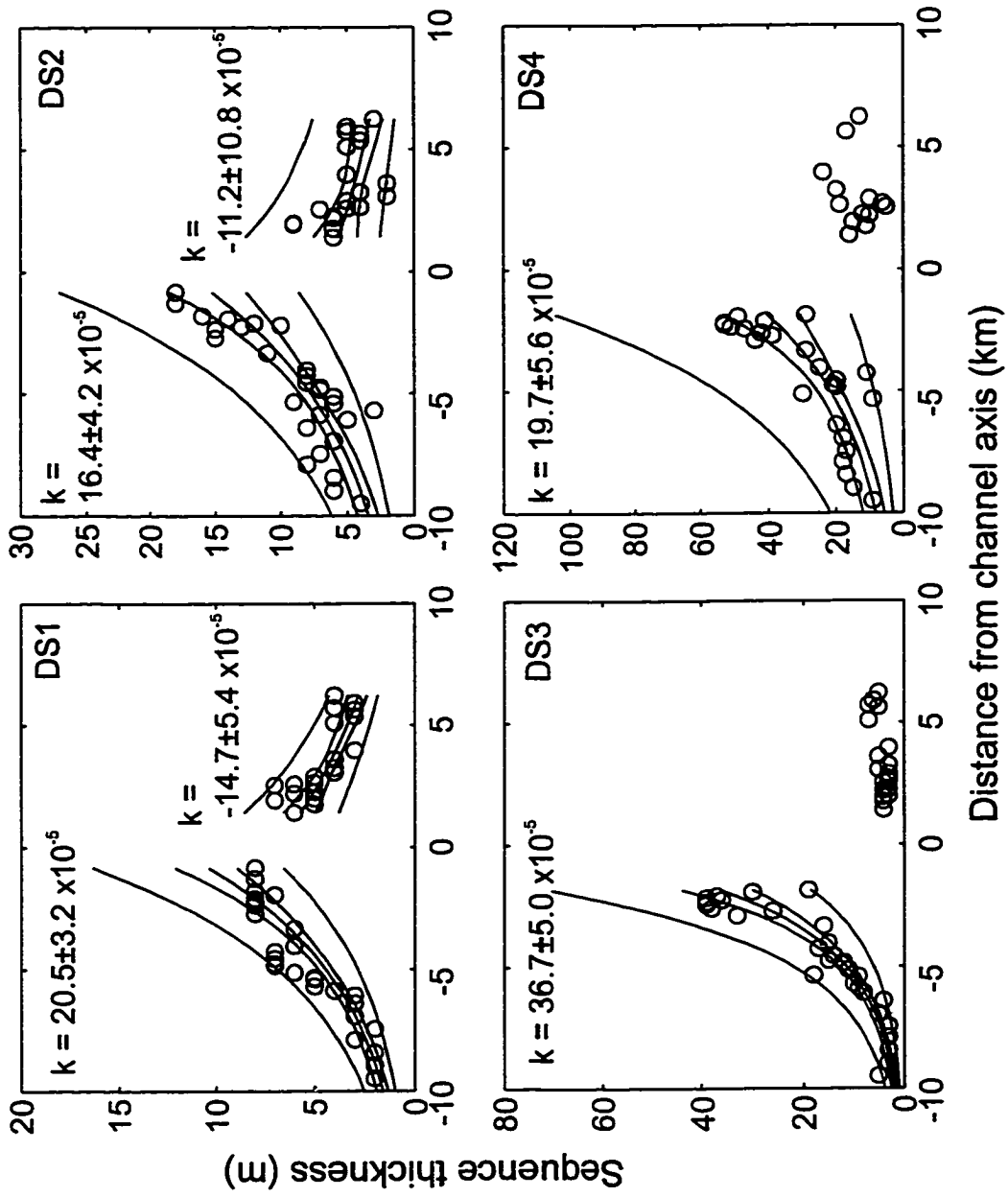


Figure 4.19. Thickness data from cross-section 1 showing data points (open circles), regression line, confidence intervals, and prediction intervals. For each significant ($p < 0.05$) regression the value of k is given along with the 95% confidence limits on k .

Table 4.3. Regression data for cross-section 1: western levee. DS = depositional sequence, k ($\times 10^{-5} \text{ m}^{-1}$) = decay constant, δk ($\times 10^{-5} \text{ m}^{-1}$) = 95% confidence limit on k , η_0 (m) = y-intercept of regression, $\delta \eta_0$ (m) = 95% confidence limit on η_0 , r = correlation coefficient, y_{lc} (km) = distance from channel axis to levee crest, and η_{lc} (m) = calculated thickness of depositional sequence at levee crest.

DS	k	δk	η_0	$\delta \eta_0$	r	y_{lc}	η_{lc}
1	20.5	3.2	12.3	2.2	0.93	-2.0	8.2
2	16.4	4.2	17.5	4.0	0.84	-2.0	12.6
3	36.7	5.0	71.7	19.6	0.94	-2.0	34.4
4	19.7	5.6	58.4	19.8	0.82	-2.0	39.4

At cross-section 2, thickness data from west of Hueneme Channel show that each depositional sequence thins away from the channel (Figure 4.20). The data are more scattered than at cross-section 1; as a result the correlation coefficients for the regression lines are less, and the error estimates are greater (compare Table 4.3 and Table 4.5). The levee crests west of the channel again appear to be stable through time (Figure 4.16). DS1 and DS2 possess nearly identical decay constants while the calculated thickness of sediment at the levee crest is greater for DS2 and DS1 (Figure 4.20 and Table 4.5). Like cross-section 1, DS3 possesses the highest decay constant. The decay constant for DS4 is much smaller at cross-section 2 than at cross-section 1, although the thickness data at cross-section 2 show a great deal of scatter.

Table 4.4. Regression data for cross-section 1: eastern levee. See Table 4.3 for explanation of data and symbols. Only significant ($p < 0.05$) results shown. For non-significant results, k is not significantly different from zero as for DS4. In this case, the average value of η is reported.

DS	k	δk	η_0	$\delta \eta_0$	r	y_{lc}	η_{lc}
1	-14.7	5.4	7	0.7	0.78	2	5.2
2	-11.2	10.8	6.6	1.5	0.41	2	5.3
3	14.4	7.4	2.2	0.3	0.45	2	4.0
4	0					2	12.0

Hueneme Fan: Cross-section 2

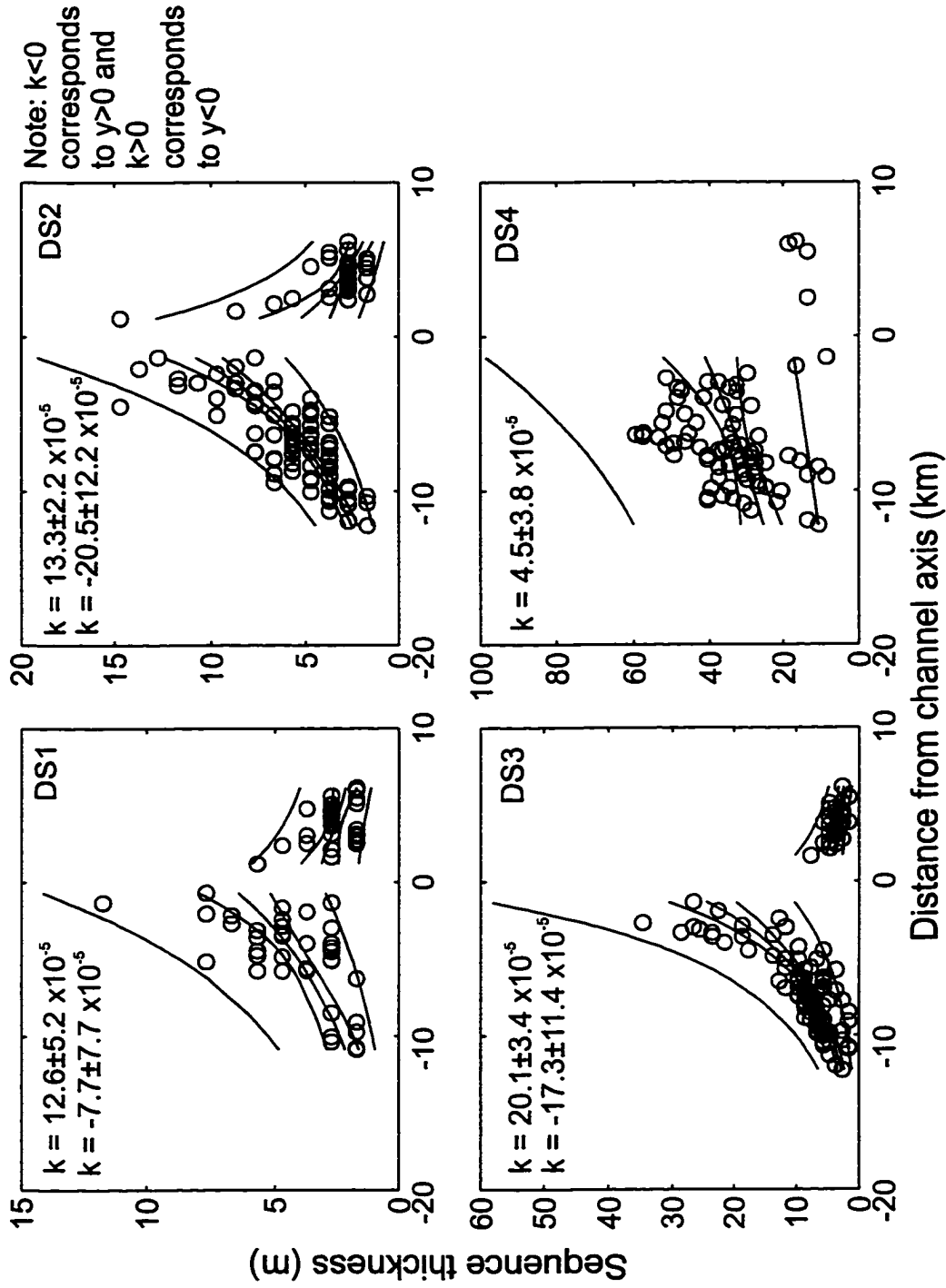


Figure 4.20. Thickness data from cross-section 2 showing data points (open circles), regression line, confidence intervals, and prediction intervals. For each significant ($p < 0.05$) regression the value of k is given along with the 95% confidence limits on k .

Table 4.5. Regression data for cross-section 2: western levee. See Table 4.3 for explanation of data and symbols.

DS	k	δk	η_o	$\delta\eta_o$	r	y_{lc}	η_{lc}
1	12.6	5.2	7	2.2	0.68	-2	5.4
2	13.3	2.2	12.9	2.2	0.78	-2	9.9
3	20.1	3.4	32.2	8.6	0.78	-2	21.5
4	4.5	3.8	43.8	12.6	0.27	-2	40.0

East of Hueneme Channel, only DS2 and DS3 show thinning that could be statistically explained by the exponential model. Characterization of DS4 suffers from a lack of data (Figure 4.20). The regression parameters for DS1 are reported but are not significant ($p = 0.11$). Even the regression parameters for DS2 and DS3 show relatively low correlation coefficients and high error estimates (Table 4.6). The difficulties with establishing significant patterns for the eastern levee may correspond to the difficulties in correlating reflectors in this region.

Table 4.6. Regression data for cross-section 2: eastern levee. See Table 4.3 for explanation of data and symbols.

DS	k	δk	η_o	$\delta\eta_o$	r	y_{lc}	η_{lc}
1	-7.7	4.2	3.4	0.6	0.31	2	2.9
2	-20.5	6.1	6.7	1.6	0.52	2	4.4
3	-17.3	5.7	6.8	1.5	0.52	2	4.8
4	0					2	15

Thickness data from cross-section 3 continue the apparent trend of increasing deviation from a simple thinning of depositional sequences away from the channel (Figure 4.21). West of Hueneme Channel, only DS3 shows thinning away from the channel. Data from DS1 and DS2 display no apparent pattern. DS4 thickens away from the channel. The lack of a pattern in thickness variations for DS1 and DS2 could result from the difficulty of correlating sub-bottom horizons across sediment waves. The available data, however, suggest that the depositional sequences are predominantly uniform in thickness. The thickness of DS1 is almost exclusively 3-5 m while DS2 is slightly more variable with most of the data lying between 5-8 m. All that can be rigorously stated about these patterns is that any thinning that may occur does so at

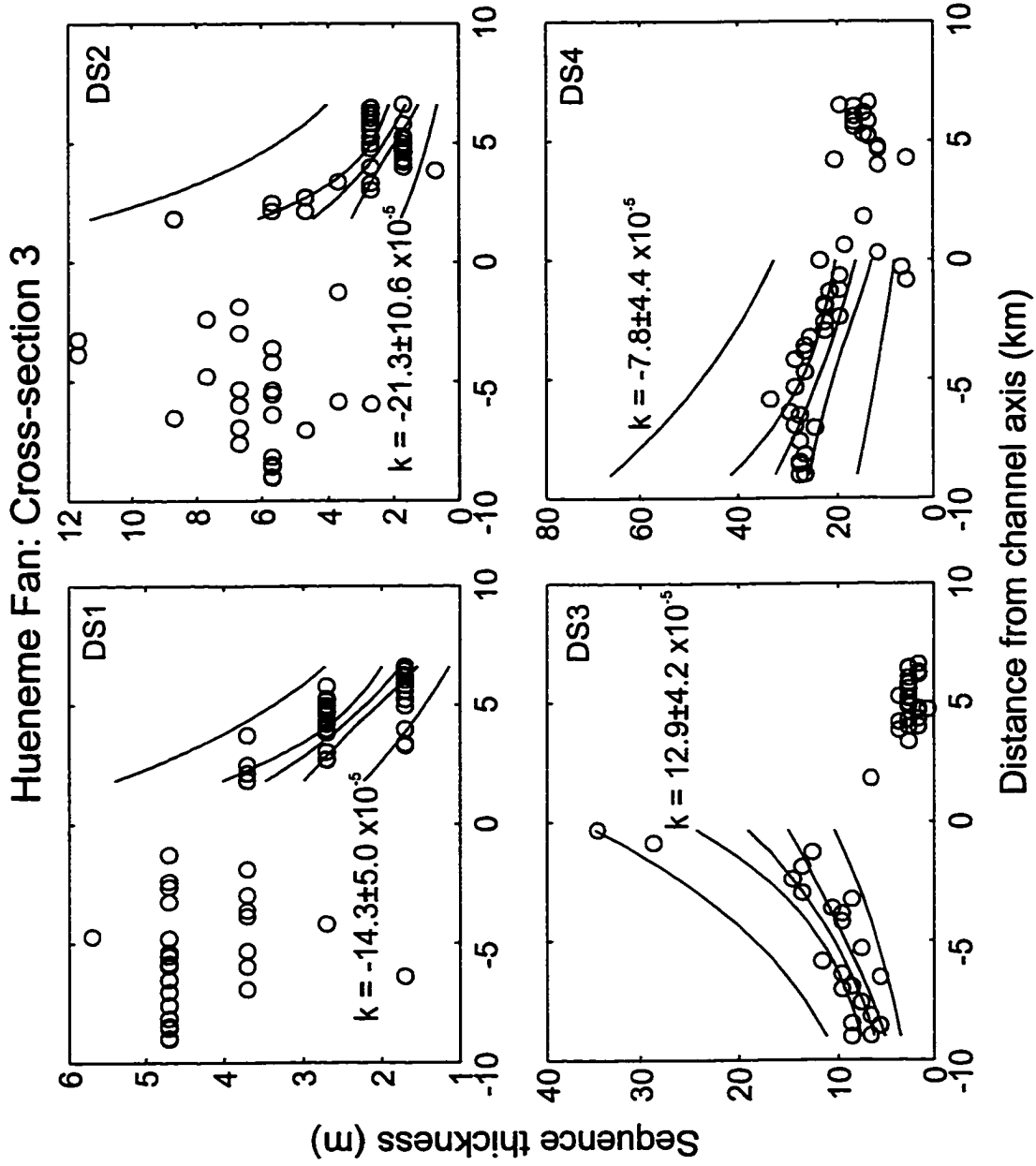


Figure 4.21. Thickness data from cross-section 3. Note that k for DS4 west of Hueneme Channel is less than zero; the depositional sequence thickens away from the channel (see Figure 4.12).

lengthscales far exceeding the data coverage. Consequently, the regression analysis shows k to be not significantly different from zero (Table 4.7).

Table 4.7. Regression data for cross-section 3: western levee. See Table 4.3 for explanation of data and symbols.

DS	k	δk	η_o	$\delta\eta_o$	r	y_{lc}	η_{lc}
1	0					-2	4.5
2	0					-2	7.0
3	12.9	2.1	19.9	2.5	0.8	-2	15.4
4	-7.8	2.2	16.1	1.9	0.57	-2	18.8

East of Hueneme Channel, only DS1 and DS2 show thinning that can be significantly described by the regression parameters (Figure 4.21, Table 4.8). Neither DS3 nor DS4 have any recognizable pattern in depositional sequence thickness. The average thickness of DS3 is about 3-4 m while DS4 is around 15 m thick. The same arguments applied to DS1 and DS2 west of the channel apply to DS3 and DS4 east of the channel; thinning may be occurring at lengthscales much greater than represented by the available data.

Table 4.8. Regression data for cross-section 3: eastern levee. See Table 4.3 for explanation of data and symbols.

DS	k	δk	η_o	$\delta\eta_o$	r	y_{lc}	η_{lc}
1	-14.3	2.5	4.5	0.5	0.7	2	3.4
2	-21.3	5.3	6.6	1.6	0.58	2	4.3
3	0					2	3.4
4	0					2	15

Across-channel Asymmetry

Assessing levee asymmetry development on Hueneme Fan is hampered by the lack of channel-perpendicular crossings. Estimates can be made, however, by reconstructing the levee development using the depositional sequence thickness data presented in the previous section. These thickness data represent an average over approximately 5 km of channel length, and therefore have a low resolution in the down-channel direction, but they at least offer a consistent method of estimating levee

asymmetry not otherwise available. They also provide estimates of asymmetry at a directly comparable resolution to the analysis of thickness patterns presented above.

Recall that the initial surface for the development of the most recent channel-levee system on Hueneme Fan began at J and that the paleobathymetry of horizon J shows a distinct levee east of the modern trend of Hueneme Channel (Figure 4.15). Taking this initial asymmetry into account, the reconstruction of levee crest elevations (Table 4.9) closely resembles that seen in oblique channel profiles (Figure 4.9). The modern levee crest elevation difference predicted from the reconstruction compares well with the observed levee asymmetry of the modern channel, thereby offering some constraint on the results.

Using the initial asymmetry of the system as a starting point, the eastern levee is higher than the western levee until after deposition of R (Table 4.9). By the time horizon G was deposited, the levees had begun to take the form of the modern system with the western levee higher than the eastern levee. Channel width, defined as levee crest to levee crest width, remained constant at about 3.5–4 km. It should be noted that while the evidence does suggest that the position of the levee crest west of Hueneme Channel has been stable through time at about 2 km from the modern channel axis, the position of the

Table 4.9. Reconstruction of Hueneme Fan levee crest asymmetry taking account of the paleobathymetry on J (Figure 4.15). Tabulated values correspond to elevation above J west of the channel. At horizon J, the eastern levee is higher than the western levee because of the presence of the buried levee east of Hueneme Channel.

Reflector	Cross-section 1		Cross-section 2		Cross-section 3	
	Western Levee (m)	Eastern Levee (m)	Western Levee (m)	Eastern Levee (m)	Western Levee (m)	Eastern Levee (m)
Surface	95	77	77	67	45	41
L	86	71	71	64	40	38
G	74	66	62	60	34	33
R	39	62	40	55	19	30
J	0	50	0	40	0	15

eastern levee crest through time is not so confidently established. The western levee crest coincides with the position where depositional sequence thickness is greatest. Using maximum thickness as the criterion for identifying levee crests east of the channel consistently places them at 2 km from the modern channel axis. Using thickness to

identify levee crests rather than elevation does presuppose no shifting of the levee crests through time. The across-channel slope, ∇H (Table 4.10), mirrors the evolution of the elevation difference between levee crests, starting at large positive values where the western levee is lower than the eastern levee and decreasing to large negative values where the western levee is higher than the eastern levee.

Table 4.10. Across-levee elevation difference calculated from data in Table 4.9 and across-levee slope calculated using channel width equal to 4 km

Reflector	Cross-section 1		Cross-section 2		Cross-section 3	
	ΔH (m)	∇H (m km ⁻¹)	ΔH (m)	∇H (m km ⁻¹)	ΔH (m)	∇H (m km ⁻¹)
Surface	-18	-4.50	-10	-2.50	-4	-1.00
L	-15	-3.75	-7	-1.75	-2	-0.50
G	-8	-2.00	-2	-0.50	-1	-0.25
R	23	5.75	15	2.75	11	2.75
J	50	12.5	40	10.0	15	3.75

The asymmetry in the channel morphology develops in the absence of a simple relationship in the asymmetry of the thickness patterns. Where decay constants could be compared across the channel they are not significantly different (Figure 4.22a). Asymmetry in depositional sequence thickness favours accumulation of sediment on the western levee (Figure 4.22b). Superficially, this would suggest that the value of the decay constant on conjugate levees does not depend on either the elevation difference between conjugate levees or ∇H . However, this behaviour only characterizes four of the 12 cases, in particular, DS1 and DS2 at cross-sections 1 and 2 where values of ∇H are most negative. Where ∇H is only slightly negative or positive, the decay constants from conjugate levees display complex relationships. The largest value of k on the western levee occurs for DS3 during deposition of which ∇H changed from positive values to negative values. During this time, approximately uniform deposition occurred east of the channel. Uniform deposition also occurred east of the channel for DS4 when ∇H was the most positive. West of the channel the decay constants for DS4 vary from weakly negative (thickening away from the channel at cross-section 3) to weakly positive (at cross-section 2) to strongly positive (at cross-section 1). Finally, when ∇H was

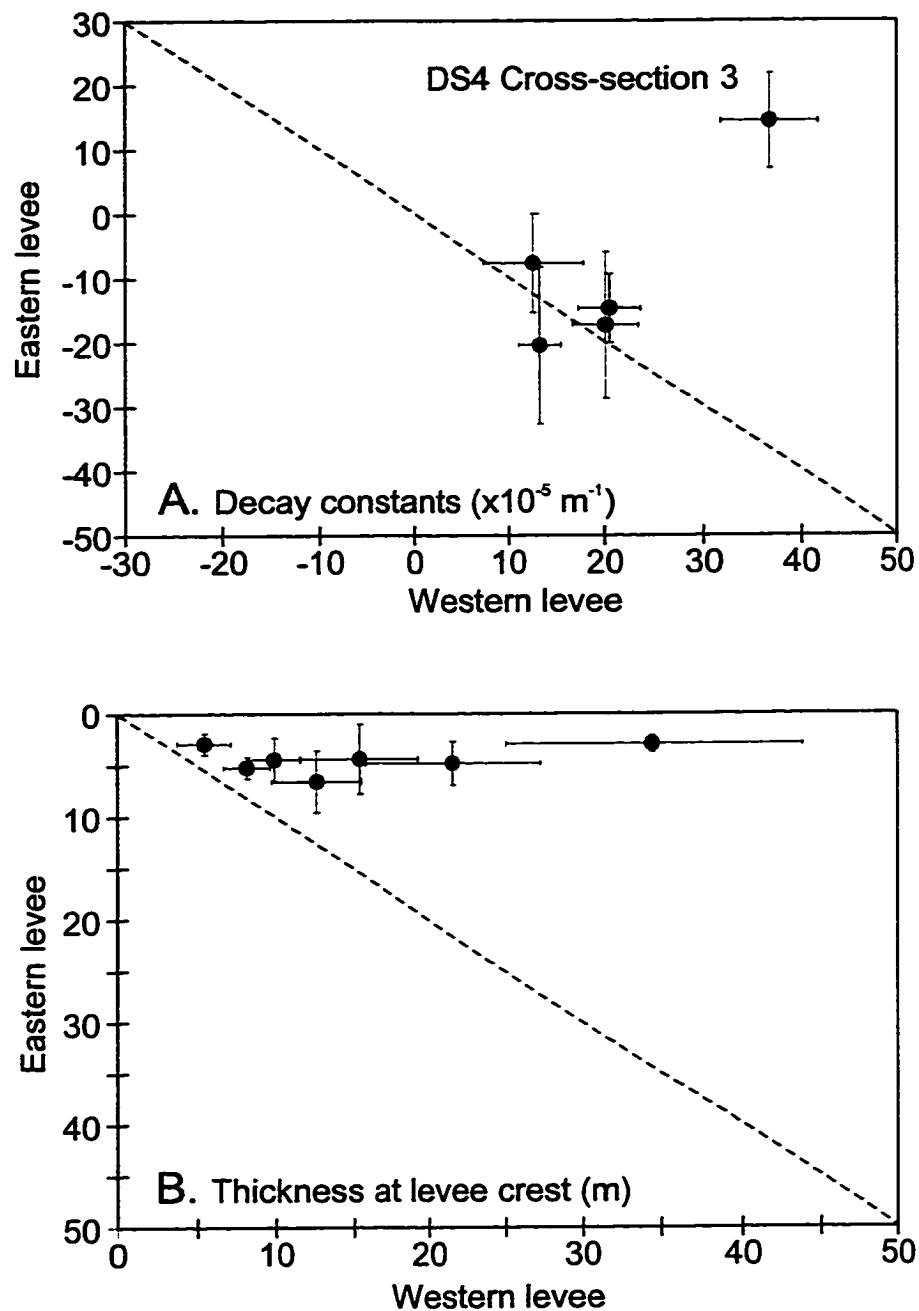


Figure 4.22. Asymmetry of regression parameters. A. Comparison of decay constant from conjugate levees. B. Comparison of thickness at levee crest. Note that when decay constants can be compared they are about the same for conjugate levees while the thickness of sediment at the levee crest is always greater west of the channel.

slightly negative as it is at cross-section 3 for DS1 and DS2, uniform deposition characterized the western levee while thinning depositional sequences occurred east of the channel.

Sediment Waves

The sediment waves on Hueneme Fan display a complex spatial and stratigraphic evolution. Their surface expression apparent in detailed bathymetry of the fan (Figure 4.3) shows that the wave crests are aligned oblique to the channel trend, having wavelengths that vary between 200 m and 500 m, decreasing with distance from the channel. The amplitude of the waves is generally less than 10 m.

The sediment waves prograded downfan between deposition of horizon R and G. Piper et al. (1998b, submitted) stated that the stratigraphic development of the waves displayed periods of active wave growth alternating with periods where sediment draped the waves and infilled wave troughs. In line 46 (Figure 4.11), one can see the initial formation and upstream migration of the sediment waves above horizon R. Up to G, the migration and growth of the waves appears progressive with increasing amplitude and $SRR > 1$. After deposition of horizon G, upstream migration is more difficult to detect and even the few waves shown in the figure display different behaviour along equivalent stratigraphic horizons: some showing progressive migration, some showing simple aggradation suggesting inactivity. Between horizons G and L, wave amplitude tends to decrease and the SRR approaches unity. Above L, the development of sediment waves appears to have ceased.

Topographic Features

Besides the effect of the buried levee on the evolution of across-channel asymmetry and thickness patterns, buried topographic highs west of Hueneme Channel play a role in determining thickness patterns. A major topographic feature affects the deposition of DS4 (Figure 4.7). This feature has approximately 40 m of relief. Near the base of DS4, reflections onlap this feature. Onlapping, where reflections terminate against this feature, eventually gives way to the deposition of sediments that are acoustically continuous across the feature but pond against it. At the transition between onlapping and ponding, the subsurface high had an apparent relief of approximately 10 m. The onlapping and then ponding of sediments continued throughout most of the

deposition of DS4. By the time of horizon R, the subsurface high was no longer a positive topographic feature and thus after R, the subsurface high did not control variations in depositional sequence thickness.

Farther north, another topographic high appears to affect depositional sequences post-R. Reflections are continuous across the feature suggesting continuity of deposition, but inter-reflection thickness increases near the base of the feature indicative of ponding (Figure 4.23). The relief of this feature is not well-constrained by seismic data but the bathymetry suggests that it presently has as much as 25 m of relief (Figure 4.3).

4.5 Synthesis of Levee Architecture

This section compiles the data on the levee architecture of Hueneme Fan in order to investigate the potential existence of trends and relationships between trends in the downstream, stratigraphic, and across-channel variations in levee architecture.

4.5.1 Downchannel Variability

Variations in ΔH and ∇H display the most prominent downchannel pattern in levee architecture (Figure 4.24). Superimposed on the general pattern of decreasing asymmetry are changes in the decay constant (Figure 4.25). The elevation difference between conjugate levee crests and the magnitude of the cross-channel slope both decrease for the modern sea floor, horizon L, and horizon G. In other words, the channel-levee geometry becomes more symmetric downchannel. For cross-sections 1 and 2, this downchannel decrease in asymmetry occurs without a significant change in the decay constant (Figure 4.25a). At cross-section 3, where asymmetry is at a minimum, the value of k for the western levee is not significantly different from zero while the eastern levee has decay constants around $20 \times 10^{-5} \text{ m}^{-1}$. In the upper two depositional sequences levees of the proximal channel are symmetrical in shape (denoted by similar values of k), but asymmetric in levee crest elevation. Downchannel, the levees are asymmetrical in shape but have low across-channel asymmetry.

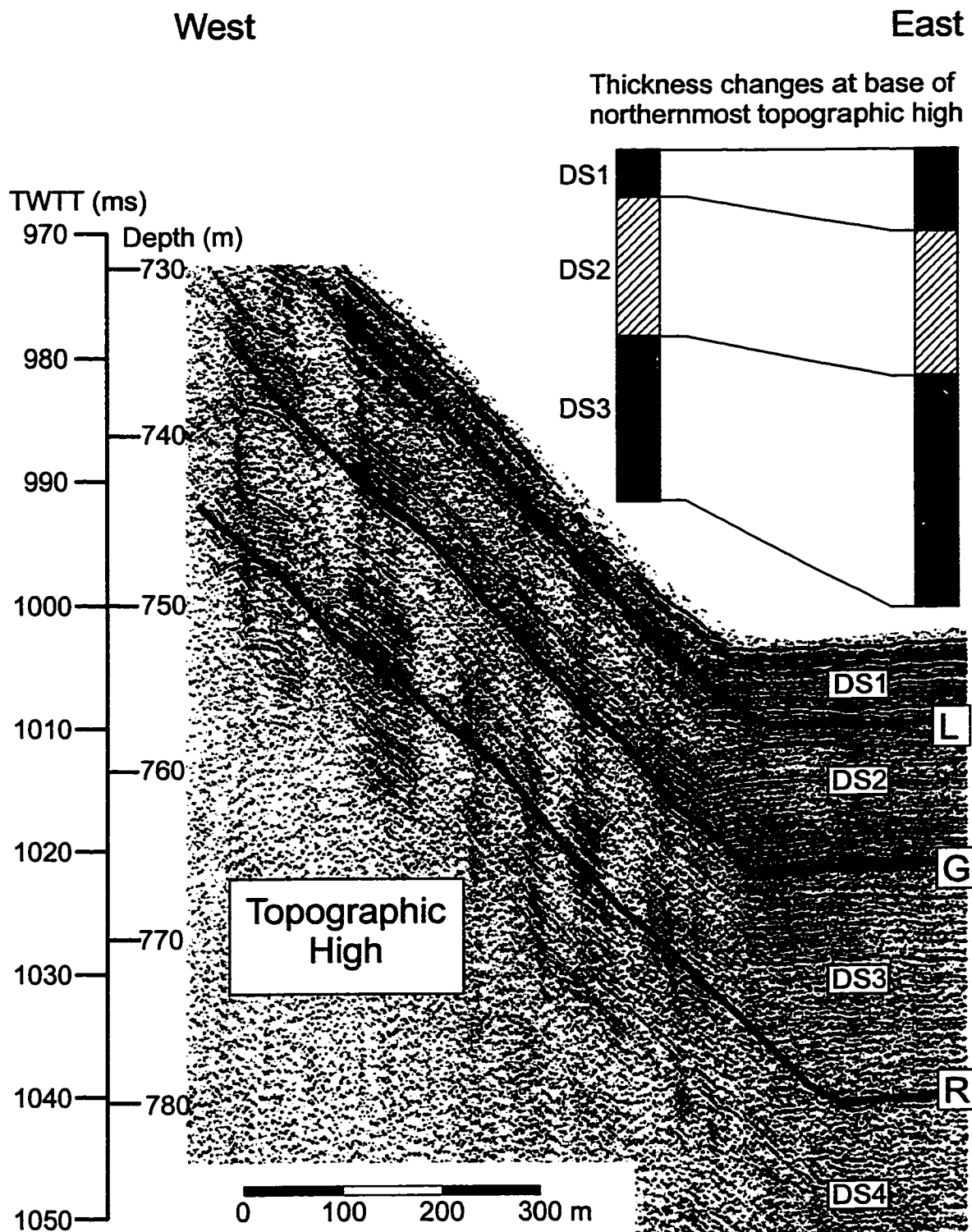


Figure 4.23. Huntce DTS profile (Line 36) showing relationship between depositional sequences and northernmost topographic high observed in modern bathymetry (Figure 4.3) and paleobathymetry of horizon J (Figure 4.15). Note continuity of reflections but abrupt westward thinning of individual depositional sequences indicative of ponding of sediment against this feature.

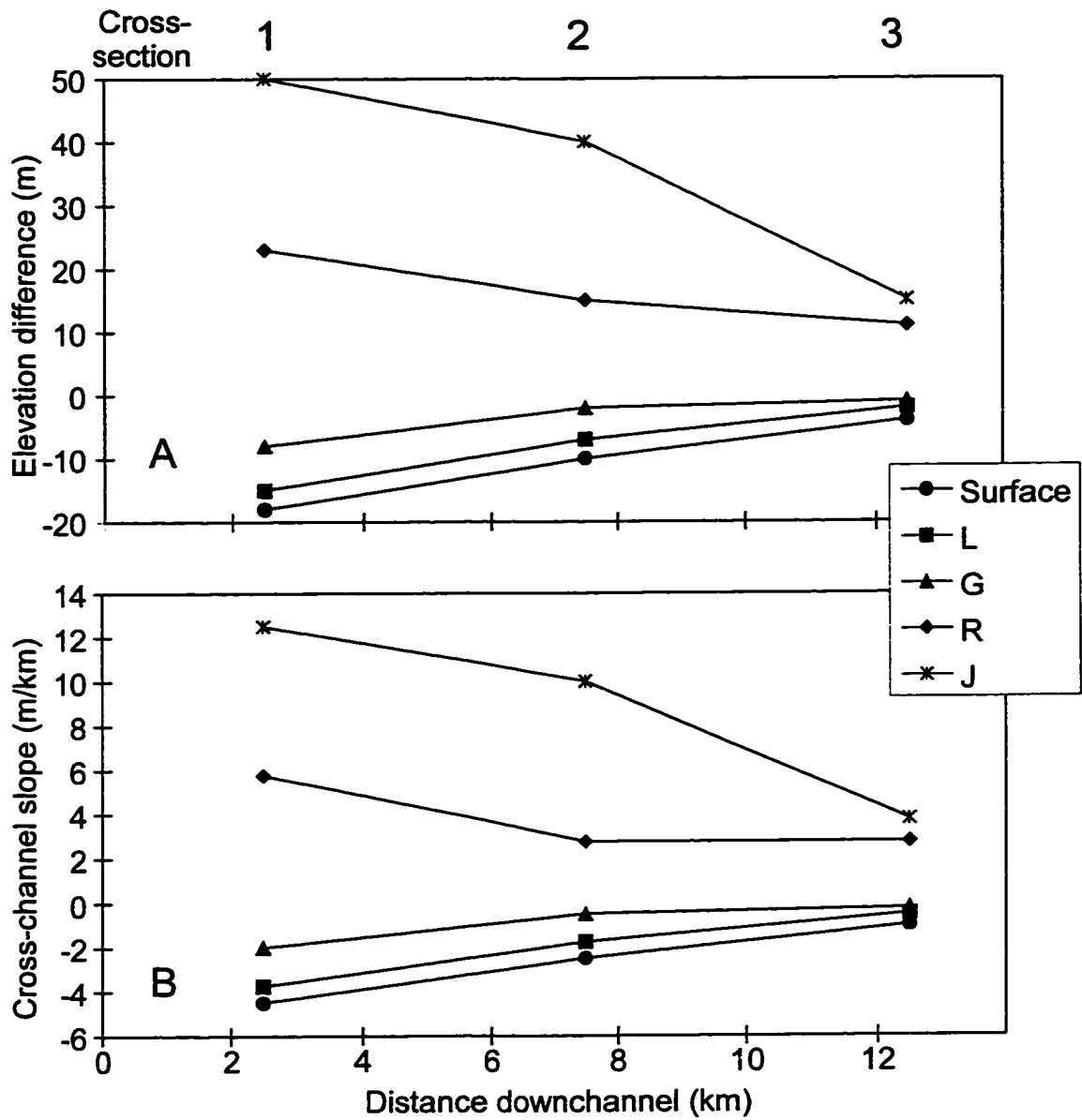


Figure 4.24. A. Downchannel plot of the elevation difference between conjugate levee crests. B. Downchannel plot of cross-channel slope.

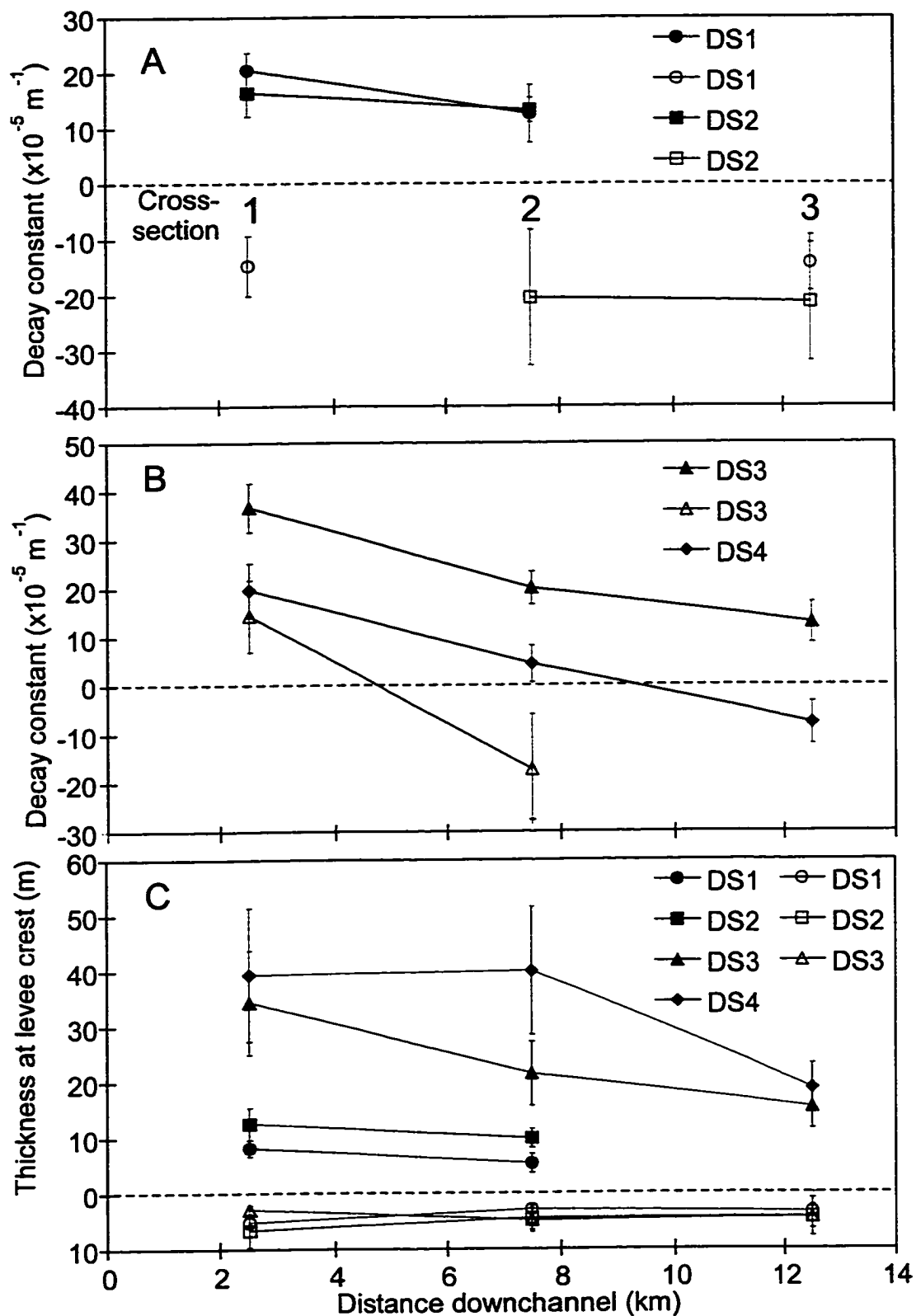


Figure 4.25. Downchannel variations; A. decay constants for DS1 and DS2. B. decay constants for DS3 and DS4. C. thickness at levee crest. In Figure 4.25a and Figure 4.25b, the change in sign of the decay constant denotes a change in the direction of thinning from away from the channel axis to toward the channel axis.

Thickness of sediment at the levee crest shows downchannel decreases for each depositional sequence, but the data are sparse. However, because J could be widely correlated, the thickness of sediment between horizon J and the sea floor could be widely mapped. The downchannel variation in thickness of sediment at the western levee crest above horizon J shows a dramatic decrease in sediment thickness over the upper reach of Hueneme Channel followed by a much slower decrease in thickness (Figure 4.26). At the very distal end of Hueneme Channel, sediment thickness above J again begins to fall off rapidly.

Deposition of DS3 between horizons R and G spans the transition from positive to negative values for ∇H . The downchannel trend for DS3 still shows decreasing asymmetry whether measured at horizon G (becoming less negative) or R (becoming less positive). This pattern coincides with a downchannel decrease in k (Figure 4.25b) on the western levee while uniform thickness of sediments appear to characterize the eastern levee. Examination of the thickness of sediments at the levee crest also shows a weak downchannel decrease on the western levee while the eastern levee has no trend (Figure 4.25c). Except for cross-section 3, DS4 shows features similar to DS3 (Figure 4.25b) with non-zero decay constants on the western levee that decrease downchannel and uniform sedimentation to the east of the channel.

4.5.2 Stratigraphic Variability

The stratigraphic evolution of levee architecture is dominated by the asymmetry of the channel-levee system that existed prior to the most recent phase of channel-levee growth and the overcoming of this pre-existing asymmetry through time. The stratigraphic evolution of asymmetry shows consistent trends in both ΔH and ∇H . ∇H started at large positive values and progressed to large negative values, crossing through zero sometime between deposition of R and G. The asymmetry developed due to preferential deposition of sediment west of the channel.

At cross-sections 1 and 2 on the western levee, a complete record of variations in the decay constant is available (Figure 4.27). The stratigraphic evolution of k lacks a discernible trend, with k having “background” values of around $20 \times 10^{-5} \text{ m}^{-1}$ at cross-section 1 and a value of about $10 \times 10^{-5} \text{ m}^{-1}$ for cross-section 2. At both cross-sections, k

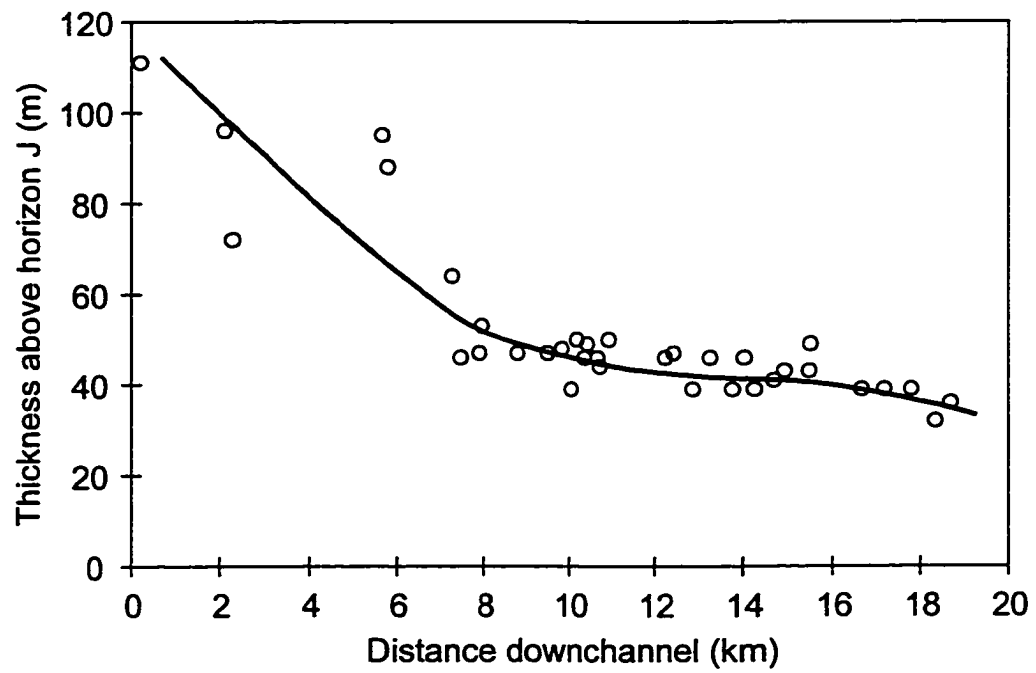


Figure 4.26. Thickness of sediment at western levee crest above horizon J plotted against distance downchannel.

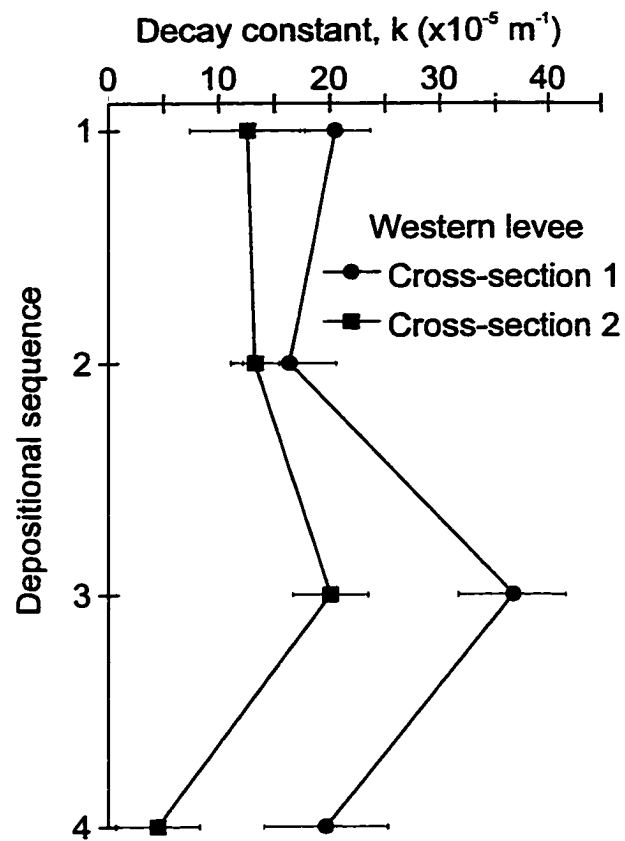


Figure 4.27. Stratigraphic evolution of decay constants for DS1 and DS2 calculated for the western levee at cross-sections 1 and 2.

for DS3 stands out above this background, increasing to $36.7 \times 10^{-5} \text{ m}^{-1}$ at cross-section 1 and about $20 \times 10^{-5} \text{ m}^{-1}$ at cross-section 2. The maximum in k for these cross-sections occurred at a time when the eastern levee of Hueneme Channel passed from being bathymetrically higher to bathymetrically lower than the western levee. This maximum also coincided with the downfan progradation of sediment waves and evidence for active sediment wave growth.

4.6 Key Features

1. Hueneme Fan provides information on the general behaviour of channel-levee architecture over the distal reaches of a submarine channel-levee system. Its channel morphology differs from that of the Northwestern Atlantic Mid-ocean Channel (Chapter 3) and represents part of the continuum of channel-levee architecture being studied in this thesis.
2. When depositional sequences thin perpendicular to channel trend their thickness variations can be described by an exponential model. Of the 24 cases investigated, 15 could be statistically fit to the model.
3. Several instances exist when k is not significantly different than zero (seven of 24). These instances characterize proximal locations east of Hueneme Channel and distal locations west of Hueneme Channel. Two cases showed patterns where thickness increased away from the channel.
4. Differences in the elevation of conjugate levee crests evolved because of preferential deposition of sediment west of Hueneme Channel. This deposition eventually produced a western levee crest that was bathymetrically higher than its conjugate eastern levee crest. The transition from positive ∇H to negative ∇H occurred during deposition of DS3.
5. Where asymmetry, whether measured as ΔH and ∇H , is greatest, the value of k on conjugate levees is approximately equal. During times when ∇H was positive, the eastern levee has uniform thickness depositional sequences while the western levee possessed non-zero decay constants. Instances where ∇H is negative but small, occurring at the distal end of Hueneme Channel, the western levee has uniform thickness depositional sequences while the eastern levee has non-zero decay constants.

6. Cross-channel slope shows the strongest downchannel trend of the architectural parameters and this trend is a response to preferential accumulation of sediment on the western levee. The decay constant shows a downchannel decrease, especially for DS3 on the western levee. Thickness of sediment at the levee crest is relatively uniform on the eastern levee at successive locations downchannel. Sediment thickness on the western levee shows a weak downchannel decrease between cross-sections. The downchannel pattern in thickness of sediment at the western levee crest above horizon J shows a strong decrease in thickness over the upper reach of Hueneme Channel, followed by smaller decreases in thickness. At the very distal end of Hueneme Channel, sediment thickness again begins to fall off rapidly.
7. Cross-channel slope shows a coherent stratigraphic trend, evolving from positive to negative values through time. Decay constants show no systematic trend with the only notable behaviour being a maximum in k for DS3 at each cross-section.
8. The stratigraphic evolution of sediment waves shows the development and channelward migration post-deposition of R. Between R and G sediment wave growth continued and after G but before L the sediment wave amplitude decreased. Some waves show periods of draping sedimentation alternating with periods of channelward migration. After deposition of L, deposition draped the relief created by the sediment waves.
9. The thickness of DS4 in relation to a bathymetric high on the western levee (Line 16 and Line 20-21) suggests that prior to deposition of R, local relief of up to 40 m was enough to affect sediment distribution patterns, creating onlapping reflections. At more proximal locations (Line 36) ponding against a different bathymetric high affected all deposition post-J. In the modern bathymetry this feature has up to 25 m of relief. The ponding, rather than onlapping, of reflections in relation to this feature suggests that it was not of sufficient size to interrupt sediment distribution patterns but large enough to affect them. In general, the control of pre-existing topography on levee architecture is pronounced on Hueneme Fan because of the short timescale for the most recent phase of channel-levee growth. Before Holocene transgression

reduced sediment delivery to Hueneme Fan, deposition had only begun to eliminate these topographic obstacles and create a more typical channel-levee morphology.

Chapter 5

Levee Architecture of Other Systems

5.1 General Statement

The previous two chapters presented detailed investigations of submarine channel-levee systems, isolating key features in levee architecture. These features include: 1) thickness patterns both across-levee and downchannel; 2) asymmetry of levees across the channel, parameterized by cross-channel slope and thickness patterns on conjugate levees; 3) sediment waves, described in terms of the stratigraphic evolution of wave morphology; and 4) the stratigraphic evolution of levee crests. This chapter looks at these features on Reserve, Amazon, and Var fans. For each system, a general setting of the channel-levee system is provided that includes location, channel morphology, and general stratigraphy. This background is then followed by identification of the key features in levee architecture. The observations of levee architecture from these systems supplement data from Hueneme Fan and NAMOC, adding to the database of architectural observations of channel-levee systems. These systems also have data that help to constrain the nature of levee architecture, including boreholes on Amazon Fan and current-meter data on Reserve Fan. Var Fan was analyzed because of data availability and because it has features in common with Hueneme Fan and the more complex Laurentian Fan presented in the next chapter.

5.2 Reserve Fan

Reserve Fan formed due to the discharge of mine tailings into Lake Superior (Figure 5.1) over about 20 years (Normark & Dickson, 1976a, b). The tailings were fed on to a subaerial delta at an average rate of $40.5 \times 10^6 \text{ kg day}^{-1}$ by two launders (open flumes) elevated 3 m above the delta surface which were periodically extended to keep pace with delta progradation. In the early 1970's, the delta was approximately 1.5 km wide and had prograded about 1 km from the original lake shore (Normark & Dickson, 1976b). The bathymetry presented by Normark & Dickson (1976a,b) shows that Reserve Fan begins basinward of an abrupt change in regional slope around the 180 m isobath. Landward of the 180 m isobath is a steep ($< 300 \text{ m km}^{-1}$ or $< 17^\circ$) prodelta slope.

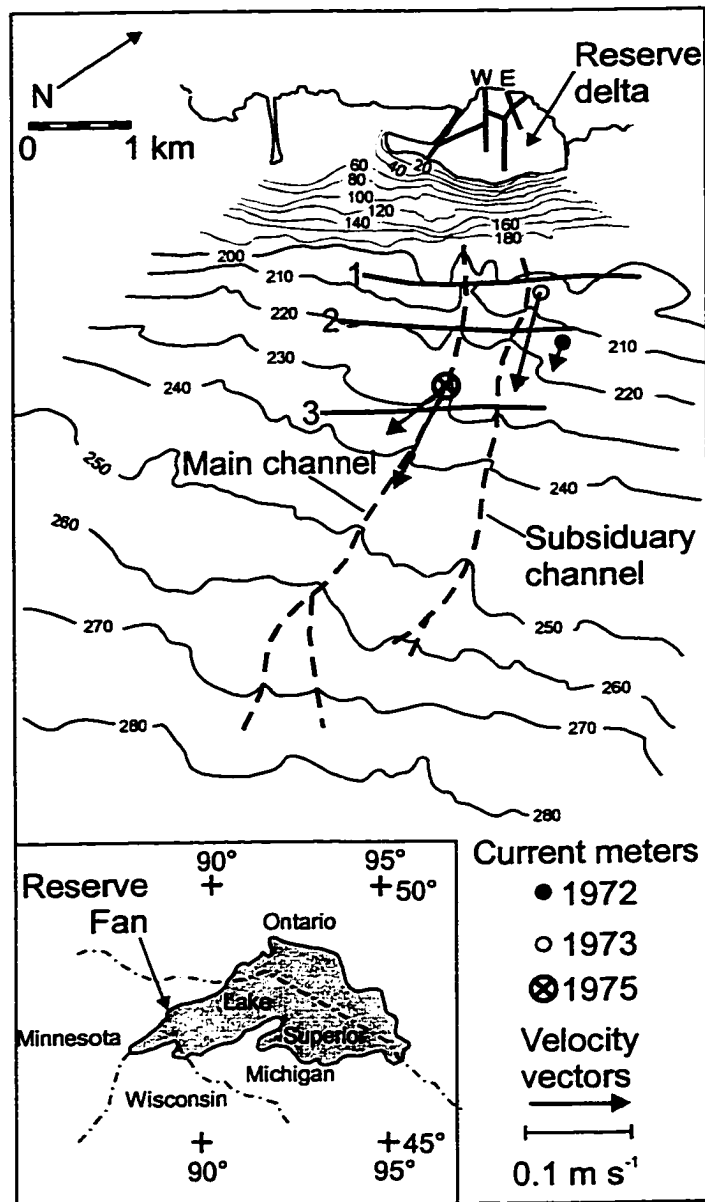


Figure 5.1. Bathymetry of Reserve Fan showing location of current meter stations and acoustic profiles. Reserve Fan occurs distal of Reserve Delta with the main fan channel beginning around the 200 m isobath. A minor channel occurs east of the main channel. The current meter stations are plotted along with velocity vectors that show the mean value of flow speed and direction. Inset shows general location of Reserve Fan within Lake Superior.

Basinward from the 180 m isobath, the slope decreases to 20 m km^{-1} . Reserve Fan covers an area of approximately 20 km^2 extending from the 180 m isobath to the 285 m isobath. The fan has two leveed channels: a main channel and a smaller subsidiary channel to the east (Figure 5.1). Slope of the main channel averages 20 m km^{-1} while channel width averages 500 m and channel depth averages about 4 m. The main channel and the subsidiary channel begin around the 200 m isobath and lose their bathymetric expression around the 280 m isobath, covering a distance of about 5 km. The abrupt appearance of a leveed channel at the base of the prodelta slope was attributed by Normark & Dickson (1976b) to a hydraulic jump.

Mapping of the tailings deposit by Normark & Dickson (1976b) using closely-spaced ($\sim 35 \text{ m}$) high resolution seismic profiles and calculation of sediment volumes from mine records, suggests that 45% of the sediment introduced at the launders became incorporated into the fan. The majority of this sediment was deposited on the western levee of the main channel. In cores, fan sediments are easily differentiated from normal lake sediments because of their exotic colour and mineralogy. Typical lake sediment consists of reddish sandy-to-silty clay whereas the tailings deposit is greyish-black with significant proportions of magnetite (7%) in addition to quartz (50%) and amphibole (43%). The mean grain size on the fan ranges from $17\text{-}53 \mu\text{m}$ (Table 5.1). Generally, the channel floors have the coarsest grains, with maximum grain sizes of up to $250 \mu\text{m}$. The levee crests have finer-grained sediment than the adjacent channel floors and become progressively finer with distance from the channel.

The sediment character and morphology of Reserve Fan are well-constrained by previous investigations (Normark & Dickson, 1976a,b). First, as the serendipitous result of current meter moorings in 1972 and 1973 (Normark & Dickson, 1976a), and then in 1975 by a dedicated scientific investigation (Normark, 1989), turbidity current flow down Reserve Fan was monitored. From these investigations, many through-channel flow parameters are known, including sediment discharge, $J \text{ (m}^3 \text{ s}^{-1}\text{)}$, volume discharge, $Q \text{ (m}^3 \text{ s}^{-1}\text{)}$, velocity, $u \text{ (m s}^{-1}\text{)}$, flow thickness, $H \text{ (m)}$, volume concentration, C , and particle settling velocity, $w_s \text{ (m s}^{-1}\text{)}$ (Table 5.2). Behaviour of the turbidity currents on the prodelta slope is also constrained by observation. Divers reported continuous downslope flow of turbidity currents 3-5 m thick in water depths less than 60 m (Normark &

Dickson, 1976a). Direct measurement also constrains the volume concentration at which tailings enter the basin at about 0.02 (Normark & Dickson, 1976b).

Table 5.1. Mean grain size characterizing general location on Reserve Fan (data from Normark & Dickson, 1976b). Coarsest sediment found in channels and on depositional lobe while finer sediment occurs on levees and at locations distal of the depositional lobe. Also note the fining of the mean grain size between the crest and flank of the western levee.

General location	Mean Grain Size (μm)
Main channel	53
Subsidiary channel	42
Crest of western levee	31
Flank of western levee	22

Table 5.2. Values of channel dimensions and flow parameters taken from Normark (1989) at 2 km downchannel at the site of the 1975 current meter location (Figure 5.1).

Variable	Value	Source
W (channel width)	500 m	Bathymetry, Normark & Dickson (1976a)
D (channel depth)	4 m	Bathymetry, Normark (1989)
u (velocity)	0.1 m s^{-1}	Current meter, Normark (1989)
C (volume concentration)	1.8×10^{-5}	Sampling of flow, Normark (1989)
H (flow thickness)	16 m	Sampling of flow, Normark (1989)
w_s (settling velocity)	0.001 m s^{-1}	Normark & Dickson (1976b)
Q (volume discharge)	$800 \text{ m}^3 \text{ s}^{-1}$	uhW
J (sediment discharge)	$0.0144 \text{ m}^3 \text{ s}^{-1}$	uhWC

5.2.1 Levee Architecture

Three cross-sections, associated with the locations of the current meter deployments, were selected from the literature (Normark & Dickson, 1976b) for analysis of thickness patterns. Sediment on the eastern levee of the main channel was too thin to accurately reconstruct thickness patterns. From the isopach map drawn by Normark & Dickson (1976b, their figure 5) thickness on the eastern levee is variable but averages approximately 3 m, extending about 2 km from the main channel. Sediment thickness, even on the western levee, was not sufficient to isolate reflections within the tailings deposit. Consequently, the levee architecture of Reserve Fan can only be characterized by looking at the entire deposit and then only on the western levee of the main channel. A more detailed stratigraphy was not possible.

Variations in thickness across the western levee show rapid thinning at all the cross-sections (Table 5.3, Figure 5.2). Visual inspection of the thickness plots, values for the correlation coefficient, and the error estimates all suggest that depositional sequence thickness conforms to the exponential model outlined in Chapter 2. Small-scale relief on the western levee appears to increase between cross-section 1 and 3 (compare Figure 5.2a, Figure 5.2c, Figure 5.2e). The hyperbolic reflections that these features return to the surface represent short wavelength (< 200 m) oscillations in lake floor relief. Normark & Dickson (1976b) postulated that this relief was the result of small overflow channels; however, they also noted a lack of continuity of these features between successive profiles. Such evidence suggested to them that these features represent discontinuous depressions that may be remnants of old overflow channels. Their internal morphology was not well-established by the acoustic profiles presented by Normark & Dickson (1976b), consequently, the interpretation of this relief as sediment waves can be neither supported nor refuted.

Table 5.3. Summary of regression parameters for western levee of Reserve Fan. Location of cross-sections given in Figure 5.1. Distances given in column 1 are measured from the 180 m isobath, the start of channel relief on the fan. k = decay constant, δk = 95% confidence limits around decay constant, η_{lc} = thickness at levee crest, $\delta\eta_{lc}$ = 95% confidence limits around thickness at levee crest, r = correlation coefficient.

Cross-section	$k \times 10^{-5}$ (m^{-1})	$\delta k \times 10^{-5}$ (m^{-1})	η_{lc} (m)	$\delta\eta_{lc}$ (m)	r
1 (0.5 km)	104.9	12.4	12.5	1.1	0.96
2 (1 km)	110.9	14.0	7.6	0.7	0.96
3 (2 km)	117.5	31.2	6.0	1.0	0.88

5.2.2 Synthesis of Levee Architecture on Reserve Fan

The spatial decay constant, k , for the western levee of the main channel on Reserve Fan shows a downchannel increase (Table 5.3, Figure 5.3). However, the increase is within the 95% confidence limits on k , reflecting no significant downchannel trend in k between the three cross-sections. The thickness of sediments on the levee crest decreases from about 18 m to 3 m over a distance of 5 km, following what appears to be an exponential pattern. Regression analysis performed on these downchannel variations

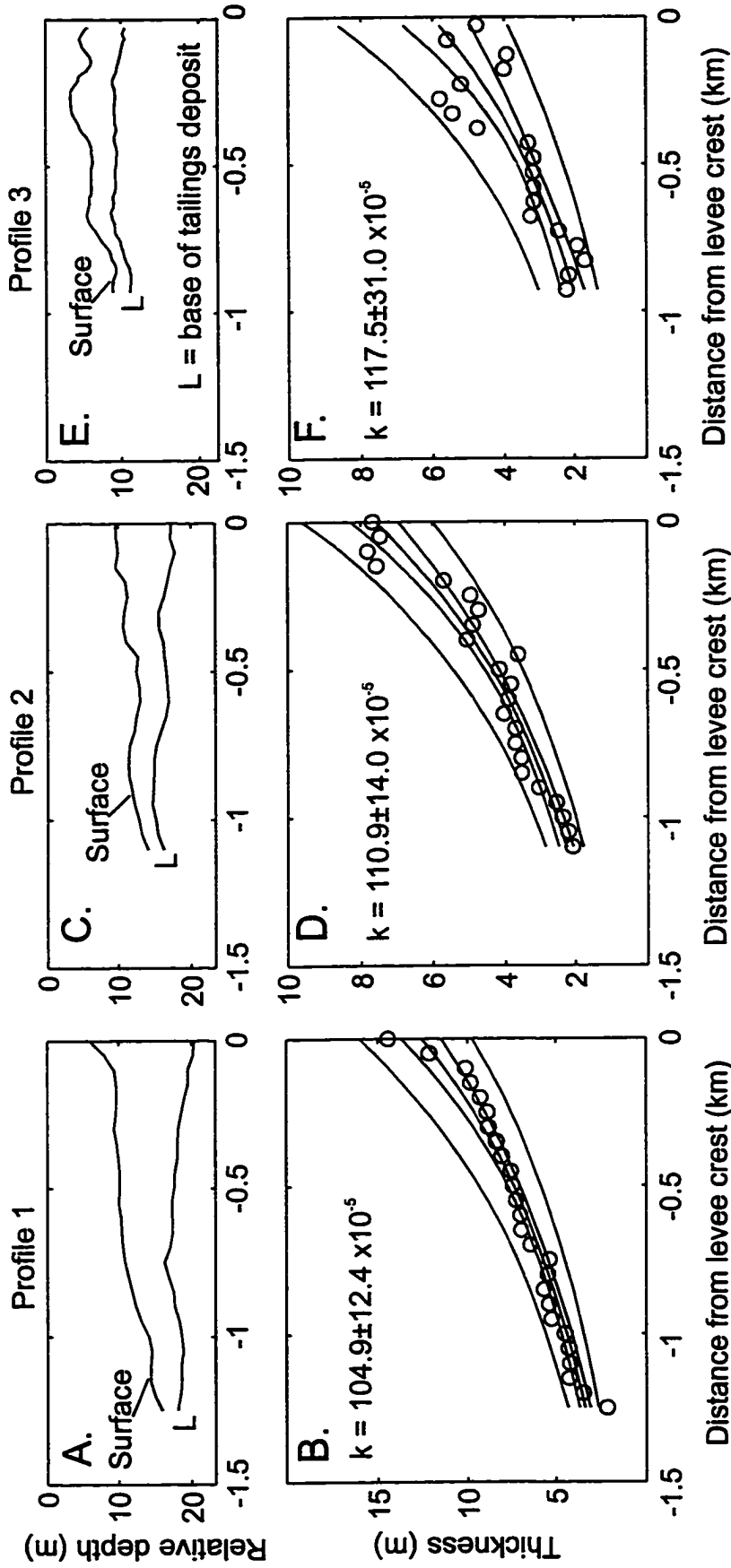


Figure 5.2. Data from profiles 1 to 3 on Reserve Fan: A. Line drawing of profile 1 across western levee; B. Thickness data for profile 1; C. Line drawing of profile 2; D. Thickness data for profile 2; E. Line drawing of profile 3; F. Thickness data for profile 3. Original data presented by Normark & Dickson (1976a,b). Decay constants for across-levee variations in thickness, k , quoted with 95% confidence limits used to denote error.

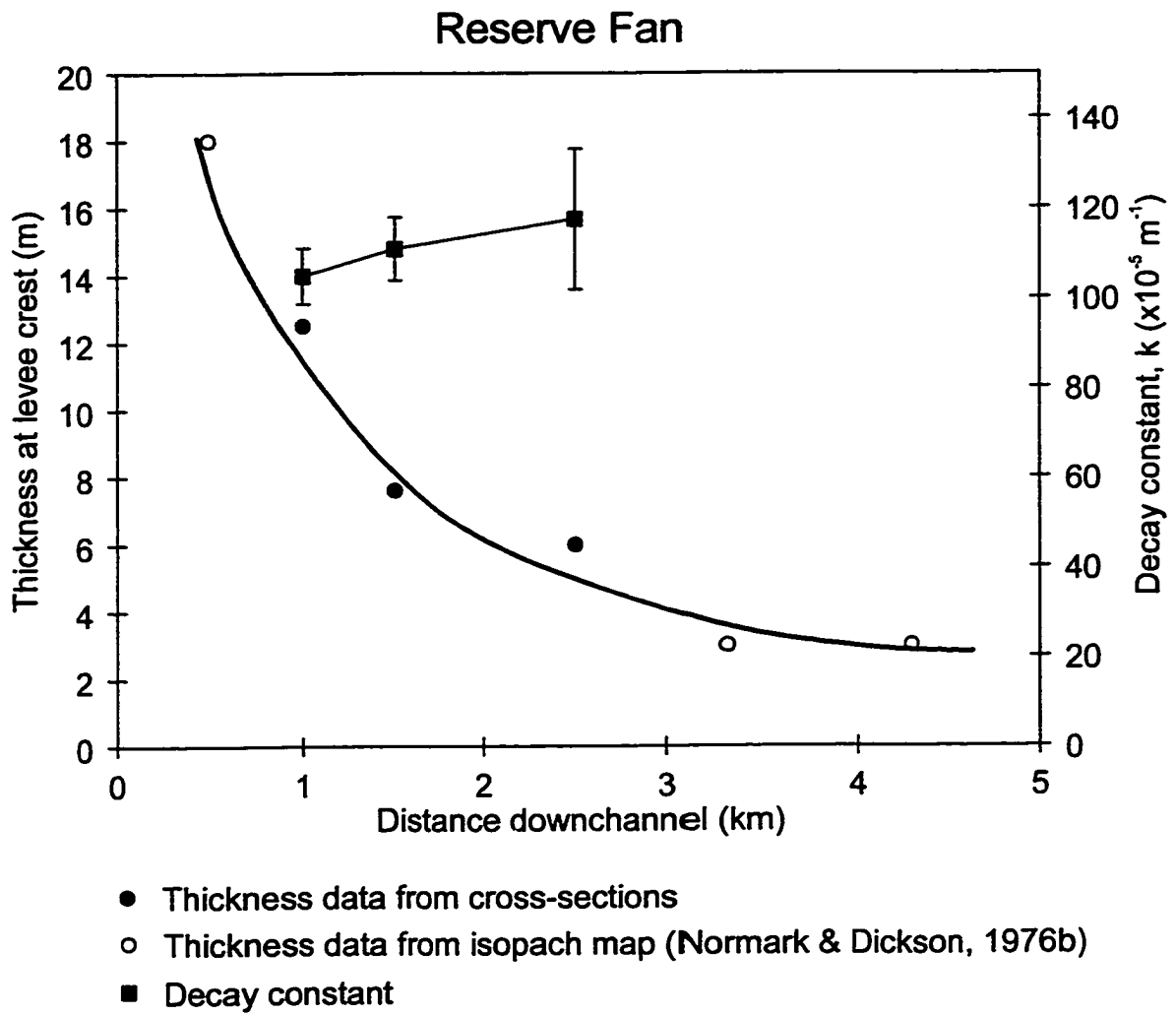


Figure 5.3. Downchannel variation in spatial decay constant, k , and thickness of sediment at the levee crest on western levee of Reserve Fan.

confirms the statistical significance of this exponential pattern ($p < 0.05$, $r^2 = 0.93$), having a downchannel decay constant of about $48.6 \pm 18.9 \times 10^{-5} \text{ m}^{-1}$. Thus, the western levee of Reserve Fan displays exponential thinning both across the levee and down the channel. The patterns in exponential thinning across the levee do not show any significant differences downchannel and the rate of thinning across the levee is about twice that of the thinning downchannel.

The spatial scale of Reserve Fan distinguishes it from all the other systems investigated in this thesis. It has large decay constants ($\sim 100 \times 10^{-5} \text{ m}^{-1}$) compared to NAMOC ($\sim 1-10 \times 10^{-5} \text{ m}^{-1}$, Chapter 3) and Hueneme Fan ($\sim 10-20 \times 10^{-5} \text{ m}^{-1}$, Chapter 4). The current-meter data reported by Normark (1989) suggest that the patterns in levee architecture were formed from flows that had through-channel velocities of about $0.1-0.3 \text{ m s}^{-1}$. By way of comparison, the flow parameter reconstructions that have been conducted on NAMOC and Hueneme Fan suggest through-channel flow velocities of $1-10 \text{ m s}^{-1}$ on NAMOC and $< 1 \text{ m s}^{-1}$ on Hueneme Fan. Although the estimates from NAMOC and Hueneme Fan derive from indirect methods whereas those on Reserve Fan come from direct measurements, an inverse relationship between flow velocity and the across-levee spatial decay constant, k , is suggested.

5.2.3 Key Features

1. Reserve Fan is small system with channel half-widths of $< 250 \text{ m}$ and channel relief $< 4 \text{ m}$, both less than the channel dimensions observed in other systems (e.g., NAMOC, Chapter 3; Hueneme Fan, Chapter 4). In many ways, Reserve Fan represents an end-member in the continuum of architectural observations being assembled in this study.
2. Thickness patterns across the western levee of Reserve Fan follow an exponential pattern that can be parameterized by a spatial decay constant, k , and the thickness of sediment at the levee crest, η_{lc} .
3. Downchannel variations in the thickness of sediment at the levee crest also follow an exponential pattern. The spatial decay constant that parameterizes this behaviour is about half that of the decay constant, k , that describes the across-levee variations in levee thickness. The downchannel variations in thickness do not correlate with any noticeable downchannel trend in k .

5.3 Amazon Fan

Amazon Fan lies off the northeast coast of Brazil (Figure 5.4), seaward of the mouth of the Amazon River. It has been the subject of numerous studies that have described its evolution (e.g., Manley & Flood, 1988), its planform morphology (Damuth et al., 1988; Pirmez & Flood, 1995), its surficial sediment cover (e.g., Flood et al., 1991), and its Quaternary history (Manley & Flood, 1988; Flood, Piper, Klaus et al., 1995). For the purposes of this study, the morphology of Amazon Channel as revealed by multibeam bathymetry and reported by Pirmez (1994) and Pirmez & Flood (1995) was used in conjunction with 3.5 kHz and watergun seismic profiles supplied by Lamont-Doherty Earth Observatory.

5.3.1 General Setting

The stratigraphy of Amazon Fan shows the interfingering of channel-levee systems with mass transport complexes composed of slides and debris flows. Manley & Flood (1988) recognized the stacking of three mid-fan channel-levee complexes -- upper (ULC), middle (MLC), and lower (LLC) -- each composed of many channel-levee systems (Figure 5.5). Underlying the upper levee complex (ULC) is an acoustically transparent unit that blankets the pre-existing topography and was initially interpreted as a debris flow complex (Manley & Flood, 1988). Results of recent ODP drilling have suggested that this unit may be a series of slides (Flood, Piper, Klaus et al., 1995). Preliminary chronologies, later confirmed by ODP drilling, suggested that the ULC represents deposition during the last glacial period (Manley & Flood, 1988), encompassing isotopic stages 4-2. The most recent phase of channel-levee growth, the Amazon system, occurred during the last deglacial period (Piper et al., 1997).

The ULC consists of several individual channel-levee systems. Except for the most recent system, termed Amazon, Manley & Flood (1988) distinguished previous channel-levee systems by colours and using stratigraphic relationships assigned relative ages. In order of increasing age these channel-levee systems include Amazon, Brown, Aqua, Purple, Blue, and Orange. The different systems are thought to have formed in response to successive avulsions. Downstream of an avulsion site, initial deposition is

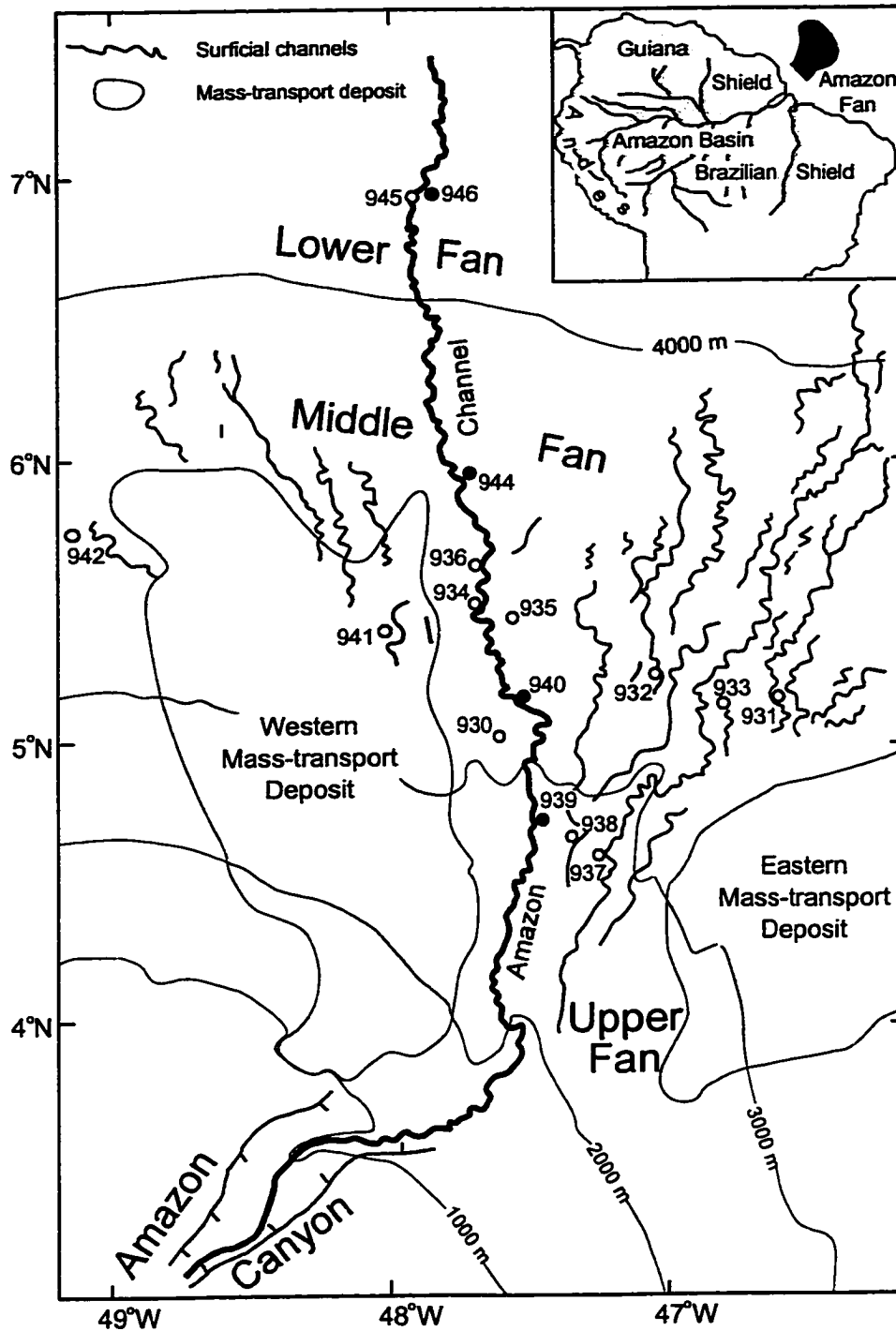


Figure 5.4. Location map for Amazon Fan showing the general bathymetry, trend of modern Amazon Channel along with previous channels, surface debris flows, and ODP sites (modified from Damuth et al., 1988, and Manley & Flood, 1988). Filled circles denote ODP sites used in the thesis.

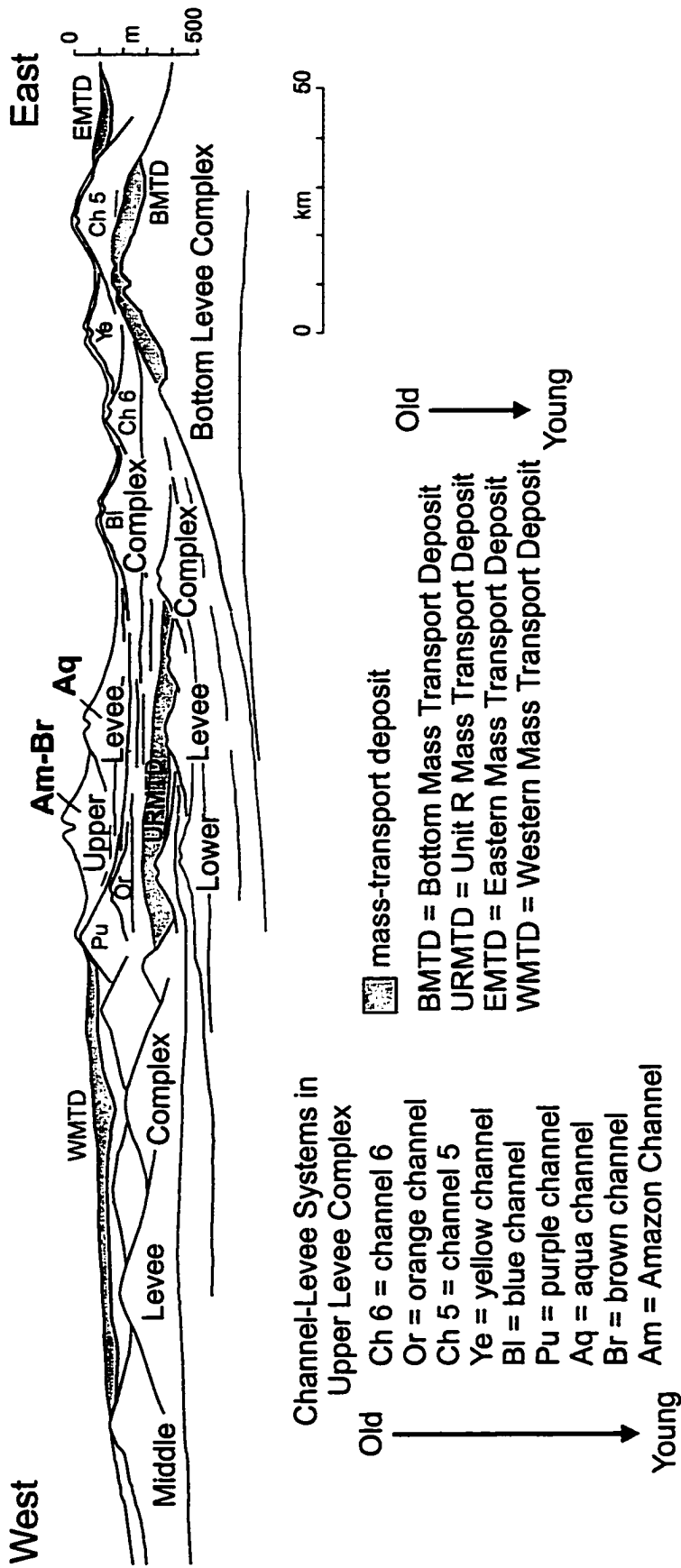


Figure 5.5. Schematic cross-section showing middle fan architecture (modified after Flood, Piper, Klaus et al., 1995). Four major channel-levee complexes are identified, ULC (upper levee complex), MLC (middle levee complex), LLC (lower levee complex), and BLC (bottom levee complex). Each complex consists of several channel-levee systems; for ULC these have been given designations. Also shown are mass transport deposits that cover the modern fan surface and stratigraphically divide levee complexes in the sub-surface.

characterized by evenly stratified, high-amplitude packages of reflectors, termed HARPs, that drilling has confirmed to be principally sands. Above the HARP, a channel-levee complex developed, having a cone-shaped zone of high amplitude reflectors (HARs) flanked by distally-thinning wedges of sediment with low amplitude reflections. The HARs were originally interpreted as channel fill sands, later confirmed by drilling results, but their geometry may result, in part, from hyperbolic reflections returned by the channel walls (Flood, 1987). Upstream of an avulsion site, deposition of the channel-levee system continued. Channel avulsions get progressively younger downfan. Consequently, the more proximal reaches along Amazon Channel have been active conduits for longer periods of time than more distal reaches.

Channel Morphology

Amazon Channel extends for over 1000 km from the base of the continental slope to the basin plain. Damuth et al. (1983) initially documented the highly sinuous nature of this deep-sea channel with apparent meander cut-offs based on GLORIA sidescan sonar. Damuth et al. (1983) traced the modern surficial channels establishing the history of channel bifurcations giving each a numeric designation, one through six.

The morphology of Amazon Channel has recently been investigated by Pirmez (1994) and Pirmez & Flood (1995) based on SeaBeam bathymetric profiles. Based on the elevation of the channel floor relative to the surrounding sea floor, Pirmez & Flood (1995) subdivided the channel-levee system into several segments. The first 100 km represents the canyon, the next 200 km is defined as the upper fan, the following 400 km represents the middle fan and the last 100 km is classified as the lower fan. Sinuosities on the upper fan are generally less than 1.5; on the middle fan, sinuosity increases to 1.5-2.5; on the lower fan sinuosity decreases to generally less than 1.5. Channel slope is locally variable, but generally decreases downstream from 8 m km^{-1} to 1 m km^{-1} (Figure 5.6). Over the entire length of Amazon Channel, the regional downslope gradient is higher than the along-channel gradient. Seaward of Amazon Canyon, which has a maximum depth of 400 m, channel depth decreases from about 150 m to 30 m. Channel width decreases from around 10 km to 1 km over the first 300 km, remains at 1 km between 300 km and 600 km and slightly increases to 2 km over the next 200 km (Figure 5.6). Pirmez (1994) also calculated what he termed total aggradation of the levee crest which represents the thickness of

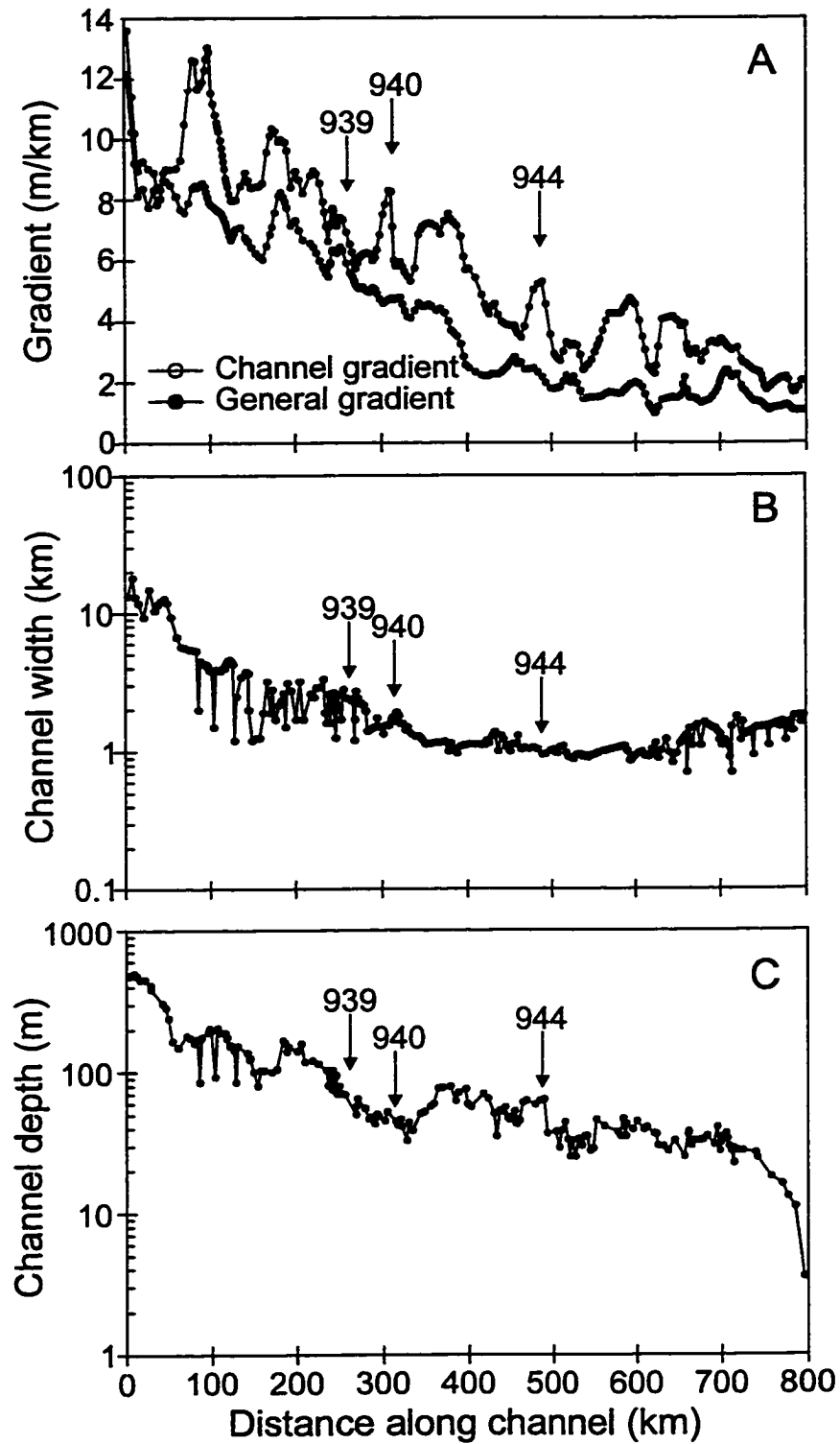


Figure 5.6. Morphology of Amazon Channel: A. downchannel and regional gradient; B. channel width; C. channel depth. Data taken from Pirmez (1994).

sediment from the stratigraphic base of the ULC to the levee crest of Amazon Channel (Figure 5.7). Although not a direct measure of the thickness of any particular channel-levee system making up the ULC, the variations in total aggradation do give some indication of the downchannel variations in sediment thickness, showing that sediment thickness decreases downchannel.

The morphology of Amazon Channel reflects an apparent balance between changes in sinuosity and entrenchment or aggradation of the channel thalweg (Pirmez & Flood, 1995). Pirmez (1994) and Pirmez & Flood (1995) pointed out the relationship between the existence of knickpoints in the channel profile and bifurcation sites. Pirmez & Flood (1995) postulated that avulsion leads to entrenchment of the channel upstream of the bifurcation site and aggradation downstream of the site as the channel regraded after the perturbation to the channel profile caused by avulsion. Periods of enhanced channel-levee progradation in response to increased terrigenous sediment flux may cause avulsion to occur (Pirmez & Flood, 1995); consequently, avulsions may record major changes in the character of turbidity currents moving down the system.

Sediment Delivery

Milliman & Meade (1983) reported that the Amazon River delivers $10^9 \text{ m}^3 \text{ yr}^{-1}$ of sediment. This present day rate of sediment input accounts for the volume of sediments contained within the upper levee complex (ULC) deposited over the last glacial-interglacial period (Manley & Flood, 1988). The present day distribution of sediments shows medium sand (1.5-3 ϕ) covering the outer shelf and coarse silt to clay (4-8 ϕ) making up the modern delta and inner shelf (Nittrouer et al., 1982). The outer shelf sands are well-sorted and likely represent relict shoreface sediments dating from the last glacioeustatic lowstand of sea level (Nittrouer et al., 1982). The inner shelf and deltaic sediments represent the character of sediments delivered by the Amazon River and thus probably reflect the dominant grain sizes delivered to the fan during lowstands of sea level when the Amazon River crossed the continental shelf and fed sediment directly to the continental slope.

Initiation

A large, relatively clean river like the Amazon is a poor candidate for the generation of hyperpycnal inflows (Mulder & Syvitski, 1995). A more likely initiation

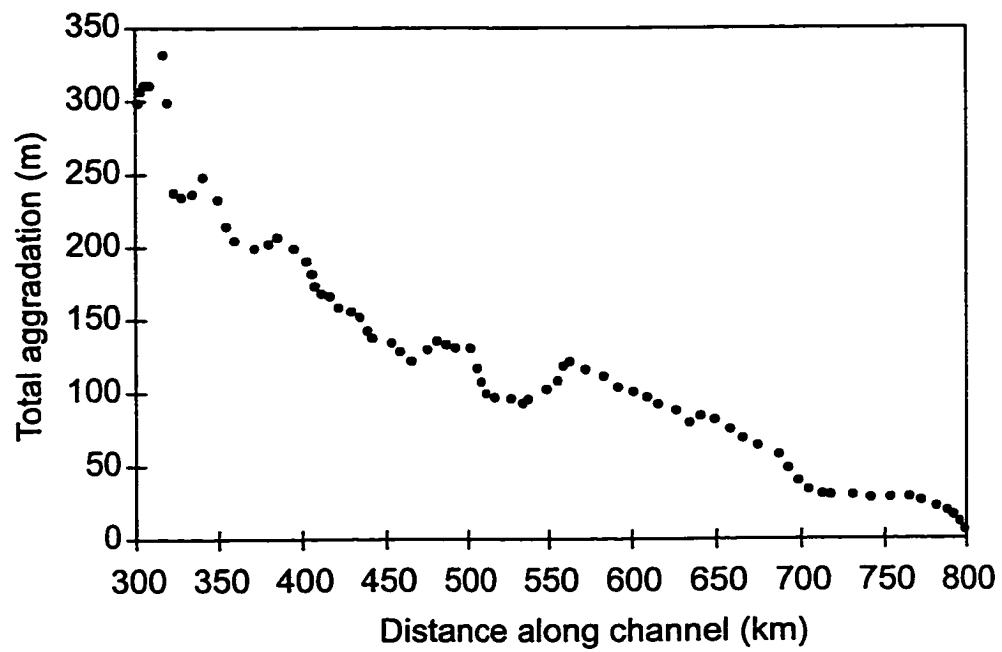


Figure 5.7. Total aggradation of Amazon system measured from base of ULC to modern levee crest of Amazon Channel (data from Pirmez, 1994).

mechanism for the Amazon system may be failure of rapidly deposited deltaic sediments during delta progradation on to the continental slope. The long (>1000 km), meandering (sinuosity>1.5) travel path of channels on Amazon Fan suggests that flows remain intricately related to the channel. The capacity of the channel is likely related to the average size of individual flows. From boreholes collected by ODP Leg 155, Piper & Deptuck (1997) estimated that the frequency of turbidity currents was at least on the order of one every ten years and could possibly be annual. In addition, the presence of sediment waves and tractional bedding features in individual turbidites suggest prolonged flow (Normark & Piper, 1991). This combination of evidence suggests that the initiation mechanism active on Amazon Fan created frequent, relatively small-volume, but long-duration flows. Frequent events have smaller volumes because the time between events along with the sediment input rate sets the amount of sediment that can accumulate in the source area (e.g., Adams, 1989). The coincidence of small volume events with long duration implies low volume concentration. A potential mechanism for creating low concentration, long duration flows from slumps has recently been postulated by Piper et al. (1998a, submitted) whereby slumps evolve into debris flows through incorporation of water. The debris flows, in turn, transform into turbidity currents through hydraulic jumps. If the failure is widespread then drainage of the upper slope failures by debris flows could occur over a prolonged period, sustaining a long duration turbidity current (Piper et al., 1998a, submitted). The most likely position for a hydraulic jump would be near the canyon mouth where slopes drop under 7 m km^{-1} , below which Froude number would be less than unity (Middleton, 1966).

Flow Parameter Reconstructions

The flow parameters of turbidity currents on Amazon Fan have been reconstructed by Pirmez & Flood (1995), Pirmez (1994), Hiscott et al. (1997), and Piper & Deptuck (1997). Pirmez (1994) and Hiscott et al. (1997) reported values of velocity, volume concentration, and thickness for the upper, middle, and lower fan reaches of Amazon Channel. On the upper fan, velocity estimates from grain size using suspension criteria and channel curvature using Komar's (1969) model range from $0.05\text{-}0.1 \text{ m s}^{-1}$ with volume concentrations of about 5×10^{-5} and thicknesses on the order of 100 m. On the middle fan, velocity estimates centre around 0.5 m s^{-1} , volume concentrations at 0.005

and flow thickness at 50-100 m or 1-2 times channel depth. On the lower fan, velocity estimates increase to about 1.1 m s^{-1} with volume concentrations of 0.01 and flow thicknesses between 40-60 m. The apparent downfan increases in velocity and volume concentration may reflect "reconcentration" owing to the removal of the dilute upper portions of the flow by overbanking (Pirmez, 1994; Hiscott et al., 1997). This "reconcentration" of the flow potentially occurs as turbidity currents reach an equilibrium between entrainment of water through the upper flow interface, loss of volume due to flow spilling, and the downfan decrease in channel depth (Pirmez, 1994; Hiscott et al., 1997). Although the equilibrium suggested by the continuous overspill model for overbanking explains a great deal about the levee architecture of many systems (e.g., long distance correlation of levee turbidites on NAMOC, Hesse, 1995), the model does not require the "reconcentration" suggested initially by Pirmez (1994) to occur. Alternatively, these apparent downfan increases in flow parameters may simply reflect landward migration of fan sedimentation during the last sea level rise. The deposits upon which most the velocity estimates were based were not necessarily the result of a single generation of flows. The lower fan sediments that result in higher velocity estimates may pre-date the upper fan sediments that lead to lower velocity estimates. For the "reconcentration" process to be plausibly demonstrated using the data from Amazon Fan the time equivalence of the depositional units used to reconstruct flow parameters would have to be demonstrated.

5.3.2 Levee Architecture

The architecture of levees from Amazon Fan was investigated using 3.5 kHz profiles near three ODP sites -- 939, 940, and 944. The data from each of these sites are presented in turn. Unlike the presentation of other systems, the levee stratigraphy and analysis of levee architecture are presented together for each cross-section.

Site 939

Site 939 sampled the upper 100 m of the eastern (right-hand looking downstream) levee of Amazon Channel (Figure 5.8). Hole 939A is closest to Amazon Channel lying about 1.6 km from the modern channel axis; Hole 939B lies 480 m east of 939A (Figure 5.9). The 3.5 kHz data across site 939 show that the boreholes penetrated a succession of

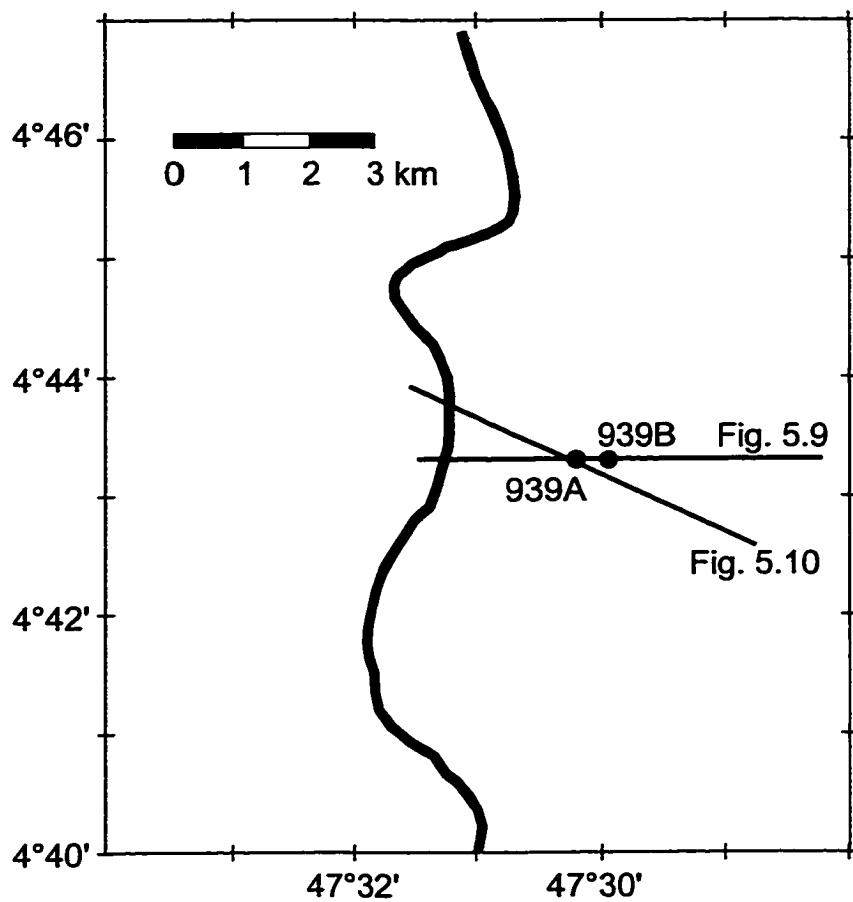


Figure 5.8. Trend of Amazon Channel in the vicinity of Site 939 showing location of boreholes and 3.5 kHz profiles.

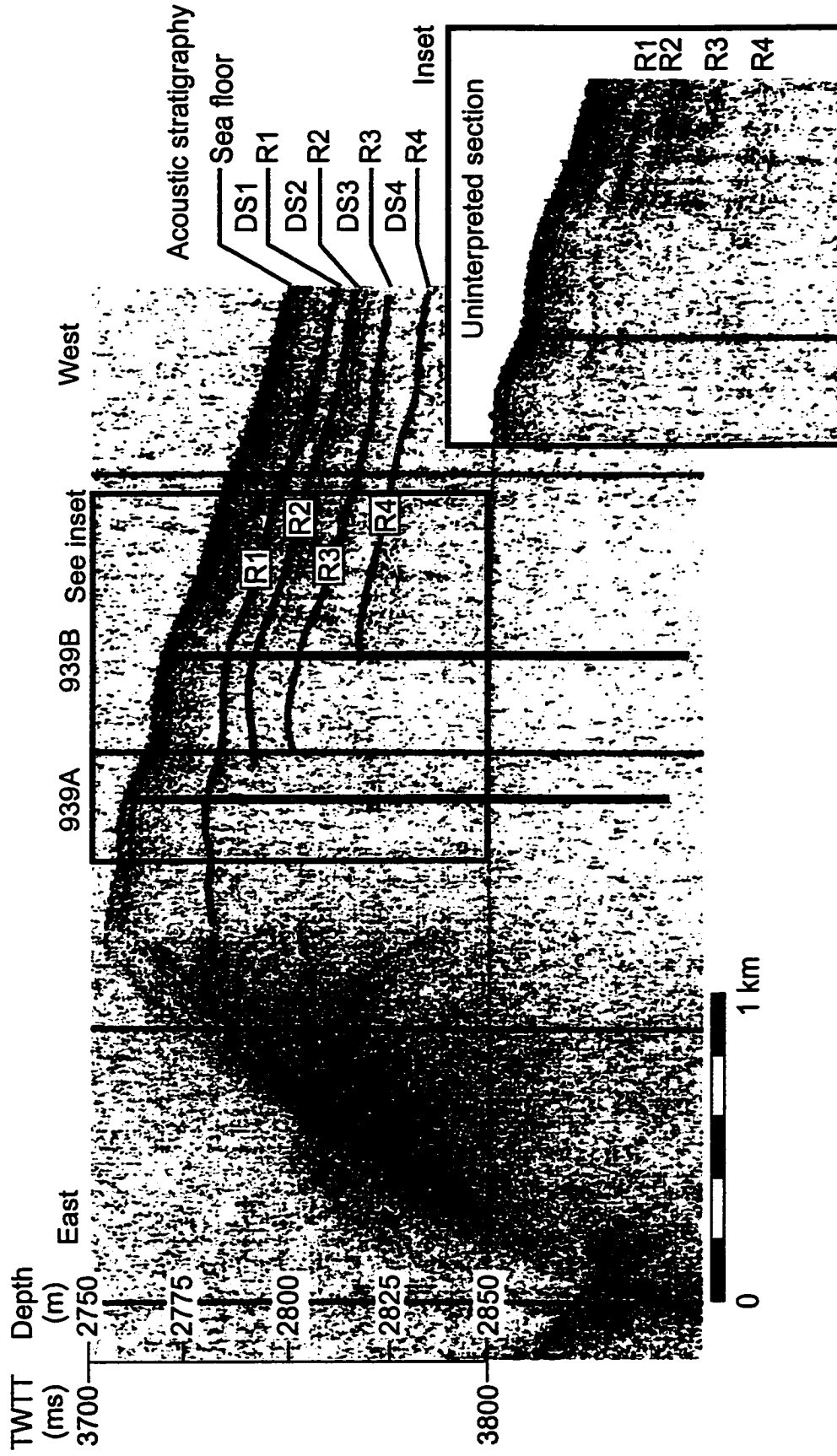


Figure 5.9. 3.5 kHz profile over Site 939. Inset shows uninterpreted section reproduced at higher resolution. Boreholes and seismic reflectors also shown. Location given in Figure 5.8.

acoustically transparent sediments interspersed with weakly-stratified packages (Figure 5.9). In this succession, four sub-bottom horizons were identified, termed R1-R4, bounding four depositional sequences, DS1-DS4. DS1 between the sea floor and R1 appears acoustically transparent to weakly acoustically stratified and becomes particularly transparent on approaching the channel. DS2, between R1 and R2 appears acoustically transparent throughout. DS3 between R2 and R3 has better acoustic stratification, but again this acoustic character grades laterally into a transparent acoustic character moving toward the channel. DS4 between R3 and R4 is acoustically transparent.

The modern levee crest is about 500 m west of Hole 939A and about 90 m above the channel floor, but subsurface levee crests may be much closer to 939A or in between holes 939A and 939B (Figure 5.9). The poor quality of the data reproduction does not immediately show evidence for shifts in the position of subsurface levee crests although some indication of reflectors dipping toward the channel axis appears in the sub-surface. Better evidence of the subsurface levee crests can be seen in 3.5 kHz data collected near Site 939 in 1984 (Figure 5.10). The location of these subsurface levee crests correlates with low amplitude relief at the sea floor, suggesting that this small scale relief preserves former levee crest positions.

Figure 5.11 shows the borehole stratigraphy for holes 939A and 939B. This figure forms a template for presentation of the other boreholes, and thus warrants a general description. For each hole presented in this section, the patterns depict different lithologies. Upper case roman numerals denote individual lithologic units with subunits denoted by lower case arabic letters. Down the left side of the graphic summary description of each hole are the sub-bottom depths of selected correlation horizons defined by Piper et al. (1997). N1-N3 horizons refer to correlation horizons based on magnetic inclination data; ha and hb refer to correlatable peaks in the oxygen isotope record from the holes; X, Y, and Z' denote correlation horizons identified in magnetic intensity records. The letters a-n correspond to the interhole correlation based on magnetic susceptibility records reported by Flood, Piper, & Klaus et al. (1997). Arrows labeled R1-R4 denote the sub-bottom depth of reflectors in the core with two-way travel time (TWTT) converted to sub-bottom depth using the time-depth models given by Flood et al. (1997). Because direct correlation of reflectors between sites was not possible, the

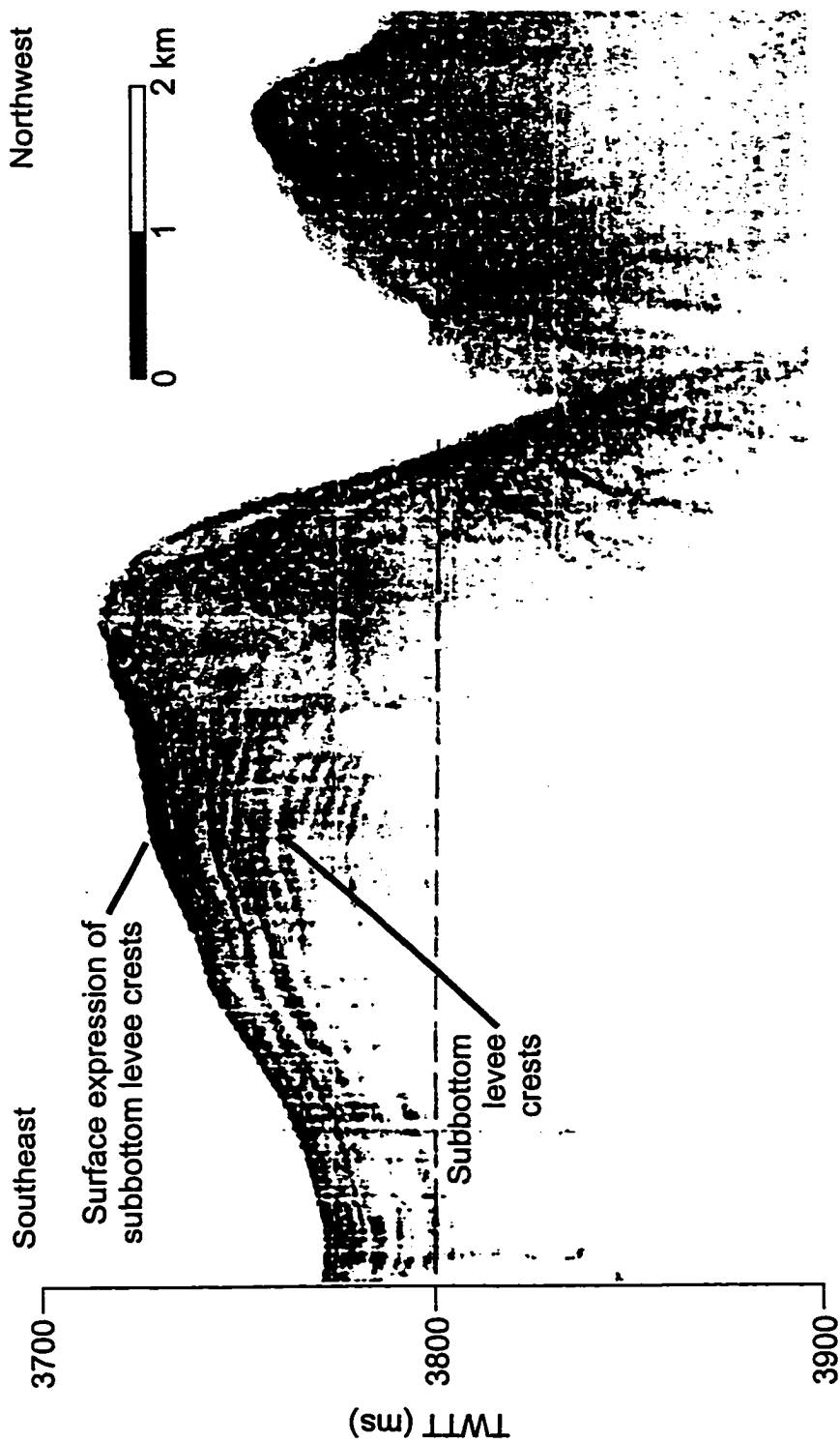


Figure 5.10. 3.5 kHz profile across Site 939 collected in 1984 by RV Conrad. Location given in Figure 5.8.

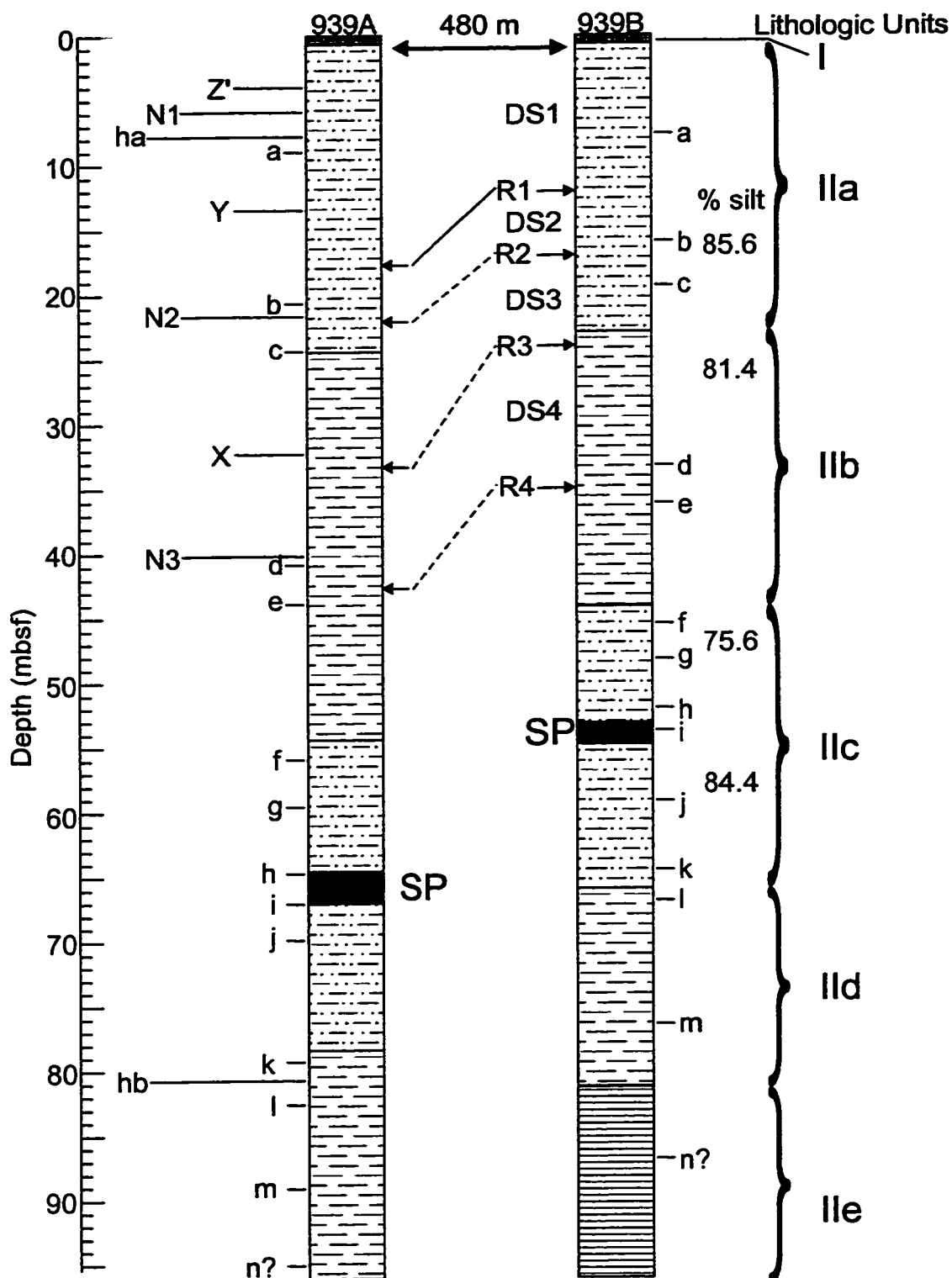


Figure 5.11. Borehole stratigraphy at Site 939. Correlation of R1 between holes A and B based on direct tracing in seismic profile. Correlation of R2, R3, and R4 from Hole 939B to 939A based on magnetic susceptibility correlations developed in Flood, Piper, Klaus et al. (1995). See text for further discussion. SP = silt packet (see Figure 5.13). Fills used to distinguish lithologic units not to denote a particular lithology. mbsf = metres below seafloor.

reflectors and depositional sequences can only be correlated from site to site based on their stratigraphic position within the magnetic or isotopic stratigraphies.

Two major lithologic units occur at Site 939 (Flood, Piper, Klaus et al., 1995). Unit I consists of bioturbated, carbonate-rich mud interpreted to be Holocene deposition of hemipelagic sediments. At all sites, Unit I refers to this hemipelagic sediment. Unit II consists of muddy silt and is divided into subunits on the basis of lamina abundance. Overall, this unit reflects Pleistocene deposition of turbidites. The break between Unit IIa and IIb was placed at the first occurrence of a silt lamina. For these holes and for sites 940 and 944, this criterion distinguishes Units IIa and IIb. At Site 939, Unit IIc distinguishes itself from IIb by the lack of silt laminae except for an interval (SP = silt packet) characterized by abundant laminae. Unit IId resembles IIb, consisting of muddy silt with silt laminae. Unit IIe was distinguished from IId by a reduction in the number of apparent silt laminae and is separated from IId by a bed of structureless silty mud.

Reflectors R1-R4 could be identified in Hole 939B. R4 lies within Unit IIb. R3 lies near the boundary between Unit IIa and IIb. R1 and R2 lie within Unit IIa and R1 could be placed in 939A also within unit IIa. Based on the magnetic susceptibility correlation, R2 (between b and c in 939B) would fall within unit IIa in 939a. R3 lies below c in 939B so it would be within unit IIb in 939A. From these correlations, DS1, beneath a thin cap of hemipelagic sediments, consists of massive muddy silt turbidites in which most of the primary sedimentary structures have been partially to completely destroyed by bioturbation. Grain size data from Manley et al. (1997) suggest that these sediments consist of over 80% silt with minor contributions of clay and sand (Figure 5.11). DS2 also consists of massive muddy silt turbidites. DS3 spans a transition from laminated muddy silt turbidites to massive muddy silt turbidites. The laminated muds may account for a greater proportion of DS3 in Hole 939A than 939B. DS4 consists of laminated muds in both holes. Percent silt within the laminated muddy silt turbidites is also greater than 80% (Figure 5.11, Manley et al., 1997). R1 lies between horizons Y and N2 in the magnetostratigraphic correlation scheme constructed by Piper et al. (1997), and below ha in the isotopic stratigraphy of Piper et al. (1997).

Although the high percentage of silt suggests that these sediments may be more properly called silts, comparison of the grain size data with visual core descriptions

suggest that the data of Manley et al. (1997) based on laser diffraction may be biased towards the coarser grain sizes. They are reported here because these data represent the only characterization of grain size common to all the cores presented. The important use of these data is comparison between lithologic units and between sites and not their absolute values.

For the laminated muddy silt turbidites, the detailed onboard descriptions reported by Piper & Deptuck (1997) provide some indication of turbidite character (Figure 5.12). The summary core description on the right side of Figure 5.12 uses vertical arrows to denote inferred turbidite thickness. The horizontal arrows pointing to various sub-bottom depths show the location of grain size analyses; those that are labeled are displayed on log-probability plots on the left side of Figure 5.12. Turbidite thickness varies from 0.03-0.06 m. At the sub-centimetre scale the beds show upward-fining of the median grain size. The grain size distributions show a change in slope at 6-7 ϕ , separating a well-sorted medium silt to fine sand population from a more poorly-sorted fine silt and clay population.

The correlation of the silt packet (SP in Figure 5.11) seen in holes 939A and 939B is supported by the magnetic susceptibility correlation and thus attempts were made to refine the correlation down to the event level (Figure 5.13). The first and last occurrence of silt beds or laminae with centimetre- (rather than decimetre) scale spacing constrain the thickness of the silt packet. The basal silt beds in both holes overlie thick sequences of massive muddy silt turbidites which in turn overlie laminated muddy silt turbidites. The packet is 2.43 m thick in Hole 939A and 2.16 m thick in Hole 939B, thinning by about 10% over 480 m. The correlation is based on the equivalence of the bottom silt beds and the correlation of the top two silt beds in 939A with the thin intervals of closely-spaced laminae (CSL) in 939B. All correlations beyond these general relationships are tentative. Six silt beds occur in 939A while only one silt bed occurs in 939B. The thick units of colour-banded muds in 939A also have no apparent correlative unit in 939B. Consequently, the character of individual turbidites appears to change dramatically over distances of less than 500 m.

The thickness patterns for the four depositional sequences identified at Site 939 show exponential thinning perpendicular to channel trend that can be reasonably well-

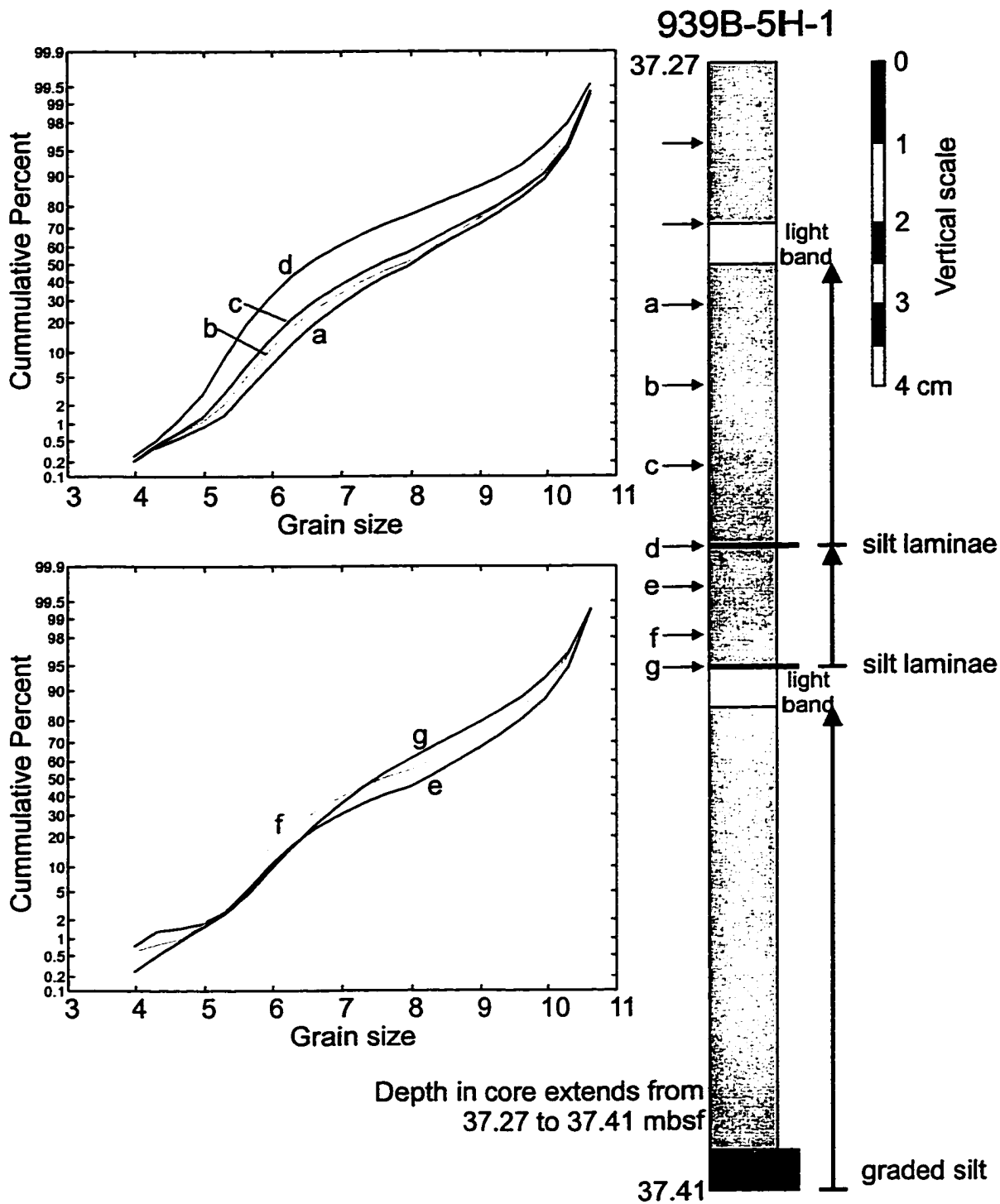


Figure 5.12. Turbidite character at Site 939. Core description and grain size data taken from Piper & Deptuck (1997). Cumulative grain size distributions plotted on log-probability paper.

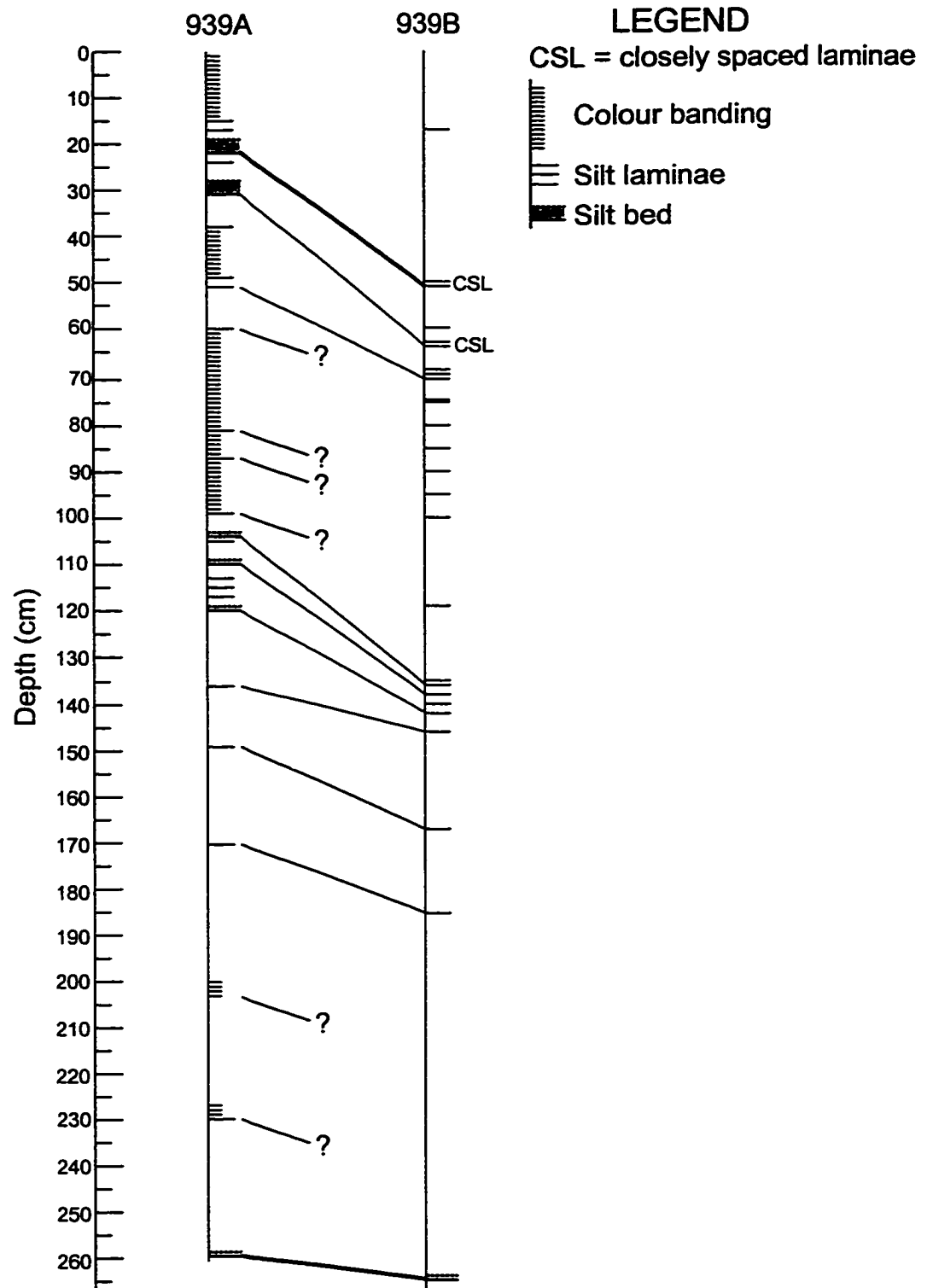


Figure 5.13. Bed to bed correlation of silt packet identified at Site 939.
 Vertical scale in cm.

described by a regression equation (Table 5.4, Figure 5.14) . Except for DS3, depositional sequences have a decay constant whose magnitude averages about $24 \times 10^{-5} \text{ m}^{-1}$. DS3 has a significantly smaller decay constant indicative of a more uniform depositional sequence. The decay constants show no correlation with lithology. DS1 and DS2 consist of massive muddy silt turbidites while DS4 consists entirely of laminated muddy silt turbidites. Comparison of the decay constants for these sequences shows no significant difference. However, DS3 includes sediments from both lithologic units and its decay constant is notably less than the other sequences.

Table 5.4. Summary of regression parameters at Site 939 for depositional sequences identified in 3.5 kHz data. DS = depositional sequence, k = decay constant, δk = 95% confidence limit around decay constant, η_o = y-intercept of regression equation, $\delta \eta_o$ = 95% confidence limit around y-intercept, r = correlation coefficient, y_{lc} = distance from channel axis to levee crest, η_{lc} = thickness at levee crest.

DS	$k \times 10^{-5}$ (m^{-1})	$\delta k \times 10^{-5}$ (m^{-1})	η_o (m)	$\delta \eta_o$ (m)	r	y_{lc} (km)	η_{lc} (m)
1	-28.8	3.8	24.2	2.6	0.93	1.0	18.1
2	-20.4	6.0	7.8	1.4	0.79	1.5	5.7
3	-7.6	3.8	8.0	1.0	0.61	1.5	7.1
4	-23.6	5.2	17.4	2.6	0.90	1.5	12.2

Site 940

Site 940 sampled about 250 m of the eastern levee of Amazon Channel about 4 km from the channel axis (Figure 5.15). This site lies downstream of the Aqua avulsion site (Figure 5.15), so that sediment at Site 940 records the history of channel-levee development, spanning two major avulsion episodes (i.e., Aqua to Brown, Brown to Amazon). A line drawing of the two major reflectors, R1 and R2, identified in 3.5 kHz profiles across the channel shows that depositional sequences thin away from the channel axis and some small scale relief at the surface that may reflect the location of a previous levee crest like at site 939 (Figure 5.16). The modern levee crest at Site 940 is about 1 km from the channel axis and about 75 m above the channel floor. The inferred paleo-levee crest occurs about 500 m east of the modern levee crest. A watergun profile collected concurrently with the 3.5 kHz data shows the deeper structure of Amazon Channel (Figure 5.17). The basal reflector defines the top of the Aqua HARP (high

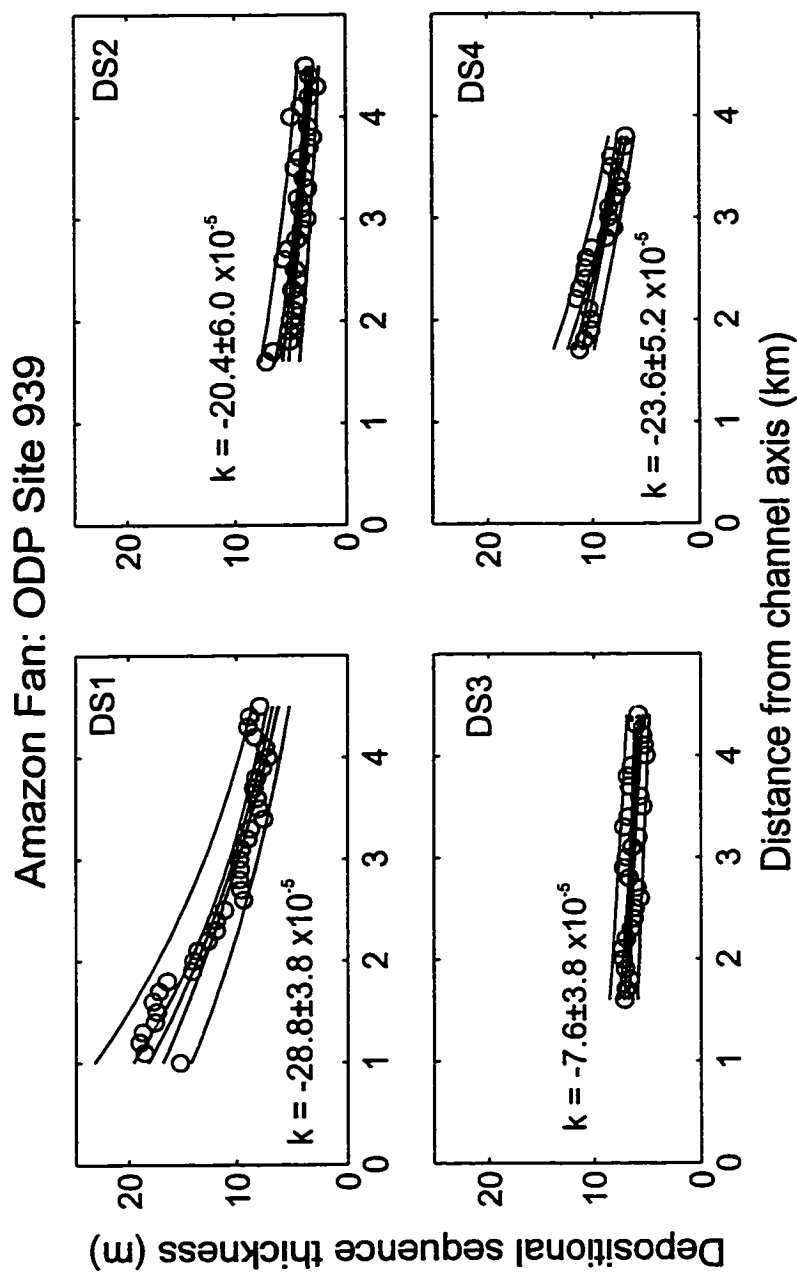


Figure 5.14. Thickness variations across the eastern levee of Amazon Channel at Site 939. Depositional sequences defined in text. Regression parameters tabulated in Table 5.4.

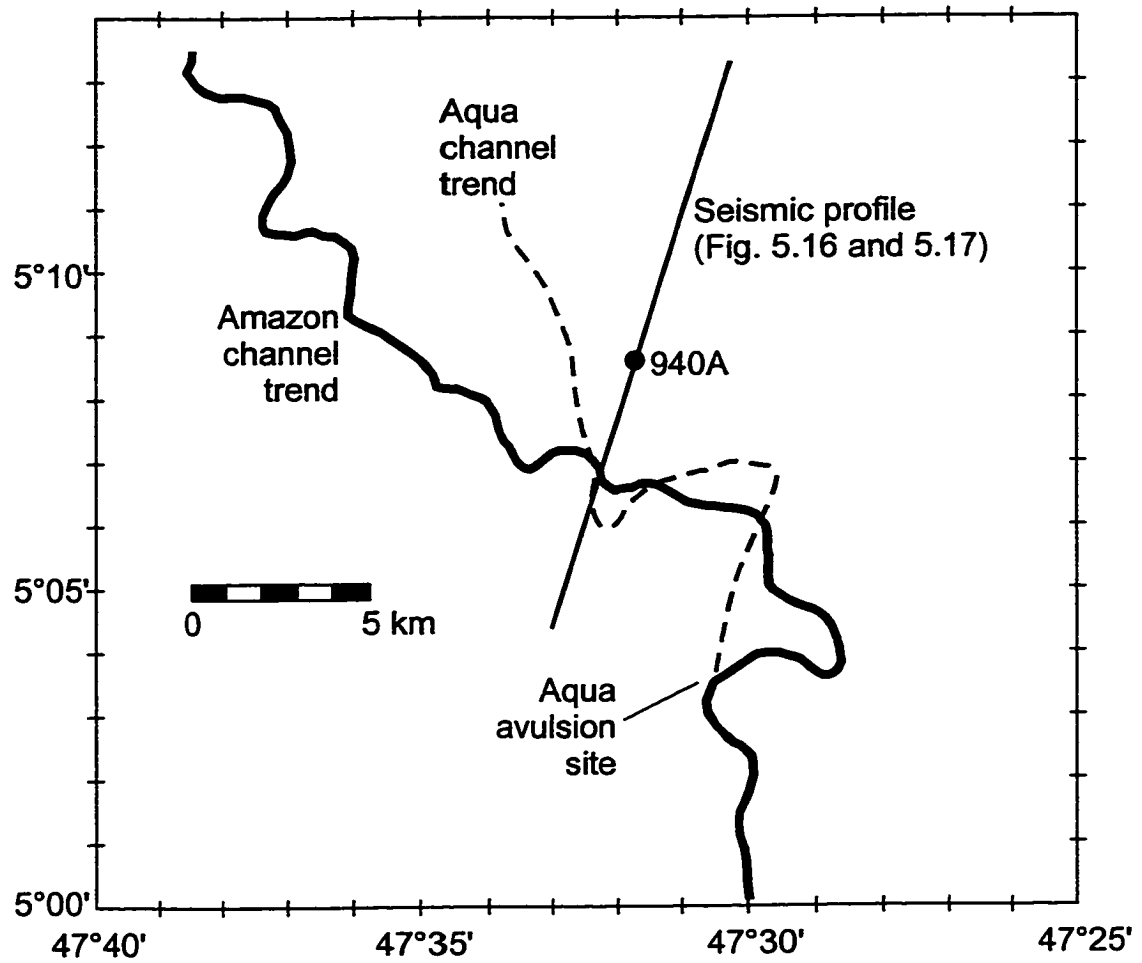


Figure 5.15. Channel trend in the vicinity of Site 940 showing location of borehole and seismic profile. Also shown is approximate location of Aqua avulsion site.

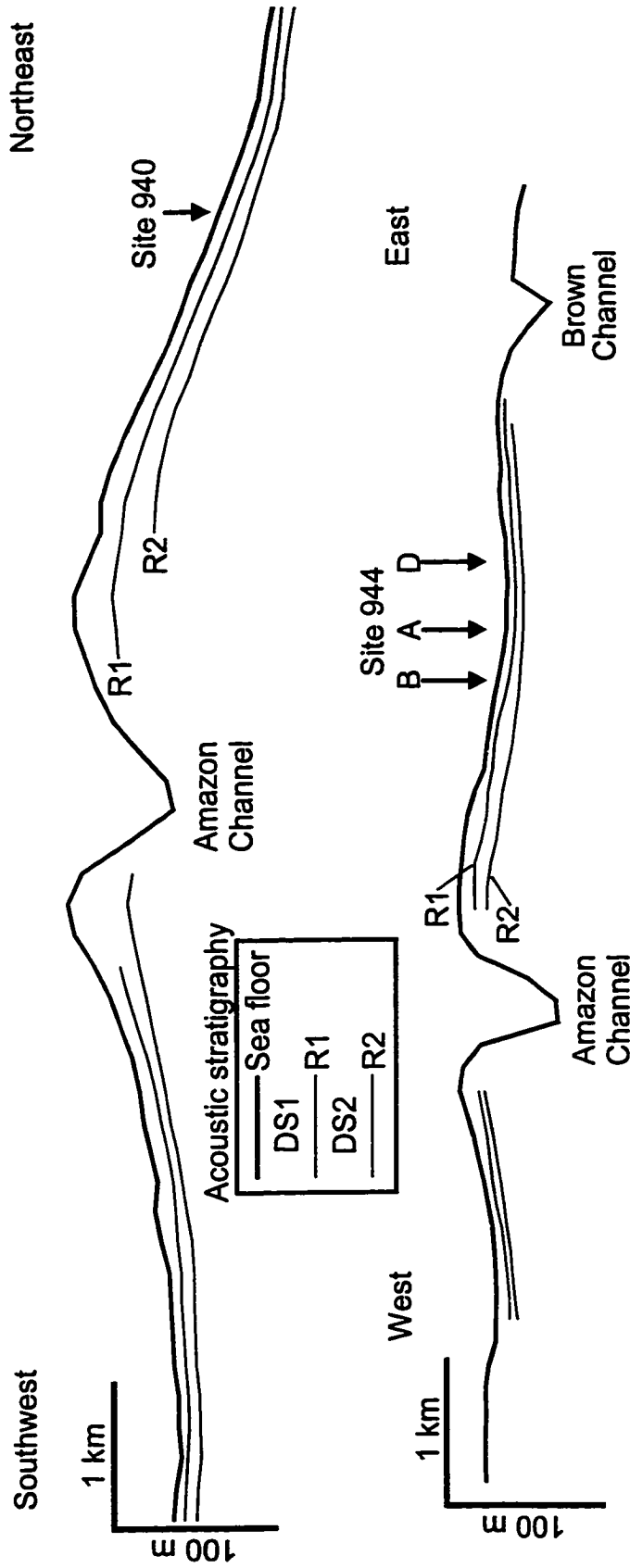


Figure 5.16. Line drawings of 3.5 kHz profiles across sites 940 and 944 showing location of boreholes relative to Amazon Channel. Profile across Site 944 also crosses brown channel. DS1 = depositional sequence bounded by sea floor and R1; DS2 = depositional sequence bounded by R1 and R2

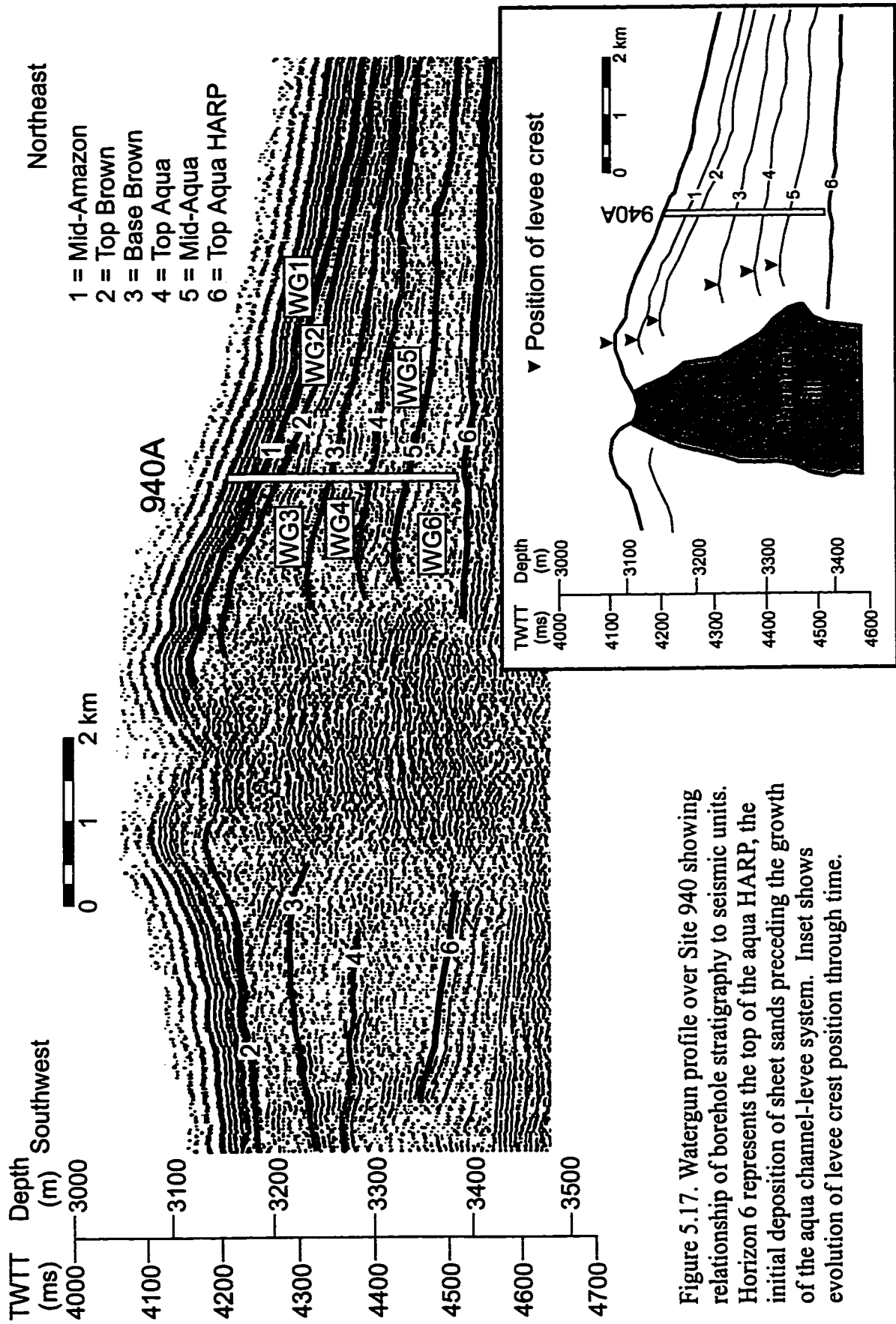


Figure 5.17. Watergun profile over Site 940 showing relationship of borehole stratigraphy to seismic units. Horizon 6 represents the top of the aqua HARP, the initial deposition of sheet sands preceding the growth of the aqua channel-levee system. Inset shows evolution of levee crest position through time.

amplitude reflector packet). Above the Aqua HARP horizon, five reflectors were identified that divide the levee into six depositional sequences: WG1 between the surface and mid-Amazon reflector, WG2 between mid-Amazon and top Brown, WG3 between top Brown and base Brown, WG4 between base Brown and top Aqua, WG5 between top Aqua and mid-Aqua, and WG6 between mid-Aqua and the top of the Aqua HARP.

The lithostratigraphy of the upper 100 m of Hole 940A was divided into two major units very similar to those distinguished at Site 939 (Figure 5.18). Unit I consists of hemipelagic silty mud, interpreted to be Holocene deposition. Unit II consists of muddy silts, representing Pleistocene turbidite deposition. Units IIa and IIb are distinguished by the first occurrence of a silt lamina. Unit IIc lacks silt laminae, having an appearance similar to IIa. Units IId and IIe are analogous to IIb. An important difference between the lithostratigraphy of Site 939 and Site 940 is the presence of contorted bedding at several horizons, interpreted to be slumps. The thickest slump deposit is identified as Unit IIe but thinner intervals of contorted bedding occur in IIb.

As at Site 939, the velocity model of Flood et al. (1997) was used to convert TWTT to depth in the borehole, so that the sub-bottom horizons identified in the 3.5 kHz profiles could be placed in the borehole stratigraphy. R1 occurs near the base of Unit IIa and is almost coincident with horizon N1. R2 occurs within Unit IIb just above horizon ha and several metres above horizon Y. The occurrence of R1 and R2 within the magnetic and isotopic stratigraphy at Site 940 suggests that both of these reflectors post-date the first subbottom reflector identified at Site 939. At Site 940, DS1 consists almost exclusively of massive muddy silt turbidites with about 80% silt and minor contributions of clay and sand (Figure 5.18, Manley et al., 1997). DS2 consists of laminated muddy silt turbidites with two minor slump deposits and has about 70-85% silt (Figure 5.18, Manley et al., 1997).

Depositional sequences identified in the watergun profile across Amazon Channel (Figure 5.17) could also be placed in the borehole stratigraphy from site 940 (Figure 5.19). WG6 consists of laminated muddy silt turbidites. Lamina frequency appears approximately constant at less than 20 m^{-1} , except for a maximum of 60 m^{-1} at 240 mbsf (metres below sea floor). WG5 and WG4 also consist of laminated muddy silt turbidites,

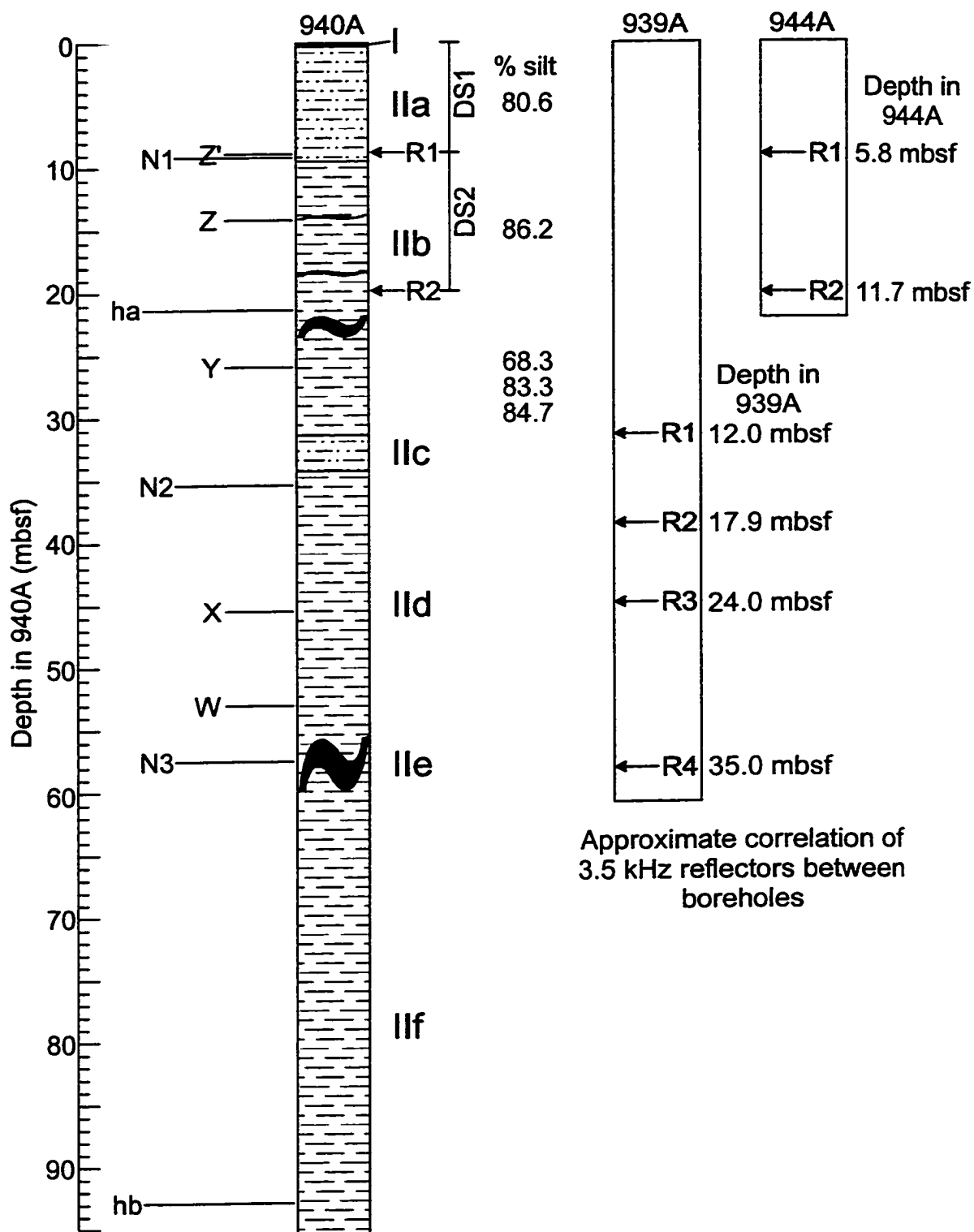


Figure 5.18. Borehole stratigraphy of the upper 95 m at Site 940. Also shown is the relative stratigraphic position of reflectors defined at sites 939 and 944. Note approximate correlation of R1 and R2 between sites 940 and 944. According to the magnetic and isotopic stratigraphy of Piper et al. (1997), R1 at Site 939 lies stratigraphically below R2 at sites 940 and 944.

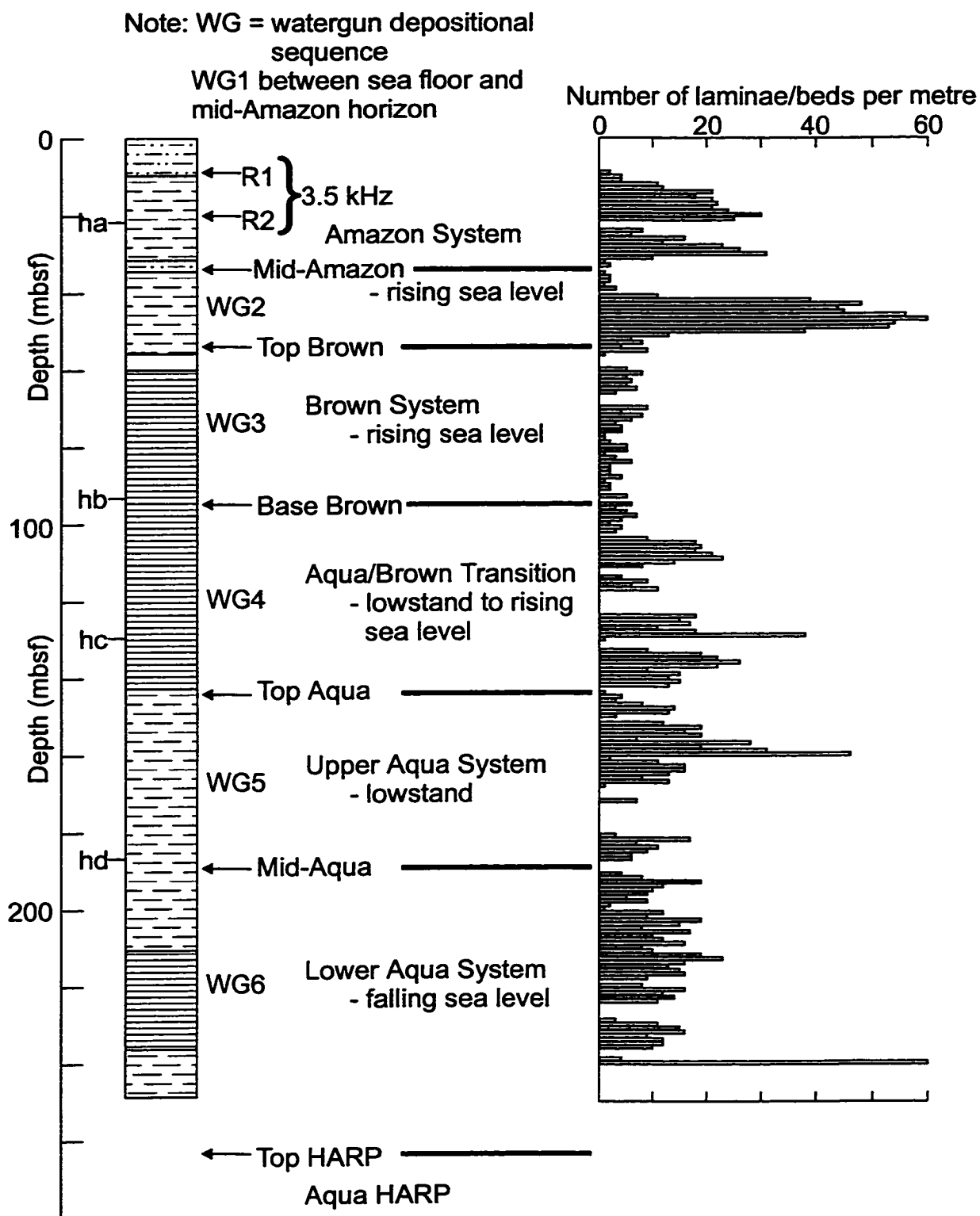


Figure 5.19. Complete borehole stratigraphy of Site 940 showing major seismic units defined in watergun and 3.5 kHz data. Relative sea level history adapted from Piper et al. (1997). Right side of figure shows histogram of number of laminae or beds per metre of section logged from shipboard core descriptions.

although lamina frequency appears to be focused into packets. Deposition characterizing the Brown system, WG3, shows a distinct decrease in lamina frequency. The most pervasively laminated sediment is WG2, associated with the initial development of the Amazon channel-levee system. Also shown on Figure 5.19 is the sub-bottom position of R1 and R2 identified in the 3.5 kHz data, as can be seen the difference between the two depositional sequences is the presence of silt laminae in DS2 (between R2 and R1) and the absence of silt laminae in DS1 (above R1). Overall, WG1, which encompasses DS1 and DS2, shows packages of laminated muddy silt turbidites interspersed with massive muddy silt turbidites.

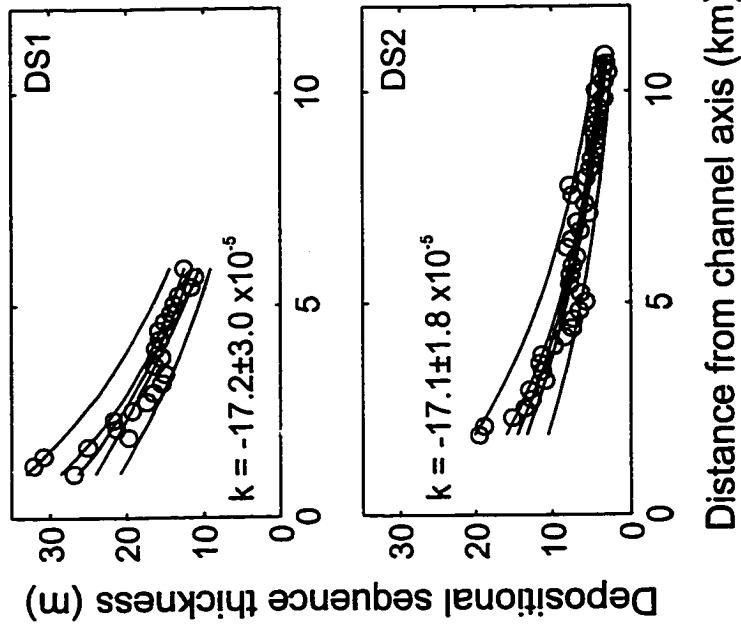
The levee crests that could be identified in the watergun profile show a progressive movement toward the modern channel axis. The movement appears most pronounced after the deposition of the top-Aqua reflector. The watergun profile across Amazon Channel also shows the apparent evolution of the channel fill. It should be recalled that the dimensions of the HARs only approximate channel-fill dimensions because of the complicating influence of hyperbolic reflections from the channel walls (Flood, 1987). With this caveat in mind, the channel fill appears to narrow through time. The narrowing of the fill does not progress smoothly. The channel appears widest overlying the Aqua HARP. It then narrows at a stratigraphic position equivalent to the eastern levee crest of the top-Aqua reflector. It then appears to have decreased gradually to the modern sea floor. Narrowing of the channel fill coincides with shifting of the levee crest toward the channel axis.

The thickness patterns observed in the high resolution data show that the observed thinning can be well-explained by the exponential model (Table 5.5, Figure 5.20a). The depositional sequences show no significant difference in the magnitude of the decay constant.

Table 5.5. Summary of regression parameters at Site 940 for depositional sequences identified in 3.5 kHz data. See Table 5.4 for explanation of symbols.

DS	$k \times 10^{-5}$ (m^{-1})	$\delta k \times 10^{-5}$ (m^{-1})	η_o (m)	$\delta\eta_o$ (m)	r	y_{lc} (km)	η_{lc} (m)
1	-17.2	3.0	31.4	3.6	0.93	1.2	25.5
2	-17.1	1.8	20.1	2.4	0.95	1.2	16.4

A. Amazon Fan: ODP Site 940



B. Amazon Fan: ODP Site 944

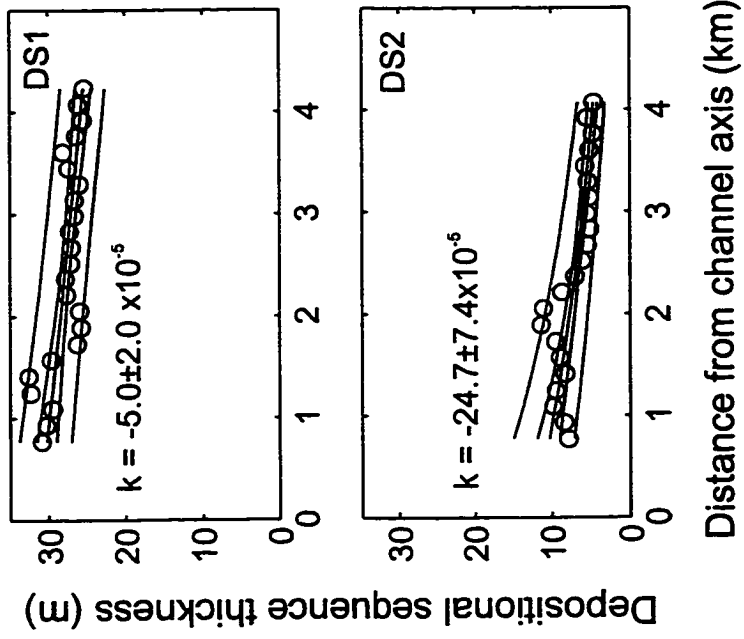


Figure 5.20. Thickness data from sites 940 and 944 for depositional sequences defined in 3.5 kHz profiles. For Site 940, regression data tabulated in Table 5.5; for Site 944, regression data tabulated in Table 5.7.

The thickness patterns as observed in the watergun data show more variability (Table 5.6, Figure 5.21). Four of the six depositional sequences – WG6, WG4, WG3, and WG2 – have decay constants within the range of $11\text{-}14 \times 10^{-5} \text{ m}^{-1}$. WG1 and WG5 stand out from the other sequences in having much lower decay constants. Both of these sequences show laminae occurring in packets, as does WG4. The higher resolution data also show that within WG1, the depositional sequences (DS1 and DS2) have higher decay constants than the decay constant calculated for WG1 as a whole.

Table 5.6. Summary of regression parameters at Site 940 for depositional sequences identified in watergun data. WG = watergun depositional sequence. See Table 5.4 for explanation of other symbols.

WG	$k \times 10^{-5}$ (m^{-1})	$\delta k \times 10^{-5}$ (m^{-1})	η_o (m)	$\delta \eta_o$ (m)	r	y_{lc} (km)	η_{lc} (m)
1	-2.4	0.6	37.3	1.6	0.78	1.0	36.4
2	-11.5	2.4	34.0	6.6	0.80	1.0	30.3
3	-13.4	1.4	70.4	7.0	0.94	1.4	58.4
4	-14.2	2.8	62.1	9.2	0.87	2.0	46.7
5	-5.5	0.8	58.3	3.6	0.90	2.1	51.9
6	-11.7	0.8	100.7	6.0	0.98	2.2	77.8

Site 944

A transect of three boreholes sampled the eastern levee of Amazon Channel at Site 944 (Figure 5.22). Hole 944B lies about 2 km from the modern channel axis, Hole 944A lies 250 m east of 944B and Hole 944D lies 350 m east of 944A. Two subbottom horizons, R1 and R2, could be identified and traced in the 3.5 kHz profile (Figure 5.16) and their sub-bottom depths projected into the boreholes (Figure 5.23). These reflectors form the bounding surfaces of two depositional sequences that show evidence of thinning away from the channel axis. About 4 km east of Amazon Channel lies the Brown Channel (Figure 5.16, Figure 5.22). The modern bathymetry and the subbottom reflectors rise slightly toward this feature. The depositional sequences do not, however, thicken toward the Brown channel and thus they do not appear to be levee sequences associated with flow down the Brown channel. The geometry here suggests that the depositional sequences drape the pre-existing topography created during activity of the Brown channel-levee system.

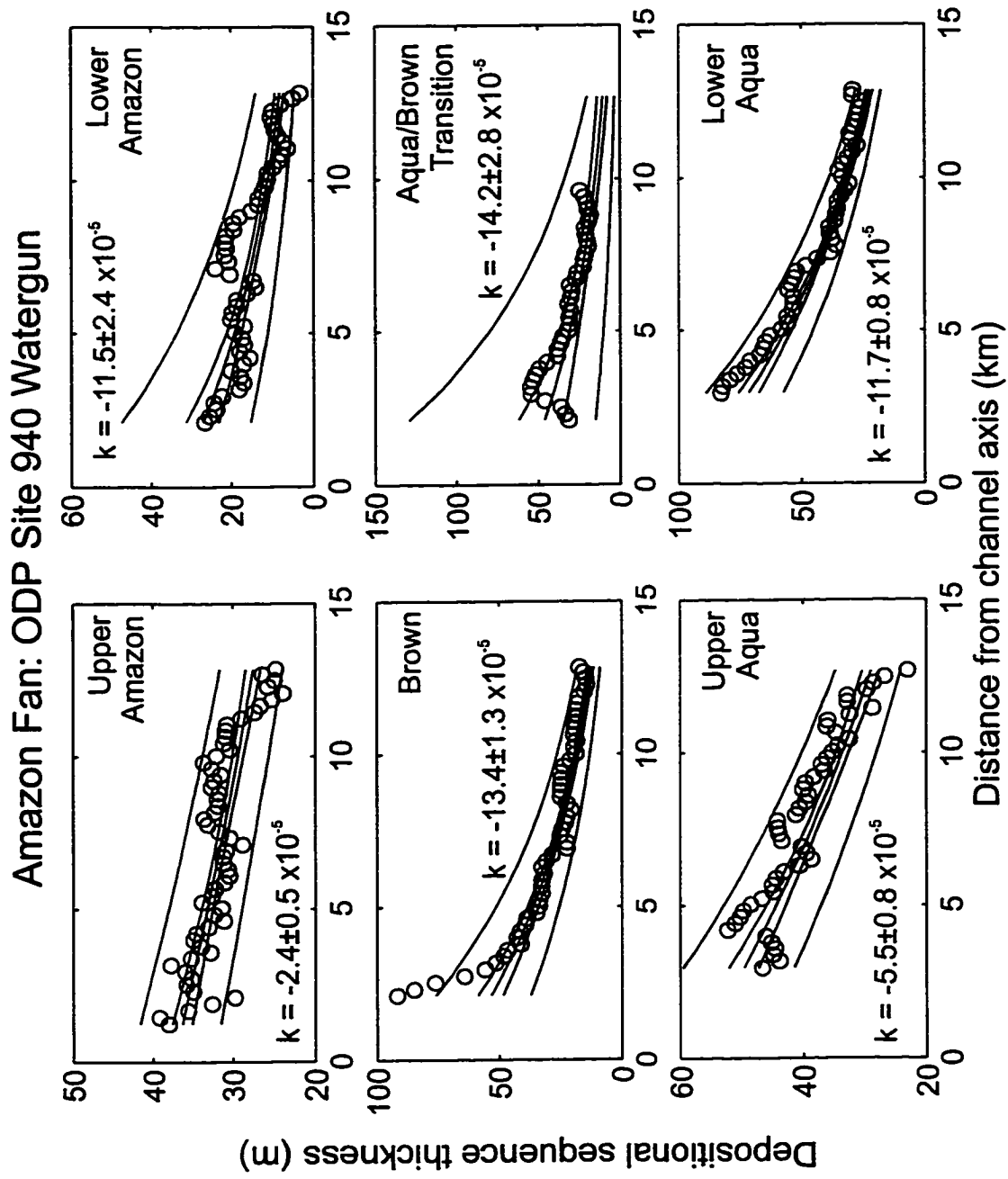


Figure 5.21. Thickness variations across eastern levee of Amazon Channel in vicinity of Site 940 for depositional sequences defined in watergun seismic profile. Regression data tabulated in Table 5.6.

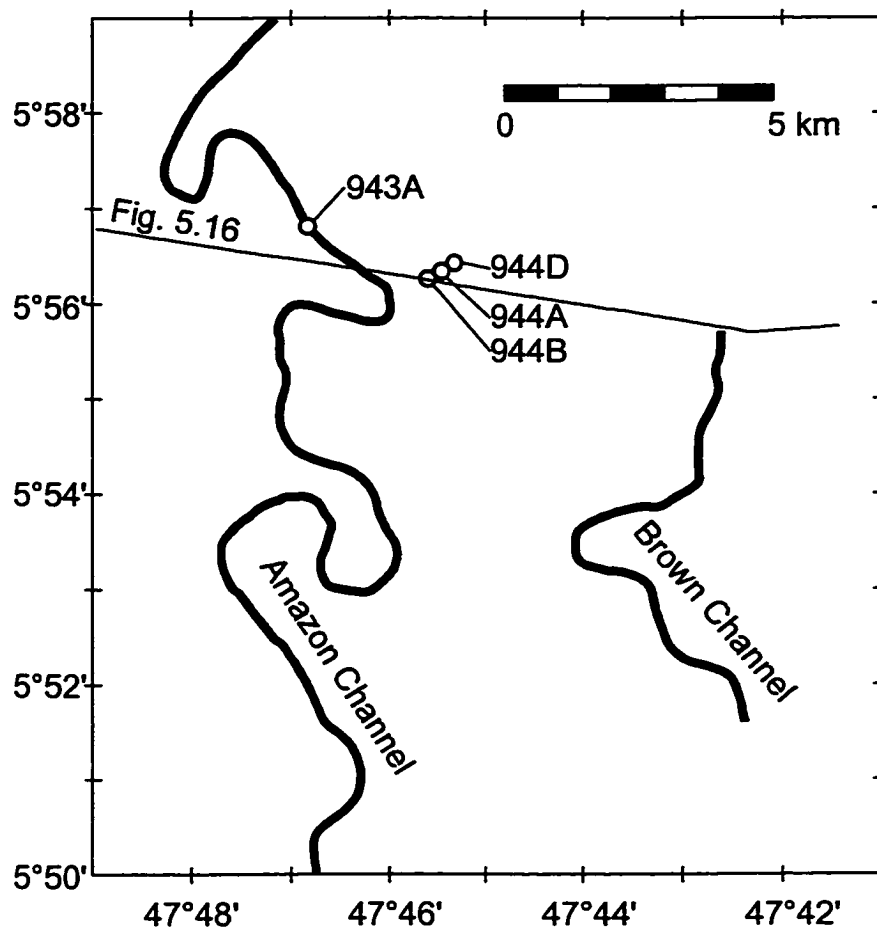


Figure 5.22. Channel trend in the vicinity of Site 944 showing location of boreholes and 3.5 kHz profile. Also shown is the trend of the Brown channel east of Amazon Channel.

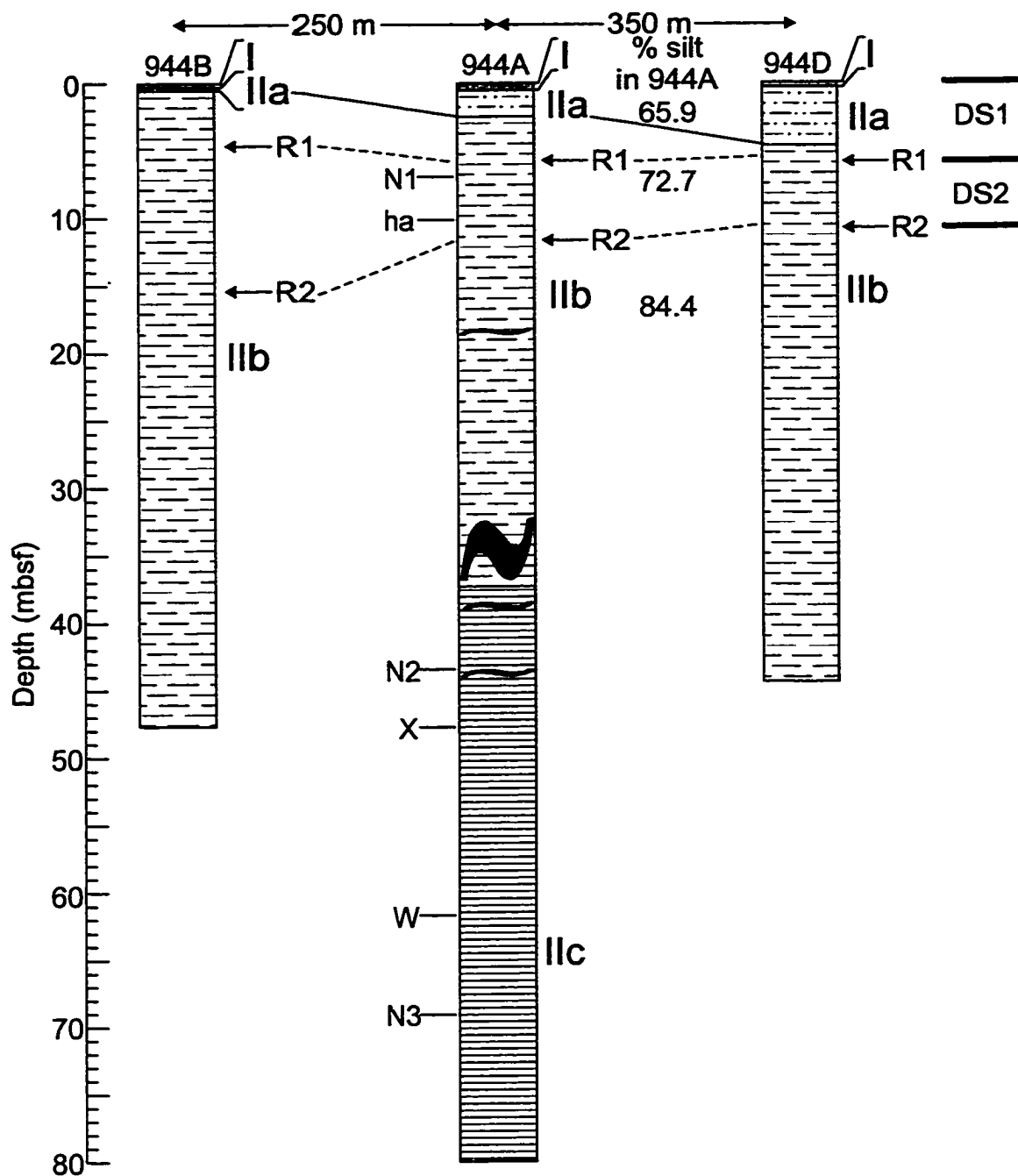


Figure 5.23. Borehole stratigraphy of upper 80 m of section at Site 944.

The modern levee crest occurs about 500 m from the channel axis and is about 60 m above the channel floor. Although difficult to trace into the channel-proximal sediments, R1 and R2 appear to form levee crests directly beneath the modern levee crest. The data show no small-scale relief in the modern bathymetry that would indicate previous locations of subsurface levee crests (Figure 5.16).

The investigation at Site 944 was restricted to the levee morphology as imaged by 3.5 kHz data and thus only the upper 80 m of section are presented (Figure 5.23). Unit I consists of hemipelagic sediment; Unit II consists of muddy silt. As at the other sites the boundary between IIa and IIb was placed at the first sub-bottom occurrence of an identifiable silt laminae. Unit IIb, in Hole 944A shows some contorted bedding interpreted as slumps, but these features occur below the depositional sequences defined in the 3.5 kHz data, i.e., below R2. Unit IIc consists of abundantly laminated muddy silt. R1 in Hole 944A occurs near horizon N1 and thus is approximately coeval with R1 as defined at Site 940 (Figure 5.18). R2 in Hole 944A occurs just below horizon ha and correlates approximately with R2 at Site 940 (Figure 5.18). Across the levee, DS1, above R1, changes in character. At Hole 944B, DS1 consists primarily of laminated muddy silt turbidites (Unit IIb) capped by a thin layer of massive muddy silt turbidites (Unit IIa). At Hole 944A, DS1 can be divided into two layers of approximately equal thickness: a basal layer made up of laminated muddy silt turbidites and an upper layer of massive muddy silt turbidites. At Hole 944D, DS1 consists predominantly of massive muddy silt turbidites underlain by a thin layer of laminated muddy silt turbidites. DS2, on the other hand, consists entirely of laminated muddy silt turbidites (Unit IIb).

The variations in the thickness of the two depositional sequences at site 944 show apparently similar patterns, but very different regression parameters (Table 5.7, Figure 5.20b). The difference between the two depositional sequences lies in their absolute thickness. For DS1, the depositional sequence thins from around 30 m to about 22 m over a distance of about 3 km. DS2 thins from about 10 m to about 2 m over the same distance. They thin by the same absolute amount but in a relative sense, DS1 is much more uniform in thickness than DS2. It is this difference that shows up in the decay constants, with k for DS2 being about five times greater than k for DS1. The more uniform character of DS1 coincides with the lateral change in character of the

depositional sequence from laminated muddy silt turbidites to massive muddy silt turbidites.

Table 5.7. Summary of regression parameters at Site 944 for depositional sequences identified in 3.5 kHz data. See Table 5.4 for explanation of symbols.

DS	$k \times 10^{-5}$ (m^{-1})	$\delta k \times 10^{-5}$ (m^{-1})	η_o (m)	$\delta\eta_o$ (m)	r	y_{lc} (km)	η_{lc} (m)
1	-5.0	2.0	31.4	1.8	0.73	0.8	30.2
2	-24.7	7.4	12.4	2.4	0.83	0.8	10.2

Grain Size Data

Overall, the levees of Amazon Fan consist of sediments whose grain size distributions show two general patterns, depending on average grain size. Piper & Deptuck (1997) focused their attention on muddy turbidites from Amazon Fan and most of these sediments display a relatively uniform, or linear, distribution across size classes up to around 10 μm when plotted on log-log graphs (Figure 5.24) similar to grain size distributions from turbidites reported by Kranck (1984). Above 10 μm , the grain size distribution tails off dramatically, following a quadratic form. Slight differences between samples can be observed in the slope of grain size distribution below 10 μm , but in general they all possess the same form. Some of the samples reported by Hiscott et al. (1997) also show this pattern (Figure 5.25). Most of the turbidites sampled by Hiscott et al. (1997) and some of the silt laminae sampled by Piper & Deptuck (1997) show a slightly different distribution. In these sediments the silt fraction forms a prominent mode in the distribution that lies between 20-30 μm (right side of Figure 5.24 and Figure 5.25), also observed by Kranck (1984).

5.3.3 Synthesis of Levee Architecture on Amazon Fan

The borehole data from Amazon Fan constrain the character of the depositional sequences described by the regression parameters at two different scales of observation: high resolution 3.5 kHz and low resolution watergun data. Generally, the thickness patterns isolated in the 3.5 kHz data have decay constants greater $17 \times 10^{-5} m^{-1}$, lacking any suggestion of spatial or stratigraphic trends. Total aggradation of the levee crest above the base of the upper levee complex shows a downchannel decay (Figure 5.7).

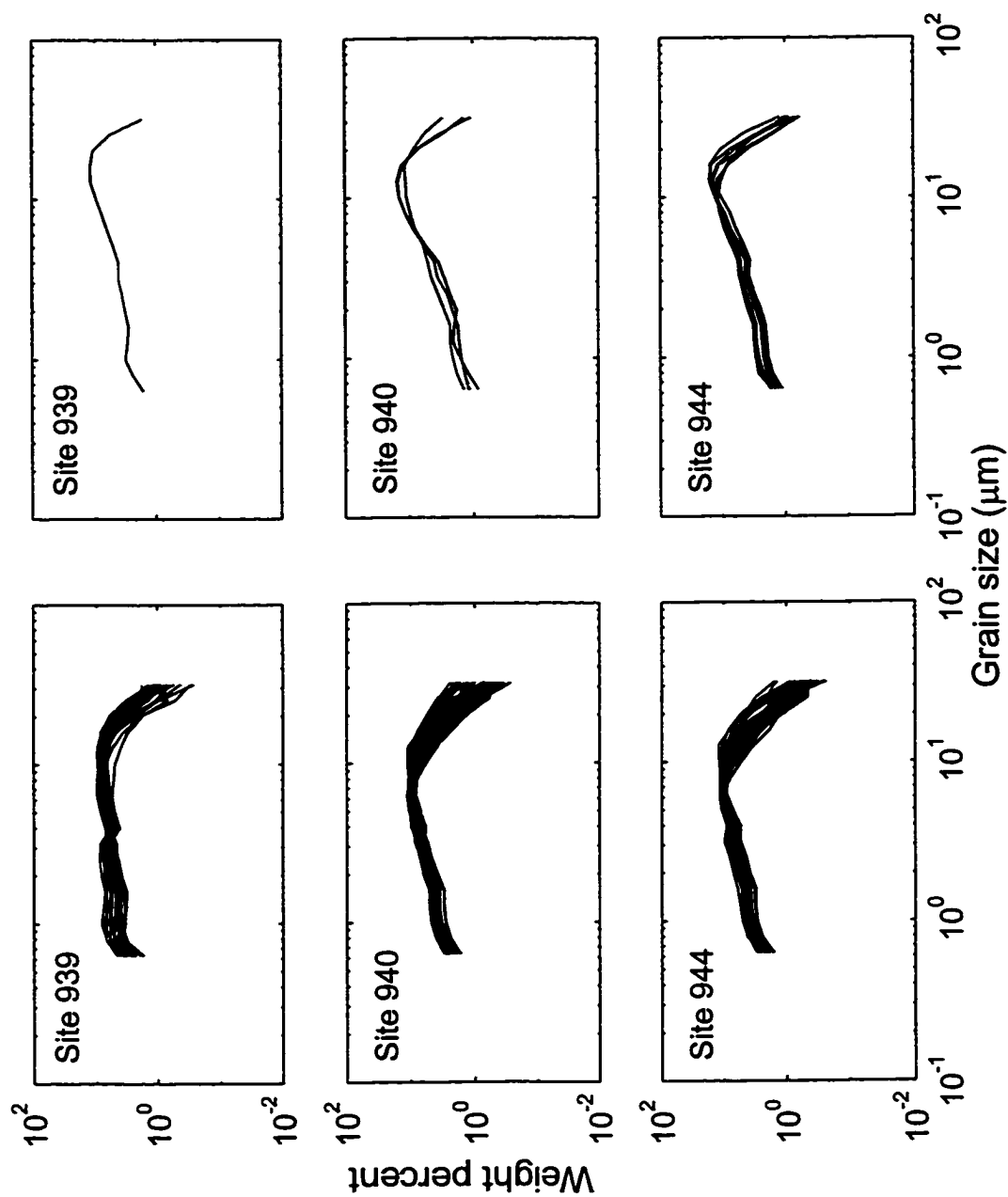


Figure 5.24. Grain size data for sites 939, 940 and 944 taken from Piper & Deptuck (1997). Left-hand column of plots shows samples that have relatively uniform distributions of fine silt and clay with small amounts of medium silt to fine sand. Right-hand column of plots shows samples that have a strong mode in the silt fraction.

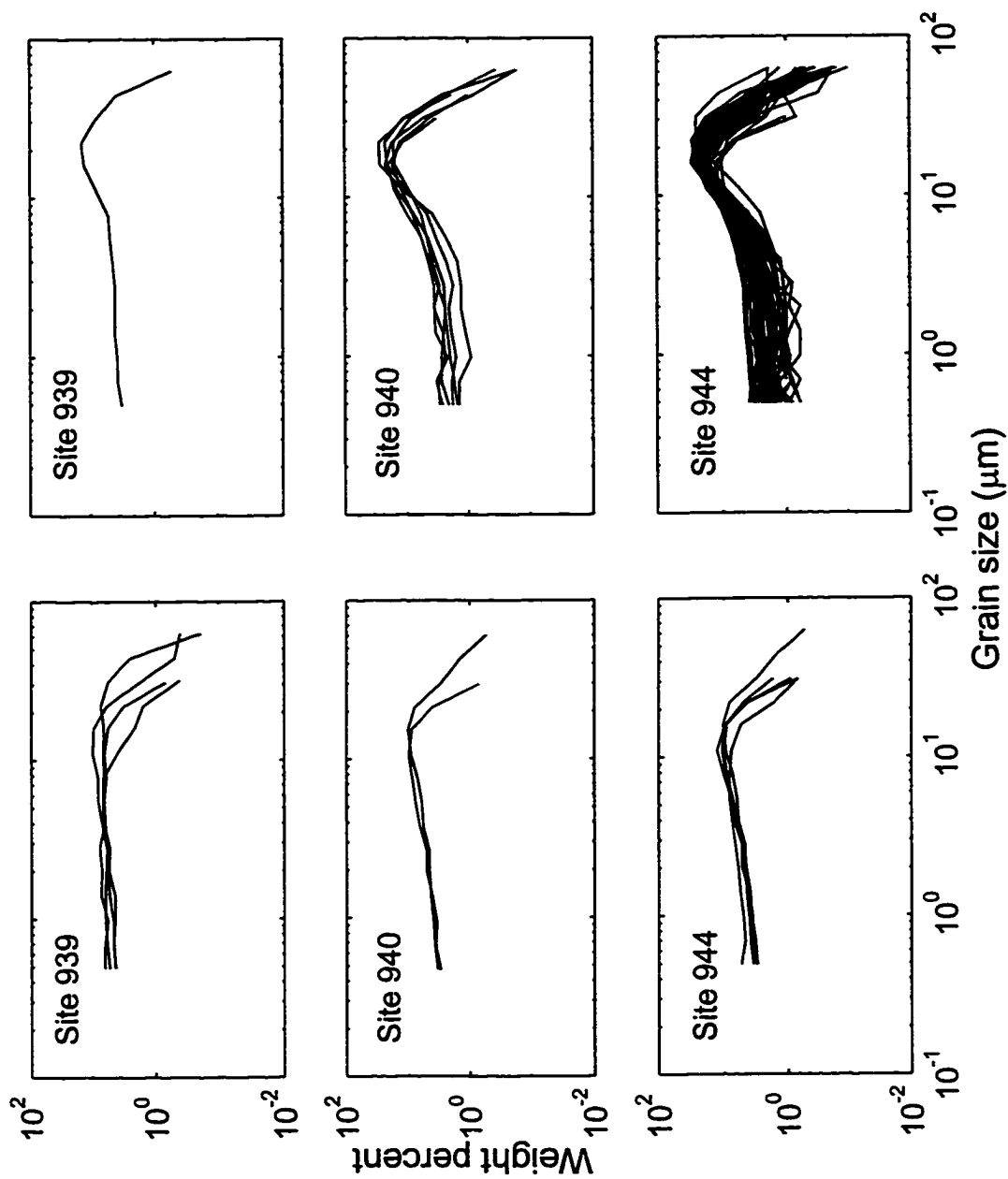


Figure 5.25. Grain size data for sites 939, 940 and 944 taken from Hiscott et al. (1997). Left-hand column of plots shows samples that have relatively uniform distributions of fine silt and clay with small amounts of medium silt to fine sand. Right-hand column of plots shows examples of samples that have a strong mode in silt fraction.

This may in part reflect downchannel thinning of sediment at the levee crest. However, it also reflects the avulsion history of Amazon Channel, i.e., more distal channel segments have been active for less time than more proximal channel segments. As such these data should be regarded as only a guide to the downchannel variation in individual depositional sequence thickness.

The lack of a significant downchannel trend in the decay constants coincides with the approach to relatively uniform values for the cross-channel slope (Figure 5.26). Because of the equatorial position of Amazon Fan, Coriolis force plays a small role in the development of across-channel asymmetry compared with channel curvature. Using the model of Komar (1969) and assuming that channel depth is a reasonable estimate of flow thickness, the approach to uniform values of cross-channel slope suggests spatially-uniform values of the Froude number and consequently spatially uniform flow conditions.

For two depositional sequences the decay constant drops below $10 \times 10^{-5} \text{ m}^{-1}$: DS3 at Site 939 and DS1 at Site 944. In both of these depositional sequences, the boreholes show that the depositional sequences encompass more than one lithostratigraphic unit. At Site 939, Hole 939A shows that DS3 possesses about equal amounts of units IIa (massive muddy silt turbidites) and IIb (laminated muddy silt turbidites) while 480 m east at hole 939B, DS3 consists primarily of Unit IIa. A similar transition is seen in more detail at Site 944. At Hole 944B, DS1 consists predominantly of Unit IIb. At Hole 944A, DS1 consists equally of units IIa and IIb while at Hole 944D, Unit IIa makes up most of DS1. These observations suggest that the effect of having depositional sequences composed of heterogeneous lithologies acts to reduce the thinning. This is not to say, however, that a particular lithology shows a distinct spatial decay constant. At Site 940, DS1 consists exclusively of Unit IIa while DS2 consists exclusively of Unit IIb, yet no difference in the thinning of these depositional sequence can be detected. The same is true of the depositional sequences isolated at Site 939. Only DS3 has a decay constant that is significantly different and this depositional sequence consists of both Unit IIa and IIb.

The stratigraphic evolution of the levee at Site 940 since its inception above the Aqua HARP shows that the occurrence of silt laminae and the lithologic character of the depositional sequences is variable. The decay constants for four of the six depositional

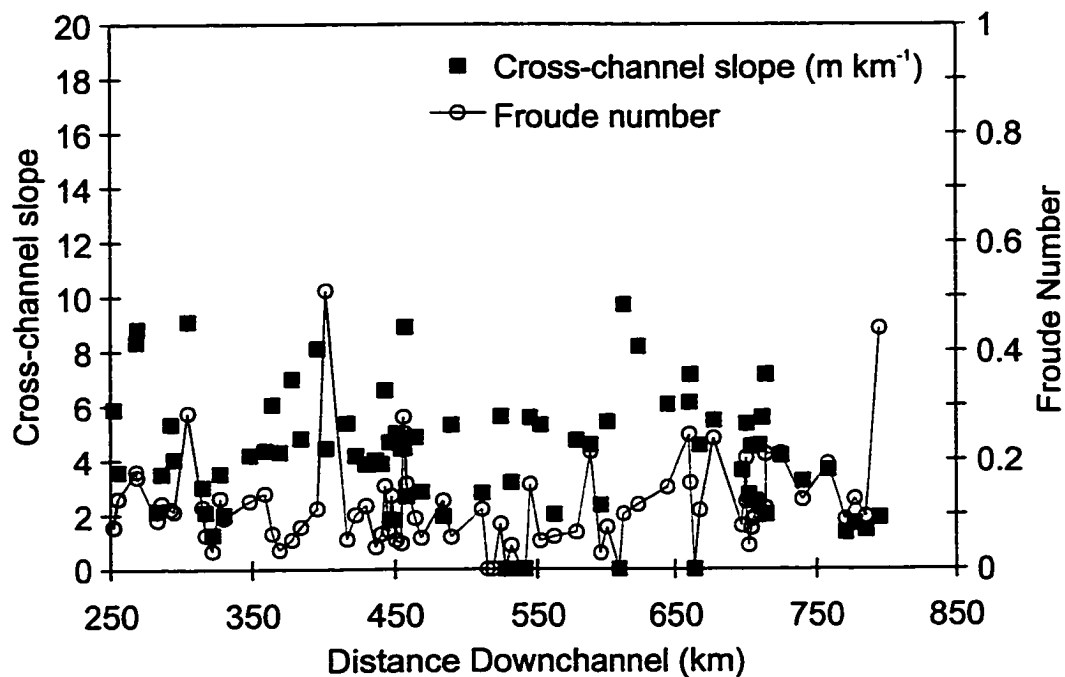


Figure 5.26. Downchannel variation in cross-channel slope of Amazon Channel and Froude number calculated from Komar's (1969) model assuming that flow thickness equals channel depth. Data taken from Pirmez (1994). Note that although the data is variable, all Froude numbers imply subcritical flow.

sequences (WG2-WG4, WG6) fall into a narrow range between $11\text{-}14 \times 10^{-5} \text{ m}^{-1}$. WG2 has the highest frequency of silt laminae, while WG3 possesses the overall lowest frequency of silt laminae. WG3 and WG6 display a uniform distribution of laminae while the silt laminae in WG4 occur in discrete packets. WG5 has a decay constant ($5.5 \times 10^{-5} \text{ m}^{-1}$) that is about half that of the other depositional sequences, but it, like WG4, has silt laminae that occur in packets. WG1 encompasses the depositional sequences defined in the 3.5 kHz data. It shows two major silt packets, one of which is bounded between R1 and R2 (i.e., DS2 in the 3.5 kHz data). It may be that the difference between the decay constants in the 3.5 kHz data and the decay constant for WG1 again reflects the mixture of different lithologies.

According to the chronostratigraphy proposed by Piper et al. (1997), only WG5 corresponds to deposition during a sea-level lowstand. The underlying depositional sequence, WG6, was deposited during a sea-level fall while the overlying depositional sequences, WG1-WG4, were deposited during rising sea-level. The levee architecture, as parameterized by the decay constant appears to show little relation with sea-level. The decay constant does show a local minimum at the lowstand, but it may also show a minimum in WG1 during the Holocene transgression.

The long term evolution of the levee at Site 940 shows two phases of growth. The first phase is characterized by a wide channel with aggradational eastern levees. This phase occurs up to deposition of top-Aqua. After top-Aqua, the width of the channel fill gradually decreases and the levee crests moved toward the channel axis. Both of these phases have basal depositional sequences with decay constants greater than $10 \times 10^{-5} \text{ m}^{-1}$ capped by much more uniform depositional sequences. Across-channel correlation of the reflectors shows that evidence for a levee morphology on the western levee characterizes the succession above top-Aqua. The base-Brown and top-Brown reflectors display levee crests and these levee crests moved toward the channel. These crests are higher on the western levee than the eastern levee, the same as for the modern levee crest.

The grain size data from the levees of Amazon Fan, at least for sites 930, 940 and 944, show two discrete distributions: one dominated by single-grain settling and the other dominated by floc settling. A uniform distribution across size classes in the bottom sediments suggests that the material in suspension was incorporated into flocs (e.g.,

Kranck, 1984; Schell, 1996). On the other hand, single grain settling produces a relatively well-sorted distribution dominated by a single grain size (e.g., Kranck, 1984). In those samples dominated by single-grain settling the modal silt size varies over a narrow range between 15-20 μm , subtly decreasing downfan (Figure 5.25). In those samples dominated by floc settling, the break between the linear and quadratic parts of the distributions varies also varies over a narrow range of between 7-10 μm ; again this break point appears to decrease slightly downfan (Figure 5.24). The slope of the linear portion of these distributions also shows a subtle downfan evolution, increasing between sites 939 and 944.

5.3.4 Key Features

1. ODP boreholes from Amazon Fan provide groundtruthing of depositional sequences defined in acoustic data that is not available from other systems, allowing the relationship between the sedimentology of levees and large-scale morphology of levees to be investigated. In addition, Amazon Fan has a long, meandering channel with channel dimensions, width and relief, roughly similar to Hueneme Fan which has a short, straight channel.
2. Depositional sequences identified in 3.5 kHz data have across-levee thickness patterns that could be described reasonably well by the exponential model with the majority of the depositional sequences having decay constants between $17 \times 10^{-5} \text{ m}^{-1}$ and $29 \times 10^{-5} \text{ m}^{-1}$. Indirect data, topographic aggradation, on downchannel variations in sediment thickness at the levee crest also suggest downchannel thinning.
3. The boreholes constrain the lithologies of these depositional sequences and show that when they consist of a single lithologic unit, either massive muddy silt turbidites (Unit IIa) or laminated muddy turbidites (Unit IIb), no major difference in the values of k can be detected.
4. Two depositional sequences identified in 3.5 kHz data have decay constants between $5-8 \times 10^{-5} \text{ m}^{-1}$. These depositional sequences consist of mixtures of lithologic unit IIa, massive muddy silt turbidites, and unit IIb, laminated muddy silt turbidites. Given that the reflectors defining the boundaries of depositional sequences represent isochronous horizons, these two depositional sequences possess significant lateral

changes in lithology that may be acting to produce more uniform depositional sequences, i.e., lower values of the spatial decay constant, k .

5. Correlation of the silt packet at Site 939 suggests that while correlation at the metre scale can be successfully demonstrated, correlations at the event level suffer, perhaps due to strong lateral facies gradients. Within the silt packet in hole 939A, six silt beds occur while in hole 939B only one silt bed is found. The tentative correlation of the silt beds in hole 939A with silt laminae in hole 939B suggests that the depositional lengthscale across the levee for bedded silt must be less than 480 m at this location.
6. The long term evolution of the channel-levee system at site 940 shows that overall the levee has grown in two phases. The first phase was characterized by a wide channel with an aggradational eastern levee. The western levee displays a complex pattern of internal reflections not immediately recognizable as a levee feature. The second phase of levee evolution saw the gradual channelward movement of the levee crests on both the western and eastern levees. Width of the channel fill also decreased.
7. No direct sedimentological control of the thickness patterns is suggested. Grain size spectra show only minor changes downfan. In addition, links between lamina abundance and thickness patterns are not apparent. Thickness patterns do not relate simply to sea level fluctuations or to the morphological evolution of the levee.

5.4 Var Fan

Var Fan lies off Nice, France in the Ligurian Sea, western Mediterranean Sea (Figure 5.27). It occurs seaward of the Var delta and extends to the continental slope off Corsica, covering an area of 16 200 km². The fan has been the subject of several studies most recently by Savoye et al. (1993) and Piper & Savoye (1993). The growth of Var Fan revealed by airgun seismic reflection data was investigated by Savoye et al. (1993). The data available from Var Fan consist of six airgun seismic profiles that obliquely cross the middle fan valley (Figure 5.28). These lines form a subset of the data used by Savoye et al. (1993).

5.4.1 General Setting

The continental shelf off Nice is narrow (0-3 km) and the continental slope is

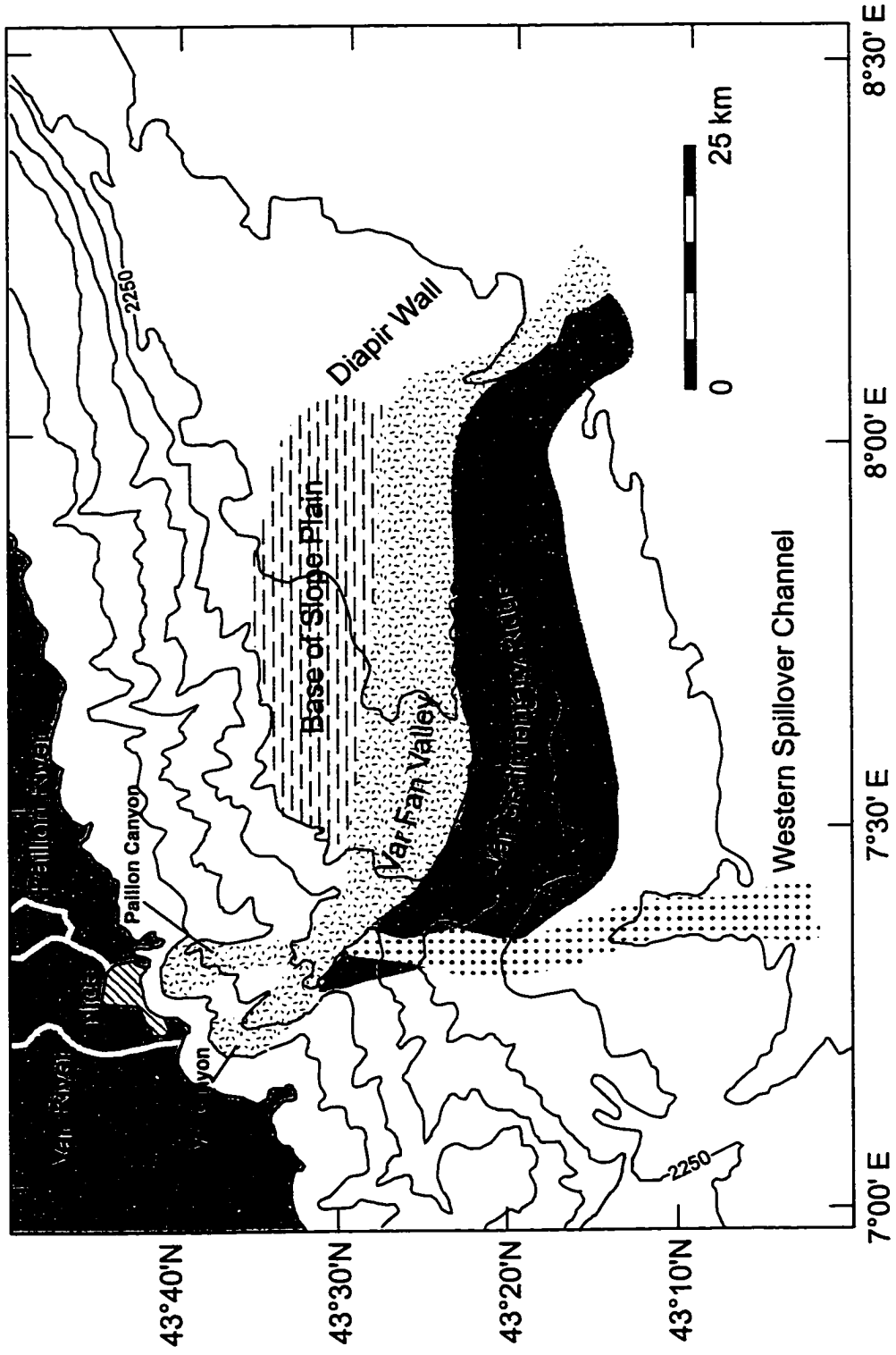


Figure 5.27. Location of Var Fan showing major geomorphological zones referred to in text.

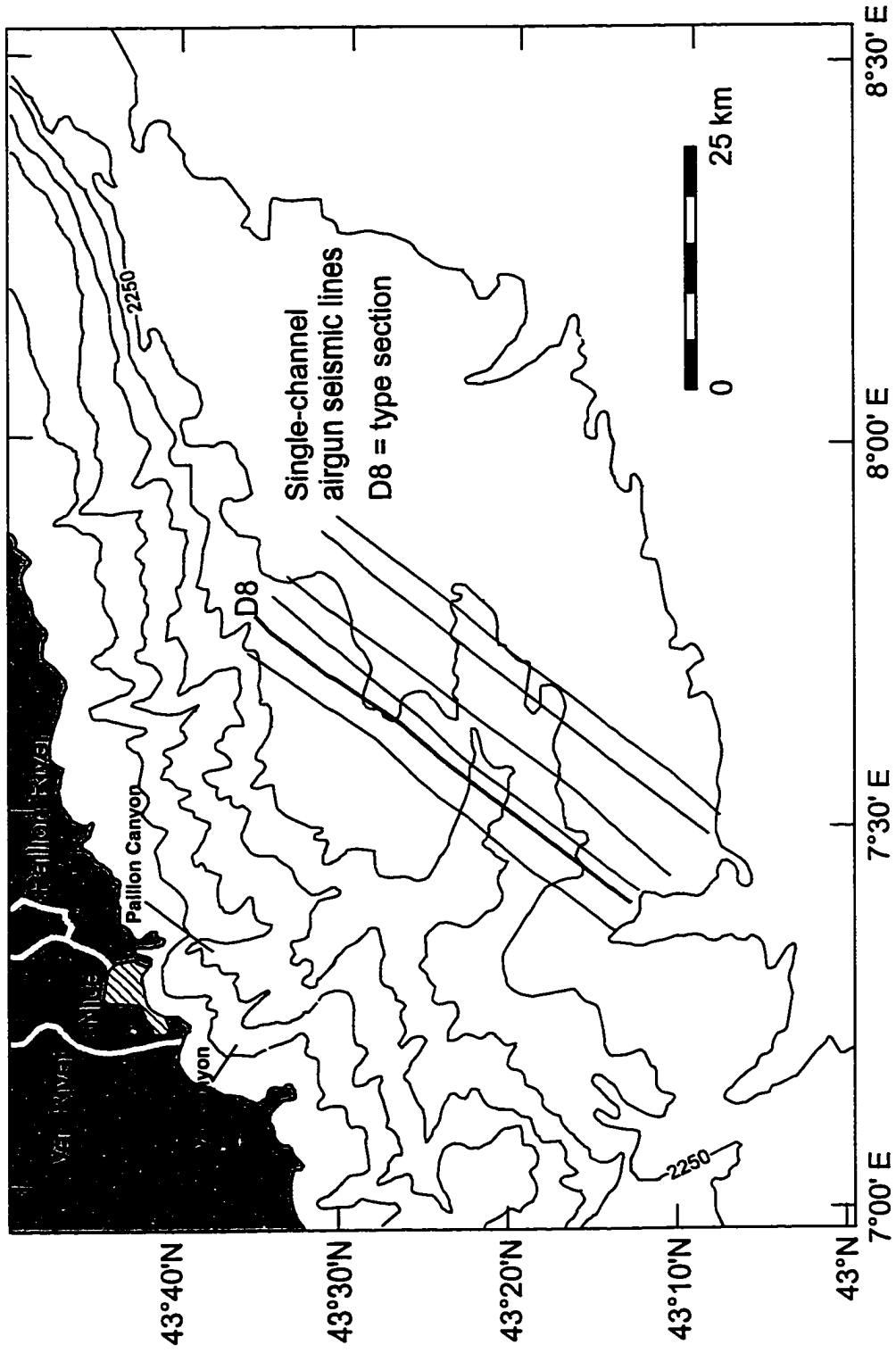


Figure 5.28. Seismic lines available for study of Var Fan.

steep ($< 200 \text{ m km}^{-1}$). The upper fan valley trends south of Var Canyon and is approximately 5 km wide and 600 m deep at the base of the slope (Piper & Savoye, 1993). The middle fan valley runs east-west, bounded to the south by the Var Sedimentary Ridge (VSR) with up to 300 m of relief (Figure 5.27, Figure 5.29). No significant levee exists north of the valley where sediments tend to onlap the base of the continental slope. Together, the canyon and fan valley are 130 km long. The water depth of the channel displays a concave-upward profile with channel gradients decreasing from 80 m km^{-1} in the canyon to about 10 m km^{-1} in the middle fan valley (Figure 5.29).

Savoye et al. (1993) reconstructed the paleogeographic evolution of the Var Fan, concluding that channel patterns controlled its growth. These workers mapped the regional occurrence of four reflectors (I-IV) that they tentatively dated as mid-Pliocene (reflector I), late Pliocene (reflector II), base Quaternary (reflector III), and mid-Quaternary (reflector IV) (Savoye et al., 1993, their Figure 14). Development of the channel-levee system began after deposition of reflector II. At reflector III, large sediment waves developed on the VSR. Channels on Var Fan, associated with fan development, first trended due south of Var Canyon. After deposition of reflector III, the VSR developed and the main fan valley trended west. Savoye et al. (1993) also correlated fan development with events affecting the Var delta. The most important of these is the rapid uplift of more than 300 m inferred from raised delta deposits and correlated with the stratigraphic interval between reflectors III and IV. The presence of the stage 5 highstand deposits at +8 m, near the level of stage 5 elsewhere in the world (e.g., Gallup et al., 1994; Carew & Mylroie, 1995), suggests that the rate of uplift decreased substantially in the late Quaternary. The general style of levee growth on the VSR was progradational. Evidence presented by Savoye et al. (1993) suggests that the VSR has prograded downfan since deposition of reflector IV, if not since deposition of reflector II. This evidence included the general increase in inter-reflector spacing in channel-parallel seismic lines. They suggested that rapid levee progradation resulted from flow expansion and overbank deposition where the levee was no longer high enough to contain average through-channel flows.

In 1979, land-filling operations at the Nice Airport led to slope failure. The failure generated a turbidity current that broke two submarine telecommunication cables.

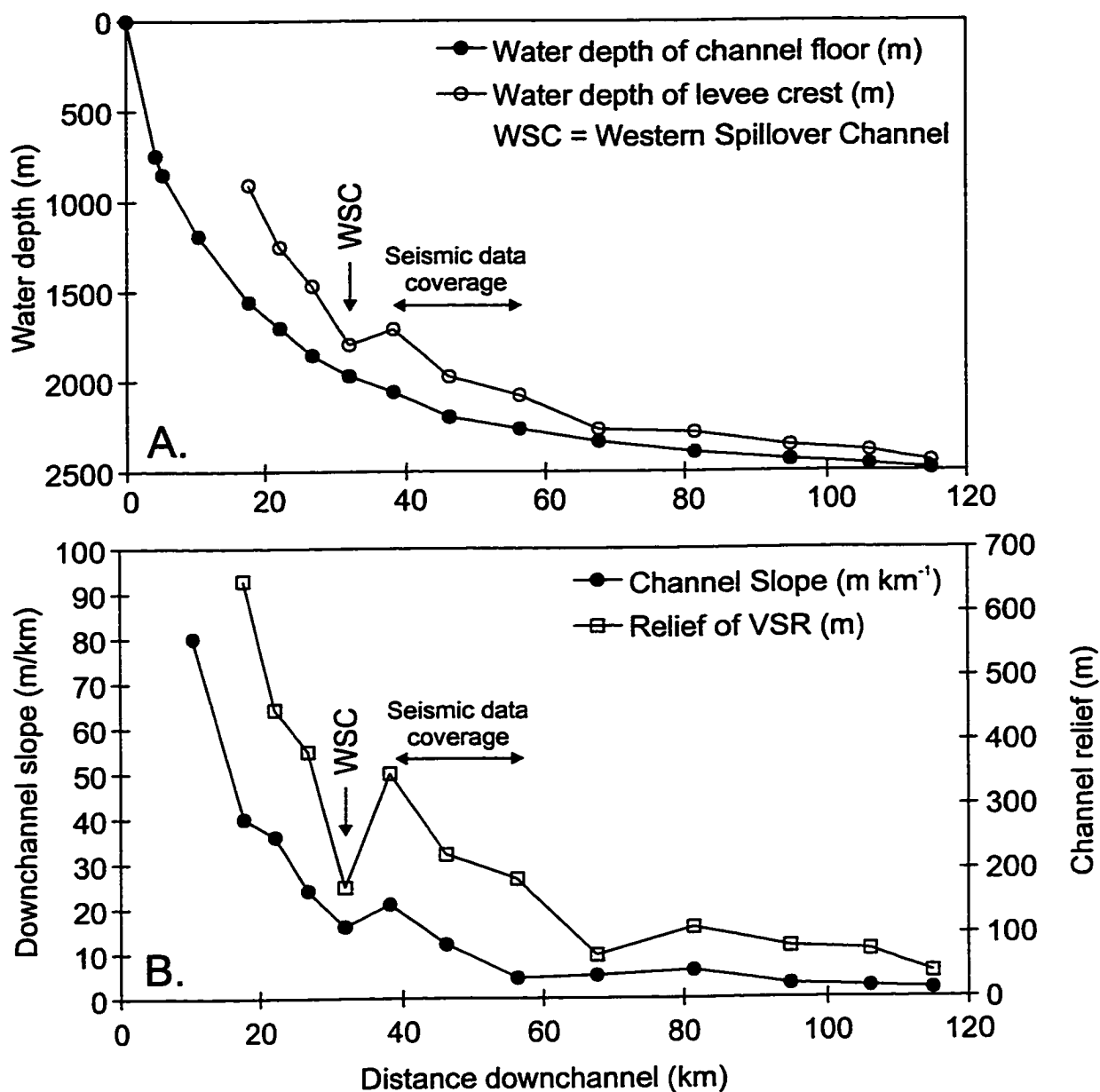


Figure 5.29. Morphology of Var fan valley (data taken from Piper & Savoye, 1993): A. longitudinal profile of water depth of the channel axis and levee crest; B. downchannel variation in channel slope and relief between channel floor and Var Sedimentary Ridge. Also shown is the approximate extent of seismic data coverage of the fan system. Note the abrupt decrease in relief of the Var Sedimentary Ridge associated with the head of the Western Spillover Channel.

The location and time elapsed between cable breaks, submersible observations of the failure and flow path, and detailed bathymetric and seismic surveys of the fan allowed Piper & Savoye (1993) to reconstruct the flow of this turbidity current and to compare its deposits with those sampled by piston cores, thereby constraining the nature of late Pleistocene turbidity currents on Var Fan. Piper & Savoye (1993) provided evidence for up to five different types of flow active in the late Quaternary evolution of Var Fan. Sandy flows like the 1979 event had only limited spillover onto the VSR and were characterized mostly by channel erosion and sand and mud deposition on the abyssal plain. Holocene flows carrying both sand and mud flowed down the Western Spillover Channel (Figure 5.27) and overbanked the eastern VSR depositing mud on the VSR and sand and mud in the channel and on the abyssal plain. Sandy, erosive, Late Pleistocene flows overbanked along almost the entire VSR, eroding the channel and VSR and depositing sand and mud on the abyssal plain. Bankfull late Pleistocene flows displayed limited spillover on the western VSR and covered the eastern VSR. These flows deposited thin sands and mud on the eastern VSR and sand and mud on the abyssal plain. Finally, thick muddy late Pleistocene flows covered the entire VSR and were responsible for sediment wave deposition. These flows deposited only limited sand and mud in the channel and mud on the VSR and abyssal plain.

By applying the cross-channel slope model of Komar (1969), Piper & Savoye (1993) estimated that the average through-channel velocity of the flows responsible for the deposition of the VSR was about 0.35 m s^{-1} . Using the length of sediment waves and the antidune model of Normark et al. (1980), the overbanking flows were estimated to have thickness of several hundred metres on the VSR. This estimate along with the channel relief suggested that through-channel flow thickness was greater than 500 m. This information incorporated into the Chezy equation of turbidity current flow with F_i estimated between 1-2, produced estimates of volume concentration on the order of 10^{-4} . Using McCave & Swift's (1976) equation for fine-sediment deposition and bed thicknesses of tens of centimetres on the VSR, flow durations were calculated to be on the order of a few days to weeks. Thus, the flows responsible for construction of the VSR were thick, slow-moving, and of long duration according to Piper & Savoye (1993). They further suggested that these flows were the result of hyperpycnal inflow of cold,

sediment-laden water from the braided Var River which acted as a proglacial, meltwater stream during the Pleistocene glaciation of the Alpes Maritimes.

5.4.2 Levee Architecture

Levee Stratigraphy

Line D8 crosses the middle fan valley and VSR and was used as a type section. In line D8, six sub-bottom horizons could be identified, termed R1 through R6 (Figure 5.30). These reflectors formed the bounding surfaces of six depositional sequences, D1-D6 (Figure 5.30). R6, R4, and R3 are equivalent to regional reflectors II, III, and IV, respectively of Savoye et al. (1993). Above R4, the VSR consists of continuous, moderately acoustically stratified sediments. Below R4, the sediments have weak acoustic stratification and moderate continuity. Also below R4, is a package of short discontinuous reflections. This acoustic character is very similar to the present channel fill and it likely represents a previous location of the fan valley (termed C6 by Savoye et al., 1993). R1 could be correlated to lines D7 and D9-D13; thus the character of the depositional sequence between the sea floor and R1 could be mapped along the channel (Figure 5.31). A fault cuts through the levee flank, offsetting reflectors by as much as 50 m. However, thinning of the depositional sequences continues uninterrupted except within 1 km of the fault; thicknesses of the depositional sequences are not substantially affected by this feature.

According to the paleogeographic reconstruction of Savoye et al. (1993), at the time of R6 a leveed fan valley ran directly south of Var Canyon. During deposition of DS5, between R5 and R4, the leveed fan valley established its modern morphology, trending east-west. In line D8, R5, R4 and R3 rise to form a levee crest adjacent to the package of discontinuous, high amplitude reflections indicative of channel fill that lies stratigraphically above R6. The geometry of the weakly stratified sediments and their proximity to inferred channel fill suggests that this feature represents the former location of a fan valley. Relief between the levee crest at R3 and the top of the channel fill is about 40 m. The total thickness of this channel fill is approximately 120 m. Almost immediately after deposition of R3, the sediments have continuous reflections above the

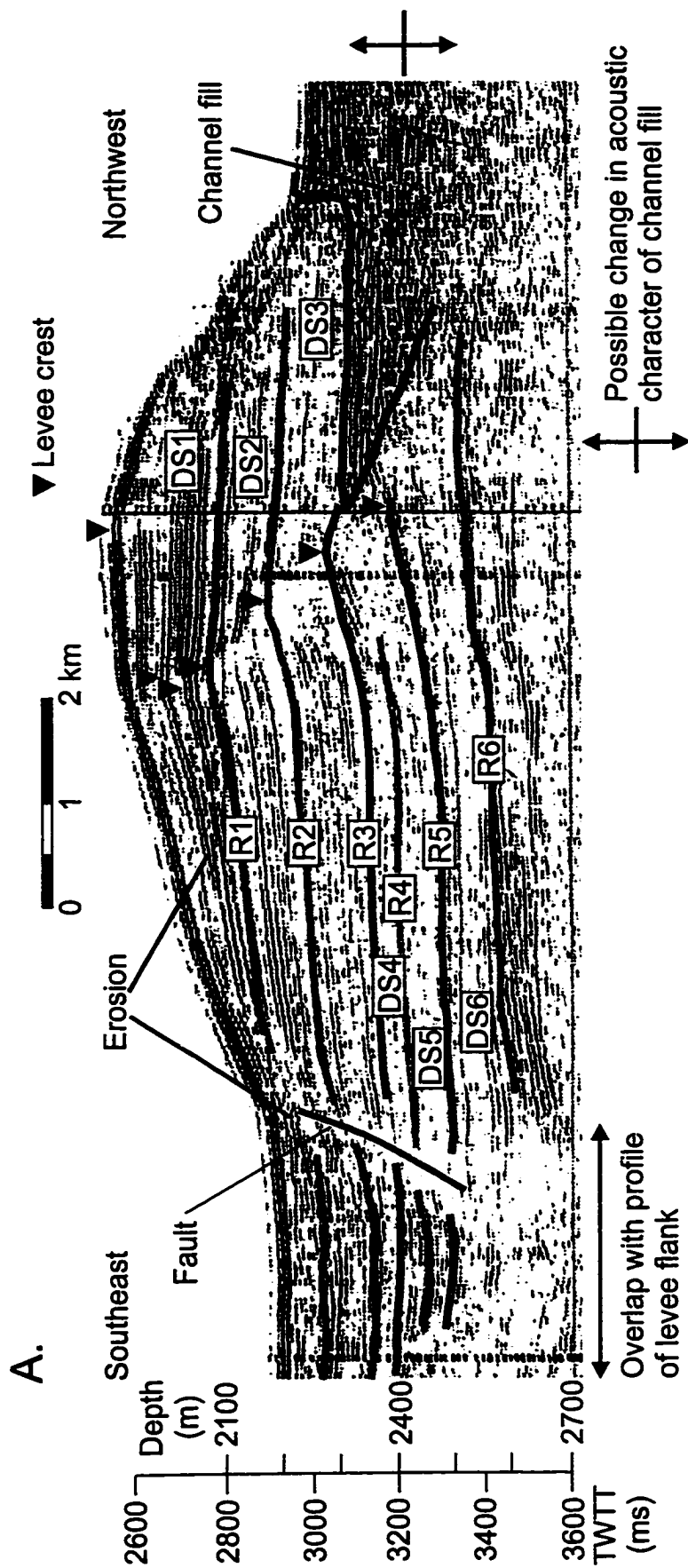


Figure 5.30. Airgun seismic profile, D8 showing acoustic stratigraphy developed for Var Fan: A. profile over levee crest; B. extension of profile over levee flank. See text for discussion of labeled features. Location given in Figure 5.28.

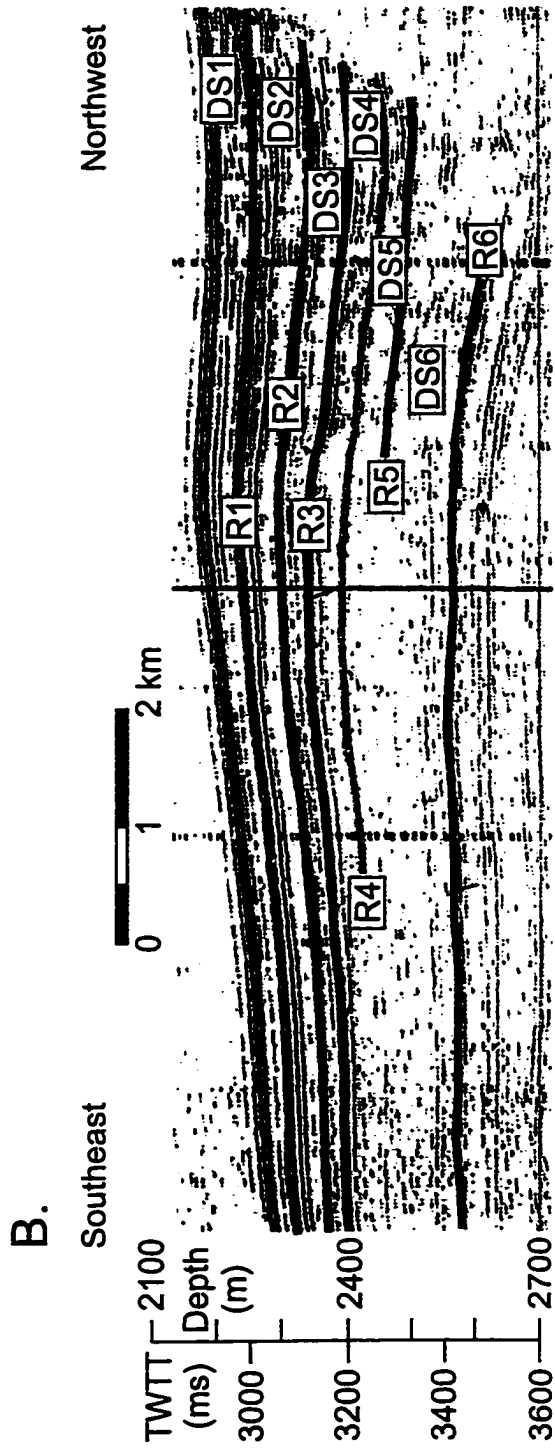


Figure 5.30. *Continued.*

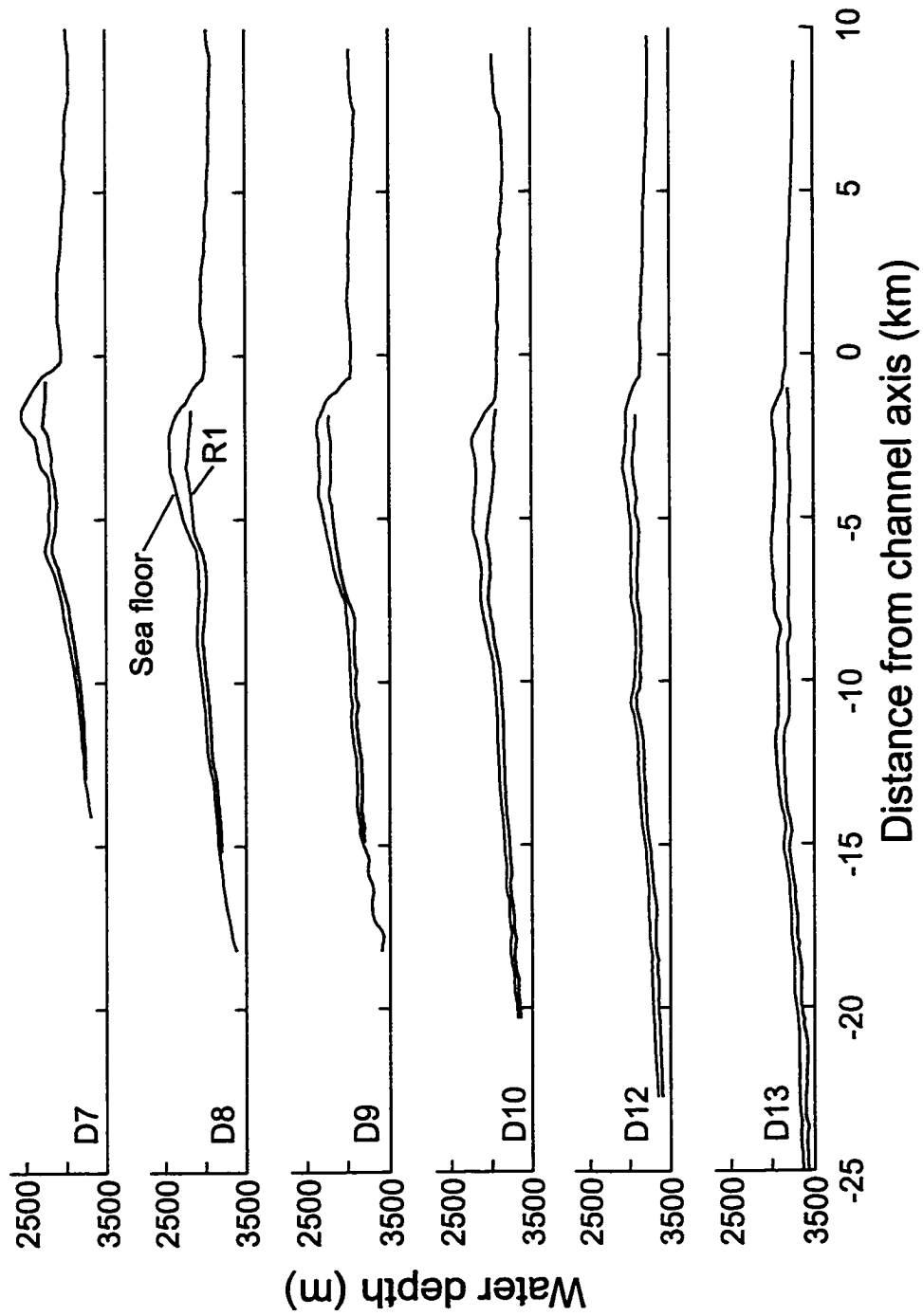


Figure 5.31. Line drawings of successive downchannel profiles, D7, D8, D9, D10, D12, D13. Locations given in Figure 5.28.

buried channel feature, suggesting that the channel position changed abruptly, most likely northward to near its present location (Savoye et al., 1993).

After deposition of R3, relief on the VSR increased, outpacing aggradation of the channel floor. Presuming that the top of the buried channel is near the stratigraphic base of the present channel, then no more than 100 m of sediment accumulated in the present channel while over 400 m of sediment have accumulated on the VSR. If the base of the modern channel corresponds to the change in acoustic character of the channel fill at about the same stratigraphic position as base of the former fan valley (Figure 5.30) then about 200 m of sediment have accumulated in the channel while 400 m of sediment accumulated on the VSR. Above R3, the levee crest of the VSR shifted away from the channel axis until after deposition of R1. After R1, the levee crest moved toward the channel taking up its modern location. None of the three depositional sequences (DS1-DS3) shows a significant change in thickness associated directly with this propagation of the levee crest through time.

Horizon R1 in line D8 could be correlated to lines D7, D9, D10, D12, and D13 based on direct tracing and reflector character. In line D8, R1 appears about mid-way between the modern channel floor and levee crest (Figure 5.30 and Figure 5.31). The sediments above R1 thin away from the channel and grade laterally, showing good acoustic stratification near the channel to becoming increasingly acoustically transparent with distance from the channel. The relative position of R1 at the channel edge evolves such that R1 is closer to the modern channel floor moving downchannel (Figure 5.31). By line D13, the stratigraphic position of R1 coincides with the elevation of the modern channel floor.

The levee crest was defined in Chapter 2 as the stratigraphically highest point on the levee dividing reflectors that dip away from the channel from those dipping toward the channel. In line D8, this position moves away from the channel for horizons from R3 to just above R1 (Figure 5.30). Above about midway between R1 and the surface, the levee crest moved toward the channel. This behaviour above R1 is better seen in line D10 (Figure 5.32a) which shows that the outer levee crest formed the stratigraphically highest point up to horizon a (Figure 5.32b). At horizon a, the inner and outer levee

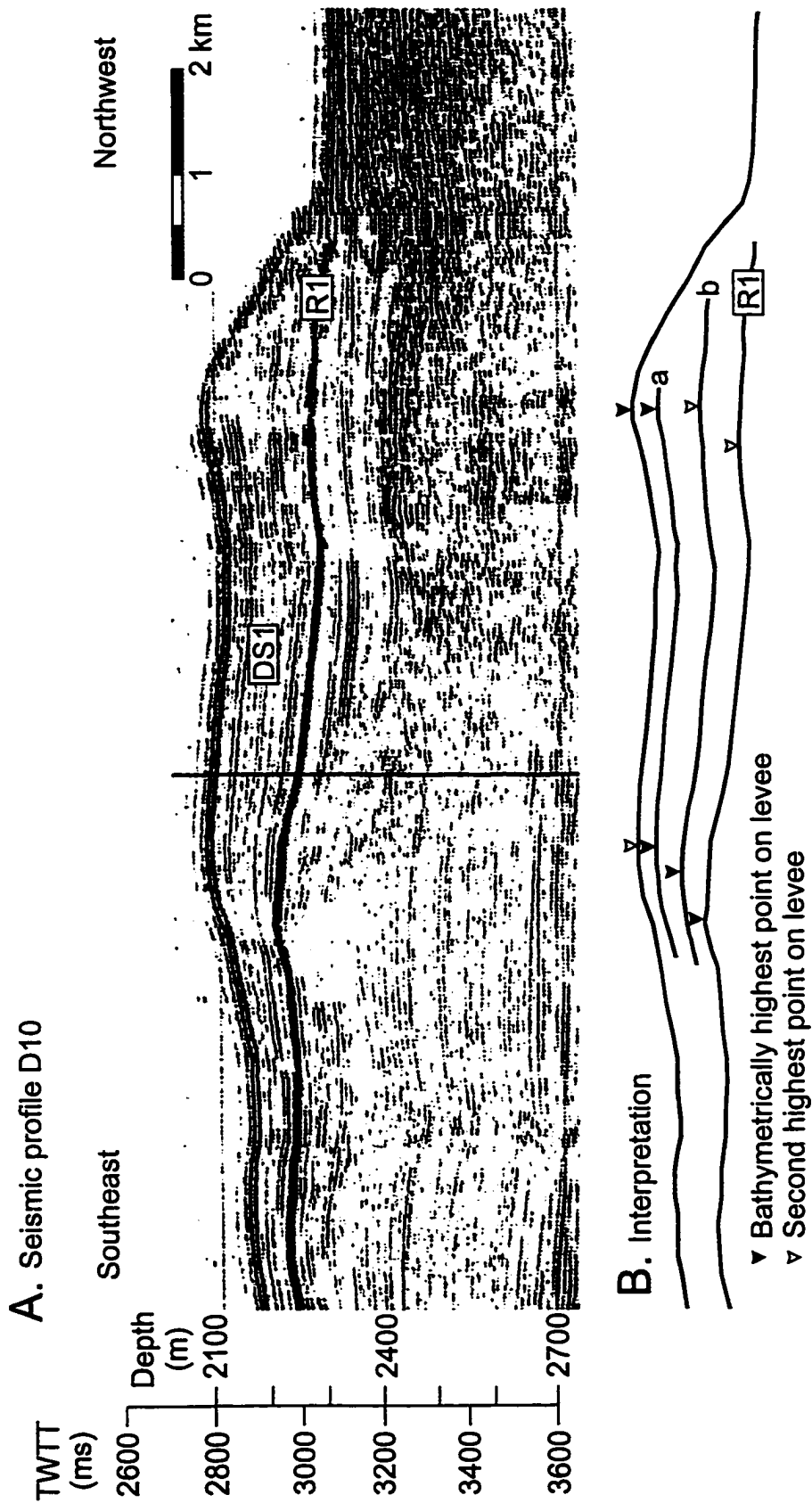


Figure 5.32. Seismic profile D10 on Var Fan: A. profile showing outer and inner levees on Var Sedimentary Ridge; B. interpretation showing evolution of levee crest. Small arrows in B denote location of bathymetrically highest points on inner and outer levees; filled arrow denotes location of highest point, open arrows denote location of second highest point. Prior to horizon a the outer levee crest is higher than the inner levee crest. At horizon a, the inner and outer levee crests have about the same elevation. Above horizon a, the inner levee crest is higher than the outer levee crest.

crests had about the same elevation; above horizon a, the inner levee crest increased in elevation above the outer levee crest (Figure 5.32b).

Levee Architecture

The seismic profiles across the VSR were all collected at oblique angles to the modern channel trend, although they tended to be more perpendicular than parallel to the modern channel trend (Figure 5.28). Consequently the thickness patterns may represent apparent channel-perpendicular variations, depending on the exact position and trend of the channel through time. Savoye et al. (1993) suggested that the middle fan valley ran east-west since deposition of R6 (II). Below R6, the channel ran south. The seismic lines all run approximately northeast-southwest, thus if the channel was trending west they cross the channel at a 45° angle to the channel trend. In the regression results presented below, distances across-levee have been projected to distances perpendicular to the channel trend (i.e., multiplied by $\cos(45^\circ)$) reflecting a truer representation of channel-perpendicular behaviour of the thickness variations. The architecture of DS1 was investigated at lines D7 to D13, covering a downchannel distance of 20 km. The stratigraphic evolution of levee architecture was investigated at line D8.

The depositional sequences identified on line D8 all thin away from the channel except for DS6. This depositional sequence shows a minimum thickness around 5 km from the modern channel axis, a maximum thickness around 9 km from the modern channel axis and then a relatively uniform thickness at distances greater than 10 km from the channel axis (Figure 5.33). DS2 to DS5 all show a relatively simple thinning pattern except for DS3 which displays some thinning across a fault that cuts through the levee flank. DS1 displays a distinct change in the rate of thinning also coincident with the surface trace of the fault. The channel-proximal levee thins from about 200 m to 100 m over a distance of less than 3 km; the distal levee thins from 100 m to 50 m over a distance of almost 10 km. This change in thinning behaviour may be the consequence of erosion of the levee flank or it may imply that DS1 has a composite nature, consisting of two subunits with different rates of thinning.

The decay constant for DS2, DS3, and DS4 on line D8 shows little variation, ranging between $8.2\text{-}9.5 \times 10^{-5} \text{ m}^{-1}$ (Table 5.8). The decay constant for DS1 is somewhat greater at $13.5 \times 10^{-5} \text{ m}^{-1}$, but this decay constant may not be a suitable descriptor of

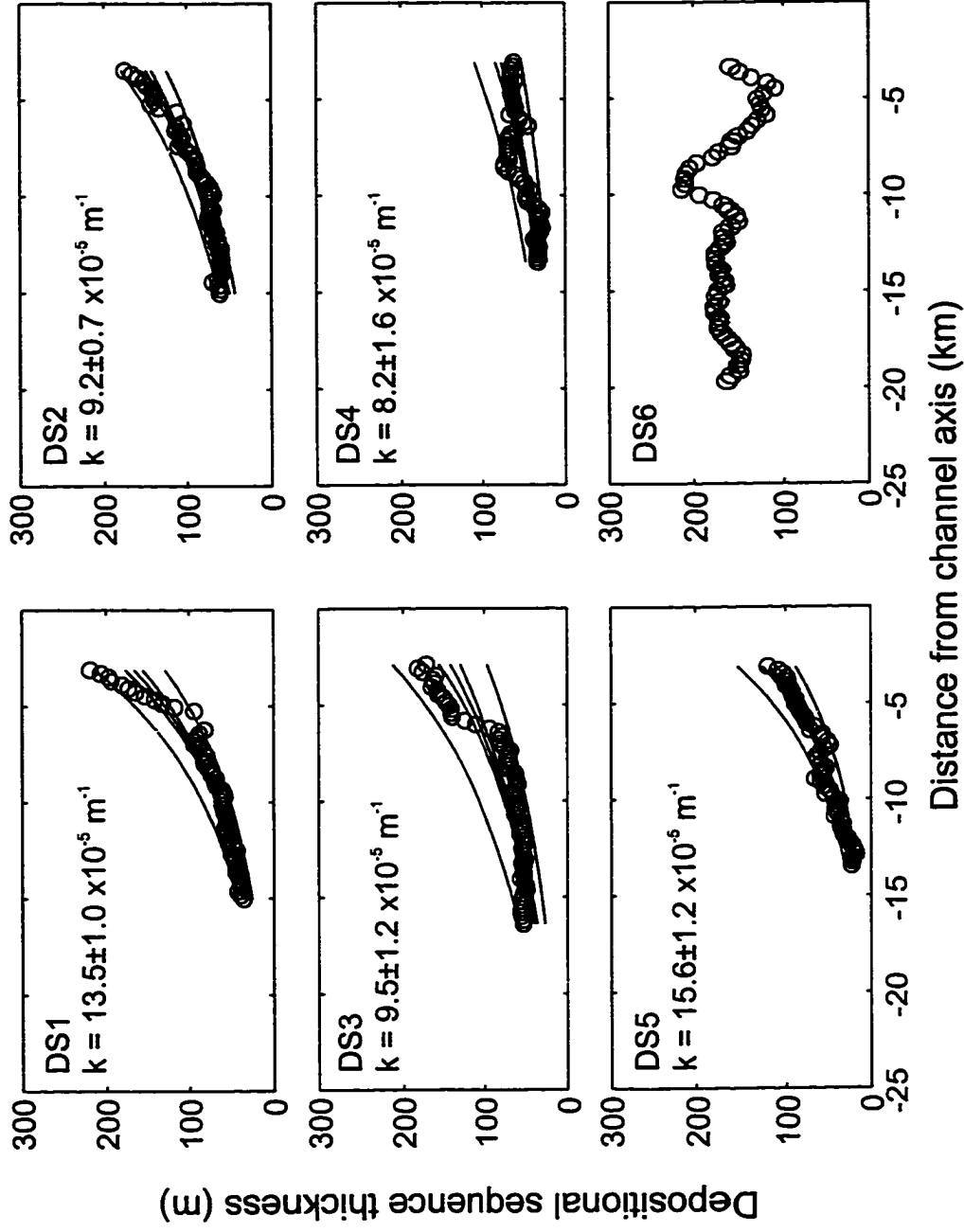


Figure 5.33. Thickness variations across Var Sedimentary Ridge for depositional sequences identified in profile D8. Values of decay constant for across-levee variations in thickness, k , also noted. Regression data tabulated in Table 5.8.

thickness variations for DS1. The decay constant for DS5, $k = 21.0 \times 10^{-5} \text{ m}^{-1}$ is about twice that of the overlying depositional sequences. The thickness variations for DS6 could not be fitted to the exponential model.

Table 5.8. Summary of regression parameters for line D8 on Var Fan. DS = depositional sequence, k = decay constant, δk = 95% confidence limit around decay constant, η_0 = y-intercept of regression equation, $\delta \eta_0$ = 95% confidence limit around y-intercept, r = correlation coefficient.

DS	$k \times 10^{-5}$ (m^{-1})	$\delta k \times 10^{-5}$ (m^{-1})	η_0 (m)	$\delta \eta_0$ (m)	r
1	13.5	1.0	252.1	23.4	0.97
2	9.2	0.7	205.1	14.2	0.96
3	9.5	1.2	188.6	23.2	0.89
4	8.2	1.6	97.8	14.2	0.81
5	15.6	1.2	191.1	21.0	.96

The thickness of DS1 was measured at five additional cross-sections where it shows a consistent pattern of thinning with increasing distance from channel axis (Figure 5.34). At lines D8 (Figure 5.33) and D10 (Figure 5.34), thickness variations proximal to the channel are greater than thickness variations on the levee flank. Nevertheless, the thickness variations as a whole could be fitted to the exponential model (Table 5.9). Between D7 and D8, the decay constant decreases from $22.0 \times 10^{-5} \text{ m}^{-1}$ to $11.2 \times 10^{-5} \text{ m}^{-1}$. From D8 to D13, the decay constant varies between 7.3 - $13.2 \times 10^{-5} \text{ m}^{-1}$, generally decreasing downchannel.

As noted for DS1 at line D8, the thickness variations for this sequence may be better described by two regression equations: one equation for the proximal levee where the spatial change in thickness is large and one equation for the levee flank where the thickness variations are much more gradual (Table 5.10). The decay constant of the proximal levee, k_p , is up to an order of magnitude greater than the decay constant for the levee flank, k_f .

Asymmetry of the VSR is an extreme example of preferential deposition on one side of the channel, but levee development did not proceed as an identifiable movement of the levee crests or simple aggradation of the levee. The present relief of the VSR

Table 5.9. Summary of regression parameters for DS1 on Var Fan. See Table 5.8 for explanation of symbols.

Line	$k \times 10^{-5}$ (m^{-1})	$\delta k \times 10^{-5}$ (m^{-1})	η_o (m)	$\delta \eta_o$ (m)	r
D7	17.5	1.4	253.3	27.6	0.96
D8	13.5	1.0	252.1	23.4	0.97
D9	10.1	0.8	187.8	14.8	0.96
D10	9.5	0.8	234.8	23.2	0.93
D12	4.4	0.6	112.8	8.2	0.84
D13	5.2	0.8	199.2	24.8	0.81

Table 5.10. Regression parameters for DS1 on Var Fan calculating different regression equations for the proximal levee and levee flank. k_p = decay constant for proximal levee, k_f = decay constant for levee flank, δk_p = 95% confidence limit around k_p , δk_f = 95% confidence limit around k_f , r = correlation coefficient, y_{of} = distance from channel axis between data used to calculate k_p and data used to calculate k_f .

Line	k_p $\times 10^{-5}$ (m^{-1})	δk_p $\times 10^{-5}$ (m^{-1})	r	y_{of} (km)	k_f $\times 10^{-5}$ (m^{-1})	δk_f $\times 10^{-5}$ (m^{-1})	r
D7	30.7	4.0	0.97	6.0	16.9	2.0	0.95
D8	34.8	5.8	0.97	6.0	10.5	0.6	0.98
D9	19.6	2.6	0.95	8.0	8.5	1.8	0.90
D10	21.4	1.8	0.98	8.0	5.8	0.8	0.86
D12	11.4	2.2	0.91	8.0	1.5	0.8	0.49
D13	12.5	1.2	0.95	14.0	0	na	0.02

(Figure 5.29) is a good approximation of the present elevation difference between conjugate levees because little or no levee exists north of the channel. If this was true throughout the development of the VSR, then the elevation difference between conjugate levee crests increased through time as the VSR grew. Stratigraphic trends in cross-channel slope are more difficult to assess because of the complex behaviour of the levee crests. At line D8, the levee crests below R4 moved southeastward and appear to be associated with the buried channel whose fill appears to widen through time. Above R4 and up to just above R1, the levee crests apparently associated with the modern channel location continued to shift to the southeast as the levee grew. The coincidence of increasing elevation differences with increasing distance of the levee crest from the channel axis could produce a cross-channel slope that remained constant through time. The modern levee crest appears to be the stratigraphically highest point on the levee and this point lies

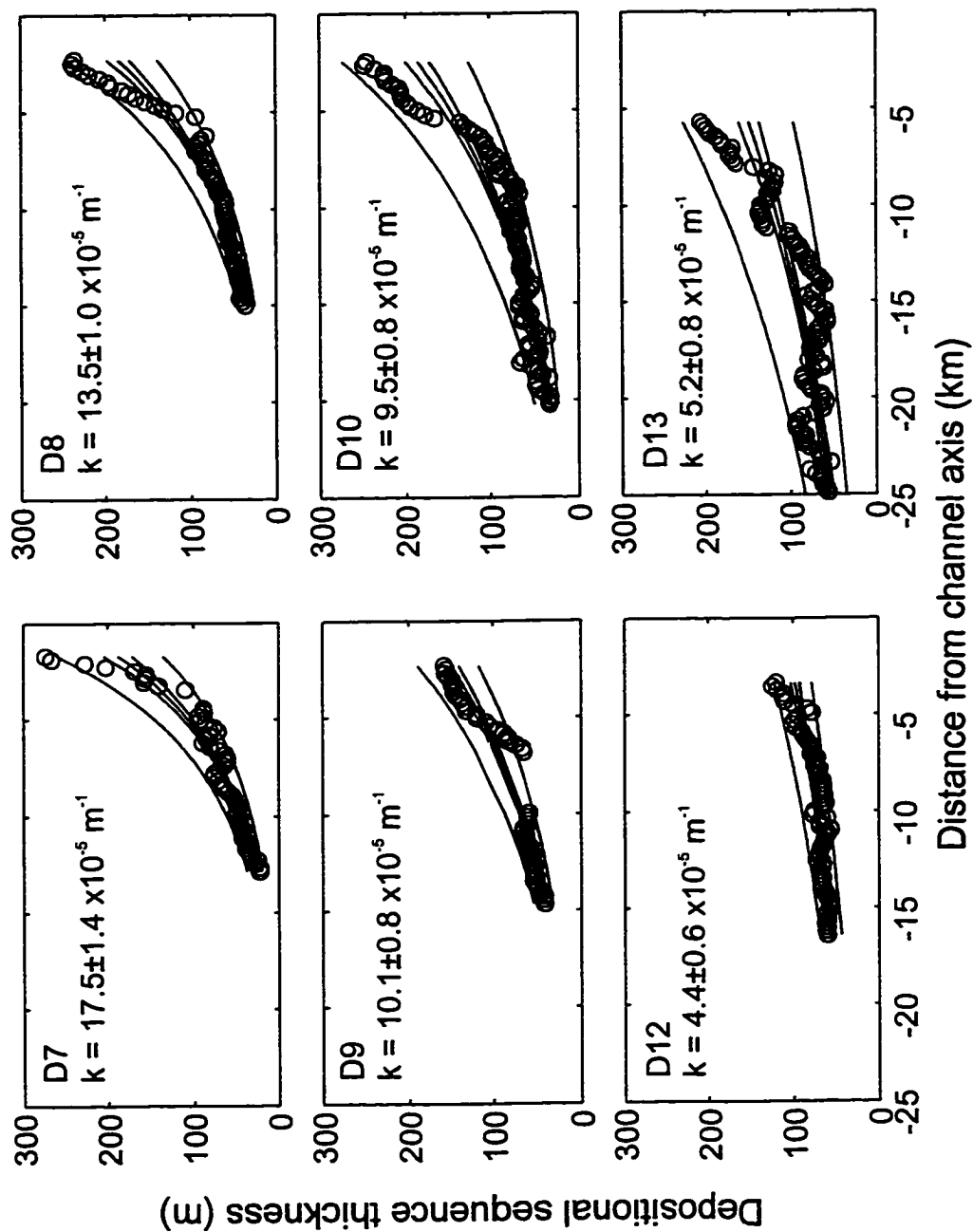


Figure 5.34. Thickness variations across Var Sedimentary Ridge for DSI identified in profiles D7, D8, D9, D10, D12, and D13. Decay constant for across-levee variations in thickness, k , also noted. Regression data tabulated in Table 5.9 and Table 5.10.

several kilometres channelward of the underlying levee crest. This suggests that during deposition of DS1, the cross-channel slope may have greatly increased.

Sediment waves developed on the VSR after deposition of R4 (Figure 5.35). The waves are aligned oblique to the modern channel trend, having amplitudes of 10-50 m and wavelengths from 1-7 km (Piper & Savoye, 1993). The stratigraphic development of the sediment waves shows three phases (Figure 5.35 and Figure 5.38). During the first (between R4 and R3) and second phase (above R3) of wave growth, the crests and troughs of the waves moved upstream by about 500 m overall. Wave amplitude increased to 15 m prior to R3 and then decreased to 7.5 m above R3 but below R1. The change from increasing to decreasing wave amplitude marks the beginning of the second phase of wave growth. During the final phase, the wave crests and troughs still moved upstream, but the overall migration was less than in the first two phases, about 250 m. Wave amplitude was relatively constant, but may have decreased around R1. The decrease in wave amplitude is especially noticeable on the upstream limb of the sediments waves. Throughout their stratigraphic development, wavelength shows little variability.

5.4.3 Synthesis of Levee Architecture on Var Fan

Prominent patterns in levee architecture from Var Fan occur downchannel. In this direction, the spatial decay constant, k , decreases as does the thickness of sediment at the levee crest (Figure 5.36). The ratio of these two parameters, η_{lc}/k , defines the volume of sediment contained within the levee per unit channel length, V_{xlc} ($m^3 m^{-1}$). This value shows a downchannel increase (Figure 5.37a). As noted by Savoye et al. (1993), the levee growth on Var Fan appears progradational. The pattern in V_{xlc} supports this contention and captures this behaviour better than the analysis of thickness variations along a single seismic profile. For example, if a seismic line ran down the levee crest then no progradational thickness trends would have been surmised; the thickness of sediment at the levee crest decreases downchannel (Figure 5.36b). However, the decrease in sediment thickness occurs at a slower rate than the decrease in k so that V_{xlc} ($= \eta_{lc}/k$) increases. Thus, the levee is progradational in the sense that more sediment is incorporated into the levee at more distal locations.

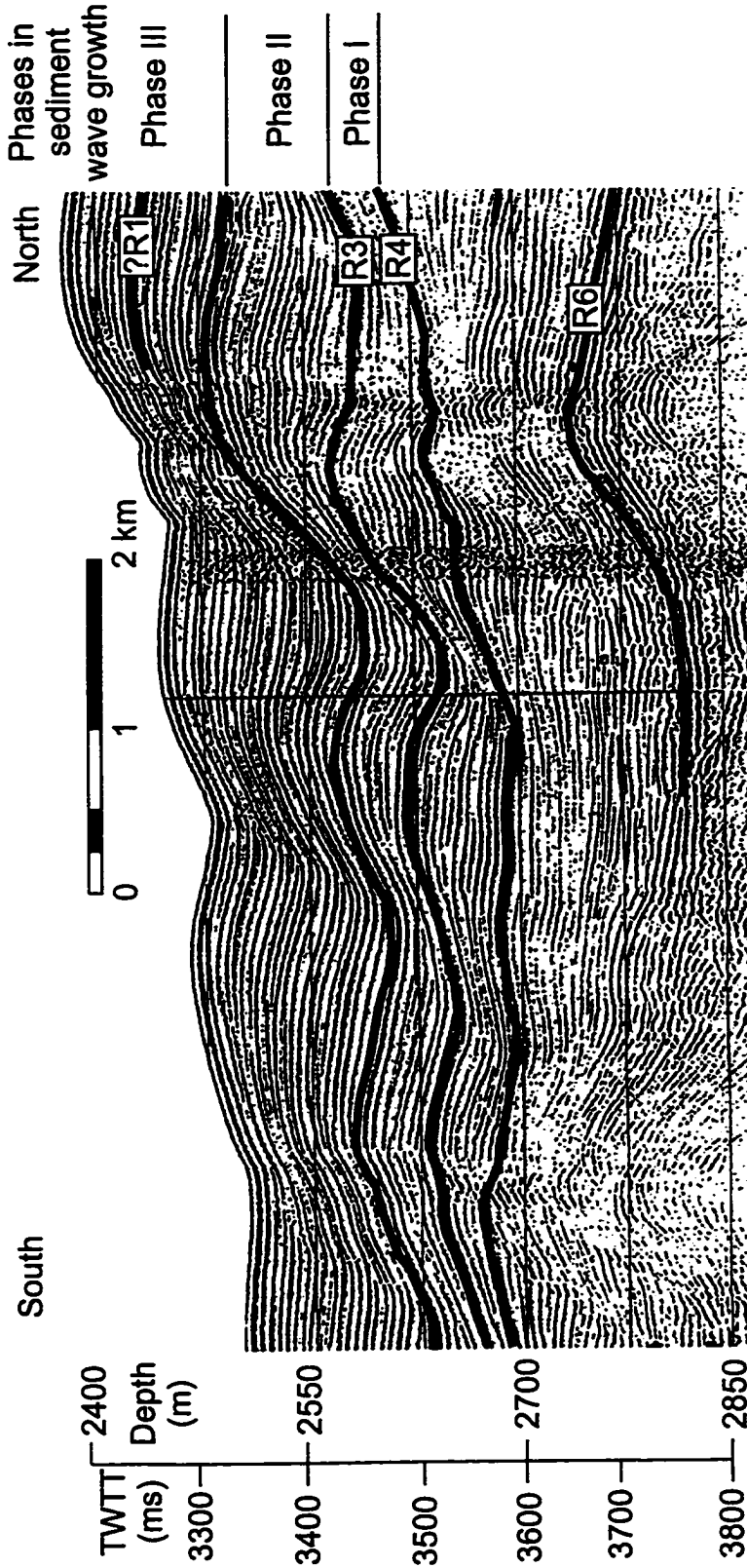


Figure 5.35. Sediment waves on Var Fan (modified after Savoye et al., 1993).

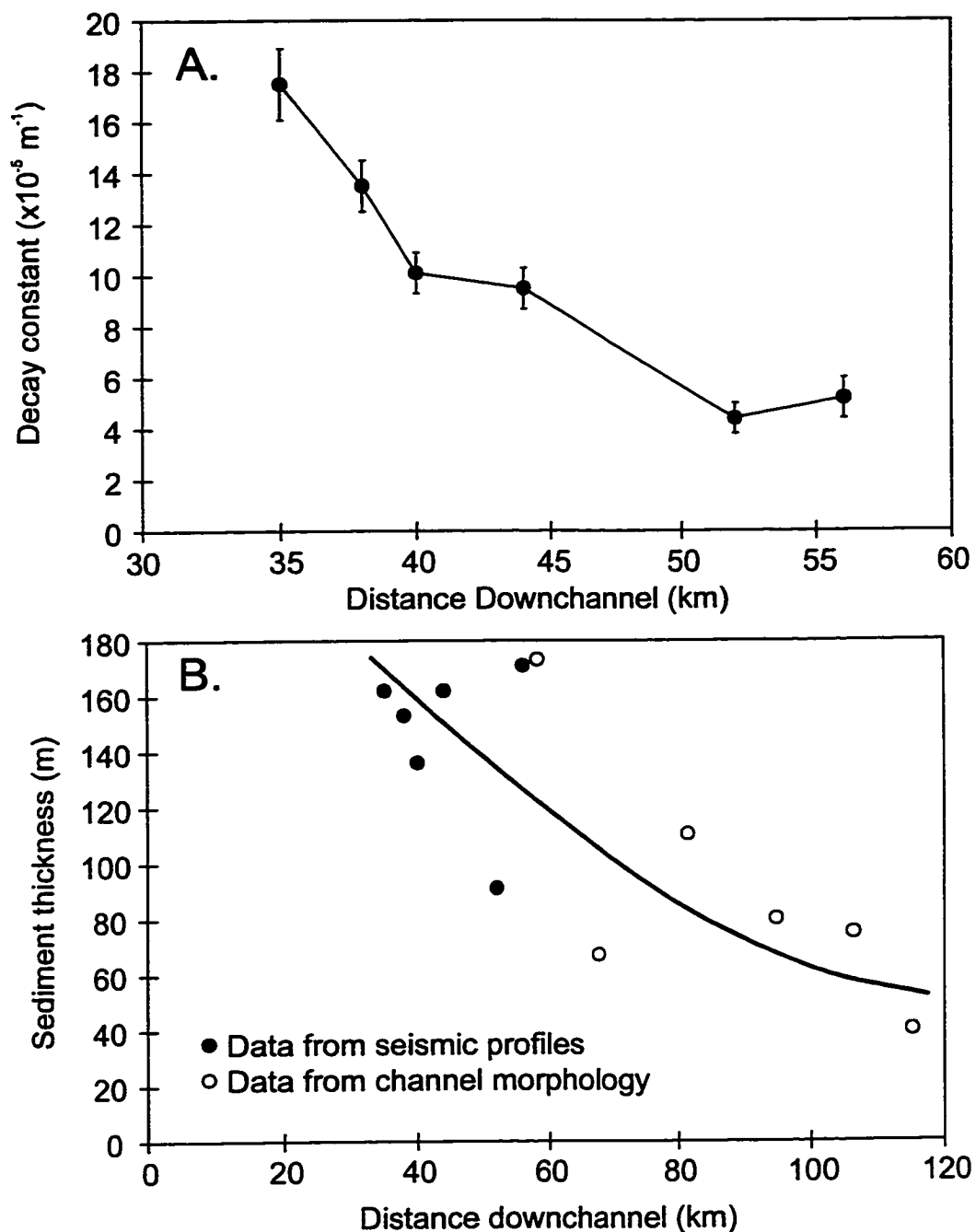


Figure 5.36. Downchannel variability in regression parameters: A. decay constant; B. thickness at levee crest. In B data come from direct measurements of thickness from seismic lines and from the modern channel relief, assuming that the elevation of R1 coincides with the elevation of the channel floor for distances greater than 60 km downchannel (see Figure 5.31).

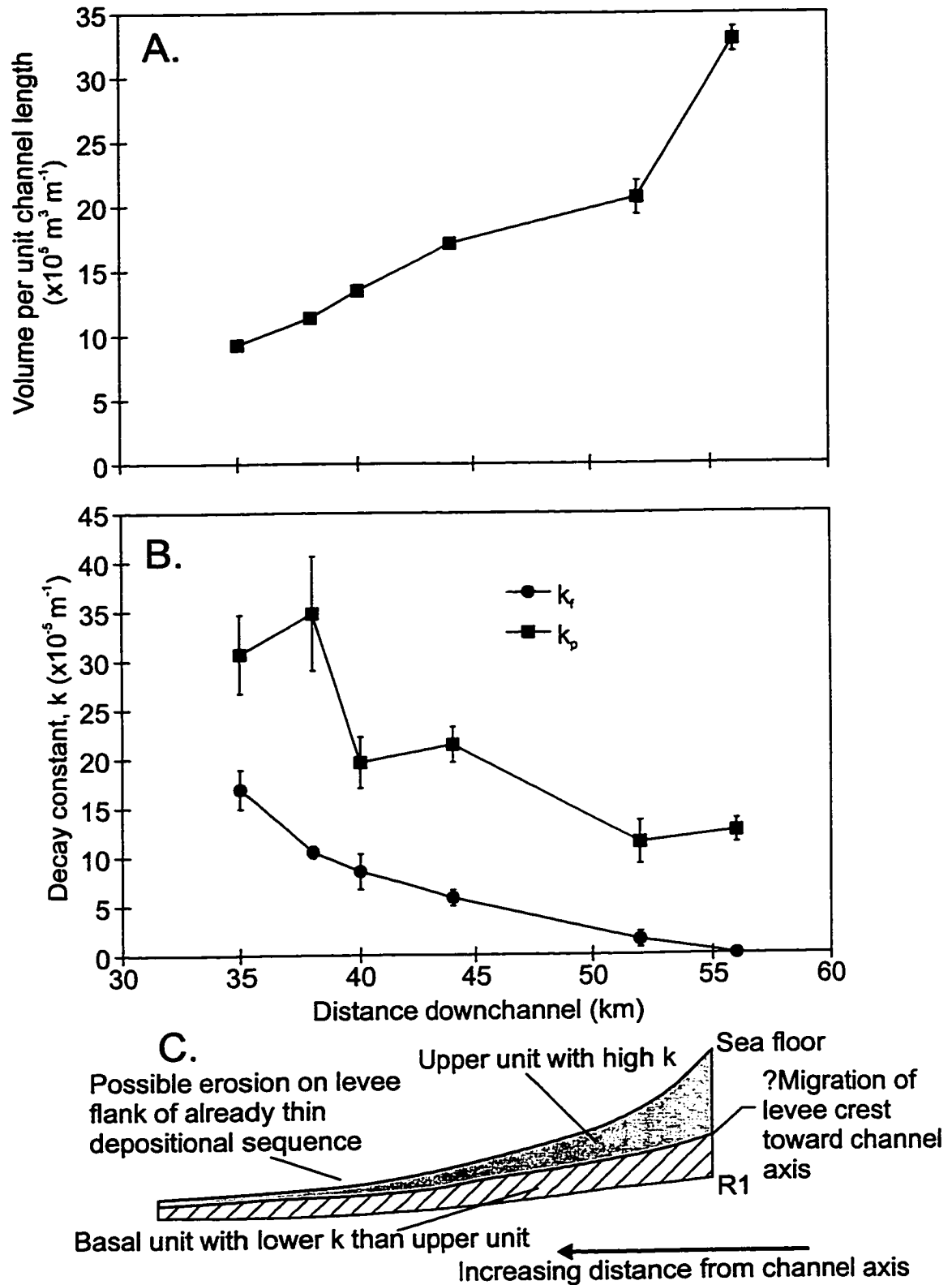


Figure 5.37. Downchannel variability in regression parameters: A. volume of sediment per unit channel length; B. decay constant for proximal levee and levee flank; C. schematic diagram showing possible composite structure of DS1 for subunits spanning the same stratigraphic interval.

DS1 shows thinning patterns that suggest two separate rates of decay: one for the proximal levee, k_p , and another for the levee flank, k_f . Calculation of these separate decay constants shows that k_p is between $10\text{-}20 \times 10^{-5} \text{ m}^{-1}$ greater than k_f (Table 5.10) and that both k_p and k_f decrease downchannel (Figure 5.37b). The existence of two distinguishable patterns in the across-levee thinning reflects a major change in the amount and distribution of sediment within a depositional sequence. The boundary between the two thickness patterns corresponds to a region of erosional truncation of reflectors above R1. This erosion in part would explain the pattern. However, reflections above R1, proximal to the channel display a strongly divergent internal geometry; the depositional sequence may already have been quite thin before being removed by erosion. The change in thickness patterns could, therefore, reflect a major change in the spatial decay of thickness within DS1; a lower unit with a decay constant best reflected by k_f and an upper unit whose decay constant is larger (Figure 5.37c).

The possibility of DS1 representing a composite of two very different thinning patterns is also suggested by the evolution of the levee crest. Between R3 and R1, the space between the levee crest and the modern channel fills with low to moderate amplitude, sub-parallel reflections indicative of muddy overbank deposits. During this time, the levee crest appears to have shifted away from the channel axis. At about midway through DS1, the position of the levee crest moved toward the channel axis. The potential change in thickness patterns within DS1 corresponds to the development of the modern levee crest closer to the channel axis, suggesting different depositional geometry for the upper portion of DS1 compared to the lower half of DS1.

Piper & Savoye (1993) used the sediment waves on Var Fan to constrain interpretation of turbidity current flow thickness on the levee. They discounted the lee wave model for sediment wave development using a Froude number argument. Fi^2 is a direct function of slope (Middleton, 1966) and for the slopes on which the sediment wave developed, of order 10 m km^{-1} , Fi would be greater than one, corresponding to supercritical flow. Piper & Savoye (1993) stated that the lee wave model does not apply for $Fi < \pi^{-1}$, well within the region of subcritical flow. Using the antidune model, the wavelengths ranging from 1-7 km suggest flow thickness on the levee of several hundred metres, assuming $Fi = 1$. Strictly speaking, the antidune model and the flow parameters

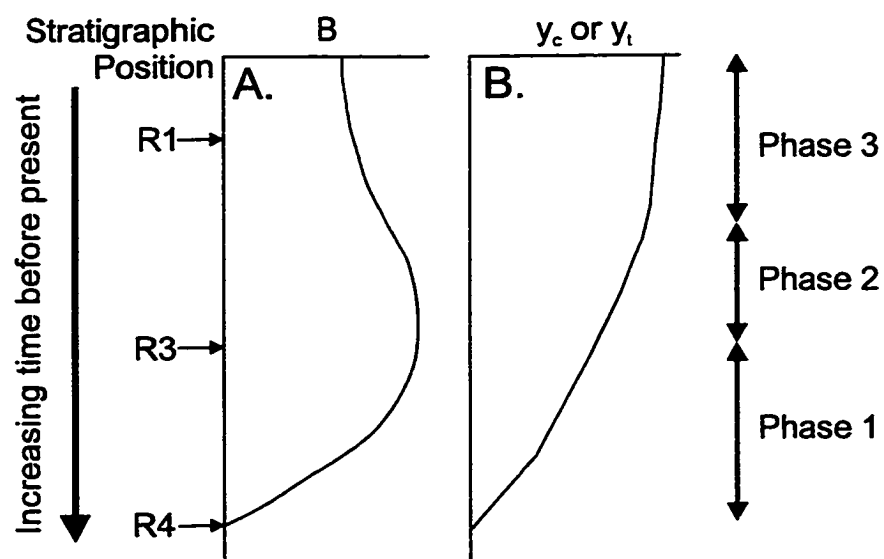


Figure 5.38. Schematic depiction of sediment wave evolution for seismic profile shown in Figure 5.35: A. wave amplitude; B. position of wave crest, y_c , or trough, y_t .

predicted by it applies only to those stratigraphic horizons where the wavelength being measured coincides with active wave growth. If upstream migration reflects wave activity, then these estimates of flow thickness reflect conditions characterizing levee development since R4 (Figure 5.38). However, if active wave growth must also include increases in wave amplitude, then flows several hundred metres thick only characterized the stratigraphic interval between R4 and R3. The decrease in wave amplitude and the reduced upstream migration above R3 may reflect a change in the average character of the overbanking flows, perhaps a decrease in flow thickness below that predicted by the antidune model and the length of the sediment waves.

5.4.4 Key Features

1. Var Fan with its straight, steep, highly asymmetric channel, is a medium-sized system within a continuum of systems having a similar gross-scale morphology, larger than Hueneme Fan and smaller than Laurentian Fan.
2. An exponential model describes the variations in depositional sequence thickness perpendicular to channel trend. In general, Var Fan consists of depositional sequences with decay constants on the order of $10 \times 10^{-5} \text{ m}^{-1}$.
3. The nature of thickness variations of DS1 suggests that two separate equations may describe the depositional sequence geometry of the proximal and distal levee. Decay constants on the proximal levee were about three times greater than decay constants for the distal levee.
4. No stratigraphic trends occur in the value of the decay constant, parameterizing across levee variations in depositional sequence thickness.
5. The decay constants decrease downchannel. V_{xlc} increases downchannel. The elevation difference between conjugate levees decreases downchannel.
6. While levee asymmetry developed due to preferential deposition on the Var Sedimentary Ridge, recognizable levee crests on the VSR are difficult to identify, because of the complex evolution of the levee above R3. Prior to about midway between R1 and the surface, an inner and outer levee developed with the stratigraphically highest point on the levee associated with the outer levee. After this

time and up to present day, the inner levee crest became the stratigraphically highest point.

7. Below R4, the levee developed levee crests that shifted away from the channel axis coincident with an apparent increase in the width of channel fill.
8. Sediment waves show three phases of development. Phase 1 was characterized by increase in wave amplitude and rapid upstream migration. Phase 2 continued the upstream migration but wave amplitude first decreased and then stabilized. The final phase of sediment wave growth saw a lessening in the rate of upstream migration and little change in wave amplitude. Throughout sediment wave development, wavelength remained virtually unchanged.

5.5 General Summary

This chapter has documented the levee architecture from three additional submarine channel-levee systems, showing that some of the features initially found on NAMOC (Chapter 3) and Hueneme Fan (Chapter 4) are more widely seen. First of all, the levees of Reserve, Amazon, and Var fans all show thinning perpendicular to channel trend that can be described by an exponential model and parameterized by a decay constant, k . These decay constants tend to be uniform within a particular system, but vary between systems from as high as $100 \times 10^{-5} \text{ m}^{-1}$ to $10\text{-}20 \times 10^{-5} \text{ m}^{-1}$ for Amazon and Var fans. With the data from NAMOC, the total range of values that k takes can range over two orders of magnitude from $1\text{-}100 \times 10^{-5} \text{ m}^{-1}$. These systems also show downchannel thinning of sediment thickness at the levee crest that coincides with no significant downchannel trend in the decay constant. Grain size data from Reserve Fan (Normark & Dickson, 1976b) and Amazon Fan (Piper & Deptuck, 1997; Hiscott et al., 1997; Manley et al., 1997) show that the levees consist of silty mud. Furthermore, evidence from boreholes on Amazon Fan suggest that variations in lamina abundance do not immediately correlate with the magnitude of k . Examination of these systems supports the contention that levees tend to be uniform in composition whereas k varies by orders of magnitude.

Chapter 6

Levee Architecture of Laurentian Fan

6.1 General Statement

Laurentian Fan, located seaward of Laurentian Channel off eastern Canada (Figure 6.1), displays a great deal of diversity within a single depositional system, perhaps more diversity than in any one of the other systems previously presented. The system distinguishes itself from others in several ways including: 1) multiple, recently-active fan valleys; 2) proximal glacial source; and 3) extremely deep and wide channels. It also has features common to the other systems studied in this thesis, including straight channels with large slopes (Hueneme, Reserve, and Var fans) and asymmetrical levees (NAMOC, Hueneme Fan, and Var Fan). The general morphology of the upper fan is different between the western and eastern sides of the system (Figure 6.2 and Figure 6.3). A network of tributaries feeds Western Valley, like those feeding NAMOC, whereas Eastern Valley receives sediment from a single channel that heads near the shelf break. Laurentian Fan offers the opportunity to study levee architecture where, within a single system, channel-levee morphology takes on radically different forms, perhaps owing to the nature of sediment delivery to the fan. Also, the proximity of Laurentian Fan to a major outlet for Laurentide ice during the Pleistocene, i.e., Laurentian Channel, suggests that its architecture may respond to ice sheet dynamics.

6.2 Data Set

The main data set for the investigation of Laurentian Fan consists of 40 in³ airgun seismic and sparker reflection profiles collected over the past three decades and made available by the Geological Survey of Canada Atlantic (Figure 6.2). The sparker data have a vertical resolution of < 20 m with navigation fixes estimated to be accurate within ± 150 m. The airgun data have a vertical resolution of < 10 m with navigation provided by LORAN C and transite satellite for cruises prior to 1992 (accuracy ± 150 m) and by GPS (accuracy ± 5 m) after this time. In addition, recent cores and high resolution 3.5 kHz data provide some groundtruth for the sediments imaged by the seismic data. These data are augmented by GLORIA, SeaMarc, and SAR sidescan sonar and SeaBeam

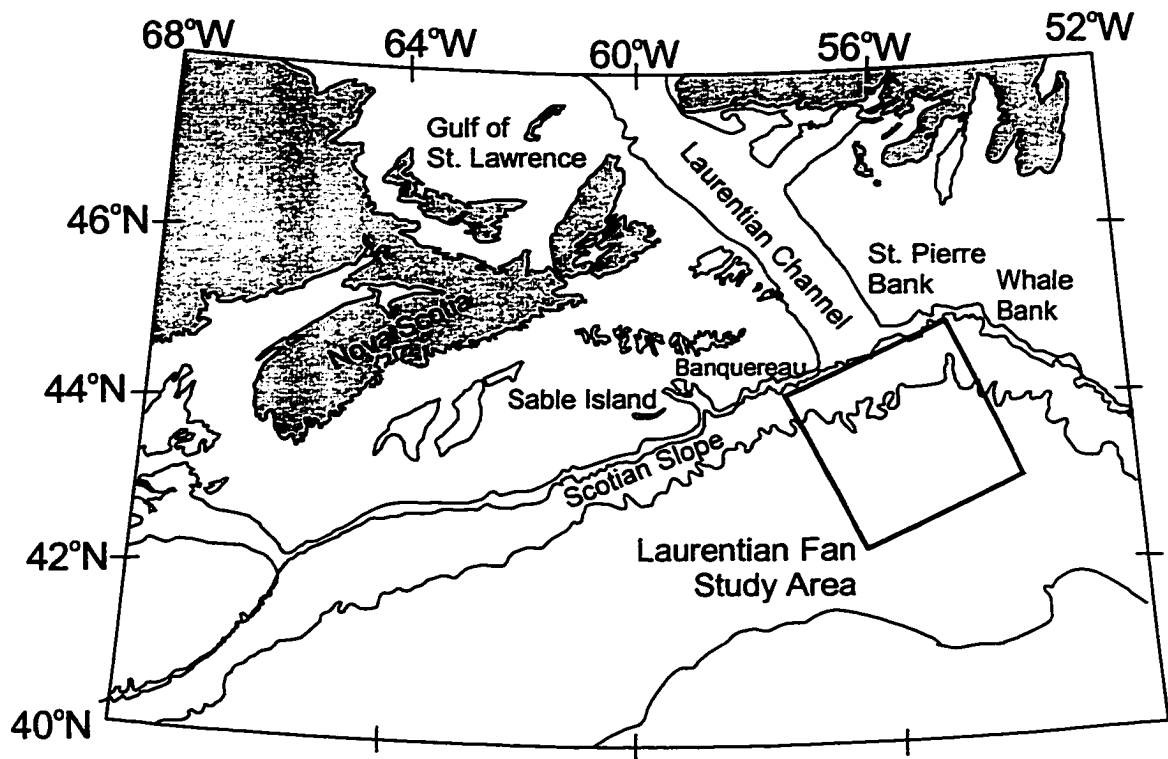
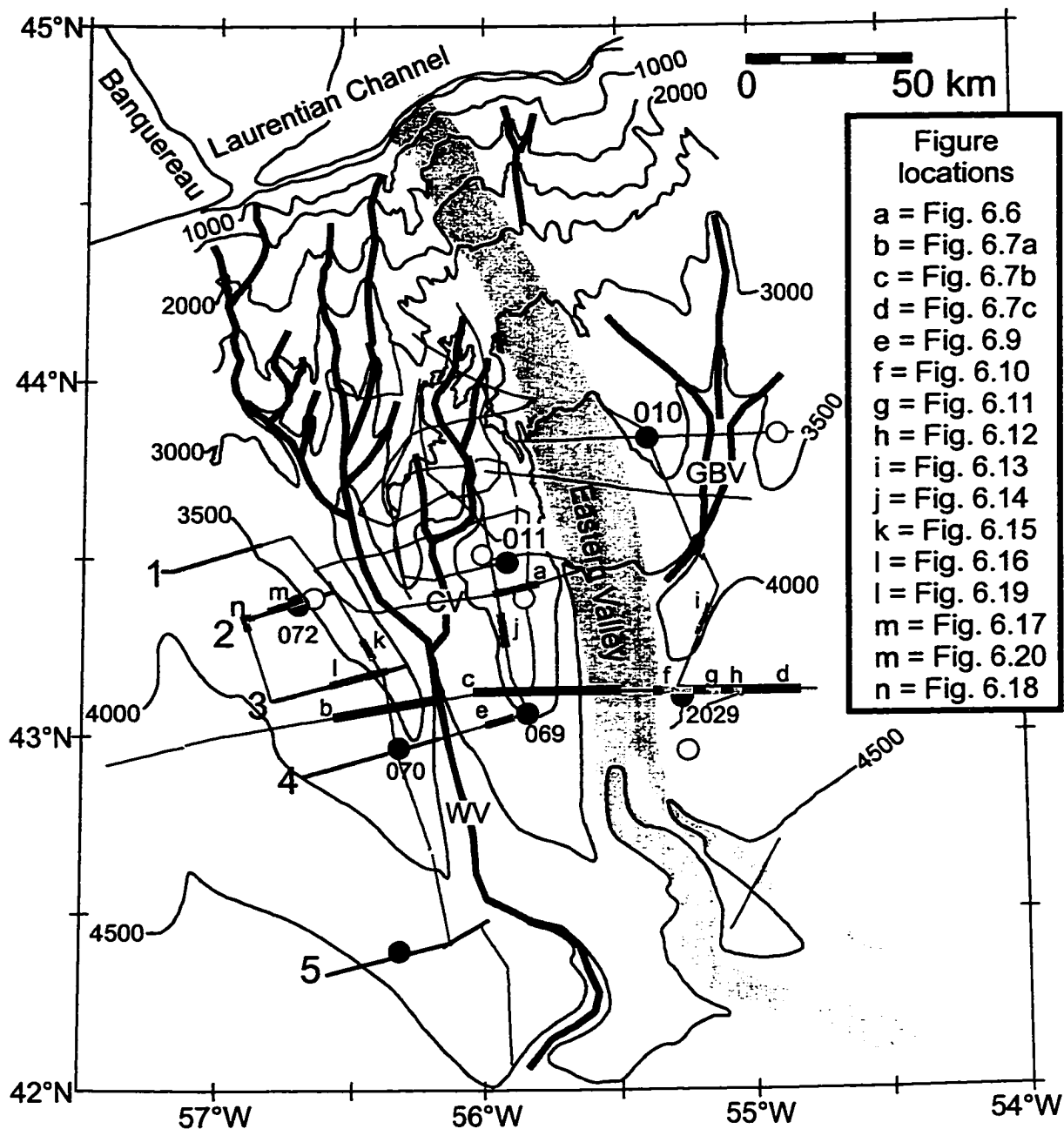


Figure 6.1. General map of the continental margin off Nova Scotia showing the location of Laurentian Fan and the study area.



- CV = Central Valley
 GBV = Grand Banks Valley
 WV = Western Valley
 ■ a-m = figure locations, black line for multichannel data
 — 1-5 = cross-sections of western levee of Western Valley
 ● 010, 011, 069, 070, 072, 2029 = cores presented in chapter
 ○ other cores described from Laurentian Fan

Figure 6.2. Data distribution for study of Laurentian Fan. Also shown are the drainage networks associated with Eastern and Western Valleys. Lower case arabic letters denote figure locations. Contour interval is 500 m.

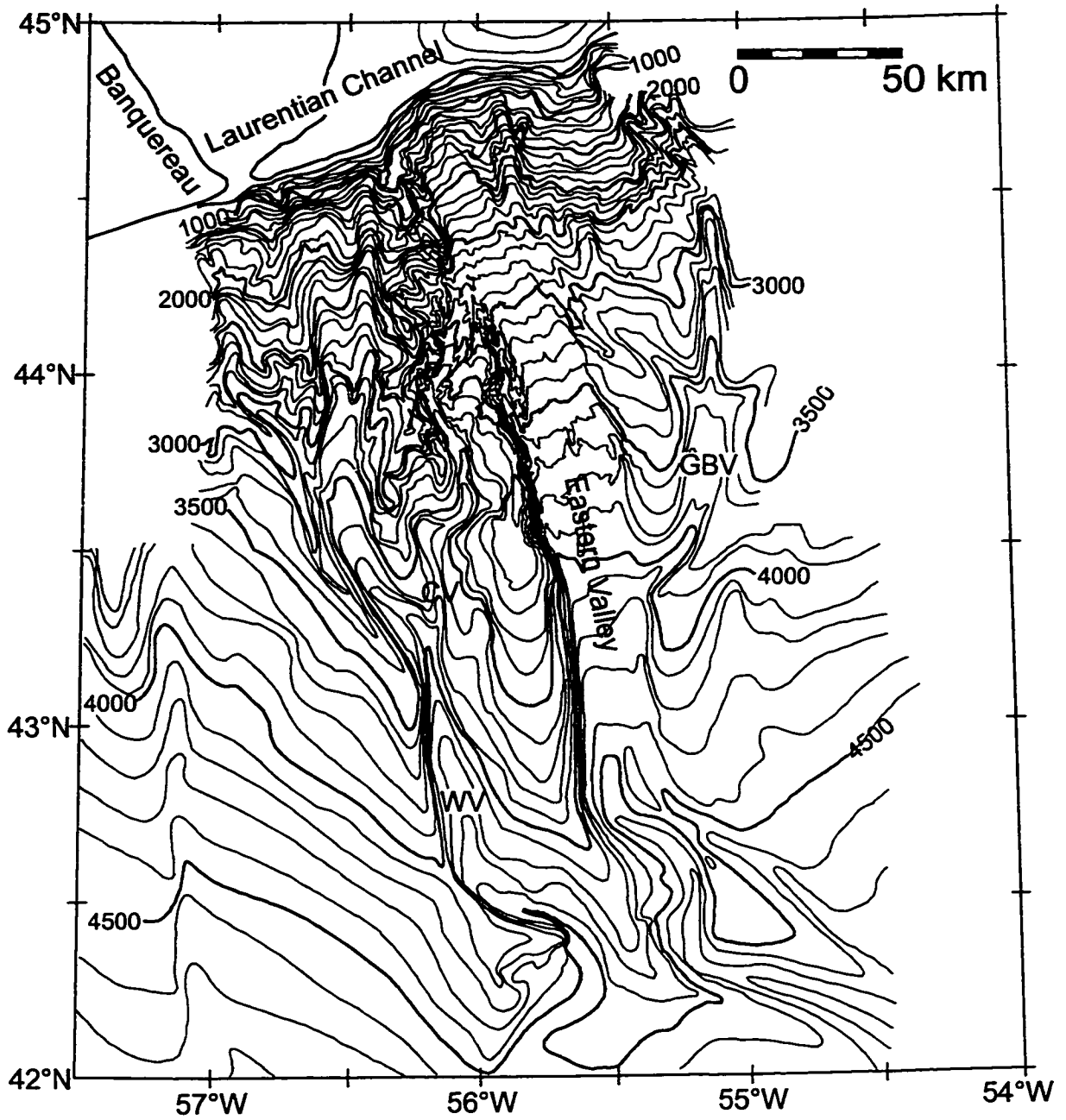


Figure 6.3. Detailed bathymetry of Laurentian Fan (after Hughes-Clarke, 1988). Contour interval is 100 m.

bathymetry of selected areas of the fan that have been reported elsewhere (e.g., Masson et al. 1985, Hughes-Clarke, 1988; Hughes-Clarke et al., 1989; Piper et al., 1998a, submitted). Sparker data collected in 1978 were presented by Piper & Normark (1982). These workers developed an acoustic stratigraphy of the fan that has been used and extended in the present study.

6.3 Setting of Laurentian Fan

Laurentian Fan occurs off the eastern Canadian continental margin (Figure 6.1), bounded to the north and east by the Grand Banks of Newfoundland. It lies seaward of Laurentian Channel, a glacially-excavated trough with an average water depth of 400 m, about 300 m greater than the regional water depth of the continental shelf. Laurentian Channel acted as a major outlet for continental ice sheets centred in eastern Canada (e.g., Piper et al., 1990). Consequently, fan growth recorded the complex interaction between ice sheet dynamics and sediment supply.

6.3.1 Channel Morphology

The channel system on the continental slope and upper fan shows two different forms (Figure 6.3). Eastern Valley heads near the present shelf break in water depths of around 400-500 m and extends as a continuous feature to water depths in excess of 4500 m. Both east and west of Eastern Valley, a complex network of tributaries drain the continental slope. In the west, this network includes drainage from the continental slope off Laurentian Channel and perhaps Banquereau (Figure 6.1) and a system of tributaries that merge into Central Valley and appear to feed from Eastern Valley (Figure 6.3). In the east, drainage from the continental slope off St. Pierre and Whale banks (Figure 6.1) first merges into a single valley, informally termed Grand Banks Valley by Masson et al. (1985) and Hughes-Clarke (1988), and then joins Eastern Valley around the 3900 m isobath (Figure 6.3).

Eastern Valley has relief up to 900 m. The relief of the western levee increases from 300 m to 900 m at about 180 km from the shelf break and then gradually decreases to 200 m around 300 km from the shelf break (Figure 6.4). Width of channel floor is about 25 km and remains uniform over nearly 200 km after which point, near the 4400 m

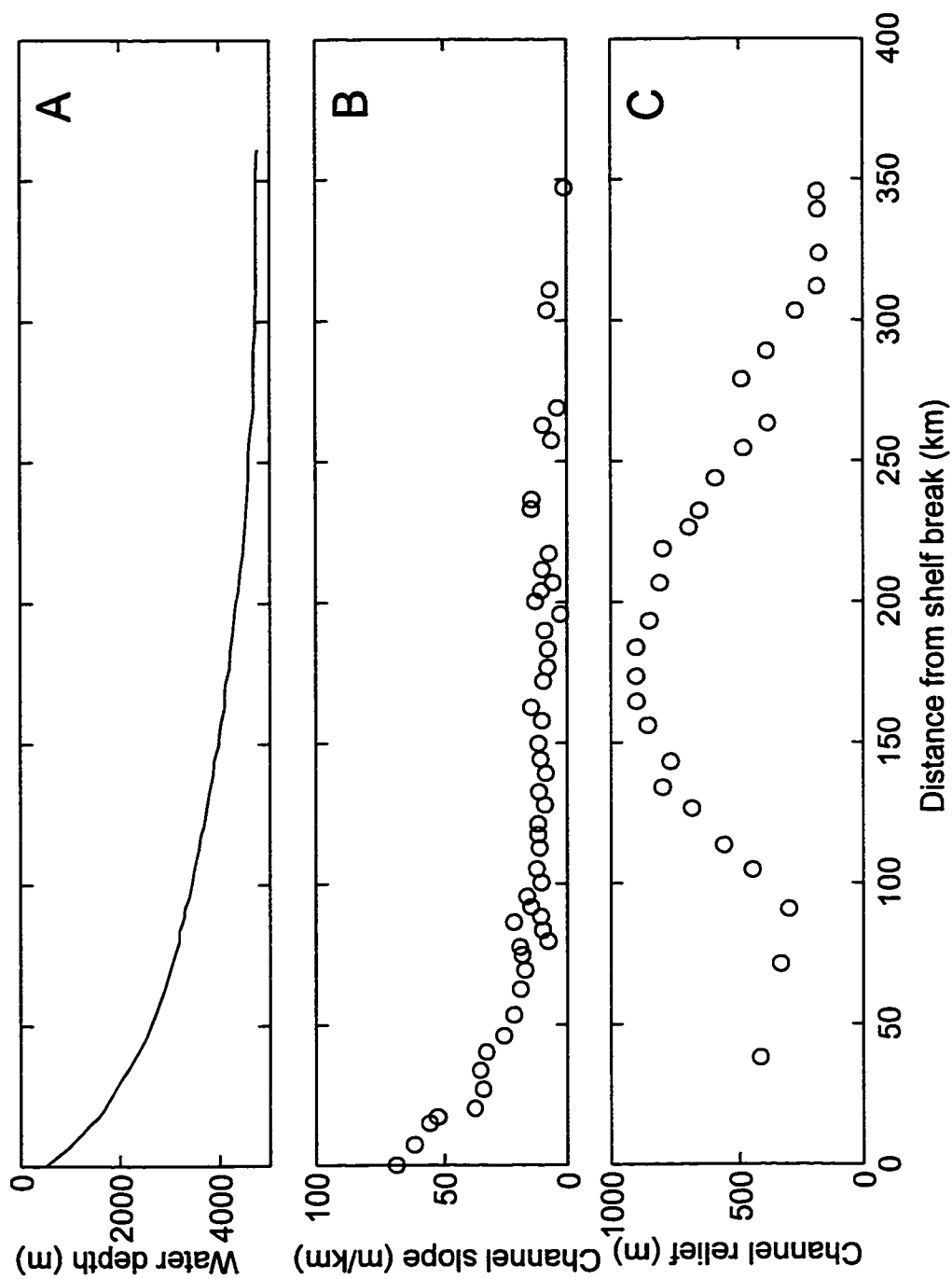


Figure 6.4. Longitudinal profiles of Eastern Valley with distances measured along the channel from the 400 m isobath: A. axial profile of channel; B. channel slope; and C. relief between channel floor and crest of western levee of Eastern Valley.

isobath, an inter-channel high splits Eastern Valley into two segments (Figure 6.3). The distance between levee crests is also uniform and averages 40 km. The western levee of Eastern Valley (WLEV) is higher than the eastern levee of Eastern Valley (ELEV) by as much as 700 m. Grand Banks Valley joins Eastern Valley around the 4100 m isobath. Its relief increases from 150 m to 400 m between the 3200 m and 3700 m isobaths and then decreases back to 150 m between the 3700 m and 4100 m isobaths (Figure 6.3). Grand Banks Valley has channel relief that is notably less than the adjacent Eastern Valley, although the channel slopes are similar at about 10 m km^{-1} .

Western Valley is smaller than Eastern Valley with a maximum relief of less than 600 m (Figure 6.3 and Figure 6.5). The channel floor of Western Valley is narrower than Eastern Valley, with widths around 10-15 km. Near the 4100 m isobath, Central Valley joins Western Valley. Relief of Central Valley decreases from greater than 400 m above the 3700 m isobath to 100 m at the 4100 m isobath. The network of tributaries feeding Central Valley appear to head on the western levee of Eastern Valley and may be spillover channels that tapped flows moving through Eastern Valley. If so, the lower part of Western Valley, $> 4100 \text{ m}$, receives drainage originating through Eastern Valley and drainage from the western continental slope off Laurentian Channel. The downchannel slope of Western Valley decreases from 40 m km^{-1} at 30 km from the shelf break to about 10 m km^{-1} at 100 km from the shelf break. After this point, slopes vary between $5\text{-}10 \text{ m km}^{-1}$ for the next 200 km.

6.3.2 Previous Work on Geology of Laurentian Fan

General Quaternary Stratigraphy

The most prominent event in the evolution of Laurentian Fan was the re-organization of the channel pattern from a single leveed fan valley to the present multiple fan valleys some time in the Quaternary. Piper & Normark (1982) suggested that the re-organization occurred in response to the glacial excavation of Laurentian Channel. A distinct reflector in multi-channel seismic records, horizon L, was identified by Uchupi & Austin (1979) as the base of Laurentian Fan, separating pelagic sediments from terrigenous turbidites. Piper & Normark (1989) tentatively dated horizon L as Late

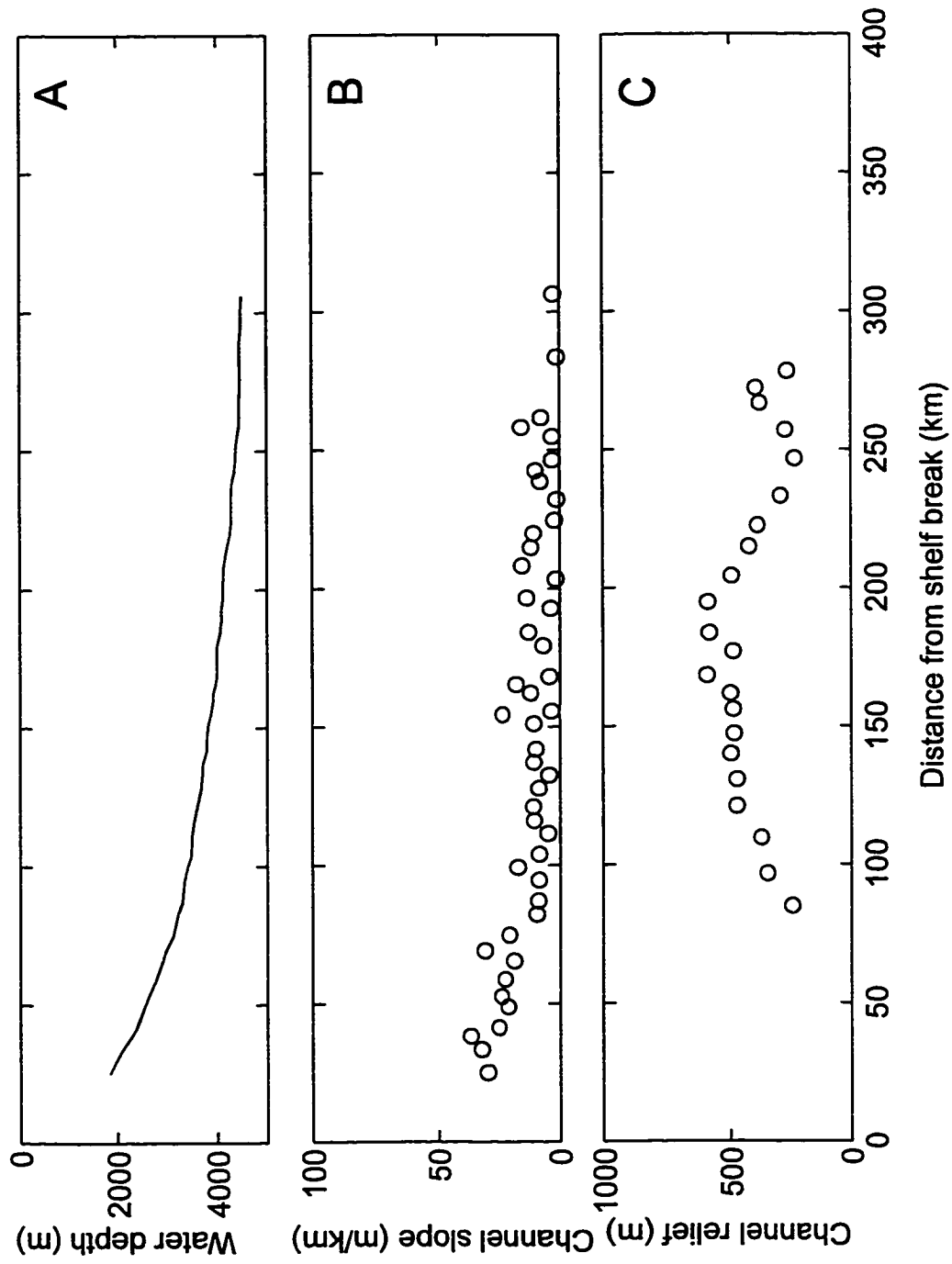


Figure 6.5. Longitudinal profiles of Western Valley with distance measured along the channel from the 400 m isobath: A. axial profile of channel; B. channel slope; and C. relief between channel floor and crest of western levee of Western Valley.

Pliocene or older based on samples recovered from sea floor outcrops by DSRV Alvin. The base of the Late Pliocene also represents the start of turbidite deposition in Deep Sea Drilling Project Site 382 from the margin of the Sohm Abyssal Plain (Tucholke et al., 1979). Above L, Piper & Normark (1982) mapped two regional reflectors, A and Q, and subdivided the evolution of the fan into several phases. From L to A, a single, leveed fan valley existed on Laurentian Fan. From the locations of buried levees below A, these workers suggested that the channel followed the modern trend of Eastern Valley. Between A and L, thickness variations appear on east-west (strike) lines but the thickness remains relatively uniform on north-south (dip) lines (Piper & Normark, 1982). Above A, the first evidence exists for multiple fan valleys. Piper & Normark (1982) suggested that Central Valley originated as a spillover channel from Eastern Valley while Western Valley was fed from the continental slope off Laurentian Channel. Thickness patterns in the section above A show little variation in both across- and downfan directions, except where removed by erosion north of 44°N and across pre-existing relief (Piper & Normark, 1982).

General Late Quaternary Stratigraphy

The late Quaternary stratigraphy of Laurentian Fan revealed by shallow (<30 m) piston cores can be generally divided into units by sediment colour and core location. Understanding of this stratigraphy is primarily the result of work by Stow (1977) who investigated piston cores on the middle fan between the 3500 m and 4000 m isobaths. Sediments flooring the fan valleys consist of sands and gravels. The levees commonly show two stratigraphic units: reddish-brown, muddy turbidites commonly with a basal silt lamina or laminae and olive-grey, bioturbated silty mud. The red sediments are generally considered to be Pleistocene in age, supplied by the glacial erosion of Carboniferous red beds in the Gulf of St. Lawrence. The olive-grey mud represents hemipelagic deposition (e.g., Hill, 1984) with the uppermost occurrence of olive-grey mud interpreted to be of Holocene age.

Recent work by Piper & Skene (1998) detected the presence of detrital carbonate beds on Laurentian Fan which radiocarbon dates bracket between 14.5 ka and 14 ka. The event appears to correlate with the episodic discharge of icebergs through Hudson Strait, termed Heinrich events (e.g., Bond et al., 1992; Dowdeswell et al., 1995). These beds

occur above the reddish-brown muddy turbidites, suggesting that the turbidites pre-date 14.5 ka. One core examined by Piper & Skene (1998) from the eastern levee of Eastern Valley penetrates the entire section of reddish-brown muddy turbidites. It shows that they are underlain by a second gravelly-mud unit, rich in detrital carbonate that may correspond to H2 (Heinrich event 2) which dates from 21 ka. If so, then the succession of reddish-brown muddy turbidites typically sampled in shallow piston cores from Laurentian Fan represents deposition starting just before the glacial maximum and terminating before 14.5 ka. Within the turbidite unit, thin intervals of olive-grey sediment, typically less than 0.05 m, interrupt the otherwise monotonous succession of reddish-brown sediments (Stow, 1977). These units resemble the overlying Holocene hemipelagic sediments and may reflect cessation of turbidite deposition.

6.3.3 Nature of Turbidity Currents

Sediment Delivery

Sediment delivery to the continental slope off Laurentian Channel potentially occurred due to glacio-marine processes including transport by proglacial, englacial, and supraglacial meltwater, ice-rafting, and even ice-contact deposition. The magnitude of sediment delivery, as in any glacial system, is difficult to gauge precisely, but can be indirectly estimated from the amount of sediment incorporated into the fan. The volume of sediments comprising the fan is estimated at 10^{15} - 10^{16} m³, deposited since the middle to late Pliocene, yielding an estimate for sediment delivery of 10^9 - 10^{10} m³ yr⁻¹: equal to or perhaps greater than the sediment delivery estimated for NAMOC using the same type of calculation (Chapter 3). Sediments recovered from the channel floors and observed during submersible dives suggest that a wide range of grain sizes are supplied to fan, from gravel to clay (Stow, 1977; Hughes-Clarke et al., 1989).

Initiation

In 1929, a magnitude 7.2 earthquake with its epicentre located on upper St. Pierre Slope (Figure 6.1) instantaneously broke several deep-sea telegraph cables on the upper continental slope (Heezen & Ewing, 1952; Hughes-Clarke, 1988). The event also produced cable breaks at progressively greater distances downslope and at successively later times. The instantaneous cable breaks were attributed to sediment failure caused by

the earthquake. The delayed cable breaks were interpreted to have resulted from the downslope flow of a turbidity current spawned by upper slope sediment failure. This turbidity current eroded the channel floors, thereby increasing its sediment load and excess density and promoting acceleration, a process termed ignition (Parker et al., 1986). From high resolution sidescan sonar on the upper St. Pierre Slope, Piper et al. (1998a, submitted) reconstructed the evolution of the seismically triggered slump into a turbidity current, suggesting that fluid entrainment associated with a hydraulic jump was responsible for the generation of a turbidity current. Furthermore, they argued that drainage of the upper slope by debris flows would occur, not instantaneously, but over a finite time period. Thus, the feeding of turbidity currents by debris flows could potentially take place over a prolonged period. While loading by an earthquake was responsible for the 1929 Grand Banks event, sediment failure of upper slope sediment supplied by ice-rafting, meltwater or grounded ice may have been active during the Pleistocene (Piper & Normark, 1982).

A completely separate initiation mechanism for turbidity currents on Laurentian Fan is associated with episodic outbursts of subglacial meltwater (Piper et al., in prep.). Based on isotopic evidence for meltwater dilution in the Gulf of Mexico, Emiliani et al. (1978) proposed that massive floods emerged from beneath the Laurentide ice sheet near the end of the Late Wisconsinan glaciation. Shaw & Kvill (1984) and Shaw & Sharpe (1987) interpreted many glaciogenic features on land to have resulted from the flow of subglacial, sediment-laden water rather than ice. Such floods might generate hyperpycnal inflows and may have been responsible for the molding of gravel waves on the floor of Eastern Valley.

Flow Parameter Estimates

For the 1929 event, the known distances between cables and the elapsed time between cable breaks has been used to establish average flow velocities (Heezen & Ewing, 1952). These data suggest velocities of 10 m s^{-1} to 20 m s^{-1} . The nature of the flow and its deposits have been studied in detail using sidescan sonar and submersible observations (e.g., Hughes-Clarke, 1988; Hughes-Clarke et al., 1989). Erosional trimlines on the walls of Eastern Valley suggest that the flow increased in thickness downstream from about 150 m to as much as 300 m (Hughes-Clarke, 1988). Using the

Chezy equation for velocity of a turbidity current, estimates of flow thickness from trimlines and velocity estimates from cable breaks, Hughes-Clarke (1988) calculated volume concentrations between 0.04 and 0.06. These data can be combined to estimate a sediment discharge which in turn yield estimates of flow duration ranging from 4-11 hours (Hughes-Clarke, 1988). The sediment budget for the 1929 event also shows that the volume of sediment contained in the turbidite ($< 200 \times 10^9 \text{ m}^3$) does not account for more than $20 \times 10^9 \text{ m}^3$ of mud (Piper & Aksu, 1987) which was possibly advected south in the Western Boundary Undercurrent (Piper & Aksu, 1987; Hughes-Clarke, 1988).

The 1929 event was a fast-moving, thin, high concentration flow that did not apparently overtop the levees of Eastern Valley. Such a flow is very different than the thick, slow-moving, low concentration, Late Pleistocene flows suggested by Stow & Bowen (1980) from analysis of laminated muds collected from the levees. For these flows, the analysis of Stow & Bowen (1980) suggested velocities of $0.1\text{-}0.15 \text{ m s}^{-1}$ with volume concentrations of 10^{-3} to 10^{-4} and durations of several days to weeks.

6.4 Levee Architecture of Laurentian Fan

6.4.1 Levee Stratigraphy

Prominent reflectors were identified on WLEV (Figure 6.6) and correlated throughout the available seismic data. In order of increasing sub-bottom depth these reflectors are O, Q, B, and A. A and Q are the same horizons as were originally defined by Piper & Normark (1982). At the type section location, the seismic profile consists of alternating packages of acoustically transparent and acoustically well-stratified sediments. Horizon A occurs at the top of a thin package of acoustically well-stratified sediments that is overlain by more acoustically transparent sediment. The transparent package is overlain by another thin package of acoustically well-stratified sediments, the top of which corresponds to horizon B. The pattern is repeated above horizon B with horizon Q identified at the top of an acoustically well-stratified interval. Horizon O occurs at the base of weakly acoustically stratified to acoustically transparent sediments. Between Q and O, the sequence appears weakly acoustically stratified throughout. In general, each horizon on WLEV tends to be flat-lying, with the only significant relief

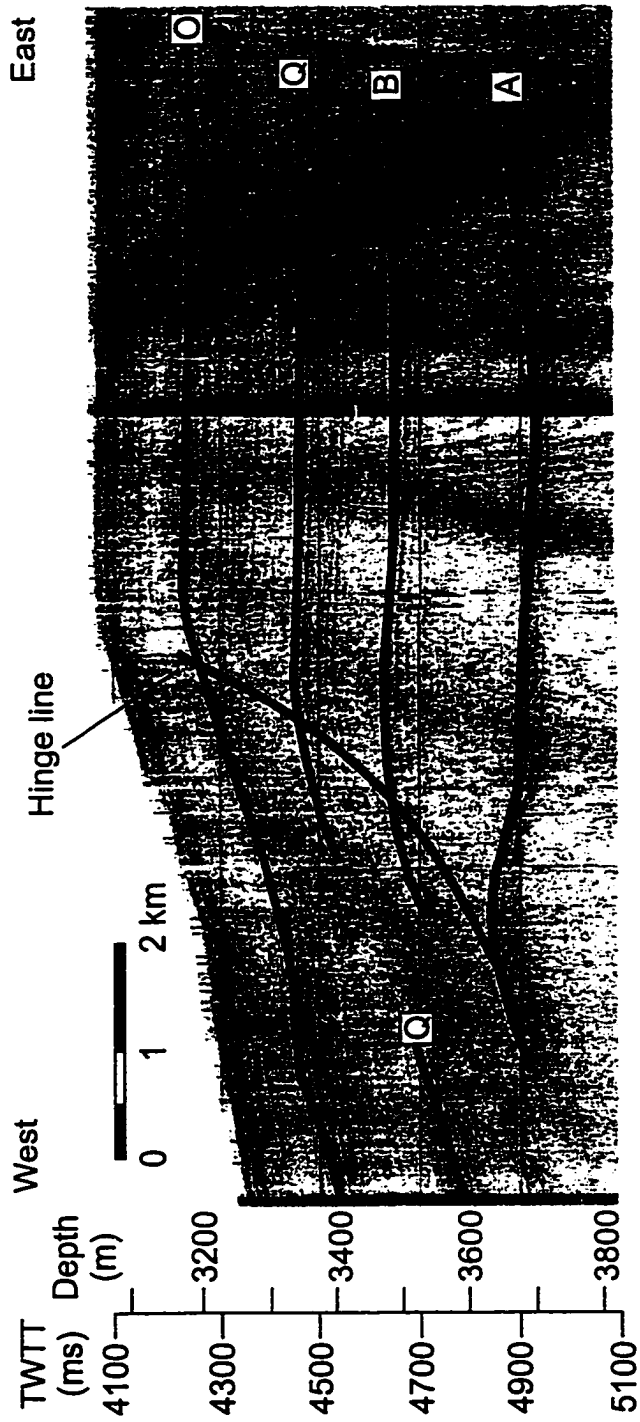


Figure 6.6. Sparker seismic profile across WLEV showing the four regional reflectors identified in this study. Horizon A and Q are identical to reflectors defined by Piper & Normark (1982). Location given in Figure 6.2.

associated with a hinge line (Figure 6.6) identified by Piper & Normark (1982). The thinning of depositional sequences across the hinge line represents the only significant across-levee change in thickness on WLEV. At the resolution of the data, the levee sequence of WLEV appears conformable.

The reflectors were correlated across the channels based on reflector character and stratigraphic position. Horizon A was identified on a multi-channel seismic line (GAD008) where it could be traced from the western levee of Western Valley (WLWV) to the western edge of Eastern Valley (Figure 6.7a, b). Horizon L could be identified under the western levee of Western Valley by correlation with data of Piper & Normark (1982) and Uchupi & Austin (1979). An additional reflector, horizon L', was identified, which overlies horizon L and represents the stratigraphic change from continuous high amplitude reflections to lower amplitude reflections on WLWV. On approaching Western Valley, horizons L and L' merge (Figure 6.7a). Horizon A was correlated across Eastern Valley on the basis of reflector character and relative stratigraphic position above L' (Figure 6.7b,c).

This multi-channel seismic line, GAD008 (Figure 6.7), provides a clear picture of the large-scale structure of Laurentian Fan. The section between L' and A doubles in thickness across Eastern Valley (Figure 6.8). Above horizon A, sediment thickness on WLEV and WLWV is everywhere greater than on ELEV. Thickness of sediment between horizons A and Q is about the same on WLEV and WLWV; however, above Q, the sediment thickness of WLWV is greater than on WLEV, suggesting a westward shift of the locus of maximum sediment accumulation. These patterns suggest that the western side of Eastern Valley has always been the preferential site for sediment accumulation; however, after horizon Q, the western levee of Western Valley received more sediment than western levee of Eastern Valley.

A single-channel airgun seismic profile across WLEV near GAD008 (Figure 6.9) shows a similar, but higher quality, image of the acoustic stratigraphy compared to the sparker (Figure 6.6) or multi-channel data (Figure 6.7b). It shows the same alternation between acoustically well-stratified and acoustically poorly stratified sediments and the same relative thickness between reflectors. In this case, correlation across the hinge line is easier and shows that the thinning of depositional sequences associated with this

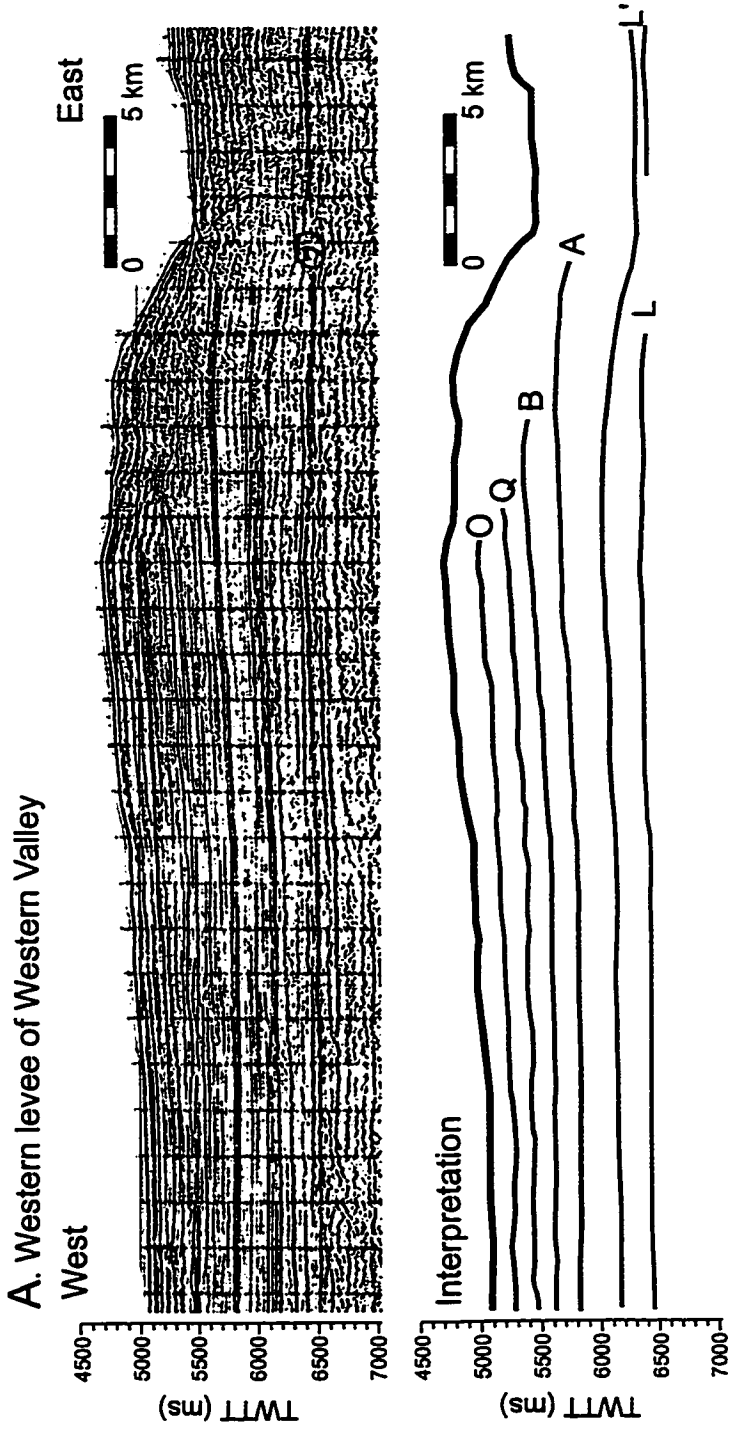


Figure 6.7. A. Multichannel seismic line, GAD008, across WLWV (top) and interpretation (bottom); B. Multichannel seismic line, GAD008, across WLEV (top) and interpretation (bottom); C. Multichannel seismic line, GAD008, across ELEV (top) and interpretation (bottom). Locations given in Figure 6.2.

B. Western levee of Eastern Valley

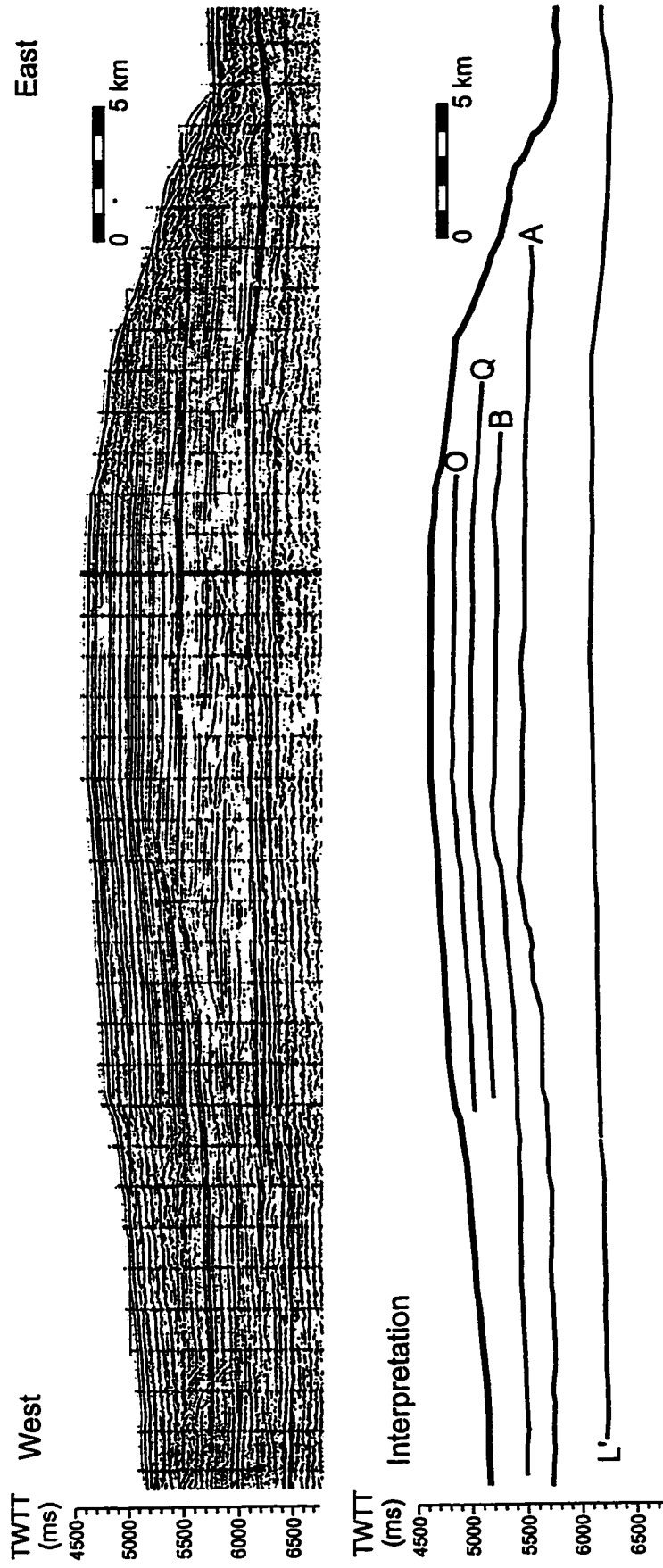


Figure 6.7. Continued.

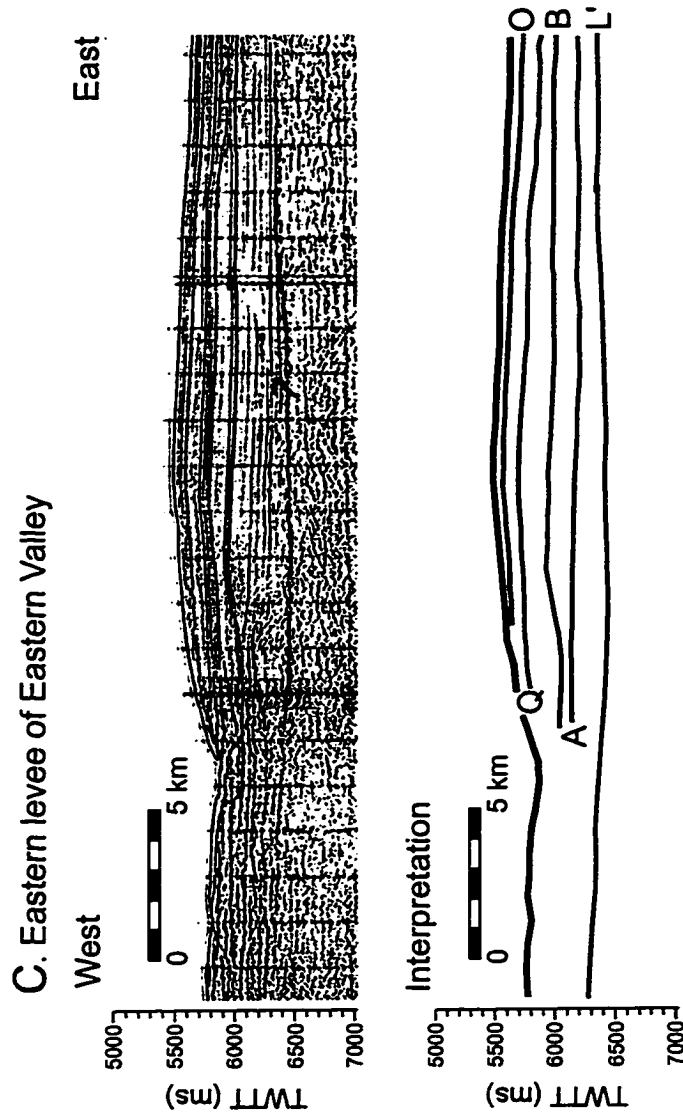


Figure 6.7. Continued.

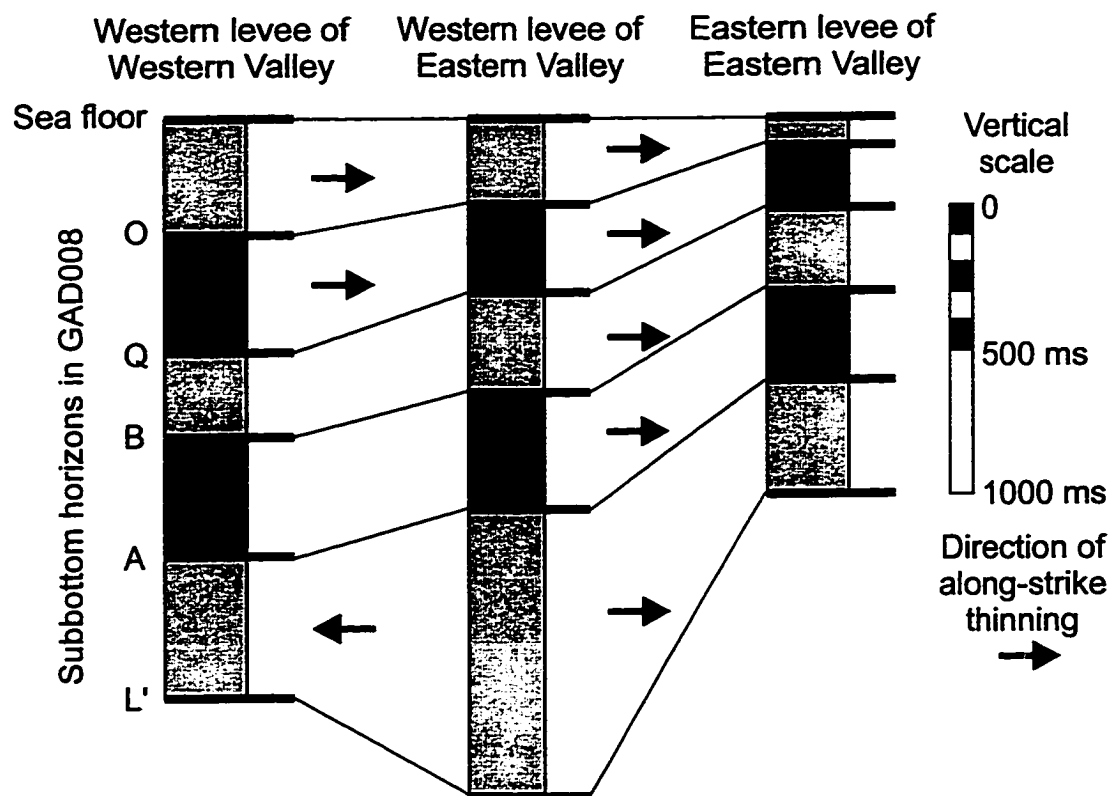


Figure 6.8. Comparison of sediment thickness at crest of fan valleys on Laurentian Fan showing the predominance of sediment accumulation west of Eastern Valley since horizon L' and the shift of maximum sediment accumulation to west of Western Valley since horizon Q.

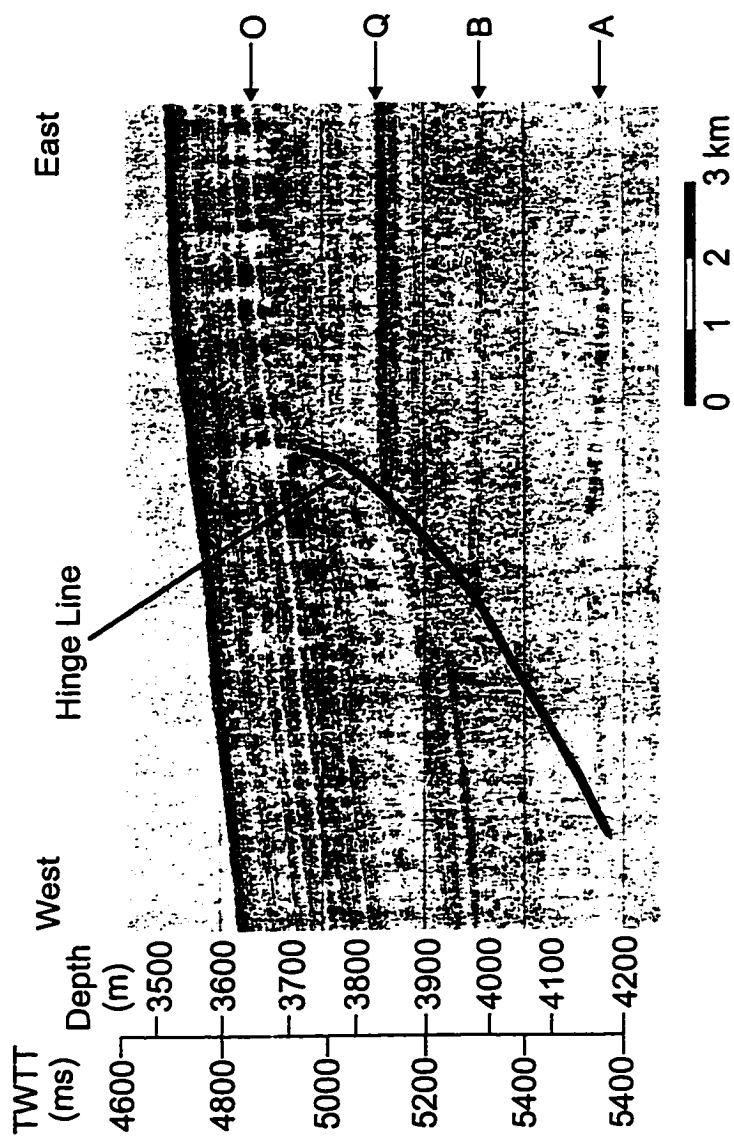


Figure 6.9. Sleevegun seismic profile across WLEV south of type section shown in Figure 6.6. Location given in Figure 6.2.

feature is greatest for the interval between horizons B and Q.

Single-channel airgun data across ELEV (Figure 6.10) close to GAD008 show that this levee has an acoustic character similar to WLEV (Figure 6.6 and Figure 6.9). Again, the levee consists of alternating sequences of acoustically well-stratified sediment and poorly acoustically stratified to transparent sediment. This section also shows several erosional events that post-date horizon A (denoted by arrows in Figure 6.10). The oldest and most significant (i.e., greatest relief) of these occurs about midway between horizons A and B. The erosion appears focused close to the channel. After the erosional event, sediments filled the space apparently created by this channel-widening erosion, first onlapping (labeled OL in Figure 6.10) the relief and then draping it. The next major erosional horizon corresponds to horizon B. Its relief is less than the underlying erosional event, but it is likewise overlain by reflectors that are continuous across the erosional relief. Between B and Q, a package of acoustically well-stratified sediment was deposited that shows only minor evidence for erosion, which is focused above the inflection point in horizon B. Horizon O also corresponds to an erosional horizon. Its relief is mostly inherited from the preexisting topography, and its erosional nature is mainly indicated by hyperbolic returns, indicating a rough surface. These hyperbolic echoes also characterize the seafloor returns suggesting relatively recent erosion of ELEV. The erosional character of ELEV does not extend far from the channel. Away from the channel (toward the east in Figure 6.10), the levee consists of a conformable succession at the resolution of the data. In Figure 6.10 one can see the abrupt transition from eroded levee to conformable levee sediments.

A feature, grossly similar to the hinge line seen on WLEV (Figure 6.9), occurs on ELEV (Figure 6.11). The relief on this feature, unlike the hinge line, appears to coincide with erosion at horizon B that truncates a package of flat-lying reflectors. It is somewhat similar to the erosion seen near Eastern Valley (Figure 6.10), but this surface appears related to erosional downcutting associated with a subsurface debris flow (Figure 6.12). This debris flow appears to erosionally truncate horizon B and thus post-dates this reflector. A second debris flow occurs above horizon Q (Figure 6.12).

ELEV also has a prominent toplap surface (Figure 6.13) that occurs downfan of the confluence between Grand Banks Valley and Eastern Valley. Stratigraphically, the

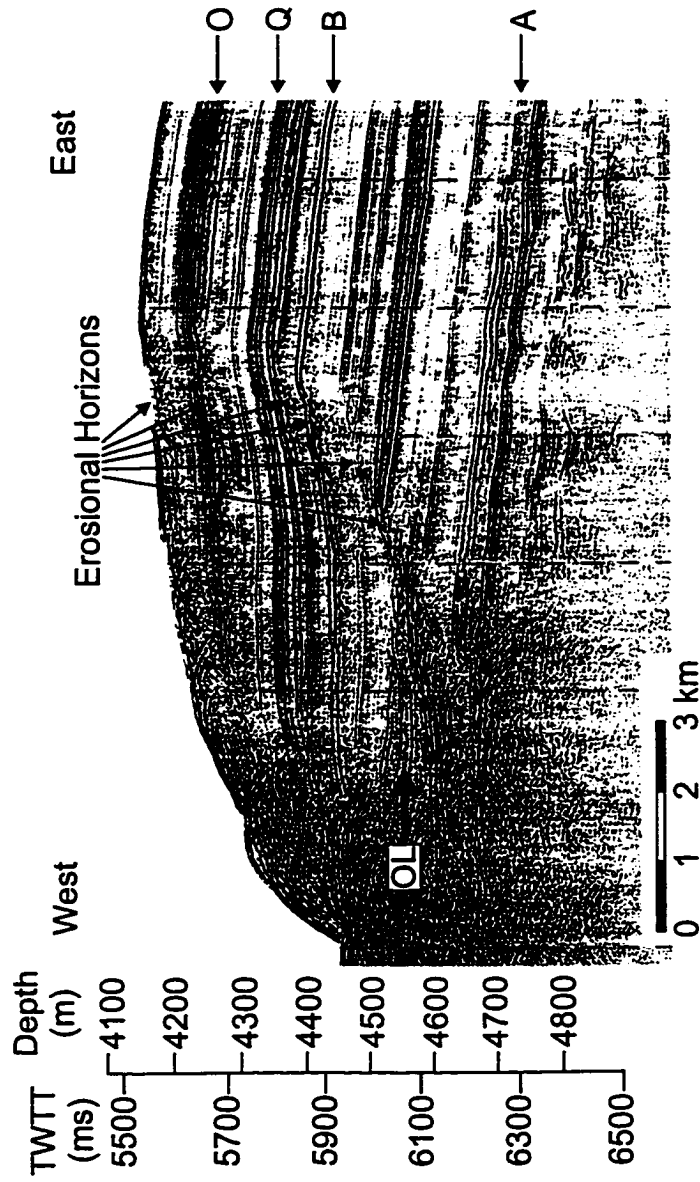


Figure 6.10. Airgun seismic profile across ELEV. Location given in Figure 6.2.

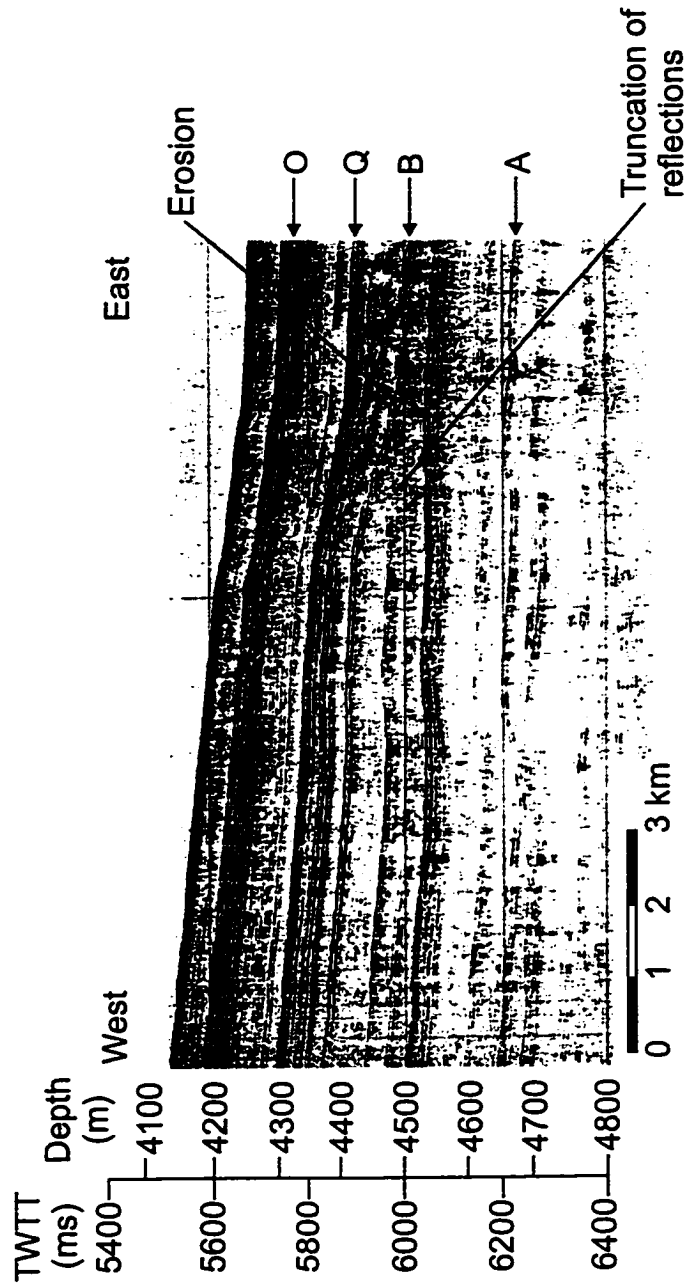


Figure 6.11. Sleevegun seismic profile across ELEV showing erosional surface associated with debris flow. Location given in Figure 6.2.

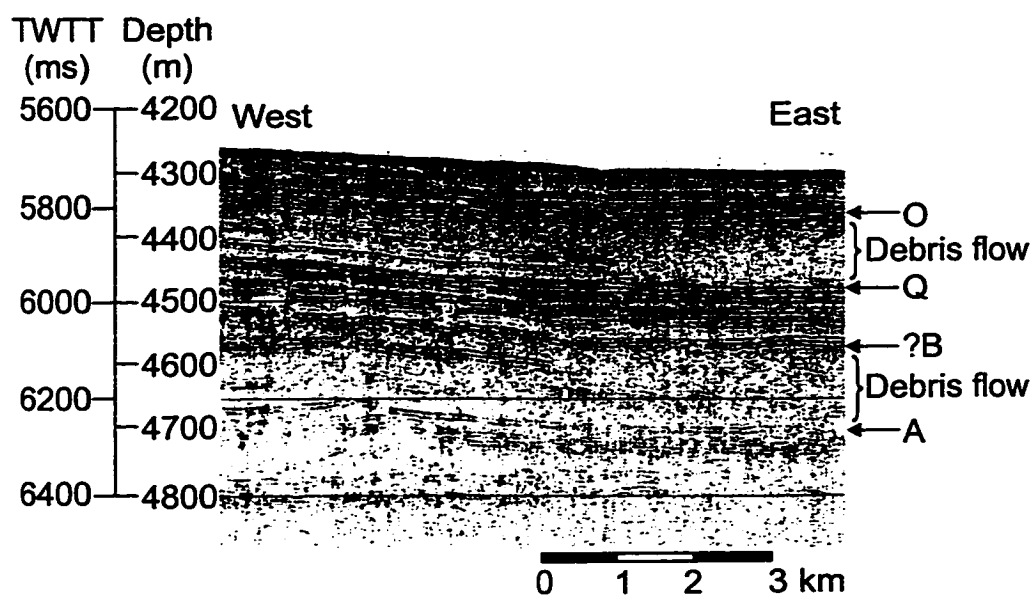


Figure 6.12. Sleevegun seismic profile across ELEV showing debris flows above horizons B and Q. Location given in Figure 6.2.

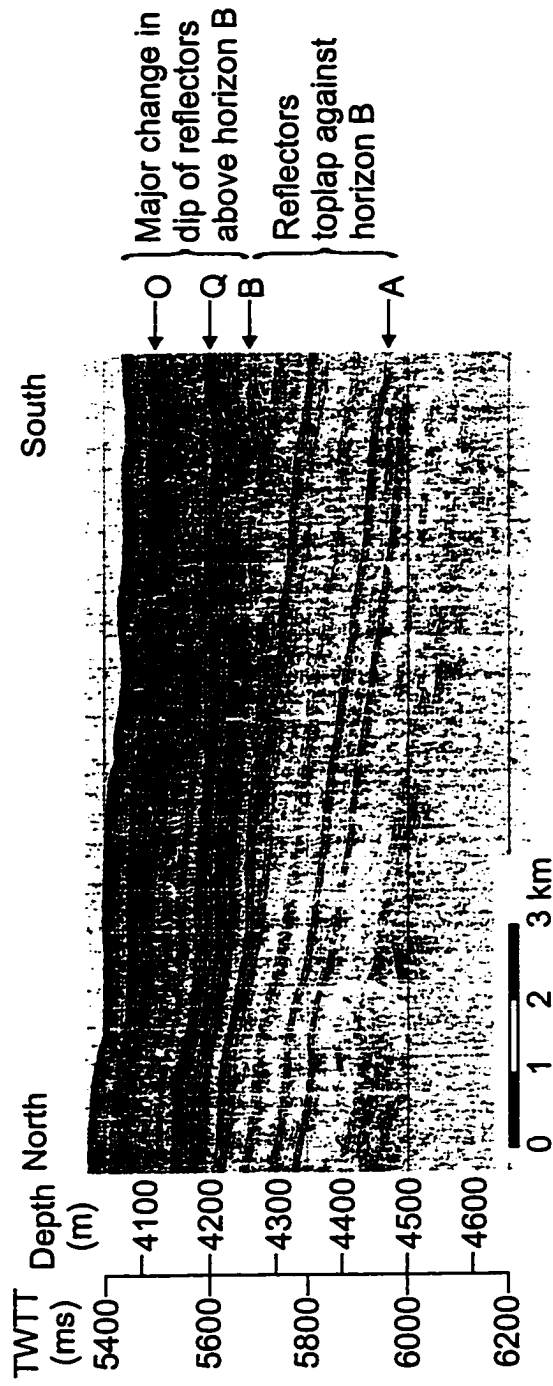


Figure 6.13. Airgun seismic profile along ELEV showing toplap at horizon B. Location given in Figure 6.2.

surface coincides with horizon B, marking an abrupt change in the regional dip of reflectors. Below B and including horizon A, reflectors dip southward at 12 m km^{-1} . Above horizon B, the dip of reflectors decreases by about half to 5 m km^{-1} . In contrast, dip lines along WLEV and WLWV display sub-parallel reflectors, gently dipping south (Figure 6.14 and Figure 6.15).

On WLWV, the regional stratigraphy could be correlated into four of five channel-perpendicular cross-sections spanning a distance of 140 km down Western Valley (Figure 6.2). At cross-sections 3 (Figure 6.16) and 4, two additional horizons were correlated, G and P, refining the stratigraphy of the sequence above horizon O. At cross-section 3 on WLWV, which has a similar acoustic stratigraphy to cross-sections 4 and 5, horizons A and B appear as low relief reflectors, consisting of moderate amplitude reflections. The interval between A and B, like on WLEV and ELEV, spans acoustically transparent to weakly acoustically stratified sediment. Horizon Q at this cross-section has moderate relief. The interval between B and Q shows two phases of development. The basal sequence unit consists of subparallel, low amplitude reflections that is qualitatively similar to the underlying interval between A and B. The overlying sequence shows relief development. This relief appears to be predominantly depositional and may reflect the growth of sediment waves. The interval between Q and O also can also be divided in two sequences, based on reflection amplitude and topographic relief. The basal sequence comprises low amplitude reflections and shows some evidence for upslope migration of the wave forms. The overlying sequence consists of high amplitude reflections; the wave forms still show evidence for upslope migration, but wave amplitude decreases upsection until only subtle relief exists at horizon O. Horizon O returns hyperbolic echoes in some places, suggesting increased surface roughness probably due to erosion. Above O, the sediments appear acoustically well-stratified. No significant change in acoustic character differentiates the intervals between O and P, P and G, and G and the seafloor.

At cross-section 2 on WLWV, only horizon O and Q could be confidently identified (Figure 6.17). Horizon Q at cross-section 2 has low relief, markedly different from its character at cross-section 3. The observable sequence above Q is no more than 150 m thick, substantially thinner than at cross-section 3 where this same interval is around 300 m thick. Direct comparison of thickness is hampered by the limited data

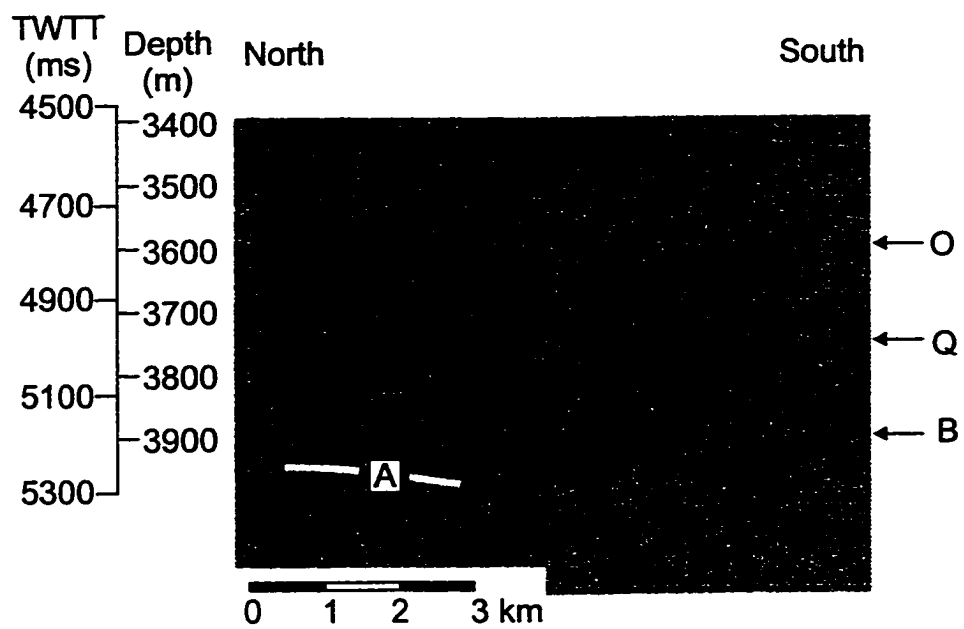


Figure 6.14. Sleevegun seismic profile along WLEV. Location given in Figure 6.2.

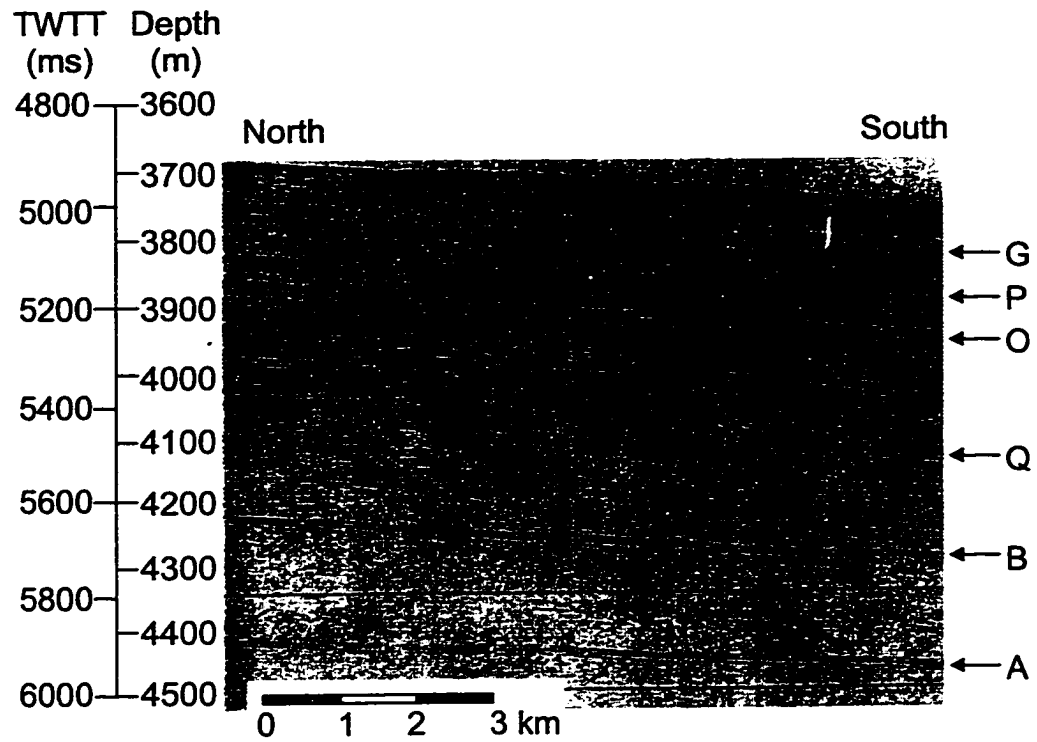


Figure 6.15. Sleevegun seismic profile along WLWV.
Location given in Figure 6.2.

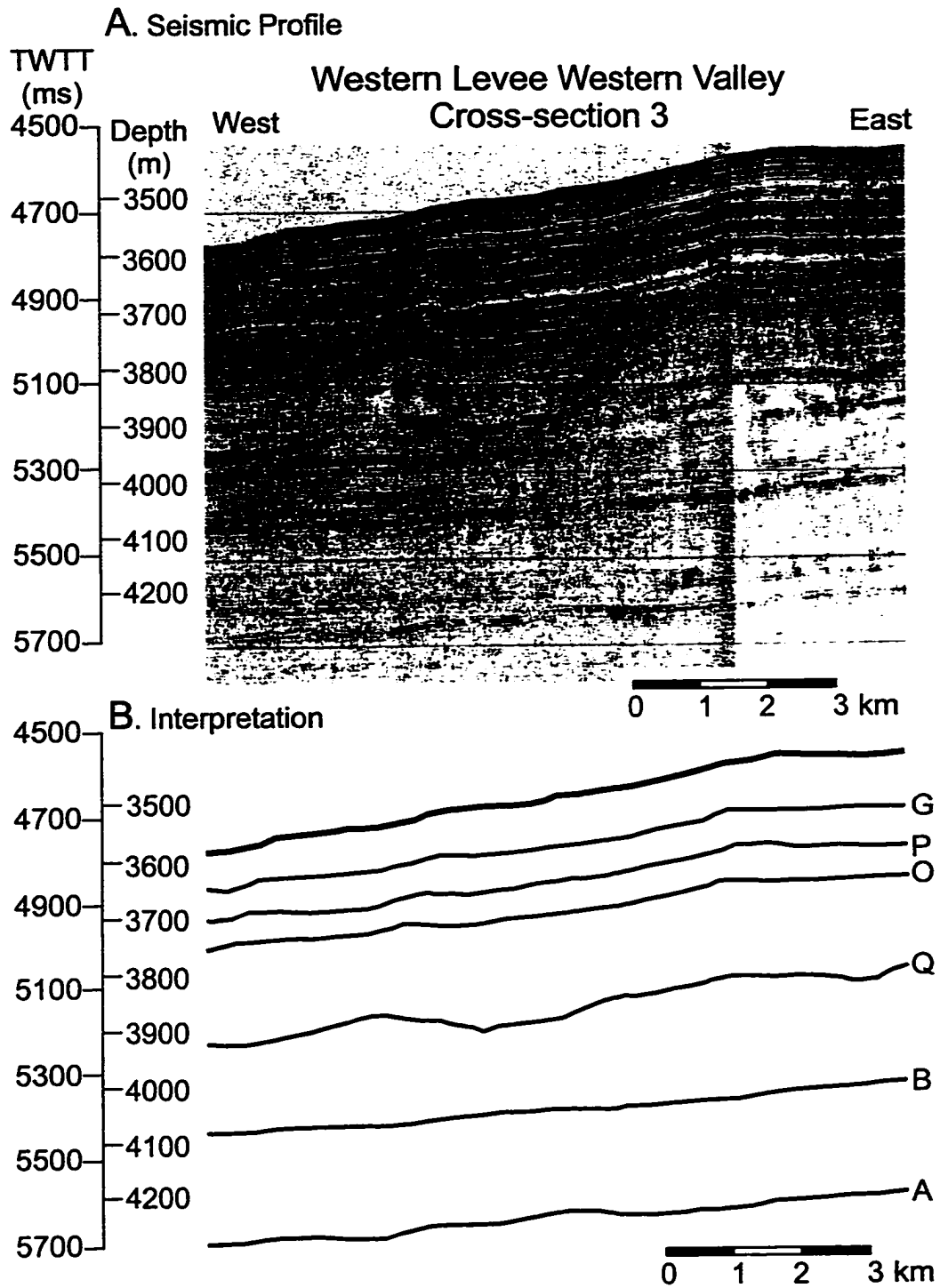


Figure 6.16. Sleevegun seismic profile of WLWV at cross-section 3. Location given in Figure 6.2.

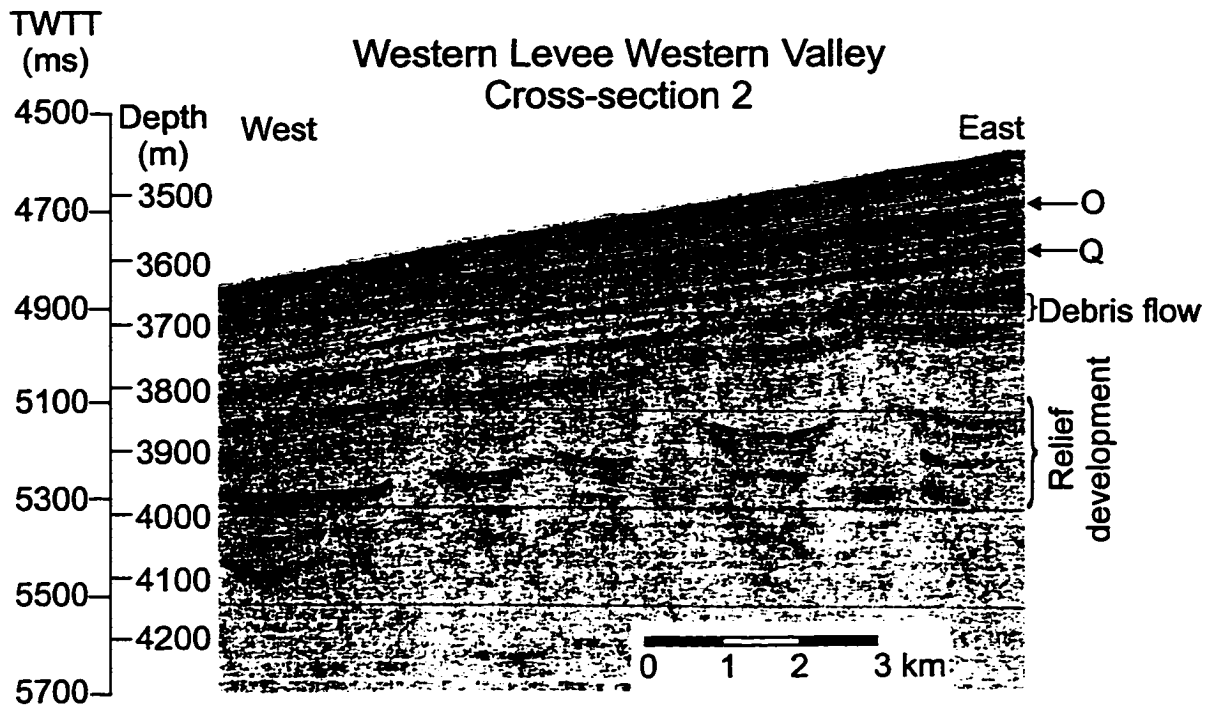


Figure 6.17. Sleevegun seismic profile of WLWV at cross-section 2. Location given in Figure 6.2.

coverage and the erosive character of the levee crest at cross-section 2. The simplest interpretation of the change in thickness between cross-sections 2 and 3 is that the sediment eroded from the levee crest at cross-section 2 was deposited at cross-section 3 and beyond. However, the levee becomes depositional at a distance of 15 km from the channel axis, only 5 km from the eroded levee crest, and the thickness of sediment above Q at this location is approximately 150 m. At cross-section 3, the sequence above Q is not observed to decrease to a thickness of 150 m where the levee is depositional. Projecting the spatial rate of thinning for the interval above Q suggests that this interval would be around 150 m thick at distances more than 50 km from the channel axis. While it cannot immediately discount erosion as an important factor in the downchannel channel increase in thickness, the geometry of the levees tends to support the contention that the increase in sediment thickness between cross-section 2 and 3 is accounted for by more than just erosional removal of sediment.

On WLWV at cross-section 2, the stratigraphy below horizon Q is masked by the presence of a debris flow (Figure 6.17). The debris flow thickens to the west (Figure 6.18) where it can be tentatively placed above horizon B. A surface debris flow is apparent near cross-section 2 which, while smaller than the subsurface example, has similar acoustic character. This debris flow also thickens westward. Beneath horizon Q, the reflectors have high relief (labelled relief development on Figure 6.17) which may be sediment waves, an artifact in the data, or result from the presence of gas in the sediments.

High quality 3.5 kHz profiles were analyzed at cross-section 2 and 3 in order to quantify the near surface geometry of levee architecture. A sub-bottom horizon, R1, could be directly correlated between the cross-sections. At cross-section 3 (Figure 6.19), this horizon occurs within an otherwise acoustically transparent interval above a distinct package of acoustically well-stratified sediments. Above R1, the sediments are moderately acoustically stratified. At cross-section 2 (Figure 6.20), the sediments above R1 also show moderate acoustic stratification. Beneath R1, the distinct package of acoustically well-stratified sediment has substantially lower amplitude.

Four cores from Laurentian Fan were chosen to constrain the late Quaternary stratigraphy and sedimentology of the levees (Figure 6.21). Three of these cores, MD95-

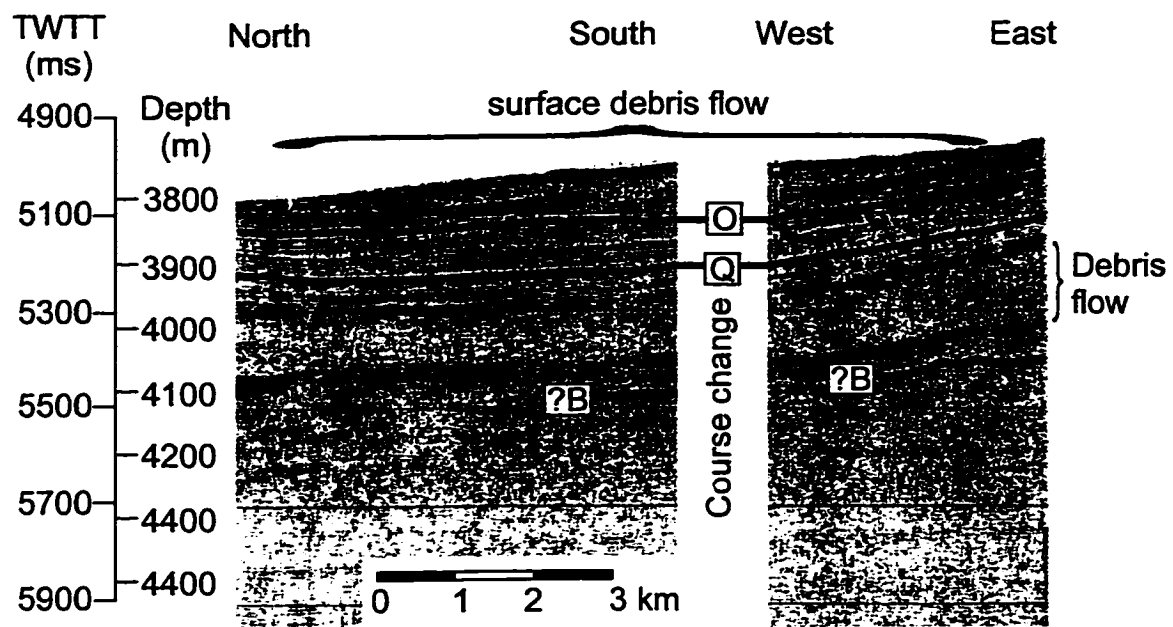


Figure 6.18. Sleevegun seismic profile of WLWV near cross-section 2 showing debris flows. Location given in Figure 6.2.

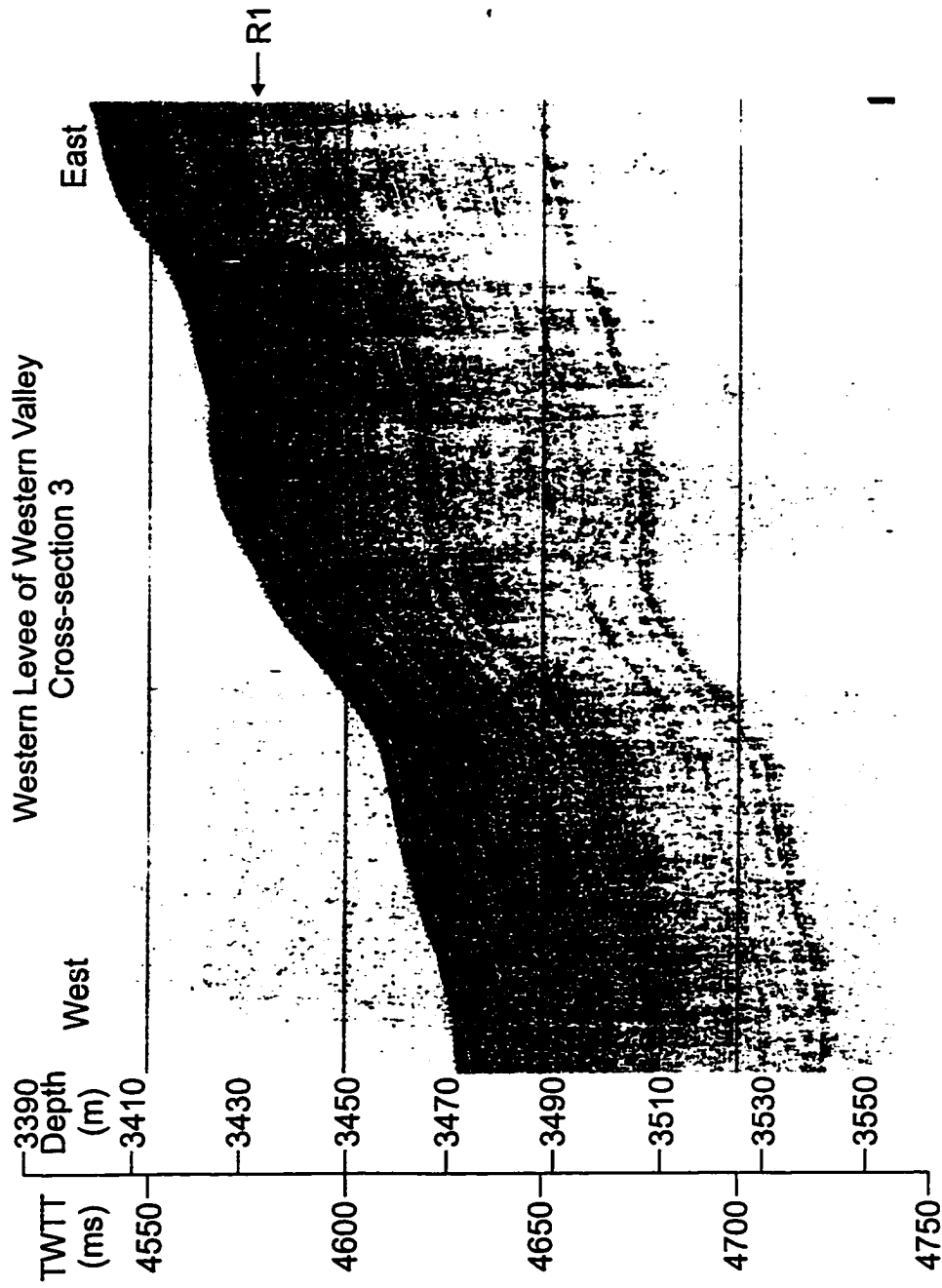


Figure 6.19. 3.5 kHz profile of WLWV at cross-section 3. Location given in Figure 6.2. Apparent sediment wave morphology inherited from relief developed around horizon Q.

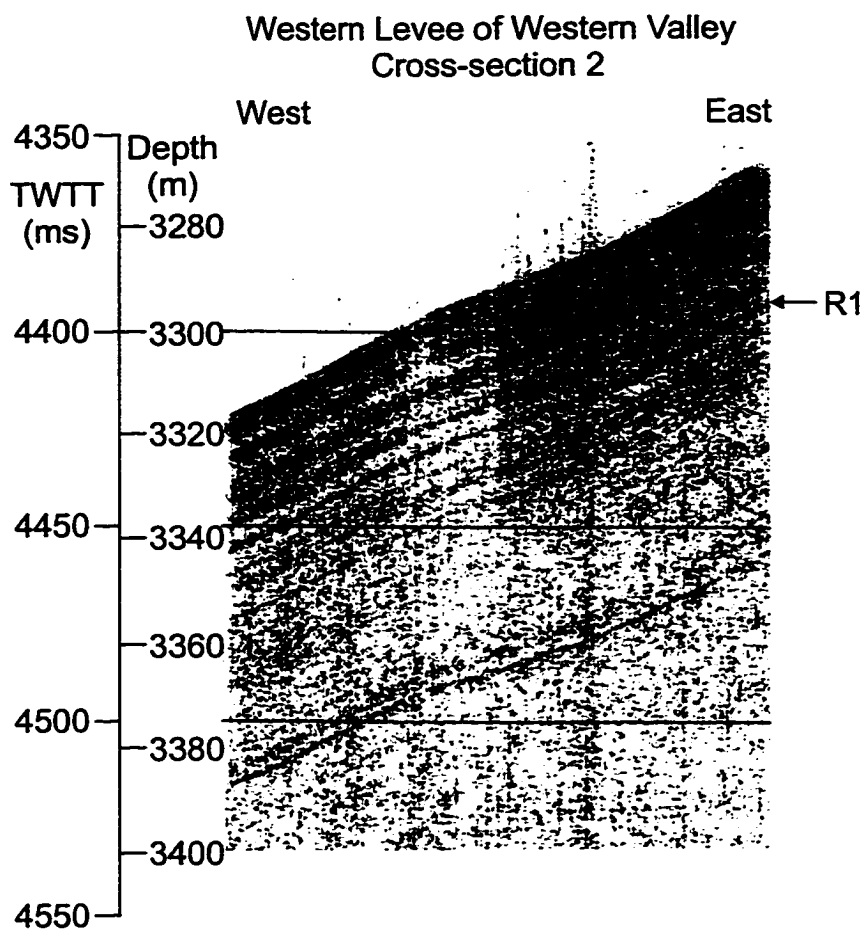


Figure 6.20. 3.5 kHz profile of WLWV at cross-section 2.
Location given in Figure 6.2.

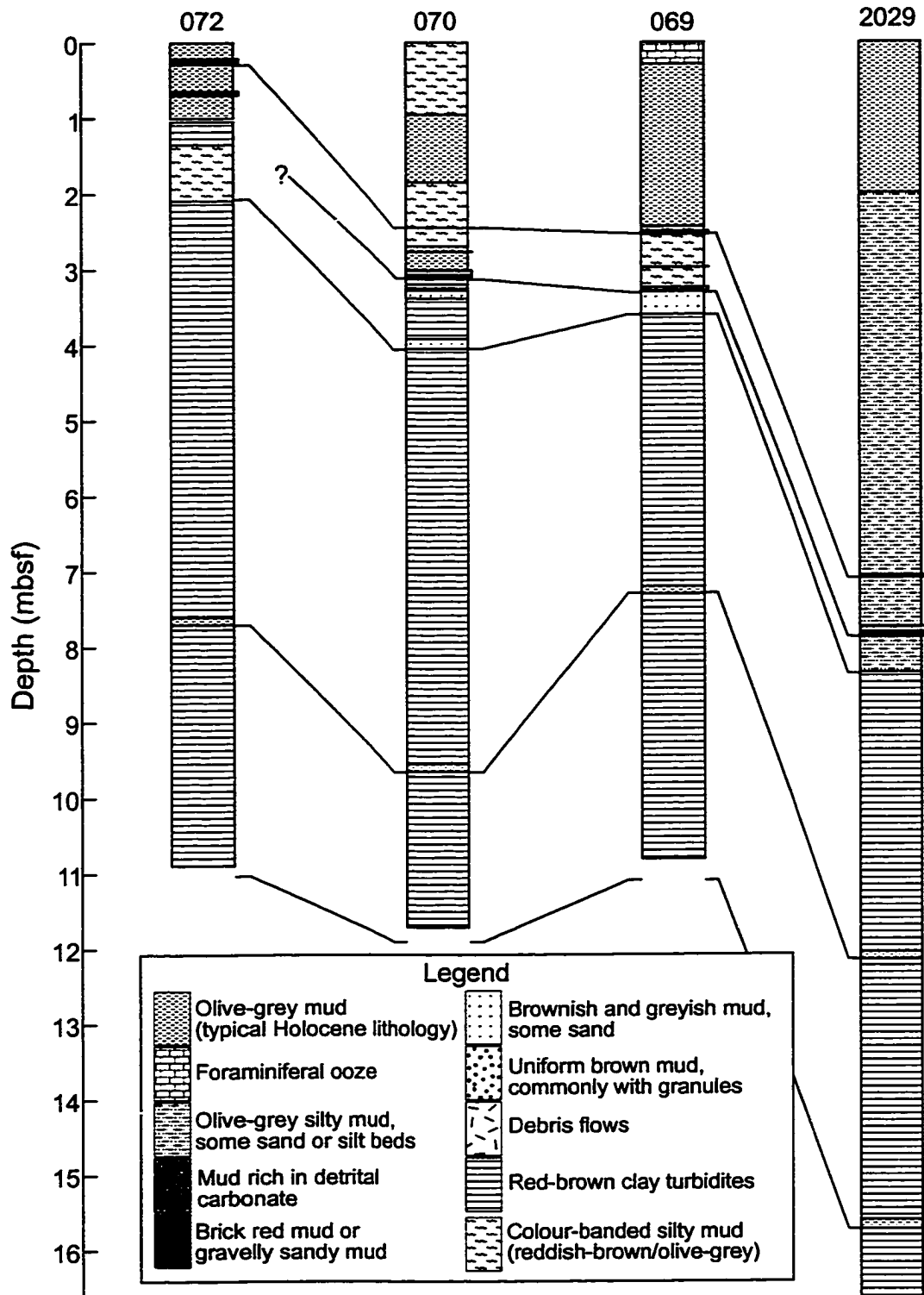


Figure 6.21. Summary descriptions of selected piston cores. Correlations based on sub-bottom occurrence of marker beds including brick-red sandy muds, light grey, gravelly muds rich in detrital carbonate, and intervals of bioturbated, olive-grey silty mud within the reddish-brown laminated muds.

2029 (core 2029), 92029-069 (core 069), and 92069-070 (core 070) form an east-west transect across Laurentian Fan, each sampling sediments from a levee crest (Figure 6.2): core 2029 was collected from the crest of ELEV, core 069 was collected from the crest of WLEV, and core 070 was collected from the crest of WLWV. Core 070 coincides with cross-section 4. The fourth core, 96029-072 (core 072) samples the flank of WLWV at cross-section 2.

Core 2029 is the longest piston core collected from Laurentian Fan, penetrating over 30 m below the seafloor, although coring disturbance may have expanded muddy sections by as much as 50%. The stated sub-bottom depths for core 2029 are uncorrected for possible disturbance. In its upper 16 m, core 2029 has three major lithologic units, interspersed with several key marker beds (Figure 6.21). The uppermost lithologic unit consists of olive-grey, bioturbated silty mud, generally thought to reflect Holocene hemipelagic deposition on the eastern Canadian continental margin (e.g., Hill, 1984). The middle unit consists of olive-grey mud with several fine sand beds. Within this unit, three marker beds occur. Two of these are brick-red sandy muds and the third is a light grey, sandy mud, rich in detrital carbonate. Reddish-brown muddy turbidites, many with basal silt laminae, compose the third unit in core 2029. This unit extends from about 8.2 m to 27 m in core 2029. Within the turbidite unit, thin intervals of bioturbated, olive-grey silty mud occur that divide the reddish-brown turbidites into discrete units.

The marker beds allow for a detailed correlation between the cores, showing two major features. Correlation of the thin hemipelagic units within the reddish-brown turbidite succession suggests that the uppermost sequence of turbidites thickens to the west. It is 3-4 m thick in cores 2029 and 069 and over 6 m thick in cores 070 and 072. These cores along with those presented by Stow (1977) suggest that deposition of reddish-brown, fine-grained turbidites was widespread and represents deposition between 21 ka and > 14.5 ka, spanning the last glacial maximum and early deglacial period (Piper & Skene, 1998). Correlation of the ice-rafted deposits suggests that the late deglacial history of Laurentian Fan, i.e., post 14.5 ka, displayed a complex interplay between shifts in sediment source and changes in depositional mechanism.

Turbidite deposition on Laurentian Fan represented by the laminated reddish-brown muds does not show any significant change within the section sampled by piston

cores. For cores 069, 070, and 072, in lieu of measuring bed thickness, the number of laminae per metre was tabulated in order to investigate possible trends in turbidite character (Figure 6.22). These data show that sediment character in terms of laminae per metre is uniform down core 069, slightly more variable down core 070, and shows a weak increase down core 072.

The same uniformity in sediment character appears in grain size analyses (Figure 6.23). For core 2029, core 010, and core 011, selected grain size analyses performed by Schell (1996) are presented. In all these analyses, the grain size spectra are similar, suggesting no major changes in the grain size of the levee sediments. In a more detailed study of grain size variations in these and other cores from Laurentian Fan, Schell (1996) reported no major downcore trends.

6.4.2 Stratigraphic Evolution

From horizon L to A, Laurentian Fan had a single leveed fan valley that followed the trend of the present Eastern Valley (Piper & Normark, 1982). Within Eastern Valley, acoustically stratified, intrachannel highs exist, suggesting that Eastern Valley was narrower than at present (Piper & Normark, 1982). Even with the erosional widening of Eastern Valley, the relative elevation difference of horizon A across Eastern Valley places an upper limit of 400 m on the elevation difference between conjugate levees around A. This substantial asymmetry could be entirely due to the action of the Coriolis force, as has been suggested on Var Fan (Savoye et al., 1993; Piper & Savoye, 1993). Although erosional widening of the channel has removed the eastern levee crest, the dip of reflectors suggests that it would not have been much less than 300 m below the western levee crest. Beneath the present western levee of both Eastern and Western Valley, the levee sediments deposited between L and A consist of acoustically transparent material that thins to the west. The sediments beneath the eastern levee of Eastern Valley have a similar acoustic character and thin eastward. Above A, ELEV has 500 m of sediment compared to over 1 km of sediment beneath WLEV and 900 m of sediment beneath WLWV. Sediment accumulation was focused to the west in accordance with either deflection of flows by the Coriolis force or bottom currents. Comparison of any particular interval shows that preferential sediment accumulation west of Eastern Valley

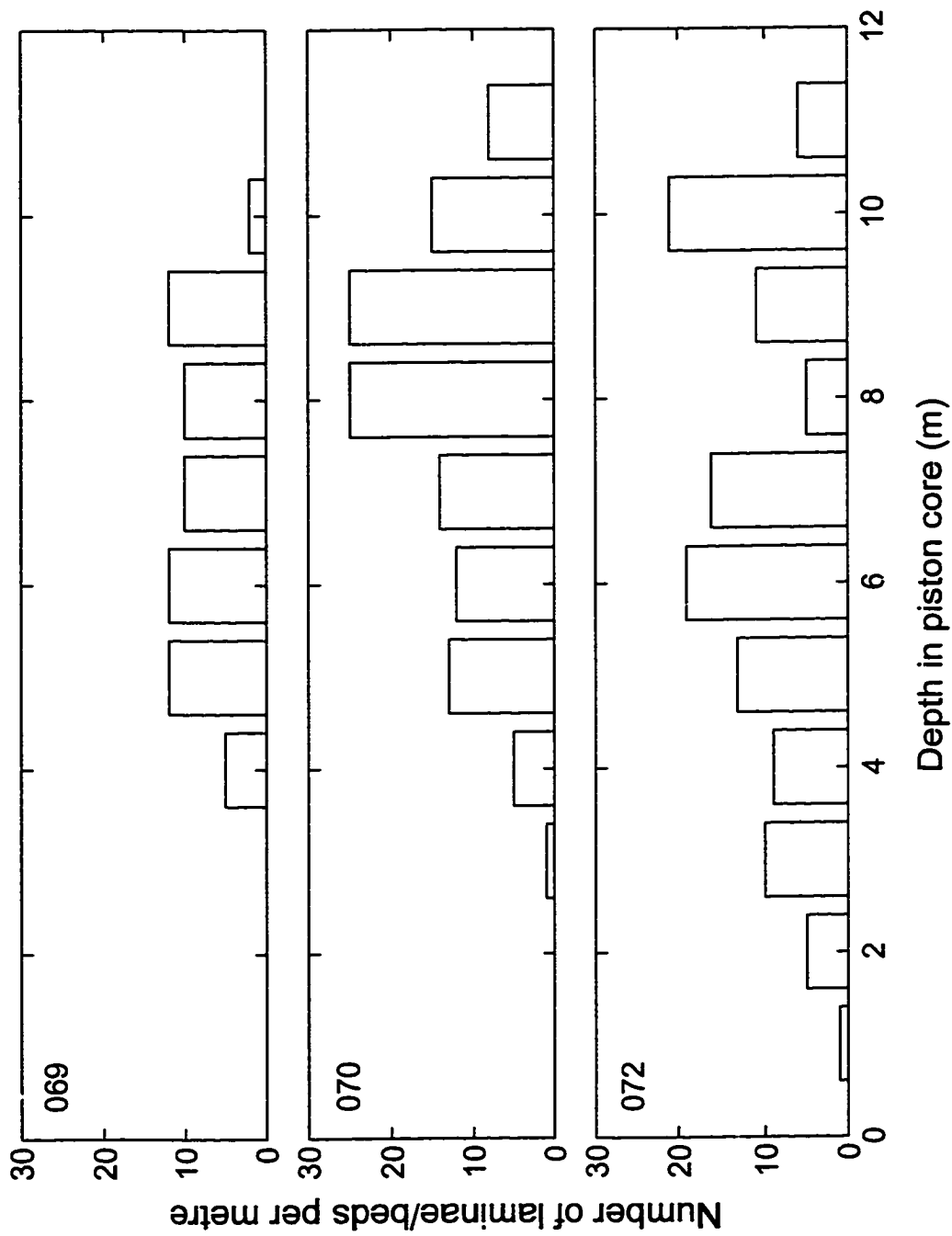


Figure 6.22. Frequency of laminae or beds per metre of sections for cores 069, 070, and 072.

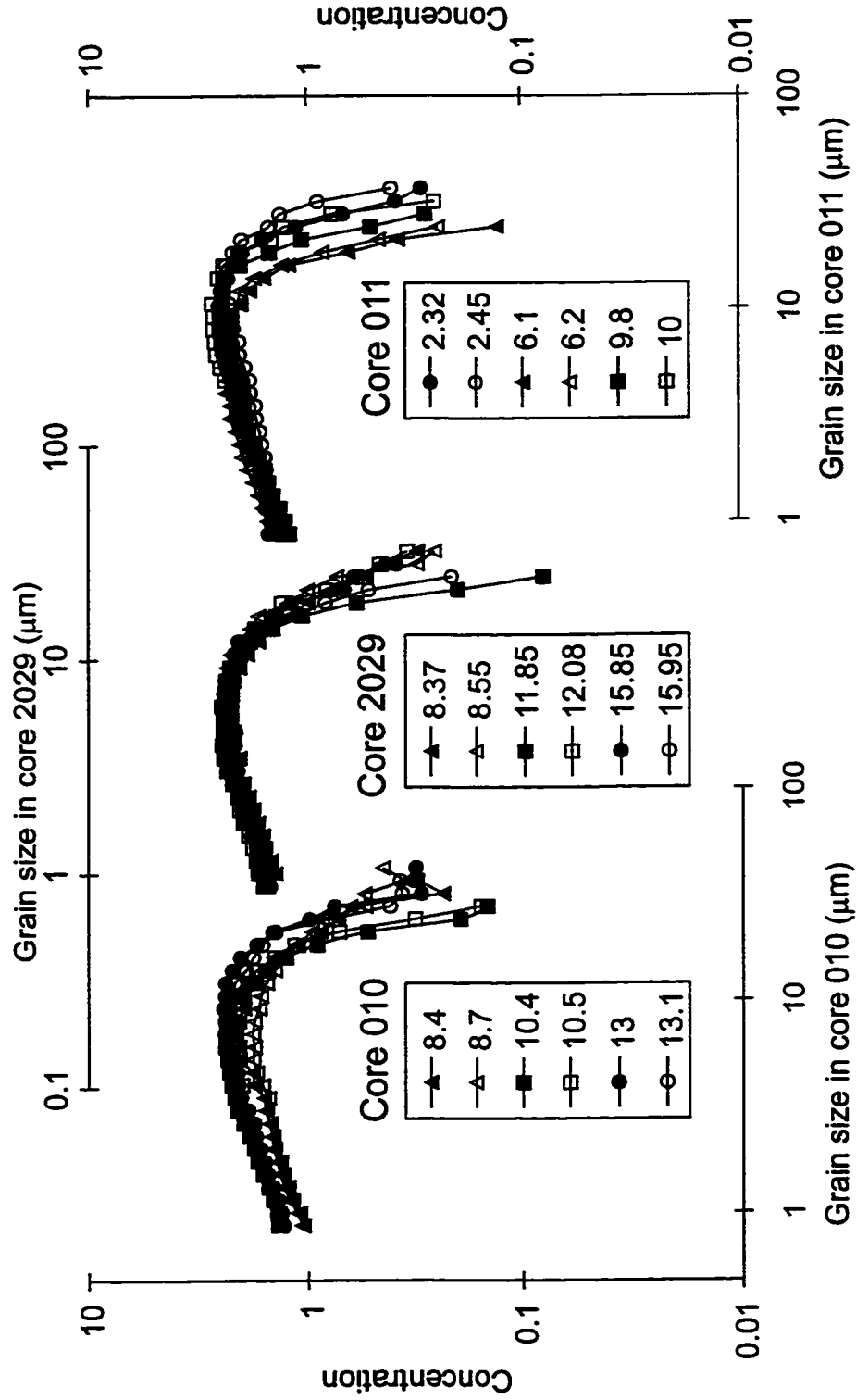


Figure 6.23. Summary of grain size analyses on Laurentian Fan (data from Schell, 1996). Legend for each core denote depth in piston from which sample was taken.

persisted throughout the history of the fan, but may have moved from WLEV to WLWV above Q.

Between horizons A and B, the sediments accumulated without a significant stratigraphic change in character. Beneath WLWV, WLEV, and on the distal portion of ELEV the sediments appear acoustically transparent to weakly stratified. Relief developed on horizon A created a hinge line on WLEV. Piper & Normark (1982) interpreted the thinning of depositional sequences across the hinge line to be the result of local flow acceleration and reduced deposition. Such an interpretation suggests that flows originated from Eastern Valley. Another notable feature associated with Eastern Valley is the presence of a prominent erosional horizon adjacent to the channel (Figure 6.10). This erosion appears to have removed channel-proximal sediment, leaving a high relief surface during the time between A and B that was filled by onlapping and then draping sediments. The acoustic character of the onlapping sediment fill suggests sandier sediments. Above this, a package of continuous, low amplitude reflections overlies the erosion surface, suggesting a return to deposition of predominantly muddy sediments. At horizon B, the ELEV displays a toplap relationship with underlying reflectors (Figure 6.13) which suggests a major reorganization of depositional patterns at least for the eastern side of Laurentian Fan. This change could correlate with the formation of Grand Banks Valley.

The interval between B and Q displays several events. Just above B, a debris flow is found on the flank of WLWV and could be associated with the initial excavation of Western Valley. On WLWV, the interval between B and Q below the confluence of Western Valley with Central Valley shows the development of local relief that could be sediment waves. These wave forms appear to migrate eastward suggesting that they were sourced from flows originating to the east and may represent the initial deposition associated with flow down Western Valley. Beneath WLEV, the interval between B and Q is almost identical to the underlying sequence between A and B. The hinge line continued to be the only major influence of depositional patterns. On ELEV, horizon B corresponds to an erosional event similar to that seen between horizons A and B. This event did not create as much erosional relief as the previous episode.

Between horizons Q and O, the irregular relief on WLWV gradually lessened until it was essentially removed by erosion at O. The interval between Q and O displays a distinct change in reflection amplitude that correlates with the decrease in wave migration. The relief developed on horizon Q decreased only slightly within the low amplitude interval, but lessened substantially within the overlying, higher amplitude sequence. Active migration of the wave forms characterized the low amplitude zone; during deposition of the high amplitude reflections, movement of the wave forms lessened substantially and their relief gradually diminished. Again, WLEV showed no change in depositional character. Between Q and O on ELEV, deposition continued to be influenced by erosional events that appear to have removed channel proximal sediments. These events did not create the same level of erosional downcutting, suggesting less powerful flows.

Above horizon O, the levees continued to aggrade. On both WLWV and WLEV, the depositional sequence above O consists of weakly to moderately acoustically stratified sediments. The relief on WLWV created by sediment waves below O propagated upsection, but no evidence for wave migration or increases in wave amplitude is seen. Thus the flow conditions responsible for sediment wave growth did not characterize flows above O. Erosional events still appear to have affected the architecture of ELEV, but these events have even less downcutting than the underlying interval between Q and O, suggesting a continued decrease in flow power, perhaps because levee aggradation increased channel depth, tending to contain more of the erosive portion of flows within the channel.

6.4.3 Levee Architecture

Thickness Patterns

Thickness patterns on the levees of Laurentian Fan were investigated for the western levee of Western Valley (WLWV) at four cross-sections. Architecture was studied at the highest possible resolution allowed by the available data. At cross-sections 2 and 3, this meant the investigation of 3.5 kHz profiles. However, because high quality 3.5 kHz data were not available for each cross-section, the airgun data were also used to characterize levee architecture above horizon O. For cross-sections 3 and 4, the

stratigraphy could be refined to include horizons G and P. The thickness patterns identified in the airgun data are for the interval between O and the seafloor for cross-sections 2 and 5 and for the interval between G and the seafloor at cross-sections 3 and 4.

The depositional sequence between R1 and the seafloor was identified in 3.5 kHz data from cross-sections 2 and 3 (Figure 6.24a,b). These data show that the near-surface sediments thin away from the channel axis. The regression data show that this thinning conforms to an exponential trend (Table 6.1). The decay constant, k , and thickness at the levee crest, η_{lc} , both increase between cross-section 2 and 3.

The thickness patterns for two depositional sequences were quantified. The first depositional sequence lies between horizon G and the surface. It could be identified at cross-section 3 and 4. Like in the high resolution data the depositional sequence thins with increasing distance from the channel axis. For this sequence, however, the thinning appears to be more linear than exponential (Figure 6.24c, d). Nevertheless, the data could be adequately fit by the exponential model (Table 6.2) and such was done so as to retain consistency between systems. Even though the interval between horizon G and the seafloor is more than twice as thick at the levee crest than the high resolution depositional sequence, the value of k is not statistically different at the 95% confidence level (compare Table 6.1 and Table 6.2). Between cross-sections 3 and 4, the decay constant for the interval between horizon G and the seafloor is not statistically different while η_{lc} decreases.

Table 6.1. Summary of regression parameters calculated for thickness patterns in 3.5 kHz data. k = decay constant, δk = 95% confidence limits around decay constant, η = y-intercept of regression equation, $\delta \eta$ = 95% confidence limits around y-intercept, r = correlation coefficient, y_{lc} = distance from channel axis to levee crest, η_{lc} = depositional sequence thickness at levee crest.

Section	k $\times 10^{-5}$ (m^{-1})	δk $\times 10^{-5}$ (m^{-1})	η (m)	$\delta \eta$ (m)	r	y_{lc} (km)	η_{lc} (m)
2	1.5	0.2	34.9	2.1	0.95	-10.33	29.9
3	2.3	0.4	47.5	2.1	0.95	-11.38	36.6

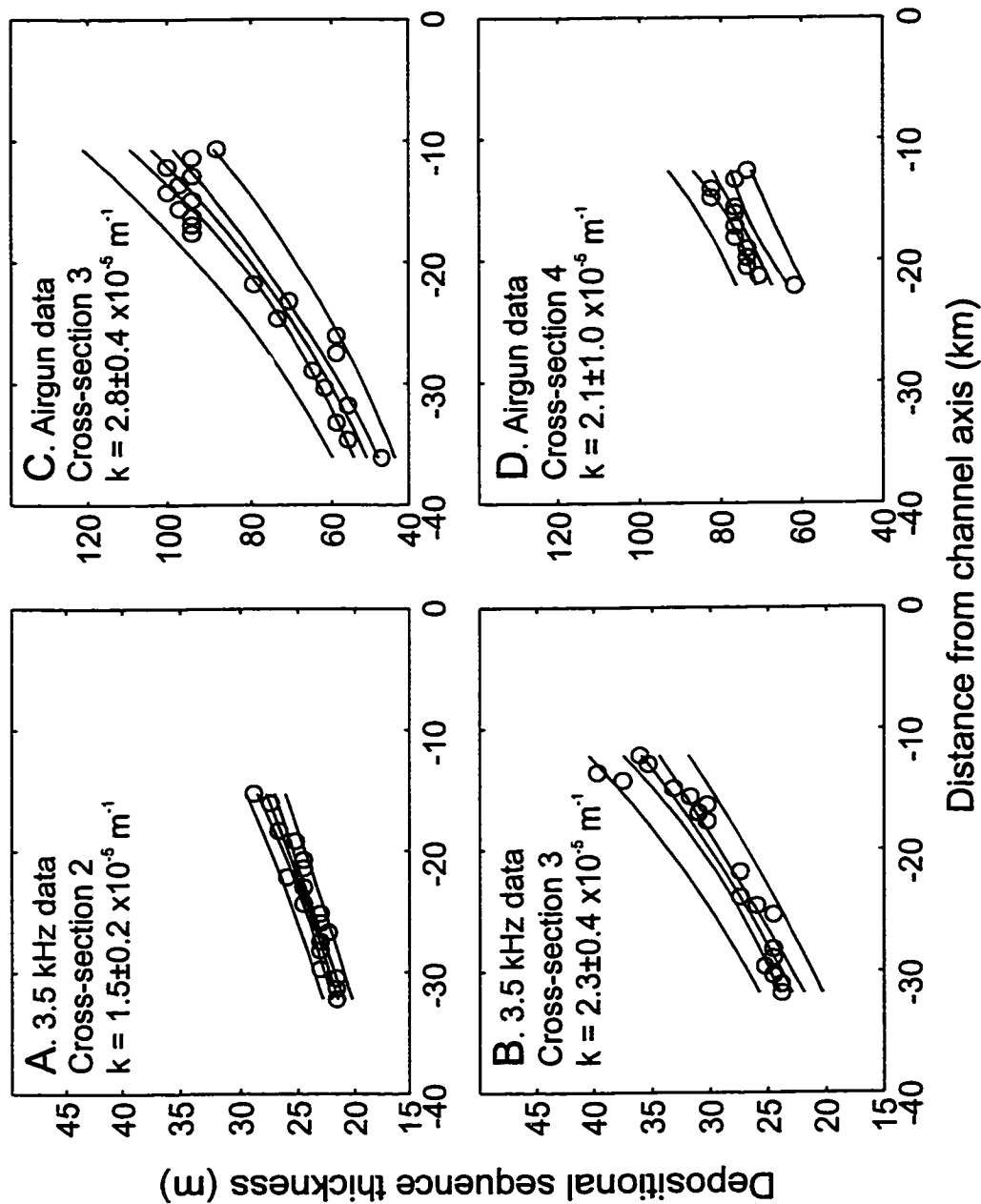


Figure 6.24. Thickness variations for interval above R1 in 3.5 kHz data: A. cross-section 2; and B. cross-section 3. Thickness variations for interval above horizon G in airgun data; C. cross-section 3; and D. cross-section 4. Location of cross-sections given in Figure 6.2. Value of decay constant for across-levee variations in thickness, k , also reported with 95% confidence limits.

Table 6.2. Summary of regression data for thickness variations between horizon G and the surface. See Table 6.1 for explanation of symbols.

Section	k $\times 10^{-5}$ (m^{-1})	δk $\times 10^{-5}$ (m^{-1})	η (m)	$\delta\eta$ (m)	r	y_{lc} (km)	η_{lc} (m)
3	2.8	0.4	140.1	12.6	0.95	-11.38	101.9
4	2.1	1	107.0	20.2	0.76	-10.14	86.5

The second depositional sequence identified in the airgun data lies between horizon O and the seafloor. It is the only depositional sequence that could be identified at all four cross-sections. The variations in the thickness of this depositional sequence also display thinning with distance from the channel axis (Figure 6.25). Again, the thinning could be described as linear, but instead it was fit to an exponential model. Compared to cross-sections 1 and 4, the decay constant is low for cross-sections 3 and 4 while η_{lc} is much greater. Comparison of Table 6.2 and Table 6.3 shows that the decay constant calculated for the interval above horizon G is slightly greater than for the interval overlying horizon O. It is likely that, between horizons O and G, thickness is more uniform. However, taking into account the errors on k , the difference between the two depositional sequences is very minor. In fact all the data for Laurentian Fan, regardless of the resolution at which depositional sequences are defined suggest that the decay constant varies between $1-3 \times 10^{-5} m^{-1}$.

Table 6.3. Summary of regression data for thickness variations between horizon O and the surface. See Table 6.1 for explanation of symbols.

Section	k $\times 10^{-5}$ (m^{-1})	δk $\times 10^{-5}$ (m^{-1})	η (m)	$\delta\eta$ (m)	r	y_{lc} (km)	η_{lc} (m)
2	2.3	0.2	126.6	6.4	0.98	-10.33	99.8
3	1.6	0.4	303.0	26.4	0.89	-11.38	252.6
4	1.2	0.2	213.9	12.4	0.88	-10.14	189.4
5	2.8	0.4	168.9	18.1	0.92	-8.04	134.9

Levee Asymmetry

The asymmetry of the levees of Laurentian Fan cannot be easily quantified because, except for the modern channels, levee crests are difficult to detect. The present elevation difference on the conjugate levees of Eastern Valley varies from less than 100

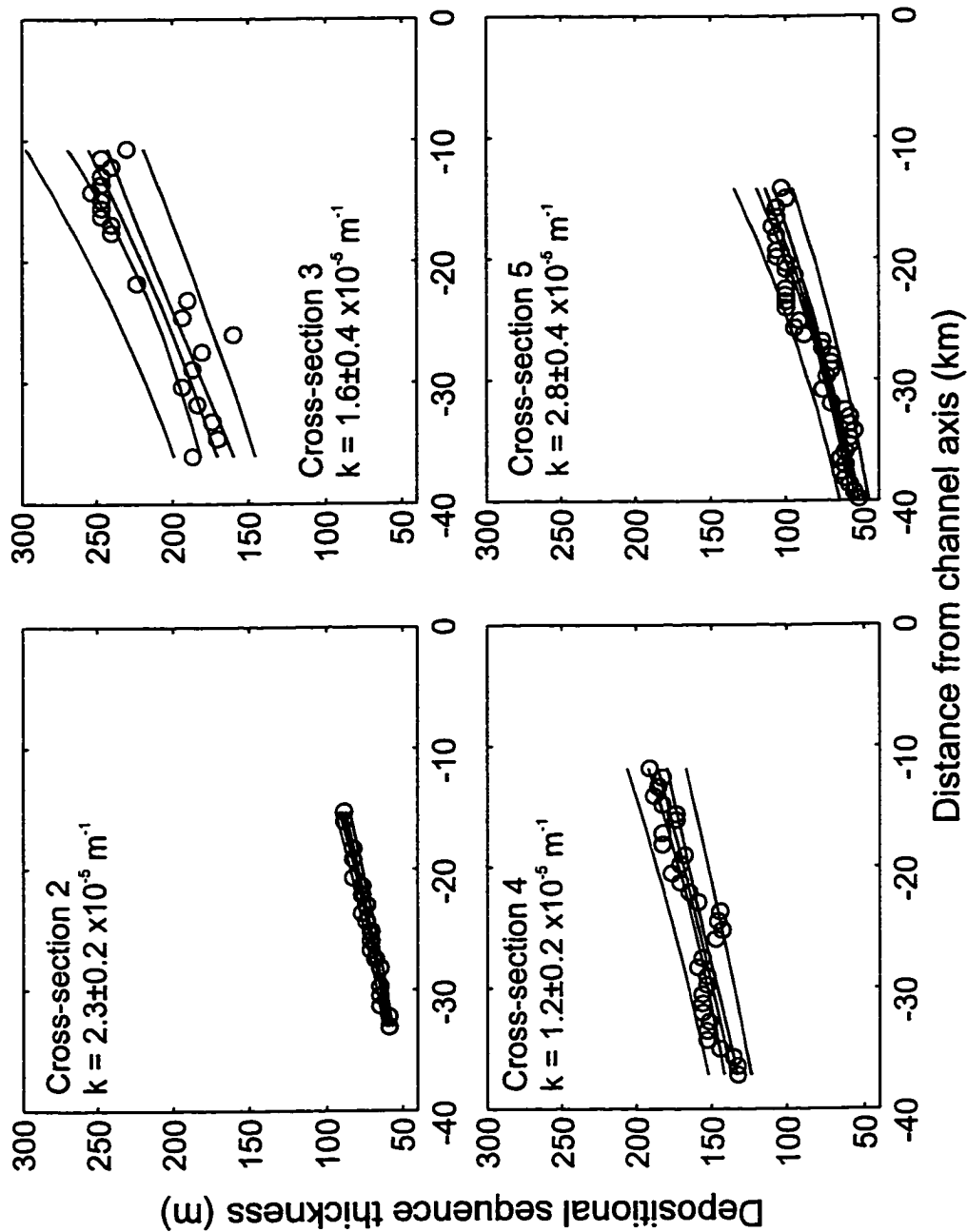


Figure 6.25. Thickness variations for interval above horizon O at cross-sections 2-5. Locations given in Figure 6.2. Value of decay constant for across-levee variations in thickness, k , also reported with 95% confidence limits.

m to greater than 600 m. The relief of ELEV is approximately 200 m and does not change significantly between the 3000 m and 4500 m isobaths (Figure 6.3). Conversely, the relief of WLEV increases to 900 m around the 4000 m isobaths and then decreases to less than 300 m around the 4500 m isobath (Figure 6.3 and Figure 6.4). Distance between conjugate levee crests averages 40 km with only minor variability. From these data, the cross-channel slope, ∇H (m km^{-1}), of Eastern Valley ranges from less than -5 m km^{-1} to more than 15 m km^{-1} (Figure 6.26a). The downchannel variability in ∇H occurs independent of variations in channel slope that average 10 m km^{-1} over this channel reach.

Even the present asymmetry of Western Valley is difficult to gauge because of its proximity to Eastern Valley. The crest of WLWV is bathymetrically lower than WLEV by as much as 300 m. Comparison of sediment thickness between WLEV and WLWV through time suggests that WLWV became the preferential site for deposition after horizon Q (Figure 6.8). Relative to sediment thickness on WLEV, WLWV is as much as 50% thicker. Prior to Q, across-fan variations in thickness show minor thinning to the west and east of Eastern Valley. Thus, while the crest of WLWV remains bathymetrically lower than WLEV, the preferential deposition on WLWV after Q had begun to decrease the elevation difference.

Sediment Waves

Possible sediment waves on WLWV characterize the interval between just below horizon Q and horizon O. The topographic expression, however, extends to the seafloor (Figure 6.19). The sediment waves have a wavelength of 5-7 km and amplitudes between 5-15 m. The waves appear to migrate eastward toward the channel axis between just below Q and O. Minor discontinuities in reflections can be seen on the upslope limb of the sediment waves at some horizons, suggesting erosion. The evolution of wave position and amplitude shows three phases (Figure 6.27). In the first phase, amplitude increases and the waves migrated upstream. Decreasing amplitude coupled with limited upstream migration characterized the second phase of wave growth. In the third phase, wave amplitude continued to decrease and the position of sediment waves remained fixed. This phase was terminated by erosion at horizon O that removed most of the

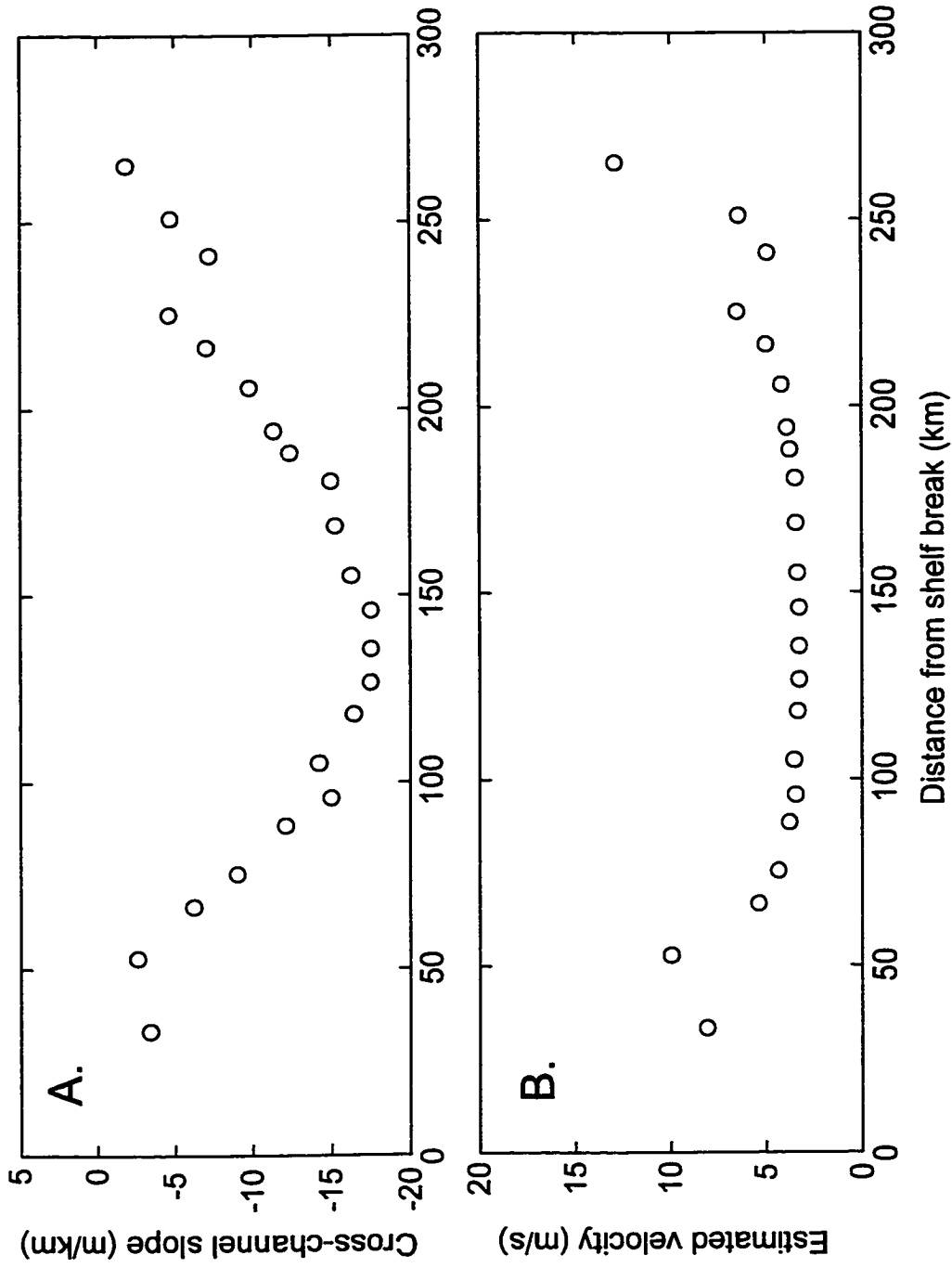


Figure 6.26. Longitudinal profiles of Eastern Valley showing: A. cross-channel slope; and B. estimated through-channel velocity from cross-channel slope.

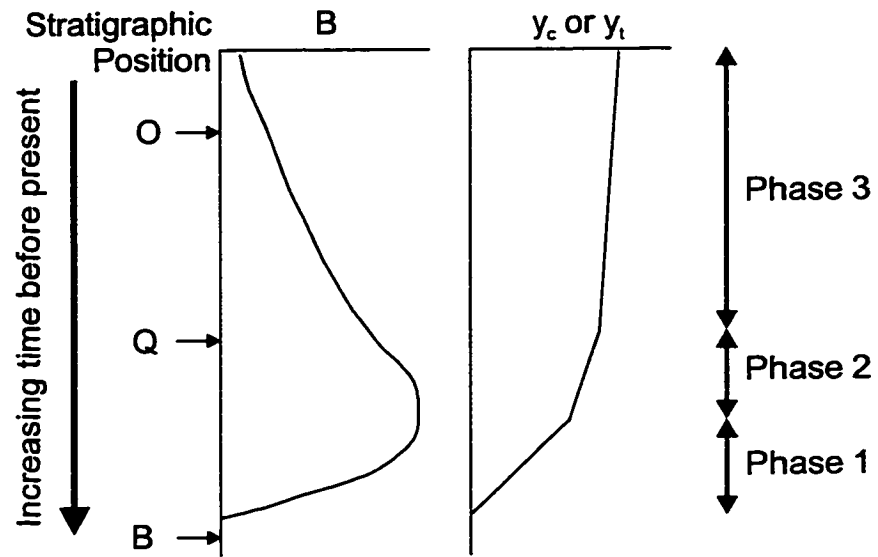


Figure 6.27. Schematic depiction of sediment wave evolution on WLWV.
 B = wave amplitude; y_c = position of wave crest; y_t = position of wave

seafloor relief associated with the sediment waves, although minor relief has persisted to the present.

Hinge Lines

The stratigraphic evolution of the hinge line on WLEV shows that its effect on the thickness of overlying depositional sequences decreased through time (Figure 6.6 and Figure 6.9). Above horizon A the depositional sequence thins between 40% to 50% across the hinge line (Figure 6.28). Successive horizons show a decrease in the amount of thinning until, above horizon O, the thickness over the hinge line is 90% of its thickness on either side of the hinge line. The evolution of thinning over the hinge line shows slight differences at different distances downfan. At the more proximal location, the percent thinning follows a linear trend from 0.4 to 0.9. At the more distal location, thinning decreases from 0.7 to 0.9. These data suggest that the control of the hinge line on depositional sequence thickness has both spatial and temporal components. The temporal component consists of the overall decrease in the control of the hinge line through time. The spatial component consists of an apparent decrease in the affect of the hinge line downfan: its influence on thickness patterns decreases downfan.

Levee Erosion on Eastern Levee of Eastern Valley

On ELEV, erosional horizons appear to be focused over short horizontal lengthscale and they create relief. Adjacent to Eastern Valley, this erosion may be associated with widening of the channel. After each erosional event, there was a return to continuous deposition across the relief created by the erosional event. One exception to this pattern occurs after the first erosional surface above horizon B. Subsequent to this event, channel proximal reflectors that appear to onlap the erosional surface. Overlying this package of acoustically stratified sediment, some indication of a second erosional surface is present. Above this second erosional surface, the sediments appear weakly acoustically stratified to acoustically transparent and they are continuous across the underlying relief.

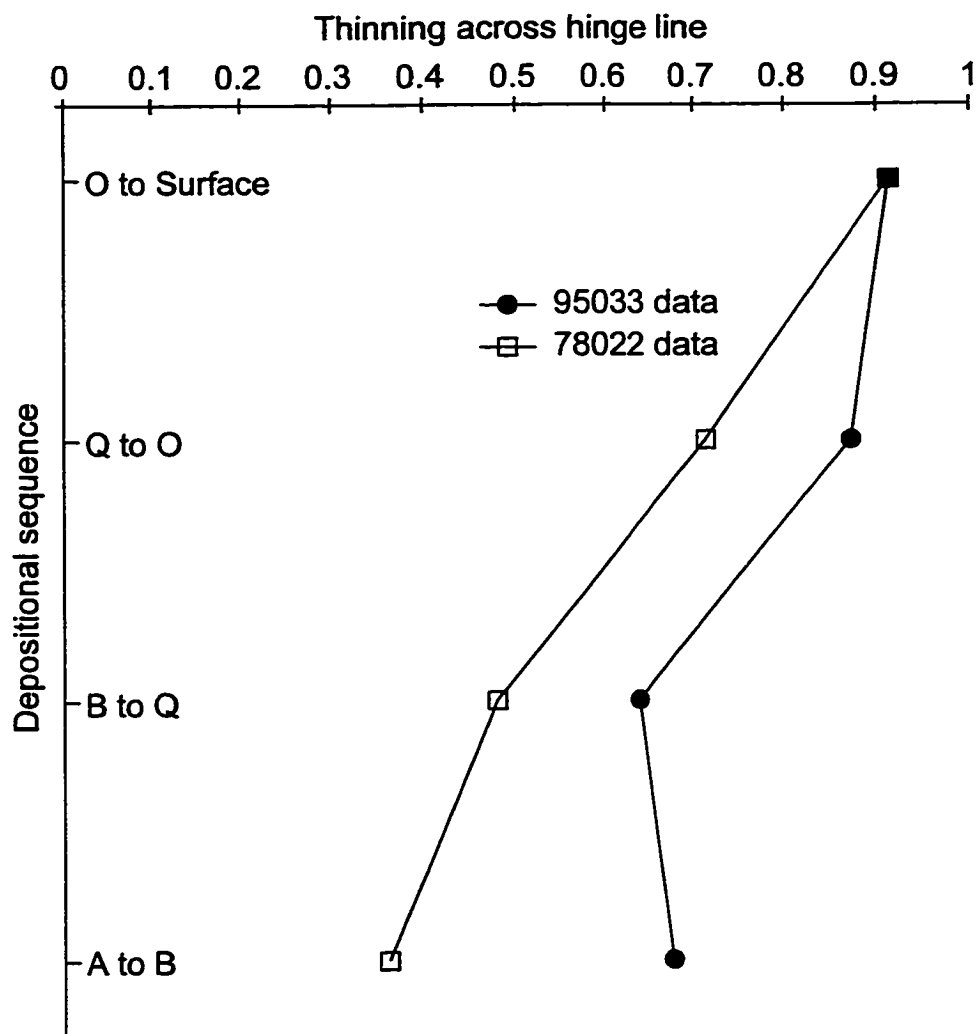


Figure 6.28. Stratigraphic variation in amount of thinning across hinge line on WLEV. Data from 78022 shown in Figure 6.6 and data from 95033 shown in Figure 6.9.

6.5 Synthesis of Levee Architecture

6.5.1 Downstream Variability

Spatial decay constants which parameterize the variation in depositional sequence thickness across a levee range from $1-3 \times 10^{-5} \text{ m}^{-1}$, showing no trend over a downchannel distance of over 100 km (Figure 6.29a). The thickness of sediment at the levee crest above horizon O is variable but shows a gradual decrease downchannel over more than 250 km (Figure 6.29b). At the distal end of the Western Valley, sediment thickness decreases abruptly.

The only other coherent downchannel trend that characterizes Laurentian Fan is the variation in ∇H (Figure 6.26). The cross-channel slope equation of Komar (1969), assuming that $Fi^2 = 1$ and that average channel depth equals flow thickness, yields estimates of the bankfull, through-channel velocity and volume concentration. These estimates suggest that through-channel flows traveling less than 4 m s^{-1} (Figure 6.26b), having volume concentrations less than 0.002 can easily account for the observed asymmetry.

The pattern in asymmetry may have more to do with erosion than with the balance between cross-flow forces. The pattern in asymmetry is entirely the result of variations in the relief of WLEV. As noted by Piper & Normark (1982), the levees north of 44°N are erosional. Thus, part of the increase in channel relief on Eastern Valley reflects the transition from an erosional to depositional levee. ELEV displays evidence for multiple erosional events. Its present relief does not vary substantially downchannel and averages 200 m. Lacking data from ELEV seaward of the data shown in Figure 6.10, one cannot demonstrate that ELEV is characterized by erosional events along its entire length. Given that the present asymmetry has likely been erosional modified, flow parameters calculated from this asymmetry must be viewed with skepticism.

6.5.2 Stratigraphic Variability

Stratigraphic variability on Laurentian Fan can only be demonstrated at very large scales. Laurentian Fan displays an evolution from a relatively simple system with a single fan valley and sediment source to a more complex system with multiple fan valleys and potential sediment pathways (Piper & Normark, 1982). The history of Laurentian

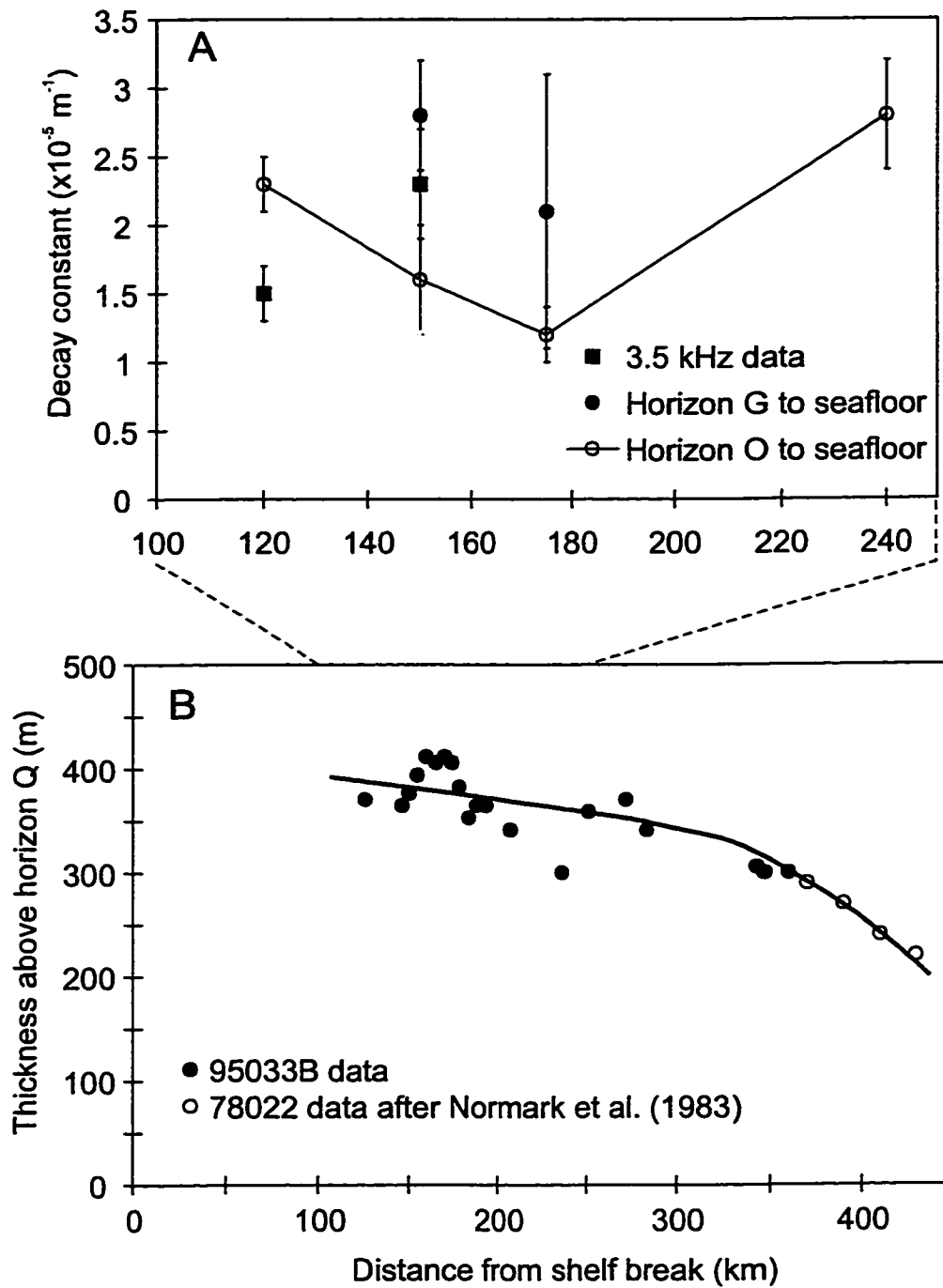


Figure 6.29. Downchannel variation in regression parameters: A. decay constant; and B. thickness of sediment at levee crest (m). Note different horizontal scales for A and B.

Fan has been refined stratigraphically and extended spatially with the new data. Points important to the present study of levee architecture are that: 1) Central Valley has existed since before deposition of horizon B; 2) Western Valley became active after deposition of B. In the GAD008 profile (Figure 6.7), the location of maximum sediment thickness appears to migrate westward through time. Prior to horizon B, WLEV received the bulk of sediment deposition consistent with Eastern Valley acting as the primary sediment transport path. After Q, WLWV was the depocentre. It suggests that flows through Eastern Valley contributed proportionally less to levee deposition west of the channel than flows through Western Valley. Asymmetry of this kind is also seen in the piston cores where the upper red mud unit appears thickest in cores 072 and 070 on WLWV.

6.6 Key Features

1. Laurentian Fan is large submarine fan having channel dimensions that are greater than any other channel-levee system studied in this thesis, while still possessing some gross-scale morphological features in common with Hueneme and Var fans, allowing the scale relationships between levee architecture and system size to be investigated among generically-related systems.
2. Whereas thickness variations show thinning with distance from the channel axis, these variations can, in some instances, be indistinguishable from linear decreases in thickness. Nevertheless, thickness variations could be fit to the exponential model for depositional sequences above horizon O.
3. The decay constants range from $1-3 \times 10^{-5} \text{ m}^{-1}$, among the smallest values determined for levee depositional sequences.
4. The decay constants calculated for the western levee of Western Valley show no downchannel trend for the interval above horizon O. The thickness of sediment at the levee crest is variable but shows a gradual downchannel decrease. At the distal end of Western Valley, sediment thickness at the levee crest decreases abruptly.
5. Levee asymmetry was created by preferential deposition on the western side of channel, but downchannel patterns in asymmetry may be controlled more by erosion.

Chapter 7

Synthesis of Levee Architecture

7.1 General Statement

Imaging of levees in modern environments by conventional seismic reflection profiles shows that they preserve a wealth of stratigraphic and morphological information. However, the use of levee architecture to unravel the dynamics of channel-levee development has suffered because a quantitative understanding of the links between levee architecture and through-channel flow character is lacking. This study has identified parameters that systematically describe levee architecture, something not previously attempted. The challenge taken up in this chapter is to determine how levee architecture relates to channel morphology and potentially to the character of the through-channel turbidity currents.

Observations of levee architecture from the several fans studied include across-levee and downchannel variations in depositional sequence thickness, differences in the architecture of conjugate levees, i.e., asymmetry, the stratigraphic evolution of levee crests, and the stratigraphic development of sediment waves. The goals of this chapter are to establish which aspects of levee architecture correlate with channel morphology and to explore causative explanations for the observed relationships.

7.2 Observations of Levee Architecture

7.2.1 Thickness Patterns

The spatial decay constant, k , quantifies variations in depositional sequence thickness perpendicular to channel trend. The inverse of this decay constant, k^{-1} , defines the distance over which sediment thickness decreases by a factor of $1/e$ and represents a quantitative definition of levee width. The variability of k within any particular system, with some minor exceptions, shows little evidence for systematic trends, either downchannel or stratigraphically. The exceptions include examples from NAMOC, Hueneme Fan, and Var Fan. On NAMOC, the decay constant for DS1 on the western levee increases from $2 \pm 0.4 \times 10^{-5} \text{ m}^{-1}$ to $9.1 \pm 2.4 \times 10^{-5} \text{ m}^{-1}$ over a downchannel distance of over 300 km (Fig. 3.26). On the Var Sedimentary Ridge, the decay constant decreases

downchannel by a factor of 3-4 over a distance of about 20 km (Fig. 5.36). On the western levee of Hueneme Fan, the decay constants for DS1 and DS3 show a downchannel decrease (Fig. 4.25). The only consistent downchannel trend that emerges is a decrease in k along the distal reaches of a submarine channel-levee system.

Thickness of sediment at levee crests decreases downchannel. Along the upper reach of channels, thickness apparently decays exponentially downchannel (Figure 7.1). In some cases (particularly along Western Valley, Laurentian Fan) which otherwise show an exponential downchannel decay, sediment thickness at the levee crest decreases abruptly at the distal end of the channel (Figure 7.1). Regression analysis of thickness variations along the upper reaches of channels produces statistically significant exponential fits (Figure 7.1, Table 7.1). The distance over which thickness decreases by a factor of $1/e$, λ^{-1} (m), defines the e-folding length for downchannel changes in sediment thickness at the levee crest and represents a quantitative definition of levee length. Most importantly, k^{-1} shows little downchannel variability and the channel reaches for which k^{-1} is uniform downchannel display exponential thinning of sediment thickness at the levee crest in the downchannel direction.

Table 7.1. Summary of regression results from exponential fit to downchannel variations in sediment thickness at levee crest. Error in decay constant reflects 95% confidence limit on decay constant. λ^{-1} = e-folding length or inverse of decay constant, r = correlation coefficient.

System	Decay constant ($\times 10^{-5} \text{ m}^{-1}$)	Error ($\times 10^{-5} \text{ m}^{-1}$)	λ^{-1} (km)	r
NAMOC	-0.21	± 0.17	476.2	0.92
Hueneme	-8.80	± 2.67	11.4	0.88
Reserve	-48.64	± 18.86	2.1	0.96
Amazon	-0.38	± 0.03	263.2	0.96
Var	-1.35	± 0.67	74.1	0.70
Laurentian	-0.13	± 0.03	769.2	0.87

Between systems, the decay constant, k , varies by two orders of magnitude having a maximum of greater than $100 \times 10^{-5} \text{ m}^{-1}$ on Reserve Fan and a minimum of around $1 \times 10^{-5} \text{ m}^{-1}$ on NAMOC and Laurentian Fan. The magnitude of channel dimensions also shows such variability. Channel half-width, W (m), and channel relief, D (m), vary by

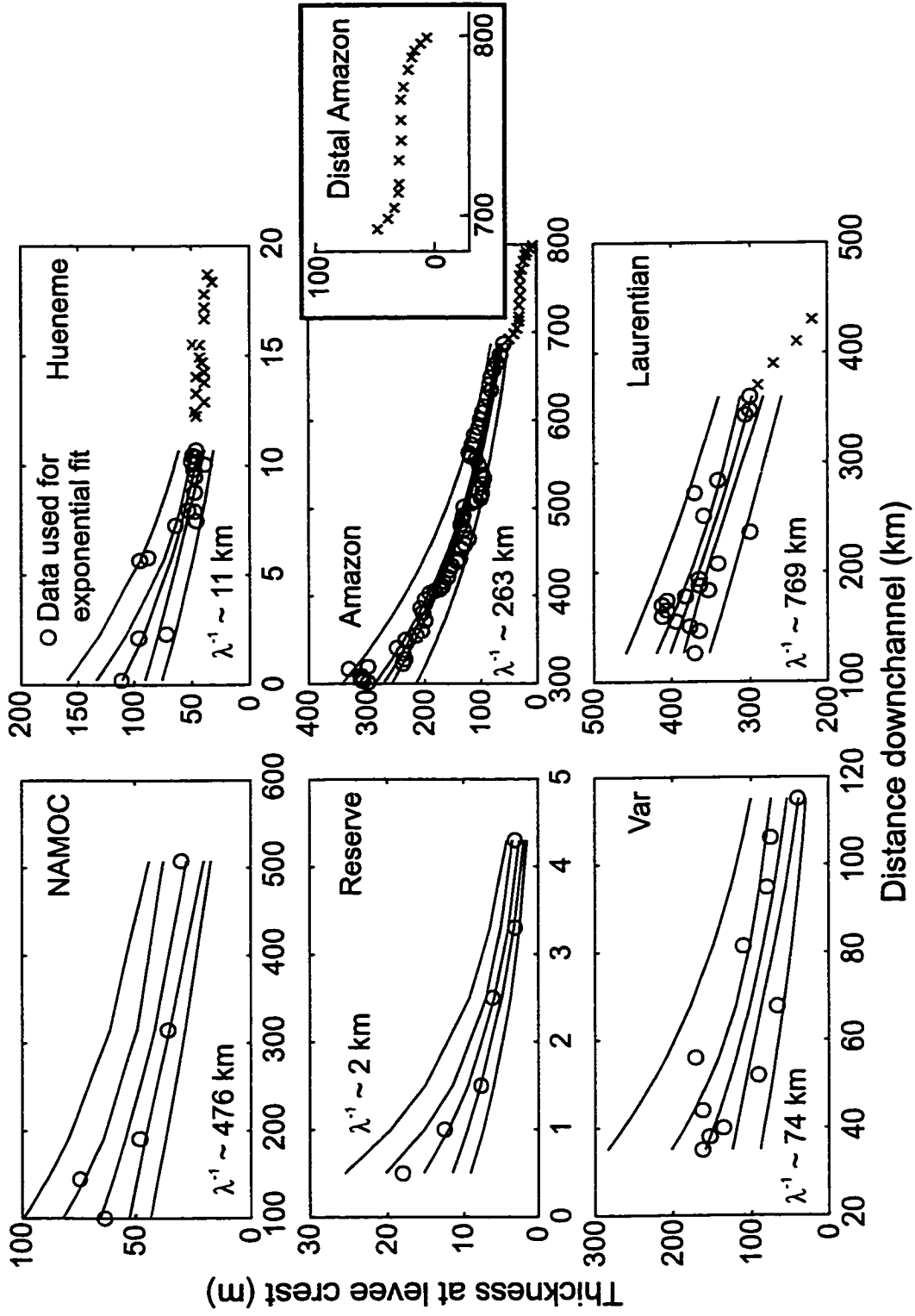


Figure 7.1. Downchannel variations in sediment thickness at levee crest for all systems plotted with regression line, confidence and prediction intervals. Also reported are the values of e-folding length, λ^{-1} , for each regression. Open circles denote data points used in regression, crosses denote distal data not used to calculate λ^{-1} . Regression data summarized in Table 7.1.

about two orders of magnitude while channel slope spans about one order of magnitude. A plot of the inverse of the decay constant, k^{-1} (m), versus the half-width of the channel shows a positive relationship (Figure 7.2) when plotting data from all systems together. A positive relationship also occurs between k^{-1} and channel relief (Figure 7.3). The inverse relationship between k^{-1} and downchannel channel slope (Figure 7.4) is weak, but statistically significant.

The magnitude of λ^{-1} also varies by about two orders of magnitude between systems, having a maximum of greater than 700 km on Laurentian Fan and a minimum of about 2 km on Reserve Fan (Table 7.1); however, determination of this parameter is limited by the downchannel coverage of the available data (Figure 7.5a). A plot of λ^{-1} versus average channel half-width over the same reach of the channel used to define λ^{-1} shows a positive relationship (Figure 7.5b), suggesting that wide channels have more gradual variations in sediment thickness at the levee crest than narrower channels. A similar relationship exists between λ^{-1} and channel relief, D (Figure 7.5c), suggesting that deep channels have more gradual downchannel variations in sediment thickness at the levee crest than shallow channels.

The relationships between levee architecture and channel morphology plotted on log-log graphs display linear trends that can be quantified using regression analysis. The general form of the regression equation equates some feature of levee architecture, Y , to some measure of channel morphology, X , according to

$$Y = 10^{a \pm \delta a} X^{b \pm \delta b} \quad (7.1)$$

where a is the intercept of the regression line and b is the slope of the regression line. The errors on a and b reflect the 95% confidence limits on the regression parameters.

The value of λ^{-1} scales directly with channel width (Figure 7.5a) according to

$$\lambda^{-1} \sim W^{1.31 \pm 1.16} \quad (7.2)$$

with $r^2 = 0.71$. The relationship between λ^{-1} and D (Figure 7.5b) is given by

$$\lambda^{-1} \sim D^{1.25 \pm 0.67} \quad (7.3)$$

with $r^2 = 0.87$. These relationships imply that the downchannel lengthscale over which sediment thickness at the levee crest varies scales with the size of the channel.

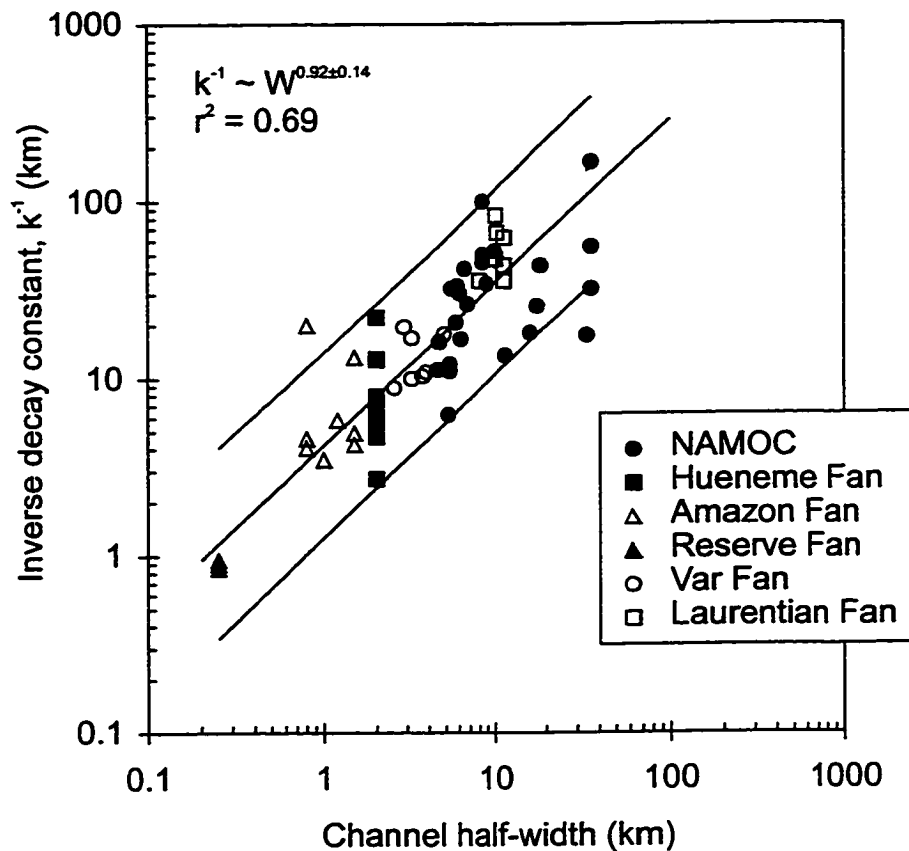


Figure 7.2. Relationship between inverse decay constant, k^{-1} , and channel half-width where channel half-width is defined as the distance between the channel axis and the levee crest and the inverse decay constant represents the distance across a levee over which sediment thins to $1/e$ or about 37%. Also reported is the relationship between k^{-1} and W predicted from linear regression and its r^2 value. Regression line and 95% prediction intervals plotted as solid lines.

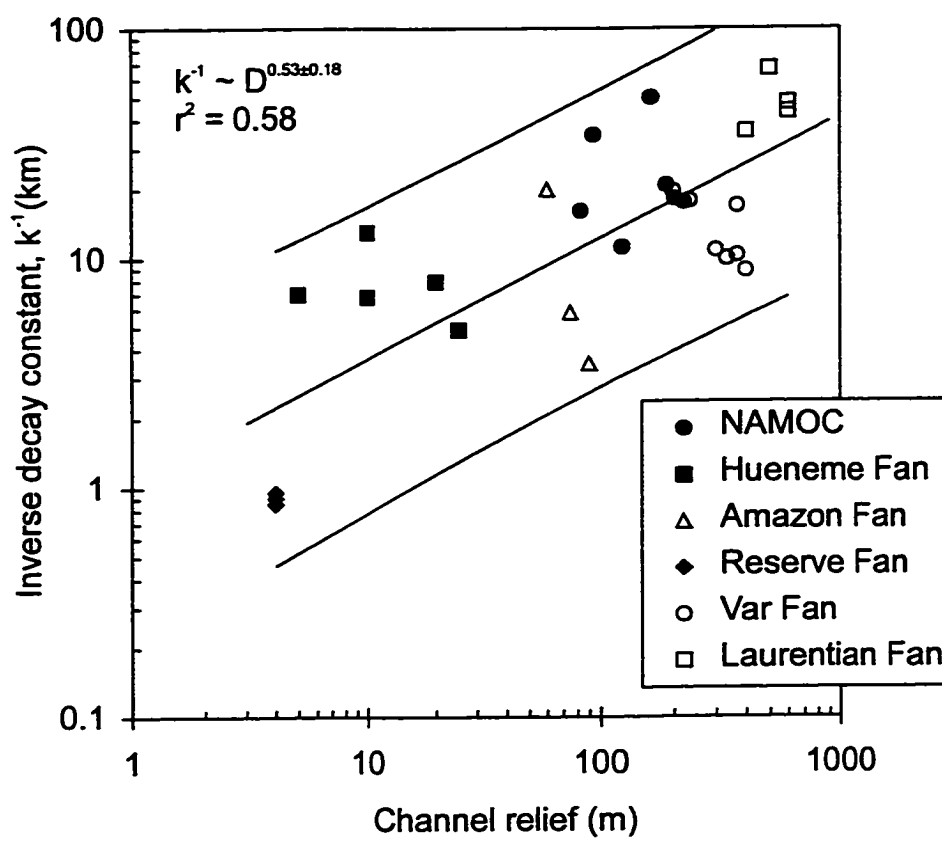


Figure 7.3. Relationship between inverse decay constant for across-levee variations in depositional sequence thickness, k^{-1} , and channel relief where channel relief is defined as the elevation difference between the levee crest and the channel floor.

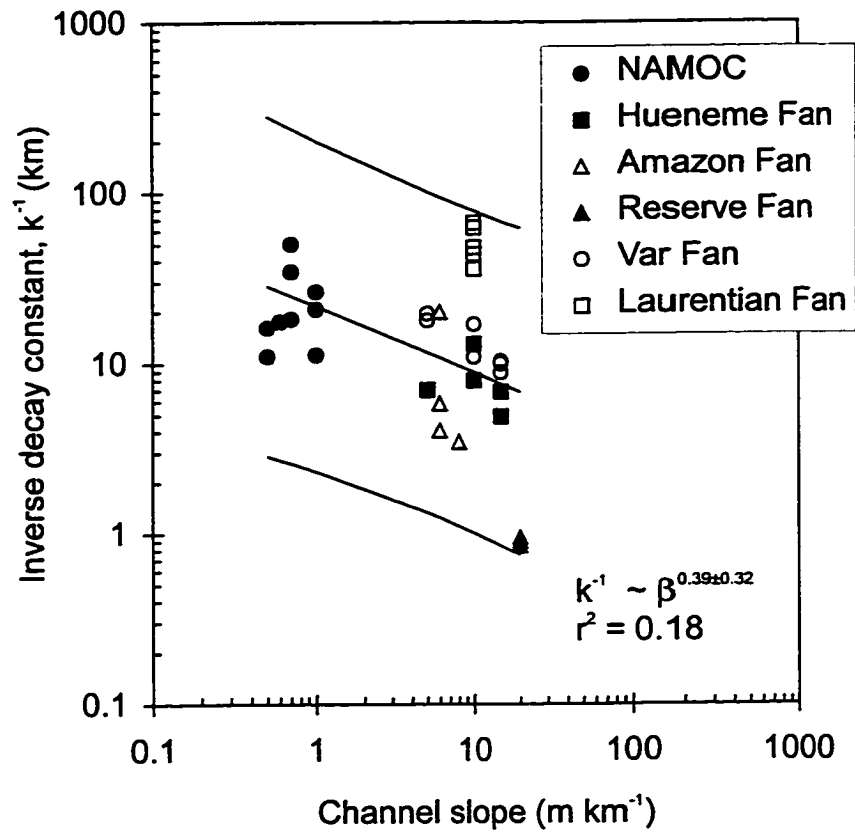


Figure 7.4. Relationship between inverse decay constant for across-levee variations in thickness, k^{-1} , and downchannel slope.

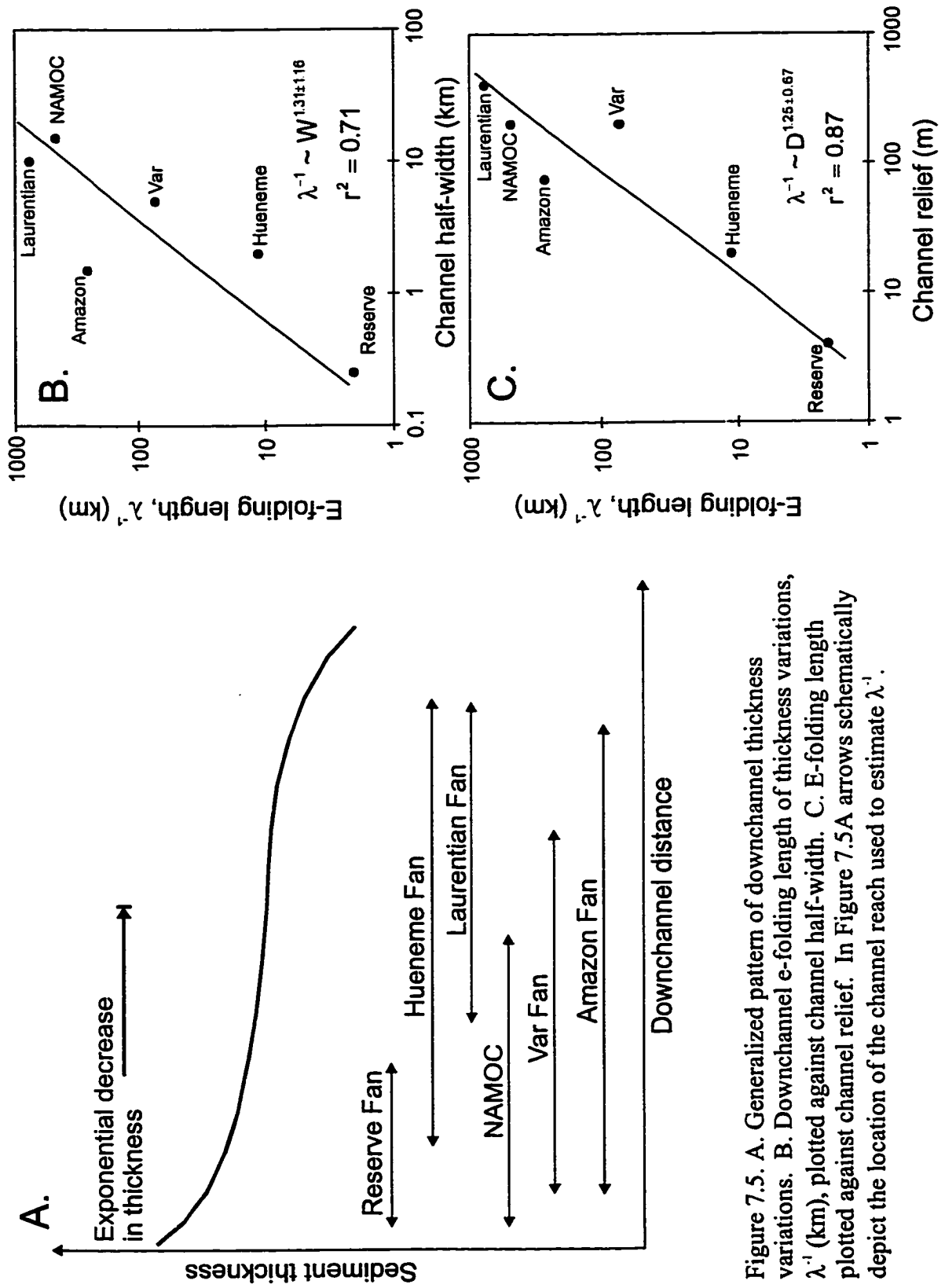


Figure 7.5. A. Generalized pattern of downchannel thickness variations. B. Downchannel e-folding length of thickness variations, λ' (km), plotted against channel half-width. C. E-folding length plotted against channel relief. In Figure 7.5A arrows schematically depict the location of the channel reach used to estimate λ' .

The observations of levee architecture suggest a direct relationship between channel relief and the inverse decay constant, k^{-1} , defined by across-levee variations in depositional sequence thickness (Figure 7.3). Channel relief scales with k^{-1} according to

$$k^{-1} = 10^{3.03 \pm 0.37} D^{0.53 \pm 0.18} \quad (7.4)$$

with $r^2 = 0.58$. Within the 95% confidence limits of the regression equation, k^{-1} scales with $D^{1/2}$. The relationship between k^{-1} and W (Figure 7.2) suggests that k^{-1} scales with W according to

$$k^{-1} = 10^{0.62 \pm 0.09} W^{0.92 \pm 0.14} \quad (7.5)$$

with $r^2 = 0.69$. The dependence of k^{-1} on both channel relief and channel half-width might result from the covariance of channel relief with channel half-width. A plot of log of channel half-width versus log of channel relief (Figure 7.6) displays a dependence of width on relief according to

$$W = 10^{2.48 \pm 0.51} D^{0.52 \pm 0.24} \quad (7.6)$$

with $r^2 = 0.45$. The relationship between W and D , rather than the relationship between k^{-1} and W , may reflect a fundamental characteristic of submarine channels, further supported by the inclusion of data from other submarine channel-levee systems (Figure 7.6). The regression equation that fits the entire data set predicts that W scales with D according to

$$W = 10^{2.12 \pm 0.31} D^{0.62 \pm 0.16} \quad (7.7)$$

with $r^2 = 0.54$ which has a slightly different exponent than (7.6); however, the two equations agree within the 95% confidence limits. The relationship between k^{-1} and downchannel slope, β , varies according to

$$k^{-1} = 10^{1.34 \pm 0.29} \beta^{-0.39 \pm 0.32} \quad (7.8)$$

with $r^2 = 0.18$.

The empirical relationships between levee architecture and channel morphology suggest that levee architecture scales with channel dimensions — half-width and relief — but inversely with downchannel slope and then only weakly. Because channel morphology is generally thought to reflect the hydrodynamics of the through-channel turbidity currents, these empirical relationships may help to isolate the functional dependence of levee architecture on through-channel flow character.

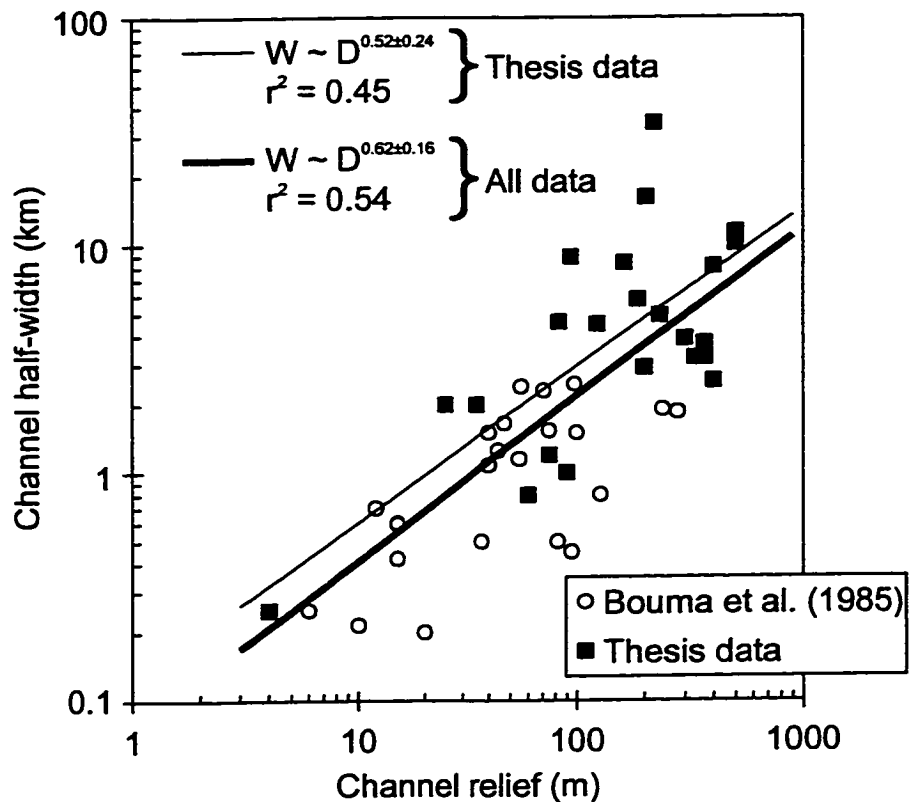


Figure 7.6. Relationship between channel width and channel depth for channel-levee systems in this study (filled squares), including data from the literature (open circles) taken from maps published in Bouma et al. (1985). The two scale relationships refer to regressions performed only on data presented in this thesis (thesis data) and on the entire data set (all data).

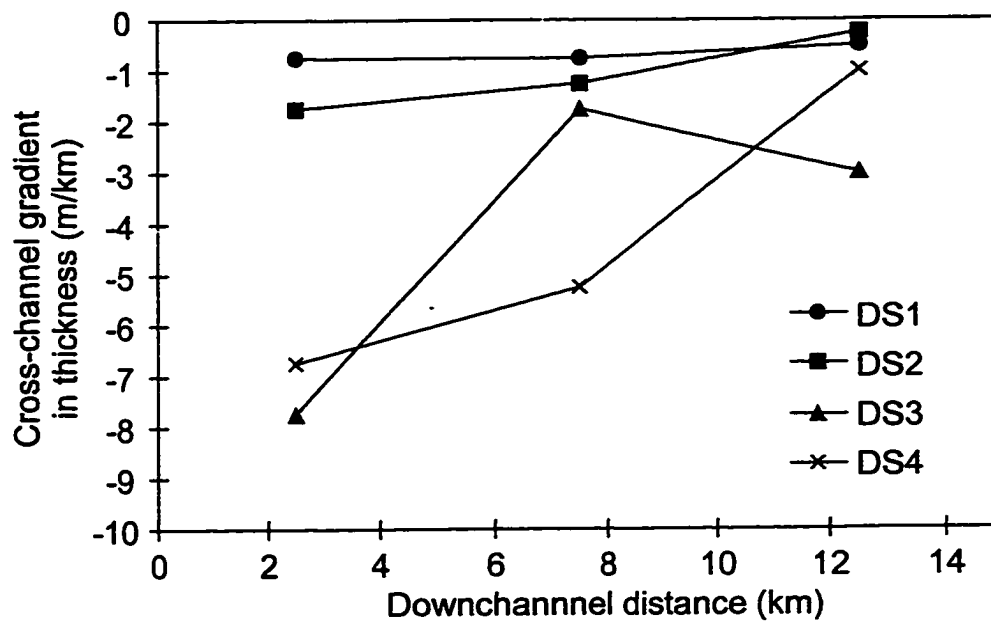
7.2.2 Levee Asymmetry

The cross-sectional profile of a channel-levee system commonly displays a pronounced asymmetry, parameterized by ∇H , the elevation difference between conjugate levee crests divided by the horizontal distance between levee crests. Komar (1969) suggested that the elevation difference between conjugate levees reflects flow deflection caused by the Coriolis force owing to the Earth's rotation and/or the centrifugal force arising from channel curvature. Flow deflection promotes deposition on one side of the channel thereby creating the observed differences in the elevation of conjugate levee crests. Observations of levee asymmetry show that changes in ∇H can arise because of changes in the horizontal distance between levee crests without significant changes in the elevation difference between conjugate levee crests. Table 7.2 summarizes the observations of asymmetry made in previous chapters.

Table 7.2. Dominant control, origin, and patterns in cross-channel slope. These systems have relatively straight channels and thus asymmetry is likely controlled by the balance between Coriolis force and the cross-channel pressure gradient. N/A = not available.

System	Principal control of ∇H	Origin of pattern	Down-channel trend in $-\nabla H$	Strati-graphic trend in $-\nabla H$
NAMOC	Coriolis	initially preferential deposition then reduction in channel width	increase	increase
Hueneme	Coriolis	preferential deposition	decrease	increase
Var	Coriolis	preferential deposition	decrease	N/A
Laurentian	Coriolis	preferential deposition	decrease	N/A

On NAMOC, asymmetry *increases* downchannel (Fig. 3.28) as a result of reductions in channel width. Approximately equal amounts of sediment accumulated on conjugate levees during the latest phase of channel-levee growth. On Hueneme (Fig. 4.24), Var (Fig. 5.29), and Laurentian (Fig. 6.26) fans asymmetry *decreases* downchannel as a result of decreases in sediment thickness on the right-hand levee relative to sediment thickness on the left-hand levee (e.g., Figure 7.7). The difference in sediment thickness on conjugate levee crests divided by the distance between levee crests is denoted by $\nabla \eta$.



Definition of cross-channel thickness gradient, $\nabla\eta$

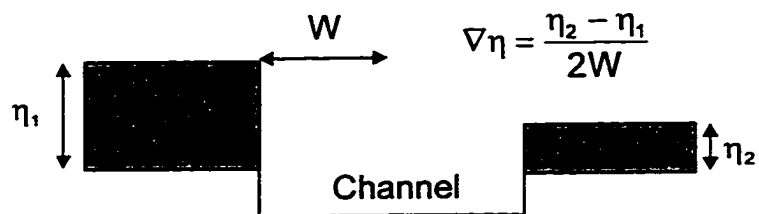


Figure 7.7. (Top) Downchannel trend in cross-channel thickness gradient (m km⁻¹) on Hueneme Fan. (Bottom) Definition sketch showing parameters used to calculate the cross-channel gradient in sediment thickness at the levee crest.

Differences in the elevation of conjugate levees reflect preferential deposition on one side of the channel and these differences may arise from deflection of the flow by Coriolis and/or centrifugal forces. Where the radius of channel curvature is very large, Komar's (1969) model for levee asymmetry balances the cross-channel pressure gradient against the Coriolis force such that

$$-\nabla H = \frac{fu}{g_o C} \quad (7.9)$$

where

$$g_o = g \frac{\rho_s - \rho}{\rho} \quad (7.10)$$

and where f (s^{-1}) is the Coriolis parameter, u ($m s^{-1}$) is the through-channel velocity, C is the volume concentration, g ($m s^{-2}$) is the acceleration due to gravity, ρ_s ($kg m^{-3}$) is grain density, and ρ ($kg m^{-3}$) is the ambient fluid density. In deriving (7.9), Komar (1969) assumed that the cross-channel gradient in flow thickness which produces the pressure gradient scales directly with ∇H and that no cross-channel gradients in volume concentration exist. The asymmetry created by through-channel flows implicitly assumes that the flows are overbanking, requiring that the flows lose sediment to the levees, promoting decreases in C . If volume concentration decreases, then the downchannel patterns in levee asymmetry, provided that levee asymmetry is given by (7.9), record the behaviour of velocity relative to volume concentration (Figure 7.8). If reductions in volume concentration occur without significant changes in velocity, perhaps because of dilution by entrainment, then asymmetry would increase downchannel (case 1, Figure 7.8) as is seen on NAMOC. If velocity varies directly with C then asymmetry would remain constant downchannel (case 2, Figure 7.8). If velocity decays more rapidly than C , implying rapid deceleration of the flow, perhaps because of decreasing slope, then asymmetry would decrease (case 3, Figure 7.8) as is the case on Hueneme, Var, and Laurentian fans.

Where the thickness of sediment on conjugate levees is equal, e.g., on NAMOC, equation (7.9) may not apply, leaving the question — does the flow deflection responsible for levee asymmetry require that depositional sequence thickness also be

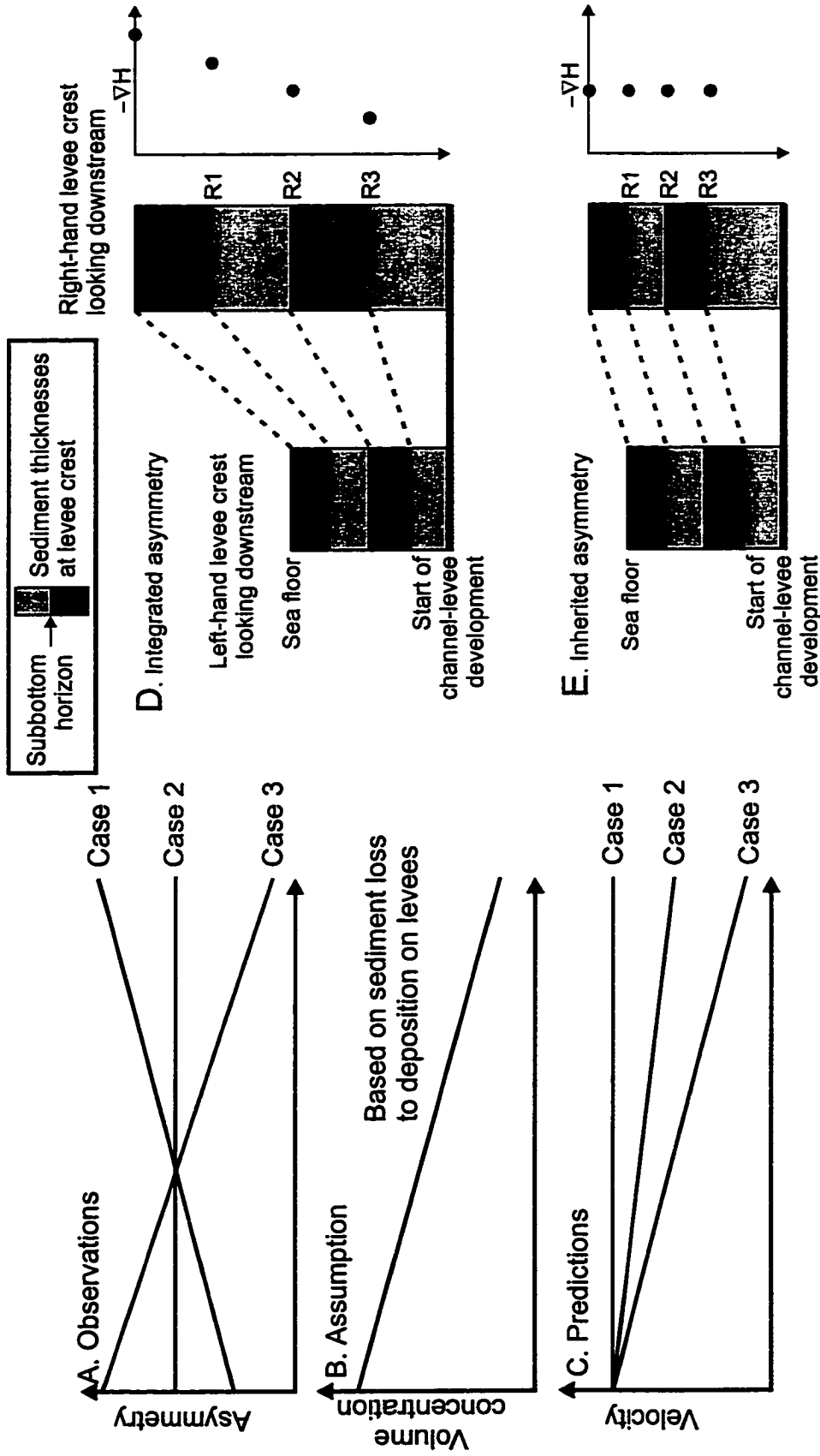


Figure 7.8. Schematic depiction of downchannel patterns in levee asymmetry, ΔH , and their physical interpretation for a straight channel; A. downchannel patterns in levee asymmetry; B. assumed decrease in volume concentration; C. downchannel evolution of through-channel velocity. Evolution of levee crest asymmetry and the interaction between elevation differences and difference in thickness at the levee crest for conjugate levees; D. modern asymmetry reflects integrated behaviour of difference in sediment accumulation since the start of channel-levee development; E. modern asymmetry reflects asymmetry inherited from horizon R3 time.

asymmetrical? The modern value of ∇H records the value of $\nabla \eta$ integrated over the entire history of the channel (Figure 7.8). A constant value of $\nabla \eta$ at successive stratigraphic horizons, a possible indication of equilibrium conditions, produces an ever-increasing value for ∇H (Figure 7.8). Alternatively, a constant value of ∇H for successive stratigraphic horizons requires that $\nabla \eta$ be zero (Figure 7.8). In this case, the value of ∇H seen at a particular stratigraphic horizon represents a value inherited from an earlier phase of channel-levee development. A question that remains unresolved in the application of (7.9) is whether ∇H measured at any particular stratigraphic horizon relates to the flow conditions active at that stratigraphic time. Because the value of ∇H represents the sum of $\nabla \eta$ over time, ∇H is more likely a measure of the integrated behaviour of the through-channel flows. On the other hand, $\nabla \eta$ reflects conditions corresponding to a particular stratigraphic interval; however, no model exists relating $\nabla \eta$ to flow parameters.

The model of Komar (1969) has been used by many workers to estimate flow parameters from levee asymmetry and should potentially represent a key tool for establishing the links between levee architecture and through-channel flow character. However, the observations of both the stratigraphic and spatial patterns in asymmetry suggest that Komar's (1969) model cannot be applied without consideration of relative contributions of preferential deposition (i.e., the stratigraphic evolution of $\nabla \eta$) and changes in channel width to asymmetry. Even then predictions about the stratigraphic or downchannel evolution of flow parameters may not be easily extracted without a refined model.

7.2.3 Levee Crest Evolution

The levee crest represents a fundamental morphological feature common to all channel-levee systems. Its elevation plays a role in defining channel depth, its horizontal position in defining channel width. The levee crest represents the topographically highest point on the levee, separating strata that dip toward and away from the channel. Most levee crests migrate toward the channel axis through time. On NAMOC (Fig. 3.10, Fig. 3.11), the western levee crest at cross-sections 4 and 5 moved gradually whereas the eastern levee crest moved abruptly between horizons R and G, and more gradually

thereafter. Similarly on Amazon Fan, the levee crests shift toward the channel axis as the width of the channel fill decreases (Fig. 5.17).

Two different stages of levee crest development are seen on Hueneme and Var fans (Figure 7.9). On Hueneme Fan, deposition on the inner levee was insufficient to raise its crest above the outer levee crest, and consequently, the outer levee crest remained stable. On Var Fan, however, one sees a later phase in the development of an inner levee. At horizon R1, the inner levee crest occurs at a lower elevation than the outer levee crest, similar to the present morphology on Hueneme Fan. After deposition of R1, the space between the outer levee crest and the channel filled such that by horizon a, the inner and outer levee crests had about the same elevation. Further deposition after horizon a produced the modern levee crest substantially closer to the channel axis than its position at R1.

Laurentian Fan has levee crests that shifted away from the channel (Figure 7.10). On the western levee of Western Valley, the levee crest moved away from the channel axis suggesting that the channel has widened through time. On the eastern levee of Eastern Valley, erosional events are pronounced. After each erosional event, deposition began to fill the available space by overlapping the erosional surface (OL in Figure 7.10) or draping it, but the fill never attained sufficient thickness to move the levee crest toward the channel axis. The successive erosional events presumably acted to keep the levee crest from the commonly observed behaviour of shifting toward the channel axis.

The evolution of the position of a levee crest can be predicted from a simple geometric model that relates the timing of levee crest movement to two morphologic parameters: the angle of the inner levee slope and the distribution of sediment within depositional sequences. Inner levee slope parameterizes the space available for the accumulation of sediment between the channel and the outer levee crest. Filling of this space by sediment is parameterized by a spatial decay constant and sediment thickness at the origin. Figure 7.11 schematically illustrates the evolution of a simplified levee morphology for various combinations of decay constant and inner levee slope. For all cases, the depositional sequences contain the same volume of sediment per unit channel length, i.e., η_0/k is constant. What is being varied between the cases is the distribution of

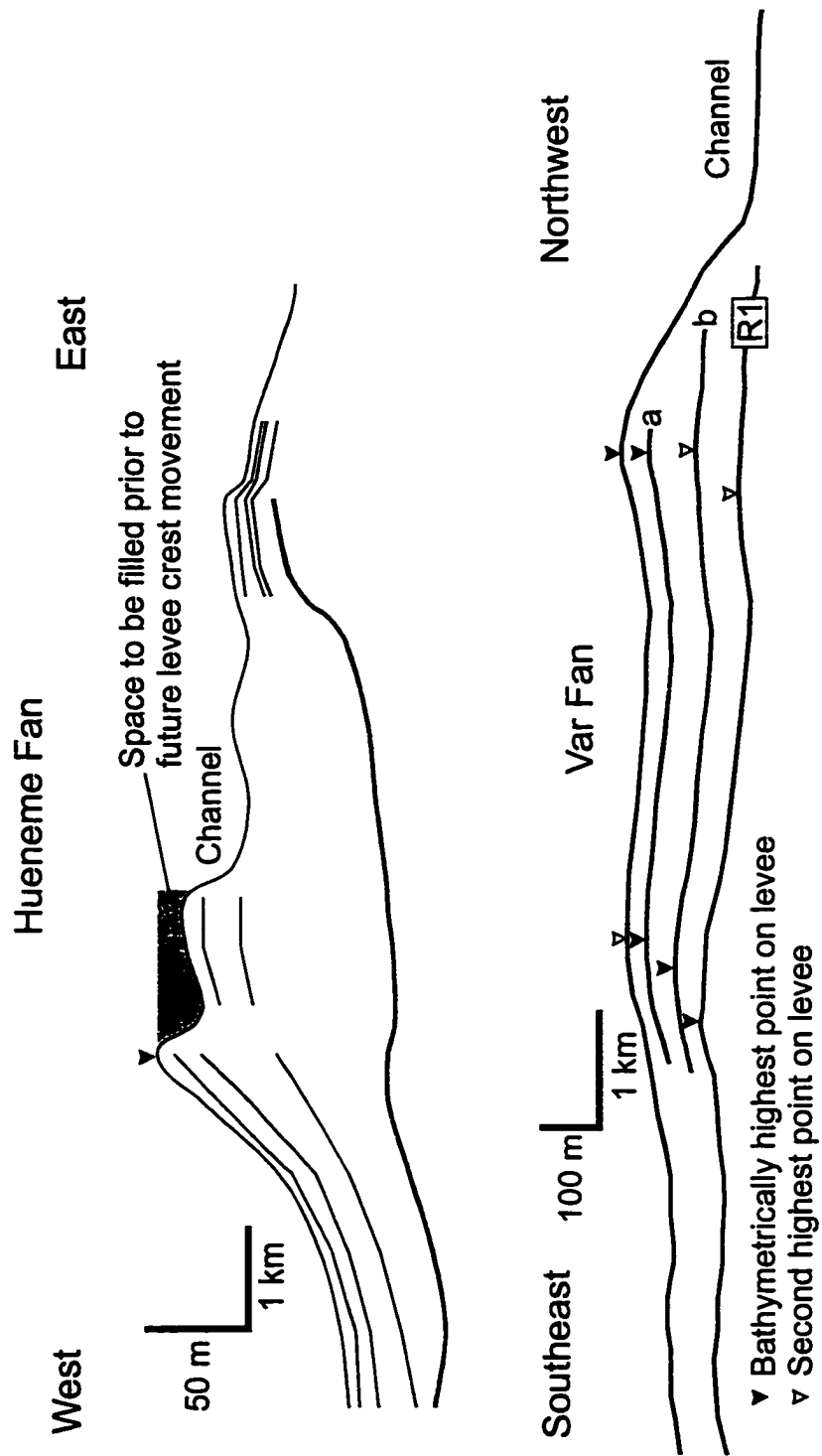


Figure 7.9. Evolution of levee crests on Hueneme Fan and Var Fan.

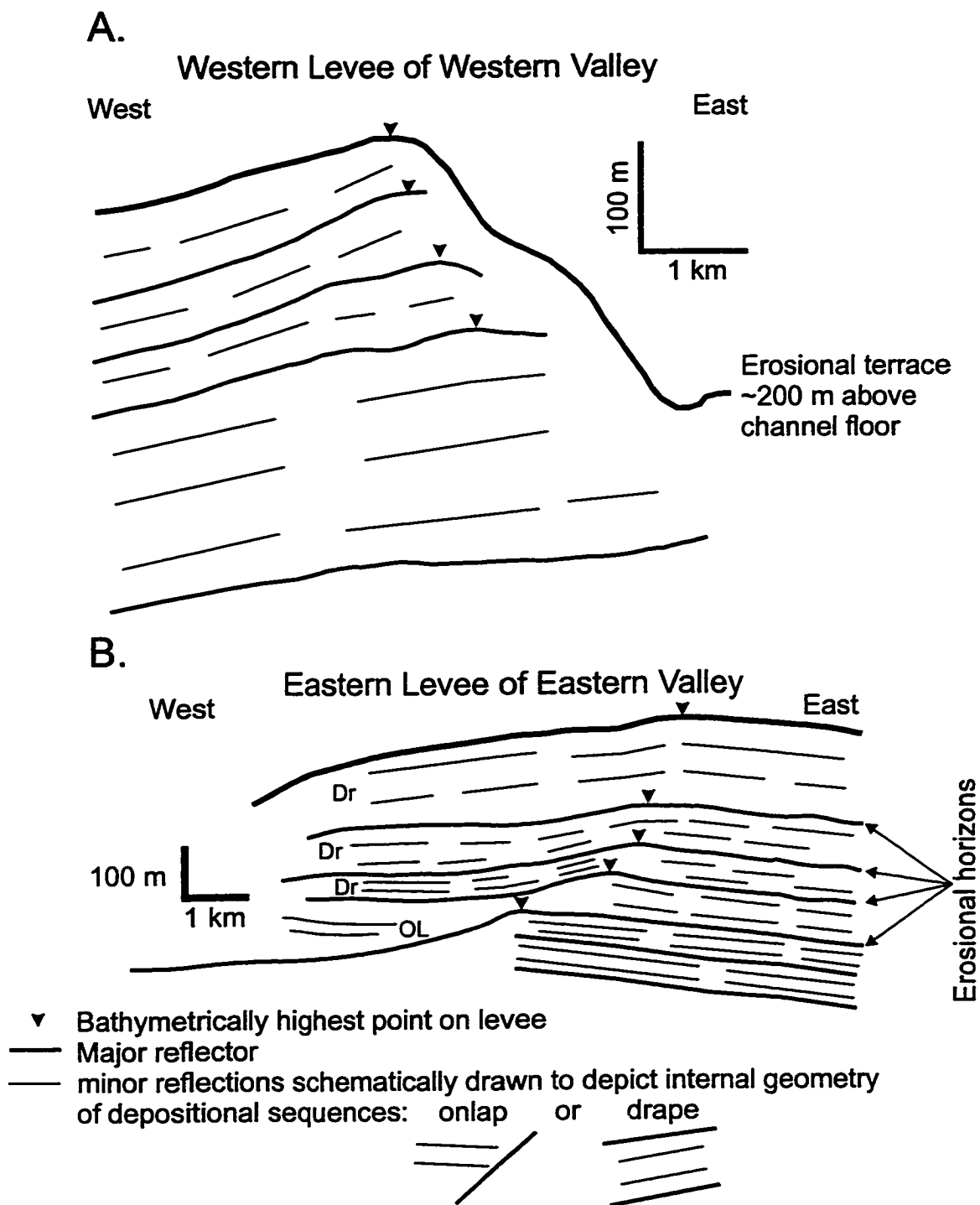
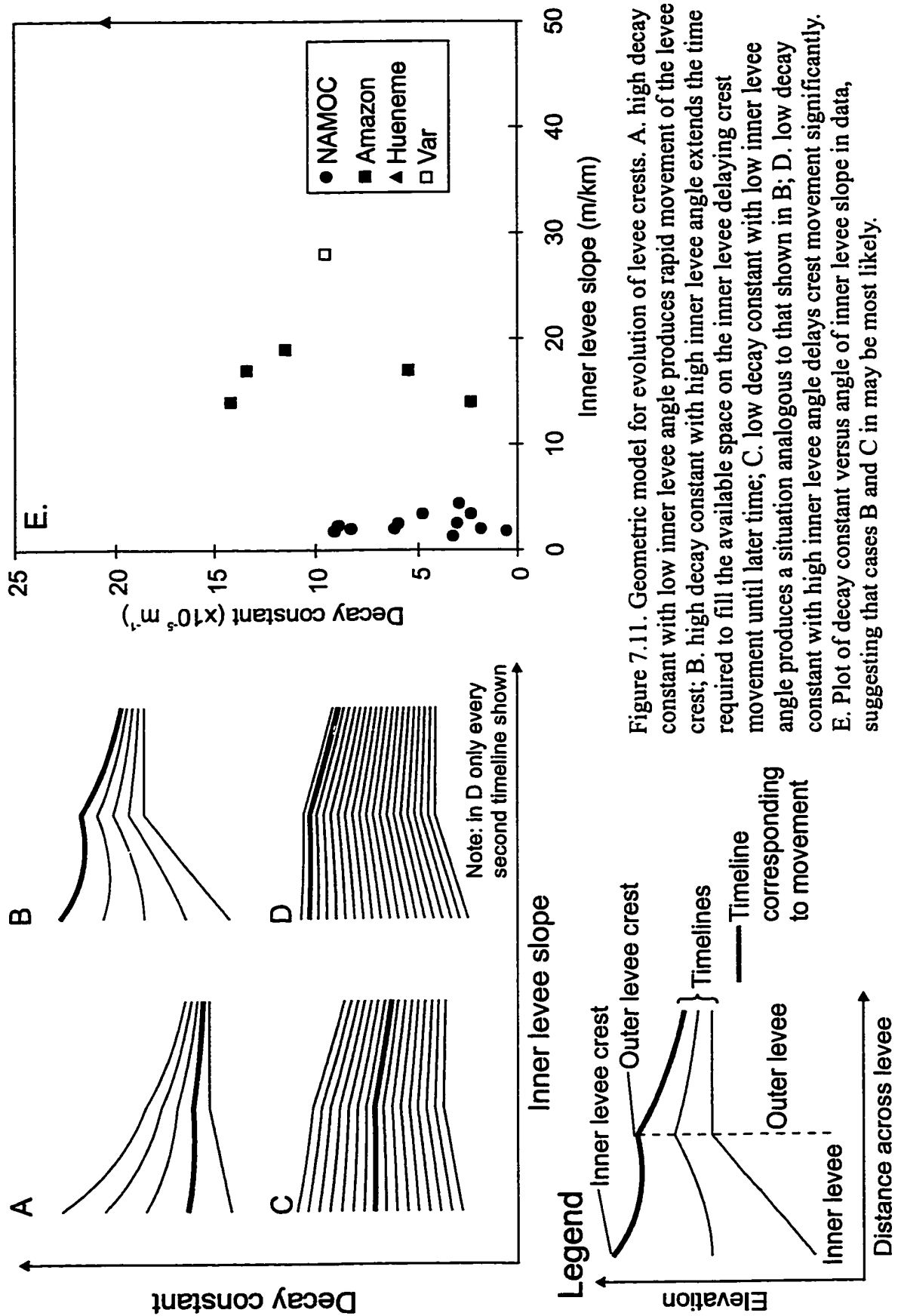


Figure 7.10. Evolution of levee crests on Laurentian Fan taken from A. western levee of Western Valley and B. eastern levee of Eastern Valley. Both show that the stratigraphically highest point on the levee moves away from the channel through time. Dr = draping reflectors, OL = onlapping reflectors.



the same amount of sediment into narrow (sediment thickness decays rapidly away from channel axis) or broad (sediment thickness more uniform) levees. Cases A and B have large values of k and η_0 corresponding to levees that are narrow, mounded features. Cases C and D have small values of k and η_0 corresponding to levees that are broad, low relief features. Levee crest movement is taken to have occurred when the position of the maximum elevation on a levee switches from the outer to inner levee crest.

Where the inner levee slope is high, the space available for sediment channelward of the levee crest is large. For high values of k , sediment deposition is focused close to the channel and the space between the channel and previous levee crest fills rapidly (Figure 7.11b). Channelward movement of the levee crest occurs even more rapidly when the initial inner levee slope is low (Figure 7.11a). Conversely, low values of k spread deposition over a larger distance. Consequently, the space available between the original levee crest and the channel fills more slowly (Figure 7.11c, d).

The most important aspect of the levee crest evolution captured by both observations and the geometric model (Figure 7.11) is that under a wide range of conditions levee crests will move channelward. However, not all combinations of decay constant and inner levee slope may be equally probable. Data from NAMOC, Hueneme Fan, Amazon Fan, and Var Fan show that the decay constant generally increases with inner levee slope (Figure 7.11e). This suggests that levee crests will shift abruptly between successive stratigraphic horizons rather than occurring gradually throughout the development of a levee. Consequently, a likely scenario for levee crest evolution, in the absence of erosion, would be to observe extended periods of levee crest aggradation followed by an abrupt movement of the levee crest toward the channel.

Channelward movement of the levee crest in the absence of erosion and at the resolution of the available seismic data appears to be an inherent behaviour of levee growth. Because movement is abrupt it is not easily related to the long-term average behaviour of through-channel flows thought to be preserved by channel morphology and possibly preserved by thickness patterns in levee architecture.

7.2.4 Sediment Waves

Sediment waves are large-scale bedforms that occur on some submarine levees. They commonly display an asymmetric morphology and their stratigraphic development appears to show upslope migration. This morphology led Normark et al. (1980) to propose that these features represent giant antidunes formed by the supercritical flow of overbanking turbidity currents. Sediment waves also form in regions where bottom currents, rather than turbidity currents, transport sediment. Observations of sediment waves off Argentina led Flood (1988) to propose that such waves formed as lee waves. The lee wave model has been applied to sediment waves formed under turbidity currents (Howe, 1996). Thus, the same bedform has two potential models explaining its formation and development.

Even in the small sampling of submarine channel-levee systems presented in this thesis, the occurrence of sediment waves spans a wide spectrum of geological environments and potential morphological controls (Table 7.3). Sediment waves form on a wide range of levee slopes and are associated with a large range of channel morphologies. While these conditions reflect areas where sediment waves occur, similar values of, for example, levee slope, occur at other locations along the channel where no sediment waves develop. The range of conditions over which sediment waves can develop appears to contradict their rather restricted occurrence within an individual system.

Although sediment waves appear to occur over a range of geological settings, their stratigraphic development in any of these settings follows a general pattern that can be differentiated into four phases (Figure 7.12). In the first phase of growth, wave amplitude increases and the waves migrate upstream. In the second phase, wave amplitude stabilizes while upstream migration continues. In the third phase of wave development, amplitude decreases. However, the reduction in amplitude can still coincide with upstream migration. Finally, in the fourth phase of growth, amplitude continues to decrease and migration ceases. Throughout wave development, wavelength remains relatively unchanged except where sediment waves coalesce upsection. In this case, wavelength increases. In other examples, larger sediment waves develop a

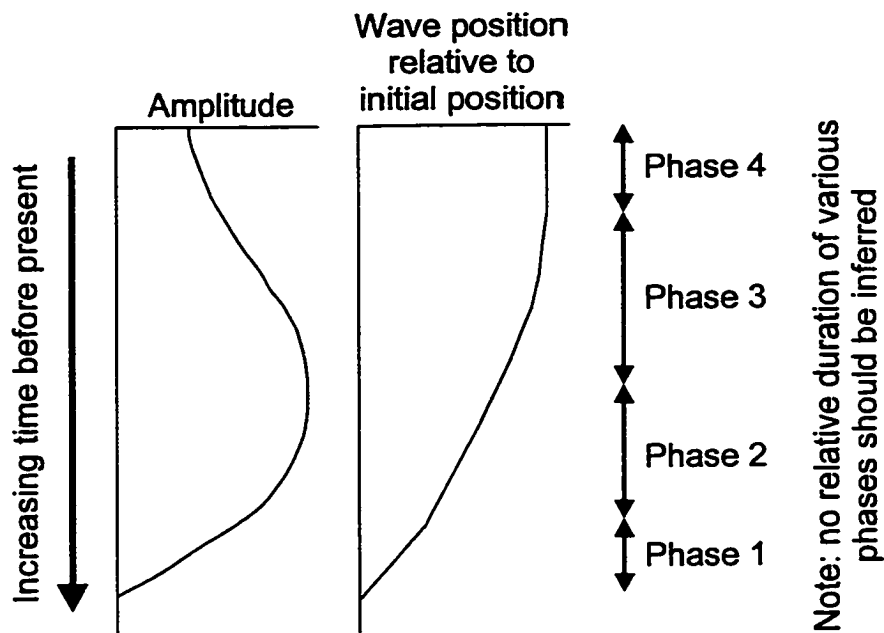


Figure 7.12. Schematic representation of the stratigraphic development of sediment waves, synthesizing observations from NAMOC, Hueneme Fan, Var Fan, and Laurentian Fan.

hummocky morphology on their downstream limb, perhaps indicating the development of smaller waveforms, analogous to ripples forming on the back of dunes.

Table 7.3. Summary of sediment wave characteristics and associated channel and levee morphology. L_{sw} = wavelength, B = amplitude. Values of channel slope and channel depth are reported for modern channel only to give some indication of the differences in channel morphology between the systems and not to suggest the possible values for channel slope and channel depth at the time of sediment wave formation.

System	L_{sw} (km)	B (m)	Levee slope (m km ⁻¹)	Channel slope (m km ⁻¹)	Channel depth (m)
NAMOC	0.5-1	2-5	~ 1	1-2	100-200
Hueneme Fan	0.2-0.5	5-10	~ 10	5-15	10-30
Var Fan	1-7	10-50	~ 10	5-10	100-300
Laurentian Fan	5-7	5-15	~ 5	~ 10	400-600

Comparison of Sediment Wave Models

The consistent stratigraphic development of sediment waves is not explicitly accounted for in the antidune model of Normark et al. (1980). Because wavelength does not vary substantially, predictions of the antidune model (see Eq. 1.16) would suggest that flow character remains unchanged in spite of the fact that wave amplitude and migration progressively change through time. Alternatively, the antidune model may only apply to the initial phase of sediment wave growth

The lee wave model for sediment wave growth (Flood, 1988), of which the antidune model (Normark et al., 1980) is an end-member, predicts upstream migration of the sediment wave and changes in wave amplitude. The lee wave model (see Eq. 1.17) relates the ratio between sedimentation rates on the upstream and downstream limbs of the sediment wave, expressed as the sedimentation rate ratio (SRR), to flow velocity, wavelength, and wave amplitude. The relationships between SRR, wave amplitude, and migration rate suggest potential feedbacks between morphology of a sediment wave and wave growth. Once sediment waves begin to grow under the influence of a particular flow velocity, the SRR will promote an increase in the amplitude of the waveform and upstream migration of the wave. However, because SRR is inversely related to amplitude, an increase in amplitude will promote a decrease in the SRR. Because the SRR reflects the difference in sediment deposited on the upstream and downstream limbs,

a decrease in the SRR reflects more uniform deposition which reduces wave amplitude and decreases the apparent migration of the waves. The feedbacks predicted by the lee wave model may explain the observed stratigraphic development of sediment waves, but the model is sufficiently complex that exact predictions of sediment wave development cannot be derived easily. Furthermore, the apparently random occurrence of sediment waves on levees makes them difficult to incorporate into a model that relates levee architecture to through-channel flow character.

7.3 Physical Interpretation of Depositional Lengthscales in Levee Architecture

A major finding of this thesis has been that identifiable lengthscales exist in levee architecture. These lengthscales include k^{-1} , defined by the variations in depositional sequence thickness perpendicular to channel trend, and λ^{-1} , the lengthscale for downchannel variations in sediment thickness at the levee crest. Parameterizing levee architecture in such a manner allows for the investigation of quantitative relationships between these measures of levee architecture and measures of channel morphology, including channel half-width, W , channel relief, D , and downchannel slope, β . The extension of the quantifiable parameters of a channel-levee system to explicitly include levee architecture represents a fundamental improvement on the description of these systems and facilitates comparison between submarine channel-levee systems and fluvial systems. Furthermore, the relationships between levee architecture and channel morphology suggest that physical parameters of through-channel turbidity currents may be recorded by levee architecture.

In this section, simple models are constructed to explain the physical dependence of the depositional lengthscales in levee architecture on the character of the through-channel flow. Because levee deposits record sediment removal from the through-channel flow, levee architecture may respond to through-channel flow character. Furthermore, it is generally thought that channels evolve so as to reflect the hydrodynamics of through-channel flows (e.g., Komar, 1973; Clark et al., 1992). Consequently, correlation of the across-levee lengthscale for thickness variations, k^{-1} , and the downchannel lengthscale for thickness variations, λ^{-1} , with channel morphology may reflect the control of flow character not only on channel morphology but also on levee architecture. Therefore,

changes in levee architecture may reflect changes in channel morphology and flow character.

7.3.1 General Interpretation of Across-Levee Lengthscale

An important feature of thickness patterns is the distribution of this sediment across the levee, parameterized by a spatial decay constant, k . A simple scaling argument balancing the flux of sediment to the bed, $w_s L_y C$ ($\text{m}^2 \text{s}^{-1}$), against the flux of sediment across the levee originating from the channel, vhC ($\text{m}^2 \text{s}^{-1}$), yields

$$k^{-1} \sim \frac{vh}{w_s} \quad (7.11)$$

where C is the volume concentration of sediment, L_y (m) is levee width and estimated using the inverse decay constant, k^{-1} (m), vh ($\text{m}^2 \text{s}^{-1}$) is the volume flux across the levee, and w_s (m s^{-1}) is the settling velocity of particles deposited on the levee. The vh term represents the product of across-levee velocity, v (m s^{-1}), and overbank flow thickness, h (m). The relationship given by (7.11) would also arise from the steady-state balance between the time scale for removal of particles from the flow, h/w_s and the time scale for movement of sediment across the levee, L_y/v . A simplified but more formal presentation of the steady-state balance describing across-levee variations in volume concentration is given by

$$\frac{\partial C}{\partial y} = -\frac{w_s}{vh} C \quad (7.12)$$

which, when vh and w_s are constants, suggests that C varies across a levee according to

$$C = C_o \exp\left(-\frac{w_s}{vh} y\right) \quad (7.13)$$

A simple model for sediment deposition (e.g., McCave & Swift, 1977) suggests that sediment thickness across a levee scales with volume concentration according to

$$\eta_{lc} \sim w_s C n \tau \quad (7.14)$$

where, n is the number of events and τ (s) is the average duration of an event, neither of which should vary substantially either across a levee or downchannel. Substituting (7.13) into (7.14) yields

$$\eta \sim w_s C_o n \tau \exp\left(-\frac{w_s}{vh} y\right) \quad (7.15)$$

which suggests that the spatial decay constant calculated from variations in sediment thickness perpendicular to channel trend is given by w_s/vh . At the levee crest sediment thickness, η_{lc} , is given by

$$\eta_{lc} \sim w_s C_o n \tau \exp\left(-\frac{w_s}{vh} y_{lc}\right) \quad (7.16)$$

The balance of fluxes across a levee, (7.11), or solution of a simple sediment conservation equation, (7.13), suggests that large values of k^{-1} correspond to either large values of vh or small values of w_s . It should be noted that k^{-1} , calculated from a depositional sequence, reflects the integrated behaviour of many flows. Because of this, the vh term estimated from k^{-1} represents an average value for the flux of fluid transferred to the levee from the typical through-channel flow. Although not necessarily at the scale of individual events, the internal reflection geometry of depositional sequences is conformable and divergent. Such a simple internal geometry favours limited variability in the flow character of individual events making up a depositional sequence. If flows possessed a wide range of thicknesses and/or velocities on a levee, it is likely that such behaviour would be expressed in the acoustic character of depositional sequences (especially when imaged by high resolution instruments). Furthermore, depositional sequences composed of turbidites deposited under widely variable flow conditions might not be expected to conform to an exponential pattern.

The w_s term in (7.11) represents the average settling velocity of the particles deposited on the levee and does not appear to vary significantly between systems. Levees tend to be fine-grained monotonous successions of muddy silts commonly with intervening silt and fine sand beds, providing further evidence for the limited variability in vh . Core data from the systems studied here suggest that levees consist of turbidites whose character does not radically change either within a system or between systems. Some minor variability can be seen in modal grain size on Amazon Fan (Chapter 5; Fig. 5.24-5.25). The frequency of laminae also varies, but this only appears to affect the depositional style of the silt fraction and not the overall grain size of the levee sediments. The lowest decay constants characterize NAMOC (Chapter 3; Tables 3.2-3.9) and

Laurentian Fan (Chapter 6; Tables 6.1-6.3), but cores show the levees to be muddy silt to silty mud with silt laminae. Amazon Fan (Chapter 5; Tables 5.4-5.7) has decay constants up to an order of magnitude greater than on NAMOC or Laurentian Fan, yet the levee sediments still consist of muddy silts with silt laminae. On Reserve Fan (Chapter 5; Table 5.1) where decay constants are greatest, the levees consist of muddy silts. Consequently, over two-orders-of-magnitude difference in the decay constant between systems is not readily explained by such a range in the settling velocity of the particles deposited on the levees. Although the effects of flocculation complicate the relationship between grain size of the deposit and particle size within the flow (e.g., Kranck, 1984), one might reasonably expect that if settling velocity varied by two orders of magnitude that some indication would be present in the character of the turbidites deposited on the levees of different systems.

The relative uniformity of the sediments on levees and, by inference, the limited variability in particle settling velocity leaves the vh term in (7.11) as the potential source of differences in k^{-1} between systems. Furthermore, the simple internal reflection geometry of depositional sequences and the limited variability in bedding character in levee sediments suggests that the vh calculated from k^{-1} represents a meaningful ensemble average. The large values of k^{-1} characterizing systems like NAMOC and Laurentian Fan reflect flows where vh is large whereas smaller values of k^{-1} such as those on Hueneme, Amazon, and Reserve fans suggest that the vh term is small. On Reserve Fan ($k^{-1} \sim 1$ km), where the flow was monitored directly (Normark, 1989), through-channel velocity was estimated to be about 0.1 m s^{-1} . On Amazon Fan ($k^{-1} \sim 5$ km), velocity estimates derived from the grain size of particles deposited by the flow and from application of the cross-flow slope equation (Komar, 1969) are on the order of 1 m s^{-1} (e.g., Pirmez & Flood, 1995). On NAMOC ($k^{-1} > 20$ km), similar indirect methods suggest velocities of several metres per second (Klaucke et al., 1997). This evidence suggests that vh is a direct function of flow velocity, but says little about the exact form that this dependence might take. What is needed to link levee architecture to the character of through-channel flows is a model relating the magnitude of fluid losses to levees, vh , to through-channel flow character.

7.3.2 Constant Thickness Model

Consider a turbidity current flowing through a channel of depth, D , that entrains ambient fluid through its upper interface and because flow thickness, H , exceeds local channel relief, the flow discharges fluid from the channel to the levees (Figure 7.13). Furthermore, assume that the flux to the levees is kinematically defined such that the flux of fluid to levees exactly balances entrainment and divergence of the through-channel advective flux. In such a flow, the turbidity current maintains a constant thickness while volume concentration of sediment decreases downchannel; clean water enters the flow from above and an equal volume of sediment-laden fluid exits the flow out the sides. If fluid losses to the levees outpace fluid gains due to entrainment, flow thickness would decrease and overbanking could cease. Consequently, this type of flow represents conditions for the maximum, sustainable loss of sediment to the levees while remaining consistent with the observed downchannel continuity of levee deposition. Appendix A reports the full derivation of the equations for conservation of water, sediment, and momentum describing such a flow.

The model envisioned above makes several simplifying assumptions about channel morphology, namely that channel size and slope are constant in the downchannel direction. In most of the systems presented in this thesis, channel width (or half-width) is uniform downchannel over the channel reach characterized by levee deposition (Hueneme Fan, Fig. 4.3; Reserve Fan, Fig. 5.1; Laurentian Fan, Fig 6.3). On Amazon Fan (Fig. 5.6), channel width is relatively uniform over about 400 km of the middle channel reach (from 300 - 700 km downchannel), increasing slightly over the last 100 km. The most significant changes in channel half-width are seen on NAMOC (Fig. 3.6). However, most of the variability characterizes the upper reach of NAMOC. Between cross-section 3 and 5, a distance of approximately 300 km, half-width decreases from about 8 km to about 5 km and between cross-sections 4 and 5, a distance of about 200 km, half-width does not change significantly, averaging about 5 km.

Slope does tend to decrease downchannel, but the variability in slope within a system is small relative to the variability in slope between systems. On NAMOC, slope

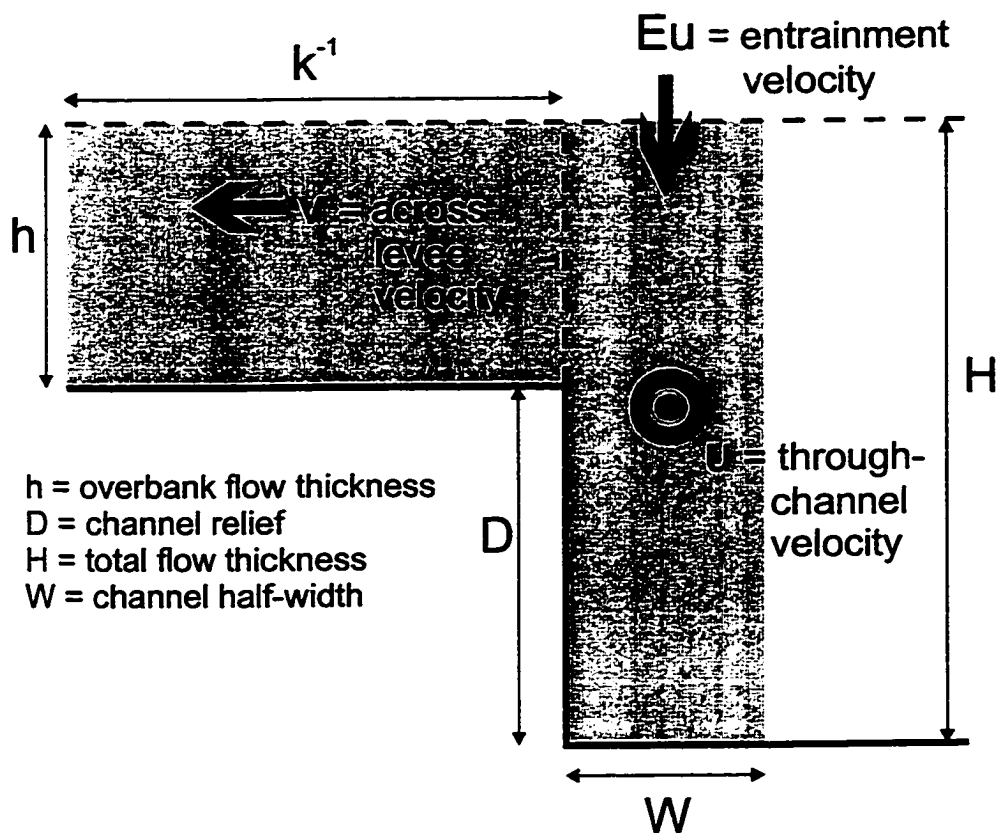


Figure 7.13. Definition sketch for constant thickness model.

does not change significantly from an average value of about 0.7 m km^{-1} (Fig. 3.3). A gradual decrease in slope characterizes Amazon Fan, but this decrease from about 8 m km^{-1} to around 2 m km^{-1} (Fig. 5.6) occurs over a distance of 700 km. Slopes on Hueneme Fan decrease as well from about 18 m km^{-1} to about 5 m km^{-1} ; however, this decrease includes the region of the fan where the channel merges with the depositional lobe. On Laurentian and Reserve fans, variability in slope is small with Laurentian Fan having average channel slopes of 10 m km^{-1} (Fig. 6.5) and Reserve Fan having slopes of about 20 m km^{-1} .

A similar trend can be seen in channel relief; it also tends to decrease downchannel, but not dramatically. The largest channel relief is seen on Laurentian Fan where along Western Valley it averages about 500 m along the upper reach of the channel (over a distance of up to 150 km) before decreasing (Fig. 6.5). Over the upper reaches of Hueneme Channel ($< 10 \text{ km}$ downchannel), channel relief decreases from about 30 m to 20 m. It then declines sharply as the channel merges with the depositional lobe. More subtle changes in channel relief occur on Amazon Fan where channel relief varies between 50 m and 100 m over the lower 500 km of the channel (Fig. 5.6) and NAMOC where channel relief decreases from 220 m to about 100 m over 400 km.

The simplified equations for conservation of momentum, water, and sediment arising from the assumptions of constant channel morphology and a kinematic definition of fluid losses to the levees can be written as

$$\frac{\partial u^2}{\partial x} = 2g_o \sin\beta C - 2 \frac{(E + C_D)}{H} u^2, \quad (7.17)$$

$$vh = EuW - HW \frac{\partial u}{\partial x}, \quad (7.18)$$

and

$$\frac{\partial C}{\partial x} = -\frac{EC}{H}, \quad (7.19)$$

respectively, where $u \text{ (m s}^{-1}\text{)}$ is the layer- and width-averaged velocity downchannel, $v \text{ (m s}^{-1}\text{)}$ is the layer-averaged cross-levee velocity at the channel edge ($y = W$), $h \text{ (m)}$ is the overbank flow thickness, and $H \text{ (m)}$ is the through-channel flow thickness. Provided that the entrainment coefficient and slope are constants, (7.19) has the solution

$$\frac{C}{C_o} = \exp\left(-\frac{Ex}{H}\right), \quad (7.20)$$

suggesting that volume concentration decreases exponentially with distance. Under the assumptions of the model, the transfer of sediment from the through-channel flow to the levees is responsible for the decay in volume concentration. The entrainment coefficient, E , is not well constrained but is known to be a direct function of slope and an inverse function of Richardson number (Ellison & Turner, 1959). In turn, Richardson number may be an inverse function of slope (Middleton, 1966b; Bowen et al., 1984). Consequently, the relatively uniform values of slope characterizing individual submarine channels argues in favour of the entrainment coefficient being approximately constant.

Equation (7.20) can be substituted into (7.17) yielding a first-order differential equation whose solution is given by

$$\left(\frac{u}{u_o}\right)^2 = \Gamma_2 e^{-Ex/H} + (1 - \Gamma_2) e^{-2(E+C_D)x/H} \quad (7.21)$$

where

$$\Gamma_2 = \frac{2g_o \sin\beta C_o H}{(E + 2C_D)u_o^2} = \frac{2Ri_o \sin\beta}{(E + 2C_D)} \quad (7.22)$$

and where Ri_o is the initial bulk Richardson number of the flow and is given by

$$Ri_o = \frac{g_o C_o H}{u_o^2} \quad (7.23)$$

The second term in (7.21) reflects near-field effects imposed by the somewhat artificial initial conditions for flow that are used to solve the equations. The initial conditions are artificial in the sense that the flow is required to start off exceeding local channel depth by some specified amount. Such conditions may occur where the start of the leveed channel coincides with a break in slope that produces a hydraulic jump which abruptly increases flow thickness above channel relief. On the other hand, a perhaps more plausible condition would have the flow begin confined within the channel and then, because of entrainment, it would progressively increase in thickness eventually growing to exceed channel relief. Nevertheless, although the initial conditions for flow have been

chosen carefully in order to simplify the governing equations, their effect dies out quickly.

The first term on the right-hand side of (7.21) contains the relevant physics describing the large-scale behaviour of the flow, i.e., after the effect of the initial conditions has decayed, and is of primary interest here. Retaining this term, the solution for velocity simplifies to

$$\left(\frac{u}{u_0}\right)^2 = \Gamma_2 e^{-Ex/H} \quad (7.24)$$

This equation can be recast into a more familiar form given by

$$u^2 = g_0 CH \frac{\sin\beta}{\left(\frac{1}{2}E + C_D\right)} \quad (7.25)$$

which is equivalent to the Chezy equation for turbidity current flow (e.g., Komar, 1977; Bowen et al., 1984; Stacey & Bowen, 1988a) with a slightly modified form for the frictional drag on the flow.

Substituting (7.24) and its derivative with respect to x into (7.18) yields

$$vh = \frac{3}{2}EuW, \quad (7.26)$$

suggesting that vh depends on the product of the entrainment coefficient, E , the through-channel velocity, u , and channel half-width, W . Unfortunately, u is unknown and E is not well-constrained, although it is a function of slope and bulk Richardson number (e.g., Ellison & Turner, 1959).

Figure 7.14 graphically depicts the variation of u/u_0 and vh/EuW described by (7.21) and the full solution of vh given in Appendix A by (A.35) for various values of Γ_1 (see Appendix A for definition) and Γ_2 (Table 7.4). In all cases, velocity decreases downchannel (Figure 7.14a) and the value of vh/EuW converges to 1.5. This behaviour occurs for values of E/C_D that span about two orders of magnitude (Table 7.4), suggesting that the model is relatively insensitive to these rather poorly known parameters.

Table 7.4. Values of Γ_1 and Γ_2 and the corresponding value of E/C_D used to produce model results in Figure 7.14.

Γ_1	Γ_2	E/C_D
0.6	1.07	0.14
0.8	1.20	0.5
1.0	1.33	1
1.25	1.50	2
1.75	1.83	10

Because the model suggests that vh depends on unknowns, additional information is required to test the model against observations. Using the simple equation of sediment deposition, (7.14), downchannel patterns in η_{lc} likely scale with downchannel patterns in volume concentration. In the model, volume concentration decays exponentially, suggesting that sediment thickness at the levee crest decays exponentially. Substituting (7.20) into (7.14) yields

$$\frac{\eta_{lc}(x)}{\eta_{lc}(0)} \cong \exp\left(-\frac{Ex}{H}\right), \quad (7.27)$$

providing a physical interpretation of the downchannel lengthscale for variations in sediment thickness at the levee crest parameterized by λ^{-1} . Note that in using (7.14) the same assumptions concerning limited variability in flow conditions are being made as was done in relating k^{-1} to vh/w_s . But again, the internal geometry of the depositional sequences shows no evidence for such variability in flow conditions.

In the model, the lengthscales for levee deposition depend upon flow parameters. The model suggests that downchannel variations in sediment thickness, parameterized by λ^{-1} , is given by

$$\lambda^{-1} \cong \frac{H}{E} \quad (7.28)$$

Using (7.11) and (7.26), the lengthscale for variations in sediment thickness across the levee, k^{-1} , is given by

$$k^{-1} \cong \frac{3 EuW}{2 w_s} \quad (7.29)$$

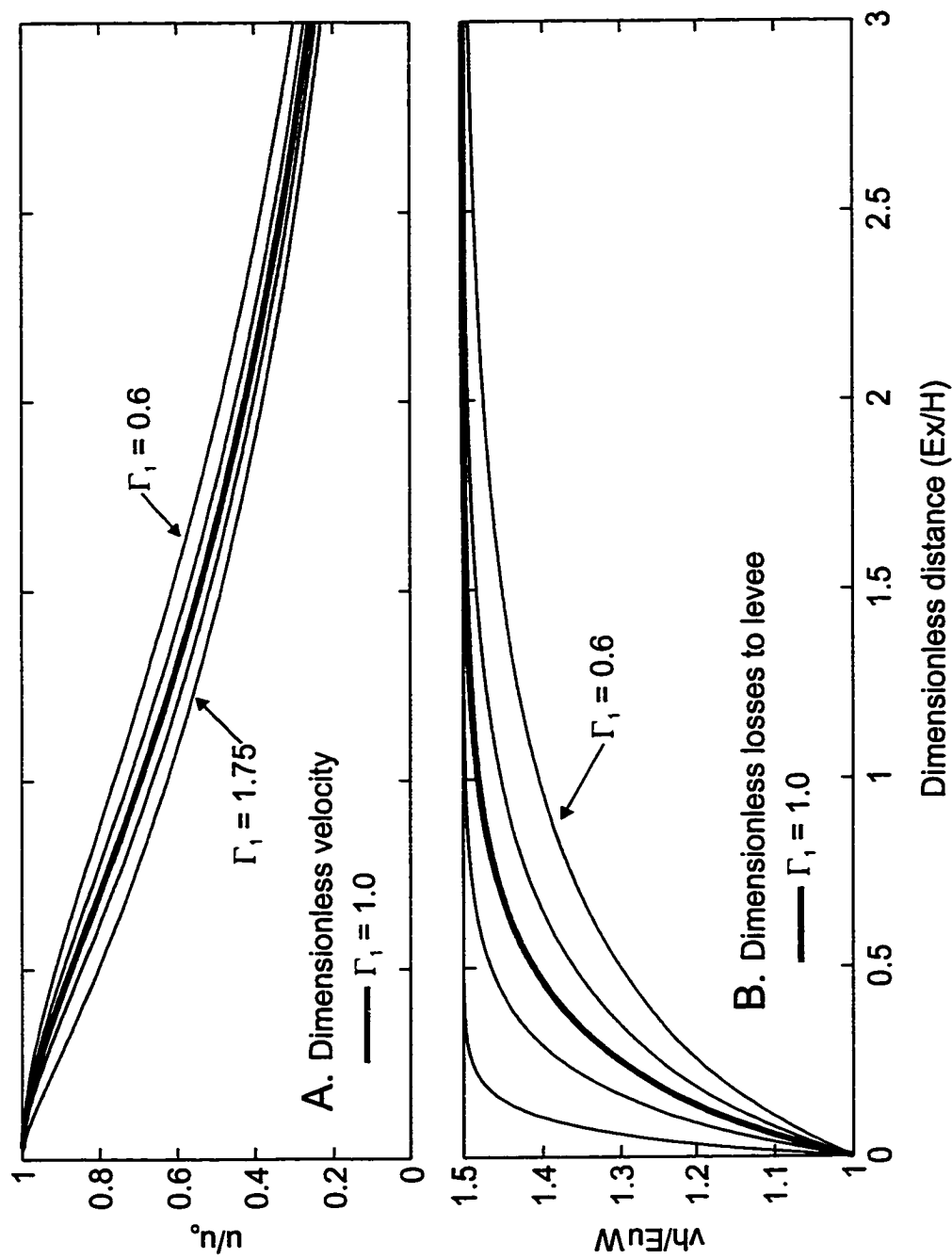


Figure 7.14. Flow behaviour in constant thickness model for values of Γ_1 given in Table 7.4: A. dimensionless velocity; B. dimensionless loss to levees as a function of dimensionless distance downchannel.

To assess the validity of the model using either (7.28) or (7.29) requires knowledge of the entrainment coefficient, E . However, the product of (7.28) and (7.29) removes the effect of the entrainment coefficient and is given by

$$k^{-1}\lambda^{-1} \equiv \frac{3 u_{HW}}{2 w_s} = \frac{3 Q}{2 w_s} \quad (7.30)$$

where Q ($\text{m}^3 \text{s}^{-1}$) is through-channel volume discharge; unfortunately, Q is also an unknown parameter.

For fluvial systems, the relationships between volume discharge and channel parameters like width, depth, and velocity, are described by the hydraulic geometry of the channel (Leopold & Maddock, 1953). Each of the three main channel parameters — width, depth, and velocity — vary with discharge according to power laws given by

$$\begin{aligned} \text{width} &\sim Q^b \\ \text{depth} &\sim Q^f \\ \text{velocity} &\sim Q^m \end{aligned} \quad (7.31)$$

where b , f , m are empirical or theoretical exponents. The exponents have been assessed empirically for a large number of rivers and the values of the exponents vary because of such variables as climate, bedrock type, and channel form (e.g., Ritter, 1986). Studies that have synthesized the world-wide variability in these exponents (Knighton, 1975; Park, 1977; Rhodes, 1977) all show that the exponents have a wide range of values. Rhodes (1977) suggested that the exponents should be expected to take almost any combination of values and that their actual values may be useful in the development of an empirical classification of channels. His study highlights the fact that hydraulic geometry represents a simple description of a complex process. However, Langbein & Leopold (1964) derived equilibrium values for b , f , and m by assuming that work done by a river at a particular cross-section is distributed uniformly. In the absence of interactions between sediment load, flow resistance, flow depth, and flow velocity, a uniform distribution of work requires that each exponent equal 0.33. But because such interactions do occur (for example, resistance to flow in river channels scales with flow depth; Langbein & Leopold, 1964) the theoretically-derived values for b , f , and m are 0.23, 0.42, and 0.35, respectively. Agreement between these theoretical values and the original estimates of Leopold & Maddock (1953) was favourable (Langbein & Leopold,

1964) and has led to their general acceptance in geomorphology literature (e.g., Ritter, 1986).

In deriving their values of b , f , and m , Langbein & Leopold (1964) required that W scale as $D^{0.55}$, a relationship that holds for a flow where the forces applied to the bed and banks are distributed uniformly (Nizery & Braudeau, 1955). In a preceding section, it was shown that there is a relationship between channel half-width and channel relief (Figure 7.6), i.e., $W \sim D^{0.62 \pm 0.16}$. This relationship is very close to the relationship of Nizery & Braudeau (1955) which in turn forms the basis for the equilibrium hydraulic geometry relationships of Langbein & Leopold (1964). Although it cannot be further tested given the available data from submarine channels, if the equilibrium hydraulic geometry relationships also hold for submarine channels then the product of k^{-1} and λ^{-1} should scale as $D^{2.38}$, i.e., using $f = 0.42$ and where $D \sim Q^{0.42}$.

The product of k^{-1} and λ^{-1} varies with D (Figure 7.15) according to

$$k^{-1}\lambda^{-1} \sim D^{2.00 \pm 0.83} \quad (7.32)$$

with $r^2 = 0.92$. At the 95% confidence level the observed relationship between $k^{-1}\lambda^{-1}$ and D cannot be considered different from the relationship derived from hydraulic geometry and accounts for a significant amount of the variance in the data. This suggests that the physical interpretation of depositional lengthscales given by the constant thickness model may represent a reasonable, albeit simplified, depiction of an overbanking flow with losses to the levees from overbanking, vh , scaling as EuW .

7.4 Discussion

The present study of levee architecture has developed empirical relationships between levee and channel morphology and has proposed a simple model to account for the potential physical parameters of through-channel turbidity currents recorded by levee deposition. The following section discusses some outstanding issues that have arisen from this study including, how the empirical relationships might be applied to the study of channel-levee systems, the origin of variability between systems, and the development of a tentative model encompassing the expected downchannel structure of channel-levee systems.

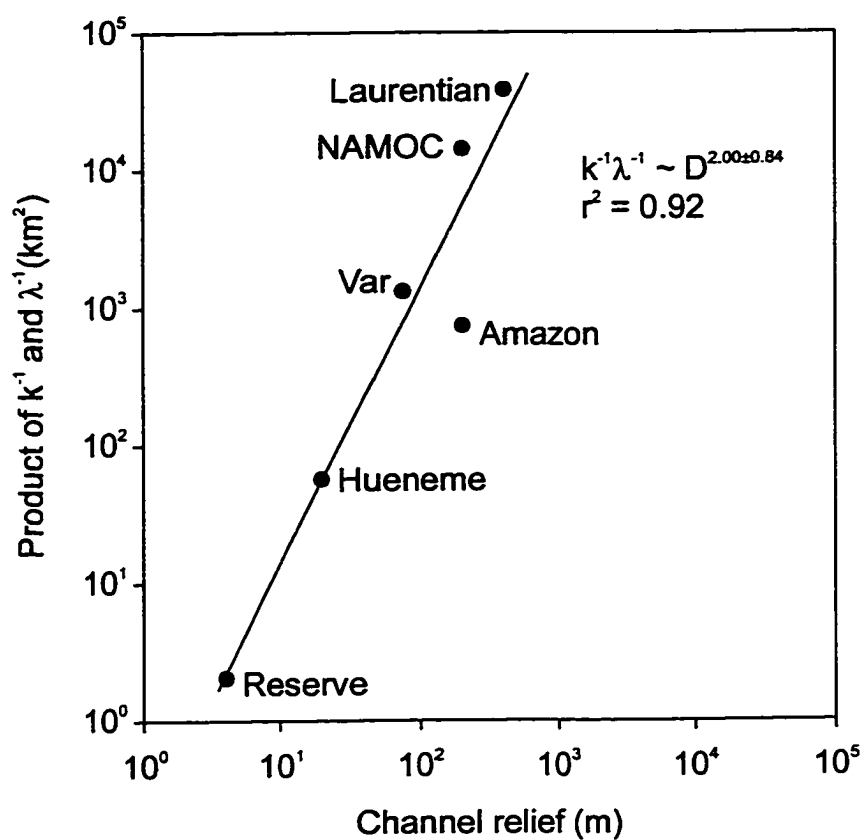


Figure 7.15. Observed relationship between channel relief, D , and the product of k^{-1} and λ^{-1} . Using the constant thickness model and the hydraulic geometry relationships of Langbein & Leopold (1964), this product should scale as $D^{2.38}$.

7.4.1 Application of the Empirical Relationships

In developing the empirical relationships between measures of levee architecture and channel morphology, data were taken from a wide variety of channel-levee systems, spanning different geological settings. Consequently, the relationships capture the mean behaviour of channel-levee architecture, just as the compilations of hydraulic geometry from many rivers reflect the mean behaviour of fluvial systems. It has often been noted that for a particular section of a particular river the relationships predicted by the general hydraulic geometry equations do not hold. This lack of agreement between theoretical relationships and observations generally has led fluvial geomorphologists to investigate other factors that may influence the behaviour of a river, such as bedrock type, climate, or vegetation (e.g., Ritter, 1986). In rivers, the hydraulic geometry relationships describe a quasi-equilibrium condition (e.g., Langbein & Leopold, 1964). This same reasoning can be applied to the scale relationships derived for submarine channel-levee systems. The scale relationships themselves provide an indication of equilibrium behaviour which can be applied to an individual system. What now exists because of this study is a standard for comparison, providing a means for quantitatively assessing the information recorded in channel-levee architecture.

Both channel half-width and levee width scale approximately with the square root of channel depth. Wide channels are deep and have wide levees; narrow channels are shallow and have narrow levees. For modern channels, the history of channel filling is poorly resolved by standard seismic reflection profiling because channel floor sediments have high reflectivity that prevents penetration of acoustic energy and if mud is lacking, do not possess impedance contrasts. However, the levees, comprising alternating silt and mud tend to well resolved by seismic reflection profiling. Provided that the relationships advanced here are correct, the scaling between channel relief and levee width provides a method for estimating past values of channel depth. Coupled with the elevation of buried levee crests, estimates of past channel depths provide estimates of the thickness of channel fill over a particular stratigraphic interval, indirectly providing a stratigraphy for the channel fill within the limits of error associated with the empirical relationships.

This procedure for indirectly estimating past channel depth and channel fill stratigraphy was applied to Hueneme Fan. On Hueneme Fan all that is known unequivocally about the channel fill is that since deposition of horizon J about 75 m of sediment have accumulated. During this same interval, the levee stratigraphy can be divided into four discrete time slices (Chapter 4). Using the relationships derived from the analysis of levee thickness patterns, a history of channel fill can be proposed (Figure 7.16). Application of (7.4) predicts that channel depth was at a minimum during deposition of DS3 and that post-dating horizon G but pre-dating horizon L, the channel was erosionally deepened. The timing of this channel deepening generally correlates with a time of widespread sand deposition on the distal fan (Piper et al., 1998b, submitted).

In order to test the validity of the empirical relationships between levee architecture and channel morphology, they need to be applied to a channel-levee system not used in the regression analysis. One such system is Zaire Fan off the west coast of Africa, studied most recently by Droz et al. (1996). This channel-levee system has sinuosities comparable to Amazon Channel (Chapter 5), averaging 1.85. Channel relief decreases from about 300 m on the upper fan to < 100 m on the lower fan. Channel slope also decreases downchannel from about 8 m km^{-1} to 3.1 m km^{-1} . Using a middle fan seismic line published by Droz et al. (1996; their Fig. 3b), the levee architecture of Zaire Fan channel can be assessed (Figure 7.17). The decay constant for Zaire Fan is approximately $16.4 \pm 1.8 \times 10^{-5} \text{ m}^{-1}$ which equates to a levee width of 6.1 km. The predicted value of levee width from channel relief is 14.7 km with a range that lies between 5.9 km and 36.7 km. The predicted value of levee width from channel half-width is 3.2 km with the 95% confidence limits encompassing a range from 1.2 - 8.8 km. For both relationships, the observed value of k^{-1} lies within the confidence intervals of the expected values of k^{-1} , lending support for the estimated regression equations. Application of the relationships also shows the large errors associated with using the scaling relationships for individual systems.

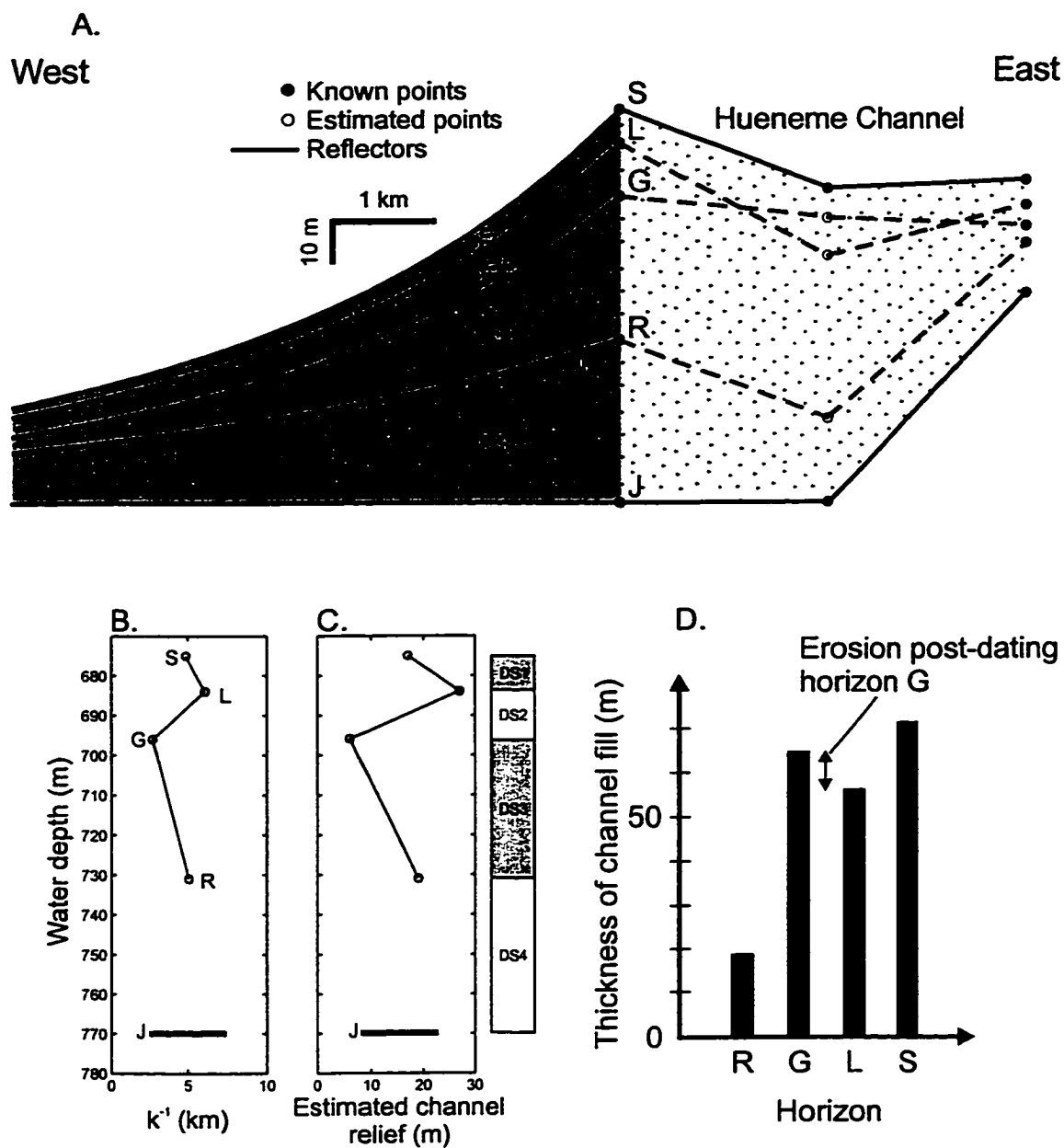


Figure 7.16. A. Schematic depiction of western levee and reconstruction of channel fill history at cross-section 1 of Hueneme Fan. B. Stratigraphic variation in k^{-1} for western levee of Hueneme Fan. C. Estimates of channel depth related to values of k^{-1} . D. Bar graph shows thickness of channel fill at increasingly younger stratigraphic horizons. The decreases in channel fill thickness between G and L suggests erosion of the channel at some time between these horizons.

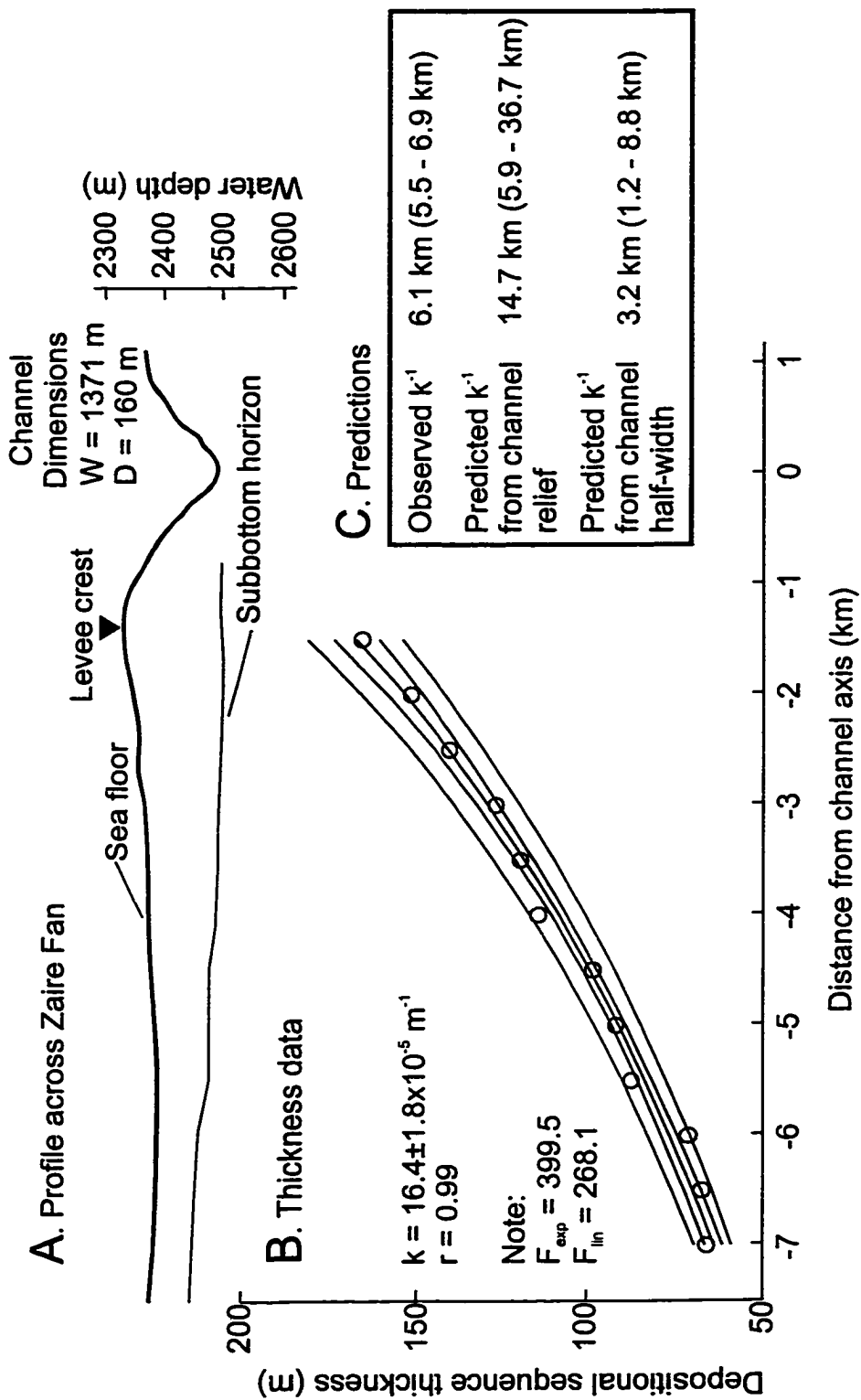


Figure 7.17. Application of empirical relationships to levee architecture from Zaire Fan; A. Interpreted line drawing of seismic profile; B. Thickness data plotted against distance from channel axis; C. Predictions of scaling relationships. Original seismic profile published in Droz et al. (1996; their Fig. 3b).

The empirical relationships between levee architecture and channel morphology also play a role in subsurface and outcrop mapping of ancient channel-levee systems. In outcrop mapping of channel-levee systems, it is the thickness rather than horizontal extent of features that can be determined most easily, simply because exposures are rarely widespread enough to display a complete channel-levee cross-section. In subsurface mapping, owing to the vertical resolution of typical industry seismic data, it is the horizontal extent of features that is better defined. However, horizontal lengthscales in channel-levee systems like levee and channel width are intimately related to vertical lengthscales like channel depth. In subsurface studies, for example, estimates of channel depth can be made from mapping the width of channel features and using the correlation between channel width and channel relief. Furthermore, the width of a channel sets the width of the levees; consequently, mapping of an individual channel provides an estimate of the areal extent of overbank deposition. Channel width also scales with the e-folding length of a channel-levee system, λ^{-1} , so that measurement of a single feature, channel width, can potentially determine the large-scale structure — channel relief, channel length, and levee width — of a submarine channel-levee system.

7.4.2 Differences Between Channel-Levee Systems

The initial sections of Chapters 3-6 presented detailed examinations of individual channel-levee systems, focusing on the such parameters as magnitude and nature of sediment delivery, initiation mechanisms and estimates of turbidity current frequency. When viewed in total, the sample set of channel-levee systems spans a wide range of conditions that could potentially control channel-levee architecture. However, what has been found in the thesis is that the structure of channel-levee systems parameterized by variations in depositional sequence thickness and channel size conforms to simple empirical relationships in spite of differences in source area dynamics or initiation mechanisms. No major outliers exist in correlations between channel morphology and levee architecture that systematically point to differences between systems like NAMOC and Laurentian Fan fed by continental glaciers and systems like Amazon and Hueneme Fan fed by rivers. Furthermore, Amazon and Hueneme Fan have depositional channels (*sensu* Nelson and Kulm, 1973) whereas NAMOC, Laurentian Fan, and Reserve Fan

have depositional-erosional channels. It also appears that planform geometry of the channel, i.e., meandering versus straight, is not immediately related to levee architecture. Hueneme and Amazon Fan have approximately equal values of k^{-1} , but Hueneme Channel is relatively straight whereas Amazon Channel is highly sinuous. Clark et al. (1992) showed that channel slope may play a role in determining sinuosity and therefore the relatively weak dependence of k^{-1} on channel slope is consistent with the weak dependence of thickness patterns on planform geometry.

Faced with numerous sources of variability between systems, it would be natural to presume that levee architecture might well be exceedingly complex. However, the lack of a distinct expression of this variability in levee architecture suggests that an underlying physical process is responsible for the patterns, namely the exponential decay of thickness both across-levee and downchannel and the correlation of this structure with channel morphology. That is not to say that such factors as sediment delivery or initiation mechanisms do not play role in determining channel-levee morphology. It does suggest that the expression of such factors cannot be found in the large-scale structure of levees, potentially limiting the search for causal mechanisms responsible for overall submarine fan morphology to the mechanisms that control channel size. Simply stated, the question that remains unanswered is what is the origin of a particular channel size. Theoretical and experimental work on channel inception (e.g., Imran et al., 1998) may provide insight into this fundamental question.

7.4.3 Physical Process of Overbanking

Most if not all flows will overtop their channels (Clark & Pickering, 1996), but what happens to a flow once it has begun to overbank? The model for overbanking flows presented in this thesis suggests that the depositional lengthscales both across-levee, k^{-1} , and downchannel, λ^{-1} , can be explained by a kinematic balance between losses to the levees, vh , and gains due to entrainment, EuW . Such a balance has been proposed, but not well justified, by Pirmez (1994) and Hiscott et al. (1997).

The kinematic balance that forms the basis for the constant thickness model represents a simplified description of overbanking flow. It does suggest relationships that may be reasonable and that are consistent with observations. It does not, however,

represent a model that explains all observations of levee architecture. In particular, the direct relationship between v_h and through-channel flow velocity suggests that v_h and, therefore, levee width should decrease downchannel because velocity in the model decreases downchannel. Such behaviour is not consistent with observations that show no systematic behaviour of k^{-1} within an individual channel-levee system. It could be that the decreases in through-channel velocity are small or occur over greater downchannel lengthscales than the lengthscales over which observations of k^{-1} have been made. Note that the constant thickness model suggests that e-folding length for downchannel variations in velocity is $2H/E$, twice that of the e-folding length for variations in volume concentration (i.e., H/E). Given the errors in determining k^{-1} and that the uniformity of k^{-1} occurs for distances on the order of H/E or less, it is perhaps to be expected that a demonstrable trend in k^{-1} could not be observed.

Alternatively, velocity could remain approximately uniform if the volume concentration of sediment transferred from the through-channel flow to the levees represented only a fraction of the layer- and width-averaged volume concentration. This might occur where flows possess vertical gradients in volume concentration (e.g., Stacey & Bowen, 1988a). In such cases, the upper portions of the flow would be more dilute than the average volume concentration of the flow and the loss of sediment to the levees may not substantially deplete the gravitational driving force of the flow. If under such conditions v_h still scaled with EuW , then the downchannel variation in u would be smaller than that given by the constant thickness model and thus downchannel variation in v_h and k^{-1} would also be small.

As a third alternative, losses of fluid to the levees may represent some fraction of the gains of fluid caused by entrainment, i.e., less than that suggested by the constant thickness model. Similar to the effect of vertical gradients in volume concentration, the downchannel variations in velocity would be less than suggested by the constant thickness model. In such cases, thickness of the through-channel flow would tend to grow downchannel, but at a lesser rate than caused by entrainment in a confined flow. Eventually, a state may be reached where the channel no longer acts to confine the majority of the flow and a transition may occur from overbanking flow to spreading flow.

The potential consequences of this transition in the downchannel structure of channel-levee systems are further explored in the next section.

7.4.4 Implications for Downchannel Structure of Channel-Levee Systems

Observations of the downchannel structure of channel-levee systems have previously been synthesized into generic patterns for the evolution of channel depth (Menard, 1964), longitudinal profiles (e.g., Pirmez & Flood, 1995), and slope-sinuosity relationships (Clark et al., 1992). The importance of these studies has been to characterize the general behaviour of a channel-levee system to which individual systems can be compared, thereby highlighting potentially anomalous features requiring further investigation. The present study extends the quantifiable parameters of a channel-levee system to include levee width and depositional sequence thickness at the levee crest, finding that the downchannel evolution of these features can be placed within a generic pattern as well. The pattern highlights the nature of correlation between these features of channel-levee architecture that distinguish a channel-levee system into two discrete reaches.

Figure 7.18 summarizes the downchannel patterns of the two most important parameters describing the large-scale structure of levee architecture (Figure 7.18a, b) and the relative average values for channel half-width and channel relief (Figure 7.18c) along with the horizontal extent of individual channel-levee systems used to groundtruth the downchannel patterns. Figure 7.18d schematically depicts the differences in overbanking flow character responsible for the potential bipartite division of a channel-levee system. A primary feature of channel-levee architecture is the observation that decay constants, which parameterize the variations in depositional sequence thickness perpendicular to channel trend, along the upper reach of a channel show little or no systematic trend over distances that can exceed several hundred kilometres (NAMOC, Chapter 3; Laurentian Fan, Chapter 6; Figure 7.18a). When trends in decay constants occur they show a

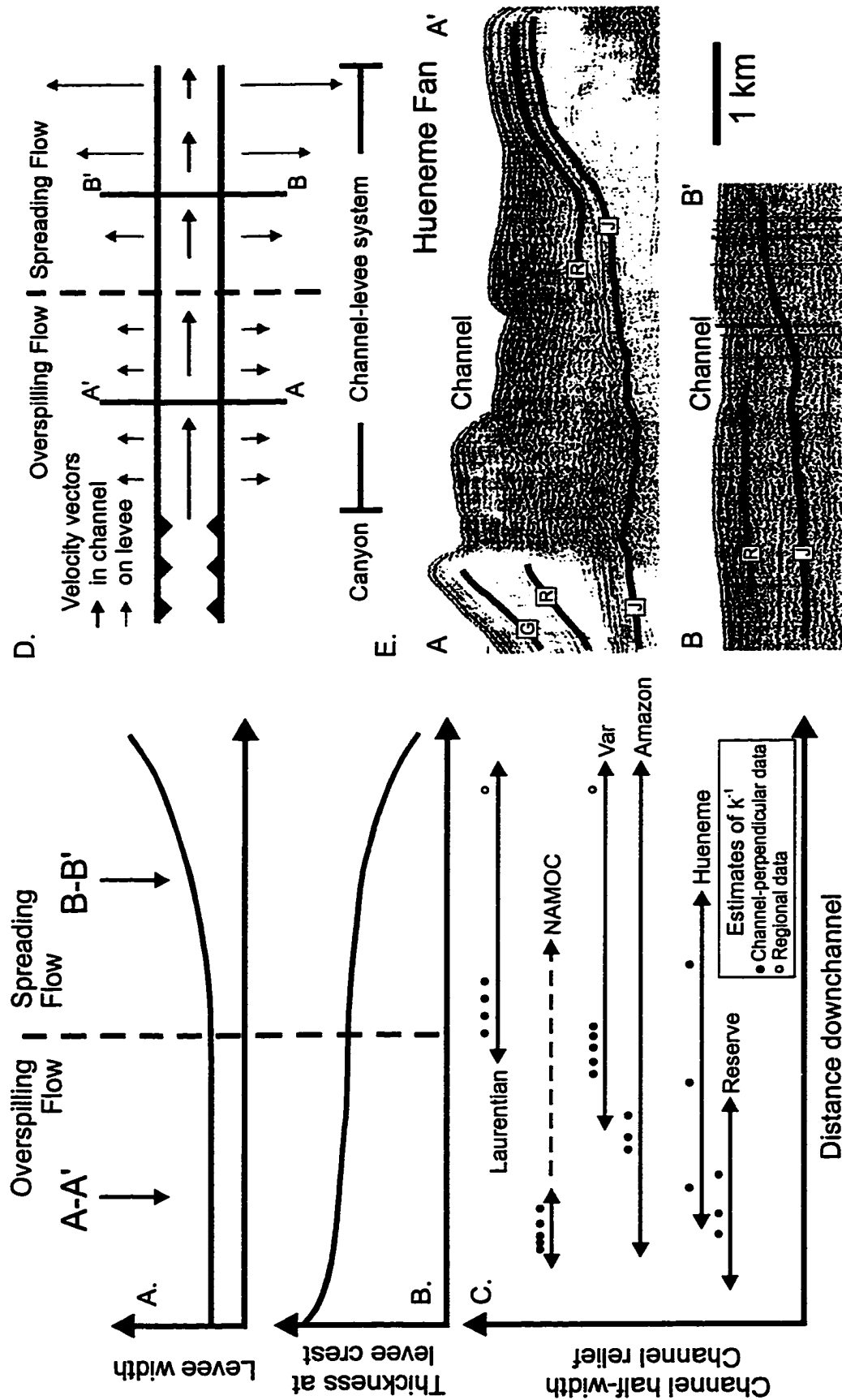
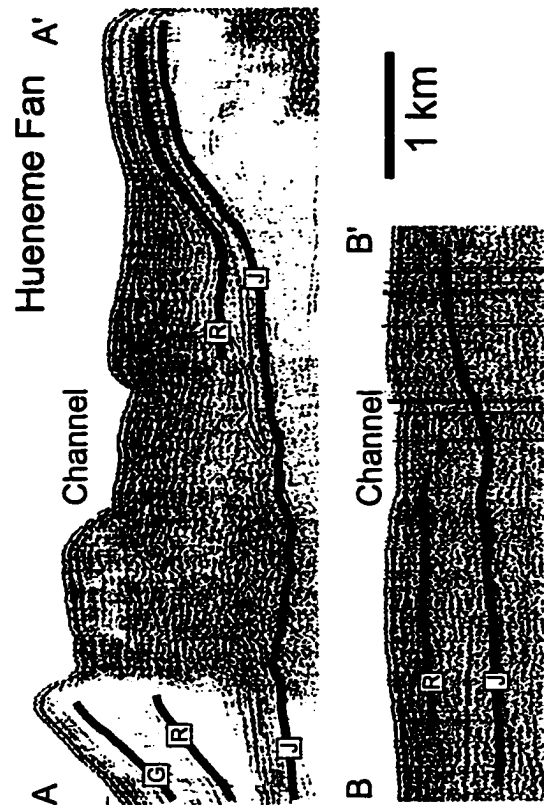


Figure 7.18. General downchannel patterns in A. levee width and B. sediment thickness at levee crest. C. Extent of data used to ground-truth patterns and schematic representation of average channel dimensions (estimates from regional data have unknown stratigraphic age). D. Potential difference in flow processes responsible for bipartite division of channel. E. Expression of overspilling and spreading flow on Hueneme Fan.



decrease at the distal ends of channel levee systems (Hueneme Fan, Chapter 4, Figure 7.18a). Where k^{-1} is uniform, thickness at the levee crest decays exponentially (Figure 7.18b). As k^{-1} increases (i.e., k decreases) on the lower reaches of a channel-levee system, thickness at the levee crest is uniform or decays abruptly.

In terms of flow processes, the inter-relationships between various parameters can be explained by the division of a through-channel flow into two regimes (Figure 7.18d). In the first regime, termed overspilling flow, the channel acts as the main conduit for the downslope transport of sediment. The flow loses sediment to the levees, but does so at a rate that is some fraction of the gains of fluid caused by entrainment. Such a flow will gradually increase in thickness. Continuous depletion of sediment from the through-channel flow, no matter how small, will eventually lead to deceleration of the flow. This deceleration will also tend to increase flow thickness, forcing more of the flow above the confines of the channel. Under these conditions, termed spreading flow, the flow is no longer significantly confined by the channel. Such a flow would produce levees which would increase in width as the flow decelerated.

The downchannel changes in sediment thickness at the levee crest resulting from spreading flow are difficult to predict. Both uniform sediment thickness and abrupt decreases in sediment thickness have been observed along the distal reaches of the systems studied here and in flume experiments studying spreading and axisymmetric turbidity currents. In experiments studying the flow of spreading turbidity currents (Luthi, 1981), a linear decay of velocity with distance coincides with a linear increase in the half-width of the deposit (Figure 7.19). Sediment thickness decays exponentially with distance. Linear decreases in velocity with distance also characterize axisymmetric turbidity currents (Figure 7.20) studied experimentally by Bonnetcaze et al. (1995). In these experiments, a sector tank was used which widened with distance at an angle of 8° (Figure 7.20). Although not free to spread, these flume results show that the decay of velocity behaves linearly as flow width increases linearly. In these flows, the deposit displays regions of relatively uniform thickness interrupted by regions of abrupt decreases in thickness. While the division of the flow into an overspilling portion and a spreading portion remains tentative at this point, this model explains most of the overall downchannel structure of a channel-levee system.

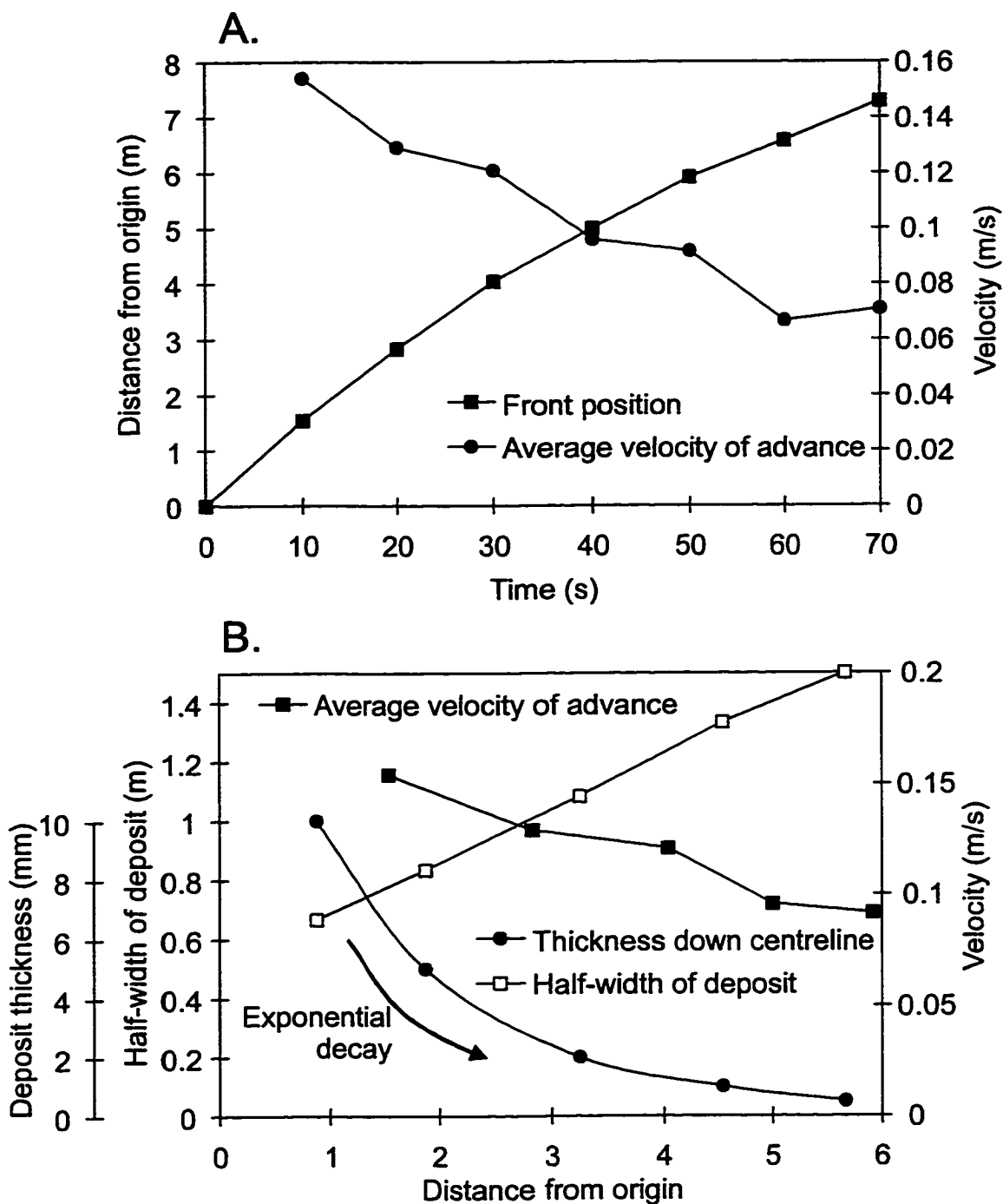


Figure 7.19. Experimental results from investigation of spreading turbidity currents by Luthi (1981); A. flow parameters versus time showing advance of the flow and the velocity of this advance; B. flow and deposit parameters versus distance down flume. Sediment grains used were quartz silt with a mean grain size of 37 μm .

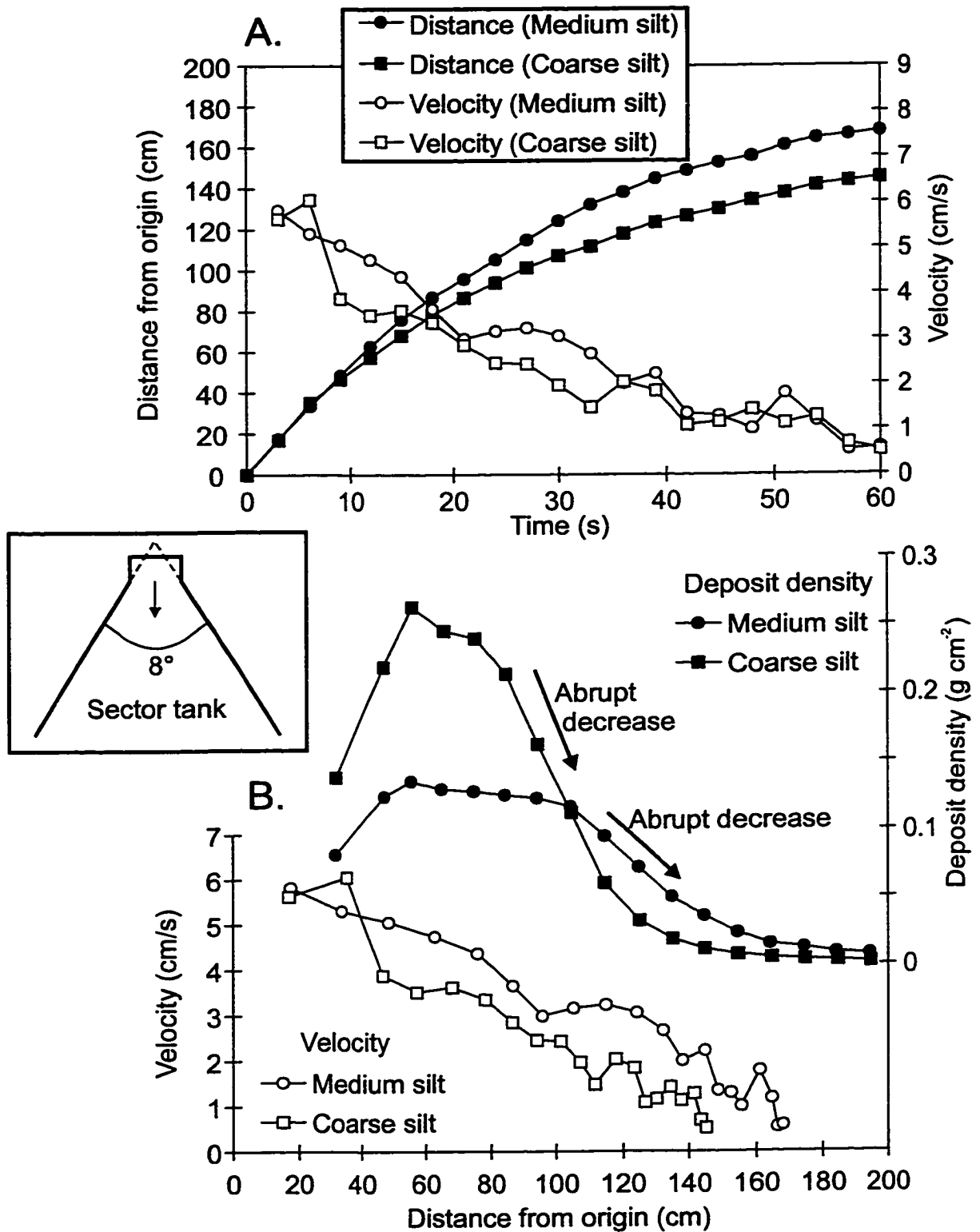


Figure 7.20. Experimental results from the investigation of axisymmetric turbidity currents by Bonnecaze et al. (1995); A. flow parameters versus time; B. flow and deposit parameters versus distance. Medium silt denotes experiment that used $37\ \mu\text{m}$ silicon carbide particles; coarse silt denotes $53\ \mu\text{m}$ silicon carbide particles. Inset shows sector tank geometry.

The downchannel structure of an entire fan system is best represented by data from Hueneme Fan (Figure 7.18e). The expression of overspilling flow is evident on the upper fan (profile A-A') where a well-developed levee shows an obvious contrast in acoustic character with channel fill. This morphology gives way to a more subtle channel-levee system that lacks significant differences in acoustic character between the channel fill and the levee sediments (profile B-B'). This downchannel pattern suggests that separation between channel filling processes and levee growth on the upper fan progressively changes to more uniform deposition. The difference in character on the upper fan indicates different types of sediment and presumably different processes acting in the channel compared to on the levees. In the simple model for downchannel structure of channel-levee systems differences arise because the channel acts as the primary conduit for downslope movement of sediment while the levees passively receive sediment from this downslope flow. On the lower fan, the more uniform character of the sediments both acoustically and in terms of thickness suggests more uniform downslope flow. More uniform conditions perpendicular to channel trend characterize the spreading flow phase. It is suggested that where entire systems can be investigated the downchannel structure schematically depicted in Figure 7.18 should generally be seen.

The division of channel-levee systems into two discrete reaches potentially provides a quantitative method of classifying systems. Although there is no generally accepted definition of the terms upper, middle, and lower fan, the channel extends downslope from the transition between the canyon and channel to the transition between the channel and depositional lobe. It is proposed that a channel-levee system can be divided into two reaches based on the architecture of the levees and channel and the differences in flow behaviour that characterize these reaches. The transition from fan valley to depositional lobe is simply an extension of the spreading flow behaviour established over the lower reaches of a channel-levee system. In addition, because levees are on average almost an order of magnitude more areally important than channels (i.e., levees are approximately eight times wider than channels) their downchannel structure potentially controls the seismic expression of submarine fans in low resolution industry seismic profiles. Because channel-levee morphology divides into reaches characterized by fundamentally different physical processes, future investigation of channel-levee

morphology will be better able to construct relevant physical models by first recognizing where along a submarine channel-levee system the investigation is located.

7.5 Closing Statement

The most important contributions of this study concern the thickness patterns in depositional sequences on levees. The thickness patterns obey relationships that correlate with channel morphology. Because channel morphology is thought to reflect the hydrodynamics of through-channel turbidity currents, a model was sought to link levee architecture directly with through-channel flow parameters. The constant thickness model explores the flow behaviour and levee architecture resulting from the maximal, sustainable loss of sediment and fluid from the through-channel flow. The model represents a physical treatment of a balance suggested by Pirmez (1994) and Hiscott et al. (1997). Testing of the model against observations displays reasonable agreement, provided that through-channel volume discharge of turbidity currents relates to flow parameters in a way analogous to the relationships described by the hydraulic geometry of fluvial systems as given by Langbein & Leopold (1964). The observed relationship between channel half-width and channel relief for submarine systems and its agreement with the relationship describing river channels supports such a contention.

At the outset of this project, levee architecture and its importance to understanding the processes that shape the large-scale structure of channel-levee systems were largely unknown, a limitation also hampering the study of fluvial levees (Brierley et al., 1997). That is not to say that various features of levee architecture like asymmetry, sediment waves, and sediment characteristics (i.e., grain size, sedimentary structures, etc.) had not been studied. Rather, these features have been looked at extensively in the modern, and where possible, ancient record of submarine channel-levee systems, but these observations and their interpretation lacked a framework for the expected behaviour of levee architecture. This thesis has addressed what levees look like, placing important constraints on the more fundamental question, what *should* levees look like? The morphological description of levee architecture has shown that various lengthscales within a channel-levee system are related, at least at the large-scale. The physical interpretation of these lengthscales points to a conceptualization of through-channel flows

that produce levees whose thickness decays exponentially downchannel while their cross-sectional morphology, also displaying exponential patterns in thickness perpendicular to channel trend, remains uniform over downchannel lengthscales that can exceed several hundred kilometres. The absolute magnitude of these lengthscales are correlated directly with channel dimensions, ultimately suggesting that the range of channel-levee architecture, parameterized by levee width, k^{-1} , levee length, λ^{-1} , channel relief, D , and channel half-width, W , is both restricted and related to the hydrodynamics of through-channel flows.

Chapter 8

Conclusions, Contributions, and Directions for Future Research

8.1 General Statement

In Chapter 1, three objectives were presented that, if met, would lead to an improved and more quantitative understanding of levee architecture and the expression of turbidity current flow dynamics in that architecture. These objectives were (1) the systematic and quantitative characterization of levee architecture, (2) the definition of physical controls on levee architecture, and (3) investigation of the potential for using levee architecture to infer environmentally-relevant turbidity current flow parameters. In order to meet those objectives, the architecture of levees from a wide range of geological environments has been investigated. The channel-levee systems investigated include NAMOC and Hueneme, Reserve, Amazon, Var, and Laurentian fans. This chapter summarizes the major findings and conclusions of this thesis, and then briefly discusses the implications this study has for guiding future research into submarine fans and turbidity-current processes.

8.2 Characterization of Channel-Levee Architecture

Levees constitute an important element not only of submarine channel-levee systems but also of submarine fans. However, prior to this study, little attention had been paid to the systematic and quantitative analysis of levee architecture. An important contribution of this thesis has been to recognize that thickness variations in levees perpendicular to channel trend can be quantified using an exponential model (Chapter 2 for methodology, Fig. 2.5; Table 8.1 for applications to individual systems). This procedure yields a consistent and reproducible measure of the cross-sectional shape of a levee, parameterized by a spatial decay constant, k , and the thickness of a depositional sequence at the levee crest, η_{lc} . In some cases, linear trends in thickness could be seen, but for the sake of consistency between systems exponential models were favoured. Statistical comparison of exponential versus linear models for across-levee variations in thickness shows that there is either no significant difference between the two models or

that the exponential model is favoured (Fig. 2.4). The inverse of the spatial decay constant, k^{-1} , defines the e-folding length for across-levee variations in the thickness of depositional sequences. This lengthscale represents a quantitative measure of levee width.

Table 8.1. Summary of figures showing across-levee variations in depositional sequence thickness.

System	Figure reference
NAMOC	Figs. 3.20-3.24
Hueneme Fan	Figs. 4.19-4.21
Reserve Fan	Fig. 5.2
Amazon Fan	Figs. 5.14, 5.20-5.21
Var Fan	Figs. 5.24-5.25
Laurentian Fan	Figs. 6.24-6.25

The structure of levees can also be characterized by the downchannel behaviour of the spatial decay constant (e.g., Fig. 3.26, 4.25, 5.3, 6.29). The variations in k^{-1} showed no significant downchannel trends except on Hueneme Fan (Fig. 3.26) where data coverage spanned the channel-levee to lobe transition. Variations in depositional sequence thickness at the levee crest could be fit to an exponential model (Fig. 7.1; Table 7.1), parameterized by a decay constant, λ , whose inverse, λ^{-1} , defines the e-folding length for downchannel variations in the thickness of levee depositional sequences. This downchannel lengthscale represents a quantitative definition of levee length.

Calculation of these measures of levee architecture extends the quantifiable parameters of a channel-levee system beyond measures of channel morphology investigated by previous workers (e.g., Clark et al., 1992) which include, for example, channel relief, slope, width, sinuosity, and levee asymmetry — the elevation difference between conjugate levees and cross-channel slope. Although measures such as channel relief include information on the thickness of sediment on levees, channel relief does not explicitly characterize levee deposits. Whether the channel is a site of deposition, erosion, or bypass influences channel relief in manner not necessarily related to sediment accumulation on the levees. Consequently, including explicit measures of levee

architecture represents a fundamental improvement to the quantitative description of submarine channel-levee systems.

8.3 Empirical Relationships

The six systems studied in this thesis were used to develop empirical relationships describing channel-levee architecture. Between systems, the application of consistent quantitative techniques allowed direct comparison of parameters describing levee architecture with parameters describing channel morphology. Downchannel, the observations of channel-levee architecture were incorporated into a generic model tentatively describing the expected behaviour of channel-levee architecture. Stratigraphically, regular patterns were found in the evolution of levee crests and sediment waves.

8.3.1 Inter-system Variability

Quantitative measures of channel-levee morphology show variability spanning over two orders of magnitude. General relationships exist between the lengthscale for variations in depositional sequence across a levee, k^{-1} or levee width, and channel dimensions. In particular, levee width depends approximately linearly on channel half-width, W (Fig. 7.2), and the square root of channel relief, D (Fig. 7.3). Channel half-width scales as $D^{0.62 \pm 0.16}$ (Fig. 7.6).

General relationships also exist between the lengthscale for downchannel variations in depositional sequence thickness at the levee crest, λ^{-1} , and channel dimensions. Although the strength of these relationships suffers from a lack of data points (six in total), λ^{-1} scales approximately with $W^{1.31 \pm 1.16}$ (Fig. 7.5b) and $D^{1.47 \pm 0.67}$ (Fig. 7.5c). The product of the two lengthscales, $k^{-1}\lambda^{-1}$, scales with $D^{2 \pm 0.83}$ (Fig. 7.15).

These inter-system relationships exist in spite of a range of geological differences between systems. Continental glaciers influenced sediment delivery to NAMOC (Chapter 3.3.3) and Laurentian Fan (Chapter 6.3.3) while alpine glaciation may have played a role in sediment delivery to Var Fan (Chapter 5.3.1). Hueneme (Chapter 4.3.3) and Amazon (Chapter 5.3.1) fans were fed by rivers during lowstands of sea-level, but Hueneme Fan may have been more influenced by turbidity currents triggered from hyperpycnal inflow of dense river water than the failure of rapidly-deposited deltaic

sediment likely responsible for generating flows on Amazon Fan. The comparison of Amazon and Hueneme Fan is particularly intriguing considering that they have similar values of k^{-1} but very different values of slope and sinuosity (Fig. 4.4 and 5.6). In light of such variability, it might be expected that comparison of levee architecture between systems would show few relationships. The fact that such relationships do exist suggests that an underlying physical process is responsible for patterns in levee architecture.

The general relationships between levee architecture and channel morphology provide scaling relationships that are useful in the mapping and interpretation of channel-levee systems where data are limited. The intrinsic dependence of horizontal lengthscales (channel half-width, channel length, and levee width) on vertical lengthscales (channel relief, depositional sequence thickness) can be used to guide outcrop and subsurface investigations where neither of these dimensions can be completely determined from analysis of extant data.

8.3.2 Downchannel Variability

Examination of the downchannel trends in levee architecture from all the systems studied here suggests some systematic behaviour. Sediment thickness at the levee crest decreases exponentially over the upper reaches of a submarine channel (Fig. 7.1). This thinning is parameterized by λ^{-1} , and it coincides with generally uniform values of k sometimes over large downchannel distances (e.g., Fig 3.26). Sediment thickness at the levee crest over the lower reaches of some submarine channels appears uniform, but on others it decays abruptly (Fig. 7.1).

These patterns in levee architecture generally coincide with rather limited variability in channel morphology, especially in comparison to the variability in channel and levee dimensions between systems (Chapter 7.3.2). Channel width tends to be particularly uniform downchannel, whereas both channel relief and channel slope tend to decrease, but do not show variations that encompass the variation in these parameters between systems. Thus, a single value of channel width, relief, and slope, generally characterizes an individual system.

Downchannel patterns in levee asymmetry, parameterized by the cross-channel slope, ∇H , also characterize submarine channels. In the cases studied, where the cross-

channel slope increases with distance downchannel (NAMOC, Fig. 3.28), this pattern results from reductions in the distance between conjugate levee crests rather than changes in the elevation difference between conjugate levee crests. Where the cross-channel slope decreases with distance downchannel (e.g., Figs. 3.28, 5.26, 7.7), the decrease results from reductions in the elevation difference between conjugate levees. The decrease in the elevation difference arises because the cross-channel gradient in depositional sequence thickness at the levee crest, $\nabla\eta_{lc}$, decreases. In other words, deposition occurs preferentially on one side of channel along the upper reaches of the system and becomes progressively more symmetric with distance downchannel.

8.3.3 Stratigraphic Variability

Regular stratigraphic patterns were observed in the evolution of levee crests and sediment waves. The levee crest, defined as the topographically highest point on the levee separating strata that dip toward the channel from strata that dip away from the channel, shows a general tendency, in the absence of erosion, to move toward the channel axis. A geometric model (Fig. 7.11) suggests that the channelward movement of levee crests can be explained by the filling of the space that exists between the levee crest and channel. A direct relationship may exist between the angle of the inner levee slope, a measure of the available space, and the spatial decay constant which parameterizes the filling of this space (Fig. 7.11e). This relationship, guided by insight from the geometric model, suggests that, in the absence of erosion and at the resolution of available seismic data, levee crests shift abruptly after extended periods of aggradation rather than continuously migrating toward the channel axis through time.

Sediment waves develop following a consistent pattern. After their initial development, likely in response to some exceptional event given their apparently random occurrence within individual systems (Table 7.3), sediment waves proceed to grow and decay in discrete phases characterized by variations in their amplitude and rate of upstream migration (e.g., Figs. 3.7, 5.35, 6.16, 7.7). At no time in their development does wavelength show any significant variations or correlate with variations in either wave amplitude or the rate of upstream migration. Examination of existing models relating sediment wave morphology to turbidity flow parameters suggests that the lee

wave model of Flood (1988) may explain the observed stratigraphic patterns better than the antidune model of Normark et al. (1980).

The value of the spatial decay constant for across-levee variations in thickness, k , shows no systematic stratigraphic patterns (e.g., Figs. 3.29, 4.27, Tables 5.6, 5.8). In the high resolution data on systems like NAMOC and Amazon Fan, the stratigraphic interval encompassed by a depositional sequence tends to be much less than the duration of channel activity. Changes in channel morphology between successive depositional sequences are minor, and consequently the expected changes in levee architecture would be small and likely less than the errors associated with estimating the decay constant. Similarly, there are no stratigraphic trends in k for depositional sequences defined in the lower resolution seismic data. However, the stratigraphic interval between successive stratigraphic horizons is much larger in the low resolution seismic data and the past morphology of the channel is difficult to determine.

8.4 Physical Interpretation of Thickness Patterns

Submarine channels act as conduits for turbidity currents transporting terrigenous detritus to the deep-sea. Levee deposition occurs because the thickness of these through-channel turbidity currents can exceed local channel relief and spill out from the channel onto the levee. Of the features examined and quantified in this thesis only thickness patterns varied in a systematic way with channel morphology, suggesting that they may record the hydrodynamics of through-channel turbidity currents.

A simple model suggests that the depositional lengthscale for across-levee thickness variations, k^{-1} , depends on the character of the through-channel turbidity current (Chapter 7.3.1). This lengthscale scales with the flux of fluid transferred from the through-channel flow, v_h , divided by the average settling velocity of the particles on the levee, w_s . Core data suggest that all the systems have levees composed of silty mud and may have similar w_s , leaving differences in v_h as the source of variability in k^{-1} which exceeds two orders of magnitude. In addition, bedding in levee sediments shows little evidence of dramatic changes; levees are generally comprised of monotonous successions of laminated silty muds (e.g., Fig. 5.19). The divergent internal reflection geometry, conformable nature of depositional sequences (at a resolution of < 0.5 m for some seismic

data), and monotonous bedding character of turbidites on levees argue in favour of limited variability in the character of individual flows and thereby suggest that the vh term related to individual turbidity current events can be estimated from the ensemble-average represented by k^{-1} . It is unlikely that large variability in vh at the event level would produce the simple exponential thinning pattern observed in across-levee variations of depositional sequence thickness or the conformable, divergent internal reflection geometry. Evidence from direct observations of turbidity current flow (Reserve Fan) and indirect estimates of flow parameters (e.g., NAMOC and Hueneme Fan) suggest that k^{-1} , and therefore vh , scales directly with through-channel flow velocity.

Exploring the link between vh and through-channel flow parameters required construction of a model through simplifications to the equations governing the conservation of momentum, fluid mass, and sediment mass in an overbanking turbidity current (Chapter 7.3.2; Appendix A). In the constant thickness model, losses to the levees are assumed to be as large as possible while still allowing for downchannel continuity of levee deposition. The flow is envisioned to travel through a channel of constant size and uniform downchannel slope, maintaining a constant thickness because entrainment of sediment-free water through the top of the flow balances the loss of sediment-laden fluid out the sides of the flow. In this model, volume concentration (and therefore sediment thickness at the levee crest) decays exponentially downchannel. The lengthscale for this downchannel variation is given by H/E where H is the total flow thickness in channel and E is the entrainment coefficient. The model suggests that vh (and therefore, k^{-1}) scales with EuW , where u is the through-channel velocity and W is channel half-width. In the constant thickness model, the product of the two lengthscales, k^{-1} and λ^{-1} goes as volume discharge Q . Using the hydraulic geometry relationships of Langbein & Leopold (1964), Q scales with $D^{2.38}$ where D is channel relief. Observations show that $k^{-1}\lambda^{-1}$ scales with $D^{2.00\pm 0.83}$ (Fig. 7.15) which is not significantly different from the relationship suggested by the constant thickness model. Given the available data, the use of the hydraulic geometry relationships of Langbein & Leopold (1964) cannot be directly tested; however, in their theoretical derivation of the hydraulic geometry exponents, Langbein & Leopold (1964) required that W scale as $D^{0.55}$, a theoretical

condition proposed by Nizery & Braudeau (1955). This scaling relationship is not significantly different than that found for submarine channels (Fig. 7.6).

8.5 Generic Model for Channel-Levee Architecture

The large-scale structure of channel-levee systems obeys certain constraints that have been recognized empirically and supported theoretically. These constraints suggest that the dimensions of a channel-levee system are all inter-related. Exponential lengthscales characterize thickness patterns on levees (Fig. 7.1, Table 7.1, Table 8.1) and correlations exist between these lengthscales and channel morphology (Figs. 7.2-7.3, 7.5). Using the constant thickness model, the product of k^{-1} , the lengthscale for across-levee variations in thickness, and λ^{-1} , the lengthscale for downchannel variations in thickness, varies with the magnitude of the initial through-channel volume discharge. Systems with large through-channel volume discharge have wide, deep, and long channels with broad, long levees. Small through-channel volume discharge coincides with channel-levee systems having narrow, shallow, and short channels and narrow, short levees.

Regardless of system size, the downchannel structure of channel-levee architecture shows two reaches (Fig. 7.20): 1) an upper reach with uniform levee width and exponential downchannel decreases in sediment thickness at the levee crest; and 2) a lower reach with increasing levee width and more complex variations in sediment thickness at the levee crest. The morphological distinctiveness of these reaches may arise from different types of overbanking. Over the upper reach, the levees grow by deposition from overspilling turbidity currents where sediment moves from through-channel flow to the levees in manner potentially described by the constant thickness model. Over the lower reach, sediment transport through the channel progressively gives way to transport across the levee analogous to the spreading of an unconfined flow. It should be noted that such a model for downchannel structure is tentative at present because little data was available from the lower reaches of the submarine channel levee systems studied here; to propose it as a general model for channel-levee architecture requires additional investigation.

8.6 Suggestions for Future Research

1. The present study has focused on the levees of submarine channels, finding that over significant reaches of the channel they behave in a consistent manner. However, the possible models that describe their architecture would benefit from study of two very important locations along a channel-levee system: 1) the transition between the canyon and channel-levee system; and 2) the transition between the channel-levee system and depositional lobe. The correlations between channel morphology and levee architecture suggest that factors determining channel size control the large-scale structure of channel-levee systems; in addition, construction of simple flow models like the one used here requires knowledge of the initial flow conditions. Thus, study of the canyon-channel transition may provide necessary insight into the processes of channel inception and the initial conditions of through-channel flows. The tentative model for the general structure of channel-levee systems also suffers from the lack of detailed knowledge of channel-levee systems as they merge with the depositional lobe. Improved understanding of this transition will help constrain future models.
2. A major tool used by this study has been the development of empirical relationships between features of levee architecture. Extension of the study to include data from many more systems will help to refine the accuracy of these relationships. Channel-levee systems of particular interest are: 1) Indus and Bengal fans because they are the largest modern submarine fans; 2) Zaire and Rhone fans because they have a morphology similar to Amazon Fan; and 3) any or all of the numerous fans located in the California Continental Borderland because they represent a wide range of channel dimensions and levee architectures within a relatively small geographic area.
3. Application of the hydraulic geometry relationships, the work of others on submarine channel morphology (e.g., Clark et al, 1992), and anecdotal evidence from fluvial levees (Allen, 1970, p. 137) suggest similarities between submarine levees and fluvial levees that appears to be a promising avenue for future investigation.
4. A major limitation of the geological understanding of channel-levee architecture arise from the lack of theoretical and flume work on overbanking flows. This work is vital in separating the possible from the plausible when interpreting the geological record of geophysical-scale phenomena.

Appendix A:

Derivation of Constant Thickness Model

Consider a turbidity current flowing through a channel of depth, D , that entrains ambient fluid through its upper interface and because flow thickness, H , exceeds local channel relief, the flow discharges fluid from the channel to the levees. Furthermore, assume that the flux to the levees is kinematically defined such that the flux of fluid to levees exactly balances entrainment and divergence of the through-channel advective flux. In such a flow, a turbidity current maintains a constant thickness while volume concentration of sediment decreases downchannel. In this conceptualization of an overbanking flow, clean water enters the flow from above and an equal volume of sediment-laden fluid exits the flow out the sides. If fluid losses outpaced fluid gains due to entrainment, flow thickness would decrease and overbanking would cease. Consequently, this type of flow represents conditions for the maximum, sustainable loss of sediment to the levees while remaining consistent with the observed downchannel continuity of levee deposition. The following model explores the consequences of such flow on the conservation of water, sediment, and momentum.

The continuity equation for the flow can be written as

$$\frac{\partial u}{\partial x} + \frac{\partial v}{\partial y} + \frac{\partial w}{\partial z} = 0 \quad (\text{A.1})$$

where u is horizontal velocity in x , v is horizontal velocity in y , w is vertical velocity.

Averaging over the layer thickness, H , yields

$$\frac{\partial u}{\partial x} + \frac{\partial v}{\partial y} + \frac{w}{H} \Big|_{z=H} - \frac{w}{H} \Big|_{z=0} = 0 \quad (\text{A.2})$$

where u and v now represent layer-averaged values for velocity and shape-factors resulting from the integration have been assumed equal to unity. Assuming that u and w are independent of y , averaging over the channel half-width, W , yields

$$\frac{\partial u}{\partial x} + \frac{v}{W} \Big|_{y=W} - \frac{v}{W} \Big|_{y=0} + \frac{w}{H} \Big|_{z=H} - \frac{w}{H} \Big|_{z=0} = 0 \quad (\text{A.3})$$

Assuming symmetry about the channel axis, $v(0)$ equals zero. Furthermore, the vertical fluid velocity at the sediment water interface is assumed to be zero, i.e., there is no flow of water into or out of the bed. Under these conditions, (A.3) reduces to

$$\frac{v}{W}\Big|_{y=W} = \frac{w}{H}\Big|_{z=H} - \frac{\partial u}{\partial x} \quad (\text{A.4})$$

By using the entrainment assumption (Ellison & Turner, 1959), the vertical velocity at the upper interface is assumed proportional to the downchannel flow velocity yielding

$$\frac{w}{H}\Big|_{z=H} = \frac{Eu}{H} \quad (\text{A.5})$$

With this assumption, the continuity equation becomes

$$\frac{v}{W}\Big|_{y=W} = \frac{Eu}{H} - \frac{\partial u}{\partial x} \quad (\text{A.6})$$

Total flow thickness, H , is the sum of D , channel relief, and h , the overbank flow thickness and therefore, vH equals $vD + vh$. Assuming that v is zero for $z \leq D$, vH equals vh and (A.6) becomes

$$vh = EuW - WH \frac{\partial u}{\partial x} \quad (\text{A.7})$$

To investigate the behaviour of this expression of continuity requires expressions for velocity and gradients in velocity derived from equations for conservation of sediment mass and momentum in turbidity currents.

At steady-state, the equation for conservation of sediment mass can be written as

$$\frac{\partial uc}{\partial x} + \frac{\partial vc}{\partial y} + \frac{\partial wc}{\partial z} = w_s \frac{\partial c}{\partial z} + \frac{\partial}{\partial x} K_x \frac{\partial c}{\partial x} + \frac{\partial}{\partial y} K_y \frac{\partial c}{\partial y} + \frac{\partial}{\partial y} K_z \frac{\partial c}{\partial z} \quad (\text{A.8})$$

where K_x , K_y , and K_z , represent diffusion coefficients in x , y , and z respectively and arise from modelling the turbulent fluctuations in volume concentration diffusively (e.g., Stacey & Bowen, 1988a). Integrating (A.8) over the channel half-width and assuming that u , w , w_s , and c are independent of y yields

$$\frac{\partial uc}{\partial x} + \frac{vc}{W}\Big|_{y=W} + \frac{\partial wc}{\partial z} - \frac{\partial w_s c}{\partial z} = \frac{\partial}{\partial x} K_x \frac{\partial c}{\partial x} + \frac{K_y(W)}{W} \frac{\partial c}{\partial y}\Big|_{y=W} - \frac{K_y(0)}{W} \frac{\partial c}{\partial y}\Big|_{y=0} + \frac{\partial}{\partial z} K_z \frac{\partial c}{\partial z} \quad (\text{A.9})$$

If gradients in sediment concentration in y are assumed small then (A.9) becomes

$$\frac{\partial uc}{\partial x} + \frac{vc}{W} \Big|_{y=W} + \frac{\partial wc}{\partial z} - \frac{\partial w_s c}{\partial z} = \frac{\partial}{\partial x} K_x \frac{\partial c}{\partial x} + \frac{\partial}{\partial z} K_z \frac{\partial c}{\partial z} \quad (\text{A.10})$$

Integrating (A.10) over the flow thickness, H , yields

$$\begin{aligned} & \frac{\partial uC}{\partial x} + \frac{vC}{W} + \frac{wc}{H} \Big|_{z=H} - \frac{wc}{H} \Big|_{z=0} - \frac{w_s c}{H} \Big|_{z=H} + \frac{w_s c}{H} \Big|_{z=0} \\ & = \frac{\partial}{\partial x} K_x \frac{\partial C}{\partial x} + \frac{K_z}{H} \frac{\partial c}{\partial z} \Big|_{z=H} - \frac{K_z}{H} \frac{\partial c}{\partial z} \Big|_{z=0} \end{aligned} \quad (\text{A.11})$$

where C is the layer-averaged volume concentration. At $z = 0$, the flux can be specified by

$$\frac{wc}{H} \Big|_{z=0} - \frac{w_s c}{H} \Big|_{z=0} - \frac{K_z}{H} \frac{\partial c}{\partial z} \Big|_{z=0} = 0 \quad (\text{A.12})$$

provided that there is no net deposition, i.e., the settling flux (second term in (A.12)) offsets the diffusive flux (third term in (A.12)). At $z = H$, the flux can be specified by

$$\frac{wc}{H} \Big|_{z=H} - \frac{w_s c}{H} \Big|_{z=H} - \frac{K_z}{H} \frac{\partial c}{\partial z} \Big|_{z=H} = 0 \quad (\text{A.13})$$

and assuming a local balance between the downward settling flux and the upward diffusive flux and the interface at $z = H$ represents a fixed surface that allows sediment-free fluid into the flow that can only be exported out the sides of the flow. These boundary conditions simplify (A.11) to

$$\frac{\partial uC}{\partial x} + \frac{vC}{W} \Big|_{y=W} - \frac{\partial}{\partial x} K_x \frac{\partial C}{\partial x} = 0 \quad (\text{A.14})$$

and using (A.6), (A.14) can be written as

$$u \frac{\partial C}{\partial x} - \frac{\partial}{\partial x} K_x \frac{\partial C}{\partial x} = -\frac{EuC}{H} \quad (\text{A.15})$$

Scale analysis shows that the diffusive term in (A.15) is small relative to the other terms and can be neglected. Consider a downchannel lengthscale for x of H/E (Ellison & Turner, 1959) and that K_x scales with BUH where B is a coefficient near unity (Csanady, 1982). With these scales the terms in (A.15) go as

$$\frac{U}{H} + \frac{EBU}{H} \sim \frac{U}{H} \quad (\text{A.16})$$

Because $E \ll 1$ — maximum values is around 0.09 (Ellison & Turner, 1959) — diffusion can be neglected and (A.15) becomes

$$\frac{\partial C}{\partial x} = -\frac{EC}{H} \quad (\text{A.17})$$

which, if E is constant, has the solution

$$C = C_o \exp\left(-\frac{E}{H}x\right), \quad (\text{A.18})$$

predicting that volume concentration of the flow decays exponentially downchannel because of losses of sediment to the levees.

At steady-state, the equation for conservation of downchannel momentum can be written as

$$\frac{\partial u^2}{\partial x} + \frac{\partial uv}{\partial y} + \frac{\partial uw}{\partial z} = g_o \sin\beta c + \frac{\partial}{\partial z} A_z \frac{\partial u}{\partial z} \quad (\text{A.19})$$

by keeping only the lowest order terms (e.g., Stacey, 1982). Averaging over the channel half-width and assuming that u , w , and c are independent of y yields

$$\frac{\partial u^2}{\partial x} + \frac{uv}{W}\Big|_{y=W} - \frac{uv}{W}\Big|_{y=0} + \frac{\partial uw}{\partial z} = g_o \sin\beta c + \frac{\partial}{\partial z} A_z \frac{\partial u}{\partial z} \quad (\text{A.20})$$

which, because $v(0) = 0$, simplifies to

$$\frac{\partial u^2}{\partial x} + \frac{uv}{W}\Big|_{y=W} + \frac{\partial uw}{\partial z} = g_o \sin\beta c + \frac{\partial}{\partial z} A_z \frac{\partial u}{\partial z} \quad (\text{A.21})$$

Averaging (A.21) over flow thickness produces

$$\frac{\partial u^2}{\partial x} + \frac{uv}{W}\Big|_{y=W} + \frac{uw}{H}\Big|_{z=H} - \frac{uw}{H}\Big|_{z=0} = g_o \sin\beta C + \frac{A_z}{H} \frac{\partial u}{\partial z}\Big|_{z=H} - \frac{A_z}{H} \frac{\partial u}{\partial z}\Big|_{z=0} \quad (\text{A.22})$$

Using

$$\frac{A_z}{H} \frac{\partial u}{\partial z}\Big|_{z=0} = \frac{C_D u^2}{H} \quad (\text{A.23})$$

and

$$\frac{uw}{H}\Big|_{z=H} - \frac{A_z}{H} \frac{\partial u}{\partial z}\Big|_{z=H} = 0 \quad (\text{A.24})$$

simplifies (A.22) to

$$\left. \frac{\partial u^2}{\partial x} + \frac{uv}{W} \right|_{y=w} = g_o \sin \beta C - \frac{C_D u^2}{H} \quad (\text{A.25})$$

Using (A.6), (A.25) becomes

$$\frac{\partial u^2}{\partial x} + \frac{Eu^2}{H} - u \frac{\partial u}{\partial x} = g_o \sin \beta C - \frac{C_D u^2}{H} \quad (\text{A.26})$$

which simplifies to

$$\frac{\partial u^2}{\partial x} = 2g_o \sin \beta C - 2 \frac{(E + C_D)}{H} u^2 \quad (\text{A.27})$$

Using (A.18), (A.27) represents a first-order differential equation whose solution is given by

$$\left(\frac{u}{u_o} \right)^2 = \frac{2g_o \sin \beta C_o H}{(E + 2C_D) u_o^2} e^{-Ex/H} + e^{-2(E+C_D)x/H} - \frac{2g_o \sin \beta C_o H}{(E + 2C_D) u_o^2} e^{-2(E+C_D)x/H} \quad (\text{A.28})$$

with the boundary condition that $u(x=0) = u_o$. Defining Γ_2 according to

$$\Gamma_2 = \frac{2g_o \sin \beta C_o H}{(E + 2C_D) u_o^2} = \frac{2Ri_o \sin \beta}{(E + 2C_D)} \quad (\text{A.29})$$

where Ri_o is the initial bulk Richardson number of the flow and is given by

$$Ri_o = \frac{g_o C_o H}{u_o^2} \quad (\text{A.30})$$

the solution of (A.27) can be written

$$\left(\frac{u}{u_o} \right)^2 = \Gamma_2 e^{-Ex/H} + e^{-2(E+C_D)x/H} - \Gamma_2 e^{-2(E+C_D)x/H} \quad (\text{A.31})$$

To solve for the losses to the levees that satisfy (A.6), (A.27) can be written as

$$H \frac{\partial u}{\partial x} = (Ri \sin \beta - E - C_D) u \quad (\text{A.32})$$

where

$$Ri = \frac{g_o CH}{u^2} = \frac{g_o C_o H}{u_o^2} e^{-Ex/H} \left(\frac{u_o}{u} \right)^2 = Ri_o e^{-Ex/H} \left(\frac{u_o}{u} \right)^2 \quad (\text{A.33})$$

which when substituted into (A.6) yields

$$\frac{vh}{uW} = (2E + C_D - Ri \sin \beta) \quad (\text{A.34})$$

or

$$\frac{vh}{EuW} = \left(\Gamma_1 - \frac{1}{2} \Gamma_2 e^{-Ex/H} \frac{u_0^2}{u^2} \right) \frac{(E + 2C_D)}{E} \quad (\text{A.35})$$

where

$$\Gamma_1 = \frac{2E + C_D}{E + 2C_D} \quad (\text{A.36})$$

The model for turbidity current flow is completely defined by (A.18), (A.31), (A.35), with two dimensionless parameters, Γ_1 and Γ_2 , given by (A.36) and (A.29), respectively. The values that the parameters may take can be investigated. The definition of Γ_1 can be rearranged to solve for E yielding

$$E = C_D \frac{2\Gamma_1 - 1}{2 - \Gamma_1} \quad (\text{A.37})$$

and since E must be greater than zero, the range of values that Γ_1 can taken fall within $0.5 < \Gamma_1 < 2$. For example, Middleton (1966) suggests $E/C_D \sim 0.43$, which equates to Γ_1 equal to about 0.75.

The second parameter in the model, Γ_2 , can be expressed in terms of Γ_1 according to

$$\Gamma_2 = \frac{2}{3} \frac{Ri_0 \sin\beta}{C_D} (2 - \Gamma_1) \quad (\text{A.38})$$

Although the range of Γ_1 is restricted, no *a priori* reason exists for a similar restriction on Γ_2 ; thus, Γ_2 is related to Γ_1 , but is not necessarily predicted by Γ_1 . However, if the initial Richardson number of the flow is given by

$$Ri_0 \sin\beta = E + C_D \quad (\text{A.39})$$

which is true for steady-uniform flow (e.g., Bowen et al., 1984; Turner, 1986) down low slopes ($\sin\beta \approx \tan\beta$), then Γ_2 depends on Γ_1 according to

$$\Gamma_2 = \frac{2}{3} (\Gamma_1 + 1) \quad (\text{A.40})$$

Under these conditions, solutions for dimensionless velocity, dimensionless volume concentration, and the non-dimensional losses of fluid to the levees as a function of Ex/H depend on a single parameter, Γ_1 , that has a restricted range of values.

REFERENCES

- Adams, J., 1989, Turbidites off the Oregon-Washington margin record paleo-earthquakes on the Cascadia subduction zone, *Geological Survey of Canada Paper*, 89-1F: 37-43.
- Albertson, M.L., Dai, Y.B., Jensen, R.A., and Hunter, R., 1950, Diffusion of submerged jets, *American Society of Civil Engineers Transactions*, 115, 639-697.
- Alldredge, A.L. & Gotschalk, C.C., 1989, Direct observations of the mass flocculation of diatom blooms: characteristics, settling velocities and formation of diatom aggregates, *Deep-sea Research*, 36: 159-171.
- Allen, J.R.L., 1970, *Physical Processes of Sedimentation*, George Allen and Unwin Ltd., London, 248 p.
- Allen, J.R.L., 1985, *Principals of Physical Sedimentology*, George Allen and Unwin Ltd., Boston, 272 p.
- Anastasakis, G.C. & Piper, D.J.W., 1991, The character of seismo-turbidites in the S-1 sapropel, Zakynthos and Strofadhos basins, Greece, *Sedimentology*, 38: 717-733.
- Bagnold, R.A., 1962, Auto-suspension of transported sediment; turbidity currents, *Proceedings of Royal Society of London, Serial A*, 265: 315-319.
- Baltzer, A., Conchonat, P. & Piper, D.J.W., 1994, In situ geotechnical characterization of sediments on the Nova Scotian Slope, eastern Canadian continental margin, *Marine Geology*, 120: 291-308.
- Bond, G.C., Heinrich, H., Broecker, W., Labeyrie, L., McManus, J., Andrews, J., Huon, S., Jantschik, R., Clasen, S. Simet, C., Tedesco, K., Klas, M., Bonani, G. & Ivy, S., 1992, Evidence for massive discharge of icebergs into the North Atlantic ocean during the last glacial period, *Nature*, 360: 245-249.
- Bonnecaze, R.T., Hallworth, M.A., Huppert, H.E. & Lister, J.R., 1995, Axisymmetric particle-driven gravity currents, *Journal of Fluid Mechanics*, 294: 93-121.
- Bouma, A.H, Normark, W.R. & Barnes, N.E., 1985, *Submarine Fans and Related Turbidite Systems*, Springer-Verlag, New York, 351 p.
- Bowen, A.J., Normark, W.R. & Piper, D.J.W., 1984, Modelling of turbidity currents on Navy Submarine Fan, California Continental Borderland, *Sedimentology*, 31: 169-185.
- Brierley, G.J., Ferguson, R.J. & Woolfe, K.J., 1997, What is a fluvial levee?, *Sedimentary Geology*, 114: 1-9.

- Brown, L.F., Jr. & Fisher, W.L., 1982, *Seismic Stratigraphic Interpretation and Petroleum Exploration*, American Association of Petroleum Geologists, Continuing Education Course Note Series 16, 56 p.
- Carew, J.L. & Mylroie, J.E., 1995, Quaternary tectonic stability of the Bahamian archipelago: evidence from fossil coral reefs and flank-margin caves, *Quaternary Science Reviews*, 14: 145-153.
- Chough, S.K. & Hesse, R., 1976, Submarine meandering talweg and turbidity currents flowing for 4,000 km in the Northwest Atlantic Mid-Ocean Channel, Labrador Sea, *Geology*, 4: 529-533.
- Chough, S.K. & Hesse, R., 1980, The northwest Atlantic mid-ocean channel of the Labrador Sea: III. Head spill vs. body spill deposits from turbidity currents on natural levees, *Marine Geology*, 50: 227-234.
- Christensen, C.J., 1991, *An Analysis of Sedimentation Rates and Cyclicity in the Laminated Sediments of Santa Monica Basin, California Continental Borderland*, Unpubl. M.Sc. Thesis, University of Southern California, Los Angeles, 143 p.
- Christensen, C.J., Gorsline, D.G., Hammond, D.E., & Lund, S.P., 1994, Non-annual laminations and expansion of anoxic basin-floor conditions in Santa Monica Basin, California Borderland, over the past four centuries, *Marine Geology*, 116: 399-418.
- Clark, J.D., Kenyon, N.H. & Pickering, K.T., 1992, Quantitative analysis of the geometry of submarine channels: implications for the classification of submarine fans, *Geology*, 20: 633-636.
- Clark, J.D. & Pickering, K.T., 1996, Architectural elements and growth patterns of submarine channels: applications to hydrocarbon exploration, *American Association of Petroleum Geologists Bulletin*, 80:194-221.
- Csanady, G.T., 1982, *Circulation in the Coastal Ocean*, D. Reidel Publishing Co., Dordrecht, Holland, 279 p.
- Dahlen, M.Z., Osborne, R.H. & Gorsline, D.S., 1990, Late Quaternary history of the Ventura mainland shelf, California, *Marine Geology*, 94: 317-340.
- Damuth, J.E., Kolla, V., Flood, R.D., Kowsmann, K.O., Monteiro, M.C., Gorini, M.A., Palma, J.J.C. & Belderson, R.H., 1983, Distributary channel meandering and bifurcation patterns on Amazon deep-sea fan as revealed by long-range side-scan sonar (GLORIA), *Geology*, 11:94-98.
- Damuth, J.E., Kowsmann, K.O., Belderson, R.H. & Gorini, M.A., 1988, Anatomy and growth pattern of Amazon deep-sea fan as revealed by long-range side-scan sonar

- (GLORIA) and high-resolution seismic studies, *American Association of Petroleum Geologists Bulletin*, 72:885-911.
- Davis, J.C., 1986, *Statistics and Data Analysis in Geology*, John Wiley & Sons, New York, 646 p.
- Dowdswell, J.A., Maslin, M.A., Andrews, J.T. & McCave, I.N., 1995, Iceberg production, debris rafting and the extent and thickness of "Heinrich layers" in North Atlantic sediments, *Geology*, 23: 301-304.
- Droz, L., Rigaut, F., Cochonat, P. & Tofani, R., 1996, Morphology and recent evolution of the Zaire turbidite system (Gulf of Guinea), *Geological Society of America Bulletin*, 108: 253-269.
- Dyer, K.R., Cornelisse, J., Dearnaley, M.P., Fennessy, M.J., Jones, S.E., Kappenberg, J., & McCave, I.N., 1996, A comparison of in situ techniques for estuarine floc settling velocity measurements, *Journal of Sea Research*, 36: 15-31.
- Dzulynski, S. & Radomski, A., 1955, Origin of groove casts in the light of turbidity current hypothesis, *Acta Geologie Pologne*, 5: 47-56.
- Ellis, D.V. & Poling, G.W., 1995, Submarine tailings disposal (STD) for mines, *Marine Georesources and Geotechnology*, 13: 1-2.
- Ellison, T.H. & Turner, J.S., 1959, Turbulent entrainment in stratified flows, *Journal of Fluid Mechanics*, 6: 423-448.
- Emiliani, C., Rooth, C. & Stipp, J.J., 1978, The Late Wisconsinan flood into the Gulf of Mexico, *Earth and Planetary Science Letters*, 41:159-162.
- Flood, R.D., 1987, Side-echoes from a sinuous fan channel obscure the structure of submarine fan channel/levee systems, Amazon Fan, *Geo-Marine Letters*, 7:15-22.
- Flood, R.D., 1988, A lee wave model for deep-sea mud wave activity, *Deep Sea Research*, 35: 943-971.
- Flood, R.D. & Damuth, J.E., 1987, Quantitative characteristics of sinuous distributary channels on the Amazon deep-sea fan, *Geological Society of America Bulletin*, 98: 728-738.
- Flood, R.D., Manley, P.L., Kowsmann, R.O., Appi, C.J. & Pirmez, C., 1991, Seismic facies and late Quaternary growth of Amazon submarine fan, in *Seismic Facies and Sedimentary Processes of Submarine Fans and Turbidite Systems*, P. Weimer & M.H. Link (eds.), Springer-Verlag, New York, 415-433.
- Flood, R.D., Pirmez, C. & Yin, H., 1997, The compressional-wave velocity of Amazon Fan sediments: Calculation from index properties and variation with clay content, in *Proceedings of the Ocean Drilling Program, Scientific Results*, 155, R.D.

- Flood, D.J.W. Piper, A. Klaus & L.C. Peterson (eds.), College Station, TX (Ocean Drilling Program), 477-496.
- Flood, R., Piper, D.J.W., Klaus, A. et al., 1995, *Proceedings of the Ocean Drilling Program, Initial Reports*, 155, College Station, TX (Ocean Drilling Program).
- Gallup, C.D., Edwards, R.L., and Johnson, R.G., 1994, The timing of high sea levels over the past 200,000 years, *Science*, v. 263, p. 796-800.
- Gorsline, D.S., 1996, Depositional events in Santa Monica Basin, California Borderland, over the past five centuries, *Sedimentary Geology*, 104: 73-88.
- Gorsline, D.S., Kolpack, R.L., Karl, H.A., Drake, D.E., Fleischer, P., Thornton, S.E., Schwabach, J.R. & Savrda, C.E., 1984, Studies of fine-grained sediment transport processes and products in the California Continental Borderland, in *Fine Grained Sediments: Deep-water Processes and Facies*, D.A.V. Stow & D.J.W. Piper (eds.), Blackwell Scientific Publications, Oxford, 395-415.
- Hack, J.T., 1957, Studies of longitudinal stream profiles in Virginia and Maryland, *U.S. Geological Survey Professional Paper 294-B*: 45-97.
- Hamilton, L.C., 1992, *Regression with Graphics, a Second Course in Applied Statistics*, Duxbury Press, Belmont, CA, 363 p.
- Hay, A.E., 1987, Turbidity currents and submarine channel formation in Rupert Inlet, British Columbia. II. The role of continuous and surge type flow, *Journal of Geophysical Research*, 92:2883-2900.
- Hecker, B., 1980, Possible benthic fauna and slope instability relationships, in *Marine Slides and Other Mass Movements*, S. Saxov & J.K. Nieuwenhuis (eds.), Plenum Press, New York, 335-347.
- Heezen, B.C., & Ewing, M., 1952, Turbidity currents and submarine slumps and the 1929 Grand Banks earthquake, *American Journal of Science*, 250: 849-873.
- Hesse, R., 1995, Long distance correlation of spillover turbidites on the western levee of the Northwest Atlantic Mid-Ocean Channel (NAMOC), Labrador Sea, in *Atlas of Deep Water Environments: Architectural Style in Turbidite Systems*, K.T. Pickering, R.N. Hiscott, F. Ricci Lucchi, R.D.A. Smith (eds.), Chapman & Hall, London, 276-281.
- Hesse, R. & Chough, S.K., 1980, The Northwest Atlantic Mid-Ocean Channel of the Labrador Sea: II. Deposition of parallel laminated levee-muds from the viscous sub-layer of low density turbidity currents, *Sedimentology*, 27: 697-711.
- Hesse, R., Chough, S.K., & Rakofsky, A., 1987, The Northwest Atlantic Mid-Ocean Channel of the Labrador Sea. V. Sedimentology of a giant deep-sea channel, *Canadian Journal of Earth Sciences*, 24: 1595-1624.

- Hesse, R., Klauke, I., Ryan, W.B.F., Edwards, M.B., Piper, D.J.W., et al., 1996, Imaging Laurentide icesheet drainage into the deep sea: impact on sediments and bottom water, *GSA Today*, 6: 3-9.
- Hill, P.R., 1984, Sedimentary facies of the Nova Scotian upper and middle continental slope, offshore Eastern Canada, *Sedimentology*, 31: 293-309.
- Hill, P.R. & Bowen, A.J., 1983, Modern sediment dynamics at the shelf slope boundary off Nova Scotia, in *The Shelf Break. Critical Interface on Continental Margins*, D.J. Stanley & G.T. Moore (eds.), *Society of Economic Palaeontologists and Mineralogists Special Publication*, 33: 265-276.
- Hiscott, R.N., Hall, F.R. & Pirmez, C., 1997, Turbidity current overspill from the Amazon Channel: texture of the silt/sand load, paleoflow from anisotropy of magnetic susceptibility, and implications for flow processes, in *Proceedings of the Ocean Drilling Program, Scientific Results*, 155, R.D. Flood, D.J.W. Piper, A. Klaus & L.C. Peterson (eds.), College Station, TX (Ocean Drilling Program), 53-78.
- Howe, J.A., 1996, Turbidite and contourite sediment waves in the northern Rockall Trough, North Atlantic Ocean, *Sedimentology*, 43:219-234.
- Hughes-Clarke, J.E., 1988, *The Geological Record of the 1929 "Grand Banks" Earthquake and Its Relevance to Deep-sea Clastic Sedimentation*. Unpubl. PhD Thesis, Dalhousie University, Halifax, Canada, 171 p.
- Hughes-Clarke, J.E., Mayer, L.A., Piper, D.J.W., & Shor, A.N., 1989, PISCES IV submersible observations in the epicentral region of the 1929 Grand Banks earthquake, in *Submersible Observations off the East Coast of Canada*, D.J.W. Piper (ed.), Geological Survey of Canada Paper 88-20: 57-69.
- Huppert, H.E., 1968, Appendix to a paper by J.W. Miles, *Journal of Fluid Mechanics*, 33:811-814.
- Imran, J., Parker, G. & Katopodes, N., 1998, A numerical model of channel inception on submarine fans, *Journal of Geophysical Research*, 103(C1): 1219-1238.
- Inman, D.L., Nordstrom, C.E. & Flick, R.E., Currents in submarine canyons: an air-sea-land interaction, *Annual Review of Fluid Mechanics*, 275-310
- Kearey, P. & Brooks, M., 1984, *An Introduction to Geophysical Exploration*, Blackwell Scientific Publications, Oxford, 296 p.
- Kineke, G.C. & Sternberg, R.W., 1989, The effect of particle settling velocity on computed suspended sediment concentration profiles, *Marine Geology*, 90: 159-174.

- Klaucke, I., 1995, *The Submarine Drainage System of the Labrador Sea: Result of Glacial Input from the Laurentide Ice Sheet*, Unpubl. Ph. D. Thesis, McGill University, Montreal, QU, Canada, 247 p.
- Klaucke, I. & Hesse, R., 1996, Fluvial features in the deep-sea: new insights from the glacial sub-marine drainage system of the Northwest Atlantic Mid-Ocean Channel in the Labrador Sea, *Sedimentary Geology*, 106: 223-234.
- Klaucke, I., Hesse, R. & Ryan, W.B.F., 1997, Flow parameters of turbidity currents in a low-sinuosity giant deep-sea channel, *Sedimentology*, 44: 1093-1102.
- Knighton, A.D., 1975, Variations in at-a-station hydraulic geometry, *American Journal of Science*, 275: 186-218.
- Komar, P.D., 1969, The channelized flow of turbidity currents with application to Monterey deep-sea fan channel, *Journal of Geophysical Research*, 74: 4544-4548.
- Komar, P.D., 1973, Continuity of turbidity current flow and systematic variations in deep-sea channel morphology, *Geological Society of America Bulletin*, 84: 3329-3338.
- Komar, P.D., 1977, Computer simulation of turbidity current flow and the study of deep sea channels and fan sedimentation. *The Sea*, 6: 603-621.
- Komar, P.D., 1985, The hydraulic interpretation of turbidites from their grain sizes and sedimentary structures, *Sedimentology*, 32: 395-408.
- Kranck, K., 1975, Sediment deposition from flocculated suspensions, *Sedimentology*, 22: 111-123.
- Kranck, K., 1984, Grain size characteristics in turbidites, in *Fine Grained Sediments: Deep-water Processes and Facies*, D.A.V. Stow & D.J.W. Piper (eds.), Blackwell Scientific Publications, Oxford, 83-94.
- Langbein, W.B. & Leopold, L.B., 1964, Quasi-equilibrium states in channel morphology, *American Journal of Science*, 262: 782-794.
- Leopold, L.B. & Maddock, T. Jr., 1953, The hydraulic geometry of stream channels and some physiographic implications, *U.S. Geological Survey Professional Paper 252*, 55 p.
- Lombard, A., 1963, Laminites — a structure of flysch-type sediments, *Journal of Sedimentary Petrology*, 33:14-22.
- Luthi, S., 1981, Experiments on non-channelized turbidity currents and their deposits, *Marine Geology*, 40: M59-M68.

- Malouta, D.N., Gorsline, D.G., & Thornton, S.E., 1981, Processes and rates of recent Holocene, basin filling in an active transform margin: Santa Monica Basin, California Continental Borderland, *Journal of Sedimentary Petrology*, 51: 1077-1095.
- Manley, P.L., Pirmez, C., Busch, W. & Cramp, A., 1997, Grain-size characterization of Amazon Fan deposits and comparison to seismic facies units, in *Proceedings of the Ocean Drilling Program, Scientific Results*, 155, R.D. Flood, D.J.W. Piper, A. Klaus & L.C. Peterson (eds.), College Station, TX (Ocean Drilling Program), 35-52.
- Manley, P.L. & Flood, R.D., 1988, Cyclic sediment deposition within Amazon deep-sea fan, *American Association of Petroleum Geologists Bulletin*, 72: 912-925.
- Masson, D.G., Gardner, J.V., Parson, L.M. & Field, M.E., 1985, Morphology of upper Laurentian Fan using GLORIA long-range side-scan sonar, *American Association of Petroleum Geologists Bulletin*, 69: 950-959.
- McCave, I.N. & Swift, S.A., 1976, A physical model for the rate of deposition of fine-grained in the deep sea, *Geological Society of America Bulletin*, 87: 541-546.
- Menard, H.W., 1964, Turbidity currents, in *Marine Geology of the Pacific*, New York, McGraw-Hill Book Co., 191-222.
- Miall, A.D., 1985, Architectural element analysis: a new method of facies analysis applied to fluvial deposits, *Earth Science Reviews*, 22: 261-308.
- Middleton, G.V. & Southard, J.E., 1984, Mechanics of Sediment Movement, *Society of Economic Palaeontologists and Mineralogists Short Course Notes No. 3*, 401 p.
- Middleton, G.V., 1966, Experiments on density and turbidity currents, II: uniform flow of density currents, *Canadian Journal of Earth Sciences*, 3: 627-637.
- Miles, J.W., 1968, Lee waves in stratified flow. Part 2. Semi-circular obstacle, *Journal of Fluid Mechanics*, 33:803-814.
- Miller, M.C., McCave, I.N. & Komar, P.D., 1977, Threshold of sediment motion in unidirectional currents, *Sedimentology*, 24: 507-528.
- Milliman, J.D. & Meade, R.H., 1983, World-wide delivery of river sediment to the oceans, *Journal of Geology*, 91:1-21.
- Mitchum, R.M., Vail, P.R. & Thompson, S., 1977, Seismic stratigraphy and global changes of sea level, Part 2: The depositional sequence as a basic unit for stratigraphic analysis, in *Seismic Stratigraphy — Applications to Hydrocarbon Exploration*, C.E. Payton (ed.), American Association of Petroleum Geologists Memoir 26, 53-62.
-

- Mulder, T. & Syvitski, J.P.M., 1995, Turbidity currents generated at mouths of rivers during exceptional discharges to the world oceans, *Journal of Geology*, 103: 285-299.
- Mutti, E., 1985, Turbidite systems and their relations to depositional sequences, in *Provenance of Arenites*, G.G. Zuffa (ed.), NATA ASI Series, D. Reidel Publishing Co., Dordrecht, Holland, 65-94.
- Mutti, E. & Normark, W.R., 1987, Comparing examples of modern and ancient turbidite systems: problems and concepts, in *Deep Water Clastic Deposits: Models and Case Histories*, J.K. Leggett & G.G. Zuffa (eds.), Graham & Trotman, London, 1-38.
- Mutti, E. & Normark, W.R., 1991, An integrated approach to the study of turbidite systems, in *Seismic Facies and Sedimentary Processes of Submarine Fans and Turbidite Systems*, P. Weimer & M.H. Link (eds.), Springer-Verlag, New York, 75-106.
- Myers, R.A. & Piper, D.J.W., 1988, Seismic stratigraphy of late Cenozoic sediments in the northern Labrador Sea: a history of bottom circulation and glaciation, *Canadian Journal of Earth Sciences*, 25: 2059-2074.
- Nardin, T.R., 1983, Late Quaternary depositional systems and sea level change — Santa Monica and San Pedro basins, California Continental Borderland, *American Association of Petroleum Geologists Bulletin*, 67: 1104-1124.
- Nelson, C.H. & Kulm, V., 1973, Submarine fans and channels, in *Turbidites and Deep Water Sedimentation*, Society of Economic Palaeontologists and Mineralogists Pacific Section, Short Course.
- Nittrouer, C.A., Sharara, M.T. & DeMaster, D.J., 1982, Variations of sediment texture on the Amazon continental shelf, *Journal of Sedimentary Petrology*, 53:179-191.
- Nizery, A. & Braudeau, G., 1955, Discussion of paper by E.W. Lane on Design of stable channels, *American Society of Civil Engineers Transactions*, 120: 1266-1269.
- Normark, W.R., 1989, Observed parameters for turbidity-current flow in channels, Reserve Fan, Lake Superior, *Journal of Sedimentary Petrology*, 59: 423-431.
- Normark, W.R. & Dickson, 1976a, Man-made turbidity currents in Lake Superior, *Sedimentology*, 23: 815-831.
- Normark, W.R. & Dickson, 1976b, Sublacustrine fan morphology in Lake Superior, *American Association of Petroleum Geologists Bulletin*, 60: 1121-1136.
- Normark, W.R. & Piper, D.J.W., 1984, Navy Fan, California Borderland: growth pattern and depositional process, *Geo-marine Letters*, 3: 101-108.

- Normark, W.R. & Piper, D.J.W., 1991, Initiation processes and flow evolution of turbidity currents: implications for the depositional record, *From Shoreline to Abyss, Society of Economic Palaeontologists and Mineralogists Special Publication No. 46*: 207-230.
- Normark, W.R., Hess, G.R., Stow, D.A.V. & Bowen, A.J., 1980, Sediment waves on the Monterey Fan levee: a preliminary physical interpretation, *Marine Geology*, 37: 1-18.
- Normark, W.R., Piper, D.J.W. & Hess, G.R., 1979, Distributary channels, sand lobes, and mesotopography of Navy Fan, California Borderland, with applications to ancient fan sediments, *Sedimentology*, 26: 749-774.
- Normark, W.R., Piper, D.J.W. & Hiscott, R.N., 1998, Sea level controls on the textural characteristics and depositional architecture of the Hueneme and associated submarine fan systems, Santa Monica Basin, California, *Sedimentology*, 45: 53-70.
- Normark, W.R., Piper, D.J.W. & Stow, D.A.V., 1983, Quaternary development of channels, levees, and lobes on middle Laurentian Fan, *American Association of Petroleum Geologists Bulletin*, 67: 1400-1409.
- Pantin, H.M., 1979, Interaction between velocity and effective density in turbidity flow: phase-plane analysis, with criteria for autosuspension, *Marine Geology*, 31: 59-99.
- Park, C.C., 1977, World-wide variations in hydraulic geometry exponents of stream channels: an analysis and some observations, *Journal of Hydrology*, 33: 133-146.
- Parker, G., 1982, Conditions for the ignition of catastrophically erosive turbidity currents, *Marine Geology*, 46: 307-327.
- Parker, G., Fukushima, Y. & Pantin, H.M., 1986, Self-accelerating turbidity currents, *Journal of Fluid Mechanics*, 171: 145-181.
- Piper, D.J.W. & Aksu, A.E., 1987, The source and origin of the 1929 Grand Banks turbidity current inferred from sediment budgets, *Geo-Marine Letters*, 7: 177-182.
- Piper, D.J.W. & Deptuck, M., 1997, Fine-grained turbidites of the Amazon Fan: facies characterization and interpretation, in *Proceedings of the Ocean Drilling Program, Scientific Results*, 155, R.D. Flood, D.J.W. Piper, A. Klaus & L.C. Peterson (eds.), College Station, TX (Ocean Drilling Program), 79-108.
- Piper, D.J.W. & Fader, G.B., 1990, Acoustic and lithological data, in *Geology of the Continental Margin off Eastern Canada*, M.J. Keen & G.L. Williams (eds.), Geological Survey of Canada, Geology of Canada, No. 2, 494-497.

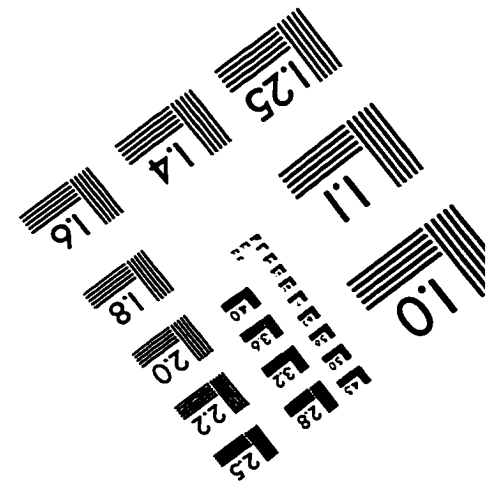
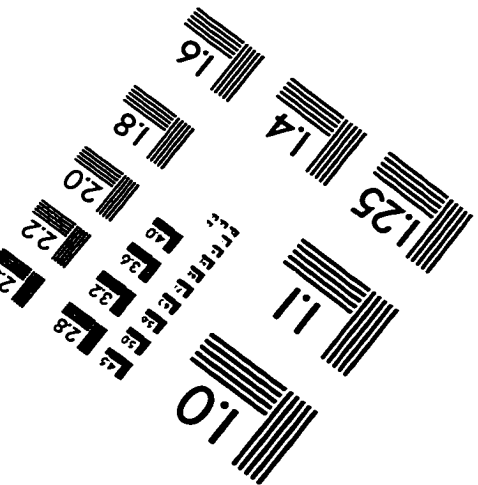
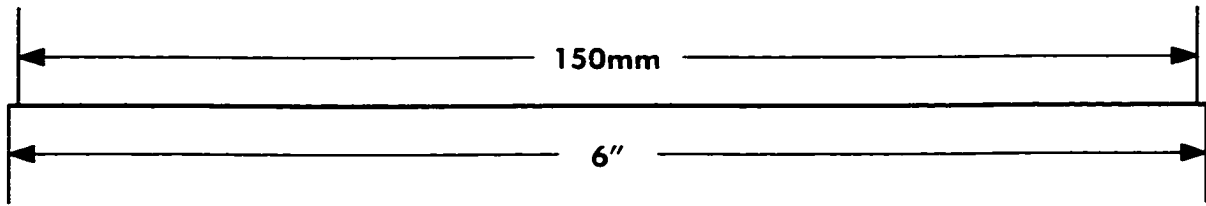
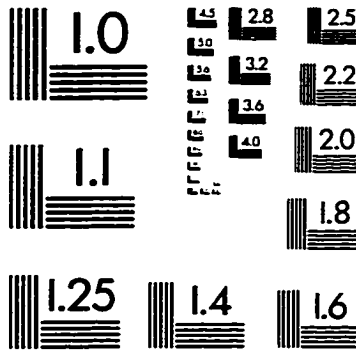
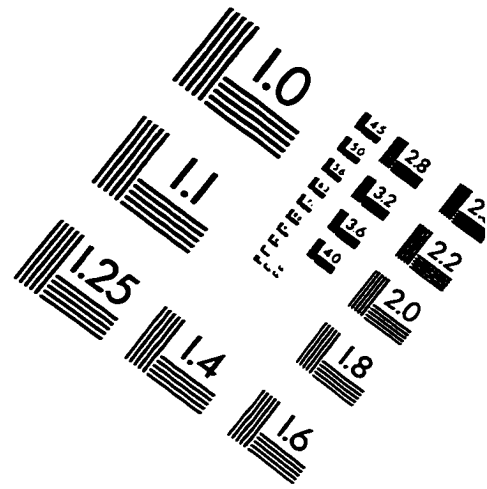
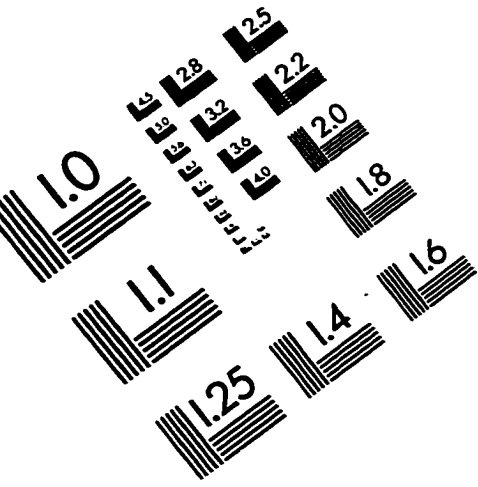
- Piper, D.J.W. & Normark, W.R., 1982, Acoustic interpretation of Quaternary sedimentation and erosion on the channelled upper Laurentian Fan, Atlantic margin of Canada, *Canadian Journal of Earth Sciences*, 19: 1974-1984.
- Piper, D.J.W. & Normark, W.R., 1983, Turbidite depositional patterns and flow characteristics, Navy submarine fan, California Borderland, *Sedimentology*, 30: 681-694.
- Piper, D.J.W. & Normark, W.R., 1989, Late Cenozoic sea-level changes and the onset of glaciation: impact on continental slope progradation of eastern Canada, *Marine and Petroleum Geology*, 6: 336-347.
- Piper, D.J.W. & Savoye, B., 1993, Processes of late Quaternary turbidity current flow and deposition on the Var deep-sea fan, north-west Mediterranean Sea, *Sedimentology*, 40: 557-582.
- Piper, D.J.W. & Skene, K.I., 1998, Latest Pleistocene ice-rafting events on the Scotian Margin (eastern Canada) and their relationship to Heinrich events, *Paleoceanography*, 13: 205-214.
- Piper, D.J.W., Cochonat, P. & Morrison, M.L., 1998a, submitted, The sequence of events around the epicentre of the 1929 Grand Banks earthquake: initiation of debris flows and turbidity current inferred from sidescan sonar, *Sedimentology*.
- Piper, D.J.W., Cochonat, P., Ollier, G., Le Drezen, E., Morrison, M. & Baltzer, A., 1992, Non-catastrophic evolution of a turbidity current from a slump: evidence from the 1929 "Grand Banks" earthquake, *Comptes Rendres Académie des Sciences Paris*, 314: 1057-1064.
- Piper, D.J.W., Flood, R.D., Cisowski, S., Hall, F., Manley, P.L., Maslin, M., Mikkelsen, N. & Showers, W., 1997, Synthesis of stratigraphic correlations of Amazon Fan, in *Proceedings of the Ocean Drilling Program, Scientific Results*, 155, R.D. Flood, D.J.W. Piper, A. Klaus & L.C. Peterson (eds.), College Station, TX (Ocean Drilling Program), 595-610.
- Piper, D.J.W., Mudie, P.J., Fader, G.B., Josenhans, H.W., MacLean, B., & Vilks, G., 1990,. Quaternary Geology, Chapter 10, in *Geology of the Continental Margin of Eastern Canada*, M.J. Keen & G.L. Williams (eds.), Geological Survey of Canada, Geology of Canada, no. 2, 475-607.
- Piper, D.J.W., Normark, W.R. & Hiscott, R.N., 1994, Holocene sand body geometry, Hueneme Fan, California Borderland, in *Atlas of Deep Water Environments: Architectural Style in Turbidite Systems*, K.T. Pickering, R.N. Hiscott, F. Ricci Lucchi, R.D.A. Smith (eds.), Chapman & Hall, London, 203-206.
- Piper D.J.W., Normark, W.R. & Hiscott, R.N., 1998b, submitted, Outcrop-scale acoustic facies analysis and the 0-15 ka development of Hueneme and Dume fans, California Continental Borderland, *Sedimentology*.

- Piper, D.J.W., Shaw, J., Skene, K.I. & Schell, T.M., in prep., Discharge of large-volume subglacial outburst floods to Laurentian Fan.
- Pirmez, C., 1994, *Growth of a Submarine Meandering Channel-levee System on the Amazon Fan*, Unpubl. Ph. D. Thesis, Columbia University, Palisade, NY, U.S.A., 587 p.
- Pirmez, C. & Flood, R.D., 1995, Morphology and structure of Amazon Channel, in Flood, R.D., Piper, D.J.W. & Klaus, A. et al., *Proceedings of the Ocean Drilling Program, Initial Reports, Ocean Drilling Program, Initial Report*, 155, College Station, TX, 23-46.
- Queney, P., 1948, The problem of air flow over mountains: a summary of theoretical studies, *Bulletin of the American Meteorological Society*, 29:16-26.
- Reynolds, S., 1987, A recent turbidity current event, Hueneme fan, California: reconstruction of flow properties, *Sedimentology*, 34: 129-137.
- Rhodes, D.D., 1977, The b-f-m diagram: graphical representation and interpretation of at-a-station hydraulic geometry, *American Journal of Science*, 277: 73-96.
- Ricci Lucchi, F., Colella, A., Gabbianelli, G., Rossi, S. & Normark, W.R., 1985, Crati Fan, Mediterranean, in *Submarine Fans and Related Turbidite Systems*, A.H. Bouma, W.R. Normark, and N.E. Barnes (eds.), Springer-Verlag, New York, 51-75.
- Ritter, D.F., 1986, *Process Geomorphology*, Wm.C. Brown Publishers, Dubuque, Iowa, 579 p.
- Rubey, W.W., 1933, Settling velocities of gravel, sand, and silt particles, *American Journal of Science*, 25: 325-338.
- Savoie, B., Piper, D.J.W. & Droz, L., 1993, Plio-Pleistocene evolution of the Var deep-sea fan off the French Riviera, *Marine and Petroleum Geology*, 10: 550-571.
- Schell, T. M., 1996, *Proximal-to-distal Trends in the Flocculation Limit of Fine-grained Turbidites*, Unpubl. MSc. Thesis, Dalhousie University, Halifax, 180 p.
- Schumm, S.A., 1960, The shape of alluvial channels in relation to sediment type, *U.S. Geological Survey Professional Paper 352-B*.
- Schumm, S.A. & Khan, H.R., 1972, Experimental study of channel patterns, *Geological Society of America Bulletin*, 88: 1755-1770.
- Seymour, R.J., 1986, Nearshore autosuspending turbidity flows, *Ocean Engineering*, 13: 435-447.

- Shanmugam, G., 1996, High-density turbidity currents: are they sandy debris flow?, *Journal of Sedimentary Research*, 66: 2-10.
- Shaw, J. & Kvill, D., 1984, A glaciofluvial origin for drumlins of the Livingstone Lake area, Saskatchewan, *Canadian Journal of Earth Sciences*, 21: 1442-1459.
- Shaw, J., & Sharpe, D.R., 1987, Drumlin formation by subglacial meltwater erosion, *Canadian Journal of Earth Sciences*, 24: 2316-2322.
- Shepard, F.P., Marshall, N.F., McLoughlin, P.A. & Sullivan, G.G., 1979, *American Association of Petroleum Geologists, Studies in Geology*, 8, 177 p.
- Shipboard Scientific Party, 1997, Site 1015, in *Proceedings of the Ocean Drilling Program, Initial Reports*, 167, M. Lyle, I. Koizumi, et al. (eds.), Ocean Drilling Program, College Station, TX (Ocean Drilling Program).
- Simpson, J.E., 1987, *Gravity Currents in the Environment and the Laboratory*, Ellis Horwood, 244 p.
- Skene, K.I., Mulder, T. & Syvitski, J.P.M., 1997, INFLO1: a model predicting the behaviour of turbidity currents generated at river mouths, *Computers & Geosciences*, 23: 975-991.
- Stacey, M.W. & Bowen, A.J., 1988a, The vertical structure of density and turbidity currents: theory and observations, *Journal of Geophysical Research*, 93: 3528-3542.
- Stacey, M.W. & Bowen, A.J., 1988b, The vertical structure of turbidity currents and a necessary condition for self-maintenance, *Journal of Geophysical Research*, 93: 3543-3553.
- Stacey, M.W. & Bowen, A.J., 1990, A comparison of an autosuspension criterion to field observations of five turbidity currents, *Sedimentology*, 37: 1-5.
- Stow, D.A.V., 1975, *The Laurentian Fan: Late Quaternary Stratigraphy*, Unpubl. Technical Report, Dalhousie University, Halifax, NS, Canada, 72 p.
- Stow, D.A.V., 1977, *Late Quaternary stratigraphy and sedimentation on the Nova Scotian outer continental margin*, Unpubl. Ph. D. Thesis, Dalhousie University, Halifax, NS, Canada, 360 p.
- Stow, D.A.V. & Bowen, A.J., 1980, A physical model for the transport and sorting of fine-grained sediment by turbidity currents, *Sedimentology*, 27, 31-46.
- Stow, D.A.V., Howell, D.G. & Nelson, C.H., 1985, Sedimentary, tectonic, and sea-level controls, in *Submarine Fans and Related Turbidite Systems*, A.H. Bouma, W.R. Normark, and N.E. Barnes (eds.), Springer-Verlag, New York, 15-22.

- Syvitski, J.P.M. & Schafer, C.T., 1996, Evidence for an earthquake-triggered basin collapse in Saguenay Fjord, Canada, *Sedimentary Geology*, 103, 1-27.
- Syvitski, J.P.M., Asprey, K. W. & Leblanc, K.W.G., 1995, In-situ characteristics of particles settling within a deep-water estuary, *Deep Sea Research*, Part II, 42: 223-256.
- Syvitski, J.P.M., Burrell, D.C. & Skei, J.M., 1987, *Fjords: Processes and Products*, Springer, New York, 375 p.
- Syvitski, J.P.M., Smith, J.N., Calabrese, E.A., and Boudreau, B.P., 1988, Basin sedimentation and the growth of prograding deltas, *Journal of Geophysical Research*, 93: 6895-6908.
- Tucholke, B.E., Vogt, P.R. et al., 1979, *Initial Reports of the Deep Sea Drilling Project, Leg 43*, U.S. Government Printing Office, Washington, D.C.
- Turner, J.S., 1986, Turbulent entrainment: the development of the entrainment assumption, and its application to geophysical flows, *Journal of Fluid Mechanics*, 173: 431-471.
- Uchupi, E. & Austin, J., 1979, The stratigraphy and structure of the Laurentian Cone region, *Canadian Journal of Earth Sciences*, 16: 1726-1752.
- Van Andel, T.H. & Komar, P.D., 1969, Ponded sediments of the Mid-Atlantic Ridge between 22° and 23° North latitude, *Geological Society of America Bulletin*, 80: 1163-1190.
- Walker, R.G., 1965, The origin and significance of the internal sedimentary structures of turbidites, *Proceedings of the Yorkshire Geological Society*, 35: 1-21.
- Wang, D. & Hesse, R., 1996, Continental slope sedimentation adjacent to an ice-margin. II. Glaciomarine depositional facies on Labrador Slope and glacial cycles, *Marine Geology*, 135: 65-96.
- Zeng, J., Lowe, D.R., Prior, D.B., Wiseman, W.J. Jr., Bornhold, B.D., 1991, Flow properties of turbidity currents in Bute Inlet, British Columbia, *Sedimentology*, 38: 975-996.

IMAGE EVALUATION TEST TARGET (QA-3)



APPLIED IMAGE, Inc
1653 East Main Street
Rochester, NY 14609 USA
Phone: 716/482-0300
Fax: 716/288-5989

© 1993, Applied Image, Inc.. All Rights Reserved